

**COLLECTED PAPERS on
Dressed Photon Science and Technology**

Vol. 30

August 2014 – August 2015

Prof. Motoichi OHTSU

MEMBERS

(From April 1, 2015)

*[I] The University of Tokyo**

Professor

Motoichi OHTSU^(a,b) (Dr. Eng.)

Associate Professor

Takashi YATSUI (Dr. Eng.)

Researcher

Teruo Murakami

Graduate Students (Doctor Candidate)

Hajime TANAKA

Jun Hyoung KIM

Graduate Students (Master Course)

Masaki IKEGAWA

Undergraduate Students

Shun OKADA

Tomohiro OKAMOTO

Yusuke NAKAHIRA

Research Assistant

Etsuko OTA

Ayako MIZUSHIMA

Secretary

Kumiko NOZAWA

Mamiko ITABASHI

Tomoko IINO

a) Also a director “International Center for Nano Electron and Photon Technology,”

The Institute of Engineering Innovation, School of Engineering The University of Tokyo”

b) Also a director, NPO-Research Institute of Nanophotonics

(*)

Department of Electronics Engineering and Information Systems,

Graduate School of Engineering,

The University of Tokyo

(Room 215, Bldg. Eng. 9)

2-11-16 Yayoi, Bunkyo-ku, Tokyo 113-8656, Japan

Phone: +81-3-5841-1189

FAX: +81-3-5841-1140

E-mail: ohtsu@ee.t.u-tokyo.ac.jp

URL:<http://uuu.t.u-tokyo.ac.jp/>

東京大学大学院 工学系研究科 電気系工学専攻

〒113-8656 東京都文京区弥生 2-11-16 工学部 9 号館 215 号室

電話: 03-5841-1189, ファックス: 03-5841-1140

E-mail: ohtsu@ee.t.u-tokyo.ac.jp

URL: <http://uuu.t.u-tokyo.ac.jp/>

[III] International Center for Nano Electron and Photon Technology*

Director

Motoichi OHTSU, Professor (core member)

Members

Kazuo HOTATE, Professor (core member)

Yuichi IKUHARA, Professor (core member)

Takao SOMEYA, Professor (core member)

Hitoshi TABATA, Professor (core member)

Masaaki TANAKA, Professor (core member)

Jean-Jacques DELAUNAY, Associate Professor

Yuichiro KATO, Associate Professor

Shinobu OHYA, Associate Professor

Masakazu SUGIYAMA, Associate Professor

Takashi YATSUI, Associate Professor

Munetoshi SEKI, Assistant Professor

(*)

Institute of Engineering Innovation,

School of Engineering, The University of Tokyo

(Room 219, Bldg. Eng. 9)

2-11-16 Yayoi, Bunkyo-ku, Tokyo 113-8656, Japan

Phone: +81-3-5841-1670

FAX: +81-3-5841-1140

E-mail: info@nanophotonics.t.u-tokyo.ac.jp

URL: <http://www.npc.t.u-tokyo.ac.jp/>

東京大学大学院 工学系研究科 総合研究機構

〒113-8656 東京都文京区弥生 2-11-16 工学部 9 号館 219 号室

電話 : +81-3-5841-1670, ファックス: +81-3-5841-1140

E-mail: info@nanophotonics.t.u-tokyo.ac.jp

URL: <http://www.npc.t.u-tokyo.ac.jp/>

[IV] Nanophotonics Engineering Organization*

Director

Motoichi OHTSU

Researcher

Tadashi KAWAZOE (Dr. Sci.)

Satoshi SUGIURA

Wataru Yamagishi

Visiting Engineers

Yuuki TSUDA^{a)}

Masashige MATSUDATE^{a)}

Kenji YAMADA^{a)}

Yuuji TSUBORI^{a)}

Satoshi KARASAWA^{b)}

Yuu KIMURA^{c)}

Research Assistant

Kazunobu HASHIMOTO

Emi NAKAGAWA

a) Sodick Co., Ltd.

b) Seiko Instruments Inc.

c) Teijin Ltd.

(*)

Nanophotonics Engineering Organization,

Specified Nonprofit Corporation

1-20-10 Sekiguchi, Bunkyo-ku, Tokyo 112-0014, Japan

Phone: +81-3-3267-6790. Fax: +81-3-5261-9788

E-mail: ohtsu-rinps@nanophotonics.t.u-tokyo.ac.jp

URL: <http://www.nanophotonics.info/>

特定非営利法人 ナノフォトンクス工学推進機構

〒112-0014 東京都文京区関口 1-20-10

電話: 03-3267-6790, ファックス: 03-5261-9788

URL: <http://www.nanophotonics.info/>

LIST OF PAPERS

[(pp. XX-XX); pages in this issue of the COLLECTED PAPERS]

[I] ORIGINAL PAPERS

- [1] H. Tanaka, T. Kawazoe, M. Ohtsu, K. Akahane, N.Yamamoto, “Evaluation of optical amplification properties using dressed photons in a silicon waveguide,” Applied Physics A, DOI 10.1007/s00339-015-9419-2, August 2015 (5 pages).

(pp. 1-5)

- [2] N. Tate, T. Kawazoe, W. Nomura, and M. Ohtsu, “Current-induced giant polarization rotation using a ZnO single crystal doped with nitrogen ions,” Scientific Reports, Vol. 5, 12762, DOI 10.1038/srep12762, August 2015 (7 pages).

(pp. 7-13)

- [3] N. Tate, M. Naruse, T. Matsumoto, M. Hoga, Y. Ohyagi, S. Nishio, W. Nomura, and M. Ohtsu, “Non-scanning optical near-field microscopy for nanophotonic security,” Applied Physics A, DOI10.1007/s00339-015-9387-6, July 2015 (5 pages).

(pp. 15-19)

- [4] T. Kawazoe, K. Nishioka, and M. Ohtsu, “Polarization control of an infrared silicon light-emitting diode by dressed photons and analyses of the spatial distribution of doped boron atoms,” Applied Physics A, DOI 10.1007/s00339-015-9288-8, June 2015 (8 pages).

(pp. 21-27)

- [5] K. Takahashi, M. Katori, M. Naruse, and Motoichi Ohtsu, “Stochastic model showing a transition to self-controlled particle-deposition state induced by optical near-fields,” Applied Physics B, Vol.120, No.2, July 2015, pp.247-254.

(pp. 29-36)

- [6] H. Tanaka, T. Kawazoe, M. Ohtsu, and K. Akahane, “Decreasing the threshold current density in Si lasers fabricated by using dressed-photons,” Fluorescent Materials, Vol. 1, Issue 1, April 2015, pp.1-7.

(pp. 37-43)

- [7] R. Hirayama, M. Naruse, H. Nakayama, N. Tate, A. Shiraki, T. Kakue, T. Shimobaba, M. Ohtsu, and T. Ito, "Design, Implementation and Characterization of a Quantum-Dot-Based Volumetric Display," *Scientific Reports*, Vol. 5, February 2015, Article number: 8472 (6 pages).

(pp. 45-50)

- [8] J. H. Kim, T. Kawazoe, and M. Ohtsu, "GaP Homojunction LEDs Fabricated by Dressed-Photon-Phonon-Assisted Annealing," *Advances in Optical Technologies*, Vol. 2015, February 2015, Article ID 236014, (2014) (8 pages).

(pp. 51-58)

- [9] T. Yatsui, W. Nomura, and M. Ohtsu, "Realization of Ultraflat Plastic Film using Dressed-Photon-Phonon-Assisted Selective Etching of Nanoscale Structures," *Advances in Optical Technologies*, Vol. 2015, February 2015, Article ID 701802 (5 pages).

(pp. 59-63)

- [10] T. Kawazoe, N. Wada, and M. Ohtsu, "Emission Spectral Control of a Silicon Light Emitting Diode Fabricated by Dressed-Photon-Phonon Assisted Annealing Using a Short Pulse Pair," *Advances in Optical Technologies*, Vol.2014, July 2014, Article ID 958327 (8 pages).

(pp. 65-72)

- [11] W. Nomura, M. Naruse, M. Aono, S.-J. Kim, T. Kawazoe, T. Yatsui, and M. Ohtsu, "Demonstration of Controlling the Spatiotemporal Dynamics of Optical Near-field Excitation Transfer in Y-Junction Structure Consisting of Randomly Distributed Quantum Dots," *Advances in Optical Technologies*, Vol.2014, April 2014, Article ID 569684 (8 pages).

(pp. 73-80)

- [12] M. Naruse, W. Nomura, M. Aono, M. Ohtsu, Y. Sonnefraud, A. Drezet, S. Huant, and S.-J Kim, "Decision making based on optical excitation transfer via near-field interactions between quantum dots," *Journal of Applied Physics*, Vol. 116, No. 15, October 2014, Article ID 154303 (8 pages).

(pp. 81-88)

- [13] M. Naruse, H. Hori, S. Ishii, A. Drezet, S. Huant, M. Hoga, Y. Ohyagi, T.

Matsumoto, N. Tate, and M. Ohtsu, “Unidirectional light propagation through two-layer nanostructures based on optical near-field interactions,” *Journal of Optical Society of America B*, Vol. 31, No. 10, October 2014, pp. 2404-2413.

(pp. 89-98)

[14]T. H. H. Le, K. Mawatari, Y. Pihosh, T. Kawazoe, T. Yatsui, M. Ohtsu, and T. Kitamori, “Novel sub-100 nm surface chemical modification by optical near-field induced photocatalytic reaction,” *Microfluidics and Nanofluidics*, Vol. 17, Issue 4, September 2014, pp. 751-758.

(pp. 99-106)

[15]P. N. Hai, T. Yatsui, M. Ohtsu, and M. Tanaka, “High-field electroluminescence in semiconductor tunnel junctions with a Mn-doped GaAs layer,” *Journal of Applied Physics*, Vol. 116, Issue 11, September 2014, Article ID 113905 (6 pages).

(pp. 107-112)

[16]T. Matsumoto, M. Hoga, Y. Ohyagi, M. Ishikawa, M. Naruse, K. Hanaki, R. Suzuki, D. Sekiguchi, N. Tate, and M. Ohtsu, “Nano-artifact metrics based on random collapse of resist,” *Scientific Reports*, Vol.4, February 2015, Article number: 6142 (5 pages).

(pp. 113-117)

[17]W. Nomura, T. Kawazoe, T. Yatsui, M. Naruse, and M. Ohtsu, “Observation and analysis of structural changes in fused silica by continuous irradiation with femtosecond laser light having an energy density below the laser-induced damage threshold,” *Beilstein Journal of Nanotechnology*, Vol. 5, August 2014, pp.1334-1340.

(pp. 119-125)

[18]M. Naruse, T. Tani, H. Yasuda, N. Tate, M. Ohtsu, and M. Naya, “Randomness in highly reflective silver nanoparticles and their localized optical fields,” *Scientific Reports* 4, August 2014, Article number 6077 (7 pages).

(pp. 127-134)

[19]M. Naruse, Song-Ju Kim, M. Aono, H. Hori and M. Ohtsu, “Chaotic oscillation and random-number generation based on nanoscale optical-energy transfer,” *Scientific Reports* 4, August 2014, Article number 6039 (9 pages).

(pp. 135-143)

[II] PRESENTATIONS IN INTERNATIONAL CONFERENCES

- [1] J.-H. Kim, T. Kawazoe, and M. Ohtsu, "The p-n homojunction GaP LED fabricated by dressed photon phonon assisted annealing," Abstracts of the 10th Asia-Pacific Conference on Near-field Optics, July 7-10, 2015, Hakodate, Japan, p.6.

(p.145)

- [2] M. Yamaguchi, T. Kawazoe, T. Yatsui, and M. Ohtsu, "Visible Si-LED with lateral p-n homojunction," Abstracts of the 10th Asia-Pacific Conference on Near-field Optics, July 7-10, 2015, Hakodate, Japan, p.7.

(p.147)

- [3] H. Tanaka, T. Kawazoe, M. Ohtsu, K. Akahane, and N. Yamamoto, "Evaluation of optical gain using dressed photons in a Si laser waveguide," Abstracts of the 10th Asia-Pacific Conference on Near-field Optics, July 7-10, 2015, Hakodate, Japan, p.8.

(p.149)

- [4] M. Naruse, W. Nomura, M. Aono, M. Ohtsu, A. Drezet, S. Huant, and S.-J. Kim, "Decision Making Based on Optical Excitation Transfer via Near-Field Interactions," Abstracts of the 10th Asia-Pacific Conference on Near-field Optics, July 7-10, 2015, Hakodate, Japan, p.23.

(p.151)

- [5] M. Ohtsu, "Who has seen the optical near field? ," Abstracts of the 10th Asia-Pacific Conference on Near-field Optics, July 7-10, 2015, Hakodate, Japan, p.43.

[Invited Presentation]

(p.153)

- [6] N. Tate, M. Naruse, T. Matsumoto, M. Hoga, Y. Ohyagi, S. Nishio, and M. Ohtsu, "Non-scanning optical near-field microscopy for nanophotonic security," Abstracts of the 10th Asia-Pacific Conference on Near-field Optics, July 7-10, 2015, Hakodate, Japan, p.47.

(p.155)

- [7] W. Nomura, T. Yatsui, T. Kawazoe, N. Tate, and M. Ohtsu, "High-speed flattening of a composite crystallized glass material by dressed-photon—phonon etching," Abstracts of the 10th Asia-Pacific Conference on Near-field Optics, July 7-10, 2015, Hakodate, Japan, p.87.

(p.157)

- [8] M. Ikegawa, T. Kawazoe, and M. Ohtsu, "Blue-ultraviolet Si photodetector with optical gain due to dressed photons," Abstracts of the 10th Asia-Pacific Conference on Near-field Optics, July 7-10, 2015, Hakodate, Japan, p.106.

(p.159)

- [9] K. Nishioka, T. Kawazoe, T. Yatsui, and M. Ohtsu, "Polarization control of Si-LED by photon breeding effect," Abstracts of the 10th Asia-Pacific Conference on Near-field Optics, July 7-10, 2015, Hakodate, Japan, p.107.

(p.161)

- [10] M. Ohtsu, "Dressed photon technology for silicon photon breeding devices," Proceedings of the Northern Optics & Photonics 2015, June 2-4, 2015, Lappeenranta, Finland, p.18.

[Plenary Talk]

(p.163)

- [11] N. Tate, T. Kawazoe, and M. Ohtsu, "Giant-magneto-optic light modulator using p-n homojunction-structured ZnO crystal," Proceedings of The Fourth Japan-Korea Workshop on Digital Holography and Information Photonics, December 16-18, 2014, Okinawa, Japan, pp. 36-37.

[Invited Presentation]

(pp.165-166)

- [12] N. Tate, T. Kawazoe, and M. Ohtsu, "Speckle Reduction by Current-Induced Magneto-Optical Effect Using P-type ZnO Device," Proceedings of the 21st International Display Workshops (IDW14), December 3-5, 2014, Niigata, Japan, pp. 1090-1093.

[Invited Presentation]

(pp.167-170)

- [13] T. Kawazoe, K. Nishioka, and M. Ohtsu, "SiC light emitting diode and its polarization control using dressed photons," Proceedings of the 21st International Display Workshops (IDW14), December 3-5, 2014, Niigata, Japan, pp. 1061-1063.

[Invited Presentation]

(pp.171-173)

- [14] M. Ohtsu, "Dressed photon technology," Technical Digest of the Core-to-Core Japan Workshop 2014, November 17-18, 2014, Tokyo, Japan, pp. 4-5.

[Invited Presentation]

(pp.175-176)

- [15]M. Yamaguchi, T. Kawazoe, and M. Ohtsu, “Visible Si-LED with lateral pn junction for efficient light extraction,” Technical Digest of the Core-to-Core Japan Workshop 2014, November 17-18, 2014, Tokyo, Japan, p.32.

(p.177)

- [16]H. Tanaka, T. Kawazoe, M. Ohtsu, K. Akahane, “Ultralow-threshold current density Si lasers using dressed photons,” Technical Digest of the Core-to-Core Japan Workshop 2014, November 17-18, 2014, Tokyo, Japan, p.33.

(p.179)

- [17]J.-H. Kim, T. Kawazoe, and M. Ohtsu, “GaP homojunction LEDs fabricated by dressed-photon-phonon assisted annealing,” Technical Digest of the Core-to-Core Japan Workshop 2014, November 17, 2014, Tokyo, Japan, p.34.

(p.181)

- [18]N. Tate, M. Naruse, T. Kawazoe, and M. Ohtsu, “Processing based on fluctuations in a nanometric space and corresponding optical applications in a macroscopic space,” Abstracts of the 2014 International Symposium on Nonlinear Theory and its Applications (NOLTA 2104), September 14-18, 2014, Luzern, Switzerland, pp.586-589.

[Invited Presentation]

(pp.183-186)

- [19]M. Naruse, M. Aono, S.-J. Kim, N. Tate, and M. Ohtsu, “Near-field Nanophotonics for Intelligent Information Functions,” Abstracts of the 2014 International Symposium on Nonlinear Theory and its Applications (NOLTA 2104), September 14-18, 2014, Luzern, Switzerland, p.498.

[Invited Presentation]

(p.187)

[III] REVIEW PAPERS

- [1] M. Ohtsu, "Past, present, and future of near field optics," *Optical and Electro-optical Engineering Contact*, Vol.53, No.6, June 2015, pp.3-13.

【大津元一、「近接場光学の過去、現在、未来」、光技術コンタクト、第53巻、第6号、2015年6月、pp. 3-13】

(pp. 189-199)

- [2] M. Ohtsu, "Science and Technology of Optical Near Fields," *Parity*, Vol.30, No.5, May 2015, pp.26-27.

【大津元一、「近接場光の科学と技術」、パリテイ、第30巻、第5号、2015年5月、pp. 26-27】

(pp. 201-202)

- [3] M. Ohtsu, "From Classical to Modern Near-Field Optics and the Future," *Optical Review*, Vol.21, No.6, June 2014, pp.905-910.

(pp. 203-208)

- [4] M. Ohtsu and T. Kawazoe, "Bulk Crystal Silicon Light Emitting Devices Using Dressed Photons," *Japanese Journal of Optics*, Vol.43, No.8, August 2014, pp.366-370.

【大津元一、川添忠、「ドレスト光子によるバルク結晶シリコン発光素子」、光学、第43巻、第8号、2014年8月、pp. 366-370】

(pp. 209-213)

[IV] PUBLISHED BOOKS

[1] T. Tadokoro and K. Ishikawa, “Illustrated Science of Light,” (supervision of M. Ohtsu), Asakura Publishing Co, Tokyo, October 2014, (128 pages).

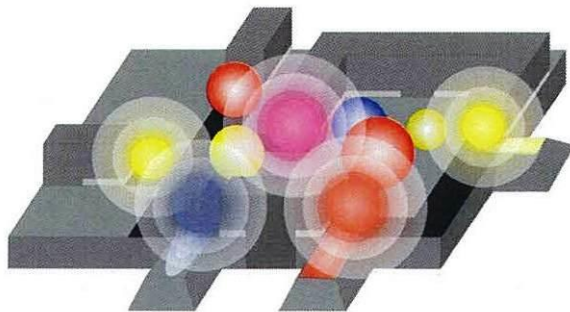
【大津元一（監修）、田所利康・石川謙（著）「イラストレイテッド 光の科学」、朝倉書店、東京、2014年10月、（128ページ）】

(pp. 215-216)

[V] AWARDS

- [1] M. Yamaguchi, The Best Presentation Award, “Visible Si-LED with lateral p-n homojunction,” The 10th Asia-Pacific Conference on Near-field Optics (APNFO10), July 7-10, 2015.
- [2] J.-H. Kim, “The p-n homojunction GaP LED fabricated by dressed photon phonon assisted annealing,” The Best Presentation Award, The 10th Asia-Pacific Conference on Near-field Optics (APNFO10), July 7-10, 2015.
- [3] H. Tanaka, “Evaluation of optical gain using dressed photons in a Si laser waveguide,” The IAC Presentation Award, The 10th Asia-Pacific Conference on Near-field Optics (APNFO10), July 7-10, 2015.
- [4] R. Nagumo, “Spectral control of nanodiamond by dressed photon-phonon etching,” The IAC Presentation Award, The 10th Asia-Pacific Conference on Near-field Optics (APNFO10) July 7-10, 2015.
- [5] K. Nishioka, “Polarization control of Si-LED by photon breeding effect,” The IAC Poster Award,” The 10th Asia-Pacific Conference on Near-field Optics (APNFO10) July 7-10, 2015.
- [6] M. Yamaguchi, “Visible Si-LED with lateral p-n homojunction for increasing light extraction coefficient,” The Best Master Thesis Award, March 2015.
【山口真生、「優秀修士論文賞」受賞対象題目「光取り出し効率向上のための横接合型可視発光 Si-LED の開発」(2015 年 3 月)】
- [7] T. Kawazoe, K. Nishioka, and M. Ohtsu, “SiC light emitting diode and its polarization control using dressed photons,” The Best Paper Award, The 21st International Display Workshops (IDW14), December 3-5, 2014, Niigata, Japan.

[I] ORIGINAL PAPERS



Evaluation of optical amplification properties using dressed photons in a silicon waveguide

H. Tanaka¹ · T. Kawazoe^{1,2} · M. Ohtsu^{1,2,3} · K. Akahane⁴ · N. Yamamoto⁴

Received: 22 June 2015 / Accepted: 7 August 2015
© Springer-Verlag Berlin Heidelberg 2015

Abstract We fabricated an optical waveguide having a high optical confinement effect using a silicon-on-insulator substrate, and we eliminated the difficulty involved with optical alignment for making laser light pass through a p–n homojunction that is transparent to infrared light. Laser light was introduced via one of the cleaved edges of the optical waveguide and was guided to the transparent p–n homojunction, and the power of the light emitted from the other edge was measured. As a result, we successfully evaluated the optical amplification properties with high precision. For light with a wavelength of 1.31 μm , we obtained a differential gain coefficient of $g = 2.6 \times 10^{-2} \text{ cm/A}$, a transparency current density of $J_{\text{tr}} = 1 \text{ mA/cm}^2$, and a saturation optical power density of $P_{\text{sat}} = 30 \text{ kW/cm}^2$. The observation of gain saturation due to the incident optical power shows that this measurement method was suitable for evaluating the optical amplification properties.

1 Introduction

Silicon (Si) is an indirect transition-type semiconductor and has therefore been considered unsuitable as a material for light-emitting devices. However, if an infrared laser could be fabricated using Si bulk crystal as the lasing material, the transparency current density, J_{tr} , would become extremely small, and consequently, there would be a possibility of achieving an extremely small threshold current density, J_{th} . The main reason for this is that light absorption loss is small because the photon energy of infrared light is smaller than the bandgap energy, E_{g} , of Si. Other advantages include the natural abundance of Si as a raw material, the ease of integration with electronic circuits, and the ability to make use of the wealth of existing processing technologies that have already been developed for Si electronic devices [1].

Stimulated Raman scattering [2–5], crystal defects [6], Si nanocrystals [7], B-doped SiGe/Si quantum wells [8], etc. have recently been used to realize Si lasers; however, researchers have encountered problems that prevent the realization of practical devices, such as the difficulty of achieving room-temperature operation via current injection and insufficient quantum efficiency. To solve these problems, we have proposed a light emission principle based on dressed photons (DPs) [9], as well as a novel fabrication technique called dressed photon–phonon (DPP)-assisted annealing. A DP is a quasiparticle that represents a coupled state between a photon and an electron–hole pair in a nanoscale region [9]. DPs also couple with multimode coherent phonons [9], and the quasiparticle representing this coupled state is a DPP. By using this technique, we fabricated the world’s first infrared Si laser having a p–n homojunction structure and achieved continuous oscillation at room temperature (oscillation wavelength approximately

✉ H. Tanaka
tanaka@nanophotonics.t.u-tokyo.ac.jp

¹ Department of Electrical Engineering and Information Systems, Graduate School of Engineering, The University of Tokyo, 2-11-16 Yayoi, Bunkyo-ku, Tokyo 113-8656, Japan

² Specified Nonprofit Corporation Nanophotonics Engineering Organization, 1-20-10, Sekiguchi, Bunkyo-ku, Tokyo 112-0014, Japan

³ International Center for Nano Electron and Photon Technology, Graduate School of Engineering, The University of Tokyo, 2-11-16 Yayoi, Bunkyo-ku, Tokyo 113-8656, Japan

⁴ The National Institute of Information and Communications Technology, 4-2-1, Nukui-Kitamachi, Koganei, Tokyo 184-8795, Japan

1.3 μm ; threshold current density 1.2 kA/cm^2) [10]. More recently, we fabricated a laser having an optical waveguide with a large optical confinement factor and achieved a remarkably low threshold current density of 40 A/cm^2 [11].

In order to design a high-performance infrared Si laser, it is important to evaluate the optical amplification properties with high precision. In a conventional infrared laser using a direct-transition-type semiconductor, the optical amplification properties are evaluated by introducing light into the optical waveguide from the outside and measuring the power ratio relative to that of the emitted light [12]. In contrast to this approach, until now we have evaluated the optical amplification properties by using the photocurrent density generated in a Si photodetector (Si-PD) with optical gain [13]. By using this method, we can evaluate the features of Si as the laser medium, such as the optical gain and transparency current density, even though the device has a very small optical confinement factor, like a PD [11].

In the present research, we solved these technical problems and evaluated the optical amplification properties with high precision by using the evaluation method employed for conventional semiconductor lasers. To do so, we fabricated a wide optical waveguide using a silicon-on-insulator (SOI) substrate, and by increasing the optical confinement factor, we improved the alignment precision of the light incident on one cleaved edge of the optical waveguide and the measurement precision of the intensity of light emitted from the other edge. This enabled us to evaluate the saturation optical power density with high precision. This paper reports the results of this evaluation.

2 Device structure and DPP-assisted annealing conditions

The light emission principle, the structure of the SOI substrate used, the ion implantation profile for introducing boron (B) atoms, which are p-type dopants, and so forth were the same as those for the case of the infrared Si laser reported in our previous paper [11]. However, as shown in Fig. 1a, the width of the optical waveguide was increased to 750 μm (compared with 8 μm in the previous paper [11]). An overview of the SOI substrate is as follows. The device layer in the SOI substrate was P-doped n-type Si (resistivity 0.020–0.034 Ωcm) with a thickness of 15 μm . The thickness of the SiO_2 insulation layer was 2 μm , and the thickness of the Si support substrate was 575 μm . The concentration of B atoms doped in the device layer was $1 \times 10^{19}/\text{cm}^3$ (the maximum acceleration voltage for ion injection was 700 keV). From simulation calculations, the p–n homojunction interface was found to be at a depth of 1.5–2.5 μm from the surface of the SOI substrate.

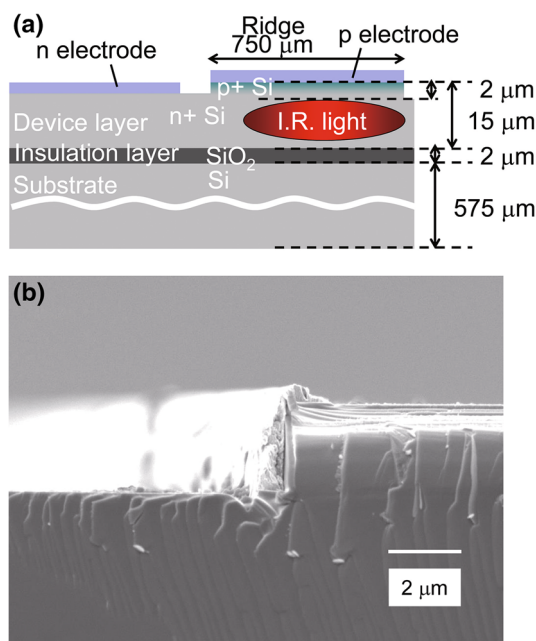


Fig. 1 **a** Schematic diagram of optical waveguide and **b** SEM image of edge of waveguide

After ion implantation, the substrate was cleaned by SPM (a 1:1 by volume solution of sulfuric acid/hydrogen peroxide) at 150 $^{\circ}\text{C}$ for 30 min and was washed with hydrofluoric acid. Next, we performed the following processes.

1. Chromium/platinum films (5-nm Cr/670-nm Pt) were deposited on the entire surface of the SOI substrate by RF sputtering.
2. The Cr/Pt films on the SOI substrate were coated with electron beam (EB) resist (OEBR-CAP112) by spin-coating. Then, the EB resist was patterned by EB lithography to leave a 750- μm -wide stripe.
3. The Cr/Pt films were etched by ICP-RIE using argon (Ar) gas.
4. Using the 750- μm -wide Cr/Pt stripe formed in Step 3 as a mask, the SOI substrate was etched with CF_4 gas to form a ridge-type optical waveguide (thickness 2 μm ; width 750 μm).
5. For use as current injection electrodes, Cr/Pt/Au films (with thicknesses of 5 nm/400 nm/400 nm) were deposited by RF sputtering.
6. To form positive (p) and negative (n) electrodes, the SOI substrate was again coated with an EB resist film, and EB lithography was performed.
7. The Cr/Pt/Au films were etched by ICP-RIE using Ar gas so as to form two separate electrodes, serving as positive and negative electrodes on the p layer and the n layer, respectively. Multiple optical waveguides were fabricated on the SOI substrate via the above processes.

8. The SOI substrate was diced by using stealth dicing to separate adjacent optical waveguides. The two edges of the optical waveguides were also cut by stealth dicing. The ridge-type optical waveguides had a width of 750 μm , a length of 2000 μm , and overall dimensions of 1.5 mm \times 2.0 mm.

Figure 1b is an SEM image of the edge of one of the waveguides after completing the processing. We confirmed that vertical etching was performed and that the ridge height was 2 μm , as designed.

DPP-assisted annealing was performed for 1 h by introducing laser light with a photon energy of $h\nu_{\text{anneal}} = 0.95$ eV (wavelength 1.31 μm) and a power of 40 mW via one of the cleaved edges of the optical waveguide while simultaneously injecting a triangular-wave current (current density 0–40 A/cm^2 , voltage 0–3 V, frequency 1 Hz) to bring about Joule heating. With this procedure, we fabricated an infrared Si light amplification device which was suitable for evaluating the optical amplification properties with high precision.

3 Measurement of differential gain coefficient, transparency current density, and saturation optical power

It is known that an infrared Si laser [10, 11] and an infrared Si LED [14] fabricated by DPP-assisted annealing emit light having the same energy as the photon energy, $h\nu_{\text{anneal}}$, of the light radiated during annealing. Therefore, we measured the optical amplification properties for light having a photon energy of $h\nu_{\text{anneal}} = 0.95$ eV (corresponding to a wavelength of 1.31 μm). Laser light was made to enter one of the cleaved edges of the optical waveguide (optical power, P_{in}), and after being guided through the optical waveguide, the power, P_{out} , of the light emitted from the other edge was measured. To take the measurement, we used an infrared camera having an InGaAs detector array (Xeva-1.7-320 manufactured by Xenics, wavelength range 0.9–1.7 μm). A triangular-wave current identical to that injected during annealing (current density 0–40 A/cm^2 , voltage 0–3 V, frequency 1 Hz) was injected into the device in order to amplify the incident optical power.

The measured dependency of the emitted optical power, P_{out} , on the injected current is shown in Fig. 2. The incident optical power, P_{in} , was 11 mW. We confirmed that the emitted optical power increased with increasing injected current. The relationship between the differential gain coefficient, g , and the injected current density, J , was determined from the expression $P_{\text{out}}/P_{\text{out}}(J = 0) = \exp(gJd)$, with reference to the value of P_{out} when the

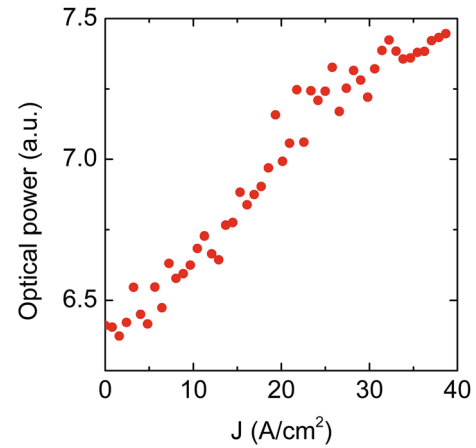


Fig. 2 Dependency of emitted optical power on injected current density at wavelength of 1.31 μm ($P_{\text{in}} = 11$ mW)

injected current density was 0. Here, d is the length of the waveguide ($\approx 2,000$ μm). The value of the optical gain G can be obtained from $G = gJ - \alpha$, based on the absorption loss of Si ($\alpha = 2.7 \times 10^{-5}/\text{cm}$) at the wavelength of 1.31 μm [15].

Figure 3 shows the measurement results for the dependency of G on J and the incident optical power, P_{in} . G was measured at 36 points in the range of incident optical powers $P_{\text{in}} = 0.6$ –140 mW. Figure 4 shows the dependency of G on J at $P_{\text{in}} = 11$ mW. The inset is a magnified view at $J = 0$. From these figures, since G was proportional to J at $J < 25$ A/cm^2 , these measurement results were fitted with a straight line. From the intersection of this straight line with the horizontal axis, the value of the transparency current density, J_{tr} , was determined to be 1 mA/cm^2 . In this measurement, the length of the gain layer through which the laser light passed was 1×10^3 times larger than that of the previous measurement using a

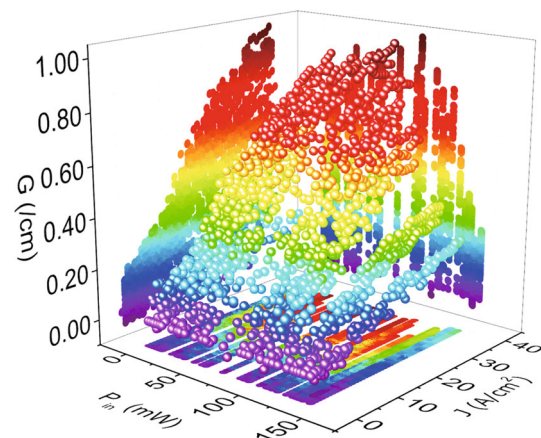


Fig. 3 Dependency of optical gain on incident optical power and injected current density at wavelength of 1.31 μm

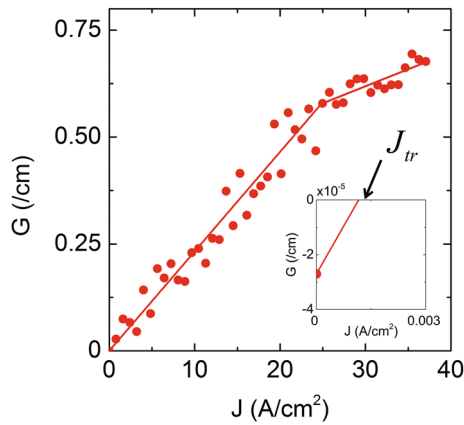


Fig. 4 Dependency of optical gain on injected current density at wavelength of 1.31 μm ($P_{\text{in}} = 11 \text{ mW}$)

Si-PD, and we could measure the amplified light precisely by making the spot size of the laser light ten times larger than that of the previous measurement. Thus, the volume involved with the optical gain was 1×10^4 times larger than the previous measurement. Therefore, the value of J_{tr} measured this time is different. Since we could estimate the value with higher precision in this measurement, we conclude that this value should be used in the design of future devices. In the region $J > 25 \text{ A/cm}^2$ in Fig. 4, the slope of the gain coefficient decreased slightly. In other words, slight gain saturation was observed. This is considered to be due to leakage current.

Figure 5 shows the dependency of the differential gain coefficient, g , on P_{in} . From this figure, at $P_{\text{in}} < 40 \text{ mW}$, g does not take a constant value but decreases as P_{in} decreases. This is because, when P_{in} is small, most of the electroluminescence (EL) is spontaneously emitted light, which spatially diverges, and therefore, it was not possible to collect and measure all of the emitted light. However, as

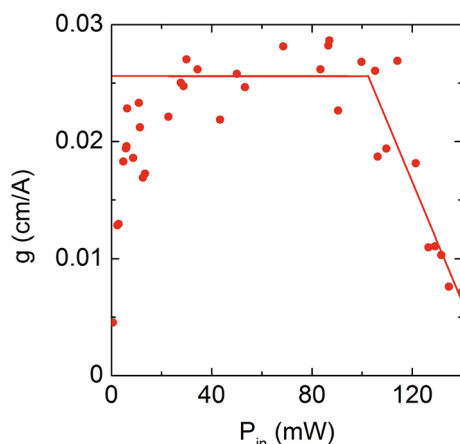


Fig. 5 Dependency of differential gain coefficient on incident optical power at wavelength of 1.31 μm

P_{in} increases, the EL power due to stimulated emission increases, and the directionality of the emitted light also increases, and therefore, the measurement precision for measuring P_{out} is improved. As a result, at $P_{\text{in}} > 40 \text{ mW}$, the measured value of g reaches a constant value of $2.6 \times 10^{-2} \text{ cm/A}$. On the other hand, at $P_{\text{in}} > 100 \text{ mW}$, g decreases as P_{in} increases. This indicates saturation of the optical gain. The above measurement results were fitted by the two straight lines in Fig. 5. This gain saturation has also been observed in conventional optical amplifiers using compound semiconductors [16], and therefore, we can conclude that this measurement method is suitable for evaluating the optical amplification properties. Although g takes a constant value of $2.6 \times 10^{-2} \text{ cm/A}$ in the center part of this figure, as described above, by estimating the value of P_{in} at which g is reduced by 3 dB from that value using the fitted straight line, a saturation power density of $P_{\text{sat}} = 30 \text{ kW/cm}^2$ was obtained.

4 Summary

We fabricated an optical waveguide having a high optical confinement effect using an SOI substrate, and the waveguide was endowed with gain by subjecting it to DPP-assisted annealing. Infrared laser light was introduced into the waveguide from one of the cleaved edges and was guided to the gain layer, which was formed of a p-n homojunction that was transparent to infrared light, and the power of light emitted from the other edge was measured. As a result, we were able to evaluate the optical amplification properties with high precision. For light with a wavelength of 1.31 μm , we obtained a differential gain coefficient of $g = 2.6 \times 10^{-2} \text{ cm/A}$, a transparency current density of $J_{\text{tr}} = 1 \text{ mA/cm}^2$, and a saturation power density of $P_{\text{sat}} = 30 \text{ kW/cm}^2$. Since we were able to observe gain saturation due to the incident optical power, we confirmed that this measurement method is suitable for evaluating the optical gain.


Acknowledgments This research was supported in part by Grant-in-Aid for JSPS Fellows Number 25 905 and the JSPS Core-to-Core Program, A. Advanced Research Networks. This research was performed in part by the Advanced ICT Research Institute of NICT.

References

1. L. Di, J.E. Bowers, Nat. Photonics **4**, 511 (2010)
2. H. Rong, A.L. Richard, J.O. Cohen, D.H.R. Nicolaescu, A. Fang, M. Paniccia, Nature **433**, 725 (2005)
3. R. Claps, D. Dimitropoulos, B. Jalali, IEEE Electron. Lett. **38**, 1352 (2002)
4. R.L. Espinola, J.I. Dadap, R.M. Osgood Jr, S.J. Mcnab, Y.A. Vlasov, Opt. Express **12**, 3713 (2004)

5. Y. Takahashi, Y. Inui, M. Chihara, T. Asano, R. Terawaki, S. Noda, *Nature* **498**, 470 (2013)
6. S.D. Cloutier, P.A. Kossyrev, J. Xu, *Nat. Mater.* **4**, 887 (2005)
7. M.J. Chen, J.L. Yen, J.Y. Li, J.F. Chang, S.C. Tsai, C.S. Tsai, *Appl. Phys. Lett.* **83**, 2163 (2004)
8. I.V. Altukhov, E.G. Chirkova, V.P. Sinis, M.S. Kagana, Y.P. Gousev, S.G. Thomas, K.L. Wang, M.A. Odnoblyudov, I.N. Yassievich, *Appl. Phys. Lett.* **79**, 3909 (2001)
9. M. Ohtsu, *Dressed photons-concepts of light matter fusion technology* (Springer, New York and London, 2013)
10. T. Kawazoe, M. Ohtsu, K. Akahane, N. Yamamoto, *Appl. Phys. B* **107**, 659 (2012)
11. H. Tanaka, T. Kawazoe, M. Ohtsu, K. Akahane, *Fluoresc. Mater.* (2015). doi:[10.1515/fma-2015-0001](https://doi.org/10.1515/fma-2015-0001)
12. Z.I. Kazi, T. Egawa, T. Jimbo, M. Umeno, *IEEE Photonics Technol. Lett.* **11**, 1563 (1999)
13. H. Tanaka, T. Kawazoe, M. Ohtsu, *Appl. Phys. B* **108**, 51 (2012)
14. T. Kawazoe, M.A. Mueed, M. Ohtsu, *Appl. Phys. B* **104**, 747 (2011)
15. M.A. Green, M.J. Keevers, *Prog. Photovolt.* **3**, 189 (1995)
16. J.L. Pleumeekers, M. Kauer, K. Dreyer, C. Burrus, A.G. Dentai, S. Shunk, J. Leuthold, C.H. Joyner, *IEEE Photonics Technol. Lett.* **14**, 12 (2002)

SCIENTIFIC REPORTS



OPEN

Current-induced giant polarization rotation using a ZnO single crystal doped with nitrogen ions

Naoya Tate¹, Tadashi Kawazoe², Wataru Nomura¹ & Motoichi Ohtsu³

Received: 01 April 2015

Accepted: 10 July 2015

Published: 06 August 2015

Giant polarization rotation in a ZnO single crystal was experimentally demonstrated based on a novel phenomenon occurring at the nanometric scale. The ZnO crystal was doped with N⁺ and N²⁺ ions serving as p-type dopants. By applying an in-plane current using a unique arrangement of electrodes on the device, current-induced polarization rotation of the incident light was observed. From the results of experimental demonstrations and discussions, it was verified that this novel behavior originates from a specific distribution of dopants and the corresponding light–matter interactions in a nanometric space, which are allowed by the existence of such a dopant distribution.

Oxide semiconductors are widely used direct-transition materials having a large bandgap. Due to their natural abundance, innocuousness, and transparency to visible light, they are expected to be widely employed for fabricating various electrical and optical devices^{1–10}. Although such oxide semiconductors are highly promising from the viewpoint of social needs, it is technically difficult to implement electro- or magneto-induced optical functions using the standard doping methods used with other types of semiconductors, because acceptors from the dopants are generally compensated with donors from the numerous oxygen vacancies and interstitial metals in the crystal. According to recent research by the authors' group^{11–19}, novel electro-optical characteristics using various indirect- and direct-transition semiconductors have been successfully demonstrated by employing our original annealing method which exploits the characteristic behavior of dressed photons (DPs)²⁰. A technique known as DP-assisted annealing has been used to autonomously form a dopant distribution that works as an appropriate p–n homojunction layer to effectively induce DPs by light irradiation. Specifically, by using an n-type bulk zinc oxide (ZnO) crystal, which is one of the most common oxide semiconductors, a p–n homojunction-structured LED that emits light at room temperature has been successfully realized¹². One of the fundamental points of this method is that the dopants form not only a spatially homogeneous distribution necessary for higher electrical conductivity but also nanometrically-clustered structures, which are autonomously optimized for generating DPs in their surroundings. According to recent theoretical discussions and experimental demonstrations by the authors' group^{21–25}, DPs were generated by irradiating light that is strongly coupled with phonons in the material, so that characteristic light–matter interactions occur via these DPs.

Magneto-optical effects are one of the most commonly known aspects of light–matter interactions. In particular, in the effect known as Faraday rotation, while light propagates through a specific material, that is, a magneto-optical material, under a large magnetic field, the polarization of the light rotates. Polarization rotation is a fundamental technology for several applications utilizing the polarization degree-of-freedom, such as ellipsometry and optical computing. The former is based on precise measurement and analysis of the polarization of reflected light from a target material, which requires a sophisticated polarization rotator. In particular, in recent research on ellipsometry, there has been a strong need for two-dimensional polarization rotators that can perform dynamic polarization modulation^{26–28}. In optical computing, particularly the previously proposed polarization-encoded optical

¹Kyushu University, 744 Motooka, Nishi-ku, Fukuoka 819-0395, Japan. ²Nanophotonics Engineering Organization, 1-20-10, Sekiguchi, Bunkyo-ku, Tokyo 112-0014, Japan. ³The University of Tokyo, 2-11-16 Yayoi, Bunkyo-ku, Tokyo 113-8656, Japan. Correspondence and requests for materials should be addressed to N.T. (email: tate@ed.kyushu-u.ac.jp)

computing method^{29,30}, advanced polarization rotators are required for processing. Furthermore, more recently, advanced polarization rotators are essential elements for realizing optical quantum computing and related research^{31–33}, which is based on polarization-encoding of photons.

In the work described in this paper, we focused on a ZnO device as a polarization rotator. In this device, the dopant distribution is expected to be suitable for inducing polarization modulation due to the characteristic behavior of DPs. The ZnO device was fabricated by using the DP-assisted annealing method, and by means of a unique electrode arrangement, different from the arrangement normally used for LEDs, the device demonstrated novel functionality as a polarization rotator. The device was irradiated with linearly polarized light in the vertical direction, and extremely large polarization rotation of the incident light was observed. The phenomenon is quite similar to conventional magneto-optical effects, but exhibited a much higher level. In addition it does not require any external equipment for applying a strong electric or magnetic field, nor a long light propagation length for ensuring a sufficient interaction time for the modulation. We quantitatively evaluated the performance of our ZnO device when functioning as a novel optical rotator, and we discuss the origin of this phenomenon on the basis of DPs.

Basics

Generally, an n-type crystal is doped by implanting p-type dopants during the crystal growth process. Previously, several techniques for doping ZnO crystals with p-type dopants using nitrogen have been demonstrated. These techniques have been applied to various methods of growing ZnO crystals, such as molecular beam epitaxy (MBE)^{34,35}, chemical-vapor deposition (CVD)^{36–38}, and magneto-sputtering^{39–42}. However, in the case where oxide semiconductors such as ZnO are used, the self-compensation effect⁴³ between acceptors and donors and dissipation of dopants has been still fundamental issues to achieve favorable p-type doping method.

In this study, an n-type bulk ZnO crystal was implanted with N^+ and N^{2+} ions serving as p-type dopants *after* the growth process using the hydrothermal growth method¹². According to previous reports by the authors' group^{11–19}, novel electro-optical functionalities in various types of indirect-transition semiconductors have been successfully implemented. The unique characteristics of these functionalities are fundamentally due to a specific distribution of dopants used for generating DPs in each material. A DP is a quasi-particle which represents the coupled state of a photon and an electron²⁵. A DP excites a coherent phonon in a nanometric material, and the state of the DP is coupled with the states of the excited phonon. During the electron transition process in the material, this coupled state behaves as an intermediate state; hence, multistep transitions and corresponding optical functions are allowed. In order to realize effective generation of DPs, in our previous work, the device was subjected to DP-assisted annealing to optimize the dopant distribution for generating DPs; namely, they were annealed with Joule heating due to the application of a current while the device was irradiated with light having a lower photon energy than the bandgap energy of the material. The basics of the DP-assisted annealing method are explained below.

First, while Joule heat is generated by the application of a forward bias current to the device, the dopants try to randomly diffuse in the material to converge to a homogeneous distribution. However, at the same time, DPs tend to be generated by irradiation of light in the vicinity of the exciton polaritons. Here, the generation of DPs is due to the formation of localized electrons and holes at regions of a specific distribution of the dopants. In the case where the photon energy of the irradiated light is lower than the bandgap energy of the material, as in our method, the photon energy is not absorbed in the material and can reach the distribution of dopants, where it generates DPs. The generated DPs, which behave as localized energy fields^{21–25}, can excite multimode coherent phonons in the material, and a coupled state of the DPs and phonons can be excited; in other words, a multi-step electron transition occurs via energy levels corresponding to the coupled state. Consequently, part of the energy due to Joule heat is converted to the photon energy of stimulated emission via the DPs, which is associated with the multi-step transition. Subsequently, Joule heat is lost and diffusion of the dopants necessarily stops. Now, the distribution of dopants works as an appropriate structure for effective generation of DPs. On the other hand, other dopants where DPs are hardly generated in their vicinities continue to diffuse in the material until they form the required specific distribution, and subsequent stimulated emission occurs. Finally, a high DP generation efficiency is exhibited in all regions, and the temperature drops in all regions of the device. More detailed theoretical descriptions of the DP-assisted annealing method and related achievements have been reported in previous papers by authors' group^{11–19}.

Experiment

In order to use the ZnO device as a polarization rotator, input light whose polarization direction was perpendicular to the crystal axis of the material was made incident on the device. Here, an original arrangement of electrodes was prepared for applying an in-plane current to the device. Details of the fabrication of the device and discussion of mechanism of the polarization rotation are given in the Methods and Discussion sections, respectively. Figure 1(a) shows a photograph of the fabricated ZnO device. The dopant implantation depth was confirmed by secondary ion mass spectrometry (SIMS) to be about 2 μm , as shown in Fig. 1(b). In a related study, the detailed dopant distribution formed by the DP-assisted annealing has been previously confirmed in the case of Si by using a three-dimensional atom probe (3DAP) method¹⁷.

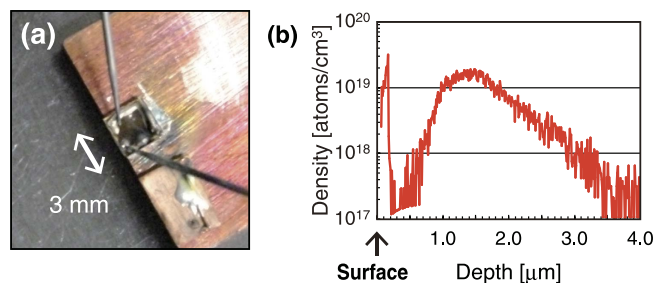


Figure 1. (a) Photograph of the fabricated ZnO device. (b) The dopant density versus implantation depth in the device.

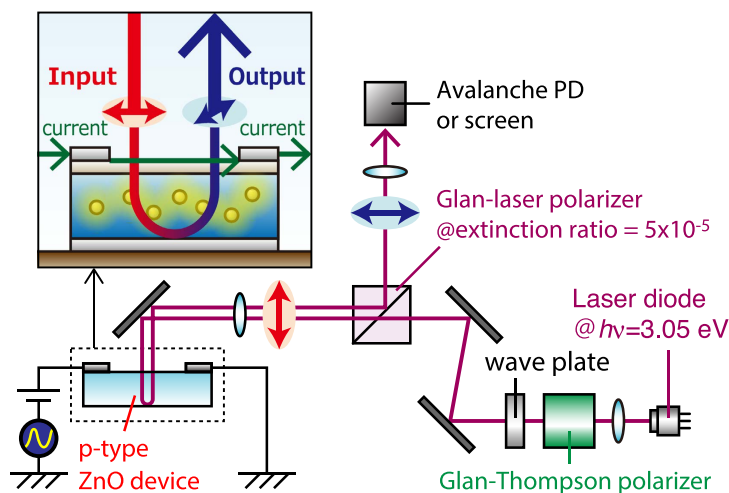


Figure 2. Schematic diagram of setup used for observing polarization rotation based on cross-Nicol method.

The experimental setup used for demonstrating polarization rotation is shown in Fig. 2. The setup was constructed to observe modulated light among the incident linearly-polarized light. The important point is that, as shown in the inset of Fig. 2, a current flowed in the in-plane direction of the device via surface electrodes formed of an indium tin oxide (ITO) layer. The applied voltage was sinusoidally modulated by a function generator. Linearly-polarized light having a photon energy $h\nu = 3.05$ eV, to which the device is transparent, was radiated in the vertical direction onto the device and was output in the opposite direction by reflection at the back side of the device. During propagation in the device, the incident light was expected to be affected by the applied current via interactions between the material and DPs. The mechanism is briefly discussed in the next section. As a result, corresponding polarization rotation was observed as a variation in the optical intensity of the reflected light by using a Glan-laser polarizer.

Figure 3(a) shows the modulated output projected on a phosphor screen, which was set at the output port. In order to clearly represent the spatial dependency of the modulation, the input light was radiated onto the device using an off-focus setup. Therefore, one cycle of varying brightness, between bright and dark parts at each area, corresponds to modulation of π radians. As shown, the spatial modulation of the polarization was found to depend on the applied current.

To quantitatively evaluate the polarization rotation shown in Fig. 3(a), input light was focused onto the device, and the intensity of the output light was observed by using an avalanche photodiode (PD). Fig. 3(b) shows an example of the output light intensity observed with 100 mHz sinusoidal modulation of an 18 V applied voltage. As shown, spatial modulation of the output signal amplitude was clearly observed. Importantly, Fig. 3(b) shows that, while the applied voltage was increased to 18 V during a half cycle of applied voltage, the polarization of the input light was rotated by more than 6π radians.

Discussion

In order to explain the large amount of polarization rotation achieved by our device, the relation between the applied current I_{IN} and the polarization rotation θ_{rot} is plotted by using the measured I-V relation of the device. As shown in Fig. 4, the device achieved a polarization rotation of more than 20π radians by

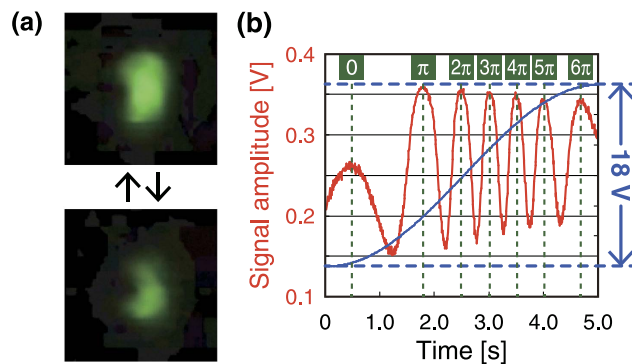


Figure 3. (a) Modulated output images, which were projected on a phosphor screen. (b) Experimentally observed relations between output light intensity (red line) and voltage applied to the device (blue line), where the maximum voltages were 18 V.

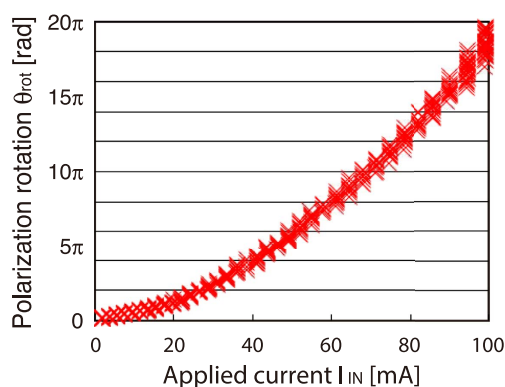


Figure 4. Relation between applied current I_{IN} and polarization rotation θ_{rot} .

applying 100 mA of current. By description with amounts of Faraday rotation, it reveals at intermediate between dielectric semiconductors and magnetic metals.

The important point of our approach is that such a giant polarization rotation does not require any external equipment for applying a strong magnetic field, unlike the conventional magneto-optical effect. Also, it does not require a long propagation distance of the incident light; the effective propagation distance for the modulation was less than $5\ \mu\text{m}$, because of the back and forth propagation in the device, as indicated by the SIMS results shown in Fig. 1(b). The basic mechanism of such a large polarization rotation is discussed below.

Simple and direct propagation of light in the material under a current-induced magnetic field is hardly expected to reveal such an effect, and therefore, the involvement of DPs must be considered. Namely, incident light induces DPs in the surroundings of the dopants, and, at the same time, current-induced magnetic fields strongly affect the phase of the DPs via the distribution of dopants. In such a situation, the incident optical energy and magnetic fields are allowed efficiently interact with each other via the DP states, where the DP states are efficiently energetically coupled with the phonon states of the material. After the interaction, reconversion of optical energy from the DPs to propagating light occurs, and other interactions are induced in surroundings of other dopants. While the expected amount of modulation in a single process is not large enough, after a number of iterations of this process, finally a large amount of modulation is realized. We expect that the theoretical relation between the phase of the DPs and magnetic fields will be clarified by future experiments.

Additionally, practical specifications for use as an optical device, namely, switching speed and power consumption, are theoretically estimated as follows: From the size of the surface ($5\ \text{mm} \times 5\ \text{mm}$) and the thickness ($500\ \mu\text{m}$), our ZnO device is estimated to have a capacitance of 30 pF, which will require $6\ \text{nC}$ ($=30\ \text{pF}/500\ \mu\text{m}$) of electric charge to achieve a single operation, namely π radians of polarization rotation. By referring to the results of our experimental demonstration shown in Fig. 5, if 10 mA of current is assumed to be applied, a switching speed of 120 ns ($=6\ \text{nC}/50\ \text{mA}$) is expected. On the other hand, energy of 60 nJ ($=6\ \text{nC} \times 10\ \text{V}$) is required for a single operation.

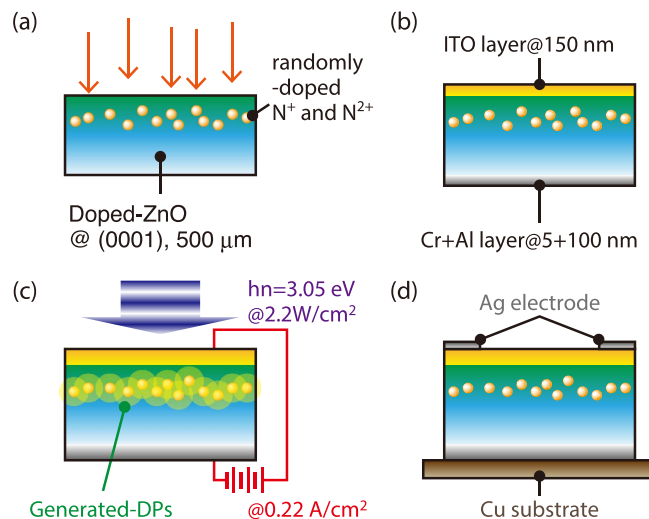


Figure 5. Basic process for fabricating a ZnO device. (a) Implantation of N⁺ and N²⁺ ions into n-type ZnO single crystal. (b) Depositing electrode layers at the front side and back side of the crystal. (c) Application of forward bias current and irradiation of light for the DP-assisted annealing. (d) Deposition of Ag electrode on the crystal and bonding of crystal to Cu substrate for heat dissipation.

Conclusion

In the work described in this paper, giant polarization rotation was experimentally demonstrated using a ZnO single crystal doped with N⁺ and N²⁺ ions. This giant polarization rotation is fundamentally due to an optimized distribution of dopants in the ZnO crystal achieved by DP-assisted annealing, which allowed DPs to be effectively induced by incident light, and application of an in-plane current to the device by using a unique electrode arrangement. As a result, polarization rotation of more than $\pi/3$ radian per volt, which is the amount required in practice to implement optical rotation, was successfully observed without using any external equipment for applying a large magnetic field, and with an effective light propagation distance of less than 5 μm in the device. Based on the results of demonstrations, we considered that this giant polarization rotation was fundamentally due to the repeated interactions between current-induced magnetic fields and localized DPs generated in the regions around dopants in a nanometric space.

Methods

Preparation of ZnO device: To fabricate the prototype device, we used commercially available n-type ZnO single crystal with a thickness of 500 μm, which is prepared by the hydrothermal growth method⁴⁴. The crystal axis orientation was (0001), and the initial electrical resistivity of the crystal was 50–150 Ω cm. The basic process for fabricating a junction ZnO device is schematically shown in Fig. 5.

N⁺ and N²⁺ ions were implanted into the crystal in six steps at energies of 20, 50, 100, 200, 400, and 600 keV for producing a broad distribution of dopants. The ion dose densities were set to 4.20×10^{13} , 9.00×10^{13} , 2.25×10^{14} , 2.75×10^{14} , 4.50×10^{14} , and $4.50 \times 10^{14} \text{ cm}^{-2}$, respectively (Fig. 5(a)). By using multi-step implantation with these parameters, the implanted dopants were distributed in a broad region in the crystal to form a p-type layer. Then, using radio-frequency sputtering, a 150 nm-thick ITO layer was deposited on the front side of the sample, and a 5 nm-thick Cr layer and a 100 nm-thick Al layer were deposited on the back side of the sample to serve as electrode layers (Fig. 5(b)). After deposition, DP-assisted annealing was performed (Fig. 5(c)). During Joule heating by application of a forward bias current, the device was irradiated with laser light having a photon energy $h\nu = 3.05 \text{ eV}$, which is lower than the bandgap energy of the ZnO crystal (3.40 eV). The forward bias current density was set to 0.22 A/cm², which was as high as possible without causing thermal destruction of the device, and the power of the irradiated light was set to 2.2 W/cm², which was as high as possible without causing the crystal temperature to become too high. According to the previous work by the authors' group¹², the surface temperature rose to nearly 100 °C under similar experimental conditions, and then dropped to a constant temperature 70 °C. As we described in the Basics section, this drop in temperature corresponds to the generation of DPs, bringing about stimulated emission, and indicates successful completion of the annealing process for fabricating an appropriate distribution of dopants to efficiently generate DPs in the material. Then, Ag electrodes were deposited for applying an in-plane current to the device, in a direction perpendicular to direction during the annealing process. Finally, the crystal was bonded on a Cu substrate for heat dissipation while working as a polarization rotator (Fig. 5(d)). The Cr and Al layers were utilized as a reflecting surface for the incident light applied to the device.

References

- N. Yamazoe "New approaches for improving semiconductor gas sensors," *Sens. Actuators B: Chem.* **5**, Issue 1–4, 7–19 (1991).
- K. D. Schierbaum, U. Weimar & W. Göpel "Comparison of ceramic, thick-film and thin-film chemical sensors based upon SnO₂," *Sens. Actuators B: Chem.* **7**, Issues 1–3, 709–716 (1992).
- G. Kiss *et al.* "Study of oxide semiconductor sensor materials by selected methods," *Thin Solid Films* **391**, Issue 2, 216–223 (2001).
- K. Nomura *et al.* "Room-temperature fabrication of transparent flexible thin-film transistors using amorphous oxide semiconductors," *Nature* **432**, No. 7016, 488–492 (2004).
- J. S. Park, W.-J. Maeng, H.-S. Kim, and J.-S. Park "Review of recent developments in amorphous oxide semiconductor thin-film transistor devices," *Thin Solid Films* **520**, Issue 6, 1679–1693 (2012).
- E. Fortunato, P. Barquinha & R. Martins "Oxide Semiconductor Thin-Film Transistors: A Review of Recent Advances," *Adv. Mater.* **24**, Issue 22, 2945–2986 (2012).
- R. Singh, K. Rajkanan, D. E. Brodie & J. H. Morgan "Optimization of oxide-semiconductor/base-semiconductor solar cells," *IEEE Trans. Electron Devices* **27**, Issue 4, 656–664 (1980).
- K. Tennakone *et al.* "Sensitization of nano-porous films of TiO₂ with santalin (red sandalwood pigment) and construction of dye-sensitized solid-state photovoltaic cells," *J. Photochem. Photobiol. A* **117**, Issue 28, 137–142 (1998).
- H. Arakawa & K. Sayama "Oxide semiconductor materials for solar light energy utilization," *Res. Chem. Intermediat.* **26**, Issue 2, 145–152 (2000).
- Y.-S. Choi, J.-W. Kang, D.-K. Hwang & S.-J. Park "Recent Advances in ZnO-Based Light-Emitting Diodes," *IEEE Trans. Electron Devices* **57**, No. 1, 26–41 (2010).
- T. Kawazoe, M. A. Mueed & M. Ohtsu "Highly efficient and broadband Si homojunction structured near-infrared light emitting diodes based on the phonon-assisted optical near-field process," *Appl. Phys. B* **104**, No. 4, 747–754 (2011).
- K. Kitamura, T. Kawazoe & M. Ohtsu "Homojunction-structured ZnO light-emitting diodes fabricated by dressed-photon assisted annealing," *Appl. Phys. B* **107**, No. 2, 293–299 (2012).
- T. Kawazoe, M. Ohtsu, K. Akahane & N. Yamamoto "Si homojunction structured near-infrared laser based on a phonon-assisted process," *Appl. Phys. B* **107**, No. 3, 659–663 (2012).
- H. Tanaka, T. Kawazoe & M. Ohtsu "Increasing Si photodetector photosensitivity in near-infrared region and manifestation of optical amplification by dressed photons" *Appl. Phys. B* **108**, No. 1, 51–56 (2012).
- N. Wada, T. Kawazoe & M. Ohtsu "An optical and electrical relaxation oscillator using a Si homojunction structured light emitting diode" *Appl. Phys. B* **108**, No. 1, 25–29 (2012).
- M. A. Tran, T. Kawazoe & M. Ohtsu "Fabrication of a bulk silicon p–n homojunction-structured light-emitting diode showing visible electroluminescence at room temperature," *Appl. Phys. A* **115**, Issue 1, 105–111 (2014).
- N. Wada, M. A. Tran, T. Kawazoe & M. Ohtsu "Measurement of multimode coherent phonons in nanometric spaces in a homojunction-structured silicon light emitting diode," *Appl. Phys. A* **115**, Issue 1, 113–118 (2014).
- M. Yamaguchi, T. Kawazoe & M. Ohtsu "Evaluating the coupling strength of electron-hole pairs and phonons in a 0.9 μm-wavelength silicon light emitting diode using dressed-photon-phonons," *Appl. Phys. A* **115**, Issue 1, 119–125 (2014).
- T. Kawazoe & M. Ohtsu "Bulk crystal SiC blue LED with p–n homojunction structure fabricated by dressed-photon-phonon-assisted annealing," *Appl. Phys. A* **115**, Issue 1, 127–133 (2014).
- T. Kawazoe, K. Kobayashi, S. Takubo & M. Ohtsu "Nonadiabatic photodissociation process using an optical near field," *J. Chem. Phys.* **122**, No. 2, 024715 (2005).
- K. Kobayashi, S. Sangu, H. Ito, M. Ohtsu "Near-field optical potential for a neutral atom," *Phys. Rev. A* **63**, 013806 (2001).
- M. Ohtsu & K. Kobayashi *Optical near fields* (Springer, 2004).
- Y. Tanaka & K. Kobayashi "Spatial localization of an optical near field in one-dimensional nanomaterial system," *Physica E* **40**, Issue 2, 297–300 (2007).
- Y. Tanaka & K. Kobayashi "Optical near field dressed by localized and coherent phonons," *J. Microsc.* **229**, 228–232 (2008).
- M. Ohtsu Dressed Photons - Concepts of Light-Matter *Fusion Technology* (Springer, 2013).
- J.-L. Stehle *et al.* "Multi-pass spectroscopic ellipsometry," *Thin Solid Films* **555**, 143–147 (2014).
- Y.-H. Chang *et al.* "Polarization modulation polarimeter for measuring two-dimensional distribution of five cell parameters of a twisted nematic liquid crystal display," *Thin Solid Films* **571**, 527–531 (2014).
- H. Arwin "Application of ellipsometry techniques to biological materials," *Thin Solid Films* **519**, 2589–2592 (2011).
- M. A. Karim, A. A. Awwal & A. K. Cherri "Polarization-encoded optical shadow-casting logic units: design," *Appl. Opt.* **26**, 2720–2725 (1987).
- Y. Li, G. Eichmann & R. R. Alfano "Optical computing using hybrid encoded shadow casting," *Appl. Opt.* **25**, 2636–2638 (1986).
- J. L. O'Brien "Optical Quantum Computing," *Science* **318**, 1567–1570 (2007).
- Pieter Kok, W. J. Munro, Kae Nemoto, T. C. Ralph, Jonathan P. Dowling & G. J. Milburn "Linear optical quantum computing with photonic qubits," *Rev. Mod. Phys.* **79**, 135–174 (2007).
- S. Gasparoni *et al.* "Realization of a Photonic Controlled-NOT Gate Sufficient for Quantum Computation," *Phys. Rev. Lett.* **93**, 020504 (2004).
- K. Iwata *et al.* "Nitrogen-induced defects in ZnO: N grown on sapphire substrate by gas source MBE," *J. Cryst. Growth* **209**, 526–531 (2000).
- A. B. M. A. Ashrafi, I. Suemune, H. Kumano & S. Tanaka "Nitrogen-Doped p-Type ZnO Layers Prepared with H₂O Vapor-Assisted Metalorganic Molecular-Beam Epitaxy," *Jpn. J. Appl. Phys.* **41**, L1281 (2002).
- K. Minegishi *et al.* "Growth of p-type Zinc Oxide Films by Chemical Vapor Deposition," *Jpn. J. Appl. Phys.* **36**, L1453 (1997).
- X. Wang, *et al.* "Nitrogen doped ZnO film grown by the plasma-assisted metal-organic chemical vapor deposition," *J. Cryst. Growth* **226**, 123–129 (2001).
- J. Lu *et al.* "Structural, electrical and optical properties of N-doped ZnO films synthesized by SS-CVD," *Mater. Sci. Semicond. Process* **5**, 491–496 (2002).
- C.-C. Lin, S.-Y. Chen, S.-Y. Cheng & H.-Y. Lee "Properties of nitrogen-implanted p-type ZnO films grown on Si₃N₄/Si by radio-frequency magnetron sputtering," *Appl. Phys. Lett.* **84**, 5040–5042 (2004).
- C. Wang *et al.* "p-Type ZnO thin films prepared by oxidation of Zn₃N₂ thin films deposited by DC magnetron sputtering," *J. Cryst. Growth* **259**, 279–281 (2003).
- Z.-Z. Ye *et al.* "Preparation and characteristics of p-type ZnO films by DC reactive magnetron sputtering," *J. Cryst. Growth* **253**, 258–264 (2003).
- J. Lu *et al.* "p-type ZnO films deposited by DC reactive magnetron sputtering at different ammonia concentrations," *Mater. Lett.* **57**, 3311–3314 (2003).
- E.-C. Lee, Y.-S. Kim, Y.-G. Jin & K. J. Chang "Compensation mechanism for N acceptors in ZnO," *Phys. Rev. B* **64**, 085120 (2001).
- T. Sekiguchi *et al.* "Hydrothermal growth of ZnO single crystals and their optical characterization," *J. Cryst. Growth* **214–215**, No. 2, 72–76 (2000).

Acknowledgements

This work was partially supported by the JSPS Core-to-Core Program (A. Advanced Research Networks).

Author Contributions

N.T., T.K. and M.O. directed the project; N.T. and T.K. designed the experiments; N.T. and W.N. performed optical characterizations; N.T., T.K. and M.O. contributed to the discussions.

Additional Information


Competing financial interests: The authors declare no competing financial interests.

How to cite this article: Tate, N. *et al.* Current-induced giant polarization rotation using a ZnO single crystal doped with nitrogen ions. *Sci. Rep.* **5**, 12762; doi: 10.1038/srep12762 (2015).



This work is licensed under a Creative Commons Attribution 4.0 International License. The images or other third party material in this article are included in the article's Creative Commons license, unless indicated otherwise in the credit line; if the material is not included under the Creative Commons license, users will need to obtain permission from the license holder to reproduce the material. To view a copy of this license, visit <http://creativecommons.org/licenses/by/4.0/>

Non-scanning optical near-field microscopy for nanophotonic security

Naoya Tate¹  · Makoto Naruse² · Tsutomu Matsumoto³ · Morihisa Hoga⁴ · Yasuyuki Ohyagi⁴ · Shumpei Nishio⁴ · Wataru Nomura¹ · Motoichi Ohtsu⁵

Received: 1 July 2015 / Accepted: 22 July 2015
© Springer-Verlag Berlin Heidelberg 2015

Abstract We propose a novel method for observing and utilizing nanometrically fluctuating signals due to optical near-field interactions between a probe and target in near-field optical microscopy. Based on a hierarchical structure of the interactions, it is possible to obtain signals that represent two-dimensional spatial patterns without requiring any scanning process. Such signals reveal individual features of each target, and these features, when appropriately extracted and defined, can be used in security applications—an approach that we call nanophotonic security. As an experimental demonstration, output signals due to interactions between a SiO₂ probe and Al nanorods were observed by using near-field optical microscopy at a single readout point, and these signals were quantitatively evaluated using an algorithm that we developed for extracting and defining features that can be used for security applications.

1 Introduction

In the critical-security battlefield, a defender tries to produce novel patterns that are difficult to accurately copy, and an attacker seeks a method to counterfeit such patterns [1]. Artifact metrics [2] is one of the most promising concepts for security applications. Artifact metrics utilizes various physical features unique to individual objects in terms of their physical properties, including their electromagnetic [3, 4], mechanical, and optical properties [5, 6]. Some results have been reported in actual implementations, such as ordinary paper [6], paper containing magnetic microfibers [7], plastics, and semiconductor chips. In particular, the essential characteristics of artifact metrics have been ascribed to a physical unclonable function [8]. On the other hand, recent technological advancements in micro-fabrication show promise for realizing various novel technologies that go beyond unclonable functions those developed so far, which have been limited to micrometer-scale precision. Against this background, we recently proposed and demonstrated the concept of *nano-artifact metrics*, which uses nanometer-scale unclonable patterns organized in a random manner [9], which is expected to offer robustness against cloning attacks.

As a further development of nano-artifact metrics, here we propose the concept of *nanophotonic security*, which is realized by combining nanophotonic principles [10–12] with the basics of nano-artifact metrics. Nanophotonics is a novel optical technology utilizing local interactions between nanometric particles via optical near fields. The optical near fields behave as a virtual cloud of photons that is constantly localized around nanometric materials illuminated by incident light. Since the virtual cloud of photons is localized in a region close to the electrons in the material, they can effectively interact with the materials in a unique manner [13].

✉ Naoya Tate
tate@ed.kyushu-u.ac.jp

¹ Faculty of Information Science and Electrical Engineering, Kyushu University, 744 Motooka, Nishi-ku, Fukuoka 819-0395, Japan

² Photonic Network Research Institute, National Institute of Information and Communications Technology, 4-2-1 Nukui-kita, Koganei, Tokyo 184-8795, Japan

³ Graduate School of Environment and Information Sciences, Yokohama National University, Hodogaya, Yokohama, Kanagawa 240-8501, Japan

⁴ Dai Nippon Printing Co. Ltd., 250-1 Wakashiba, Kashiwa, Chiba 277-0871, Japan

⁵ Department of Electrical Engineering and Information Systems, The University of Tokyo, 2-11-16 Yayoi, Bunkyo-ku, Tokyo 113-8656, Japan

Exploiting the characteristic behavior of optical near fields for implementing optical devices and systems enables novel functions that would otherwise be impossible as long as conventional propagating light is used. In nanophotonic security, signals are read out by a nanometric *reader* from a nanometric *device*. Because such signals necessarily reveal specific individuality not only about the device but also about the reader, they are fundamentally difficult to be known from the nanometrical patterns of the reader and the device. Of course, unclonability of their nanometrical patterns is assured due to the basic concept of nano-artifact metrics. Based on these factors, nanophotonic security merits attention and is expected to be lead to novel optical security techniques that will be essential for our sophisticated information society of the future.

Here, as an experimental demonstration of nanophotonic security, we propose using near-field optical microscopy (NOM) *without a scanning process* as a reader. In general, use of NOM entails a scanning process for observing a high-resolution two-dimensional image of spatially distributed optical near fields. However, such a process is not necessarily required in the case of our security applications, because only individual features of each device are required. Instead, appropriate definitions, evaluation of features, and corresponding signal processing are required. In this paper, first the concept and basic procedure of nanophotonic security based on non-scanning NOM are described. Then, results of some experimental demonstrations are shown, and the validity of our approach in an actual application is discussed.

2 Basic procedure

During the readout process in NOM, optical near-field interactions are induced between the nanometrical tip of a probe and a target. Due to these interactions, the readout signals reflect the degree of molecular attraction and the optical responses. By employing an autonomous control mechanism via a feedback structure in the setup, the probe is kept at a constant distance from the target. Here, we focus on inevitable fluctuations of the probe position during the readout process. Based on the concept of the inherent *hierarchy* of optical near-field interactions [14], interactions at various spatial scales are necessarily induced during these fluctuations. That is to say, NOM sequentially observes *compressed* information [15–17] about spatial patterns of the target from a single readout point, in other words without any scanning process. Figure 1 schematically summarizes the basic procedure of our proposed nanophotonic security system based on non-scanning NOM, from readout of the signals to extraction and evaluation of their features.

First, constantly fluctuating signals consisting of the optical responses and signals due to molecular attraction are read out by the non-scanning NOM. Generally, the frequency of such fluctuations can be directly controlled by setting the parameters of the experimental setup. Because the two fluctuating signals in Fig. 1a are obtained with the same time sequence, they can be combined to the single result shown in Fig. 1b. We plotted signals due to molecular attraction on the horizontal axis and signals due to optical responses on the vertical axis. Due to the feedback structure in the setup, the results show orbit-like modulation during the processing time. To allow simple evaluation of the result in Fig. 1b, binary image coding is performed, as shown in Fig. 1c, and the filled-in binary image is subjected to feature extraction. In this paper, the coordinates of corners in the image are defined and utilized as features of the obtained signals. In order to define and determine the coordinates of corners in the image, we employed the features from the accelerated segment test (FAST) [18] method. While various feature extraction methods have been actively studied [19–21] for realizing high-speed classification and searching of images, the FAST method is known to be one of the most effective methods. In the FAST method, only corners are defined as features of a target image, and decision tree analysis is employed to realize real-time processing. Finally, the coordinates of the corners found in each image are defined as individual features of the readout signals and corresponding device.

3 Experimental demonstration

In order to experimentally demonstrate our basic procedure, non-scanning NOM with a SiO₂ probe and Al nanorods was used as a reader and a device, respectively. The radius of curvature of the tip of the probe was less than 20 nm, and the tip was covered with a 50-nm-thick Au layer formed by sputtering, as shown in Fig. 2a. A resonance oscillator with an oscillating frequency of 32 kHz was attached to the probe for detecting molecular attraction between the probe and the device. The distance between the probe and the nanorods was set to be less than 50 nm. The nanorods were grown on a Si substrate by the glancing angle deposition (GLAD) method [22]. This method can realize various sizes, shapes, and constituents of nanorods by controlling multiple independent magnetron sources and three-dimensional rotation stage, which perform the deposition of materials by positioning a sample substrate over each magnetron at the appropriate distance and angle. We prepared two types of device, called *device 1* and *device 2*, which consisted of elements having diameters of 30 nm and 70 nm, as shown in Fig. 2b, c, respectively. All nanorods were grown in the direction vertical to the substrate, and they are slightly less than 200 nm in heights, in

Fig. 1 Basic procedure of nanophotonic security based on non-scanning NOM consists of **a** readout of optical responses and fluctuating signals due to molecular attraction, **b** producing two-dimensional plots of obtained signals, **c** image coding to produce filled-in binary patterns of the plotted results, and **d** feature extraction. In this paper, the coordinates of corners in each coded image are defined as features of the optical near-field interactions between the reader and the device

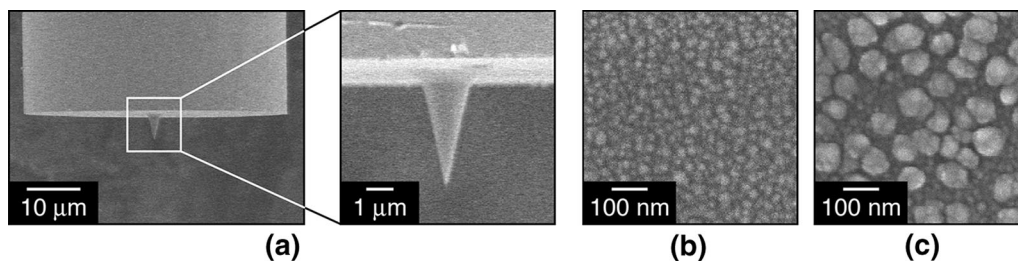
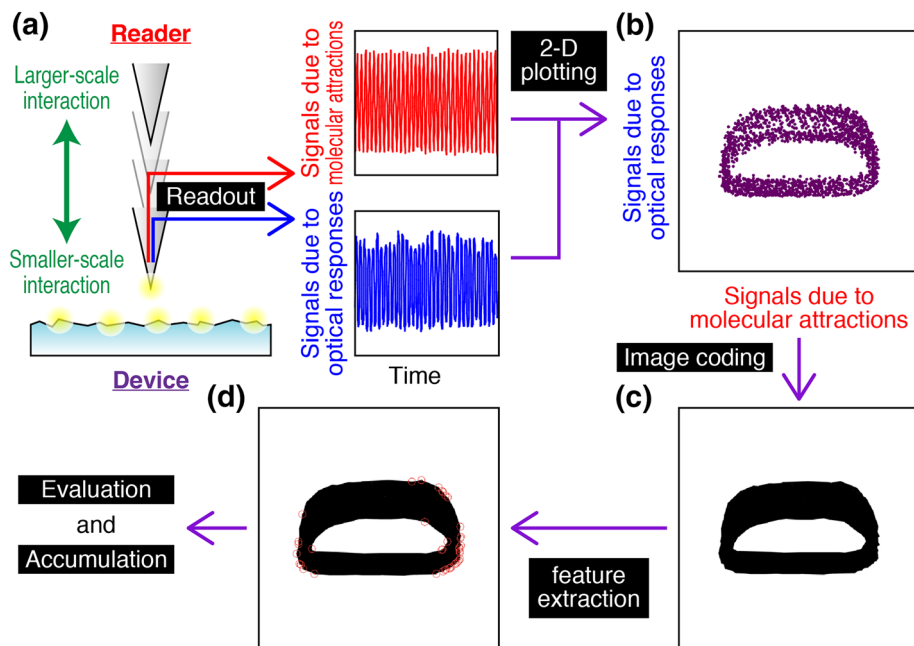


Fig. 2 SEM images of **a** tip of the probe of non-scanning NOM, and top views of nanorods in **b** device 1 and **c** device 2

both devices. A laser with a wavelength of 532 nm was used to induce optical near-field interactions and corresponding molecular attractions and optical responses. Signals due to the optical responses were detected by a photo-multiplier R-3896, manufactured by Hamamatsu Photonics, Japan, and read out as electrical signals, as well as molecular attractions.

Figure 3 shows the two-dimensional plot of the readout signals due to molecular attraction and the optical responses. For comparison, a single reader and two types of devices, device 1 and device 2, were used, and readout distances between the reader and each device are set at less than 50 nm; the plots for these devices are shown in Fig. 3a, b, respectively. A clear difference can be recognized between the two results.

To quantitatively evaluate the difference between the two results, both results were coded to produce filled-in binary patterns, and then, their corners were extracted as their individual features, as we described in the previous section. Then, in order to quantitatively evaluate these results,

we calculated *similarity values* by comparing the coordinates of the extracted corners of both images. Generally, the similarity value is defined as the Hamming distance between two sets of data. In our case, the coordinates of the corners were coded to a binary data set, and the two sets of data were compared with the other. As a result of this calculation, the similarity value between the two was calculated to be 0.10, when normalized to a maximum value of 1.00 in the case of self-similarity. The difference between the two values, 0.10 and 1.00, is sufficiently large for actual authentication between device 1 and device 2.

4 Discussion

In order to experimentally verify the validity of our proposed method and to quantitatively evaluate it using similarity values, other similarity values were obtained for various readout points on the target. We read out signals at discrete points on a single device and coded the results to

Fig. 3 Two-dimensional plots of readout signals by using non-scanning NOM with **a** device 1 and **b** device 2

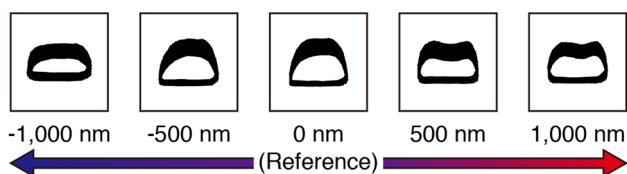
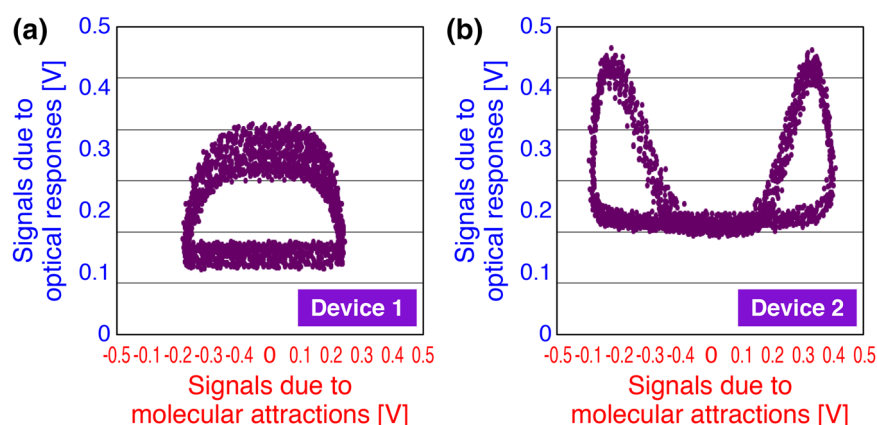


Fig. 4 Filled-in binary images obtained at discrete points on device 1, -1000 nm to $+1000$ nm away from a reference point

produce filled-in binary images, as shown in Fig. 4, which is the result with device 1.

One image is defined as a reference image, and we calculated the relative similarity values between the reference image and the others. Figure 5a, b shows calculated similarity values in the case of using device 1 and device 2, respectively. Additionally, at each point, we set two readout distances between the probe and the nanorods: One distance was set at about 100 nm, which we refer to as *farther readout*, and the other distance was set at less than 50 nm, which we refer to as *nearer readout*. In the case of farther readout, the spatial scale of the interactions between the probe and the device was much larger than in the case of nearer readout.

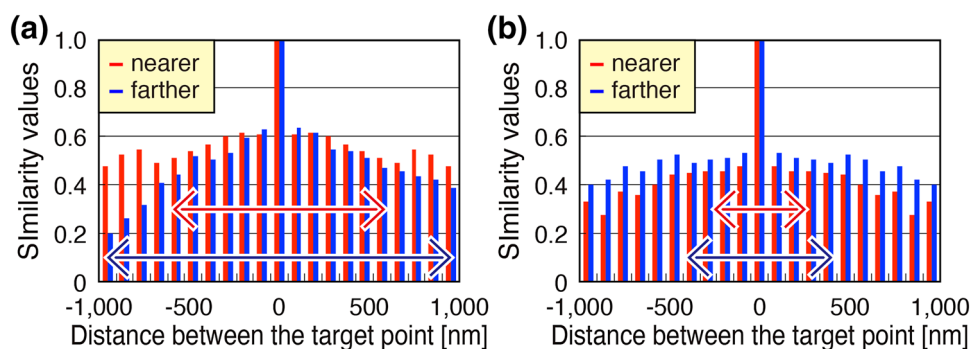
The main finding shown in these results is that all similarity values exhibited periodical increasing and decreasing. This indicates that the obtained signals at each

single readout point are the result of interactions between the probe and the spatial patterns of the nanorods, as we described in the previous section. If this were not the case, the fluctuations of the similarity values would be more random and steeper, but this was not observed. Furthermore, the difference in periods between the results of nearer readout and farther readout corroborates our hypothesis. For example, when using device 1, as shown in Fig. 5a, the pitches of the troughs are about 1200 nm and 2000 nm in the case of nearer readout and farther readout, respectively. Because the signals obtained with farther readout correspond to a larger spatial scale of interactions, the pitch of the increasing and decreasing similarity values becomes necessarily large. In the case of nearer readout, the opposite tendency was revealed. A similar comparison and reasoning also applies in the case where device 2 is used, as shown in Fig. 5b, where the results of nearer readout and farther readout showed trough pitches of about 500 and 800 nm, respectively.

5 Summary

With the goal of verifying the validity and effectiveness of nanophotonic security, we demonstrated the definition and acquisition of individual features of nanometric patterns

Fig. 5 Similarity values between the reference image and other discretely obtained images with two different readout distances [nearer readout (*red bars*) and farther readout (*blue bars*)] using a device 1 and **b** device 2



using non-scanning NOM. Our proposed method is suitable for application to actual situations as it takes only a short amount time, less than 1 s in our demonstrations, for the readout process, because it does not require the scanning process that is normally required when using NOM. This aspect, which was realized by exploiting nanometrically fluctuating signals due to optical near-field interactions, is expected to be a conceptual breakthrough not only for security applications but also for various applications related to optical information processing. Finally, although we produced filled-in binary images from readout fluctuating signals and extracted the coordinates of the corners in each image as individual features of each device, this procedure is just one possible procedure used to demonstrate the basic idea of our proposed method. Further studies will need to be performed to optimize each step in our proposed procedure.

The authors wish to thank Y. Pihosh, K. Mawatari, and T. Kitamori in the Department of Applied Chemistry at The University of Tokyo for their technical assistance in preparing the Al nanorods used for our experimental demonstrations. This work was partially supported by the JSPS Core-to-Core Program (A. Advanced Research Networks).

References

1. R.L. van Renesse, *Optical Document Security* (Artech, Morristown, 1994)
2. H. Matsumoto, T. Matsumoto, *IPSJ J.* **44**, 1991–2001 (2003)
3. D. Lim, J.W. Lee, B. Gassend, G.E. Suh, M. van Dijk, S. Devadas, *IEEE T. VLSI Syst.* **13**, 1200–1205 (2005)
4. G. DeJean, K. Darko, *Lect. Notes Comput. Sci.* **4727**, 346–363 (2007)
5. J.D. Buchanan, R.P. Cowburn, A.V. Jausovec, D. Petit, P. Seem, G. Xiong, M.T. Bryan, *Nature* **436**, 475 (2005)
6. M. Yamakoshi, J. Tanaka, M. Furuie, M. Hirabayashi, T. Matsumoto, *Proc. SPIE* **6819**, 68190H-1–68190H-10 (2008)
7. T. Ikeda, S. Hiroe, T. Yamada, T. Matsumoto, Y. Takemura, 3rd International Conference on Anti-counterfeiting, Security, and Identification in Communication 2009, pp. 382–385 (2009)
8. R. Pappu, B. Recht, J. Taylor, N. Gershenfeld, *Science* **297**, 2026–2030 (2002)
9. T. Matsumoto, in *Proceedings of the IEICE Symposium on Cryptography and Information Security*, SCIS 97-19C (1997)
10. K. Kobayashi, S. Sangu, H. Ito, M. Ohtsu, Near-field optical potential for a neutral atom. *Phys. Rev. A* **63**, 013806 (2001)
11. M. Ohtsu, K. Kobayashi, *Optical Near Fields* (Springer, Berlin, 2004)
12. Y. Tanaka, K. Kobayashi, Spatial localization of an optical near field in one-dimensional nanomaterial system. *Phys. E* **40**(2), 297–300 (2007)
13. M. Ohtsu, *Dressed Photons—Concepts of Light-Matter Fusion Technology* (Springer, Berlin, 2013)
14. M. Naruse, H. Hori, K. Kobayashi, M. Ishikawa, K. Leibnitz, M. Murata, N. Tate, M. Ohtsu, *J. Opt. Soc. Am. B* **26**(9), 1772–1779 (2009)
15. E. Candès, J. Romberg, T. Tao, *IEEE Trans. Inf. Theory* **52**, 489–509 (2006)
16. D. Donoho, *IEEE Trans. Inf. Theory* **52**, 1289–1306 (2006)
17. J. Haupt, R. Nowak, *IEEE Trans. Inf. Theory* **52**, 4036–4048 (2006)
18. E. Rosten, T. Drummond, in *European Conference on Computer Vision*, pp. 430–443 (2006)
19. C. Harris, M. Stephens, in *Alvey Vision Conference*, pp. 147–151 (1988)
20. S.M. Smith, J.M. Brady, *Int. J. Comput. Vision* **23**, 45–78 (1997)
21. D.G. Lowe, in *International Conference on Computer Vision*, pp. 1150–1157 (1999)
22. Y. Pihosh, I. Turkevych, J. Ye, M. Goto, A. Kasahara, M. Kondo, M. Tosa, *ECS Trans.* **16**(5), 49–58 (2009)

Polarization control of an infrared silicon light-emitting diode by dressed photons and analyses of the spatial distribution of doped boron atoms

Tadashi Kawazoe^{1,2} · Katsuhiko Nishioka¹ · Motoichi Ohtsu^{1,2,3}

Received: 18 May 2015 / Accepted: 15 June 2015
© Springer-Verlag Berlin Heidelberg 2015

Abstract This paper reports the fabrication of a polarization-controlled infrared LED fabricated by dressed-photon–phonon (DPP)-assisted annealing of a bulk Si crystal. For the DPP-assisted annealing, linearly polarized infrared light with a wavelength of 1.342 μm was made normally incident on the top surface of the crystal. The photon energy at the peak of the emitted light spectrum of the fabricated LED was close to that of the light irradiated during the DPP-assisted annealing. A degree of polarization of as large as 0.07 was obtained. The spatial distribution of the doped B atoms in the fabricated LED was measured, and the following findings were obtained: (1) B atoms formed pairs in which the separation between the two B atoms was three times the lattice constant of the Si crystal; and (2) the B atom pairs were apt to orient along the direction perpendicular to the propagation direction and to the polarization direction of the light irradiated during the DPP-assisted annealing. Based on these findings (1) and (2), photon breeding was confirmed with respect to photon energy and spin, respectively.

1 Introduction

Although bulk silicon (Si) crystal has been popularly used for electronic devices, it has not been used for practical light-emitting devices such as light-emitting diodes (LEDs) and lasers. This is because Si is an indirect transition-type semiconductor, meaning that electrons in the conduction band have to change their momenta in order to produce light emission. Here, the problem is that the probability of the interaction between an electron and a phonon, indispensable for the momentum change, is very low.

In order to solve this problem, for example, porous Si [1], a super-lattice structure of Si and SiO₂ [2, 3], and Si nanoprecipitates in SiO₂ [4] have been used to emit visible light. To emit infrared light, Er-doped Si [5] and Si–Ge [6] have been employed. In these examples, the emission efficiency is too low for practical use since Si still works as an indirect transition-type semiconductor in these materials.

To drastically increase efficiency, a novel fabrication method named DPP-assisted annealing has been recently devised by the authors [7]. This method has been used to fabricate an infrared LED whose external quantum efficiency and output power were as high as 15 % and 1 W, respectively, at a wavelength of 1.32 μm (CW operation at room temperature). A visible LED [8], an infrared laser [9, 10], an optical and electrical relaxation oscillator [11], and an infrared photodetector with optical amplification [12] have also been fabricated by this method. Furthermore, visible LEDs have been fabricated by using a bulk silicon carbide (SiC) crystal, even though this material is also an indirect transition-type semiconductor [13].

The dressed photon (DP) is a quasi-particle created as a result of the interaction between a photon and an electron in a nanometric space [14]. Furthermore, the DP excites

✉ Motoichi Ohtsu
ohtsu@ee.t.u-tokyo.ac.jp

¹ Department of Electrical Engineering and Information Systems, Graduate School of Engineering, The University of Tokyo, 2-11-16 Yayoi, Bunkyo-ku, Tokyo 113-8656, Japan

² Specified Nonprofit Corporation Nanophotonics Engineering Organization, 1-20-10, Sekiguchi, Bunkyo-ku, Tokyo 112-0014, Japan

³ International Center for Nano Electron and Photon Technology, Graduate School of Engineering, The University of Tokyo, 2-11-16 Yayoi, Bunkyo-ku, Tokyo 113-8656, Japan

multimode coherent phonons, and they couple to form a novel quasi-particle called a dressed-photon–phonon (DPP), which can be used for device fabrication and operation. The phonons in the DPP contribute to the required momentum change in the electron described above. The Huang–Rhys factor, representing the coupling strength between electrons and optical mode phonons, has been evaluated to be as large as 4.08 for a fabricated silicon LED (Si-LED) [15]. This value is about 10^2 – 10^3 times that in conventional bulk Si crystals, which demonstrates the large interaction probability between the electrons and phonons in this Si-LED. Furthermore, modes of coherent phonons in the DPP have been identified by pump–probe laser spectroscopy [16].

In the case of a conventional LED, it should be pointed out that the photon energy of the emitted light is determined by the bandgap energy E_g of the semiconductor used [17]. In contrast, in the case of the present Si-LED, it is determined by the photon energy $h\nu_{\text{anneal}}$ of the light irradiated during the DPP-assisted annealing. This phenomenon has been called photon breeding [18]. In other words, the photon energy of the emitted light is identical to $h\nu_{\text{anneal}}$, because the difference between $h\nu_{\text{anneal}}$ and E_g is compensated for by the energy of the phonons in the created DPP. Therefore, even infrared light, whose photon energy is lower than E_g , can be emitted from the Si-LED based on photon breeding. Photon breeding has been confirmed also in a visible Si-LED [8] and a visible SiC-LED [13], which have been fabricated via DPP-assisted annealing by irradiating bulk Si and SiC crystals with visible light, respectively. The magnitudes of the phonon sidebands in the output light spectrum have been controlled by irradiating pairs of light pulses during the DPP-assisted annealing [19].

It is expected that photon breeding takes place not only with respect to photon energy described above but also with respect to photon spin. That is, the light emitted from the LED can be polarized if it is fabricated by irradiating the Si crystal with polarized light during the DPP-assisted annealing.

The output light from conventional LEDs is not polarized, and several methods have been proposed for polarizing it, such as using the specific anisotropic optical properties of nonpolar GaInN quantum wells [20] and installing a complicated subwavelength-size metallic nanograting [21]. Instead of these approaches, the present paper proposes a novel polarization control method for infrared Si-LEDs based on photon breeding with respect to photon spin. It also reports the results of high-spatial-resolution three-dimensional analyses of the spatial distribution of the doped B atoms, performed in order to confirm the photon breeding.

Radiation energy dissipation from relativistic jets in blazars has also been called photon breeding [22]. In this

astrophysical phenomenon, very high-energy X rays are generated from low-energy infrared or visible light by inverse Compton scattering with a charged particle. Therefore, the photon breeding discussed in the present paper, creating photons by using a DPP in a nanometric-sized space in a material, is fundamentally different from that in astrophysics. Due to this difference, the present photon breeding may have to be called “nano-photon breeding” in order to avoid confusion. However, this paper uses the name “photon breeding” for conciseness.

2 Fabrication and operation

The structure of the fabricated Si-LED is schematically shown in Fig. 1a. The fabrication method was equivalent to that in Ref. [7], except that linearly polarized light was irradiated during the DPP-assisted annealing.

2.1 Fabrication by DPP-assisted annealing

First, to form the p–n homojunction, an As-doped n-type Si crystal with a thickness of $625\ \mu\text{m}$, whose electrical resistivity was $10\ \Omega\ \text{cm}$, was used. The top surface of the Si crystal was a (001) plane. The upper part of this crystal

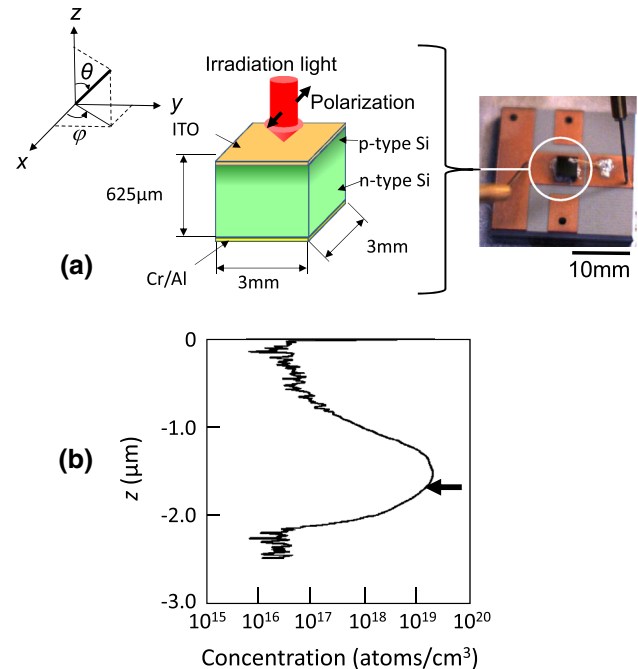


Fig. 1 Structure of the Si-LED. **a** A bird’s-eye view and photograph of the device. Definitions of the Cartesian coordinates (x , y , z), the zenith angle θ , and the azimuthal angle φ are also given. **b** Cross-sectional profile of the doped B atom concentration along the z -axis, measured by secondary ion mass spectroscopy. The *thick arrow* represents the area of the measurement, to be presented in Fig. 3

was further doped with B by ion implantation to form a p-type layer. The implantation direction was the $[00\bar{1}]$ orientation (along the z -axis in Fig. 1a, normal to the (001) plane), and the energy was 700 keV, which realized a doped B atom concentration of 10^{19} cm^{-3} , corresponding to 0.04 % of the Si atom concentration. Figure 1b shows the cross-sectional profile of this concentration along the z -axis, measured by secondary ion mass spectroscopy, which represents the p–n homojunction at a position 1.5–2.0 μm down from the top surface of the Si crystal. An ITO film (150 nm thick) was deposited on the top surface of the Si crystal. Cr and Al films were subsequently deposited on the bottom surface (5 and 100 nm thick, respectively). They were used as an anode and cathode, respectively. After depositing these films, the Si crystal was diced to form a device with an areal size of 3 mm \times 3 mm.

Second, for the DPP-assisted annealing, a forward bias voltage was applied to inject the current (170 mA: current density of 1.89 A cm^{-2}) in order to generate Joule energy, causing the B to be diffused by the Joule-heat and varying the spatial distribution of its concentration. During the annealing, infrared light, linearly polarized along the x -axis in Fig. 1a, was normally incident on the top surface of the Si crystal, through the ITO anode. Its power density, photon energy $h\nu_{\text{anneal}}$, and wavelength were 3.3 W cm^{-2} , 0.924 eV, and 1.342 μm , respectively.

Since the photon energy $h\nu_{\text{anneal}}$ of this light is lower than E_g (=1.12 eV), it can propagate through the Si crystal without suffering absorption, creating a DPP on the surface of the B atom at the p–n homojunction. The electron in the conduction band at the p–n homojunction interacts with this DPP to exchange momentum with the phonons in the DPP, and, as a result, a photon is created by stimulated emission. The created photon propagates to outside the Si crystal, which means that a part of the Joule energy is transformed to the propagating photon energy and is dissipated from the Si crystal. This dissipation decreases the diffusion rate of the B atoms, affecting the variation of the spatial distribution of B atoms. The fabrication is finished when this distribution reaches a stationary state.

2.2 Operation based on photon breeding

For the operation of the fabricated S-LED, the infrared light irradiation is not required any more; it is used only during the DPP-assisted annealing. Only forward current injection is required, as is the case of the conventional LED operation. By this forward current, an electron is injected into the conduction band at the p–n homojunction and creates a photon by spontaneous emission even though its probability is very low. However, once this photon is

created, it subsequently creates a DPP on the surface of the B atom at the p–n homojunction, and this DPP interacts with another electron in the conduction band to exchange momentum so that a secondary photon is created. By repeating these momentum exchange and photon creation processes, the emitted light intensity is amplified and reaches a stationary value within a short duration, so that light with a sufficiently high intensity is emitted from the p–n homojunction. It should be noted that the photon energy of the emitted light is identical to $h\nu_{\text{anneal}}$. This is because the spatial distribution of the B atoms has been controlled by the light irradiated during the DPP-assisted annealing, enabling most efficient stimulated emission and spontaneous emission of photons with identical photon energy. In other words, the light irradiated during the DPP-assisted annealing serves as a “breeder” that creates photons with an energy equivalent to $h\nu_{\text{anneal}}$. This is the reason why this novel phenomenon is named photon breeding with respect to photon energy.

For evaluating the polarization characteristics of the fabricated Si-LED, the emitted light was decomposed into two linearly polarized components by using a linear polarizer, and their intensities (I_{\parallel} , I_{\perp}) were acquired. The polarization directions of these components are, respectively, parallel and perpendicular to that of the light irradiated during the DPP-assisted annealing.

Their light emission spectra at an injection current of 100 mA are represented by the curves A and B in Fig. 2a, whose spectral peaks are close to $h\nu_{\text{anneal}}$ due to the photon breeding with respect to photon energy. It is seen that I_{\parallel} is larger than I_{\perp} in a wide spectral range around $h\nu_{\text{anneal}}$. Since the linearly polarized light is the superposition of the two photons with up- and down-spins, this difference between I_{\parallel} and I_{\perp} in this figure also represents the successful results of polarization control, which is due to photon breeding with respect to photon spin.

The black squares in Fig. 2b represent the measured relation between the DPP-assisted annealing time and the degree of polarization $P = (I_{\parallel} - I_{\perp}) / (I_{\parallel} + I_{\perp})$ at the photon energy $h\nu_{\text{anneal}}$. The value of P in this figure is zero at zero annealing time because the Si crystal is optically isotropic. However, this value increases with increasing annealing time and asymptotically approaches a maximum value of 0.07. This increase is not due to the optical anisotropy induced by the Joule-heat because the applied Joule energy was too low to strain or deform the Si crystal. For reference, the surface temperature was maintained at as low as 154 $^{\circ}\text{C}$ in the DPP-assisted annealing (Fig. 2 in Ref. [7]).

The measured values were fitted by the solid curve in Fig. 2b. This curve represents the result of numerical calculation based on the two-level system model, which is a theoretical model popularly used for the light-induced

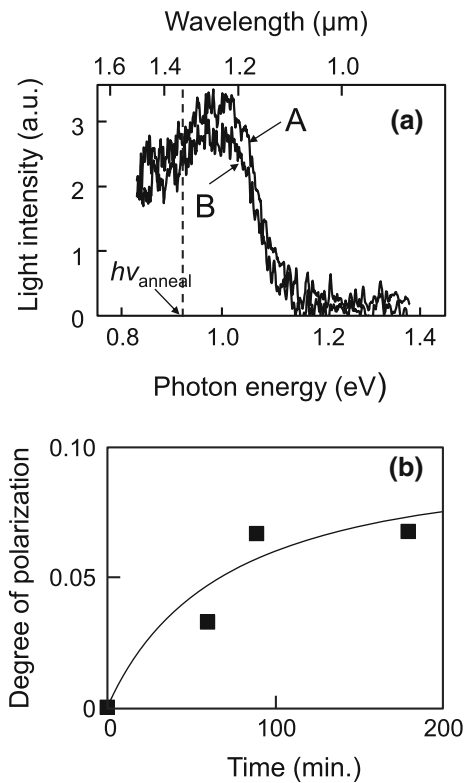


Fig. 2 Characteristics of the light emitted from the fabricated Si-LED. **a** The light emission spectra. Curves A and B are the linearly polarized components, which are, respectively, parallel and perpendicular to the direction of the linear polarization of the light irradiated during the DPP-assisted annealing. The annealing time was 180 min. **b** Relation between the DPP-assisted annealing time and the degree of polarization P at the photon energy, $h\nu_{\text{anneal}}$. Black squares represent the measured values. The solid curve represents the theoretical values, which were fitted to the measured values

variations of the configuration coordinates in several phenomena, such as spectral hole burning [23]. The agreement between this curve and the measured values suggests that the polarization was controlled by the linearly polarized light irradiated during the DPP-assisted annealing.

3 Analyses of the spatial distribution of boron atoms

To confirm the hypothesis given at the end of Sect. 2.2, this section presents the analysis results of the three-dimensional spatial distribution of the doped B atoms, which was measured by atom-probe field ion microscopy with sub-nanometer resolution [24]. The measured area is represented by a thick arrow in Fig. 1b. Figure 3 shows the measured three-dimensional spatial distribution of B atoms at the p–n homojunction. The black dots represent the positions of the individual B atoms. The distribution is projected onto the xy -, yz -, and zx -planes ((001), (100), and

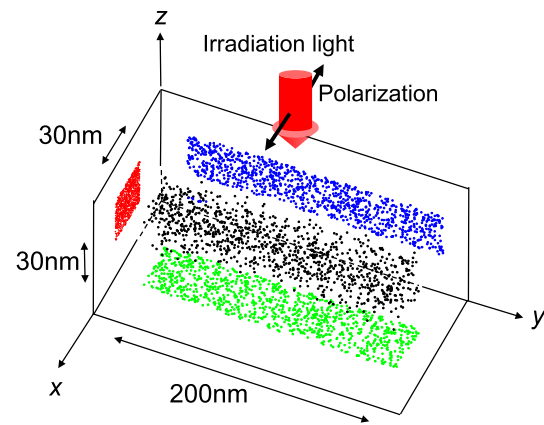


Fig. 3 Three-dimensional spatial distribution of B atoms, measured by the atom-probe ion microscopy

(010) planes), represented by green, blue, and red dots, respectively.

It should be noted that the Si crystal is composed of multiple cubic lattices with a lattice constant a of 0.54 nm [25], and its top surface lies in the xy -plane. The light irradiated during the DPP-assisted annealing is normally incident on this plane; i.e., the light propagation direction is parallel to the z -axis, which is parallel to the [001] orientation.

3.1 Separation between the boron atoms in the pair

Some of the regularly arranged Si atoms are replaced by the doped B atoms in the DPP-assisted annealing. It has been pointed out that phonons can be localized at the B atoms for creating a DPP under light irradiation because the B atoms are lighter than the Si atoms. However, for this localization, it has also been pointed out that two or more adjacent B atoms (in other words, two or more unit cells containing B atoms) are required [26]. Since the doped B atom concentration is as low as 0.04 % relative to the Si atom concentration, making it difficult for more than three B atoms to aggregate, the following discussion considers two closely spaced adjacent B atoms (a B atom pair), around which a phonon is localized for creating a DPP. That is, the pair of unit cells containing the B atoms serves as a phonon localization center.

Figure 4a, b shows the numbers of B atom pairs plotted as a function of the separation, d , between the B atoms in the pair, which were derived from the measurement results in Fig. 3. Since the distribution of the number of B atom pairs is nearly random, it can be least-squares-fitted by the Weibull distribution function (the solid curve in these figures), which is expressed as

$$p(d) = (3/\beta) \cdot (d/\beta)^2 \cdot \exp[-(d/\beta)^3], \quad (1)$$

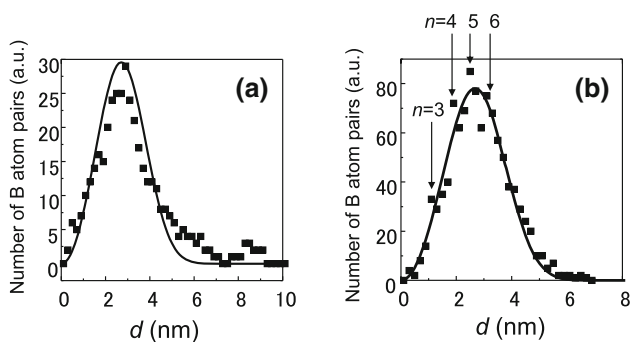


Fig. 4 Number of B atom pairs plotted as a function of the separation d between the B atoms in the pair. **a** The un-annealed Si crystal. **b** The DPP-assisted-annealed Si crystal

where δ is the concentration of the B atoms, and $\beta = \sqrt[3]{3/4\pi\delta}$. In the un-annealed Si crystal (Fig. 4a), the measured number of B atom pairs deviates from the solid curve in the range $d > 45$ nm. The deviation depends on the characteristics of the ion implantation.

In contrast, in the Si crystal after the DPP-assisted annealing (Fig. 4b), the deviation is much less than that in Fig. 4a, which means that the DPP-assisted annealing modified the spatial distribution and decreased the deviation induced by the ion implantation, making the distribution more random. However, at specific values of $d (=na$, where $n = 3, 4, 5, 6$; refer to the four downward arrows in this figure), the number of B atom pairs still deviates from the solid curve and is larger than that of the solid curve. This is explained as follows: The B atom pair with the shortest d (i.e., equal to the lattice constant a) can orient in a direction parallel to the $[1,0,0]$, $[0,1,0]$, or $[0,0,1]$ orientation because the Si crystal is composed of multiple cubic lattices. As a result, the wave-vector (momentum) of the localized phonon points in this direction, which corresponds to the $\Gamma - X$ direction in reciprocal space (Fig. 5). Thus, a photon is efficiently created because this $\Gamma - X$ direction is the same as the direction of the wave-vector of the phonon required for recombination between an electron at the bottom of the conduction band at the X -point and a hole at the top of the valence band at the Γ -point. Here, it should be noted that the absolute value of the wave-vector of the phonon has to be $1/a$ for this electron-hole recombination to take place. Furthermore, it should also be noted that, among the phonons localized at the B atom pair with separation $d (=na)$, the absolute value of the wave-vector of the lowest mode is $1/na$. By comparing these two absolute values, it is found that the DPP at this B atom pair has to create n phonons for recombination. Thus, it can be concluded that the four downward arrows in Fig. 4b indicate selective increases in the number of B atom pairs with separation $d = na$ due to the DPP-assisted annealing, and these pairs serve as localization centers for the phonons.

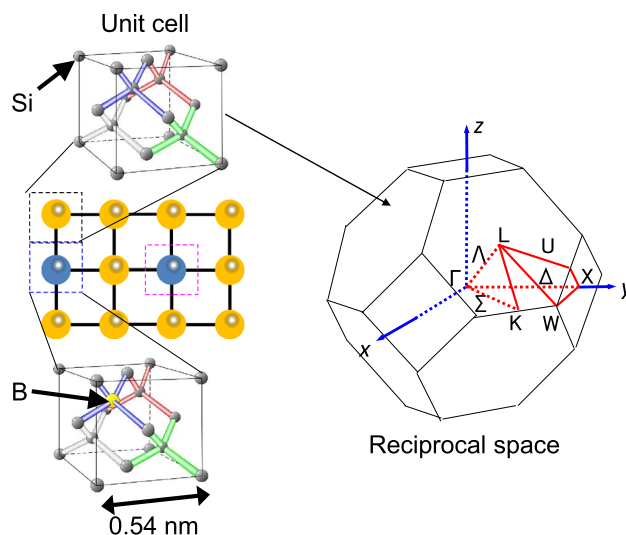


Fig. 5 Unit cell of the Si crystal in real space and in reciprocal space

Figure 6a shows the relation between n and the measured deviation in Fig. 4b. This figure shows that the deviation takes the maximum value at $n = 3$, which means that B atom pairs most efficiently create three phonons for

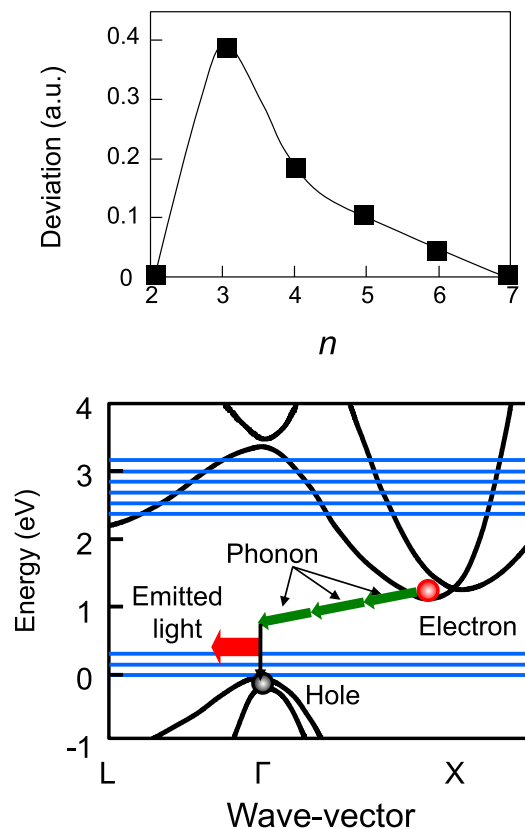


Fig. 6 Relation between n and the deviation. **a** Measured results. **b** The energy band diagram of Si and schematic explanation of light emission

light emission, as is schematically shown in Fig. 6b. This phonon creation process is consistent with the discussion in Ref. [15], in which the magnitudes of the phonon sidebands in the light emission spectra were analyzed based on the density of states of phonons and the estimated value of the Huang–Rhys factor. As a result, the emitted photon energy $h\nu_{em}$ is expressed as $h\nu_{em} = E_g - 3E_{phonon}$. By substituting the values of E_g ($=1.12$ eV) and the relevant optical mode phonon energy E_{phonon} ($=65$ meV [27]) into this equation, the value of $h\nu_{em}$ is derived to be 0.925 eV, which is identical to the photon energy $h\nu_{anneal}$ irradiated during the DPP-assisted annealing. This numerical relation confirms that photon breeding with respect to photon energy occurs.

3.2 Dependence on the zenith and azimuthal angles

Figure 4b indicates selective increases in the number of B atom pairs with separation $d = na$. This means that, since n is an integer, B atom pairs are apt to orient along a plane perpendicular or parallel to the top surface of the Si crystal (zenith angle $\theta = 0^\circ$ or 90° in Fig. 1a). Orientation along other directions in which n is not an integer ($\theta \neq 0^\circ, 90^\circ$) hardly occurs.

Figure 7a shows the relation between the zenith angle θ and the number of B atom pairs. It can be seen that this number takes the maximum value at $\theta = 90^\circ$, which means that the B atom pairs are apt to stretch in a plane (xy -plane) which is parallel to the top surface of the Si crystal, i.e., perpendicular to the propagation direction ($[00\bar{1}]$ orientation; z -axis) of the light irradiated during the DPP-assisted annealing. On the other hand, the number of B atom pairs takes the minimum value at $\theta = 0^\circ$, which means that the B atom pairs hardly orient along the propagation direction (z -axis) of the light irradiated during the DPP-assisted annealing. This is because the phonons are hardly localized along this direction since their momenta (wave-vectors) are parallel to $\theta = 90^\circ$ [28].

Figure 7b shows the relation between the azimuthal angle φ and the number of the B atom pairs. This angle is defined in the xy -plane ($\theta = 90^\circ$), and $\varphi = 0^\circ$ corresponds to the polarization direction (x -axis) of the light irradiated during the annealing. The vertical axis in Fig. 7b represents the difference in the numbers of B atom pairs after and before the DPP-assisted annealing. The negative value of this difference at $\varphi = 0^\circ$ means that the number of B atom pairs orienting to $\varphi = 0^\circ$ decreases as a result of the DPP-assisted annealing. In the region $\varphi > 45^\circ$, this difference becomes a positive value, which means that the number increased due to the DPP-assisted annealing. The number of B atom pairs takes the maximum value at $\varphi = 90^\circ$. This angular dependence means that the diffusion of the B atoms was controlled by the linearly polarized light

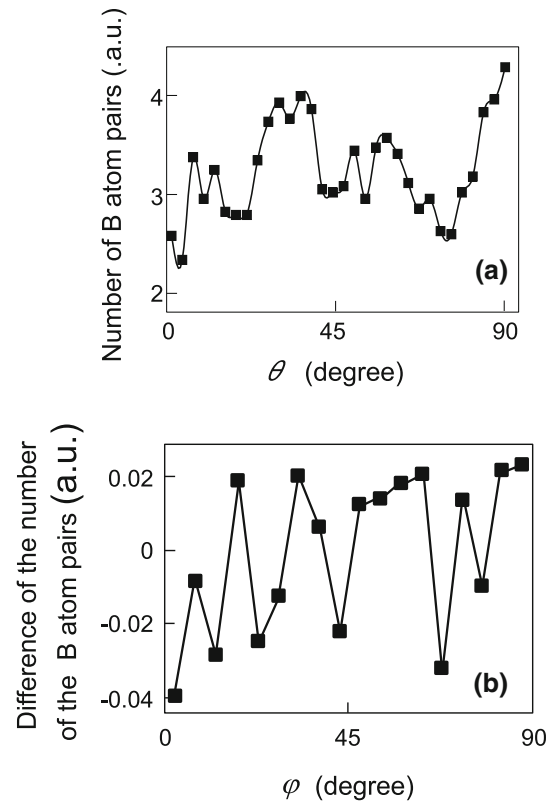


Fig. 7 Relation between the orientation angle and the number of B atom pairs. **a** Relation between the zenith angle θ and the number of B atom pairs. **b** Relation between the azimuthal angle φ and the difference in the numbers of B atom pairs after and before the DPP-assisted annealing

irradiated during the DPP-assisted annealing, with the result that the B atom pairs oriented to $\varphi = 90^\circ$.

As a result, the light emitted from the fabricated LED was polarized, and the polarization direction was governed by that of the light irradiated during the DPP-assisted annealing. There are two possible origins of this induced polarization of the emitted light: (1) Since the oriented B atom pairs work as a kind of nano-wire grid in the xy -plane (the orientation of this grid is $\varphi = 90^\circ$), the light emitted from the fabricated LED can be linearly polarized in the direction ($\varphi = 0^\circ$) perpendicular to the direction of the grid. (2) First, when the LED is fabricated by the DPP-assisted annealing, transverse optical phonons are created at the B atom pairs and couple with the DPs. The vibration direction of these phonons is parallel to that of the electric field of the polarized light ($\varphi = 0^\circ$) irradiated during the DPP-assisted annealing. Next, when the fabricated LED is operated, since these phonons are created again, the direction of the electric field vector of the emitted light becomes also parallel to the vibration direction of these phonons. Therefore, the polarization direction of the

emitted light becomes identical to that of the light irradiated during the DPP-assisted annealing.

The number of B atom pairs at $\varphi \geq 45^\circ$ in Fig. 7b is 8.6 % of the total, which corresponds to a P value of 0.07 for the 180-min annealing time. This correspondence supports the origins (1) and (2) presented above. It should be possible to increase P further by more precisely controlling the annealing parameters for orienting more B atom pairs along the direction $\varphi = 90^\circ$ (and also $\theta = 90^\circ$).

4 Summary

This paper reported the fabrication of an infrared LED by using DPP-assisted annealing of a bulk Si crystal and evaluation of its light emission characteristics. For the DPP-assisted annealing, linearly polarized infrared light with a wavelength of 1.342 μm was made normally incident on the top surface of the bulk Si crystal in order to control the polarization of the light emitted from the fabricated LED. As a result, the photon energy at the peak of the emitted light spectra of the fabricated LED was close to that of the light irradiated during the DPP-assisted annealing. A degree of polarization of as large as 0.07 was obtained.

In order to confirm the photon breeding involved in this polarization control, the spatial distribution of the doped B atoms was measured. The following findings were obtained: (1) B atoms formed a pair, in which the separation between the two B atoms was three times the lattice constant of the Si crystal. This separation is the origin of the photon breeding with respect to photon energy. (2) The B atom pairs are apt to orient in the direction $\theta = 90^\circ$ and $\varphi = 90^\circ$. The former and the latter are the values of the zenith and azimuthal angles, which are perpendicular to the propagation direction and the polarization direction of the light irradiated during the DPP-assisted annealing, respectively. These orientations are the origin of the photon breeding with respect to photon spin.

For reference, the polarization of the output light from a visible SiC-LED has also been controlled by the method devised in the present work, and a value of P as high as 0.12 was obtained at a wavelength of 480 nm [29]. Such polarization control of visible LEDs could be advantageous for reducing power consumption in backlight systems for displays and imaging applications.

Acknowledgments This work was partially supported by the Core-to-Core Program of JSPS (A. Advanced Research Network), a Grant-

in-Aid for Scientific Research (B) (No. 24360023) of MEXT, and the Exploratory Research program (No.15K13374) of MEXT.

References

1. K.D. Hirschman, L. Tysbekov, S.P. Duttagupta, P.M. Fauchet, *Nature* **384**, 338 (1996)
2. Z.H. Lu, D.J. Lockwood, J.-M. Baribeau, *Nature* **378**, 258 (1995)
3. L. Dal Negro, R. Li, J. Warga, S.N. Beasu, *Appl. Phys. Lett.* **92**, 181105 (2008)
4. T. Komoda, *Nucl. Instrum. Methods Phys. Res. SectB Beam Interact. Mater. Atoms* **96**, 387 (1995)
5. S. Yerci, R. Li, L. Dal, Negro. *Appl. Phys. Lett.* **97**, 081109 (2010)
6. S.K. Ray, S. Das, R.K. Singha, S. Manna, A. Dhar, *Nanoscale Res. Lett.* **6**, 224 (2011)
7. T. Kawazoe, M.A. Mueed, M. Ohtsu, *Appl. Phys. B* **104**, 747 (2011)
8. M.A. Tran, T. Kawazoe, M. Ohtsu, *Appl. Phys. A* **115**, 105 (2014)
9. T. Kawazoe, M. Ohtsu, K. Akahane, N. Yamamoto, *Appl. Phys. B* **107**, 659 (2012)
10. H. Tanaka, T. Kawazoe, M. Ohtsu, K. Akahane, *Fluoresc. Mater.* **1**, 1 (2015)
11. N. Wada, T. Kawazoe, M. Ohtsu, *Appl. Phys. B* **108**, 25 (2012)
12. H. Tanaka, T. Kawazoe, M. Ohtsu, *Appl. Phys. B* **108**, 51 (2012)
13. T. Kawazoe, M. Ohtsu, *Appl. Phys. A* **115**, 127 (2014)
14. M. Ohtsu, *Dressed Photon* (Springer, Dordrecht, 2013), pp. 11–18
15. M. Yamaguchi, T. Kawazoe, M. Ohtsu, *Appl. Phys. A* **115**, 119 (2014)
16. N. Wada, M.-A. Tran, T. Kawazoe, M. Ohtsu, *Appl. Phys. A* **115**, 113 (2014)
17. P.Y. Yu, M. Cardona, *Fundamentals of Semiconductors*, 4th edn. (Springer, Dordrecht, 2010), pp. 345–426
18. M. Ohtsu, *Progress in Nanophotonics 1*, ed. by M. Ohtsu (Springer, Dordrecht, 2011), pp.8–11
19. T. Kawazoe, N. Wada, M. Ohtsu, *Adv. Opt. Technol.* (2014) Article IC 958327, doi:10.1155/2014/958327
20. M.F. Schubert, S. Chhajed, J.K. Kim, E.F. Schubert, *Appl. Phys. Lett.* **91**, 051117 (2007)
21. L. Zhang, J.H. Teng, S.J. Chua, E.A. Fitzgerald, *Appl. Phys. Lett.* **95**, 261110 (2009)
22. B.E. Stern, J. Poutanen, *Mon. Not. R. Astron. Soc.* **383**, 1695 (2008)
23. R. Jankowiak, R. Richert, H. Bässler, *J. Phys. Chem.* **89**, 4569 (1985)
24. K. Hono, *Prog. Mater. Sci.* **47**, 621 (2001)
25. K. Godwod, R. Kowalczyk, Z. Szmíd, *Phys. Status. Solidi (a)* **21**, 227 (1974)
26. Y. Tanaka, K. Kobayashi, *Phys. E* **40**, 297 (2007)
27. E. Anastassakis, A. Pinczuk, E. Burstein, F.H. Pollak, M. Cardona, *Solid State Commun.* **8**, 133 (1970)
28. Y. Shinohara, T. Otobe, J. Iwata, K. Yanaba, *J. Phys. Soc. Jpn.* **67**, 685 (2012)
29. T. Kawazoe, K. Nishioka, M. Ohtsu, *Abstract of the 21st International Display Workshops*, (Soc. Information Display, 2014) PRJ-1 (Niigata, Japan, 3–5 Dec 2014)

Stochastic model showing a transition to self-controlled particle-deposition state induced by optical near-fields

Kan Takahashi¹ · Makoto Katori¹ · Makoto Naruse² · Motoichi Ohtsu³

Received: 7 November 2014 / Accepted: 3 May 2015 / Published online: 29 May 2015
© Springer-Verlag Berlin Heidelberg 2015

Abstract We study a stochastic model for the self-controlled particle-deposition process induced by optical near-fields. This process was experimentally realized by Yukutake et al. on an electrode of a novel photovoltaic device as Ag deposition under light illumination, in which the wavelength of incident light is longer than the long-wavelength cutoff of the materials composing the device. Naruse et al. introduced a stochastic cellular automaton model to simulate underlying nonequilibrium processes which are necessary to formulate unique granular Ag film in this deposition process. In the present paper, we generalize their model and clarify the essential role of optical near-fields generated on the electrode surface. We introduce a parameter b indicating the incident light power per site and a function representing the resonance effect of optical near-fields depending on the Ag-cluster size on the surface. Numerical simulation shows a transition from a trivial particle-deposition state to a nontrivial self-controlled particle-deposition state at a critical value b_c , and only in the latter state optical near-fields are effectively generated. The properties of transition in this mesoscopic surface model in nonequilibrium are studied by the analogy

of equilibrium phase transitions associated with critical phenomena, and the criteria of transition are reported.

1 Introduction

Nanophotonics, which investigates light–matter interactions on the nanometer scale, has been intensively studied from a variety of aspects ranging from fundamental interests, such as atom and optical near-field interactions [1–3], to applications including environment and energy [4, 5], health care [6], solid-state lighting [7], information and communications technologies [8, 9], among others. Precision control of the geometrical features, such as the size, layout and morphology, at the nanometer scale is important in realizing valuable functionalities [1, 3]. In this context, the nanophotonics fabrication principles and techniques have been providing interesting and important light-assisted, self-controlled nanostructures; nanoparticle array formation [10], light emission from indirect-transition-type semiconductors (such as silicon) [7], appearances of photosensitivity at wavelengths longer than the long-wavelength cutoff [5], etc. In these light-assisted material formations, while elemental physical processes indeed involve optical near-field interactions at the nanometer scale, the system is open to environment and thus is accompanied with energy flow and environmental fluctuations. For these systems, stochastic modeling [11, 12] is very useful in order to obtain deeper understandings of the underlying physical processes as well as to gain design principles for future devices and systems [3]. In the present paper, we develop the cellular automaton model [13] proposed by Naruse et al. [14], which was introduced to simulate self-controlled pattern formation of Ag film reported by Yukutake et al. [5] on the electrode of their photovoltaic device.

✉ Makoto Katori
katori@phys.chuo-u.ac.jp

Kan Takahashi
k-takahashi@phys.chuo-u.ac.jp

¹ Department of Physics, Faculty of Science and Engineering, Chuo University, 1-13-27 Kasuga, Bunkyo-ku, Tokyo 112-8551, Japan

² National Institute of Information and Communications Technology, 4-2-1 Nukui-kita, Koganei, Tokyo 184-8795, Japan

³ Nanophotonics Research Center, Graduate School of Engineering, The University of Tokyo, 2-11-16 Yayoi, Bunkyo-ku, Tokyo 113-8656, Japan

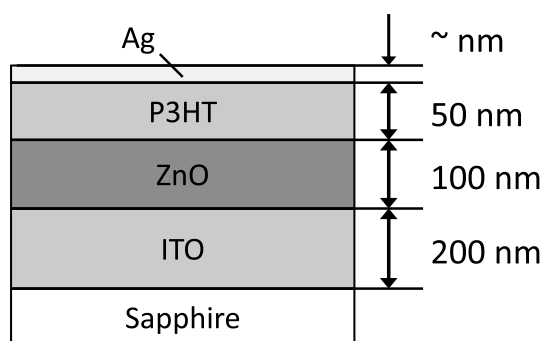


Fig. 1 Cross-sectional structure of the photovoltaic device of Yukutake et al. [5]

Figure 1 shows the cross-sectional structure of the photovoltaic device of poly-(3-hexyl thiophene) (P3HT) and ZnO sandwiched by Ag and indium tin oxide (ITO) electrodes. A P3HT layer (about 50 nm thick) and a ZnO layer (about 100 nm thick) are used as p-type and n-type semiconductors, respectively, and an ITO film (about 200 nm thick) and an Ag film (a few nanometers thick) are used as two electrodes. This multi-layered film with an area of 30 mm² is deposited on a sapphire substrate in series. At the last stage of the fabrication process of the multi-layered device, Ag was deposited on the Ag thin film. The Ag is deposited by radio frequency (RF) sputtering under light illumination while applying a reverse bias DC voltage, $V_b = -1.5$ V, to the P3HT/ZnO p-n junction. The wavelength of the incident light is 670 nm, which is longer than the cutoff wavelength $\lambda_c = 570$ nm of P3HT. Under light illumination, optical near-fields are locally generated on the Ag surface. They induce coherent phonons and form a coupled state with them, which is called a *virtual exciton-phonon-polariton* [15] or the *dressed-photon-phonon (DPP)* [3]. If the DPP field extends to the p-n junction, the two-step excitation process of electrons occurs (see [5] and Sect. 7.2.1 of [3]) and then electron-hole pairs are created at the p-n junction. As illustrated in Fig. 2, by the reverse bias voltage, the electrons and holes are separated from each other. The positive holes are attracted to the Ag film, which make the Ag film be positively charged. It was argued in [5, 14] that due to randomness in Ag deposition process by RF sputtering, the density of Ag deposits will spatially fluctuate. Since the optical near-fields are generated by short-ranged light-matter interaction, the optical near-fields will also become spatially inhomogeneous in the film. In the local area of the Ag surface, where the optical near-field is effectively induced, more positive holes are generated and transferred into the area. In such an area, which is more positively charged than other areas, the subsequent deposition of Ag will be suppressed, since the sputtering Ag is positively ionized by passing through the argon

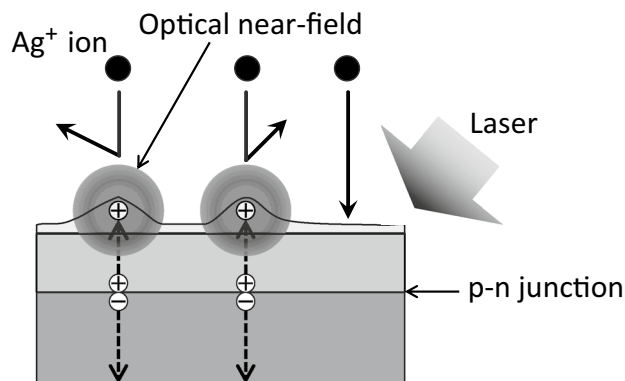


Fig. 2 Under light illumination, an optical near-field is locally generated on the Ag surface, which induces a coherent phonon at the p-n junction. Then, this generates an electron-hole pair at the p-n junction, and by the reverse bias voltage, the positive hole is attracted to the Ag film on the surface, which makes the Ag film positively charged more. Subsequent deposition of Ag⁺ ion on the electrode is suppressed by positive charge accumulated in the Ag clusters on the surface

plasma used for RF sputtering. Such a feedback mechanism induced by optical near-fields will lead to the unique and nontrivial granular structure of the Ag film, and such a self-controlled pattern formation was indeed observed in experiments [5].

Naruse et al. [14] introduced a stochastic cellular automaton model on a square lattice [13] such that each cell has one of the two values 0 and 1, which represents a vacancy and an occupation by an Ag grain, respectively. Time evolution of Ag clusters in random deposition of Ag⁺ grains on a lattice has been numerically simulated. It was assumed in their model that the repulsive force acting on an Ag⁺ grain when it is deposited on a site in the lattice is simply proportional to the total number of occupied sites in the eight neighbors (i.e., the Moore neighborhood in the square lattice). This model works well as a minimal model for the inhomogeneous pattern formation of Ag film on an electrode of the photovoltaic device, while a role of spatially inhomogeneous charge distribution due to the heterogeneous effect of optical near-fields was not clarified.

In the present paper, we propose a nonequilibrium statistical mechanics model on an $L \times L$ square lattice Λ_L , in which two kinds of stochastic variables at each site \mathbf{r} evolve in discrete time $t \in \{0, 1, 2, \dots\}$; the number of deposited grain on the site $n_t(\mathbf{r})$ and the amount of charge per site $q_t(\mathbf{r})$. These two variables are dynamically coupled as explained below. It is known that the effective potential of optical near-field is well described by a Yukawa function of a distance r , $V_{\text{eff}}(r) = e^{-r/\alpha}/r$. Here the interaction range α is proportional to the size of the matter which generates the

optical near-field under light illumination [3]. In the present situation, the range α will be approximately equal to the size s of Ag clusters. Hence, growth of sufficiently large clusters is required in order to realize the situation such that the optical near-fields generated on the Ag surface reach the p–n junction and electron–hole pairs are created (see Fig. 2). As a result, the charge increment of a cluster of Ag-deposited sites depends on the cluster size s , which is a functional of $\{n_t(\mathbf{r})\}_{\mathbf{r} \in \Lambda_L}$. We introduce a characteristic size s_0 of the cluster at which the charge increment of a cluster caused by the optical near-fields is maximized. Moreover, we assume existence of a characteristic size-variation σ^2 such that if the cluster size s deviates from s_0 by much larger than σ , that is, if $(s - s_0)^2 \gg \sigma^2$, then the effect of the optical near-fields for charging cluster becomes very small. These assumptions are due to the basic property of DPPs, the optical near-fields coupled with phonons, called the *size-dependent resonance*, and here, we use the Gaussian function

$$f(s) = \exp \left[-\frac{(s - s_0)^2}{2\sigma^2} \right] \tag{1.1}$$

to represent such size dependence (see Fig. 2.6 in Sect. 2.2.2 of [3]). Furthermore, in our numerical simulation, we perform exact calculation of long-ranged repulsive Coulomb interaction between the Ag^+ grain being deposited on a site and positively charged Ag clusters formed on the surface.

The main result of our numerical simulation of the model is that, when the lattice size L is large but finite, there are following two distinct mesoscopic states.

State A : If Ag clusters on the surface are formed with a proper size s such that $(s - s_0)^2 \leq \sigma^2$, then the optical near-fields are induced effectively to increase the charge of clusters and hence the total positive charge on the surface increases monotonically in time. It causes strong suppression of further deposition of Ag^+ grains on the surface, and then, the deposition will be stopped. As a result, a nontrivial and unique Ag film is formed.

State B : If sizes of Ag clusters on the surface tend to deviate from s_0 by more than σ , the optical near-fields are not induced effectively. In this case, the charge on surface will be saturated at a low level, and the suppression of deposition of Ag^+ grains on the surface remains weak. Hence, the random deposition process will continue without any self-control, and Ag film formation is rather trivial; as long as laser light is irradiated, the density of Ag grains on the surface gradually increases.

We will show that if we change some parameters of model, for instance, a parameter b which denotes the

incident light power per site, then there occurs a transition from State B to State A and then the self-controlled formation of Ag film is realized. We remark that in the real experiments, the p–n junction was reversely biased with a fixed voltage ($V_b = -1.5$ V). Therefore, the positive charge on the Ag surface is bounded, and it will be saturated. In order to simplify the model, however, we do not take into account such an effect in the present study.

The paper is organized as follows. In Sect. 2, the setting of the present model, the algorithm of processes and the quantities which we will calculate are explained. The results of numerical simulations are given in Sect. 3. These properties of the dynamical transition of surface state are studied by the analogy of equilibrium phase transitions associated with critical phenomena [11–13]. Section 4 is devoted to concluding remarks.

2 Discrete-time stochastic model on a lattice

Let L be an integer and consider an $L \times L$ square lattice $\Lambda_L = \{1, 2, \dots, L\}^2$. For two sites $\mathbf{r} = (x, y)$, $\mathbf{r}' = (x', y') \in \Lambda_L$ with distance $|\mathbf{r} - \mathbf{r}'| \equiv \sqrt{(x - x')^2 + (y - y')^2} = 1$, we say that they are the nearest-neighbor sites. We consider a stochastic process with a discrete time $t \in \mathbb{N}_0 \equiv \{0, 1, 2, \dots\}$. Here a particle will represent a positively charged Ag grain. At each time $t \in \mathbb{N}_0$, the following two kinds of stochastic variables will be defined,

$$\begin{aligned} n_t(\mathbf{r}) &= \text{the number of deposited particles at site } \mathbf{r}, \\ q_t(\mathbf{r}) &= \text{the amount of charge at site } \mathbf{r}, \end{aligned} \tag{2.1}$$

$\mathbf{r} \in \Lambda_L$, where $n_t(\mathbf{r}) \in \mathbb{N}_0$ and $q_t(\mathbf{r}) \in \mathbb{R}_+ \equiv \{x \in \mathbb{R} : x \geq 0\}$ (the set of nonnegative real numbers). At each time $t \in \mathbb{N}_0$, a collection of pairs of these stochastic variables over the lattice gives a *configuration* of the process, which is denoted by

$$\xi_t = \{(n_t(\mathbf{r}), q_t(\mathbf{r})) : \mathbf{r} \in \Lambda_L\}, \quad t \in \mathbb{N}_0. \tag{2.2}$$

In a given configuration ξ_t , if $n_t(\mathbf{r}) \geq 1$ and $n_t(\mathbf{r}') \geq 1$ for a pair of the nearest-neighbor sites $(\mathbf{r}, \mathbf{r}')$, we say that these two sites are *connected*. Moreover, for a pair of sites \mathbf{r} and \mathbf{r}' with $|\mathbf{r} - \mathbf{r}'| > 1$, if there is a sequence of sites $\mathbf{r}_0 \equiv \mathbf{r}, \mathbf{r}_1, \dots, \mathbf{r}_{n-1}, \mathbf{r}_n \equiv \mathbf{r}'$ in Λ_L with $|\mathbf{r}_j - \mathbf{r}_{j-1}| = 1, 1 \leq j \leq n, n \in \{2, 3, \dots\}$ such that any pair of successive sites $(\mathbf{r}_{j-1}, \mathbf{r}_j), 1 \leq j \leq n$ are connected, then we also say that \mathbf{r} and \mathbf{r}' are *connected*. For each site \mathbf{r} with $n_t(\mathbf{r}) \geq 1$, a two-dimensional *cluster* including the site \mathbf{r} is defined by

$$C_t(\mathbf{r}) = \{\mathbf{r}' \in \Lambda_L : \mathbf{r} \text{ and } \mathbf{r}' \text{ are connected}\}. \tag{2.3}$$

By definition, if \mathbf{r} and \mathbf{r}' are connected, then $C_t(\mathbf{r}) = C_t(\mathbf{r}')$. The total number of sites \mathbf{r}' included in $C_t(\mathbf{r})$ is denoted

by $|C_t(\mathbf{r})|$, which represents an area on Λ_L of the cluster of deposited particles.

We introduce the parameters in \mathbb{R}_+ as

$$\begin{aligned} b &= \text{incident light power per site,} \\ a &= \text{effective coupling constant of} \\ &\quad \text{a repulsive Coulomb potential between charges,} \\ E_{\text{th}} &= \text{threshold energy for deposition on the surface.} \end{aligned} \tag{2.4}$$

If the kinetic energy of Ag^+ grain injected to the surface by RF sputtering is relatively small, the deposition on the surface will be inhibited by the Coulomb repulsive force between the Ag^+ grain and the positively charged surface. In the present stochastic model, we do not calculate such electro-dynamical processes and simply introduce two variables a and E_{th} as parameters. We set a function $f : \mathbb{N}_0 \mapsto \mathbb{R}$, which specifies the increment ratio of charge per site and per time step as a function of cluster size to which the site belongs. We assume that f is given by (1.1) with positive constants s_0 and σ . Now we explain the elementary process, $\xi_t \mapsto \xi_{t+1}, t \in \mathbb{N}_0$.

Assume that a configuration ξ_t is given at time $t \in \{0, 1, 2, \dots\}$.

- (i) Choose a site randomly in Λ_L . The chosen site is denoted by \mathbf{x} .
- (ii) Calculate the repulsive Coulomb potential at \mathbf{x} caused by all charges on Λ_L by

$$V(\mathbf{x}) = \sum_{\mathbf{r} \in \Lambda_L} a \frac{q_t(\mathbf{r})}{|\mathbf{x} - \mathbf{r}|_+}, \tag{2.5}$$

where $|\mathbf{x}|_+ = |\mathbf{x}|$, if $|\mathbf{x}| > 0$ and $|\mathbf{x}|_+ = 1$, if $|\mathbf{x}| = 0$. (Here we consider a ‘coarse grain model’, and thus, any singularity of the Coulomb potential function should be eliminated).

- (ii-1) If $V(\mathbf{x}) \leq E_{\text{th}}$, then a charged particle is deposited at the site \mathbf{x} ;

$$n_{t+1}(\mathbf{r}) = \begin{cases} n_t(\mathbf{r}) + 1, & \mathbf{r} = \mathbf{x}, \\ n_t(\mathbf{r}), & \mathbf{r} \neq \mathbf{x}. \end{cases} \tag{2.6}$$

- (ii-2) If $V(\mathbf{x}) > E_{\text{th}}$, then let $\mathbf{y}_0 = \mathbf{x}$ and calculate $V(\mathbf{y})$ at every nearest-neighbor site of \mathbf{y}_0 , $\mathbf{y} \in \mathcal{N}(\mathbf{y}_0) \equiv \{\mathbf{y} \in \Lambda_L : |\mathbf{y} - \mathbf{y}_0| = 1\}$. If the site which attains $\min_{\mathbf{y} \in \mathcal{N}(\mathbf{y}_0)} V(\mathbf{y})$ is uniquely determined, let that site be \mathbf{y}_1 . When the minimum is attained by plural sites, we choose one of them randomly and let it be \mathbf{y}_1 . If $V(\mathbf{y}_1) > V(\mathbf{y}_0)$, then we regard that the particle is repulsed from the charged surface and cannot be deposited. Hence, the configuration is not changed at all,

$$n_{t+1}(\mathbf{r}) = n_t(\mathbf{r}), \quad \forall \mathbf{r} \in \Lambda_L. \tag{2.7}$$

If $V(\mathbf{y}_1) \leq E_{\text{th}}$, we set $\mathbf{x}^* = \mathbf{y}_1$. If $E_{\text{th}} < V(\mathbf{y}_1) \leq V(\mathbf{y}_0)$, calculate $V(\mathbf{y})$ at every $\mathbf{y} \in \mathcal{N}(\mathbf{y}_1)$ and follow the same procedure as above to determine a site \mathbf{y}_2 . If $V(\mathbf{y}_2) > V(\mathbf{y}_1)$, the deposition is not done and we have (2.7). If $V(\mathbf{y}_2) \leq E_{\text{th}}$, set $\mathbf{x}^* = \mathbf{y}_2$. If $E_{\text{th}} < V(\mathbf{y}_2) \leq V(\mathbf{y}_1)$, we repeat the similar procedure to those explained above. When $\mathbf{x}^* \in \Lambda_L$ is determined, the charged particle is deposited at the site \mathbf{x}^* ;

$$n_{t+1}(\mathbf{r}) = \begin{cases} n_t(\mathbf{r}) + 1, & \mathbf{r} = \mathbf{x}^*, \\ n_t(\mathbf{r}), & \mathbf{r} \neq \mathbf{x}^*. \end{cases} \tag{2.8}$$

Each sequence $\mathbf{x} = \mathbf{y}_0 \rightarrow \mathbf{y}_1 \rightarrow \dots \rightarrow \mathbf{y}_n = \mathbf{x}^*$ with some $n \in \{1, 2, \dots\}$ simulates a path of *drift process* on the surface performed by a particle before it is deposited at \mathbf{x}^*

- (iii) Clusters at time $t + 1$, $\{C_{t+1}(\mathbf{r}) : \mathbf{r} \in \Lambda_L\}$ are redefined for the configuration $\{n_{t+1}(\mathbf{r}) : \mathbf{r} \in \Lambda_L\}$ given by (ii). For each cluster $C_{t+1}(\mathbf{r})$, the accumulated total charge has been $\sum_{\mathbf{r}' \in C_{t+1}(\mathbf{r})} q_t(\mathbf{r}')$. In addition to that, the following amount of charge is added; $b|C_{t+1}(\mathbf{r})|f(|C_{t+1}(\mathbf{r})|)$. (See Eq. (1.1) and the explanation given above it). Then the charge at site \mathbf{r} at time $t + 1$ is given by

$$\begin{aligned} q_{t+1}(\mathbf{r}) &= \frac{1}{|C_{t+1}(\mathbf{r})|} \left\{ \sum_{\mathbf{r}' \in C_{t+1}(\mathbf{r})} q_t(\mathbf{r}') \right. \\ &\quad \left. + b|C_{t+1}(\mathbf{r})|f(|C_{t+1}(\mathbf{r})|) \right\}, \quad \mathbf{r} \in \Lambda_L. \end{aligned} \tag{2.9}$$

We note that the charge distribution in cluster can be spatially inhomogeneous in general depending on the shape of cluster on the surface. We have assumed the uniform distribution in (2.9); however, since keeping the model simple, we would like to report the advantage of introducing the variable $q_t(\mathbf{r})$, which was not considered in the previous cellular automaton model [14], in order to realize transitions between the two distinct particle-deposition states.

We start at the empty configuration $\xi_0 = \{(n_0(\mathbf{r}), q_0(\mathbf{r})) = (0, 0) : \mathbf{r} \in \Lambda_L\}$ and observe the following quantities at times $t \in \{0, 1, 2, \dots, T\}$ with a sufficiently large T ,

$$\begin{aligned} A_t &= \sum_{\mathbf{r} \in \Lambda_L} \mathbf{1}(n_t(\mathbf{r}) \geq 1), \\ Q_t &= \sum_{\mathbf{r} \in \Lambda_L} q_t(\mathbf{r}), \end{aligned} \tag{2.10}$$

where $\mathbf{1}(\omega)$ is an indicator function of a condition ω ; $\mathbf{1}(\omega) = 1$ if ω is satisfied, and $\mathbf{1}(\omega) = 0$ otherwise. The quantity A_t shows the *total area of clusters* at time t and Q_t the *total charge* of particles deposited on the surface Λ_L at time t . We set

$$R_t = \frac{A_t}{L^2}, \tag{2.11}$$

which denotes the *occupation ratio* by deposition on the surface at time t . We also define

$$Q_t^{(T)} = \frac{Q_t}{Q_T}, \quad t \in \{0, 1, 2, \dots, T\} \tag{2.12}$$

with a given T .

3 Simulation results

We performed computer simulation of the stochastic model. Here we fix the following parameters as

$$a = 1 \times 10^{-3}, \quad s_0 = 12, \quad \sigma = 2, \tag{3.1}$$

and

$$L = 64, \quad T = 10^4. \tag{3.2}$$

The parameters b and E_{th} are changed, and dependence of the process on them is studied. (We will also discuss the results on systems with different sizes L in Sects. 3.3 and 4).

3.1 Two states

Figure 3 shows time dependence of the occupation ratios by deposition on the surface, R_t (solid lines), and the total charges on the surface normalized by the values at $t = T$, $Q_t^{(T)}$ (broken lines), for $b = 0.01, 0.10, 0.30, 0.50, 0.70$ and 0.90 , when we set $E_{th} = 10$. When b is small ($b = 0.01, 0.10$ and 0.30), R_t increases monotonically and $Q_t^{(T)}$ shows saturation after some time period. When b is

large ($b = 0.50 - 0.90$), on the other hand, R_t shows saturation in time, while $Q_t^{(T)}$ increases monotonically. The results imply when b is small the system is in State B, while b is large in State A. The critical value of b will be evaluated in the next subsection as $b_c = 0.44$ in this case with $E_{th} = 10$.

3.2 Order parameter and critical exponent

When the system is in State B, R_t increases monotonically and $\lim_{t \rightarrow \infty} R_t \simeq 1$, that is, the surface will be almost covered by particles. On the other hand, in State A, the deposition is suppressed by Q_t which increases monotonically in time and the surface formation is self-controlled. As a result, we will have a nontrivial steady state, in which $\lim_{t \rightarrow \infty} R_t = R_\infty < 1$.

The vacant-site density on the surface in the steady state is defined as

$$\rho_0 \equiv 1 - R_\infty. \tag{3.3}$$

It will play a role as an *order parameter* for the transition from State B to State A.

Here ρ_0 is approximated by the value $\rho_0^{(T)} \equiv 1 - R_T$ at $T = 10^4$. For each choice of parameters, we performed ten independent simulations and studied the averaged values of $\rho_0^{(T)}$. Figure 4 shows dependence of $\rho_0^{(T)}$ on b for $E_{th} = 5, 10, 20, 30, 40$ and 50 . There $\rho_0^{(T)}$'s seem to behave as continuous functions of b . It implies that the transition is continuous and the critical value $b_c = b_c(E_{th})$ will be defined by

$$b_c(E_{th}) = \max\{b > 0 : \rho_0(E_{th}, b) = 0\}, \\ = \min\{b > 0 : \rho_0(E_{th}, b) > 0\}. \tag{3.4}$$

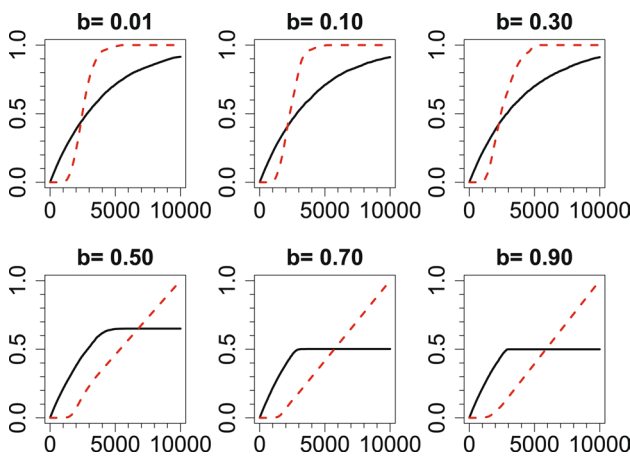


Fig. 3 R_t (solid lines) and $Q_t^{(T)}$ (broken lines) are shown as functions of time steps $t \in \{0, 1, \dots, T\}$ with $T = 10^4$ for $b = 0.01, 0.10, 0.30, 0.50, 0.70$ and 0.90 , where we set $E_{th} = 10$. The abscissas show time steps

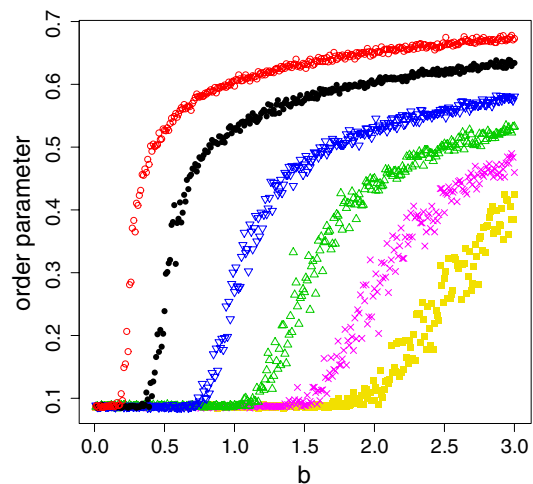


Fig. 4 Order parameters as functions of b for $E_{th} = 5$ (denoted by open circle), 10 (filled circle), 20 (inverted triangle), 30 (triangle), 40 (cross) and 50 (square)

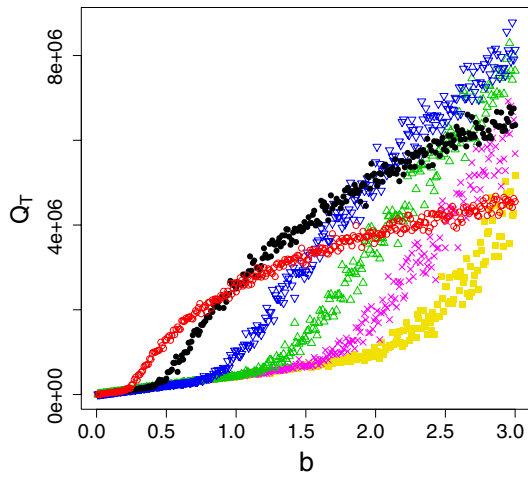


Fig. 5 Q_T with $T = 10^4$ versus b for $E_{th} = 5$ (denoted by open circle), 10 (filled circle), 20 (inverted triangle), 30 (triangle), 40 (cross) and 50 (square)

Figure 5 shows the b -dependence of $Q_T = Q_T(E_{th}, b)$ for $E_{th} = 5, 10, 20, 30, 40$, and 50. The result implies that, for $b < b_c(E_{th})$, $\lim_{t \rightarrow \infty} Q_t < \infty$, while for $b > b_c(E_{th})$, $\lim_{t \rightarrow \infty} Q_t = \infty$ (see the remark given at the end of Sect. 1). Thus, the critical value $b_c(E_{th})$ is also characterized as

$$b_c(E_{th}) = \max \left\{ b > 0 : \lim_{t \rightarrow \infty} Q_t < \infty \right\}, \tag{3.5}$$

$$= \min \left\{ b > 0 : \lim_{t \rightarrow \infty} Q_t = \infty \right\}.$$

As an analogy of the second-order phase transitions associated with critical phenomena in the equilibrium statistical mechanics, singular behavior of the order parameter in the vicinity of transition point b_c in State A is expected to be described by the following power-law,

$$\rho_0 \sim (b - b_c)^\beta, \quad 0 < b - b_c \ll 1, \tag{3.6}$$

with an exponent β [11–13].

For each value of E_{th} , we performed the numerical fitting of the data to the power-law (3.6) and evaluated values of b_c and β . For example, the curve in Fig. 6 shows the obtained curve (3.6) by fitting the data for $E_{th} = 10$, which gives $b_c = 0.44$ and $\beta = 0.34$. As we will report in the next subsection, the critical value b_c depends on E_{th} , but we found that the dependence of evaluated β on E_{th} is very small; $\beta = 0.31$ – 0.39 for $E_{th} = 5$ – 50 .

3.3 Critical line between State A and State B

We have evaluated the critical values $b_c = b_c(E_{th})$ as $b_c(5) = 0.22, b_c(10) = 0.44, b_c(20) = 0.90, b_c(30) = 1.30, b_c(40) = 1.75$ and $b_c(50) = 2.25$, respectively. They are

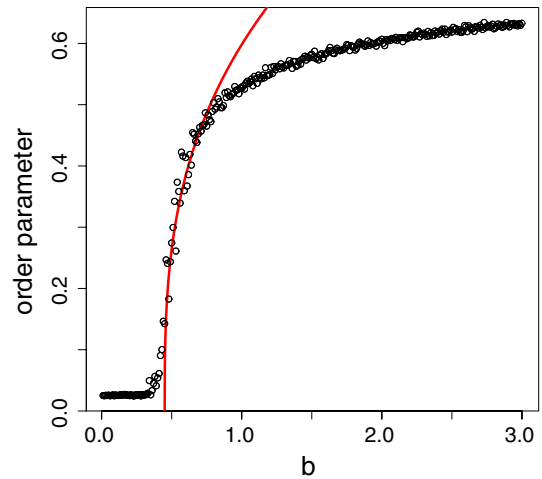


Fig. 6 Simulation result of the order parameter ρ_0 for $E_{th} = 10$. The curve shows (3.6) with $b_c = 0.44$ and $\beta = 0.34$. In the vicinity of critical value b_c in State A, the power-law behavior (3.6) is observed

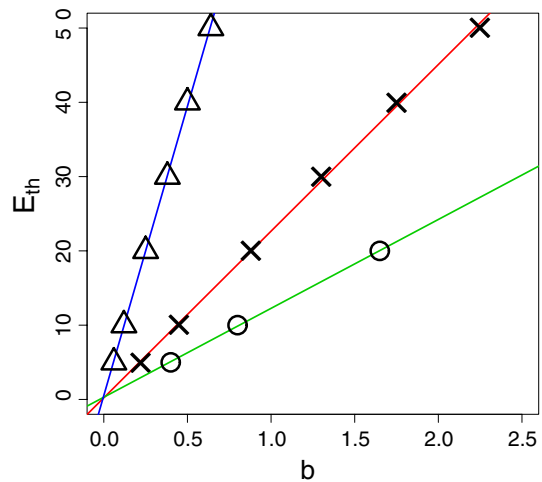


Fig. 7 The values of b_c of several E_{th} 's are shown by \times 's for the system with size $L = 64$. The critical line is well described by a straight line, $b_c = c(L)E_{th}$ with $c(L = 64) \simeq 0.045$, which divides State A (the lower right region) from State B (the upper left region). The critical values evaluated for the systems with sizes $L = 50$ and $L = 100$ are also plotted by open circle's and triangle's, respectively. We have evaluated the coefficients of critical lines as $c(50) \simeq 0.084$ and $c(100) \simeq 0.013$

plotted by cross marks in Fig. 7. We can see that the critical line is well described by a straight line,

$$b_c = cE_{th} \quad \text{with } c \simeq 0.045. \tag{3.7}$$

As discussed in Sect. 4, the critical value $b_c(E_{th})$ also depends on the lattice size L . Because of the long-ranged Coulomb potential (2.5), $b_c(E_{th})$ decreases monotonically as L increases. In other words, the coefficient in (3.7) is L -dependent; $c = c(L)$, and $\lim_{L \rightarrow \infty} c(L) = 0$.



Fig. 8 Cluster structure formed in the steady state, when $(E_{\text{th}}, b) = (10, 0.65)$. Occupied sites are *dotted*

In this sense, the transitions between State A and State B are not usual phase transitions, which should be defined in infinite-size (thermodynamic) limits. Therefore, Fig. 7 cannot be regarded as a phase diagram. In the present study, we are interested in transitions in non-equilibrium states found on a surface of device with a mesoscopic scale. The values themselves of $b_c(E_{\text{th}})$ as well as $c(L)$ reported here are not so important, since they change depending on system size. Our preliminary study by numerical simulations for different lattice sizes imply, however, that the linear dependence of b_c on E_{th} is universal as far as the system size is large but finite as shown in Fig. 7. Note that validity of the power-law (3.6) has been numerically confirmed also for different sizes of L with $\beta \simeq 0.3$.

3.4 Cluster structures in State A

For $(E_{\text{th}}, b) = (10, 0.65)$, a configuration of clusters on the surface obtained in the steady state (at $T = 10^4$) is plotted in Fig. 8, where occupied sites by particles are dotted. For $E_{\text{th}} = 10$, we have estimated $b_c = 0.44$. Then this figure shows a self-controlled surface-configuration realized in State A. Averaging over ten independent simulations, distribution of cluster size $|C_T(\mathbf{r})|$ on the steady-state surface in State A is calculated. Figure 9 shows it for $(E_{\text{th}}, b) = (10, 0.65)$. A peak is found around $s \simeq 11$, which is consistent with our choice of parameter $s_0 = 12$ in the simulation. The present results are consistent with the experimental observation reported by [5] as well as the simulation results by [14].

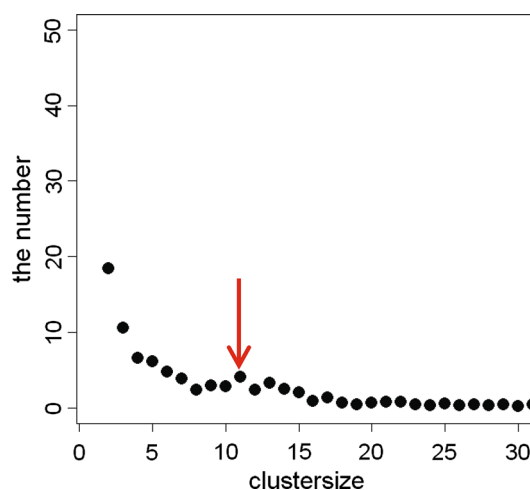


Fig. 9 Cluster size distribution in the steady state, when $(E_{\text{th}}, b) = (10, 0.65)$. As indicated by an *arrow*, a peak is found around $s \simeq 11$

4 Concluding remarks

In the present paper, we generalized the cellular automaton model [13] by Naruse et al. [14] and proposed a new stochastic model to describe the nonequilibrium dynamics of Ag film pattern formation on an electrode of the photovoltaic device of Yukutake et al. [5]. In the present new model, not only the number of deposited particle $n_t(\mathbf{r})$ but also the amount of charge $q_t(\mathbf{r})$ are considered as stochastic variables at each site \mathbf{r} in the $L \times L$ square lattice at time $t \in \mathbb{N}_0$. The previous model used the ‘pseudo-footprint’ method to take into account the repulsive interaction between an Ag^+ ion approaching the surface and positively charged Ag clusters on the surface. In the present algorithm of model, the repulsive Coulomb potential at each site caused by all charges on the lattice except the site is exactly calculated at each time step, and drift and deposition processes are simulated. The essential improvement of the model is such that we include the effect of optical near-fields generated by light–matter interaction by introducing a parameter b and a function $f(s)$. There b denotes the incident light power per site on the lattice and $f(s)$ expresses the size-dependent resonance effect of optical near-fields on matter-size s . We have regarded b as an external control parameter of the model. We have shown that, as b increases, there occurs a transition of the surface state of pattern formation with a critical value b_c , such that if $b \leq b_c$ the optical near-fields are not induced effectively (State B), while if $b > b_c$ they are induced effectively and Ag deposition process is self-controlled (State A). A nontrivial and unique Ag film is formed in State A, while in State B random Ag deposition will be continued as long as the simulation is continued.

We have discussed the transitions of surface processes from State B to State A by the analogy of equilibrium second-order phase transitions with critical phenomena [11–13]. We also studied the dependence of b_c on the threshold energy E_{th} for elementary deposition of single Ag^+ on the surface.

The transition of surface state discussed in this paper is not a phase transition in the usual sense, since our model is defined on a lattice with a finite size $L < \infty$; $L = 64$ for the simulation data reported above. In equilibrium and hence in stable systems, the $L \rightarrow \infty$ limit will provide the thermodynamic limit and it describes macroscopic behavior of materials. In the present model, however, the direct $L \rightarrow \infty$ limit may be meaningless, since the repulsive Coulomb repulsive potential (2.5) will diverge as $L \rightarrow \infty$ in the late stage of process in which sufficient amount of charge is accumulated on the surface. (It implies that b_c should be a decreasing function of L , since $V(\mathbf{x})$ given by (2.5) will take larger value as L increases, and $b_c \rightarrow 0$ as $L \rightarrow \infty$ for all $E_{th} > 0$.) In the present study, we are interested in nonequilibrium deposition dynamics of charged particles on mesoscopic materials. We should assume that the system size L of model is sufficiently large but finite.

From the view point of study of nonequilibrium statistical mechanics [11–13], it is an interesting problem to find a relevant scaling limit which can realize the present transitions of surface state as nonequilibrium phase transitions. A preliminary study by changing the lattice size L in numerical simulations implies that the parameter b should be scaled as $b = b_0 L^{-(2+\nu)}$ with a constant b_0 and a scaling exponent ν in the infinite-size limit $L \rightarrow \infty$. The dependence of $c(L)$ on L reported in Fig. 7 is consistent with it and gives a preliminary estimate $\nu \simeq 0.7$. Such a mathematical

physics aspect of the present model is also interesting and will be reported elsewhere.

Acknowledgments The present authors would like to thank S. Tojo for useful discussions on the present work. This study is supported by the Grant-in-Aid for Challenging Exploratory Research (No. 15K13374) of Japan Society for the Promotion of Science. MK is supported in part by the Grant-in-Aid for Scientific Research (C) (No. 26400405) of Japan Society for the Promotion of Science.

References

1. M. Ohtsu, T. Kawazoe, T. Yatsui, M. Naruse, *IEEE J. Sel. Top. Quantum Electron.* **14**, 1404 (2008)
2. S. Tojo, M. Hasuo, *Phys. Rev. A* **71**, 012508 (2005)
3. M. Ohtsu, *Dressed Photons: Concepts of Light-Matter Fusion Technology, Nano-Optics and Nanophotonics* (Springer, Berlin, 2014)
4. T. Franzl, T.A. Klar, S. Schietinger, A.L. Rogach, J. Feldmann, *Nano Lett.* **4**, 1599 (2004)
5. S. Yukutake, T. Kawazoe, T. Yatsui, W. Nomura, K. Kitamura, M. Ohtsu, *Appl. Phys. B* **99**, 415 (2010)
6. C. Pistol, C. Dwyer, A.R. Lebeck, *IEEE Micro* **28**, 7 (2008)
7. T. Kawazoe, M.A. Mueed, M. Ohtsu, *Appl. Phys. B* **104**, 747 (2011)
8. M. Naruse, N. Tate, M. Aono, M. Ohtsu, *Rep. Prog. Phys.* **76**, 056401 (2013)
9. M. Naruse (ed.), *Nanophotonics Information Physics: Nanointelligence and Nanophotonics Computing, Nano-Optics and Nanophotonics* (Springer, Berlin, 2014)
10. T. Yatsui, W. Nomura, M. Ohtsu, *Nano Lett.* **5**, 2548 (2005)
11. J. Marro, R. Dickman, *Nonequilibrium Phase Transitions in Lattice Models* (Cambridge University Press, Cambridge, 1999)
12. R. Mahnke, J. Kaupužs, I. Lubashevsky, *Physics of Stochastic Processes: How Randomness Acts in Time* (Wiley-VCH, Germany, 2009)
13. B. Chopard, M. Droz, *Cellular Automata Modeling of Physical Systems* (Cambridge University Press, Cambridge, 1998)
14. M. Naruse, T. Kawazoe, T. Yatsui, N. Tate, M. Ohtsu, *Appl. Phys. B* **105**, 185 (2011)
15. K. Kobayashi, S. Sangu, H. Ito, M. Ohtsu, *Phys. Rev. A* **63**, 013806 (2000)

H. Tanaka*, T. Kawazoe, M. Ohtsu, and K. Akahane

Decreasing the threshold current density in Si lasers fabricated by using dressed-photons

Abstract: We fabricated a silicon (Si) laser by applying a dressed-photon–phonon assisted annealing process to a ridge-type light waveguide that we fabricated via silicon-on-insulator (SOI) technology. We also evaluated a near-infrared Si photodiode having optical gain to estimate the differential gain coefficient for designing light waveguides. We designed light waveguides having a thickness of 15 μm to realize a large optical confinement factor. The fabricated Si laser oscillated at a wavelength of 1.4 μm . The intensity of amplified spontaneous emission (ASE) light was too low to be observed, because the threshold current density was so low that the Si laser started oscillating immediately after ASE occurred. The threshold current density for oscillation was estimated to be 40 A/cm^2 from the current–voltage characteristic. This threshold current density was twenty-eight times smaller than that of a Si laser we fabricated previously.

Keywords: Waveguide; Ridge-type; SOI; ASE; Optical confinement factor; Si-PD

DOI 10.1515/fma-2015-0001

Received January 8, 2015; accepted March 4, 2015

1 Introduction

Many passive optical devices made of Si, such as light waveguides and photodiodes, have been developed be-

cause optical devices made of Si can be easily integrated into electronic circuits. In contrast, it is difficult to develop Si-based active optical devices, such as light emitting diodes (LEDs) and lasers, because Si is an indirect transition semiconductor. Nevertheless, many researchers have been trying to realize Si lasers. For examples, optical gain from Si nanocrystals [2] and light emission from nanocrystalline Si material [3] were reported and Si lasers have been developed using the Raman effect [4] and quantum effects [5]. However, these approaches have disadvantages; from the first to the third requires photoexcitation of electrons, whereas the fourth involves a complex fabrication process, and in addition, these approaches result in low gain.

We have succeeded in developing a near-infrared Si laser that oscillated continuously at room temperature via current injection [6]. This Si laser was made of bulk Si and was based on the principle of dressed-photons. We call this device a 1G (1st Generation) Si laser. The threshold current density of the 1G Si laser was 1.1 kA/cm^2 , which was as large as that of a near-infrared semiconductor laser fabricated from InGaAsP, which is a direct-transition-type compound semiconductor [7]. A dressed-photon is a quasi-particle representing a coupled state between a photon and an electron at the nanoscale [8]. Dressed-photons can couple to coherent phonons, resulting in the emergence of new quasi-particles called dressed-photon–phonons. These quasi-particles tend to occur around impurities in nano-material crystal lattices [9]. Before realizing the 1G Si laser, our group developed a near-infrared Si LED [10], a Si optical and electrical relaxation oscillator [11], and a Si photodiode having optical gain in the near-infrared region [12]. Also, as a related device, we realized a Si LED for visible light illumination [13]. In those studies, we analyzed how the dressed-photon–phonons contribute to photon emission from the devices [14, 15].

In the present work, we focused on the fact that Si, which can emit light via the principle of dressed-photon–phonons, has a very low transparent current density in the near-infrared region, and we attempted to decrease the driving current density and the threshold current density to lower values than those of the 1G Si laser. We evaluated

*Corresponding Author: **H. Tanaka:** Department of Electrical Engineering and Information Systems, Graduate School of Engineering, The University of Tokyo, 2-11-16 Yayoi, Bunkyo-ku, Tokyo 113-8656, Japan, E-mail: tanaka@nanophotonics.t.u-tokyo.ac.jp
T. Kawazoe, M. Ohtsu: Department of Electrical Engineering and Information Systems, Graduate School of Engineering, The University of Tokyo, 2-11-16 Yayoi, Bunkyo-ku, Tokyo 113-8656, Japan and International Center for Nano Electron and Photon Technology, Graduate School of Engineering, The University of Tokyo, 2-11-16 Yayoi, Bunkyo-ku, Tokyo 113-8656, Japan
K. Akahane: The National Institute of Information and Communications Technology, 4-2-1, Nukui-Kitamachi, Koganei, Tokyo 184-8795, Japan

the differential gain coefficient, and we designed and fabricated light waveguides with a high optical confinement factor. This paper describes the light emission principle, the design and fabrication of a light waveguide, and the results of experiments to evaluate the oscillation properties.

2 Principle of laser oscillation by dressed-photons

We adopted the same fabrication method used to fabricate the 1G Si laser. Briefly, an n-type Si substrate doped with phosphorus (P) was used as the laser substrate. This substrate was implanted with boron (B) via ion implantation, for forming a p-n homojunction. After fabricating light waveguides in the Si substrate and dicing the substrate to form waveguides of the required length, we applied a dressed-photon–phonon assisted annealing process [10] to diffuse the boron. Specifically, we applied a forward current to the light waveguide, causing boron diffusing by joule heating, while the edge of the waveguide was illuminated with laser light to generate dressed-photon–phonons which were localized around the boron atoms (within approximately the Bohr-radius of a Si electron). The dressed-photon-phonons let electron–hole pairs recombine, resulting in stimulated emission. The boron diffusing rate was controlled by the decreasing joule energy because photons generated by the stimulated emission were emitted outside the device. As a result, a B concentration with a spatial distribution suitable for efficiently generating stimulated emission was formed in a self-organized manner [10]. The probability of spontaneous emission after annealing was also higher than that before annealing, because the probability of spontaneous emission is proportional to that of stimulated emission. After above annealing method, laser oscillation occurs when forward current is applied to this device. The photon energy of this device’s laser oscillation was as high as that of the laser light used for annealing because the highest probability of stimulated emission was obtained at the photon energy of the annealing light [6].

The stimulated emission occurred via a two-step transition, which is explained in [10] as stimulated emission process (1”) and (2”). These processes (1”) and (2”) are the same as those used to fabricate the Si-LED previously proposed by the authors [10].

3 Design and fabrication of a Si laser

Conventional lasers using a direct-transition-type compound semiconductor emit light whose photon energy is as high as the bandgap energy of the semiconductor. Therefore, when evaluating the differential gain coefficient g' , the edge of the light waveguide is illuminated with laser light, and the emitted light, which reflects amplification or absorption in the light waveguide, is measured from the other edge as a function of the current density [16]. However, the same measuring method cannot be adopted for this laser [6], such as one made from Si, because the photon energy of the light emitted from the Si laser in this research was 0.94 eV (wavelength, 1.32 μm), which is less than the bandgap energy of Si, and thus this light cannot be absorbed by a Si crystal.

To solve this problem, to measure the differential gain coefficient g' , we used an infrared Si photodiode (Si-PD) with optical gain, which we developed previously [12]. Fig. 1(a) shows a photograph of the Si-PD, and Fig. 1(b) shows the measuring method. Specifically, we measured the current drop when light was made incident on the surface of the Si-PD, and we used this to estimate the differential gain coefficient. The reason why the current decreased is that the number of electrons inside the Si-PD decreased in proportion to the number of photons in the amplified incident light due to stimulated emission. The photosensitivity, which is the ratio of the reduction in current to the incident light power, can be expressed by [17]:

$$\frac{\Delta I}{P} = \frac{e}{h\nu} \left[\exp \left\{ g'(J - J_{tr})L \right\} - 1 \right], \quad (1)$$

where e is the electronic charge, $h\nu$ is photon energy, J is the injected current density, J_{tr} is the transparent current density, and L is the length through which photons travel in the active layer. We assumed that L was 2 μm , because light was reflected at the back side, like Fig. 1(b), and went through the active layer (1 μm thick) two times. We could detect the incident light with high sensitivity by measuring the reduction in current because the incident light was amplified and the current density decreased when the injected current density to the Si-PD was larger than the transparent current density J_{tr} . Fig. 2 shows the dependence of the photosensitivity on the forward current density measured by the above method. The incident light wavelength was $\lambda = 1.32 \mu\text{m}$. We assumed a transparent current density J_{tr} of 5 A/cm² because we confirmed that the photosensitivity increased rapidly when the forward current density exceeded 5 A/cm². We calculated g' to be 38.4 cm/A from expression 1.

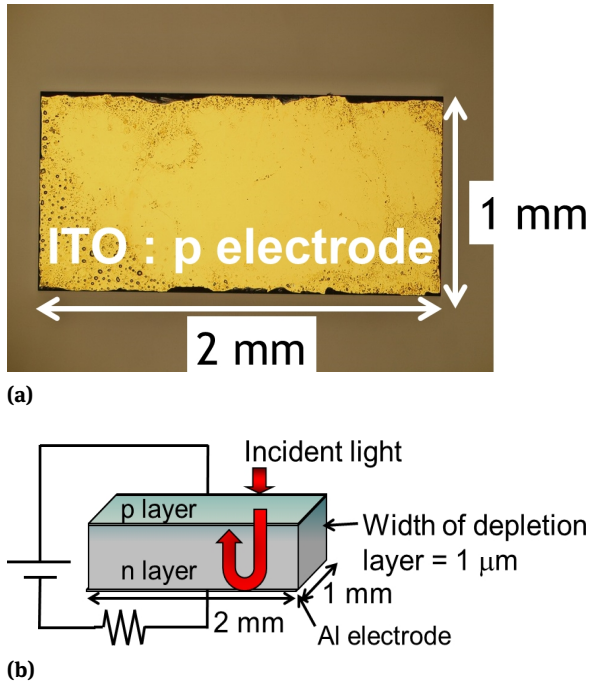


Figure 1: Estimation of the differential gain coefficient using a near-infrared Si-PD with optical gain. (a) Photograph of Si-PD, and (b) measuring method.

In addition to g' , we also need the optical confinement factor Γ to calculate the threshold current density J_{th} . We calculated Γ by the equivalent refractive index method. We used the following expression [18] to calculate J_{th} :

$$\Gamma g' (J_{th} - J_{tr}) = \alpha_{int} + \frac{1}{2l} \ln \left(\frac{1}{R_f R_b} \right), \quad (2)$$

where α_{int} is the internal loss coefficient, which consists of light absorption by the material, light leakage due to surface roughness of the walls, and so on; l is the length of the light waveguide; R_f is the reflectance of the front edge of the light waveguide from which light is emitted; and R_b is the reflectance of the back edge of the light waveguide. The optical confinement factor of the 1G Si laser was very low (4.7×10^{-4}), and R_f , R_b , J_{tr} , and l were 31%, 31%, 5 A/cm², and 250 μm respectively. Assuming that the internal loss was composed of only light absorption, we have $\alpha_{int} = 1.6 \times 10^{-5} \text{ cm}^{-1}$. By substituting these values into expression 2, we calculated $J_{th} = 2.6 \text{ kA/cm}^2$. This value of J_{th} was almost the same as a measured value of 1.1–2.0 kA/cm² reported in the literature [6], showing that this method of measuring g' by using an infrared Si-PD with optical gain was highly accurate.

The very low Γ value of the 1G Si laser allowed us to improve the Γ value, and we can considerably reduce J_{th} and the driving current density. We calculated the relationship between J_{th} and Γ first. We substituted $R_f = R_b = 31\%$,

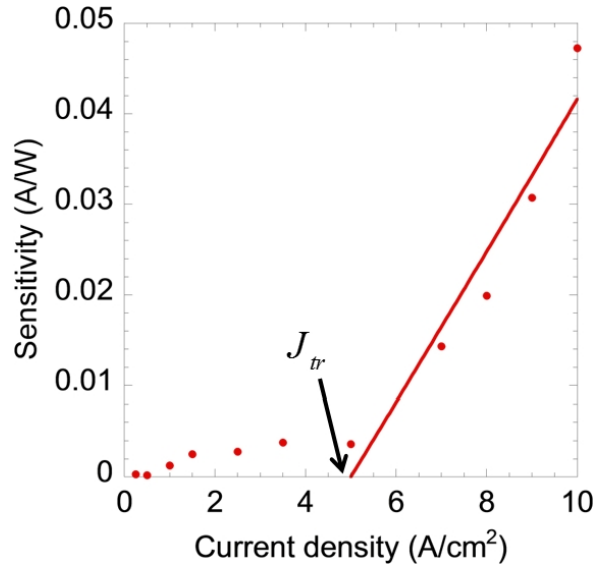


Figure 2: Measurement results of dependency of photosensitivity on forward current density for Si-PD with optical gain at wavelength $\lambda=1.32 \mu\text{m}$.

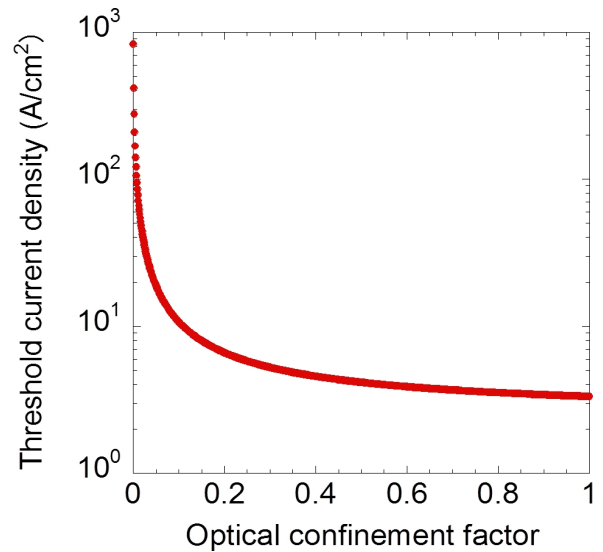


Figure 3: Calculation results showing relationship between the optical confinement factor and the threshold current density.

$J_{tr} = 5 \text{ A/cm}^2$, and $l = 500 \mu\text{m}$ into expression 2. We also assumed a waveguide optical loss of $\alpha_{int} = 1.6 \times 10^{-5} \text{ cm}^{-1}$, which is as large as that of the 1G Si laser.

Fig. 3 shows the calculated relationship between Γ and J_{th} . According to this figure, we needed to improve the optical confinement factor to more than 0.16 to obtain a J_{th} of less than 8.8 A/cm², which is less than one-hundredth that of the 1G Si laser (1.1 kA/cm²) [6].

Fig. 4 shows the schematic structure of the device we designed to obtain high Γ . The device layer was 15 μm thick, and the thickness and width of the ridge-

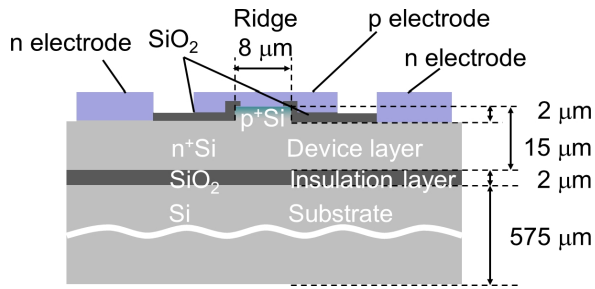


Figure 4: Schematic structure of the designed device.

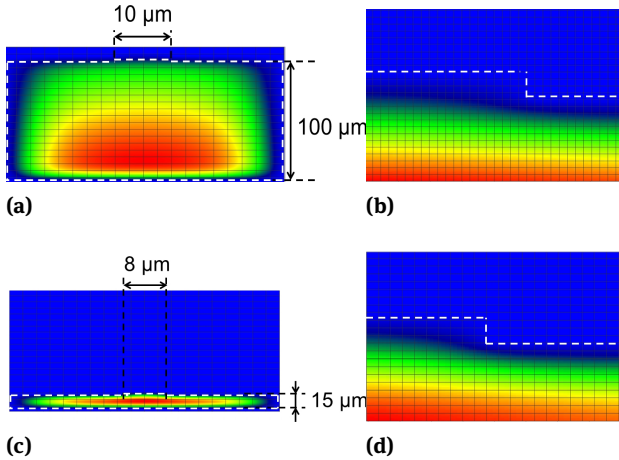


Figure 5: Cross-sectional intensity distributions of light beam that propagated inside the Si laser, calculated by simulation. White broken line: Shape of the device

- (a) Result for 1G Si laser
 (b) A magnified view of part of (a), at the corner of the waveguide ridge.
 (c) Result for the device we designed.
 (d) A magnified view of part of (c), at the corner of the waveguide ridge.

type light waveguide were 2 μm and 8 μm , respectively. We adopted the silicon-on-insulator (SOI) technique to achieve a 15 μm -thick device layer. Figs. 5(a) and (b) are cross-sections of the intensity distributions of the light that propagated inside the Si laser, calculated by simulation using the ADI-BPM method. In Fig. 5, (a) shows the result for the 1G Si laser, (b) is a magnified view of a portion of (a) at a corner of the ridge, (c) shows the result for the device we designed, and (d) is a magnified view of a portion of (c), at a corner of the ridge. These results show that the optical confinement effect of the device we designed was improved by the smaller cross-sectional shape of the light beam. The light beams in both devices were not only confined inside the ridge but propagated through the whole device layer.

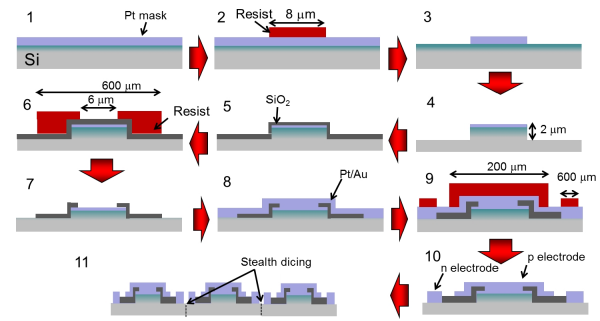


Figure 6: Overview of the fabrication process.

The SOI substrate consisted of a device layer whose material was n-type Si, doped with phosphorus, with a resistivity of 0.020–0.034 Ωcm , a SiO_2 layer (insulation layer: 2 μm thick), and a Si support substrate (575 μm thick). Boron ions were doped into the device layer by ion implantation to form a p-type layer. The highest implantation energy was 700 keV, and the boron ion concentration was $1 \times 10^{19} / \text{cm}^3$. From simulation calculations, a p-n junction interface was formed at a depth of 1.5–2.5 μm from the surface of the SOI.

After ion implantation, we cleaned the surface of the substrate with SPM (a 1:1 by volume solution of sulfuric acid: hydrogen peroxide), at 150 $^\circ\text{C}$ for 30 minutes and hydrofluoric acid. After that, we processed the SOI by following the procedure described below. Fig. 6 shows an overview of the process.

1. We deposited a chrome/platinum film (5 nm Cr, 670 nm Pt) on the surface of the SOI by RF sputtering.
2. We applied electron-beam (EB) resist (OEBR-CAP112) on the Cr/Pt layer on the SOI surface by spin coating before patterning the resist to form a stripe (8 μm width) by EB lithography.
3. We etched the chrome/platinum by ICP-RIE etching with argon (Ar) gas.
4. We used the Cr/Pt stripe fabricated by step 3 above as mask, and we etched the device layer with CF_4 gas to fabricate a ridge-type light waveguide (2 μm thick, 8 μm wide).
5. We deposited an SiO_2 film on the surface of the light waveguide by plasma CVD with TEOS gas, and we used this film as an insulating film.
6. We applied resist as in step 2 above, and then patterned the resist by EB lithography to eliminate insulating film (SiO_2 film) that was deposited on the light waveguide or part of the device layer surface.

7. We etched the SiO_2 with CHF_3 gas and to expose the top side of the light waveguide and part of the device layer surface.
8. We deposited a chrome/platinum/gold film (5 nm Cr, 400 nm Pt, 400 nm Au) by RF sputtering for use as an electrode.
9. We applied EB resist again, and patterned the resist by EB lithography to separate the p and n electrodes.
10. We etched and divided the Cr/Pt/Au film with Ar gas to fabricate p and n electrodes on a p layer and an n layer, respectively. In this way, we fabricated a number of light waveguides on the SOI substrate.
11. We diced the SOI substrate by stealth dicing to form separated light waveguides lying next to each other. We also diced the SOI substrate to fabricate both edges of a resonator.

Fig. 7(a), (b), and (c) show SEM cross-sectional images of the light waveguide edge after process steps 4, 5, and 8, respectively. Fig. 7(d) shows a photograph of the light waveguide. The fine line at the center enclosed by a rectangle indicated in a broken line is the waveguide. The length of the waveguide was $500\ \mu\text{m}$.

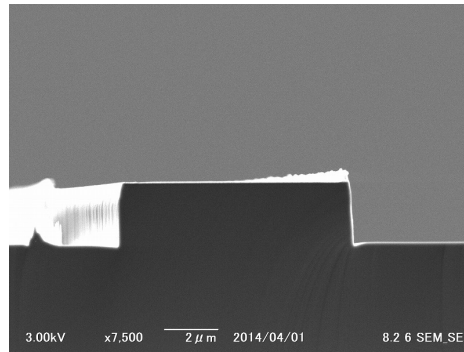
We applied dressed-photon–phonon assisted annealing to a light waveguide fabricated by the above process. Specifically, we injected current (1 kHz frequency, $100\ \mu\text{s}$ pulse width, $775\ \text{A}/\text{cm}^2$ peak current, 3.2 V peak voltage) to the light waveguide and heated it with Joule heat. Simultaneously, we illuminated the $8\ \mu\text{m}$ -wide light waveguide with laser light ($1.31\ \mu\text{m}$ wavelength, 1 mW power) to form a guided wave. The annealing time was 1.5 hours.

4 Characterization of Si laser and discussion

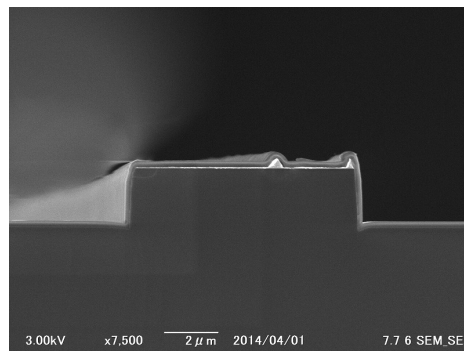
We measured the laser spectrum and estimated the threshold current density, as described below.

4.1 Laser spectrum

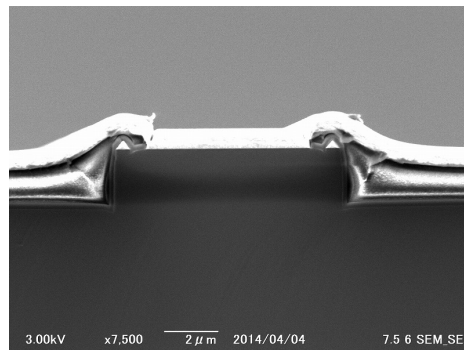
The curve in red in Fig. 8 is the laser spectrum at room temperature ($25\ ^\circ\text{C}$). The current density was $J = 42\ \text{A}/\text{cm}^2$. (When we use the value of J_{th} estimated in Subsection 2 below, we can write $J/J_{th} = 1.05$). The integration time of the spectrometer was 20 seconds, and we averaged nine laser spectra, which means that laser oscillation continued for at least 160 to 180 seconds. This spectrum showed a small width and a sharp peak at $1.4\ \mu\text{m}$. The reason why there



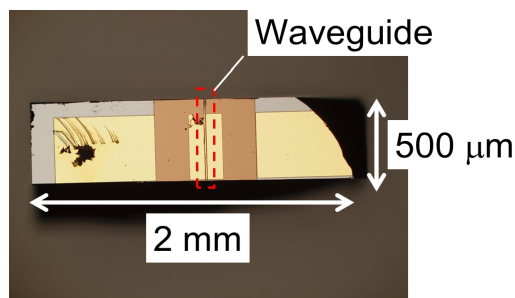
(a)



(b)



(c)



(d)

Figure 7: (a), (b), (c) SEM cross-sectional images of light waveguide edge after process steps 4, 5, and 8, respectively. (d) A light microscope image of the light waveguide.

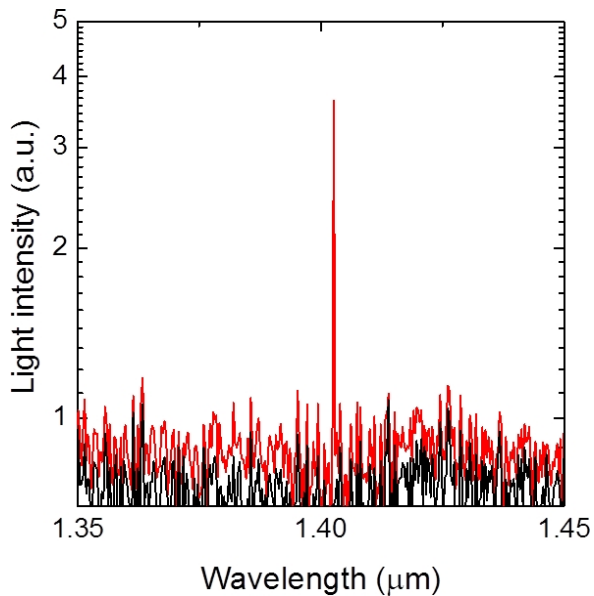


Figure 8: Measurement results of laser spectrum. Red: Above the threshold current density ($J/J_{th} = 1.05$) Black: Below the threshold current density ($J/J_{th} = 0.95$)

was only a single mode despite the relatively long cavity length is because the light absorption loss is low, and this laser starts oscillating with a low gain whose gain width is still narrow and within the homogeneous width. On the other hand, the curve in black in Fig. 8 shows the spectrum obtained when the current density was below the threshold current density (current density $J = 38 \text{ A/cm}^2$, $J/J_{th} = 0.95$) We did not observe amplified spontaneous emission (ASE). The reason for this that, because the threshold current was so low that the gain was entirely concentrated into the wavelength of spontaneous emission light when spontaneous emission was amplified, the state changed to an oscillating state at once. In other words, the Si laser started oscillating immediately after ASE occurred.

4.2 Estimation of threshold current density

We used the current–voltage characteristics to estimate the threshold current density of this Si laser. We could accurately estimate the threshold current density by measuring an extremely small current drop [19] in the current–voltage characteristics because electrical energy was immediately converted to photon energy when the current density reached the threshold current density. Fig. 9 is a current–voltage characteristic obtained 30 minutes after starting dressed-photon–phonon assisted annealing. We measured the voltage and current with an oscilloscope while applying a forward current for annealing. The ap-

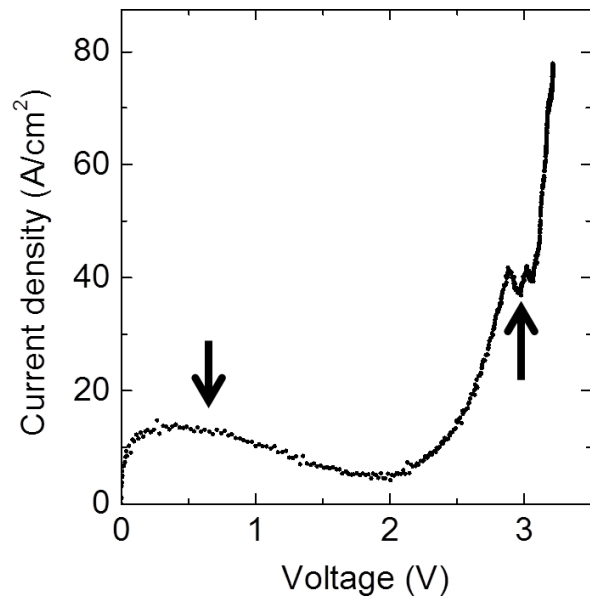


Figure 9: Measured current–voltage characteristic 30 minutes after starting dressed-photon–phonon assisted annealing.

plied current had a frequency of 1 kHz, a pulse width of $100 \mu\text{s}$, a peak voltage of 3.2 V, and a peak current density of 77.5 A/cm^2 . We observed a minuscule current drop when the Si laser started oscillating 30 minutes after starting dressed-photon–phonon assisted annealing. The upward-pointing arrow in Fig. 9 indicates the minuscule current drop around 3 V (the current density was 40 A/cm^2). We estimated the current threshold density, J_{th} , at 40 A/cm^2 from the position of this up arrow. This value of the threshold density is twenty-eight times smaller than that of the 1G Si laser ($J_{th} = 1.1 \text{ kA/cm}^2$), showing that we successfully decreased the threshold current density. In addition, this Si laser had a negative resistance property, as indicated by the downward-pointing arrow, because of floating capacitance.

The reason why the estimated threshold current density was higher than the designed value of 8.8 A/cm^2 is as follows: The actual value of the internal loss coefficient was thought to be higher than the designed value ($1.6 \times 10^{-5} \text{ cm}^{-1}$). If we assume that the value of the internal loss coefficient, α_{int} , is 20 cm^{-1} (taking the value of an InGaAsP laser [20] as reference), the optical confinement factor that corresponds to a threshold current density of 40 A/cm^2 is 0.032. This value is less than the designed value. We will attempt to achieve the designed threshold current density of 8.8 A/cm^2 by optimizing the fabrication process to decrease the internal loss coefficient and increase the optical confinement factor.

5 Summary

The objective of this research was to reduce the threshold current density of a Si laser. To achieve this, first, we evaluated a near-infrared Si photodiode having optical gain to estimate the differential gain coefficient for designing light waveguides with a high optical confinement factor. We used an SOI substrate to fabricate light waveguides with a thickness of 15 μm . We fabricated a Si laser by using dressed-photon–phonon assisted annealing. The laser oscillated at 1.4 μm . The intensity of ASE was very low because the threshold current density was so low that the Si laser oscillated immediately after ASE occurred. We estimated the threshold current density of oscillation to be 40 A/cm^2 from the current–voltage characteristic because we observed a minuscule current drop at 40 A/cm^2 when we applied a bias voltage of 3 V to the Si laser, causing the Si laser to start oscillating. This value of the threshold current density was twenty-eight times smaller than that of the Si laser we fabricated previously.

Acknowledgement: This research was supported in part by Grant-in-Aid for JSPS Fellows Number 25 905 and JSPS Core-to-Core Program, A. Advanced Research Networks.

This research was implemented in part by the Advanced ICT Research Institute of NICT.

We thank N. Yamamoto for enlightening discussions.

References

- [1] Di L. and Bowers J. E., *Nat. Photonics*, 2010, 4, 511–517.
- [2] Pavesi L., Negro L. Dal, Mazzoleni C., Franzo G., Priolo F., *Nature*, 2000, 408, 440–444
- [3] Neal R.T., Charlton M. D. C., Parker G. J., Finlayson C. E., Netti M. C. Baumberg J.J., *Appl. Phys. Lett.*, 2003, 83, 4598–4600
- [4] Takahashi Y., Inui Y., Chihara M., Asano T., Terawaki R., Noda S., *Nature*, 2013, 498, 470–474.
- [5] Saito S., Suwa Y., Arimoto H., Sakuma N., Hisamoto D., Uchiyama H., et al., *Appl. Phys. Lett.*, 2009, 95, 241101–1–3.
- [6] Kawazoe T., Ohtsu M., Akahane K., Yamamoto N., *Appl. Phys. B*, 2012, 107, 659–663.
- [7] Rosenzweig M., Mohrle M., Duser H., Venghaus H., 1991, 21, 1804–1811.
- [8] Ohtsu M., "Dressed Photons -Concepts of LightMatter Fusion Technology-," Springer, 2013
- [9] Tanaka Y., Kobayashi K., *Physica E*, 2007, 40, 297–300
- [10] Kawazoe T., Mueed M. A., Ohtsu M., *Appl. Phys. B*, 2011, 104, 747–54.
- [11] Wada N., Kawazoe T., Ohtsu M., *Appl. Phys. B*, 2012, 108, 25–29.
- [12] Tanaka H., Kawazoe T., Ohtsu M., *Appl. Phys. B*, 2012, 108, 51–56.
- [13] Tran M.A., Kawazoe T., Ohtsu M., *Appl. Phys. A*, 2014, 115, 105–111
- [14] Wada N., Tran M.A., Kawazoe T., Ohtsu M., *Appl. Phys. A*, 2014, 115, 113–118
- [15] M. Yamaguchi, T. Kawazoe, M. Ohtsu, *Appl. Phys. A*, 2014, 115, 119–125
- [16] Kimura Y., A. Ito, Miyachi M., Takahashi H., Watanabe A., H. Ota, Ito N., Tanabe T., et al., 2001 *Jpn. J. Appl. Phys.* 40 L1103–L1106
- [17] Soibel A., Mansour K., Qiu Y., Hill C. J., Yang R. Q., *J. Appl. Phys.*, 2007, 101, 093104–1–4
- [18] Kazi Z. I., Egawa T., Jimbo T., Umeno M., *IEEE Photonics Technol. Lett.*, 1999, 11, 1563–65
- [19] Agrawal G.P., Dutta N.K., *Semiconductor Lasers*. 2nd ed. New York: Van Nostrand Reinhold, 1993
- [20] Higuchi H., Namizaki H., Oomura E., Hirano R., Sakakibara Y., Susaki W., et al., *Appl. Phys. Lett.*, 1982, 41, 320–321



OPEN

SUBJECT AREAS:
QUANTUM DOTS
DISPLAYSReceived
3 October 2014Accepted
21 January 2015Published
16 February 2015Correspondence and
requests for materials
should be addressed to
R.H. (hirayama@
chiba-u.jp)

Design, Implementation and Characterization of a Quantum-Dot-Based Volumetric Display

Ryuji Hirayama¹, Makoto Naruse², Hiroataka Nakayama¹, Naoya Tate³, Atsushi Shiraki⁴, Takashi Kakue¹, Tomoyoshi Shimobaba¹, Motoichi Ohtsu⁵ & Tomoyoshi Ito¹

¹Graduate School of Engineering, Chiba University, 1-33 Yayoi-cho, Inage-ku, Chiba 263-8522, Japan, ²Photonic Network Research Institute, National Institute of Information and Communications Technology, 4-2-1 Nukui-kita, Koganei, Tokyo 184-8795, Japan, ³Graduate School of Information Science and Electrical Engineering, Kyushu University, 744 Motooka, Nishi-ku, Fukuoka 819-0395, Japan, ⁴Department of Information and Computer Engineering, Kisarazu National College of Technology, 2-1-1 Kiyomidai-higashi, Kisarazu, Chiba 292-0041, Japan, ⁵Graduate School of Engineering, The University of Tokyo, 2-1-1-16 Yayoi, Bunkyo-ku, Tokyo 113-8656, Japan.

In this study, we propose and experimentally demonstrate a volumetric display system based on quantum dots (QDs) embedded in a polymer substrate. Unlike conventional volumetric displays, our system does not require electrical wiring; thus, the heretofore unavoidable issue of occlusion is resolved because irradiation by external light supplies the energy to the light-emitting voxels formed by the QDs. By exploiting the intrinsic attributes of the QDs, the system offers ultrahigh definition and a wide range of colours for volumetric displays. In this paper, we discuss the design, implementation and characterization of the proposed volumetric display's first prototype. We developed an $8 \times 8 \times 8$ display comprising two types of QDs. This display provides multicolour three-type two-dimensional patterns when viewed from different angles. The QD-based volumetric display provides a new way to represent images and could be applied in leisure and advertising industries, among others.

Volumetric displays are one of the most interesting technologies for three-dimensional (3D) display and human-computer interactions and thus have received significant research attention^{1,2}. Unlike conventional two-dimensional displays, a volumetric display has a physical 3D architecture that enables 3D images to be observed from any surrounding viewpoint. Various volumetric displays have been proposed previously in the literature; e.g. arrays of light-emitting diodes arranged in a 3D layout or arrays of strings on which an image is projected, where the strings serve to scatter light³. However, to date, the presence of occlusion, which is the distortion of a part of the image viewed from a certain direction because of the scattering from the electrical wiring or other scattering centres, has led to a significant degradation in the quality of the 3D images (Fig. 1a).

In this paper, we present a volumetric display that eliminates occlusion by using quantum dots (QDs) arranged in a 3D manner. In our device, the light-emitting elements are formed by the QDs. Irradiation by an external invisible or visible light source excites the QDs and generates spontaneous emission; this in turn creates patterns that can be simultaneously observed from various viewing angles. Figure 1b schematically shows the concept of the volumetric display based on QD luminescence, where three different patterns ('X', 'Y', and 'Z') are observed from different viewing directions without occlusion. In addition, for simplicity, we employ other patterns in the experimental demonstrations while maintaining essential operating principles.

In addition to eliminating the electrical wiring, our QD-based volumetric display has various other unique features. The emission spectrum of the QDs depends on their size and constituent material; thus, various colours can be achieved⁴. Small-diameter QDs emit light with short wavelengths, whereas large-diameter QDs emit light with long wavelengths. Compared with other luminescence materials, the QDs exhibit higher quantum efficiencies and narrower emission spectra⁵. The 2D displays using these features of the QDs have attracted considerable attention⁶⁻⁸ and have previously been used in practical applications. Notably, these favourable properties are also important for the 3D volumetric display applications. Moreover, when the different-sized QDs are closely packed, optical energy transfer occurs among them because of the nanometre-scale near-field interactions⁹. Although this

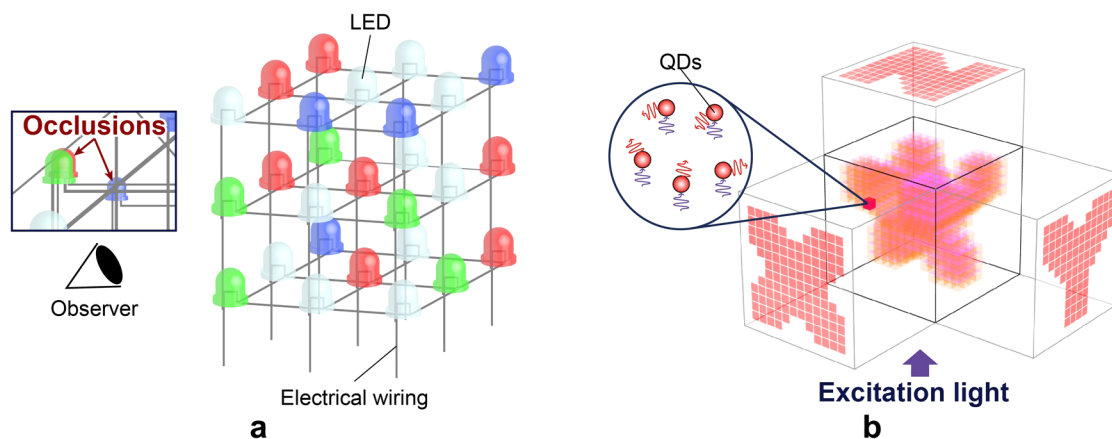


Figure 1 | Illustration of the concept of this study. (a) Occlusion occurs when a part of the image viewed from a certain direction is distorted by light scattered from the electrical wiring or other scattering centres. (b) Quantum-dot-based volumetric display exhibits different patterns when viewed from different angles. Each voxel contains quantum dots that are excited by external irradiation.

energy-transfer mechanism has not been used for the experiment reported herein, it will be exploited to provide additional functionality in future. In the sections below, we describe the design, fabrication and characterization of the proposed QD-based volumetric display.

Results

Design. In this study, we developed a QD-based volumetric display that exhibits three different images that may be viewed simultaneously from three orthogonal viewpoints. Let a voxel be denoted by V_{ijk} , where i, j and k take the values $1, \dots, N$, giving a total of N^3 voxels. The value of V_{ijk} is specified by the type of the QDs present in the corresponding voxel and is zero if there are no QDs. Let the type of a QD be given by $\{S_1, S_2, \dots, S_M\}$, where M is the number of the QD types. The images observed from the x, y and z axes are given by $A_{ij} = \sum_{k=1}^N V_{ijk}$, $B_{jk} = \sum_{i=1}^N V_{ijk}$ and $C_{ki} = \sum_{j=1}^N V_{ijk}$, respectively. Note that here, the summation does not necessarily imply arithmetic addition in the usual sense; rather, it implies the addition of the light spectra and is recognized as a given colour by the human eye. For instance, if S_1 is red and S_2 is green, the sum $S_1 + S_2$ is yellow. Furthermore, as shown below, in our experimental prototype, the sequence of S_i as observed from a viewpoint could be important depending on the absorption and transmission coefficients of each voxel.

For our experimental prototype, we selected $N = 8$, and V_{ijk} could take values of 0, red or green. Therefore, because red + green = yellow, we get a total of four colours (red, green, yellow and no colour or transparent).

To completely convey the capacity of our QD-based volumetric display, we designed the voxels for (i) the three resulting images (A, B and C) to differ from each other and (ii) yellow to appear only in one of the three images. Figure 2a schematically shows the design in which patterns A (top-left panel), B (lower-left panel) and C (lower-middle panel) differ from each other; only pattern C contains yellow. The design of each layer is presented in Fig. 2b. Although the formula described above does not enable three arbitrary patterns to be created without any artefact, Nakayama *et al.* have recently demonstrated a novel algorithm for the design of voxels that provide arbitrary numbers and arbitrary images by distributing the effects of the artefacts¹⁰. This method may be applied to the proposed QD-based volumetric display.

Implementation. Figure 3a shows a photograph of the solid blocks containing the QDs used as the light-emitting voxels. In this photograph, the blocks are exposed to ultraviolet radiation with

302 nm wavelength (AS ONE, 'MID-170', Transilluminator). The blocks containing QDs are made by encapsulating a certain amount of the QDs in a clear polydimethylsiloxane (PDMS) polymer. (Details are given in the Methods section.) The absorption spectra of the QDs are barely affected by the inclusion in the polymer because PDMS is a heat-curable resin that is transparent at visible light wavelengths. Because of its transparency, PDMS is used in various applications^{11,12}. We made two types of blocks. When irradiated by ultraviolet light, the QDs in one block emit red light, whereas those in the other block emit green light; we refer to these blocks as the 'red block' and the 'green block', respectively. They have dimensions of approximately $1 \text{ cm} \times 1 \text{ cm} \times 1 \text{ cm}$.

The solid curves in Fig. 3b show the normalized emission spectra of the red and green blocks, as well as the spectrum of the ultraviolet radiation used for excitation. The dashed curves in Fig. 3b show the absorption spectra of the red and green blocks. To obtain the emission spectra, an ultraviolet laser with 325 nm wavelength (KIMMON KOHA CO., 'IK3052R-BR') was used to excite the QD blocks. The photoluminescence spectra of the red and green blocks peaked at 629 and 541 nm, respectively. After the inclusion in polymers, the peak emissions of the red and green blocks were shifted towards longer wavelengths by 14 nm and 11 nm, respectively. These red shifts were caused by the subtle energy flow to the polymer. The photoluminescence spectra show similar red shifts; however, the red shifts were barely altered by the emission intensities. On the other hand, each absorption spectrum shows that both the red and green blocks absorbed little visible light.

To fabricate the prototype of the QD-based volumetric display with $8 \times 8 \times 8$ voxels, we followed the steps as follows: (1) We cut each block into $2.5 \text{ mm} \times 2.5 \text{ mm} \times 2.5 \text{ mm}$ cubes, which we call 'QD voxels'. (2) We arrange the QD voxels into a mould in accordance with the layer design shown in Fig. 2b. The eight layers are made separately. (3) We pour a defoamed polymer, which is a mixture of base and curing agent into the mould. (4) We solidify the polymer by heating at 130°C for approximately 3 h; the solidified polymer that includes the QD voxels becomes one of the layers. (5) By stacking the eight layers, we obtain an $8 \times 8 \times 8$ -voxel QD-based volumetric display.

Figure 4 shows the images of the resulting QD-based volumetric display acquired by a CMOS camera. Under white light irradiation, the volumetric display emits essentially no visible light (Fig. 4a). Under ultraviolet irradiation, 3D colour images appear (Fig. 4b). The chequered pattern is visible from the x, y and z directions (Fig. 4c), as are the striped (Fig. 4d) and uniform patterns (Fig. 4e).

We used the images captured by the CMOS camera to characterize the quality of the images emitted by the volumetric display. Figure 5

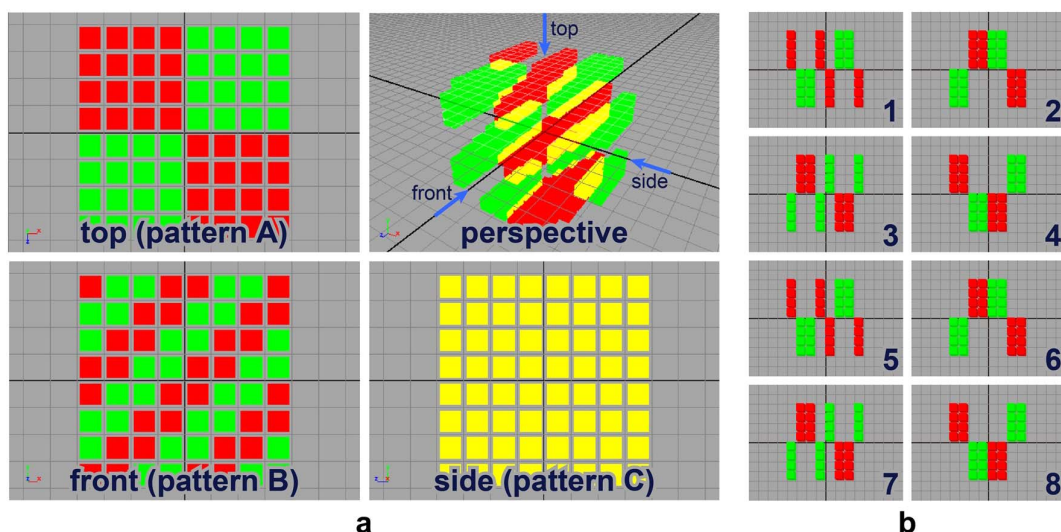


Figure 2 | Design of a QD-based volumetric-display prototype. (a) QD-based volumetric display viewed from different angles. The prototype comprises $8 \times 8 \times 8$ voxels. (b) Design data for the QD-based volumetric display consisting of eight layers.

shows the average luminance, or the RGB pixel values, of (1) the red and green blocks (Fig. 5a), (2) pattern A (emitted from the top of the volumetric display; Fig. 5b), (3) pattern B (emitted from the front; Fig. 5c) and (4) pattern C (emitted from the side; Fig. 5d). In our design, patterns A and B contain red and green pixels; four red and four green voxels yield a single projected pixel (this is the case for all the red and green pixels). In addition, the yellow pixels in pattern C consist of a combination of two red and two green voxels. Fig. 5a shows that the red and green blocks exhibit high R and G values, respectively. However, with respect to the red pixels of patterns A and B, the G and R values increase and decrease together (see Figs. 5b and 5c). We attribute the increase in the G values to the diffusion of light from the green voxels. The same trend is observed for the green pixels of patterns A and B. In addition, pattern C exhibits higher values for both R and G than the red pixels of patterns A and B, which implies that yellow is obtained by a mixture of light from the red and green voxels. Moreover, we show the maximum and minimum RGB values in Figs. 5b, 5c and 5d.

The variance in the pixel RGB values may depend in part on the nonuniformity in the voxel sizes that arises from the fabrication

process. However, the mechanism that should also be considered is as follows. As mentioned previously, when the order of the voxels changes with respect to the source of irradiation, the absorption and transmission coefficients of each voxel may cause the colour emitted in a given direction to change. We evaluated such a case by arranging a red block and a green block in series, denoted by 'RG' (Fig. 6a, left), and for the opposite order, it is denoted by 'GR' (Fig. 6a, right). The dotted and solid curves in Fig. 6b show the photoluminescence spectra of the RG and GR combinations, respectively. The peak photoluminescence from the green block (541 nm) is shifted by approximately 29% for RG vs. GR, indicating that the emitted colour depends on the order of excitation. Figure 6c shows the spectral difference in a chromaticity diagram. The chromaticity coordinates are calculated on the basis of the colour-matching function defined by the Commission Internationale de l'Eclairage. The distance between the two points on the chromaticity diagram is 3.56×10^{-2} . Near the chromaticity coordinates of the RG and GR emissions, the human eye cannot differentiate two colours separated by less than approximately 0.5×10^{-2} on the chromaticity diagram¹³. Thus, the separation of 3.56×10^{-2} between the RG and GR emis-

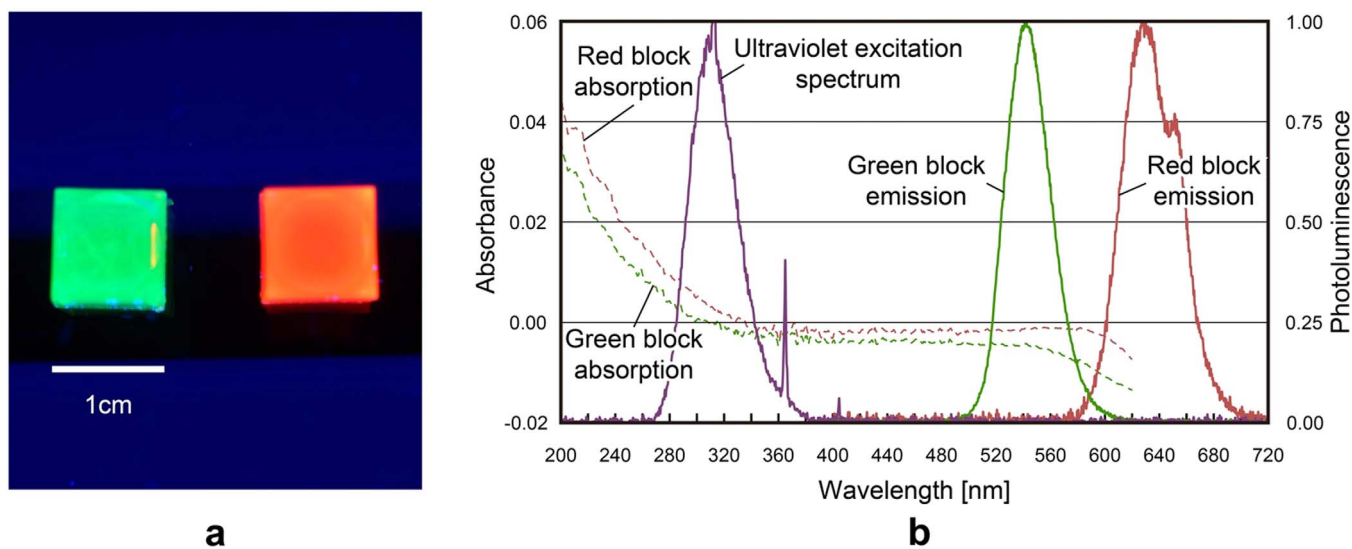


Figure 3 | Solid blocks containing QDs. (a) Photographs of the red and green blocks when excited by ultraviolet irradiation. (b) Normalized absorption and emission spectra of the red and green blocks. The spectrum of the ultraviolet excitation source used to excite the QDs is also shown.

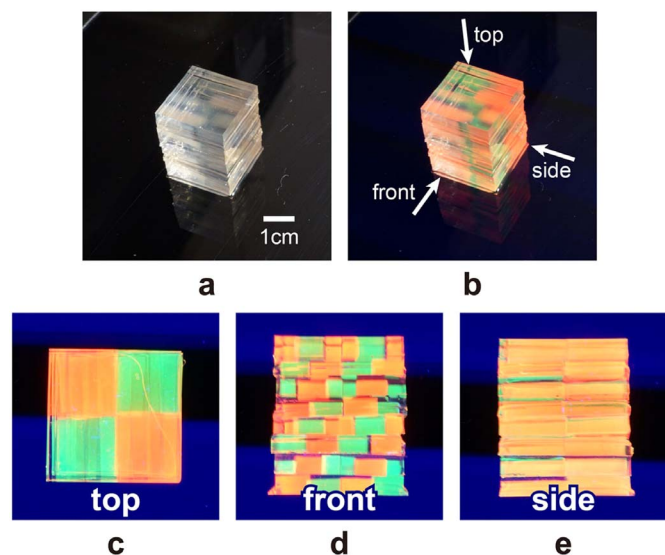


Figure 4 | Prototype of QD-based volumetric display. (a) View under natural light. (b) View when excited by ultraviolet light. Patterns when viewed from (c) the top, (d) front and (e) side.

sions is easily detected by the human eye, and therefore, different colours are observed.

Discussion

In this study, although we have only used red-light and green-light emitting QDs, QDs that emit other colours are available and can be processed in the same manner as described herein; thus, we can easily increase the types of the QDs used to diversify the available colours.

Furthermore, we confirmed that all the QD voxels were in fact excited and emitted light when excited from underneath the volumetric display. This result indicates that occlusions do not need to be considered when arranging the QD voxels. In other words, the proposed QD volumetric display offers high-definition voxels.

We have experimentally demonstrated the principle of presenting multicolour images by combining red and green blocks to obtain a yellow colour. However, the inspection of the image in Fig. 4e shows that the ‘yellow’ colour from the side pattern does not obviously differ from the red colour from the top and the front. Notably, the RGB pixel values of the ‘red’ colour area of the top (Fig. 5b) and front (Fig. 5c) patterns overlap with those of the side (Fig. 5d) when we consider the error bars. From such a quantitative perspective, the difference between ‘yellow’ and ‘red’ is not indeed clear. However, to the human eye, the colour of the side pattern is distinctly different from that of the red pixels of the top and front patterns. Note that the average G and B values of the yellow pixels from the side (Fig. 5d) are larger than those of the red pixels from the top (Fig. 5b) and front (Fig. 5c). We attribute the colour difference perceived by the human eye to such increased average G and B values. Therefore, we consider the principle of multicolour to be successfully demonstrated experimentally.

The results also show that the photoluminescence spectra depend on the order in which the QD voxels are excited. The issue of the re-absorption of light emitted from the green QDs by the red QDs is important for the discussion of the order-dependent photoluminescence. For simplicity, we consider the case that a red QD voxel and a green QD voxel are placed close to each other and only the green QDs are excited by ultraviolet irradiation. Here, the sizes of the voxels and the concentrations of QDs are under the same conditions as the experiment. Thereby, 7.1% of green light irradiated from the green QDs is re-absorbed by the red QDs (the ratio of absorption is calculated from the absorbance spectrum.) Under green-light irra-

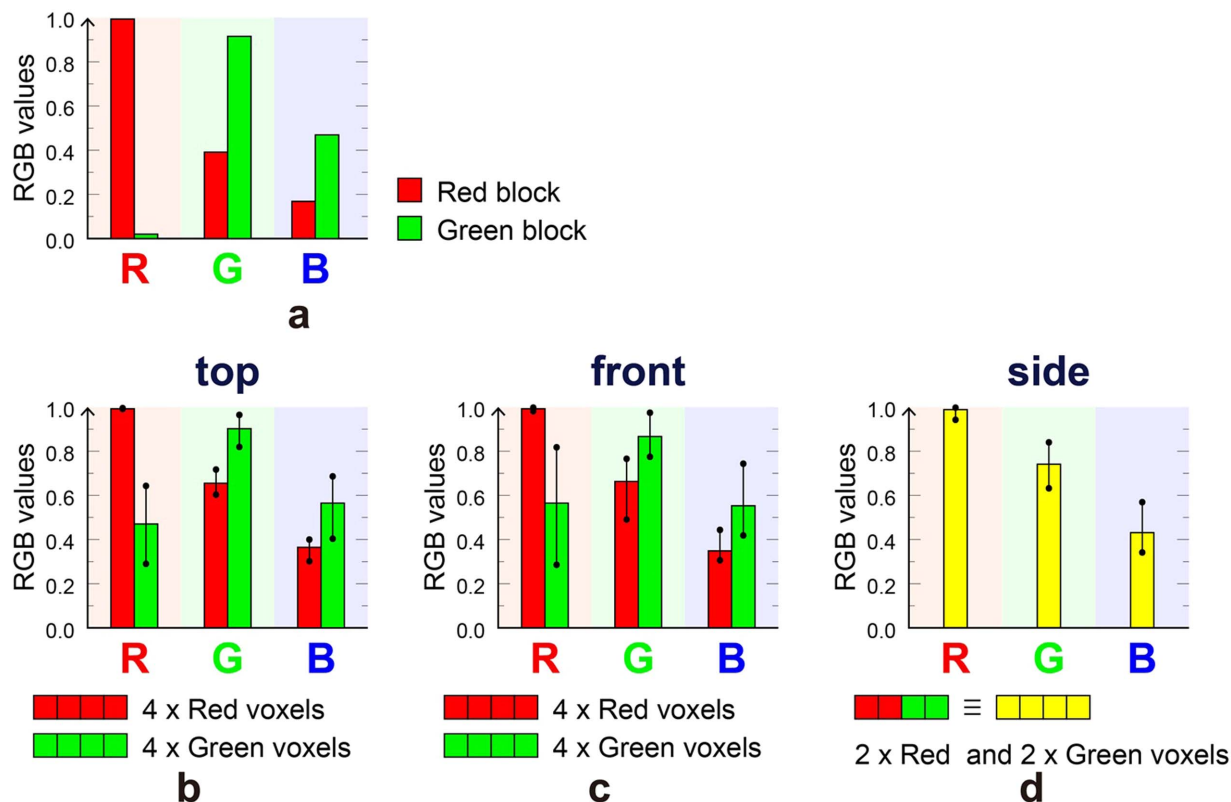


Figure 5 | Display quality. RGB values captured by CMOS camera. The labels ‘4 × red voxels’ or ‘4 × green voxels’ mean that except for four transparent voxels, there are four red voxels or four green voxels out of the eight voxels arranged in depth. (a) RGB values for pure red and green blocks. RGB values are also shown for (b) pattern A (top view), (c) pattern B (front view) and (d) pattern C (side view).

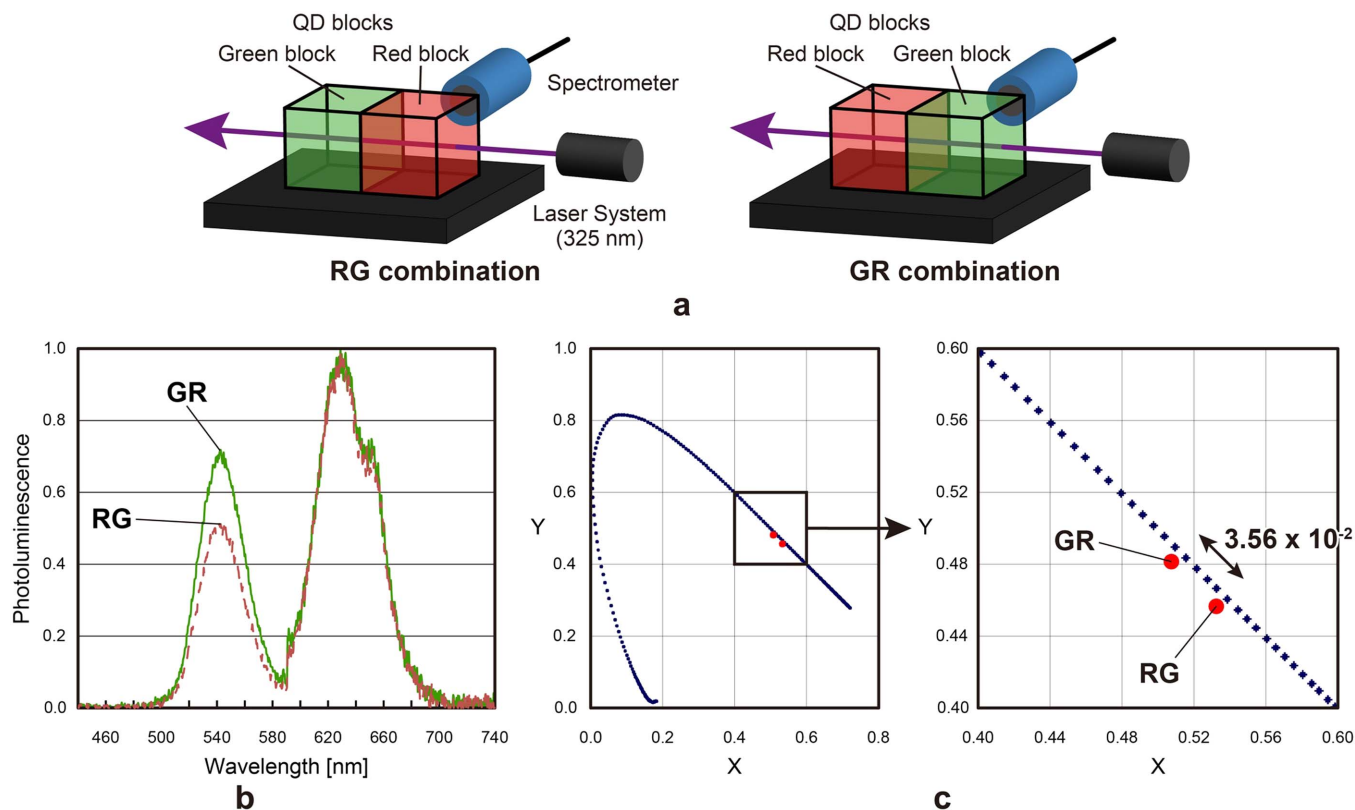


Figure 6 | Effect of QD-voxel order on proposed volumetric display. (a) Schematic of the experimental setup. (b) Observed photoluminescence spectra. (c) Effect of QD-voxel order that appears in the chromaticity diagram.

diation, the red QDs emit light that is generated from the absorbed light at an efficiency of approximately 32% (the quantum yield is obtained from the certificate of analysis by Sigma Aldrich Co.) Thus, the re-absorption can affect the colour represented by the volumetric display. However, Fig. 6b does not show the difference in the red-light emission between the RG and GR combinations. Although we do not need to consider the effect of the re-absorption for the low-integration scale of the experiment described in this study, an optimal design algorithm for the treatment of the re-absorption will be required for future applications at high definition and high integration.

In principle, the intensity of light emitted from a QD voxel can be adjusted by engineering the QD density for each specific voxel. However, this approach would make fabrication process very complicated. Thus, in future work, we will seek a strategy or a parameter regime that gives an acceptable performance for a given application. Simultaneously, we could also consider exploiting the order dependence of the photoluminescence to obtain different patterns for different viewpoints. Moreover, the excitation wavelength can be tuned to obtain interesting volumetric displays. For example, assume that we select QD_A and QD_B such that excitation E_1 excites only QD_A and excitation E_2 excites both QD_A and QD_B . This leads to an additional degree of freedom in the design and enables versatile patterns to be obtained from the QD-based volumetric displays. Furthermore, we will consider the improvement of the implementation process to achieve high definition and high integration. In addition, we will investigate the possibilities of adding further functions by using optical-near-field-mediated energy transfer between the QDs^{14–18}. For example, a QD mixture of different sizes in a voxel offers increased variety of colours because of the inter-QD energy transfer¹⁹.

In summary, we demonstrate herein a new QD-based volumetric display. Irradiation by the external light excites the QD voxels and

allows multiple patterns to be observed from various viewpoints with no occlusion. By using multiple types of QDs, a multicolour display is obtained.

Methods

QD-block preparation. A QD block is fabricated from colloidal QDs and a clear polymer. We used core-shell type CdSe/ZnS QDs (SIGMA-ALDRICH Co., Lumidot™ CdSe/ZnS) dispersed in toluene (5 mg QD per 1 mL toluene). Two types of CdSe/ZnS QDs were used: one with a peak emission at 610 nm and another with a peak emission at 530 nm. For the polymer, we used a SYLGARD 184 Silicone Elastomer Kit by Dow Corning Toray Co., which is made of PDMS and solidified by mixing two liquids (the base and the curing agent) in a ratio of 10 : 1. The base is a pre-polymer mostly consisting of dimethyl siloxane dimethylvinyl-terminated. The curing agent is primarily made of dimethyl methylhydrogen siloxane trimethylsiloxy-terminated, which yields a cross-linking of the PDMS to cure the pre-polymer by mixing the curing agent with the base. The procedure for making the QD blocks is as follows:

- (1) Stir 1.1 mL polymer (including 1.0 mL base and 0.1 mL curing agent) and 50 μ L (40 μ L) of the toluene solution that contains the CdSe/ZnS QDs for the red block (green block).
- (2) Pour the mixture into a 1 cm cube mould and defoam the mixture overnight under vacuum.
- (3) Solidify the polymer by heating at 130 °C for approximately 3 h.
- (4) Cut the solidified polymer to form the desired voxel size.

Lumidot™ CdSe/ZnS QDs are surface stabilized with organic ligands (hexadecylamine). Moreover, the QD blocks are expected to be more stable because inclusion in the polymer can prevent the effect of surface oxidation that is the main cause for the QD emission degradation. The emission intensity of a QD voxel may be adjusted by tuning the QD density. The QD density in the QD voxels is determined by the absorbance of the CdSe/ZnS QDs, the extinction coefficient of the CdSe/ZnS QDs and the toluene solution volume. In this study, the red voxels contained approximately 1.6×10^{12} of red QDs, and the green voxels contained approximately 9.3×10^{12} of green QDs per voxel.

1. Blundell, B. G., Schwarz, A. J. & Horrell, D. K. Volumetric three-dimensional display systems: their past, present and future. *Eng. Sci. Ed. J.* 2, 196–200 (1993).
2. MacFarlane, D. L. Volumetric three-dimensional display. *Appl. Optics* 33, 7453–7457 (1994).



3. Parker, M., Lumarca. *ACM SIGGRAPH ASIA 2009*. Art Gallery & Emerging Technologies: Adaptation, Yokohama, Japan, doi:10.1145/1665137.1665196 (2009, Dec. 16–19).
4. Mahler, B. *et al.* Towards non-blinking colloidal quantum dots. *Nature Mater.* **7**, 659–664 (2008).
5. Klimov, V. I. *Semiconductor and metal nanocrystals: synthesis and electronic and optical properties* (CRC Press, Boca Raton, 2003).
6. Lee, J., Sundar, V. C., Heine, J. R., Bawendi, M. G. & Jensen, K. F. Full color emission from II–VI semiconductor quantum dot-polymer composites. *Adv. Mater.* **12**, 1102–1105 (2000).
7. Coe, S., Woo, W. K., Bawendi, M. & Bulović, V. Electroluminescence from single monolayers of nanocrystals in molecular organic devices. *Nature* **420**, 800–803 (2002).
8. Wood, V. *et al.* Inkjet-printed quantum dot-polymer composites for full-color AC-driven displays. *Adv. Mater.* **21**, 2151–2155 (2009).
9. Naruse, M., Tate, N., Aono, M. & Ohtsu, M. Information physics fundamentals of nanophotonics. *Rep. Prog. Phys.* **76**, 056401 (2013).
10. Nakayama, H. *et al.* Three-dimensional volume containing multiple two-dimensional information patterns. *Sci. Rep.* **3**, 1931 (2013).
11. Wang, Y., Bish, S., Tunnell, J. W. & Zhang, X. MEMS scanner enabled real-time depth sensitive hyperspectral imaging of biological tissue. *Opt. Exp.* **18**, 24101–24108 (2010).
12. Tate, N., Nomura, W., Kawazoe, T. & Ohtsu, M. Novel wavelength conversion with nanophotonic droplet consisting of coupled quantum dots. *Opt. Exp.* **22**, 10262–10269 (2014).
13. MacAdam, D. L. Visual sensitivities to color differences in daylight. *J. Opt. Soc. Am.* **32**, 247–273 (1942).
14. Yukutake, S. *et al.* Selective photocurrent generation in the transparent wavelength range of a semiconductor photovoltaic device using a phonon-assisted optical near-field process. *Appl. Phys. B* **99**, 415–422 (2010).
15. Fujiwara, H., Kawazoe, T. & Ohtsu, M. Nonadiabatic multi-step excitation for the blue-green light emission from dye grains induced by the near-infrared optical near-field. *Appl. Phys. B* **98**, 283–289 (2010).
16. Kawazoe, T., Mueed, M. A. & Ohtsu, M. Highly efficient and broadband Si homojunction structured near-infrared light emitting diodes based on the phonon-assisted optical near-field process. *Appl. Phys. B* **104**, 747–754 (2011).
17. Kitamura, K., Kawazoe, T. & Ohtsu, M. Homojunction-structured ZnO light-emitting diodes fabricated by dressed-photon assisted annealing. *Appl. Phys. B* **107**, 293–299 (2012).
18. Kawazoe, T., Fujiwara, H., Kobayashi, K. & Ohtsu, M. Visible light emission from dye molecular grains via infrared excitation based on the nonadiabatic transition induced by the optical near field. *IEEE J. Sel. Top. Quantum Electron.* **15**, 1380–1386 (2009).
19. Naruse, M., Kawazoe, T., Ohta, R., Nomura, W. & Ohtsu, M. Optimal mixture of randomly dispersed quantum dots for optical excitation transfer via optical near-field interactions. *Phys. Rev. B* **80**, 125325 (2009).

Acknowledgments

This work is partially supported by JSPS Grant-in-Aid No. 25240015 and Core-to-Core Program, A. Advanced Research Networks.

Author contributions

R.H., M.N. and T.I. directed the project; R.H., H.N. and M.N. designed the system architecture and the experiments; N.T. and M.O. prepared the QD blocks; R.H., T.K. and N.T. performed optical characterizations; A.S. and T.S. contributed to the discussions.

Additional information

Competing financial interests: The authors declare no competing financial interests.

How to cite this article: Hirayama, R. *et al.* Design, Implementation and Characterization of a Quantum-Dot-Based Volumetric Display. *Sci. Rep.* **5**, 8472; DOI:10.1038/srep08472 (2015).



This work is licensed under a Creative Commons Attribution 4.0 International License. The images or other third party material in this article are included in the article's Creative Commons license, unless indicated otherwise in the credit line; if the material is not included under the Creative Commons license, users will need to obtain permission from the license holder in order to reproduce the material. To view a copy of this license, visit <http://creativecommons.org/licenses/by/4.0/>

Research Article

GaP Homojunction LEDs Fabricated by Dressed-Photon-Phonon-Assisted Annealing

Jun Hyoung Kim,¹ Tadashi Kawazoe,^{1,2} and Motoichi Ohtsu^{1,2}

¹Department of Electrical Engineering and Information Systems, Graduate School of Engineering, The University of Tokyo, 2-11-16 Yayoi, Bunkyo-ku, Tokyo 113-8656, Japan

²Nanophotonic Research Center, Graduate School of Engineering, The University of Tokyo, 2-11-16 Yayoi, Bunkyo-ku, Tokyo 113-8656, Japan

Correspondence should be addressed to Jun Hyoung Kim; kimjh@nanophotonics.t.u-tokyo.ac.jp

Received 5 August 2014; Revised 6 November 2014; Accepted 10 November 2014

Academic Editor: Gilles Lerondel

Copyright © 2015 Jun Hyoung Kim et al. This is an open access article distributed under the Creative Commons Attribution License, which permits unrestricted use, distribution, and reproduction in any medium, provided the original work is properly cited.

By using a homojunction-structured GaP single crystal, we generated a photon energy higher than the bandgap energy (2.26 eV). The device was fabricated by performing dressed-photon-phonon- (DPP-) assisted annealing, while applying a forward-bias current, on a p-n homojunction structure formed by implanting a dopant (Zn) into an n-type GaP substrate. The DPP-assisted annealing increased the light emission intensity in an energy band above 2.32 eV by at least 550% compared with that before annealing.

1. Introduction

In recent years, there has been interest in light-emitting diodes (LEDs) as high-efficiency light sources, and research and development has been actively carried out, resulting in remarkable technological progress, particularly in the last ten years. High-efficiency semiconductor light-emitting devices based on InGaN (for light emission in the blue-green band) and AlGaInP (for light emission in the green-red band) have been realized and are now in widespread use. However, there are a number of problems that must be solved. One of those is that a metal-organic vapor phase epitaxy (MOVPE) process, which uses toxic gases, is required for growing the substrates. The environmental load is also high since fine particles that are harmful to the human body could be produced [1]. In addition, finding the optimum conditions for the MOVPE process is not simple, and the growth conditions should be strictly controlled [2–5]. Moreover, this approach has a demerit in terms of material resources, including the need for In, which is a rare earth element.

To overcome the problems mentioned above, in this research we focused on GaP as the material and on dressed-photon-phonon- (DPP-) [6, 7] assisted annealing as the

process method. The bandgap energy, E_g , of GaP is 2.26 eV (wavelength, 548 nm). Also, GaP is a low-cost material that can be readily used to grow single crystals with the liquid encapsulated Czochralski (LEC) method, and research into light-emitting devices using GaP has been conducted for a long time, since as early as the 1960s [8, 9]. However, GaP is an indirect transition type semiconductor, and the light-emission efficiency is known to be extremely low since phonon emission and absorption are required for the radiative recombination of electron-hole pairs. A widely known technique for increasing the efficiency is to introduce isoelectronic impurities such as N atoms, and devices based on this approach are commercially available [10]. Isoelectronic impurities capture and localize electrons due to differences in electronegativity with respect to the component atoms of the host crystal. As a result, according to the uncertainty principle, the wave function of the electrons in wavenumber space becomes broader, making radiative recombination possible at yellow and green wavelengths. In addition, GaP LEDs that emit red light by the addition of Zn and O have also been reported [11]. However, the light-emission efficiency is low because of energy loss due to internal relaxation to the isoelectronic impurity levels. Furthermore, only photons

with energies lower than E_g are emitted, since light emission occurs via localized levels in the forbidden band.

On the other hand, if it were possible to effectively utilize the large E_g of GaP, it would be possible to develop a method that overcomes the environment-related problems and technical difficulties mentioned above, as well as to expand the color coverage of GaP LEDs. To this end, in this study we employed a dressed-photon-phonon- (DPP-) assisted annealing method. We have previously used DPPs to develop LEDs based on Si and SiC, which are also indirect transition type semiconductors, like GaP [12–14]. A dressed photon (DP) is a quasiparticle that represents the coupled state of a photon and an electron-hole pair in a nanosize region [7]. Similarly, a DPP is a quasiparticle that represents the coupled state of a DP and multimode coherent phonons in a nanosize region [6, 7]. In other words, by forming an impurity distribution that easily generates an interaction between electron-hole pairs, photons, and phonons inside a crystal, the limitation due to the wavenumber conservation law is relaxed, thus enabling high-efficiency radiative recombination even in an indirect transition type semiconductor [12–14]. The photon energy of this radiative recombination changes by an amount equal to the energies of multimode coherent phonons involved, and therefore, the photon energy of emitted light can be higher than E_g .

In this study, by subjecting a GaP crystal containing a p-n homojunction to DPP-assisted annealing, we obtained strong enhancement of light emission in the 520–540 nm wavelength band.

2. Principles of Light Emission and Processing Using DPPs

In this section, first we explain the principle of light emission using the DPP-assisted process, followed by a discussion of the processing principle. This is because the principle of light emission described below is also used in device processing. The DPP-assisted process [12] brought about as a result of interactions between electron-hole pairs, photons, and phonons in nanosize regions containing impurities is the basic principle of the light emission. During device processing, first, impurities are made to diffuse by changing the energy (via current and photoabsorption) given to the device into heat. In parts that have a nanostructure (impurity distribution) where the DPP-assisted process easily takes place, the energy is converted to light, and therefore, a relative cooling effect occurs [13]. Diffusion of impurities due to heat generation and maintaining the impurity distribution due to the relative cooling are the basic principles of device processing.

The light emission due to the DPP-assisted process can be understood using a model of the DPP levels as shown in Figure 1. Since the wavenumber is supplied from multimode coherent phonons, the DPP dispersion relation is represented by the horizontal green solid line in Figure 1. Since electron-hole pairs and phonons are strongly coupled, the ket vector representing this coupled state is expressed as the direct product \otimes of the electron state and the phonon state [7]. Here, el and phonon represent electrons and phonons,

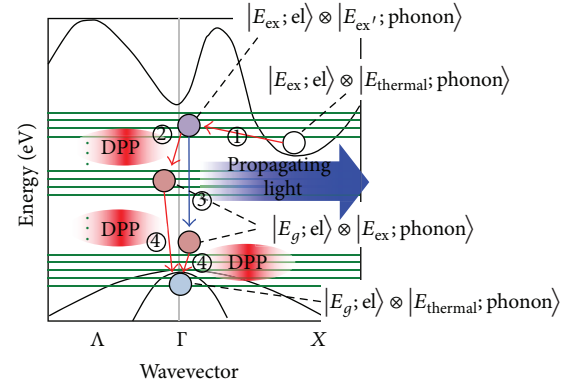


FIGURE 1: Light emission process via DPPs.

respectively, g represents the ground state, thermal represents thermal equilibrium, and ex and ex' represent excited states. First, the initial state is formed by injection of carriers from outside. In this initial state, since the electrons are in the excited state, and the phonons are in the thermal equilibrium state determined by the crystal lattice temperature, we have $|E_{ex}; el\rangle \otimes |E_{thermal}; phonon\rangle$. In this state, light emission is obtained via a process in which electrons transition to the ground state $|E_g; el\rangle \otimes |E_{thermal}; phonon\rangle$, that is to say, a process in which they transition to the valence band. This transition occurs via the intermediate states $|E_{ex}; el\rangle \otimes |E_{ex'}; phonon\rangle$ and $|E_g; el\rangle \otimes |E_{ex}; phonon\rangle$. Since transitions to the ground state via these intermediate states are electric-dipole-allowed transitions, not only are DPPs generated (Figure 1, ① \rightarrow ② \rightarrow ④), but so is propagating light (Figure 1, ① \rightarrow ③ \rightarrow ④). In addition, because of the multimode coherent phonons involved in this process, photon emission with an energy different from E_g is possible. An inverse process to this process, in other words, an absorption process due to DPPs, also exists.

Next, a processing method is described. In an indirect transition type semiconductor, since phonon absorption/emission is necessary during the emission of a photon, the radiative recombination probability is extremely low. However, in the light-emission process via DPPs, since the DP couples with multimode coherent phonons, the radiative recombination probability is high. In other words, an LED can be realized by exciting electrons to the conduction band with current injection and by using the above-described phonon absorption/emission processes. Also, the light emission wavelength of this device depends not on E_g , but on the energy of the DPPs generated in the vicinity of the p-n junction. That is to say, emitted light having an energy higher than E_g can be obtained [13, 14]. The problem is that, in the case of a normal semiconductor crystal, the DPP generation probability inside the crystal is low, and it is difficult to bring about transitions via DPP intermediate states. Here, we explain how to form, in a self-organized manner, a nanostructure that readily generates DPPs.

First, p-type impurities are implanted into an n-type substrate to form a p-n junction. Next, while irradiating the p-n junction with laser light, a forward-bias current is made to

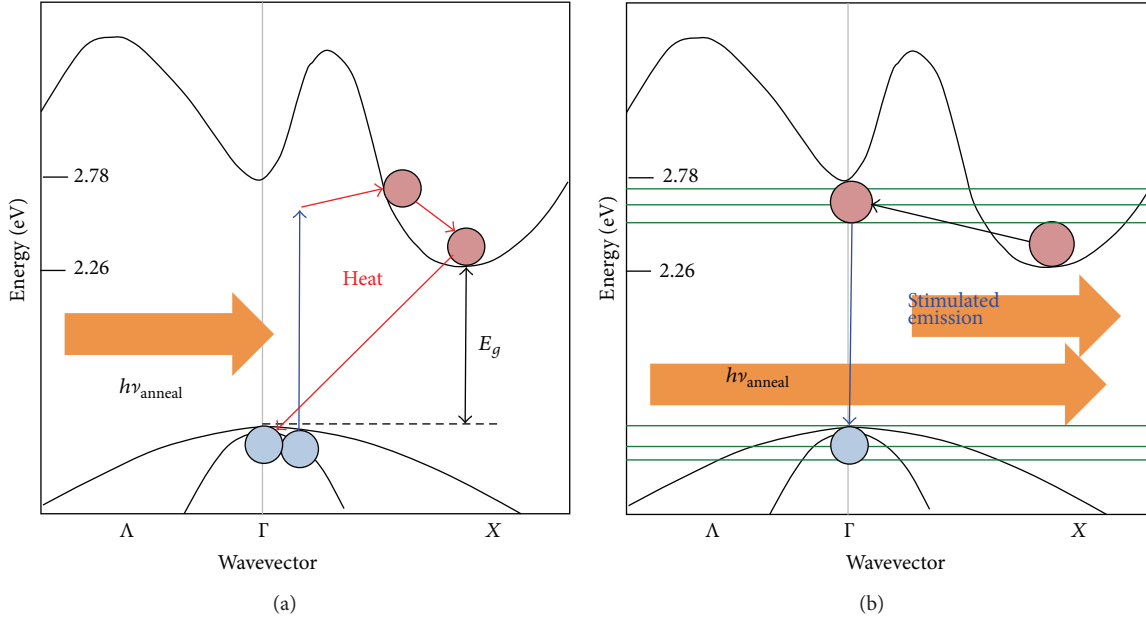


FIGURE 2: Principle of impurity diffusion by DPP-assisted annealing. (a) Heat generation due to light absorption. (b) Relative cooling due to stimulated emission.

flow to perform annealing. This processing method, known as DPP-assisted annealing [7, 12], changes the impurity distribution to a distribution suitable for generating DPPs. In the following, the processing principle is explained by dividing the distribution into a nanoregion that is not suitable for generating DPPs and a nanoregion that is suitable for generating DPPs.

(1) *Region Not Suitable for Generating DPPs.* If the photon energy of the irradiated laser light, $h\nu_{\text{laser}}$, is larger than E_g , as shown in Figure 2(a), an electron in the valence band absorbs a photon and is excited to the conduction band. This electron immediately emits a phonon due to intraband thermal relaxation and transitions to the bottom of the conduction band. Thermal energy $h\nu_{\text{laser}} - E_g$ is produced via this process. After relaxation, the electron-hole pair cannot undergo radiative recombination because of restrictions due to the wavenumber conservation law and instead undergoes nonradiative relaxation. Since this nonradiative relaxation also generates localized heat, all of the photon energy of the absorbed laser light is converted to thermal energy, causing dopant diffusion to proceed. As a result, Joule heating occurs due to the current, and heat generation occurs due to the nonradiative relaxation caused by the light irradiation.

(2) *Region Suitable for Generating DPPs.* Since a nonuniform domain boundary formed by the dopant (Zn) is formed inside the crystal by ion implantation at a high acceleration energy, the existence of a region that is suitable for generating DPPs locally can be expected. Let us assume that DPPs are generated around a certain Zn domain. In this case, as shown in Figure 2(b), at the electron-hole pairs, stimulated emission occurs via the DPP levels. As a result, unlike region (1), the locally absorbed energy is converted not only to thermal

energy but also to photon energy. Therefore, in the region around this Zn domain, heat generation is suppressed, and the diffusion rate is reduced.

In region (1), random diffusion continuously occurs, whereas in region (2), the diffusion rate is low. These diffusion processes continue until a structure suitable for generating DPPs is achieved. In addition, because the emitted light irradiates the whole device, it is not confined to the light-irradiation region but spreads in a self-organized manner throughout the whole device. When annealing is performed for a sufficiently long time, the concentration of Zn in the entire crystal is expected to take a spatial distribution that is optimal for stimulated emission via the DPP-assisted process. Moreover, since the probabilities of stimulated emission and spontaneous emission are proportional to each other [15], by using such a process, it is possible to realize an LED that emits photons.

3. Device Fabrication

The device fabrication process can be divided into two stages. First, a p-n homojunction structure is fabricated in a GaP single crystal by ion implantation. Then, the impurity distribution is altered by DPP-assisted annealing. The details of these are given below.

In the experiments performed in this study, we used an n-type (dopant: S) GaP single-crystal wafer with a thickness of $500 \mu\text{m}$ and a diameter of 50 mm , grown by the liquid encapsulated Czochralski (LEC) method. The orientation was (111), and the dopant concentration was 2×10^{17} to $4 \times 10^{17}/\text{cm}^3$ (resistivity, $0.05 \Omega\text{cm}$). This wafer was subjected to ion implantation to implant acceptors (Zn ions) with an implantation energy of 300 keV and a dose of $1.7 \times 10^{14}/\text{cm}^2$ to fabricate a p-n homojunction structure. By

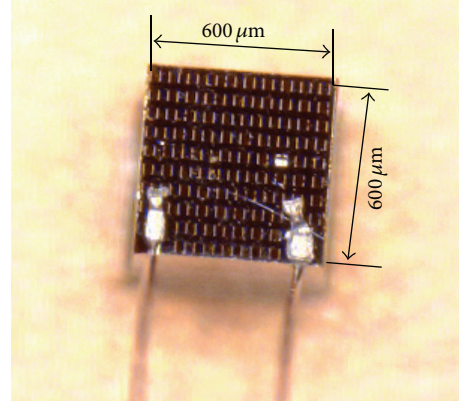
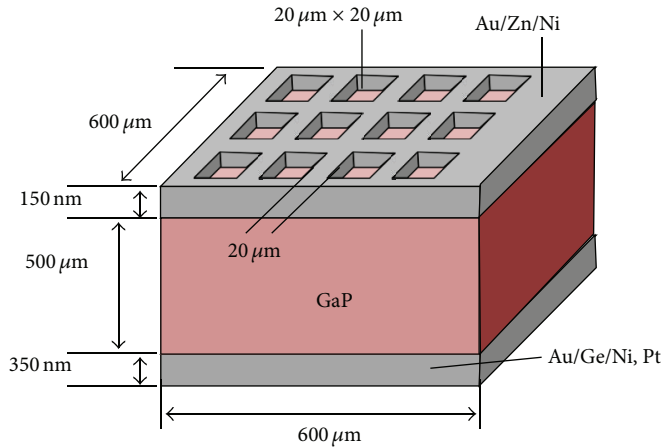


FIGURE 3: Schematic diagram of device and photograph of completed device.

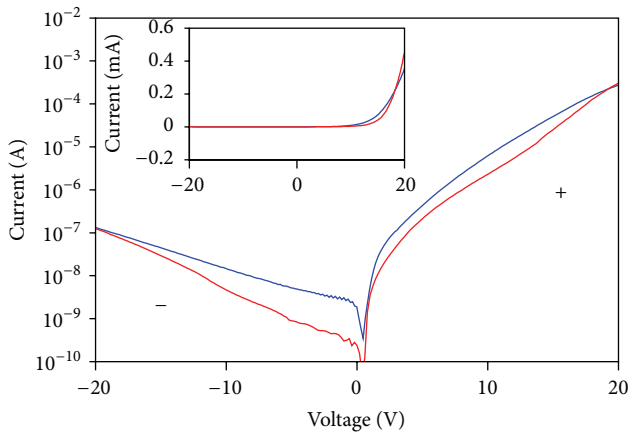


FIGURE 4: I - V characteristic of fabricated device. Red curve: before DPP-assisted annealing. Blue curve: after DPP-assisted annealing.

using such a high acceleration energy, a nonuniform domain boundary was formed, which was expected to form a region suitable for generating DPPs in a localized manner. After ion implantation, the surface was rinsed with HCl to remove excess Zn ions. After this, an Au/Zn/Ni film (150 nm) was deposited on the front surface (p-type side) of the substrate by sputtering and lift-off processing (Figure 3). The electrodes were formed in the shape of a mesh so as to facilitate light irradiation and light emission during DPP-assisted annealing and device driving, respectively. An Au/Ge/Ni film (300 nm) and a Pt film (50 nm) were sequentially deposited on the rear surface (n-type side) to serve as a negative electrode. Then, the wafer was diced into a $600\ \mu\text{m} \times 600\ \mu\text{m}$ chip and was fixed to a $20\ \text{mm} \times 20\ \text{mm} \times 1.7\ \text{mm}$ printed circuit board (PCB) by soldering the negative electrode. Finally, the positive electrode was connected to the PCB by wire bonding. The I - V characteristic of the fabricated device is shown in Figure 4 by the red curve. A rectification property was observed, indicating that a p-n junction was formed.

Next, the DPP-assisted annealing will be explained. Figure 5 shows the experimental setup used for DPP-assisted

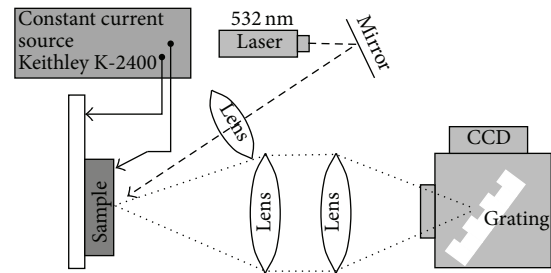


FIGURE 5: Experimental setup for DPP-assisted annealing and EL spectral measurements.

annealing and for measuring the EL spectrum. A K-2400 sourcemeter (Keithley Instruments Inc.) was used as a constant-current source for supplying current during the DPP-assisted annealing and during driving of the device. The emission spectrum of the device was measured using a spectrophotometer and a cooled Si-CCD (Roper Scientific Inc.). To make the device emit light in the green band (wavelengths around 530 nm), a forward-bias current of 30 mA ($9.9\ \text{A}/\text{cm}^2$) was applied to the device fabricated as described above while irradiating it with 532 nm wavelength ($2.32\ \text{eV}$) laser (DPSS CW laser, CNI Inc.) light. The laser power was 0.4 W, and the focal spot diameter on the surface of the device was $0.6\ \text{mm}$ ($35.4\ \text{W}/\text{cm}^2$). During the DPP-assisted annealing, the surface temperature of the device reached 40°C , while the PCB had been cooled to 26°C . As described in Section 2, the spatial distribution of the Zn ions was modified by Joule heat due to the current and by heat generated due to light absorption. The spectrum was measured every 1 hour. The processing was completed when the change in spectral intensity relative to the previous measurement was 1% or less.

4. Device Operation

4.1. Changes in Electroluminescence Spectrum due to DPP-Assisted Annealing. Figure 6(a) shows the results of

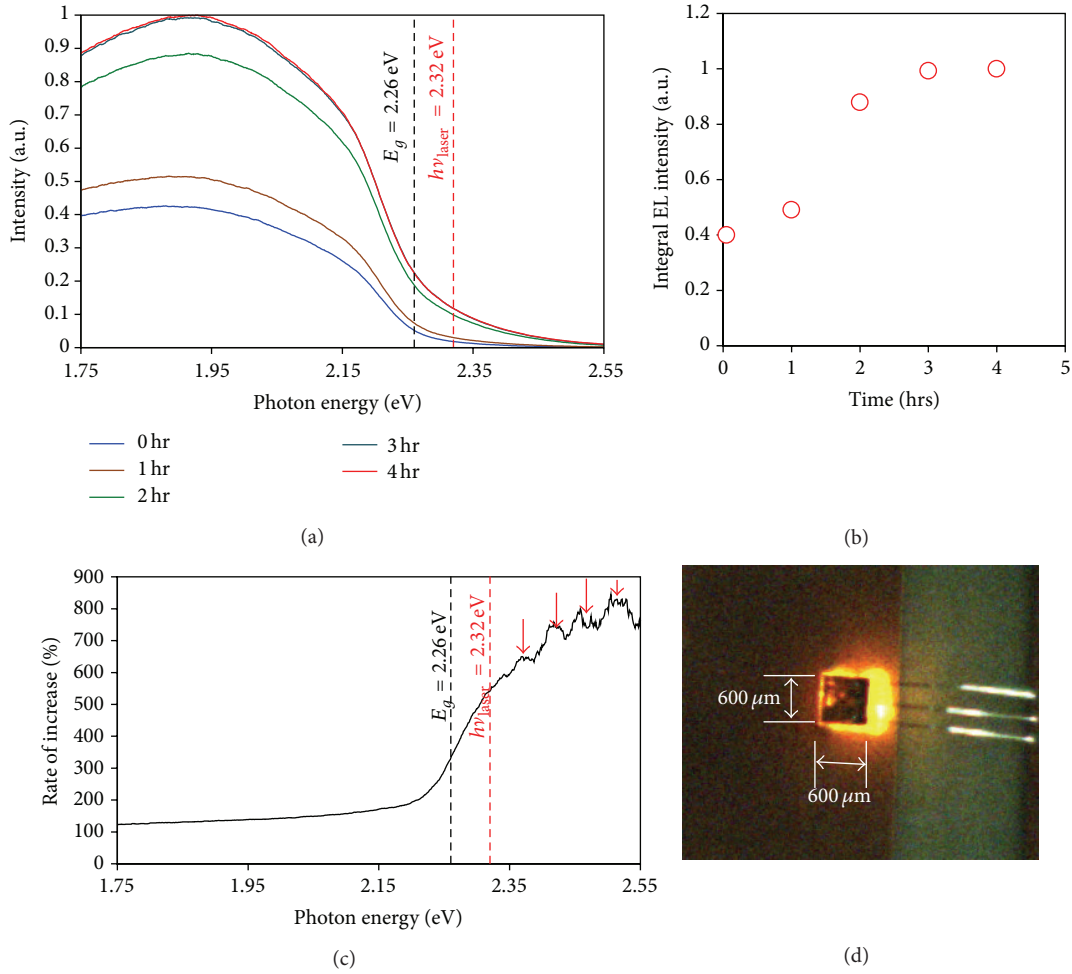


FIGURE 6: Temporal changes in EL spectra during DPP-assisted annealing of GaP LED. (a) Spectra observed during DPP-assisted annealing with a current density of 9.9 A/cm^2 while irradiating device with 532 nm laser light with power of 0.4 W. EL measurements were performed every 1 hour under the same current density conditions (9.9 A/cm^2), but without laser irradiation. (b) Total EL light emission intensity (integral of curve in (a)) versus time. (c) Measured values of R . (d) Light emission from fabricated device.

measuring the EL spectrum of the device during DPP-assisted annealing. The injection current was 30 mA. For reference, the photon energy of the irradiation light (2.32 eV) during DPP-assisted annealing and the bandgap energy of GaP (2.26 eV) are also shown by the vertical red and black dotted lines, respectively. The spectra were measured during an exposure time of 0.25 s, after the laser light irradiation was stopped. This figure shows that the light emission in the range 1.75–2.26 eV has become more intense as the annealing time was increased. Possible explanations for this include light emission from Zn-O pairs formed from Zn atoms and impurity O atoms which occupy the closely spaced Ga site and P site, respectively [16], and light emission originating from radiative recombination of electrons trapped at the donors (S) and free holes [17]. In particular, it has been reported that formation of Zn-O pairs can be explained by diffusion of Zn from the p side to the n side of the p-n junction [18]. In other words, the strong emission intensity in this region as DPP-assisted annealing progressed can be considered evidence that Zn diffusion took place. In

addition, light emission was observed from levels above E_g . This was a result of the DPP-assisted process described in Section 2. And the increase in light emission from these high energy levels was a result of the DPP-assisted annealing described also in Section 2.

Figure 6(b) shows the dependence of the total EL light emission intensity (the areas enclosed by the curves and the horizontal axis in Figure 6(a)) on the DPP-assisted annealing time. The light emission intensity saturated after about 3 hours of annealing, reaching an intensity three-times higher than the initial intensity.

Figure 6(c) shows the rate of increase R . It is the normalized emitted light intensity P of the photon energy E after saturation (after 4 hours of DPP-assisted annealing), given by the following expression:

$$R = \frac{P_{4\text{hr}}(E) - P_{0\text{hr}}(E)}{P_{0\text{hr}}(E)}. \quad (1)$$

In this figure, at photon energies below 2.2 eV ($< E_g$), R was 150–250%, whereas at photon energies higher than that of

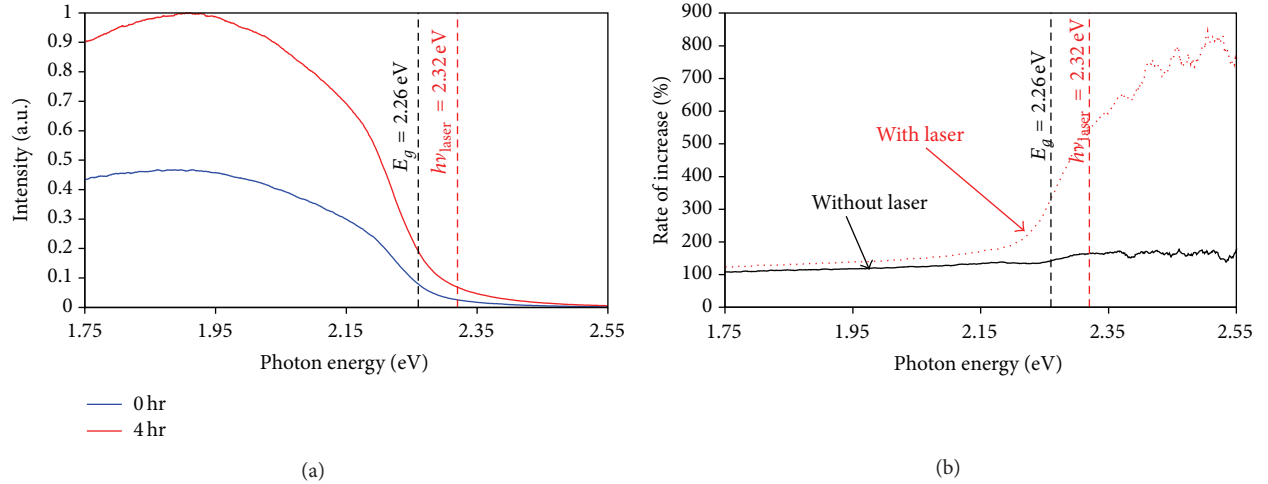


FIGURE 7: Spectrum of device annealed for 4 hours while applying current density of 9.9 A/cm^2 but no laser irradiation. (a) Blue curve shows initial spectrum, and red curve shows spectrum after DPP-assisted annealing for 4 hours. (b) Measured values of R . For comparison with case where annealing was performed without laser irradiation (black curve), the case where annealing was performed with laser irradiation is also shown (Figure 6(c), red curve).

the irradiation laser light ($h\nu_{\text{laser}}$), R was 550% or greater. This intensity variation is in agreement with that expected from the discussion in Section 2. In addition, in this figure, periodic peaks (indicated by downward red arrows) are observed at positions away from $h\nu_{\text{laser}}$ ($=2.32$ eV). These peaks were 50 meV apart, which corresponds to the energy of LO phonons in GaP. In other words, phonon sidebands appeared in the emitted light in the high-energy region, as reported in a previous study [19, 20], confirming that the light emission phenomenon was due to a DPP-assisted process via multimode coherent phonons.

Figure 6(d) is a photomicrograph showing light emission from the device. Although the value of R was large at energies higher than the photon energy of the irradiation laser light ($h\nu_{\text{laser}}$), the emission component originating from impurities or Zn-O centers [16, 17] was strong, making the emitted light appear orange.

4.2. Effect of Photon Number Density on the DPP-Assisted Annealing. Usually, GaP contains defects or impurities such as oxygen, and these form emission centers. In other words, photons with a wide range of energies are generated inside the crystal during DPP-assisted annealing, and it is thought that stimulated emission is also made possible triggered by these generated photons.

To confirm the effect of this light emission inside the crystal, we performed annealing while causing a current to flow (30 mA), but without laser irradiation. The EL spectrum obtained as a result is shown in Figure 7(a). The black curve in Figure 7(b) is the rate of increase, R , given by (1) (the red curve is a copy of Figure 6(c)). First, the values of this black curve at the low energy side were close to the values of the red curve. However, above E_g , they considerably differed. This feature can be explained as follows. In the 1.7–2.2 eV energy band, the photon number density with the corresponding energy is the same, regardless of whether or

not laser irradiation is performed, and therefore, no change occurs in the DPP-assisted process. In addition, the light emission from Zn-O or defects does not change compared with the case where laser irradiation is performed, and therefore, the rate of increase is substantially the same. In the case of the high-energy band, it is thought that there is a difference between progression and suppression of dopant diffusion depending on whether or not laser irradiation is performed. In other words, if monochromatic light of sufficient intensity is made incident, stimulated emission from an energy level corresponding to the photon energy of that monochromatic light becomes more pronounced. Therefore, this demonstrates the effectiveness of DPP-assisted annealing, in terms of the ability to control the photon energy of the light emission from the device by the photon energy, $h\nu_{\text{laser}}$, of the irradiation light rather than E_g .

4.3. The Influence of Crystallinity. In general, lattice defects occur in crystals due to impurity doping by ion implantation. In particular, with high-energy ion implantation, there is also a risk of the crystal becoming amorphous. In the present study, light emission was brought about by a DPP-assisted process. However, this process uses high energy during ion implantation, and there is also a study in which a light-emitting device was fabricated using amorphous GaP [21]; therefore, we examined the crystallinity and its influence on light emission.

We used a sample that was preliminarily annealed at 800°C for 30 minutes prior to DPP-assisted annealing, after ion implantation. Figure 8 shows the measured Raman scattering spectra (incident light: 488 nm) of the substrate before ion implantation (blue circles), the substrate after ion implantation (red diamonds), and the substrate after preliminary annealing carried out in a furnace (green triangles). In the spectrum for the substrate before ion implantation, sharp peaks appeared, which indicate the high crystal

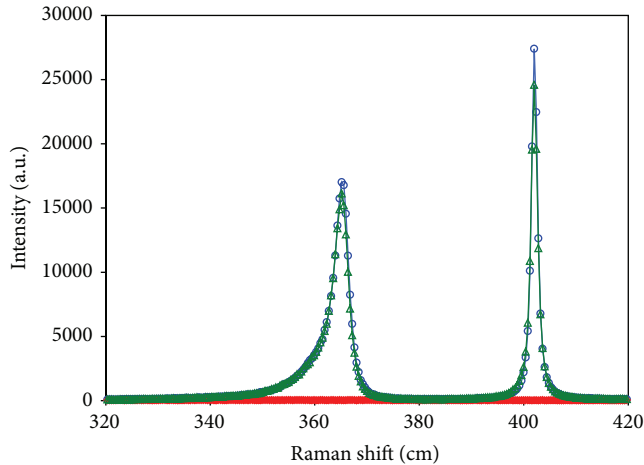


FIGURE 8: Measured Raman scattering spectra. Blue circles: substrate before ion implantation, for comparison. Red diamonds: substrate after ion implantation. Green triangles: substrate subjected to preliminary annealing after ion implantation (800°C, 30 minutes).

quality. However, after ion implantation, these peaks were not observed; therefore, it is considered that the surface changed to an amorphous structure. Also, in the spectrum for the substrate after preliminary annealing, peaks appeared again. To confirm the effect of the amorphous surface on light emission, the substrate whose surface crystallinity was restored by preliminary annealing was formed into a device and was subjected to DPP-assisted annealing under the same conditions. The results are shown in Figure 9. As can be understood from this figure, the same spectral change as shown in Figures 6(a) and 6(c) was observed also in the preannealed sample.

The results shown in Figures 8 and 9 can be explained as follows: by implanting Zn into GaP with a high acceleration energy, namely, 300 keV, the surface of the GaP crystal became amorphous. However, via the DPP-assisted process, the light emission occurs at the domain boundaries formed by the dopant (Zn) inside the crystal and does not rely on the amorphization of the crystal surface. Thus, the same results are obtained regardless of whether or not preliminary annealing is performed to recover the crystallinity.

5. Conclusion

We successfully fabricated a light-emitting device by forming a p-n junction via ion implantation in a bulk GaP crystal, which is an indirect-transition type semiconductor, and by using DPP-assisted annealing. The EL spectrum of the device fabricated by this method was governed by the light used during processing, not by the band structure of the semiconductor. In practice, the light emission from energy levels higher than 2.32 eV was increased by more than 550% (E_g of GaP is 2.26 eV) by using 532 nm (2.32 eV) light irradiation during the DPP-assisted annealing. In contrast, the rate of increase in the energy region below 2.2 eV was limited to 150–250%. By performing experiments with and without

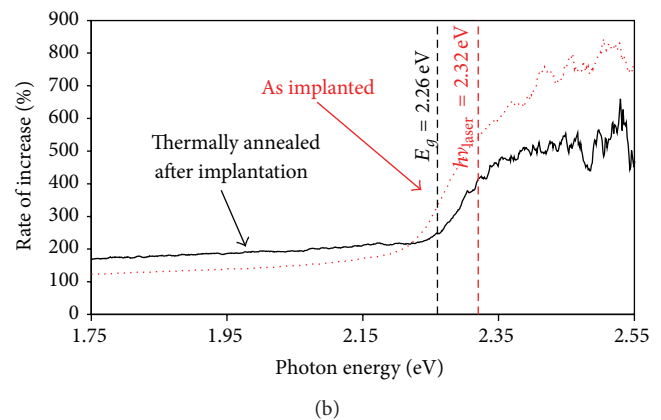
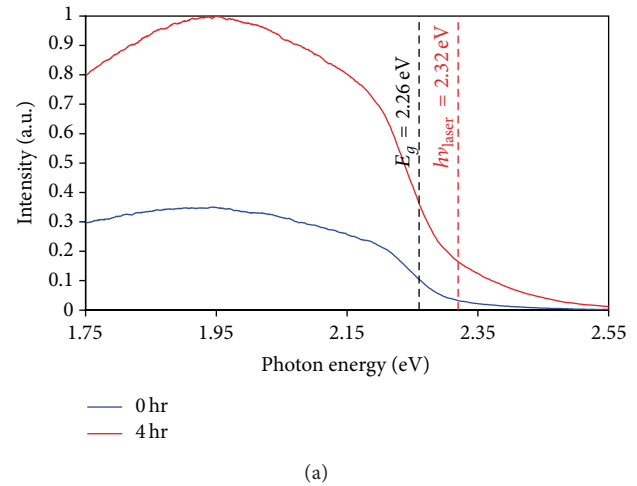


FIGURE 9: Results of DPP-assisted annealing of sample subjected to preliminary annealing after ion implantation. Processing was performed under the same conditions as in Figure 6 (applying current density of 9.9 A/cm² while irradiating the device with 532 nm laser light at power of 0.4 W). (a) Comparison of initial spectrum and spectrum obtained at saturation. (b) Rate of increase of EL spectral intensity (black solid curve). Case without preliminary annealing is also shown for comparison (Figure 6(c), red curve).

irradiation light, we also observed a phenomenon whereby the light emission intensity from higher energy levels was increased as a result of the DPP-assisted annealing, thus demonstrating the effectiveness of the DPP-assisted process. In addition, it was also confirmed experimentally that this light was emitted from a single crystal and was not due to amorphization.

Although the light emission from energy levels higher than E_g was remarkably increased, the peak position of the EL spectrum was around 630 nm due to defects and impurity O atoms. Thus, we believe that it will be possible to realize a GaP LED with an emission peak around 530 nm, provided that the crystallinity of the GaP can be improved.

Conflict of Interests

The authors declare that there is no conflict of interests regarding the publication of this paper.

Acknowledgments

The authors received support in Raman spectroscopy from Professor Dr. S. Takagi, Professor Dr. M. Takenaka, and Mr. J.-H. Han of The University of Tokyo. This work was partially supported by a Grant-in-Aid for Scientific Research (B) (no. 24360023) of MEXT and Core-to-Core Program of JSPS.

References

- [1] IARC *Monographs on the Evaluation of Carcinogenic Risks to Humans*, vol. 23 of *Some Metals and Metallic Compounds*, World Health Organization, International Agency for Research on Cancer, 1998.
- [2] M. Behet, R. Hövel, A. Kohl, A. Mesquida Küsters, B. Opitz, and K. Heime, "MOVPE growth of III-V compounds for optoelectronic and electronic applications," *Microelectronics Journal*, vol. 27, no. 4-5, pp. 297-334, 1996.
- [3] P. Fini, X. Wu, E. J. Tarsa et al., "The effect of growth environment on the morphological and extended defect evolution in GaN grown by metalorganic chemical vapor deposition," *Japanese Journal of Applied Physics Part 1*, vol. 37, no. 8, pp. 4460-4466, 1998.
- [4] D. D. Koleske, A. E. Wickenden, R. L. Henry, W. J. DeSisto, and R. J. Gorman, "Growth model for GaN with comparison to structural, optical, and electrical properties," *Journal of Applied Physics*, vol. 84, no. 4, pp. 1998-2010, 1998.
- [5] P. Gibart, "Metal organic vapour phase epitaxy of GaN and lateral overgrowth," *Reports on Progress in Physics*, vol. 67, no. 5, pp. 667-715, 2004.
- [6] Y. Tanaka and K. Kobayashi, "Optical near field dressed by localized and coherent phonons," *Journal of Microscopy*, vol. 229, no. 2, pp. 228-232, 2008.
- [7] M. Ohtsu, "Dressed photon technology," *Nanophotonics*, vol. 1, pp. 83-97, 2012.
- [8] M. Gershenson and R. M. Mikulyak, "Light emission from forward biased p-n junctions in gallium phosphide," *Solid State Electronics*, vol. 5, no. 5, pp. 313-329, 1962.
- [9] D. G. Thomas, M. Gershenson, and F. A. Trumbore, "Pair spectra and "edge" emission in gallium phosphide," *Physical Review*, vol. 133, no. 1, pp. A269-A279, 1964.
- [10] R. A. Logan, H. G. White, and W. Wiegmann, "Efficient green electroluminescent junctions in GaP," *Solid State Electronics*, vol. 14, no. 1, pp. 55-70, 1971.
- [11] J. S. Jayson, R. Z. Bachrach, P. D. Dapkus, and N. E. Schumaker, "Evaluation of the Zn-O complex and oxygen-donor electron-capture cross sections in p-Type GaP: limits on the quantum efficiency of red-emitting (Zn,O)-doped material," *Physical Review B*, vol. 6, no. 6, pp. 2357-2372, 1972.
- [12] T. Kawazoe, M. A. Mueed, and M. Ohtsu, "Highly efficient and broadband Si homojunction structured near-infrared light emitting diodes based on the phonon-assisted optical near-field process," *Applied Physics B: Lasers and Optics*, vol. 104, no. 4, pp. 747-754, 2011.
- [13] M. A. Tran, T. Kawazoe, and M. Ohtsu, "Fabrication of a bulk silicon p-n homojunction-structured light-emitting diode showing visible electroluminescence at room temperature," *Applied Physics A*, vol. 115, no. 1, pp. 105-111, 2014.
- [14] T. Kawazoe and M. Ohtsu, "Bulk crystal SiC blue LED with p-n homojunction structure fabricated by dressed-photon-phonon-assisted annealing," *Applied Physics A*, vol. 115, no. 1, pp. 127-133, 2014.
- [15] A. Einstein and P. Ehrenfest, "Zur Quantentheorie des Strahlungsgleichgewichts," *Zeitschrift für Physik*, vol. 19, no. 1, pp. 301-306, 1923.
- [16] K. Löhnert and E. Kubalek, "On the degradation of electroluminescence efficiency in gallium phosphide green light emitting diodes," *Physica Status Solidi A*, vol. 80, no. 1, pp. 173-183, 1983.
- [17] T. Kawabata and S. Koike, "High-efficiency GaP pure green light-emitting diodes of 555 nm fabricated by new liquid phase epitaxy method," *Applied Physics Letters*, vol. 43, no. 5, pp. 490-491, 1983.
- [18] K. Ždánky, J. Zavadil, D. Nohavica, and S. Kugler, "Degradation of commercial high-brightness GaP:N green light emitting diodes," *Journal of Applied Physics*, vol. 83, no. 12, pp. 7678-7684, 1998.
- [19] M. Yamaguchi, T. Kawazoe, and M. Ohtsu, "Evaluating the coupling strength of electron-hole pairs and phonons in a 0.9 μm -wavelength silicon light emitting diode using dressed-photon-phonons," *Applied Physics A*, vol. 115, no. 1, pp. 119-125, 2014.
- [20] N. Wada, M. A. Tran, T. Kawazoe, and M. Ohtsu, "Measurement of multimode coherent phonons in nanometric spaces in a homojunction-structured silicon light emitting diode," *Applied Physics A: Materials Science and Processing*, vol. 115, no. 1, pp. 113-118, 2014.
- [21] K. Tomioka and S. Adachi, "Structural and photoluminescence properties of porous GaP formed by electrochemical etching," *Journal of Applied Physics*, vol. 98, no. 7, Article ID 073511, 2005.

Research Article

Realization of Ultraflat Plastic Film Using Dressed-Photon-Phonon-Assisted Selective Etching of Nanoscale Structures

Takashi Yatsui, Wataru Nomura, and Motoichi Ohtsu

School of Engineering, The University of Tokyo, 2-11-16 Yayoi, Bunkyo-ku, Tokyo 113-8656, Japan

Correspondence should be addressed to Takashi Yatsui; yatsui@ee.t.u-tokyo.ac.jp

Received 30 September 2014; Accepted 6 November 2014

Academic Editor: Chennupati Jagadish

Copyright © 2015 Takashi Yatsui et al. This is an open access article distributed under the Creative Commons Attribution License, which permits unrestricted use, distribution, and reproduction in any medium, provided the original work is properly cited.

We compared dressed-photon-phonon (DPP) etching to conventional photochemical etching and, using a numerical analysis of topographic images of the resultant etched polymethyl methacrylate (PMMA) substrate, we determined that the DPP etching resulted in the selective etching of smaller scale structures in comparison with the conventional photochemical etching. We investigated the wavelength dependence of the PMMA substrate etching using an O₂ gas. As the dissociation energy of O₂ is 5.12 eV, we applied a continuous-wave (CW) He-Cd laser ($\lambda = 325$ nm, 3.81 eV) for the DPP etching and a 5th-harmonic Nd:YAG laser ($\lambda = 213$ nm, 5.82 eV) for the conventional photochemical etching. From the obtained atomic force microscope images, we confirmed a reduction in surface roughness, R_a , in both cases. However, based on calculations involving the standard deviation of the height difference function, we confirmed that the conventional photochemical etching method etched the larger scale structures only, while the DPP etching process selectively etched the smaller scale features.

1. Introduction

Organic materials are flexible in comparison with inorganic substrates; therefore, they are important materials as regards the development of future wearable devices [1]. Recently, organic substrates with microstructures have been prepared by mechanical pressing, an injection molding method [2], and the surface roughness values of the obtained materials have been determined by use of a pressing mold. However, because the resultant plastic is soft, these organic substrates cannot be flattened using a mechanical polishing method. Furthermore, although plastic substrates are easy to fabricate in three-dimensional structures, the side walls of these structures cannot be flattened.

In order to achieve an ultraflat surface on an inorganic material, many groups have developed a chemical mechanical polishing (CMP) method [3], resulting in a subnanometer scale flattened surface [4]. However, since CMP is a contact method, it leads to the formation of scratches or digs during polishing, while chemical materials in the slurry penetrate the polished surface, resulting in performance degradation.

Therefore, we have developed a dressed-photon-phonon (DPP) etching technique [5] as a noncontact flattening method. In this process, the free photons of propagating light are coupled with material excitation, including electrons and holes, of the nanoscale material structures; in other words, the photons interacting with the nanoscale material dress the material excitation to form a dressed photon (DP) quasiparticle. The DP also couples with multiple-mode coherent phonons in the material, which act as quasiparticle of DP and phonons (DPP). Therefore, the DPP energy is higher than that of the incident free photon; that is, the DPP realizes energy upconversion [6]. By using the energy upconversion mechanism, selective etching of the nanoscale structure can be successfully realized. Previously, we obtained ultraflat surfaces on substrates including glass [5], diamond, and GaN [7]. Since DPP etching does not require a contact pad, three-dimensional structures have also been flattened [8].

Here, we compare the effectiveness of the DPP etching technique to that of conventional photochemical etching. To evaluate the effectiveness of the DPP etching, we perform

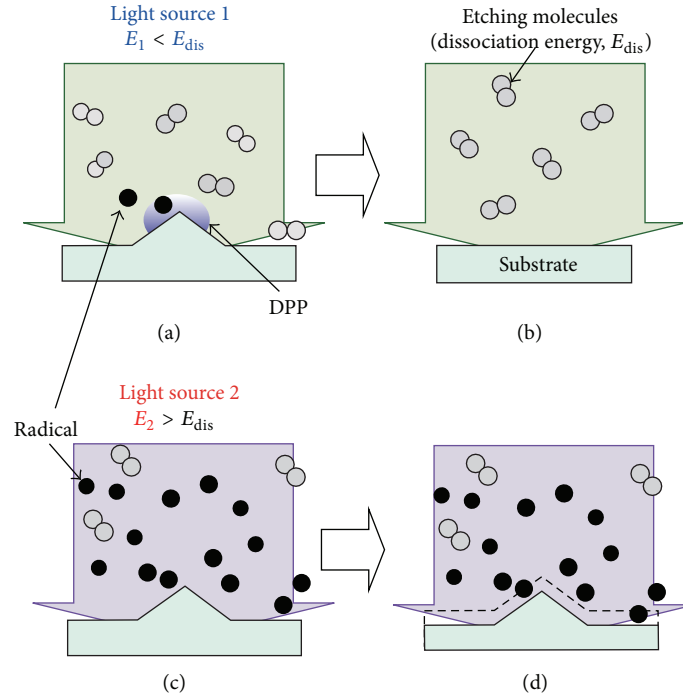


FIGURE 1: ((a) and (b)) DPP etching and ((c) and (d)) conventional photochemical etching process diagrams.

calculations based on the standard deviation of the height difference function in addition to the surface roughness, R_a . Here, we observe the wavelength dependence of photochemical etching on polymethyl methacrylate (PMMA) substrate as a plastic material.

2. DPP Etching

To realize DPP etching, the photon energy of the light source, E_1 , must be lower than the dissociation energy of the etching molecule, E_{dis} . Therefore, the incident photon cannot dissociate the etching molecules in a gas phase. However, the DPP is generated at the apex of the protrusions of the surface. Furthermore, since the DPP energy, E_{DPP} , is larger than that of E_1 , the etching molecules are dissociated selectively when they enter the proximity of the protrusions (Figure 1(a)). Consequently, the dissociated radical molecules etch away at the protrusions and, thus, the DPP etching process automatically stops when the surface is sufficiently flattened (Figure 1(b)).

In contrast to DPP etching, when conventional plasma etching or conventional photochemical etching is used, the photon energy of the light source, E_2 , is higher than E_{dis} , and the etching molecules are dissociated in all directions (Figure 1(c)). Therefore, the dissociated radical atoms etch the substrate with no position dependence (Figure 1(d)).

3. Experiment

In this study, we used a PMMA substrate prepared by injection molding in an oxygen atmosphere. Because the dissociation

energy of O_2 is 5.12 eV [9], we used a continuous-wave (CW) He-Cd laser ($\lambda = 325$ nm; 3.81 eV; excitation power: 0.8 W/cm²) for DPP etching and a 5th-harmonic YAG laser ($\lambda = 213$ nm; 5.82 eV; 20 Hz; pulse width: 5 ns) for conventional photochemical etching. The surface structure was evaluated using an atomic force microscope (AFM) with a “sampling intelligent scan” mode (Hitachi-Hitech-Science Corp.). The scanned area was 1×1 μ m and incorporated 256×256 pixels (a spatial resolution of 4 nm) and the AFM images were obtained using tilt compensation and the third-order least-squares method.

4. Results and Discussion

Figures 2(a) and 2(b) are AFM images of the surface before and after DPP etching, respectively. It was found that the surface roughness, R_a , was reduced from 0.30 to 0.22 nm following 120 min DPP etching (Figure 3). Similar R_a reduction was observed following conventional photochemical etching, as can be seen from the AFM images taken before (Figure 2(c), $R_a = 0.26$ nm) and after (Figure 2(d), $R_a = 0.20$ nm) etching, and comparison between both methods is given in Figure 3. It can be seen that the usage of conventional photochemical etching resulted in a dramatic decrease in etching time.

To investigate the surface morphology in detail, we used the method developed in our previous reports [7]. Instead of examining the value of R_a only, which is the average value of the absolute surface height deviations from the best-fitting plane (Figure 4(a)), we used the standard deviation of the height difference function. Here, the R_a value

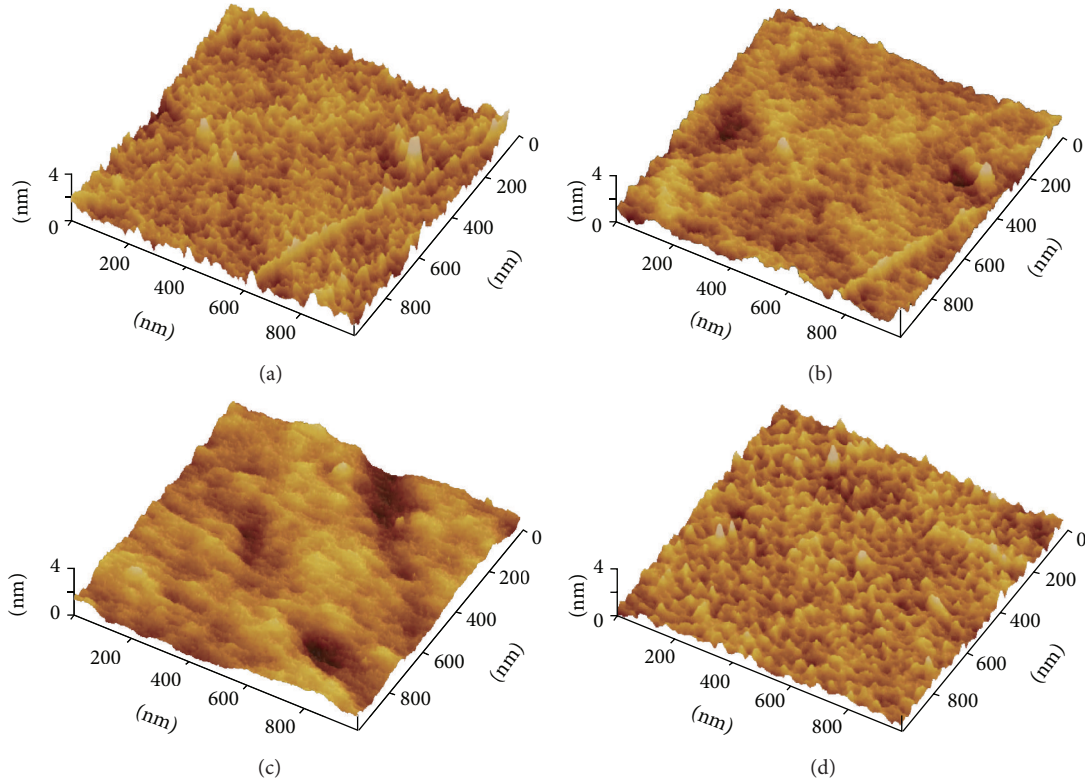


FIGURE 2: Typical AFM images of PMMA substrate (a) before and (b) after DPP etching using He-Cd laser ($\lambda = 325 \text{ nm}$, 3.81 eV). Typical AFM images of PMMA substrate (c) before and (d) after conventional photochemical etching using 5th-harmonic YAG laser ($\lambda = 213 \text{ nm}$, 5.82 eV).

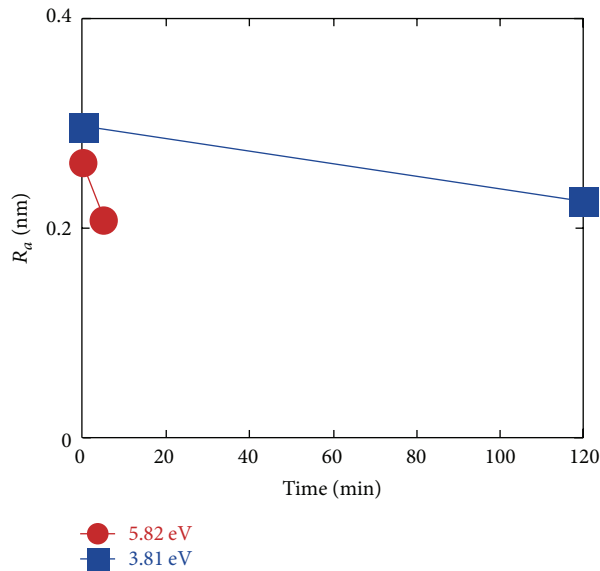


FIGURE 3: Etching time dependence of surface roughness, R_a . Blue solid squares correspond to R_a using 3.81 eV He-Cd laser (DPP etching). Red solid circles correspond to R_a using 5.82 eV 5th-harmonic Nd:YAG laser (conventional photochemical etching).

provides information about the average surface roughness for the entire scanning region. However, the standard deviation of the height difference function is given by $R(l) = \sqrt{\langle (z_{k+1}^{(l)} - z_k^{(l)})^2 / 2 \rangle}$, where l is the scale size, z is the height

from the best-fitting plane, and $\bar{z}_k^{(l)}$ is the average z value of the scale (Figure 4(b)) [10]. This $R(l)$ can be used to determine the contributions of the surface roughness values (at different length scales) to the overall surface roughness. As this value

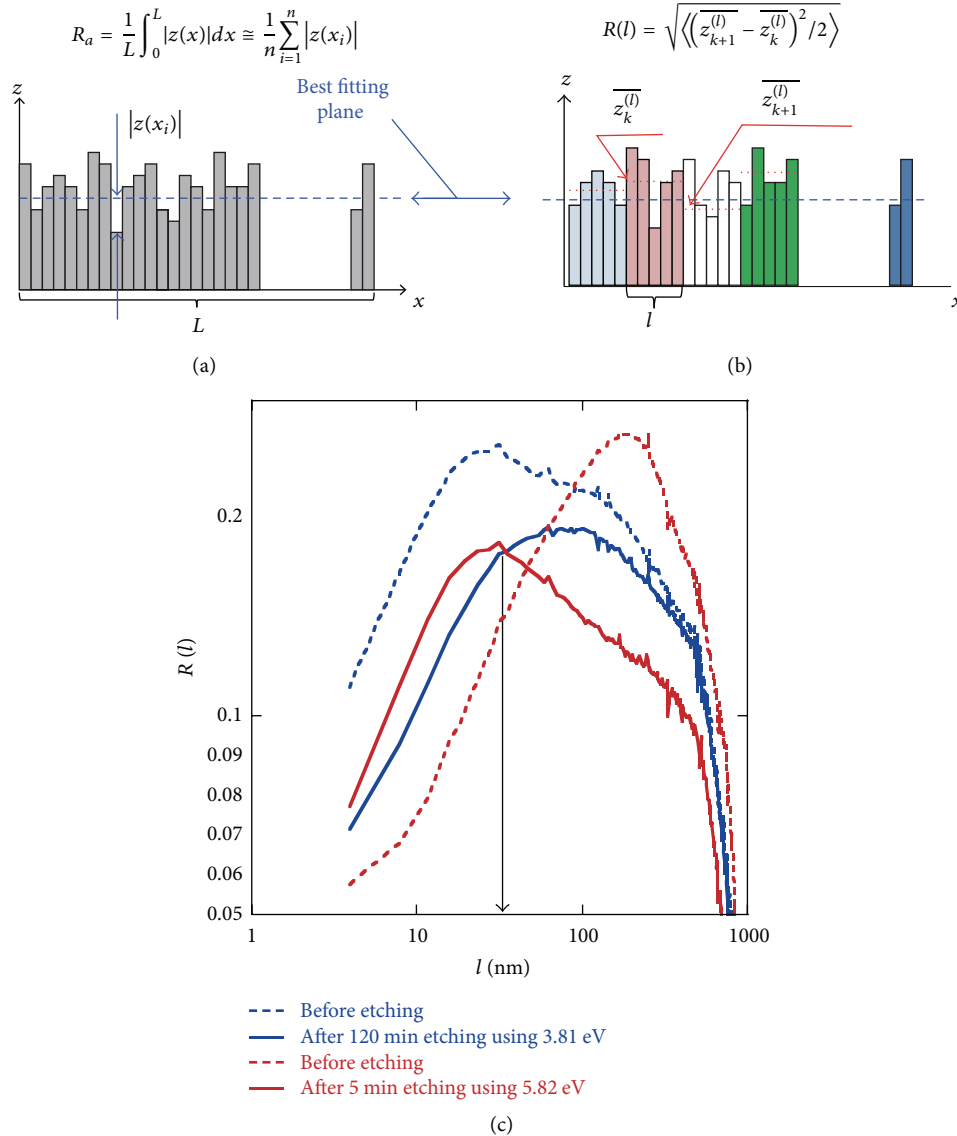


FIGURE 4: Schematic of (a) the surface roughness, R_a , and the standard deviation of the height difference function, $R(l)$. (c) Etching time dependence of the standard deviation of $R(l)$. The blue dashed curve corresponds to Figure 2(a) (before etching); the blue solid curve corresponds to Figure 2(b) (after 120 min etching using 3.81 eV DPP etching); the red dashed curve corresponds to Figure 2(c) (before etching); the red solid curve corresponds to Figure 2(d) (after 5 min etching using 5.82 eV conventional photochemical etching).

indicates the height difference of the next scale, it is known as a two-sample variance. This value is known as the Allan variance, and it is a measure of frequency stability in clocks, oscillators, and amplifiers.

Figure 4 shows the calculated $R(l)$ values from the AFM images. The maximum values of the blue curves decreased from 0.25 to 0.19 nm, which are comparable to the R_a values of Figure 2(a) (0.30 nm) and Figure 2(b) (0.22 nm) and indicate the results of the DPP etching. Similarly, the maximum values of the red curves decreased from 0.27 to 0.18 nm, which are comparable to the R_a values of Figure 2(c) (0.26 nm) and Figure 2(d) (0.20 nm) and are the photochemical etching results. It is notable that even though the R_a values vary significantly with each other, we can therefore confirm that the conventional etching etched on a scale, l , larger than

100 nm, while the DPP etching etched on a smaller scale, with l less than 100 nm. These results therefore establish that DPP etching selectively etches on a smaller scale, as the $R(l)$ value for the DPP etched is smaller than that of the conventional photochemical etching at $l < 35$ nm (indicated by the arrow in Figure 4). The increase in $R(l)$ at the smaller scale for the conventional photochemical etching case might be caused by ablation due to the higher photon energy used in this method, in comparison with that of the chemical bonding of PMMA [11].

5. Conclusion

Through an experiment on the wavelength-dependent etching of a polymethyl methacrylate (PMMA) substrate and

calculations based on the standard deviation of the height difference function of the resultant surface, we determined that dressed-photon-phonon (DPP) etching results in the selective etching of smaller scale structures in comparison with conventional photochemical etching. This information therefore supports the use of the DPP etching method for the surface finishing of organic materials. In future, by combining both DPP and conventional photochemical etching, a further decrease in the R_a value could be realized depending on the R_a value of the substance in question.

Conflict of Interests

The authors declare that there is no conflict of interests regarding the publication of this paper.

Acknowledgments

The authors wish to express special thanks to Dr. Takashi Morimoto and Mr. Yoshinori Tabata (SIGMA Koki Co., Ltd.) for their active support and discussions. This work was partially supported by a Grant-in-Aid for Scientific Research (B) (no. 26286022), the Exploratory Research program (no. 26630122) of MEXT, Core-to-Core Program of JSPS (A. Advanced Research Networks), and a research grant (Basic Research) from The Asahi Glass Foundation. They would like to thank Editage (<http://www.editage.jp/>) for English language editing.

References

- [1] M. Kaltenbrunner, T. Sekitani, J. Reeder et al., "An ultra-lightweight design for imperceptible plastic electronics," *Nature*, vol. 499, no. 7459, pp. 458–463, 2013.
- [2] B.-K. Lee, D. S. Kim, and T. H. Kwon, "Replication of microlens arrays by injection molding," *Microsystem Technologies*, vol. 10, no. 6-7, pp. 531–535, 2004.
- [3] L. Jianfeng and D. A. Dornfeld, "Material removal mechanism in chemical mechanical polishing: theory and modeling," *IEEE Transactions on Semiconductor Manufacturing*, vol. 14, no. 2, pp. 112–133, 2001.
- [4] A. J. Kadaksham, B. Lee, M. House, T. Laursen, B. Niekrewicz, and A. Rastegar, "Current status of EUV mask blanks and LTEM substrates defectivity and cleaning of blanks exposed in EUV ADT," in *Extreme Ultraviolet (EUV) Lithography II*, 79690Z, vol. 7969 of *Proceedings of SPIE*, San Jose, Calif, USA, February 2011.
- [5] T. Yatsui, K. Hirata, W. Nomura, Y. Tabata, and M. Ohtsu, "Realization of an ultra-flat silica surface with angstrom-scale average roughness using nonadiabatic optical near-field etching," *Applied Physics B: Lasers and Optics*, vol. 93, no. 1, pp. 55–57, 2008.
- [6] M. Ohtsu, "Dressed photon technology," *Nanophotonics*, vol. 1, pp. 83–97, 2012.
- [7] T. Yatsui, W. Nomura, F. Stehlin, O. Soppera, M. Naruse, and M. Ohtsu, "Challenges in realizing ultraflat materials surfaces," *Beilstein Journal of Nanotechnology*, vol. 4, no. 1, pp. 875–885, 2013.
- [8] T. Yatsui, D. Takeuchi, S. Koizumi et al., "Polarization-controlled dressed-photonphonon etching of patterned diamond structures," *Physica Status Solidi (A)*, vol. 211, no. 10, pp. 2339–2342, 2014.
- [9] D. Keilin and E. F. Hartree, "Absorption spectrum of oxygen," *Nature*, vol. 165, no. 4197, pp. 543–544, 1950.
- [10] D. W. Allan, "Statistics of atomic frequency standards," *Proceedings of the IEEE*, vol. 54, no. 2, pp. 221–230, 1966.
- [11] R. Srinivasan and B. Braren, "Ultraviolet laser ablation of organic polymers," *Chemical Reviews*, vol. 89, no. 6, pp. 1303–1316, 1989.

Research Article

Emission Spectral Control of a Silicon Light Emitting Diode Fabricated by Dressed-Photon-Phonon Assisted Annealing Using a Short Pulse Pair

Tadashi Kawazoe,^{1,2} Naoki Wada,¹ and Motoichi Ohtsu^{1,2}

¹ Department of Electrical Engineering and Information Systems, Graduate School of Engineering, The University of Tokyo, 2-11-16 Yayoi, Bunkyo-ku, Tokyo 113-8656, Japan

² Nanophotonic Research Center, Graduate School of Engineering, The University of Tokyo, 2-11-16 Yayoi, Bunkyo-ku, Tokyo 113-8656, Japan

Correspondence should be addressed to Tadashi Kawazoe; kawazoe@ee.t.u-tokyo.ac.jp

Received 24 April 2014; Accepted 5 June 2014; Published 6 July 2014

Academic Editor: Takashi Yatsui

Copyright © 2014 Tadashi Kawazoe et al. This is an open access article distributed under the Creative Commons Attribution License, which permits unrestricted use, distribution, and reproduction in any medium, provided the original work is properly cited.

We fabricated a high-efficiency infrared light emitting diode (LED) via dressed-photon-phonon (DPP) assisted annealing of a p-n homojunctioned bulk Si crystal. The center wavelength in the electroluminescence (EL) spectrum of this LED was determined by the wavelength of a CW laser used in the DPP-assisted annealing. We have proposed a novel method of controlling the EL spectral shape by additionally using a pulsed light source in order to control the number of phonons for the DPP-assisted annealing. In this method, the Si crystal is irradiated with a pair of pulses having an arrival time difference between them. The number of coherent phonons created is increased (reduced) by tuning (detuning) this time difference. A Si-LED was subjected to DPP-assisted annealing using a 1.3 μm ($h\nu = 0.94$ eV) CW laser and a mode-locked pulsed laser with a pulse width of 17 fs. When the number of phonons was increased, the EL emission spectrum broadened toward the high-energy side by 200 meV or more. The broadening towards the low-energy side was reduced to 120 meV.

1. Introduction

Direct transition type semiconductors are mainly used in semiconductor light emitting diodes (LEDs) [1, 2]. The reason for this is that the probability of electric dipole transitions, in other words, the radiative recombination probability, is high. Also, the emission wavelength is determined by the bandgap energy, E_g , of the material used. Therefore, for example, InGaAsP epitaxially grown on an InP substrate is mainly used as the active layer for near-infrared LEDs with emission wavelengths of 1.00–1.70 μm (0.73–1.24 eV), which includes the optical fiber communication wavelength band. Shortcomings with this approach are that InP is highly toxic [3], and In is a rare resource. Silicon (Si), on the other hand, is a semiconductor having low toxicity and no concerns about depletion of resources; however, its emission efficiency is low since it is an indirect transition type semiconductor.

Therefore, Si is usually not suitable as a material for use in LEDs. Nevertheless, there is a great demand for the use of Si in light emitting devices, and there has been extensive research into improving its emission efficiency. For example, there has been research into making Si emit light in the visible region by utilizing the quantum size effect of Si and by using porous Si [4], a Si/SiO₂ superlattice structure [5, 6], and Si nanoprecipitates in SiO₂ [7], as well as research into making Si emit light in the near-infrared region by doping it with light-emitting materials, such as erbium (Er)-doped Si [8] and silicon-germanium (Si-Ge) [9]. However, the reported external quantum efficiencies and power conversion efficiencies of LEDs using these materials have been low, at 0.5% and 0.8%, respectively [10].

On the other hand, using a homojunction-structured Si bulk crystal, we realized a high-efficiency, wideband LED in which the spatial distribution of the dopant density in

the Si was modified via a novel process of dressed-photon-phonon assisted annealing (DPP-assisted annealing) [11], and we achieved an external quantum efficiency of 40% and a power conversion efficiency of 50% [12]. A dressed photon (DP) is a quasi-particle created when a photon couples with an electron-hole pair in a nanometric region. Similarly, a dressed-photon-phonon (DPP) is a quasi-particle created when a DP couples with a phonon in a nanometric region. We have also succeeded in developing a Si laser [13], an infrared Si photodetector [14], and a Si relaxation oscillator [15], by using DPP-assisted annealing. These devices operate based on transitions mediated by DPPs, and the center wavelength of the electroluminescence (EL) spectrum is determined by the wavelength of the light source used for creating the DPPs. Since a DPP is a state in which a DP is coupled with a phonon in the material, the EL spectrum of the Si-LED described above has a large number of sidebands that are regularly arranged with a spacing corresponding to the optical phonon energy, centered on the photon energy of the light used in the DPP-assisted annealing. These sidebands are caused by coherent phonons (CPs) contributing to light emission. In typical light emitting devices, such sidebands originating from phonons (phonon sidebands) are observed in the photoluminescence spectrum, but are not observed in the EL spectrum. The observation of such sidebands in the EL spectrum, as described above, is a phenomenon unique to LEDs fabricated using DPPs. By using this phenomenon, it is possible to control the shape of the EL spectrum of a Si-LED by controlling the number of CPs created during the DPP-assisted annealing. In this paper, we report the results of our experiments in which we succeeded in controlling the generation of CPs by using a pair of pulses during the DPP-assisted annealing, allowing us to control the shape of the emission spectrum of a Si-LED.

2. Si-LED Fabrication and Principle of Sideband Creation

First, for fabricating a Si-LED, ion implantation is used to form an inhomogeneous spatial distribution of the dopant (boron: B) in a Si p-n homojunction substrate. Although the inhomogeneously concentrated B serves as the origin of the created DPPs, the created DPPs are not converted to propagating light that is detected outside the LED. However, if DPP-assisted annealing is used, it is possible to modify the spatial distribution of the B concentration so that the DPPs are converted to propagating light with high efficiency [12]. In the DPP-assisted annealing, a Si p-n homojunction substrate is irradiated with CW laser light while applying a forward-bias current, to control the thermal diffusion rate of the B. With this method, it has been demonstrated that the emission wavelength of a Si-LED does not depend on the bandgap energy, E_g , of the material used, but is determined by the photon energy, $h\nu_{\text{anneal}}$, of the radiated light [16]. In the present work, we performed DPP-assisted annealing by radiating CW laser light having a photon energy ($h\nu_{\text{anneal}} = 0.94$ eV) lower than E_g of silicon ($= 1.14$ eV). The principle will be described below. For more details, refer to [12].

During DPP-assisted annealing, the radiated light is not absorbed by the Si crystal at positions in the B distribution where DPPs are not created under irradiation. Thus, the energy of the electrons injected from the forward bias current is converted to thermal energy and is subsequently dissipated via intraband relaxation or nonradiative relaxation. Therefore, the B distribution randomly varies due to thermal diffusion. On the other hand, at positions where DPPs are readily created, the radiated light interacts with electron-hole pairs and phonons, whereby DPPs are created. In this case, the injected electrons emit propagating light via stimulated emission driven by localized DPPs. In other words, since part of the energy of the injected electrons is dissipated not in the form of thermal energy but in the form of optical energy, thermal diffusion becomes more difficult. In the two processes described above, the B concentration distribution in the Si crystal is modified, in a self-organized manner, to a structure suitable for the creation of DPPs and their subsequent conversion to propagating light, and then reaches an equilibrium state. The B distribution in this state is suitable for stimulated emission with the photon energy of the light irradiation, $h\nu_{\text{anneal}}$, and since the spontaneous emission probability is proportional to the stimulated emission probability, this p-n homojunction functions as a Si-LED that emits propagating light.

Next, the mechanism of sideband creation will be explained. Figure 1(a) is an energy level diagram showing electronic states in a Si-LED fabricated by DPP-assisted annealing, and Figure 1(b) is a diagram in which an intermediate DPP level has been added to the band structure. The state $|E_g; \text{el}\rangle \otimes |E_{\text{ex}}; \text{phonon}\rangle$ in the figure is a state represented by the direct product of the ground state $|E_g; \text{el}\rangle$ of the electron and the excited phonon state $|E_{\text{ex}}; \text{phonon}\rangle$. Transitions to this state $|E_g; \text{el}\rangle \otimes |E_{\text{ex}}; \text{phonon}\rangle$ have been shown to occur only due to absorption or emission of photons via DPPs [11]. When this is illustrated in the electronic band structure, it is a localized state in which DPP-mediated excitation can take place and, therefore, it is indicated by a constant-energy straight line (horizontal solid or broken line), as shown in Figure 1(b), due to wavenumber uncertainty. Although an adequate explanation of the conventional light emission process in Si-LEDs has been possible until now with only Figure 1(a), Figure 1(b) is also presented in the present paper to emphasize the significance of phonons. In the light emission process of Si-LEDs, since electrons are excited to the state $|E_{\text{ex}}; \text{el}\rangle$ by current injection, the initial state $|E_{\text{ex}}; \text{el}\rangle \otimes |E_{\text{ex}^{\text{thermal}}}; \text{phonon}\rangle$ in the light emission process exists close to the X point in the conduction band in Figure 1(b). Here, $|E_{\text{ex}^{\text{thermal}}}; \text{phonon}\rangle$ is the thermally excited state of the phonon. Similarly, since the final state $|E_g; \text{el}\rangle \otimes |E_{\text{ex}^{\text{thermal}}}; \text{phonon}\rangle$, reached after the light emission, corresponds to the energy state of holes created by the injected current, the state $|E_g; \text{el}\rangle$ concentrates in the vicinity of the Γ point at the top of the valence band. The state $|E_{\text{ex}^{\text{thermal}}}; \text{phonon}\rangle$ is limited to phonons that can exist at room temperature, according to Bose statistics. In other words, the states $|E_{\text{ex}}; \text{el}\rangle \otimes |E_{\text{ex}^{\text{thermal}}}; \text{phonon}\rangle$ and $|E_g; \text{el}\rangle \otimes |E_{\text{ex}^{\text{thermal}}}; \text{phonon}\rangle$ are the initial state and the final state in the usual indirect transition.

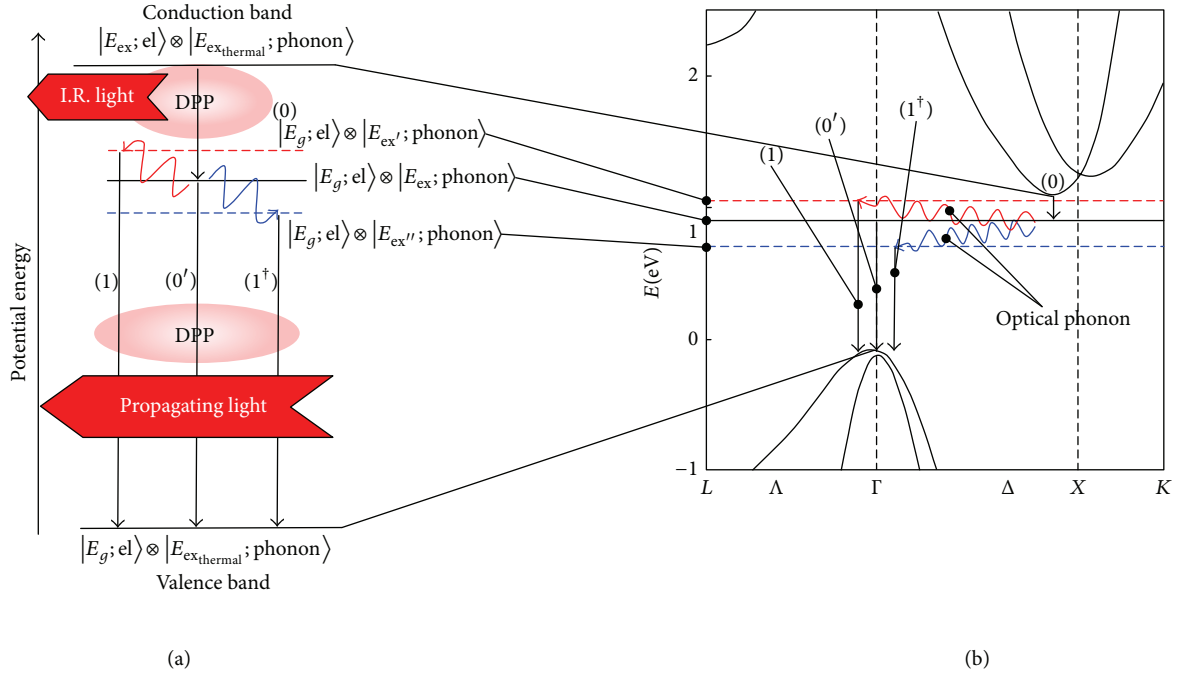


FIGURE 1: Diagram for explaining DPP-mediated transitions, showing (a) energy levels and (b) levels that can be reached via DPP-mediated transitions in electronic band structure of Si crystal.

Next, the processes (0), (0'), (1), and (1[†]) in Figure 1 will be explained. As the first-step, process (0) occurs. Processes (0'), (1), and (1[†]) occur as the second step. These processes involve externally observable transitions, in other words, photon emission. Processes (0) and (0') are transitions that do not require a phonon, whereas processes (1) and (1[†]) require an optical phonon. Similarly, (n) and (n^{\dagger}) are transitions involving n optical phonons ($n = 2, 3, 4, \dots$).

Process (0) is the first-step transition from the initial state $|E_{ex}; el\rangle \otimes |E_{ex_{thermal}}; phonon\rangle$ of electrons injected near the X point by the current to the intermediate state $|E_g; el\rangle \otimes |E_{ex}; phonon\rangle$, which can be reached via a DPP-mediated transition. It corresponds to the energy relaxation from the bottom of the conduction band ($E_g = 1.14$ eV) to the state $|E_g; el\rangle \otimes |E_{ex}; phonon\rangle$ (in this paper, the energy of this state was experimentally determined to be 0.94 eV). This transition is allowable via emission of a large number of phonons or via the emission of infrared light. However, the probability of the transition via phonon emission is small because the simultaneous emission of about 10 phonons is required at room temperature (thermal energy 25 meV). On the other hand, in the transition via infrared light emission, since the electronic state changes from $|E_{ex}; el\rangle$ to $|E_g; el\rangle$, the selection rule required for photon emission is fulfilled. In addition, this transition is a direct transition in wavenumber space, as shown in Figure 1(b). Therefore, the probability of this transition is higher than the probability of a transition via phonon emission. In real space, this process is a transition from the state $|E_{ex}; el\rangle \otimes |E_{ex_{thermal}}; phonon\rangle$, which is broadened to the extent of the electron coherence length, to the localized state $|E_g; el\rangle \otimes |E_{ex}; phonon\rangle$. The reason why infrared light can be emitted in this transition is that part of

the electron energy can be dissipated as infrared light via a DPP having an energy that is resonant with this infrared light.

Process (0') is the second-step transition from the intermediate state $|E_g; el\rangle \otimes |E_{ex}; phonon\rangle$ to $|E_g; el\rangle \otimes |E_{ex_{thermal}}; phonon\rangle$. The photon energy emitted during this process is equal to $h\nu_{anneal}$. Since this is a transition between the same electronic states $|E_g; el\rangle$, the selection rule required for photon emission is governed by a phonon, and the state $|E_g; el\rangle \otimes |E_{ex}; phonon\rangle$ is also a state that can be reached via a DPP-mediated transition. The Si-LED fabricated by DPP-assisted annealing has a high probability of conversion from a DPP to propagating light, and almost all of the electrons in the state $|E_g; el\rangle \otimes |E_{ex}; phonon\rangle$ relax by emitting photons with energy $h\nu_{anneal}$.

Process (1) is the second-step transition from the intermediate state $|E_g; el\rangle \otimes |E_{ex}; phonon\rangle$ to the final state $|E_g; el\rangle \otimes |E_{ex_{thermal}}; phonon\rangle$ by absorption of an optical phonon. Since the first-step transition due to process (0) is an infrared light emission process, optical phonons are created via the Raman process. If the electrons in the state $|E_g; el\rangle \otimes |E_{ex}; phonon\rangle$ are scattered to the Γ point by absorbing optical phonons, the second step transition from the state $|E_g; el\rangle \otimes |E_{ex'}; phonon\rangle$ to the state $|E_g; el\rangle \otimes |E_{ex_{thermal}}; phonon\rangle$ becomes possible, resulting in photon emission, as in the case of a direct transition-type semiconductor. This is process (1) shown in Figure 1(b). Here, $|E_{ex}; phonon\rangle$ and $|E_{ex'}; phonon\rangle$ are the excited states that the phonon reached before and after absorbing optical phonons. The energy of the emitted photons is $h\nu_{anneal} + h\nu_p$, where $h\nu_p$ is the energy of the optical phonon.

Process (1[†]) represents the second-step transition from the intermediate state $|E_g; el\rangle \otimes |E_{ex}; phonon\rangle$ to the final state

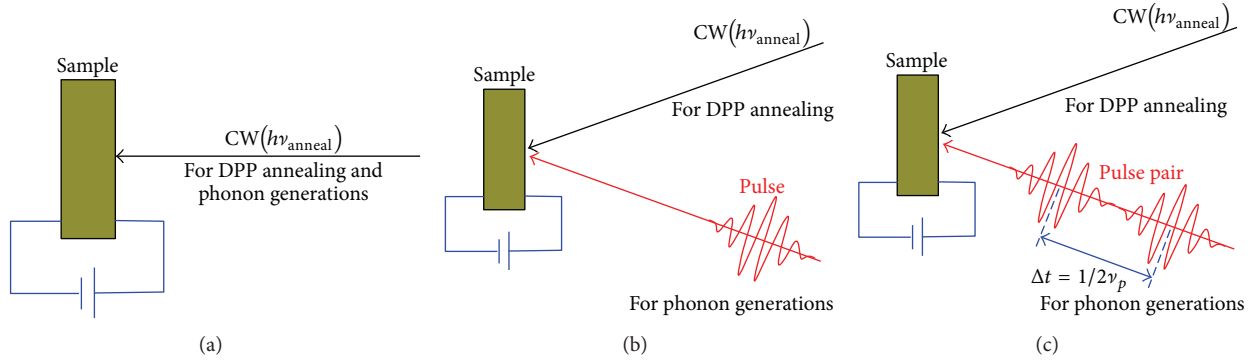


FIGURE 2: Illustration of DPP-assisted annealing using (a) CW light (conventional process); (b) CW light and a light pulse; and (c) CW light and two light pulses.

$|E_g; e\rangle \otimes |E_{\text{ex}}^{\text{thermal}}; \text{phonon}\rangle$, which occurs via emission of an optical phonon. Thus, it is conjugate to process (1). In this process, $|E_{\text{ex}}^n; \text{phonon}\rangle$ in Figure 1 shows the phonon excited state after the emission of the optical phonon. The emitted photon energy is $h\nu_{\text{anneal}} - h\nu_p$.

Similarly, processes (n) and (n^\dagger) are transitions in which n optical phonons are absorbed or emitted. Since, in practice, the processes (n) and (n^\dagger) occur simultaneously, sidebands with photon energies $h\nu_{\text{anneal}} - nh\nu_p$ and $h\nu_{\text{anneal}} + nh\nu_p$ appear in the emission spectrum. The relationship between the n th order sideband energy and the photon energy $h\nu_{\text{anneal}}$ is the same as that of an n th order Raman scattering process with respect to the zero-phonon line. As is well-known, in Raman scattering, when a large number of phonons are excited, the electrons absorb them, emitting light. On the other hand, when a small number of phonons are excited, the electrons emit phonons, emitting light [17]. Thus, the intensity of these sidebands changes according to the number of phonons. This suggests that the intensity of the sidebands can be controlled by controlling the number of phonons.

3. Principle of Controlling the Number of Phonons

The number of created phonons can be controlled by a method involving multiphoton absorption or coherent phonon (CP) excitation using pulsed light. Since the Si crystal is heated by DPP-assisted annealing in the present work, resonant absorption to a specific exciton state for creation of coherent phonons is not possible by using a high-power CW-laser optical source. This is because the high-power CW laser excitation dose not change only the phonon structures but also DP state. Therefore, we decided to selectively create phonons via CP excitation using ultrashort pulsed light. The principle of the CP excitation in this case can be understood as an impulsive stimulated Raman scattering (ISRS) process, which is a kind of stimulated Raman scattering [18]. The duration and the repetition rate of the used pulsed light were 17 fs and 80 MHz, respectively. Therefore, its duty ratio was 1.3×10^{-6} . The Raman process is based on the third order optical nonlinearity. Therefore, the enough laser power for the control of CP generation using the ultrashort pulsed light is 2.3×10^{-18} times lower than that using the CW laser.

Thus, in the experiment, the adverse effect was reduced to the negligible small coming from the DP generation by the additional laser excitation for the CP control.

In ISRS, the frequency component of the pulsed light irradiating the crystal includes coherent frequency components ν and $\nu - \nu_p$ with sufficiently high intensity, where ν_p is the phonon vibration frequency. Therefore, when the crystal is irradiated with pulsed light, the electrons absorb light with energy $h\nu$ and exhibit stimulated emission of light with energy $h\nu - h\nu_p$. At this time, it is possible to create CPs having an energy $h\nu_p$. Since these CPs are coherent, it is possible to control the creation of CPs by a single pulse or multiple pulses of light and causing them to interfere. In other words, unlike conventional DPP-assisted annealing in which the Si crystal is irradiated with CW light, CP creation is controlled by irradiating the Si crystal with pulsed light in addition to CW light. Therefore, it is possible to control the intensities of the sidebands in the EL spectrum. In the following, we describe the case where the Si-LED is irradiated with a single pulse of light during the DPP-assisted annealing and the case where the Si-LED is irradiated with a pair of light pulses.

(1) *Irradiation with a Single Light Pulse.* In the conventional DPP-assisted annealing, as shown in Figure 2(a), the CW light plays the role of decreasing the thermal diffusion rate by means of stimulated emission. In our approach, as shown in Figure 2(b), a light pulse is also radiated, together with the CW light. Since the light pulse excites multimode CPs via ISRS, the coupling probability of electron-hole pairs, photons, and CPs increases. As a result, the probability of electrons absorbing phonons and emitting light increases because the number of excited phonons increases as the light emission intensity increases. Therefore, the intensity of the sidebands having energy $h\nu_{\text{anneal}} + nh\nu_p$ increases, and the intensity of sidebands having energy $h\nu_{\text{anneal}} - nh\nu_p$ decreases. Thus, compared with an Si-LED fabricated by irradiation with only CW light, it is expected that the EL spectral shape of the Si-LED will show a higher light emission intensity at energies higher than $h\nu_{\text{anneal}}$ and conversely a lower light emission intensity at energies lower than $h\nu_{\text{anneal}}$.

(2) *Irradiation with Two Light Pulses (Light Pulse Pair).* Since the CPs created by ISRS are coherent and thus have the ability

to interfere, as described above, let us consider the case where a Si crystal is sequentially irradiated with two coherent light pulses having an arrival time difference Δt . If the value of Δt is a half-integer multiple of the vibration period, $1/\nu_p$, of the phonons ($n/2\nu_p$; $n = 1, 3, 5, \dots$), as shown in Figure 2(c), it is known that the excited CPs destructively interfere [19]. On the other hand, they constructively interfere when Δt is an integer multiple of the vibration period (n/ν_p ; $n = 1, 2, 3, \dots$). That is to say, by radiating a pair of light pulses, it is possible to control the creation of CPs so as to be suppressed or enhanced. Thus, by adjusting the value of Δt , it is possible to perform various types of sideband control as compared with (1) above.

As an example, in the case of $\Delta t = 1/2\nu_p$, we will explain how the CP creation is controlled and how, as a result of this, the EL spectrum is controlled. The value $\Delta t = 1/2\nu_p$ corresponds to one period of vibration of a phonon with frequency $2\nu_p$. Therefore, by radiating a pair of pulses having this value Δt , the number of phonons of frequency ν_p decreases, whereas the number of phonons of frequency $2\nu_p$ increases. Thus, the probability of process (1[†]) increases, by which electrons emit phonons of frequency ν_p and emit light, resulting in a higher probability of electrons absorbing phonons of frequency $2\nu_p$ and emitting light. In other words, as a result of the reduction in the number of phonons with frequency ν_p , the intensity of the sideband at energy $h\nu_{\text{anneal}} - h\nu_p$ becomes higher than that of the sideband at energy $h\nu_{\text{anneal}} + h\nu_p$. At the same time, as a result of the increase in the number of phonons with frequency $2\nu_p$, the intensity of the sideband at energy $h\nu_{\text{anneal}} - 2h\nu_p$ becomes lower than that of the sideband at energy $h\nu_{\text{anneal}} + 2h\nu_p$. The above discussion can also be extended to an explanation of the case where the sideband intensity at energy $h\nu_{\text{anneal}} - (2n - 1)\nu_p$ increases, and that at energy $h\nu_{\text{anneal}} + (2n - 1)\nu_p$ decreases. It can be also extended to the case where the sideband intensity at energy $h\nu_{\text{anneal}} - 2n\nu_p$ decreases, and that at energy $h\nu_{\text{anneal}} + 2n\nu_p$ increases. For controlling the number of phonons during the DPP-assisted annealing, we irradiate two light pulses with delay times of $\Delta t = 1/\nu_{p,\text{exp}}$ ($= 64.1$ fs), $1/2\nu_{p,\text{exp}}$ ($= 32.1$ fs), and $1/4\nu_{p,\text{exp}}$ ($= 16.0$ fs).

4. Fabrication of Si-LED and Evaluation of EL Spectrum

To fabricate a Si-LED, we doped a $625 \mu\text{m}$ -thick n -type Si (100) substrate with arsenic (As) at a concentration of about 10^{15} cm^{-3} . The resulting resistivity was $10 \Omega\text{cm}$. Next, we formed a p-n homojunction by ion implantation of boron (B) with a dose of $5 \times 10^{13} \text{ cm}^{-2}$ and an acceleration energy of 700 keV . Then, we deposited a transparent ITO film with a thickness of 150 nm on the surface of the p layer and a Cr/Al film with a thickness of 80 nm on the surface of the n layer, both by RF sputtering, to form an anode and a cathode, respectively. The device fabrication conditions up to this point were the same as those reported in [12]. In DPP-assisted annealing, we used CW laser light with energy $h\nu_{\text{anneal}} = 0.94 \text{ eV}$ (wavelength $1.3 \mu\text{m}$) as the light source for creating DPs. As the pulsed light source for creating CPs,

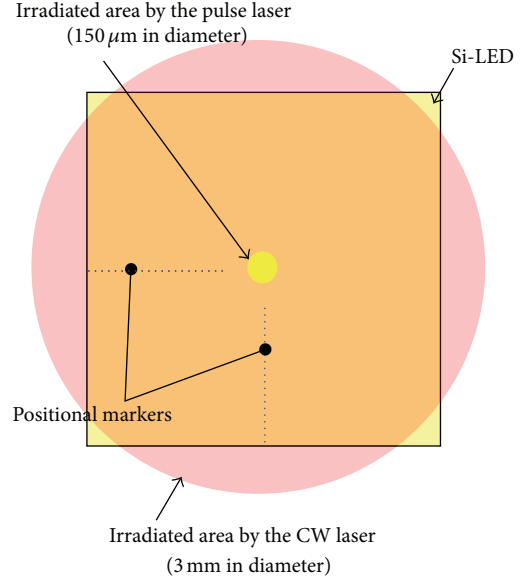


FIGURE 3: Irradiation spots of CW light and pulsed light on sample surface during DPP-assisted annealing.

we used a mode-locked laser with a photon energy of 1.55 eV (wavelength $0.8 \mu\text{m}$), a pulse width of 17 fs , and a repetition frequency of 80 MHz . To verify the DPP-assisted annealing method, we employed the following four samples.

(a) *Sample 1.* Sample 1 was irradiated with pulsed light (average power 100 mW , spot diameter $150 \mu\text{m}$) and CW light ($h\nu_{\text{anneal}} = 0.94 \text{ eV}$, power 1 W , spot diameter 3 mm). It was annealed with a voltage of 20 V and a current of 145 mA for 1 hour (Figure 2(b)).

(b) *Samples 2–4.* Of the CPs created by pulsed light irradiation, we selected optical phonons with the highest creation probability [20] ($h\nu_p = 65 \text{ meV}$ ($\nu_p = 15.6 \text{ THz}$); indicated as $h\nu_{p,\text{exp}}$ below) as the phonons to be controlled. The samples were irradiated with CW light and a pair of light pulses with $\Delta t = 1/\nu_{p,\text{exp}}$ ($= 64.1 \text{ fs}$), $1/2\nu_{p,\text{exp}}$ ($= 32.1 \text{ fs}$), and $1/4\nu_{p,\text{exp}}$ ($= 16.0 \text{ fs}$). They were annealed with a voltage of 25 V and a current of 120 mA for 1 hour (Figure 2(c)). The other experimental conditions were the same as those used for Sample 1 above. In the following, samples for $\Delta t = 1/\nu_{p,\text{exp}}$, $1/2\nu_{p,\text{exp}}$, and $1/4\nu_{p,\text{exp}}$ are referred to as Samples 2, 3, and 4, respectively.

To eliminate the contributions of variations in the sizes and shapes of the electrode and the substrate to the experimental results, the CW light was radiated onto the entire surface of the sample, and the pulsed light was radiated only at the center of the region irradiated with the CW light, as shown by the red and yellow circles, respectively, in Figure 3. With the samples prepared with this method, the EL spectral shapes in these two circles were different. By taking this difference between the intensities of these EL spectra, it was possible to eliminate the contributions above and to examine the details of the changes in the EL spectra depending on the presence/absence of the pulsed light irradiation. Experimental results are shown below.

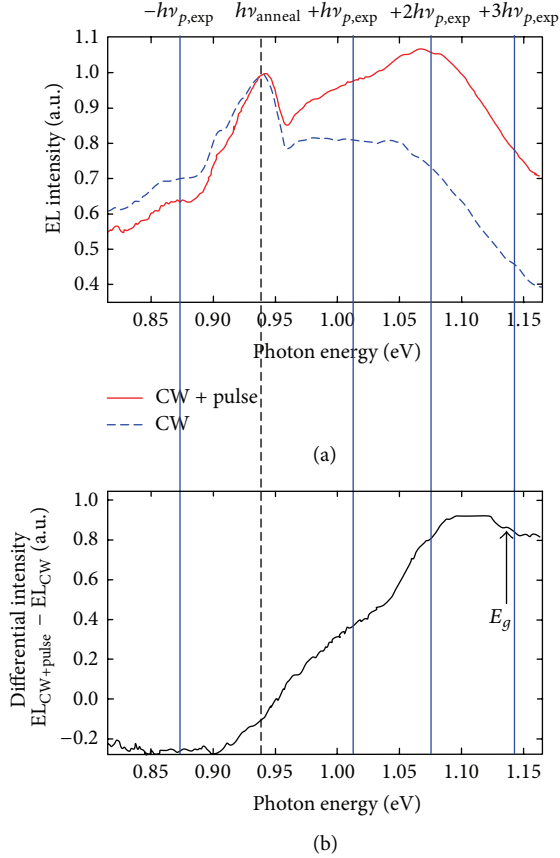


FIGURE 4: (a) EL spectra of Sample 1 after DPP-assisted annealing with the method in Figure 2(b). Red solid curve: area irradiated with CW light and pulsed light. Blue broken curve: area irradiated only with CW light. (b) Differential EL spectrum.

(a) *Sample 1.* Figure 4(a) shows, for Sample 1, the EL spectrum of the part irradiated with only the CW light (blue broken curve: EL_{CW}) and the EL spectrum of the part irradiated with the CW light and the pulsed light (red solid curve: $EL_{CW+pulse}$). Figure 4(b) shows the difference between their intensities ($EL_{CW+pulse} - EL_{CW}$; differential EL spectrum). By irradiating the sample with the pulsed light, the EL intensity at higher energies increased, and the intensity of the +1 and +2 order sidebands of the optical phonons (energy $h\nu_{p,exp} = 65$ meV) increased. In the differential EL spectrum, we also confirmed band-edge light emission and an increase in the intensity of the +3 order sideband. However, since we did not perform mode selection by using a pair of pulses, the spectra of the sidebands were extremely broad. The increase in intensity of these sidebands is explained by the creation of a large number of CPs by ISRS, using the pulsed light, as explained in Section 3. In other words, since a large number of CPs are created, the process in which CPs are absorbed becomes dominant, resulting in light emission. In addition, the increase in light emission at the band edge is considered to be a consequence of the increased number of phonons due to CP creation causing an increased probability of a direct transition between electronic bands.

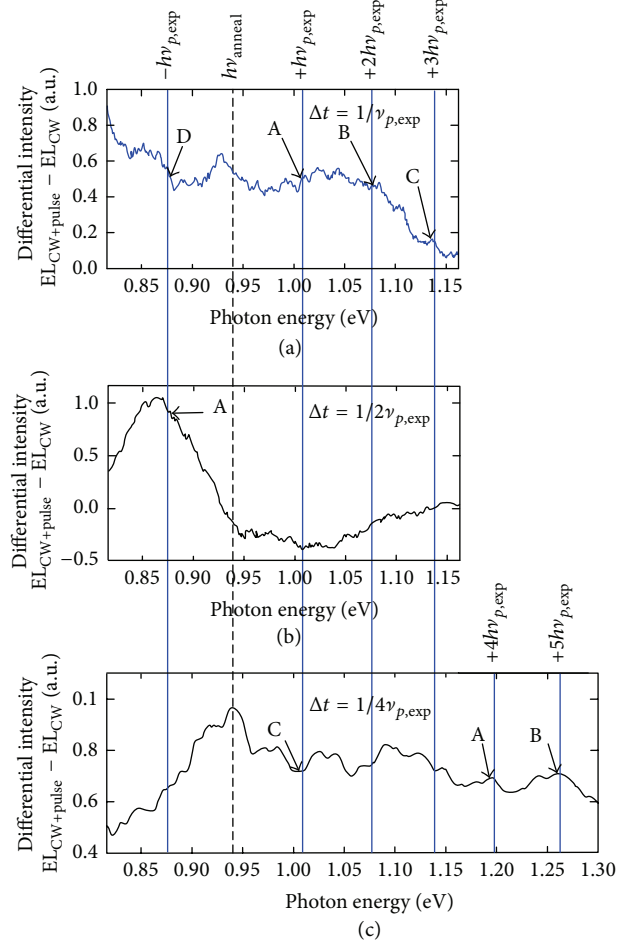


FIGURE 5: Differential EL spectra. (a) Sample 2 with $\Delta t = 1/\nu_{p,exp}$. (b) Sample 3 with $\Delta t = 1/2\nu_{p,exp}$. (c) Sample 4 with $\Delta t = 1/4\nu_{p,exp}$.

On the other hand, in the sideband corresponding to the -1 order optical phonons, the EL intensity is decreased by the incident pulsed light during DPP-assisted annealing. This is because process (1^\dagger), in which optical phonons and light are emitted, is suppressed due to CPs created by the pulsed light.

(b) *Sample 2.* Figure 5(a) shows the differential EL spectrum for Sample 2. In this sample, small bumps (arrows A, B, and C) are observed at the positions of the +1 to +3 order optical phonon sidebands ($h\nu_{p,exp} = 65$ meV). They are due to the selective creation of optical phonons $n h\nu_{p,exp}$ ($n = 1, 2, 3, \dots$), which were mode-selected by irradiating this sample with a pair of pulses with $\Delta t = 1/\nu_{p,exp}$. On the other hand, a region with reduced light emission, like that seen in Figure 4(b), was not observed in the region whose energy is lower than $h\nu_{anneal}$ (arrow D). The reason for this is that the number of created optical phonons is half or less of that in the case of Sample 1 because ISRS is a second-order nonlinear process, and the energy of the pulses irradiating this sample is one-half of the energy of the pulses irradiating Sample 1. This is due to the

suppression of process (1^\dagger), in which light emission occurs while phonons are emitted.

(c) *Sample 3.* Figure 5(b) shows the differential EL spectrum for Sample 3. In this sample, the intensity of the -1 order sideband increased (arrow A). The reason for this is that, with $\Delta t = 1/2\nu_{p,\text{exp}}$, the number of odd-numbered harmonic components was decreased, and the number of even-numbered harmonic components was increased. In other words, since the electrons had an increased probability of emitting the $+1$ order phonons, process (1^\dagger) was dominant, and the intensity of the -1 order sideband increased. On the other hand, process (1), in which light emission occurs while phonons are absorbed, is suppressed. Therefore, since the high-order modes are also suppressed, a region exhibiting reduced optical phonon sidebands is observed at energies higher than $h\nu_{\text{anneal}}$, which is the opposite to what is shown in Figure 4(b).

(d) *Sample 4.* Figure 5(c) shows the differential EL spectrum for Sample 4. The intensities of the $+1$ order and $+2$ order sidebands were decreased, and those of the $+4$ order and $+5$ order sidebands were increased. A reason for this is that, with $\Delta t = 1/4\nu_{p,\text{exp}}$, the number of $+2$ order harmonic phonons was decreased, and that the number of $+4$ order harmonic phonons was increased. The reason for the increase in the number of optical phonons in the $+5$ order is considered to be because the values of $1/4\nu_{p,\text{exp}}$ and $1/5\nu_{p,\text{exp}}$ are close. As a result, the intensity of the $+1$ order sideband is decreased. In other words, this is because the $+1$ order optical phonons are absorbed for creating the $+4$ order and $+5$ order harmonic phonons. The reason why the generation of the $+5$ order sideband dominates over generation of the $+1$ order sideband is that the energy of the $+5$ order sideband is higher than the bandgap energy, E_g , of Si, and this is a phonon scattering process that is resonant with the electronic level. As a result, process (1) is suppressed, and the intensity of the $+1$ order sideband is decreased. On the other hand, since the overall number of optical phonons is increased, process (1^\dagger) is suppressed, as in the case of Figure 4(b). As a result, a region with reduced light emission, similar to that seen in Figure 4(b), is observed in the region at energy $h\nu_{\text{anneal}} - nh\nu_{p,\text{exp}}$.

Figure 6 shows EL spectra of the regions irradiated with the light pulses for Samples 2 and 3. In Sample 2, the numbers of phonons of the fundamental ($h\nu_{p,\text{exp}}$) and the harmonics ($nh\nu_{p,\text{exp}}$; $n = 2, 3, \dots$) were all increased, and therefore, the phonon absorption probability of the electrons increased, resulting in higher light emission at higher energies. In Sample 3, on the other hand, due to the interference of CPs, the number of odd-order harmonic components of the phonons was decreased, and the number of even-order harmonic components was increased; therefore, the absorption probability of phonons of odd-order harmonic components was decreased, resulting in relatively higher light emission at lower energies. The above results indicate that the EL spectral shape of the Si-LED was successfully controlled by changing the conditions of the pair of light pulses radiated during DPP-assisted annealing. That is, the intensity at energies

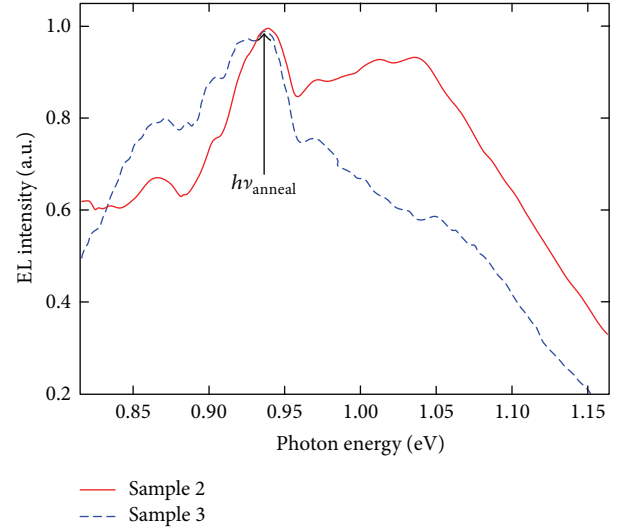


FIGURE 6: EL spectra after annealing for Samples 2 and 3.

higher than $h\nu_{\text{anneal}}$ is increased, and that at lower energies is decreased. Furthermore, conversely, the intensity at energies lower than $h\nu_{\text{anneal}}$ is increased, and that at higher energies is decreased.

In DPP-assisted annealing without using a pulsed light source, the broadening (half width at half maximum, HWHM) towards lower energies was 250 meV or greater, and the broadening (HWHM) towards higher energies was 50 meV. In contrast, in the EL spectrum of the Si-LED fabricated using a pulsed light source for creating phonons, the EL spectrum was broadened towards higher energies by 200 meV or greater (HWHM), and the broadening towards lower energies was reduced to 120 meV (HWHM).

5. Conclusion

In DPP-assisted annealing, we successfully controlled the spectral shape of a Si LED by radiating a pair of light pulses for creating CPs. In the EL spectrum, the intensity of sidebands due to phonons could be controlled by the number of phonons during DPP annealing. The peak wavelength in the EL spectrum was determined by the wavelength of the light source used in DPP-assisted annealing. In order to broaden the EL spectrum toward higher energy, a pair of light pulses having $\Delta t = 1/4\nu_{p,\text{exp}}$ was radiated. Conversely, to broaden the EL spectrum towards lower energies, a pair of light pulses having $\Delta t = 1/2\nu_{p,\text{exp}}$ was radiated. As a result, the EL spectrum was broadened towards higher energies by 200 meV or greater (HWHM), and the broadening towards lower energies was reduced to 120 meV (HWHM).

Conflict of Interests

The authors declare that there is no conflict of interests regarding the publication of this paper.

References

- [1] Z. I. Alferov, "The history and future of semiconductor heterostructures," *Semiconductors*, vol. 32, no. 1, pp. 1–14, 1998.
- [2] R. A. Milano, P. D. Dapkus, and G. E. Stillman, "An analysis of the performance of heterojunction for fiber optic communications," *IEEE Transactions on Electron Devices*, vol. 29, no. 2, pp. 266–274, 1982.
- [3] National Toxicology Program, "NTP technical report on the toxicology and carcinogenesis studies of indium phosphide (CAS No. 22398-80-7) in F344/N rats and B6C3F1 mice (inhalation studies)," Tech. Rep. NTP TR 499, U.S. Department of health and human services, Public Health Service, National Institute of Health, 2001.
- [4] K. D. Hirschman, L. Tsybeskov, S. P. Duttagupta, and P. M. Fauchet, "Silicon-based visible light-emitting devices integrated into microelectronic circuits," *Nature*, vol. 384, no. 6607, pp. 338–341, 1996.
- [5] Z. H. Lu, D. J. Lockwood, and J.-M. Baribeau, "Quantum confinement and light emission in SiO₂/Si superlattices," *Nature*, vol. 378, no. 6554, pp. 258–260, 1995.
- [6] L. Dal Negro, R. Li, J. Warga, and S. N. Basu, "Sensitized erbium emission from silicon-rich nitride/silicon superlattice structures," *Applied Physics Letters*, vol. 92, no. 18, Article ID 181105, 2008.
- [7] T. Komoda, J. Kelly, F. Cristiano et al., "Visible photoluminescence at room temperature from microcrystalline silicon precipitates in SiO₂ formed by ion implantation," *Nuclear Instruments and Methods in Physics Research B*, vol. 96, no. 1–2, pp. 387–391, 1995.
- [8] S. Yerci, R. Li, and L. Dal Negro, "Electroluminescence from Er-doped Si-rich silicon nitride light emitting diodes," *Applied Physics Letters*, vol. 97, no. 8, Article ID 081109, 2010.
- [9] S. K. Ray, S. Das, R. K. Singha, S. Manna, and A. Dhar, "Structural and optical properties of germanium nanostructures on Si(100) and embedded in high-k oxides," *Nanoscale Research Letters*, vol. 6, no. 1, article 224, 10 pages, 2011.
- [10] M. A. Green, J. Zhao, A. Wang, P. J. Reece, and M. Gal, "Efficient silicon light-emitting diodes," *Nature*, vol. 412, no. 6849, pp. 805–808, 2001.
- [11] T. Kawazoe, K. Kobayashi, S. Takubo, and M. Ohtsu, "Nonadiabatic photodissociation process using an optical near field," *Journal of Chemical Physics*, vol. 122, no. 2, Article ID 024715, 2005.
- [12] T. Kawazoe, M. A. Mueed, and M. Ohtsu, "Highly efficient and broadband Si homojunction structured near-infrared light emitting diodes based on the phonon-assisted optical near-field process," *Applied Physics B*, vol. 104, no. 4, pp. 747–754, 2011.
- [13] T. Kawazoe, M. Ohtsu, K. Akahane, and N. Yamamoto, "Si homojunction structured near-infrared laser based on a phonon-assisted process," *Applied Physics B: Lasers and Optics*, vol. 107, pp. 659–663, 2012.
- [14] H. Tanaka, T. Kawazoe, and M. Ohtsu, "Increasing Si photodetector photosensitivity in near-infrared region and manifestation of optical amplification by dressed photons," *Applied Physics B*, vol. 108, no. 1, pp. 51–56, 2012.
- [15] N. Wada, T. Kawazoe, and M. Ohtsu, "An optical and electrical relaxation oscillator using a Si homojunction structured light emitting diode," *Applied Physics B: Lasers and Optics*, vol. 108, no. 1, pp. 25–29, 2012.
- [16] M. A. Tran, T. Kawazoe, and M. Ohtsu, "Fabrication of a bulk silicon p-n homojunction-structured light-emitting diode showing visible electroluminescence at room temperature," *Applied Physics A: Materials Science and Processing*, vol. 115, no. 1, pp. 105–111, 2014.
- [17] S. K. Arora, A. J. Kothari, R. G. Patel, K. M. Chauha, and B. N. Chudasama, "Optical absorption in gel grown cadmium tartrate single crystals," *Journal of Physics*, vol. 28, no. 1, pp. 48–52, 2006.
- [18] Y.-X. Yan, E. B. Gamble Jr., and K. A. Nelson, "Impulsive stimulated scattering: general importance in femtosecond laser pulse interactions with matter, and spectroscopic applications," *The Journal of Chemical Physics*, vol. 83, no. 11, pp. 5391–5399, 1985.
- [19] M. Hase, K. Mizoguchi, H. Harima et al., "Optical control of coherent optical phonons in bismuth films," *Applied Physics Letters*, vol. 69, no. 17, pp. 2474–2476, 1996.
- [20] P. Giannozzi, S. de Gironcoli, P. Pavone, and S. Baroni, "Ab initio calculation of phonon dispersions in semiconductors," *Physical Review B*, vol. 43, no. 9, pp. 7231–7242, 1991.

Research Article

Demonstration of Controlling the Spatiotemporal Dynamics of Optical Near-Field Excitation Transfer in Y-Junction Structure Consisting of Randomly Distributed Quantum Dots

Wataru Nomura,¹ Makoto Naruse,² Masashi Aono,^{3,4} Song-Ju Kim,⁵ Tadashi Kawazoe,¹ Takashi Yatsui,¹ and Motoichi Ohtsu¹

¹ School of Engineering, The Nanophotonics Research Center, The University of Tokyo, 2-11-16 Yayoi, Bunkyo-ku, Tokyo 113-8656, Japan

² Photonic Network Research Institute, National Institute of Information and Communications Technology, 4-2-1 Nukui-kita, Koganei, Tokyo 184-8795, Japan

³ Earth-Life Science Institute, Tokyo Institute of Technology, 2-12-1 Ookayama, Meguro-ku, Tokyo 152-8550, Japan

⁴ PRESTO, Japan Science and Technology Agency, 4-1-8 Honcho, Kawaguchi-shi, Saitama 332-0012, Japan

⁵ WPI Center for Materials Nanoarchitectonics (MANA), National Institute for Materials Science, 1-1 Namiki, Tsukuba, Ibaraki 305-0044, Japan

Correspondence should be addressed to Wataru Nomura; nomura@nanophotonics.t.u-tokyo.ac.jp

Received 10 March 2014; Accepted 24 March 2014; Published 27 April 2014

Academic Editor: Chennupati Jagadish

Copyright © 2014 Wataru Nomura et al. This is an open access article distributed under the Creative Commons Attribution License, which permits unrestricted use, distribution, and reproduction in any medium, provided the original work is properly cited.

Solution searching devices that operate on the basis of controlling the spatiotemporal dynamics of excitation transfer via dressed photon interactions between quantum dots have been proposed. Long-range excitation transfer based on dressed photon interactions between randomly distributed quantum dots is considered to be effective in realizing such devices. Here, we successfully controlled the spatiotemporal dynamics of excitation transfer using a Y-junction structure consisting of randomly dispersed CdSe/ZnS core-shell quantum dots. This Y-junction structure has two “output ends” and one “tap end.” By exciting one output end with control light, we observed increased excitation transfer to the other output end via a state-filling effect. Conversely, we observed reduced excitation transfer to the output ends by irradiating the tap end with control light, due to excitation of defect levels in the tap end. These results show the possibility of controlling the optical excitation transfer dynamics between multiple quantum dots.

1. Introduction

Light excitation in quantum dots (QDs) generates dressed photons, which are light fields localized in the vicinity of the QDs, giving rise to dressed photon interactions with other nearby matter, as well as excitation energy transfer via these interactions [1]. In particular, various optical functional devices, such as logic gates called nanophotonic devices [2–4], light-harvesting devices [5], and optical signal transmitting systems [6, 7], have been realized using QDs formed of CuCl, ZnO, InAs, CdSe, and so forth, based on optical near-field excitation transfer between QDs. Nanophotonic devices have been shown to function as logic gates, such as AND, NOT, and XOR logic gates [2–4]. These devices consist of two

or three closely spaced QDs having different energy levels, and by inputting a light beam serving as a power supply and another light beam serving as a control signal, excitation energy transfer between the QDs is controlled so that the light emitted from one of the QDs serves as the output.

On the other hand, novel solution searching and decision making devices using a QD array provided with multiple output QDs have recently been proposed [8–10]. In these devices, by inputting control signals to the output QDs based on certain rules, the probability of the optical excitation being transferred uniformly to each QD is controlled to obtain a solution. In these operations, it is necessary to control the spatiotemporal dynamics of the optical excitation transfer between spatially distributed QDs. The features of these

devices are that they operate at high speed with low energy consumption since they are driven by excitation transfer based on dressed photon interactions [11]. The proposed solution searching device finds a solution to a nondeterministic polynomial (NP) time complete problem, the satisfiability problem (SAT), much faster than the WalkSAT algorithm, which is one of the fastest stochastic local search algorithms [9, 12]. The proposed decision making device exhibits high efficiency and adaptability in solving decision making problems [10].

However, although it would be ideal to utilize the models discussed in [8–10], it would be technically challenging to directly implement their architecture. One reason for this is that, in order to implement and operate this device, it is essential to fabricate a QD array in which QDs of strictly selected dimensions and number must be precisely located with nanometer-order positioning precision, as reported in [8], which is technologically demanding from the viewpoint of fabrication as the first step. In addition, another reason is the technical challenge of having to guide the control light to multiple output QDs and separately observe the output signals coming from them.

In contrast to this approach, we distributed an extremely large number of identical-size QDs randomly, and by using a structure in which an output QD is provided at the terminal end, we experimentally demonstrated the possibility of optical excitation energy transfer over distances of micrometer order via repeated dressed photon interactions between the QDs [6]. Using such a randomly distributed QD structure overcomes the fabrication difficulties mentioned above, and because of the possibility of scaling up the technique to micrometer order, it is expected that it will also be possible to overcome the technical challenges related to control and observation.

In the work reported in this paper, using a structure in which multiple QDs are randomly distributed, we experimentally investigated control of the spatiotemporal dynamics of optical excitation transfer based on dressed photon interactions between the QDs, which is a requirement for the realization of solution searching and decision making devices. Section 2 describes fundamental principles. Section 3 describes the fabricated device, experimental setup, energy transfer measurement, and characterizations. Section 4 concludes the paper.

2. Principle

First, we will explain optical excitation transfer due to dressed photon interactions and suppression of this process. As shown in Figure 1, a small QD (QD1) and a large QD (QD2) are placed in close proximity. A first excited state E11 in QD1 is resonant with a second excited state E22 in QD2 due to their size ratio of 1:1.43 [13]. When QD1 is excited by excitation light P_{in1} , a dressed photon is generated in the vicinity of QD1. The excitation energy in QD1 is transferred to E22 by dressed photon interactions and then relaxes to E21, which is the first excited state in QD2, via intersubband relaxation. Thus, the excitation energy is transferred unidirectionally (Figure 1(a)).

This is observed as emitted light P_{out2} from QD2. However, if E21, which is the level to which the excitation relaxes, has already been excited by control light P_{in2} , the excitation energy transferred to E22 cannot relax to E21, but it is transferred back to E11, and nutation occurs between E11 and E22 (Figure 1(b)). This is observed as emitted light P_{out1} from QD1, or when there is a QD in the vicinity, this leads to an increase in the probability of excitation transfer to that QD. Based on this principle, assuming that QD1, having multiple QD2's in the vicinity, is excited, by irradiating one QD2 with P_{in2} , the probability of excitation transfer to the other QD2's is changed; in other words, it is possible to control the spatiotemporal dynamics.

Next, we will explain optical excitation transfer based on dressed photon interactions in a randomly distributed QD structure. In this structure, as shown in Figure 1(c), identical-size QDs (QD1) are randomly distributed in close proximity to each other, and QD2's are placed at one location to serve as an output. The input light P_{in1} incident on the QD1's at one end undergoes repeated dressed photon interactions between the QD1's and eventually arrives at the QD2's, where it is output as emitted light P_{out2} from E21. Because the optical excitation is transferred with high probability by QDs having strong dressed photon interactions, optical excitation transfer with high energy efficiency is possible regardless of the QD1 distribution, and it has been experimentally verified that it is possible to transfer the excitation over a distance of more than 10 μm [6].

The experimental model used in this paper is shown in Figure 1(d). The green color in the figure represents a Y-junction QD1 structure consisting of a group of QD1's randomly distributed in close proximity to each other, in the form of strips with a width of 1 μm and a length of 7.5 μm extending in a radiating pattern in three directions from the center O. The ends of the Y-junction are labeled A, B, and C. QD2 structures serving as output ports, where QD2's are grouped together in squares with a side length of 3 μm , are connected at A and B so as to overlap with the QD1 structure. From A and B, called "output ends," we obtain output signals that are observed as radiation. In addition, A and B also serve as terminals for inputting control light. On the other hand, end C, which we call a "tap end," is not connected to any QD2's. The detailed experimental conditions used in this model are omitted. Figure 1(e) shows an energy band diagram in which the section including points A-O-B is illustrated one-dimensionally. When excitation light P_{in1} , serving as an input signal, is incident on the center point O in the QD1 structure, optical excitation is generated in QD1 and is transferred through the QD1 structure by undergoing repeated energy transfer due to dressed photon interactions between the QD1's. Since the optical excitation transferred to QD2 reaches E21 via intersubband relaxation, no reverse flow of the transfer occurs, and therefore the optical excitation is transferred to the ends, A and B, where the QD2 structures are provided. At this time, if end B is irradiated with control light P_{in2} that excites QD2, QD2 is excited, and the excitation light transferred from QD1 does not relax to E21, and thus excitation transfer is not observed. Therefore, a reverse flow of the optical excitation occurs at

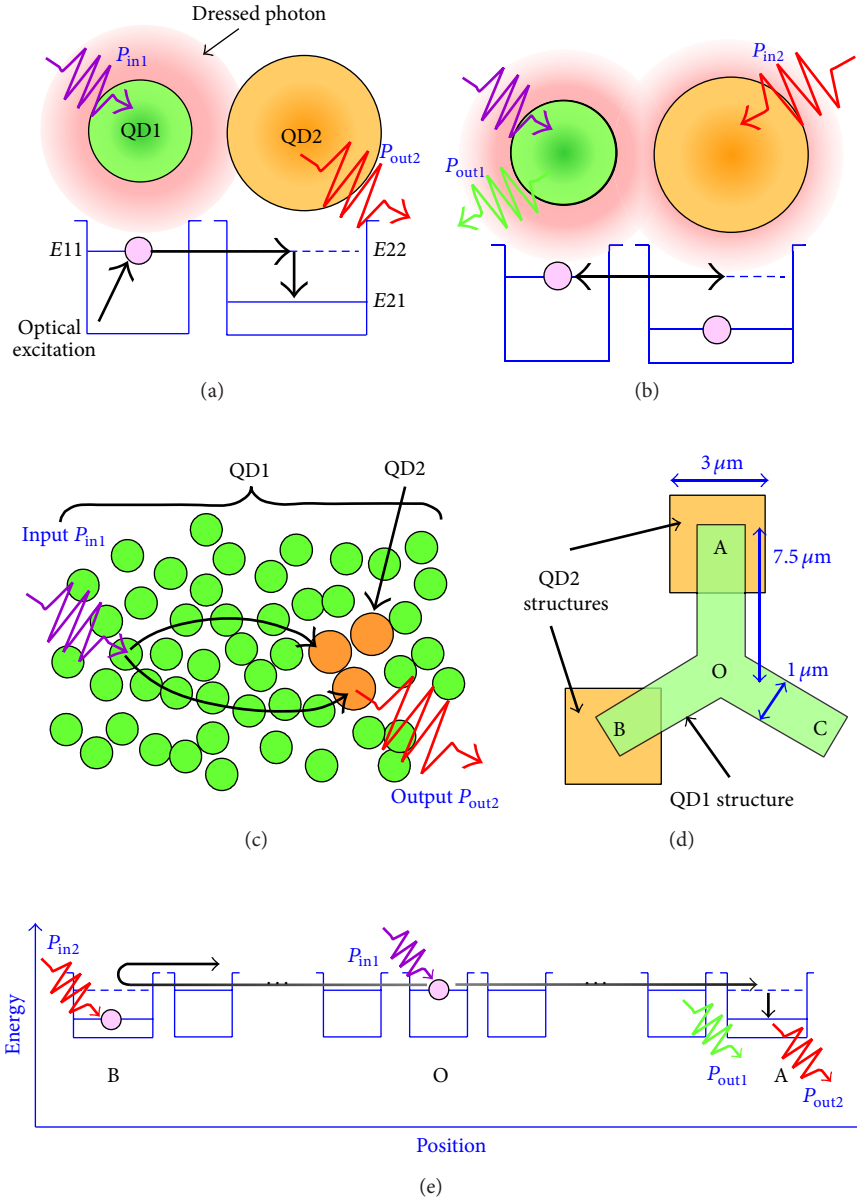


FIGURE 1: (a), (b) Schematic illustration of optical excitation transfer from QD1 to QD2 via dressed photon interactions, where (a) shows the case where energy transfer occurs from QD1 to QD2 and (b) shows the case where control light is incident on QD2, thus suppressing energy transfer. (c) Schematic diagram of long-range optical excitation transfer system. Green and yellow circles represent QD1's and QD2's, respectively. (d) Schematic diagram of experimental model. Green and yellow regions represent groups of QD1 and QD2 structures consisting of randomly distributed QD1's and QD2's, respectively. (e) Energy diagram schematically showing the experimental model from point B to point A.

end B, and the level of excitation transfer to A, which is the other output end, increases. At locations where the excitation transfer is increased, the emitted light P_{out1} and P_{out2} from QD1 and QD2 both increase, and, therefore, we can confirm that the excitation transfer is controlled by evaluating the increase in P_{out1} at end A when end B is irradiated with control light P_{in2} . Note that even if end C is irradiated with control light P_{in2} , a change like that occurring at points A and B is not expected to occur since the excitation state of the QDs does not change.

3. Experiments

3.1. Device. In our experiments, we used commercially available CdSe/ZnS core-shell QDs (manufactured by Quantum Design, Inc.). As QD1 and QD2 described in the previous section, we selected QDs with core-diameters of $d_1 = 2.5$ nm and $d_2 = 3.2$ nm, respectively. Their first excited states, estimated from absorption spectra, were $E11 = 2.36 \pm 0.08$ eV and $E21 = 2.11 \pm 0.06$ eV, respectively. As described above, E11 is resonant with E22, which is the second excited state of QD2 [14].

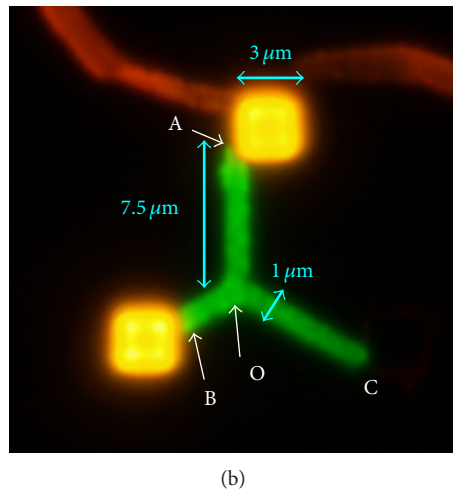
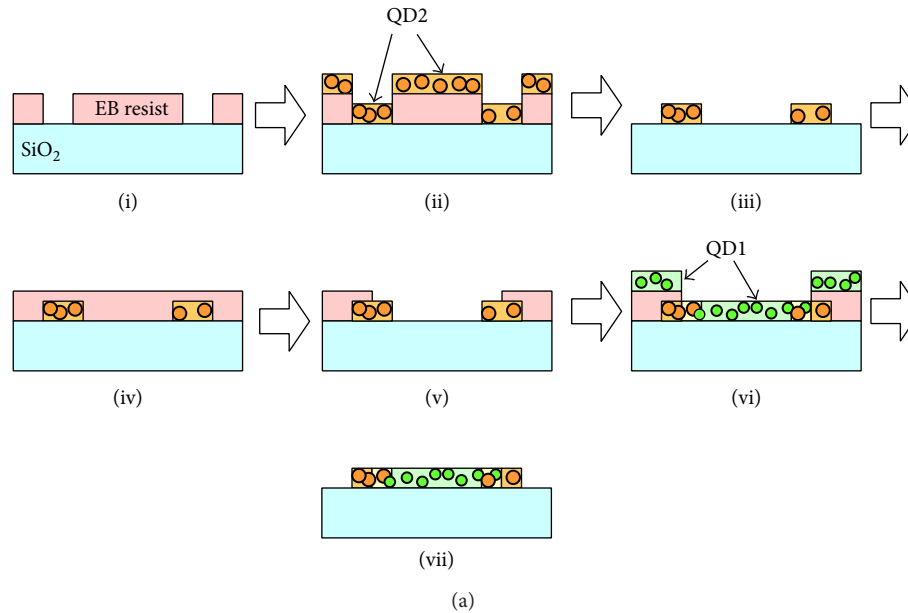


FIGURE 2: (a) Cross-sectional illustrations of sample fabrication process. (i) E-beam resist is applied to SiO₂ substrate, and regions where QD2 structures are to be formed are drawn by e-beam lithography. (ii) QD2 solution is dropped onto substrate and allowed to dry. (iii) E-beam resist is removed to obtain QD2 structures. (iv) E-beam resist is applied again. (v) Region where QD1 structure is to be formed is drawn by e-beam lithography. (vi) QD1 solution is dropped onto resist and allowed to dry. (vii) E-beam resist is removed to obtain the sample. (b) Fluorescence microscope image of sample excited by mercury vapor lamp.

The outside of the shell was modified with a carboxyl group. The solution was dropped onto a substrate and allowed to dry, affording a group of randomly distributed QDs located in close proximity with a center-to-center distance of about 10 to 20 nm.

We fabricated samples using the procedure shown in Figure 2(a). First, by using e-beam lithography on a silica substrate, in e-beam resist (ZEP-520A, Zeon Corp.), we drew locations at which QD2's were to be deposited (Figure 2(a)(i)). Next, the QD2 solution was dropped onto the substrate and allowed to dry (Figure 2(a)(ii)). Then, after removing the resist, we obtained the QD2 structure on the substrate (Figure 2(a)(iii)). Next, e-beam resist was applied on this structure (Figure 2(a)(iv)), and using e-beam lithography, we drew Y-junction locations where QD1's were

to be deposited by aligning the positions so as to contact the QD2 structure (Figure 2(a)(v)). After developing the resist, we dropped the QD1 solution onto the substrate (Figure 2(a)(vi)). Finally, the resist was removed to obtain the Y-junction QD1 structure (Figure 2(a)(vii)). Figure 2(b) shows a fluorescence microscope image obtained when the fabricated sample was excited with a mercury-vapor lamp. The QD1 structure and the QD2 structure were observed as green and yellow colors, respectively. Because points A and B were set at positions where the QD1 and QD2 structures were initially in contact, in practice the distances OA and OB of the fabricated samples were about 6.8 μm and 3.3 μm, respectively. Point C, which did not possess the QD2 structure, was set at a position 7 μm away from O.

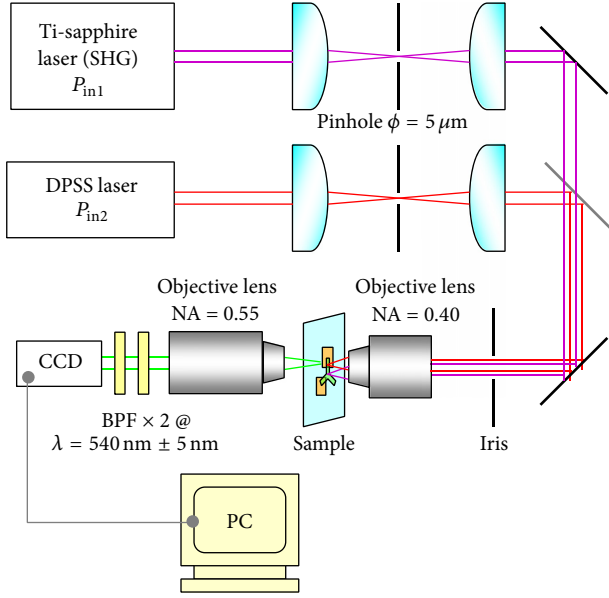


FIGURE 3: Schematic diagram of experimental setup for measurement.

3.2. Experimental Setup. The experimental setup used for performing measurements is shown in Figure 3. For the excitation light P_{in1} , we used the 2nd harmonic wave of a mode-locked Ti: sapphire laser (Mira 900, Coherent, Inc.) with a photon energy $h\nu_1 = 3.44$ eV, a pulse width of 2 ps, and a repetition frequency of 80 MHz, and for the control light P_{in2} , we used a CW diode-pumped solid state (DPSS) laser with a photon energy $h\nu_2 = 2.11$ eV. The incident powers of P_{in1} and P_{in2} were $5 \mu\text{W}$ and $10 \mu\text{W}$, respectively, and the beam spot diameters were both $5 \mu\text{m}$. The beams from the two lasers were shaped by passing them through pinholes with $5 \mu\text{m}$ diameter apertures; then, using a half-mirror, the beams irradiated the sample from the back surface of the substrate via an objective lens with a numerical aperture $\text{NA} = 0.4$. As described in the previous section, because it is possible to observe the change in excitation transfer at the output end as a variation in the emitted light P_{out1} from QD1, we evaluated this in order to make it easier to separate it from the control light. The light emitted from QD1 was observed using an electron multiplying CCD camera (Hamamatsu ImagEM C9100-13H, Hamamatsu Photonics K.K.) after passing through an objective lens with $\text{NA} = 0.55$ and two bandpass filters with transmission wavelengths of 540 ± 5 nm, which is close to the wavelength of P_{out1} . The acquired images were 512×512 pixel, 16-bit grayscale images, and the resolution was $0.37 \mu\text{m}/\text{pixel}$.

As an example of the measurement results, Figure 4(a) shows a CCD image acquired when O and A were irradiated with excitation light P_{in1} and control light P_{in2} , respectively. The green and yellow broken lines show the QD1 and QD2 structures, respectively. Point O was irradiated with P_{in1} , and we observed that the light emitted from the QD1 structure spread out in three directions due to transfer of the excitation. A cross-sectional brightness profile taken along the light-blue dotted line in this figure is shown by the red solid line in

Figure 4(b). The black solid line shows the case where point O was irradiated with only P_{in1} . The red solid line is higher in a portion of the QD1 structure serving as the transfer path OB and the point B having the QD2 structure, confirming the tendency for the optical excitation directed towards point B to be increased due to the influence of P_{in2} incident on point A.

3.3. Energy Transfer in Y-Junction Structure. To evaluate the intensity of the emitted light, we used the brightness values acquired with the CCD camera, where the total brightness of 3×3 pixels was defined as emission intensity, I . While irradiating point O with P_{in1} , we measured I_{ij} , where i indicates the output end A or B, and j indicates where the control-light P_{in2} is irradiated, that is, to the input terminal A, B, or C. Also, when no control light is irradiated, we represent this by $j = 0$. Concerning the characteristics of the device under study, described in Section 3.1, there are four representative categories:

- Reference: without any P_{in2} ($j = 0$);
- Case 1: emission end and control-light input terminal are the same point ($i = j$);
- Case 2: emission end and control-light input terminal are opposite points ($(i, j) = (A, B)$ or (B, A));
- Case 3: control-light input terminal is point C ($j = C$).

The evaluation was performed using the relative intensity change, ΔI_{ij} , defined as $\Delta I_{ij} = (I_{ij} - I_{i0})/I_{i0}$. At this time, if ΔI_{ij} is positive in Case 2, excitation transfer from one end at which the control light is input to the other end will be increased, and control of the excitation transfer will be observed.

Figure 4(c) shows a plot of ΔI_{ij} obtained in Cases 1, 2, and 3. First, we evaluated Case 1 (i.e., $i = j$), as shown by the blue bars in Figure 4(c); they took positive values $\Delta I_{AA} = 3.9 \times 10^{-2}$ and $\Delta I_{BB} = 3.7 \times 10^{-2}$, confirming that the emitted light was stronger. This is the effect of controlling the excitation transfer, and regarding energy transfer in the regions where QD1 and QD2 coexist, we obtained results showing that it is possible to control the excitation transfer also among multiple QDs. This indicates that an AND-gate operation was manifested with multiple randomly distributed QDs, as reported in [3].

Next, we evaluated Case 2 (i.e., $i \neq j = A, B$), as shown by the red bars in Figure 4(c); they also took positive values $\Delta I_{AB} = 7.3 \times 10^{-2}$ and $\Delta I_{BA} = 3.1 \times 10^{-2}$, confirming that the emitted light was stronger. ΔI_{AB} was higher than ΔI_{BA} because the wider overlapped area of QD1 and QD2 structures at point B provided more variation of excitation transfer than that at point A. This difference can be reduced by preparing finer structures and will not disturb the proper operation of solution exploring algorithms. From these results, we confirmed that the excitation transfer was suppressed by the incident control light. These results show that it is possible to control the optical excitation transfer dynamics in a randomly distributed QD structure. Since the relative change ΔI was reduced by losses involved in the optical excitation transfer, we expect that larger values will

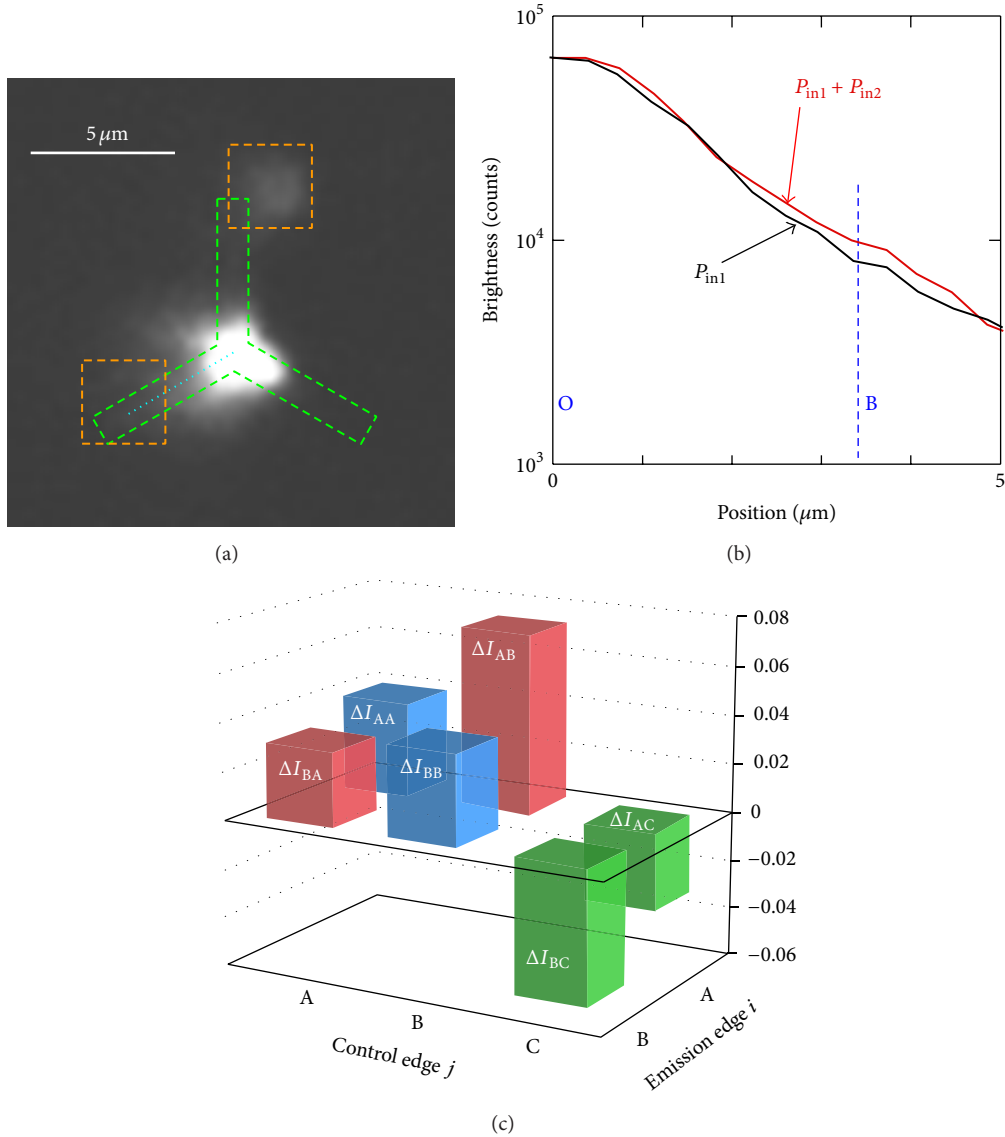


FIGURE 4: (a) Image of light emission from E11 in sample, acquired with CCD camera. Points O and A are irradiated with light P_{in1} and P_{in2} , respectively. Green and yellow broken lines represent the QD1 and QD2 structures, respectively. (b) Cross-sectional profile of emission intensity from E11, acquired with CCD. The red solid line is the cross-sectional profile taken along the light-blue dotted line in (a). The black solid line is the cross-sectional profile taken along the same location, when point O was irradiated with P_{in1} only. The $0 \mu\text{m}$ base point and the blue broken line indicate point O and point B, respectively. (c) Graph of relative change ΔI_{ij} in emission intensity from E11. Blue, red, and green bars represent Cases 1, 2, and 3, respectively.

be possible by designing a structure having shorter distances OA and OB.

3.4. Discussion on Negative Intensity Change. Moreover, we evaluated Case 3 (i.e. $j = C$), as shown by the green bars in Figure 4(c); they took negative values $\Delta I_{AC} = -3.2 \times 10^{-2}$ and $\Delta I_{BC} = -5.5 \times 10^{-2}$. Ideally, QD1 should be transparent to P_{in2} ; however, in our experiments, defect levels with energies lower than E11 in QD1 were excited by P_{in2} [15, 16]. We consider that this excitation prevented the excitation in E11 from slow and nonradiative relaxation via the defect levels.

To verify this, we performed photoluminescence measurements on the QD1 structure. In this experiment, we used samples having only the QD1 structure, fabricated with the same process as that used to fabricate the measurement samples, and we performed measurements with an experimental setup in which the bandpass filters and the CCD camera in the setup shown in Figure 3 were replaced with a spectrometer. The incident powers of P_{in1} and P_{in2} were $5 \mu\text{W}$ and $770 \mu\text{W}$, respectively, and the beams irradiated the sample in spot diameters of $10 \mu\text{m}$. The emission intensities were integrated in the range $2.25 < h\nu < 2.29 \text{ eV}$, corresponding to the peak wavelength of P_{out1} , and were normalized to the

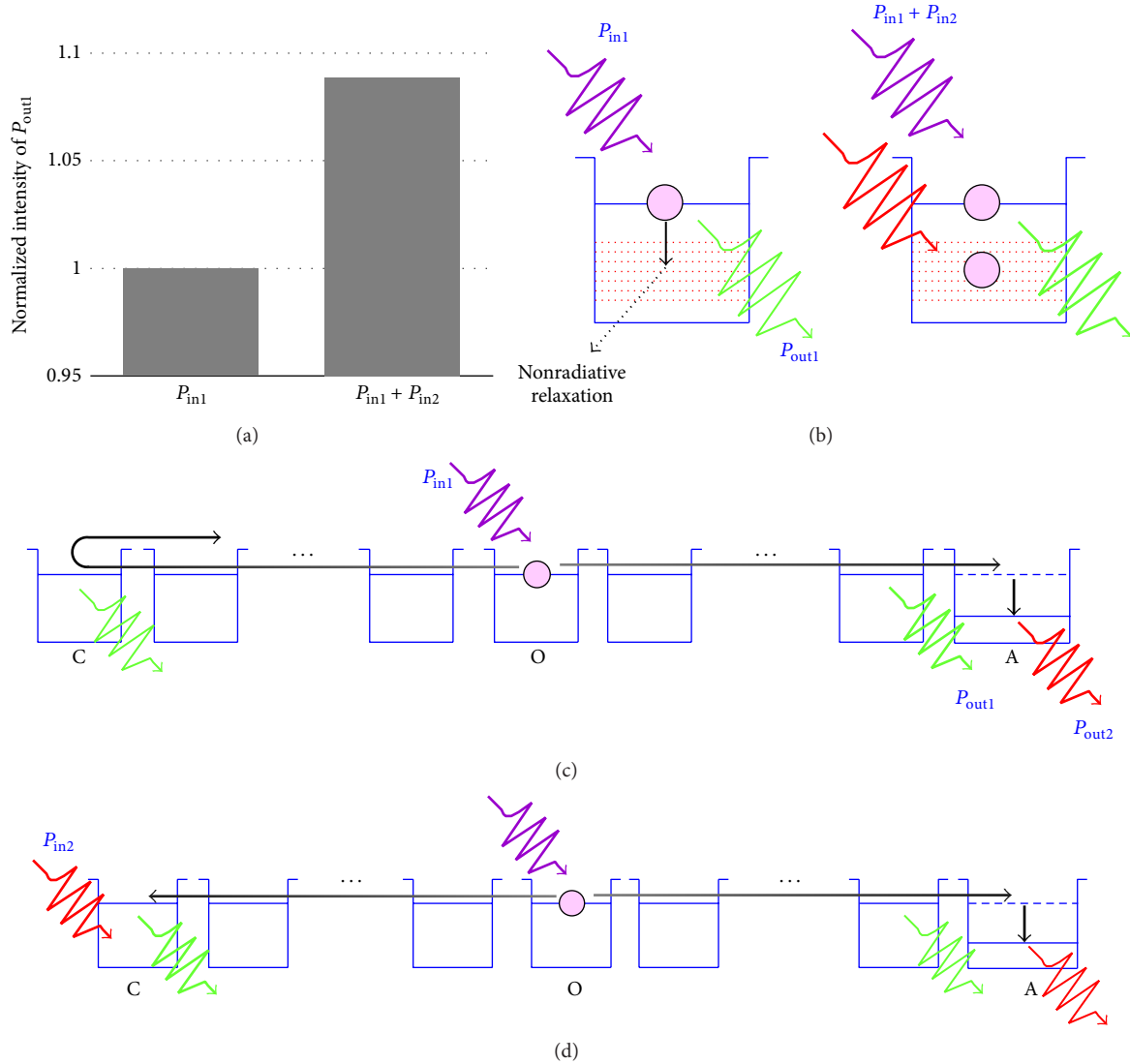


FIGURE 5: (a) Normalized intensity of emitted light P_{out1} from E11, showing cases where the QD1 structure was irradiated with only P_{in1} and with both P_{in1} and P_{in2} . (b) Schematic image of emission from QD1 with only P_{in1} or with both P_{in1} and P_{in2} . (c), (d) Energy diagram schematically showing the experimental sample from point C to point A: (c) without P_{in2} , (d) point C irradiated with P_{in2} .

emission intensity when only P_{in1} was radiated and were compared. As a result, the emission intensity for the case where P_{in1} and P_{in2} were simultaneously radiated was 1.09, showing that the emitted light was increased by radiating P_{in2} (Figure 5(a)). This was the result of defect levels in QD1 being excited by P_{in2} , suppressing the nonradiative relaxation process from E11 via defect levels, which increased the emitted light (Figure 5(b)).

From this result, the negative ΔI values in Case 3 can be explained as follows. Without P_{in2} , the excitation transferred to end C reflects and enhances P_{out1} at ends A and B (Figure 5(c)). By irradiating end C with P_{in2} , P_{out1} at C increases due to excitation of defect levels in QD1, and the reflection decreases (Figure 5(d)). As a result, P_{out1} at ends A and B decreases by irradiation of C with P_{in2} . This differs from the principle of excitation transfer suppression described

in Section 2 and Figure 1(e) but indicates the possibility of another method of controlling the spatiotemporal dynamics of excitation transfer. Also, this increased light emission due to the fact that excitation of defect levels can also occur in QD1 at points A and B; however, the energy transfer suppression effect due to excitation of E21 should be larger than this because absorption of P_{in2} ($h\nu_2 = 2.11$ eV) in QD2 is 24 times higher than that in QD1. Thus, the effect of excitation of defect levels at ends A and B is negligible.

4. Summary

In summary, to show the possibility of controlling the spatiotemporal dynamics of optical excitation transfer based on dressed photon interactions between multiple randomly distributed quantum dots (QDs), we conducted experiments

to control excitation transfer using randomly distributed QD structures. Using CdSe/ZnS core-shell QDs, we fabricated a Y-junction structure composed of randomly distributed QDs (QD1 structure). Optical excitation incident at the center of this structure was transferred to a QD2 structure serving as an output end located 3–7 μm away, and by irradiating a QD2 structure at another end with control light $P_{\text{in}2}$, we observed a maximum increase of 7.3×10^{-2} . Thus, we have shown, for the first time, that it is possible to control the spatiotemporal dynamics of optical excitation transfer in a randomly distributed QD structure. Our findings will lead to simplified implementation and driving of solution searching and decision making devices based on the optical excitation transfer dynamics between QDs and will contribute to their practical realization. On the other hand, when control light $P_{\text{in}2}$ was incident on the output end that did not have a QD2 structure, we found that the amount of excitation energy transferred to the output end was reduced by a maximum of 5.5×10^{-2} . This was thought to be because the light emission from QD1 was increased due to excitation of defect levels in QD1, and the amount of excitation energy transferred to the end provided with the QD2 structure serving as an output was reduced. This effect acted in a direction causing a reduction in excitation transfer, opposite to the increased transfer level due to excitation of the QD2 structure, indicating the possibility of a different kind of control of the spatiotemporal dynamics. This result is expected to lead to the development of novel computing device architectures in the future.

Conflict of Interests

The authors declare that there is no conflict of interests regarding the publication of this paper.

Acknowledgment

A part of this work was supported by the “Development of Next-generation High-performance Technology for Photovoltaic Power Generation System” Program, NEDO, Japan.

References

- [1] M. Ohtsu, T. Kawazoe, T. Yatsui, and M. Naruse, “Nanophotonics: application of dressed photons to novel photonic devices and systems,” *IEEE Journal on Selected Topics in Quantum Electronics*, vol. 14, no. 6, pp. 1404–1417, 2008.
- [2] T. Kawazoe, K. Kobayashi, S. Sangu, and M. Ohtsu, “Demonstration of a nanophotonic switching operation by optical near-field energy transfer,” *Applied Physics Letters*, vol. 82, no. 18, pp. 2957–2959, 2003.
- [3] T. Kawazoe, M. Ohtsu, S. Aso et al., “Two-dimensional array of room-temperature nanophotonic logic gates using InAs quantum dots in mesa structures,” *Applied Physics B: Lasers and Optics*, vol. 103, no. 3, pp. 537–546, 2011.
- [4] A. Karimkhani and M. K. Moravvej-Farshi, “Design of three-input nanophotonic and gates,” *Journal of the Optical Society of America B: Optical Physics*, vol. 26, no. 5, pp. 1084–1090, 2009.
- [5] T. Kawazoe, K. Kobayashi, and M. Ohtsu, “Optical nanofountain: a biomimetic device that concentrates optical energy in a nanometric region,” *Applied Physics Letters*, vol. 86, no. 10, Article ID 103102, pp. 1–3, 2005.
- [6] W. Nomura, T. Yatsui, T. Kawazoe, M. Naruse, and M. Ohtsu, “Structural dependency of optical excitation transfer via optical near-field interactions between semiconductor quantum dots,” *Applied Physics B: Lasers and Optics*, vol. 100, pp. 181–187, 2010.
- [7] P. Holmström, L. Thylén, and A. Bratkovsky, “Composite metal/quantum-dot nanoparticle-array waveguides with compensated loss,” *Applied Physics Letters*, vol. 97, Article ID 073110, 2010.
- [8] M. Naruse, M. Aono, S.-J. Kim et al., “Spatiotemporal dynamics in optical energy transfer on the nanoscale and its application to constraint satisfaction problems,” *Physical Review B*, vol. 86, Article ID 125407, 2012.
- [9] M. Aono, M. Naruse, S.-J. Kim et al., “Amoeba-inspired nanoarchitectonic computing: solving intractable computational problems using nanoscale photoexcitation transfer dynamics,” *Langmuir*, vol. 29, no. 254, pp. 7557–7564, 2013.
- [10] S.-J. Kim, M. Naruse, M. Aono, M. Ohtsu, and M. Hara, “Decision maker based on nanoscale photo-excitation transfer,” *Scientific Reports*, vol. 3, Article ID 2370, 2013.
- [11] M. Naruse, H. Hori, K. Kobayashi, P. Holmström, L. Thylén, and M. Ohtsu, “Lower bound of energy dissipation in optical excitation transfer via optical near-field interactions,” *Optics Express*, vol. 18, no. 23, pp. A544–A553, 2010.
- [12] U. Schöning, “A probabilistic algorithm for k-SAT and constraint satisfaction problems,” in *Proceedings of the 40th IEEE Symposium on Foundations of Computer Science*, pp. 410–414, 1999.
- [13] N. Sakakura and Y. Masumoto, “Persistent spectral-hole-burning spectroscopy of CuCl quantum cubes,” *Physical Review B—Condensed Matter and Materials Physics*, vol. 56, no. 7, pp. 4051–4055, 1997.
- [14] C. Trallero-Giner, A. Debernardi, M. Cardona, E. Menéndez-Proupín, and A. I. Ekimov, “Optical vibrons in CdSe dots and dispersion relation of the bulk material,” *Physical Review B—Condensed Matter and Materials Physics*, vol. 57, no. 8, pp. 4664–4669, 1998.
- [15] M. Y. Valakh, Y. G. Sadfyev, N. O. Korsunskaya et al., “Deep-level defects in CdSe/ZnSe QDs and giant anti-stokes photoluminescence,” *Semiconductor Physics, Quantum Electronics and Optoelectronics*, vol. 5, no. 3, pp. 254–257, 2002.
- [16] M. Danek, K. F. Jensen, C. B. Murray, and M. G. Bawendi, “Synthesis of luminescent thin-film CdSe/ZnSe quantum dot composites using CdSe quantum dots passivated with an overlayer of ZnSe,” *Chemistry of Materials*, vol. 8, no. 1, pp. 173–180, 1996.

Decision making based on optical excitation transfer via near-field interactions between quantum dots

Makoto Naruse,^{1,a)} Wataru Nomura,² Masashi Aono,^{3,4} Motoichi Ohtsu,² Yannick Sonnefraud,^{5,6} Aurélien Drezet,^{5,6} Serge Huant,^{5,6} and Song-Ju Kim⁷

¹Photonic Network Research Institute, National Institute of Information and Communications Technology, 4-2-1 Nukui-kita, Koganei, Tokyo 184-8795, Japan

²Department of Electrical Engineering and Information Systems, Graduate School of Engineering, The University of Tokyo, 2-11-16 Yayoi, Bunkyo-ku, Tokyo 113-8656, Japan

³Earth-Life Science Institute, Tokyo Institute of Technology, 2-12-1 Ookayama, Meguru-ku, Tokyo 152-8550, Japan

⁴PRESTO, Japan Science and Technology Agency, 4-1-8 Honcho, Kawaguchi-shi, Saitama 332-0012, Japan

⁵Université Grenoble Alpes, Inst. NEEL, F-38000 Grenoble, France

⁶CNRS, Inst. NEEL, F-38042 Grenoble, France

⁷WPI Center for Materials Nanoarchitectonics, National Institute for Materials Science, 1-1 Namiki, Tsukuba, Ibaraki 305-0044, Japan

(Received 13 August 2014; accepted 7 October 2014; published online 17 October 2014)

Optical near-field interactions between nanostructured matters, such as quantum dots, result in unidirectional optical excitation transfer when energy dissipation is induced. This results in versatile spatiotemporal dynamics of the optical excitation, which can be controlled by engineering the dissipation processes and exploited to realize intelligent capabilities such as solution searching and decision making. Here, we experimentally demonstrate the ability to solve a decision making problem on the basis of optical excitation transfer via near-field interactions by using colloidal quantum dots of different sizes, formed on a geometry-controlled substrate. We characterize the energy transfer behavior due to multiple control light patterns and experimentally demonstrate the ability to solve the multi-armed bandit problem. Our work makes a decisive step towards the practical design of nanophotonic systems capable of efficient decision making, one of the most important intellectual attributes of the human brain. © 2014 AIP Publishing LLC.

[<http://dx.doi.org/10.1063/1.4898570>]

I. INTRODUCTION

Optical excitation transfer between quantum nanostructures, such as quantum dots (QDs), is one of the most unique and valuable physical processes in nanophotonics.^{1–3} When QDs share common resonant energy levels mediated by optical near-field interactions, optical energy is transferred from smaller QDs to larger ones. Optical near-field interactions even allow transitions that are conventionally dipole forbidden thanks to the localized property of the optical near-fields.^{1,4} By exploiting such attributes, optical energy transfer has been applied to a wide range of applications, including energy concentration,³ logic circuits,^{5,6} and sensing.⁷ Furthermore, the possibility of *intelligent abilities* by utilizing optical energy transfer has been demonstrated theoretically; for instance, the ability to solve a constraint satisfaction problem (CSP) has been demonstrated⁸ as well as satisfiability problem (SAT),⁹ decision making problems.¹⁰ In addition, novel architectures based on recent optical technologies to accomplish computing capability have been presented.^{11–13}

In this paper, we experimentally demonstrate a decision making principle based on optical excitation transfer between two kinds of different-sized colloidal QDs formed on a geometry-engineered substrate. What we particularly

discover in our investigation of intelligence-related applications of optical excitation transfer is that, until the energy dissipation is induced, the optical excitation exists somewhere across the resonant energy levels in a nonlocalized manner, whereas it is transferred to a particular destination quantum dot when energy is dissipated. Moreover, the probability of which destination quantum dot, out of many, is chosen depends on the surrounding environment. Specifically, if the destination energy level(s) is occupied by another excitation(s), resulting in what is called state-filling effects,^{14–17} the input optical excitation is more likely to be transferred to other unoccupied energy levels. At the same time, it should also be noted that the probability of the excitation going to a dot irradiated with control light is not perfectly zero if the state-filling does not perfectly inhibit the transition.^{8–10} With these fundamental mechanisms, our work opens the way to the practical design of nanosystems capable of decision making, one of the main attributes of human intelligence.

II. QUANTUM DOT-BASED DECISION MAKER

A. Architecture

Consider the particular case of a decision making problem in which a *player* should make a quick and accurate decision in choosing, from many available ones, a *slot machine* that has the highest probability of paying out a reward so

^{a)}Electronic mail: naruse@nict.go.jp

that the player can get as much reward as possible. To accomplish this, the player should test and evaluate which machine is the best; however, too much testing or exploration to search for the best machine may result in a significant loss. Moreover, the best machine may change with time. In other words, there is a trade-off between *exploration* and *exploitation*, referred to as the *exploration–exploitation dilemma*.¹⁸ Such a problem, called the *multi-armed bandit problem* (BP), is the foundation of many important applications in information and communication technologies, such as frequency assignment in wireless communication networks,^{19,20} web-content optimization,²¹ Monte Carlo tree searches,²² etc. Decision making is also an important issue in neurosciences and even clinical implications have been discussed.²³ For the most simple case, while still preserving the essence of the problem, we restrict ourselves to choosing the best of two slot machines. We refer to the two machines as **slot machine L** and **slot machine R**, hereafter.

In Ref. 10, Kim *et al.* presented a quantum dot-based decision maker (QDM) consisting of five QDs networked via optical near-field interactions (Fig. 1). Here, we briefly outline the basic mechanism of the QDM.¹⁰ An optical excitation generated at the smaller-sized QD labeled **QD_S** in Fig. 1 can be transferred to either one of the large-sized QDs (labeled **QD_{LL}** and **QD_{LR}**) through inter-dot optical near-field interactions. This means that the photon radiation from the medium-sized QDs (denoted by **QD_{ML}** and **QD_{MR}**) is negligible. However, when the large-sized QDs, **QD_{LL}** and **QD_{LR}**, are irradiated with control light that induces state-filling effects, the probabilities of photon radiation from **QD_{ML}** and **QD_{MR}** do appear. Such a phenomenon can be regarded as if the input photon, generated at **QD_S**, is subjected to a *tug-of-war*, being pulled by the larger-size QDs on the left- and right-hand sides, meaning that when one side is pulled, the other side is immediately pushed. Such a *nonlocal correlation*, in the sense that the state-filling induced at one dot immediately alters the dynamics of the entire system, has been shown to enhance the performance in solving the BP.²⁴ Note also that fluctuation is essential in order to realize an “exploration” ability; that is to say, the probability of the excitation going to a dot irradiated with control light is not perfectly zero if the state-filling does not perfectly inhibit the transition, as mentioned earlier.

Here, we experimentally demonstrate such a mechanism by using combinations of different-sized QDs irradiated by control light patterns, evaluate the basic characteristics of

optical excitation transfer, and finally demonstrate the ability to solve decision making problems in dynamically changing environments. Note that the probabilistic nature of a photon plays a key role, as a first step toward future integrated decision making machines, and here we employ an ensemble of many quantum dots to experimentally realize optical energy transfer. The probabilistic nature is emulated by an electrical controller. In other words, the probabilistic attributes are simulated by the host controller; while its probabilities are determined by the observation of optical excitation transfer involving a large number of QDs. Nevertheless, we believe that this is an important first experimental demonstration that optical near-field-mediated energy transfer can solve decision making problems.

The idea of a tug-of-war is represented by the notion of an “intensity adjuster” (IA),¹⁰ which physically corresponds to a mechanism that modifies energy transfer patterns in the system in the following manner.

- (1) The IA’s value of “zero” indicates no imbalance of optical excitation transfer in the system. That is, control light of the same intensity is applied to *both* of the lowest energy level of **QD_{LL}** and **QD_{LR}**, which are, respectively, denoted by **LL₁** and **LR₁** in Fig. 1.
- (2) For decision making, we focus our attention on the photon radiation from the medium-size dots (**QD_{ML}** and **QD_{MR}**). The decision to choose the designated slot machine is made based on information about from which dot a photon is observed. More specifically, if a photon is observed from **QD_{ML}**, that is to say, if radiation is observed from the energy level **ML₁** denoted in Fig. 1, the decision is made to choose the **slot machine L**; whereas if a photon is observed from **QD_{MR}**, that is to say, if radiation is observed from the energy level **MR₁** in Fig. 1, the decision is made to choose the **slot machine R**.
- (3) If a reward is successfully dispensed from the selected slot machine, the IA is “moved” in the direction of the selected machine. More specifically, when the chosen machine is the **slot machine L** and a reward is successfully obtained, more control light is applied to **LL₁**, and simultaneously, less light is applied to **LR₁**. Note that the slot machines are “external” systems from the QD-based decision maker. In contrast, if no reward is dispensed, the IA is moved in the opposite direction from the machine chosen. That is to say, when the chosen

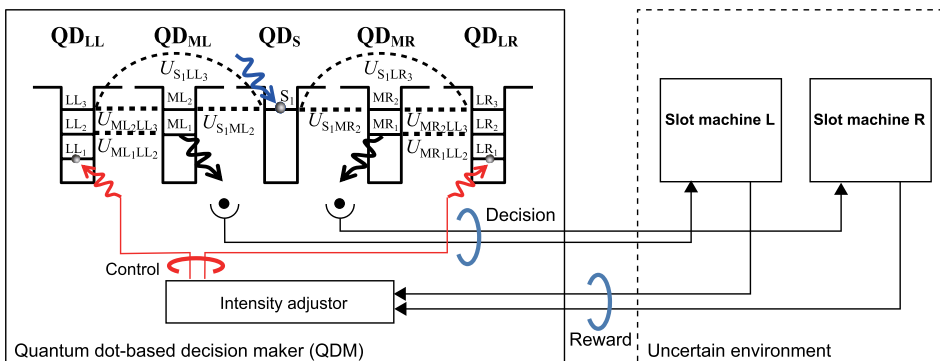


FIG. 1. Architecture and theoretical analysis of quantum dot-based decision maker (QDM). The QDM is interacting with dynamically changing external environments.

machine is the **slot machine L**, and a reward is not obtained, less light is applied to LL_1 , and more light is applied to LR_1 .

It was demonstrated that the resultant decision making performance exhibits even better performance than that of the best conventionally known algorithm called Softmax¹⁸ as shown in Ref. 10.

B. Experimental devices

In the experiment, instead of using three types of dots, we employed two types of dots, referred to as QD_S and QD_L , arranged in the configuration $QD_L-QD_S-QD_L$, as schematically shown in Fig. 2(a). As described below, there were many QD_S s and QD_L s in the experimental device. In Fig. 2(a), three QD_S s are indicated. Their energy levels are indicated by S_1 , LL_1 , LL_2 , LR_1 , and LR_2 , as shown in Fig. 2(a). (Note that “ QD_L ” in Fig. 2(a) corresponds to the “medium”-sized dot (QD_M) in the former five dot system shown in Fig. 1.) Furthermore, the experimental device, shown below, consists of a large number of smaller and larger dots arranged in a shape-engineered substrate made by lithography. The design of the experimental device is shown in Fig. 2(b). The smaller-size CdSe/ZnS core-shell QDs (QD_S s) are distributed in two 1 μm -wide lanes joined end-to-end, depicted by the dotted area in Fig. 2(b); whereas the larger-size ones (QD_L s) occupied square-shaped areas, with a side length of 3 μm , attached to the ends of the two lanes. The distance from the center of the QD_S area, indicated by P_S , and the centers of the two QD_L areas, denoted by P_L and P_R , were designed to be 7.5 μm .

Such dimensions are larger than the diffraction limit of the light used in the experiment, which in fact sacrifices one of the fundamental benefits of optical excitation transfer via near-field interactions, namely, the possibility to operate at a scale below the diffraction limit. In this paper, however, the primary focus is a first experimental demonstration of the decision making function and we consider that a macro-scale

setup suffices, as long as the underlying essential principles are preserved. We have previously confirmed optical excitation transfer mediated by near-field interactions based on these distributed colloidal quantum dots and have demonstrated optical excitation transfers over distances as long as 10 μm .²⁵ For these reasons, the fabricated experimental device was based on a large number of QDs arranged in the architecture shown in Fig. 2(b).

The input light is radiated onto the area around the position P_S in Fig. 2(b), where smaller QDs are located, corresponding to the generation of an optical excitation at the energy level S_1 in the model shown in Fig. 2(a). On the other hand, the control light for inducing state-filling effects in the energy levels LL_1 and LR_1 is radiated onto the areas occupied by the QD_L s around the positions P_L and P_R , as schematically shown by the dashed circles labeled CL and CR in Fig. 2(b). Since the two regions CL and CR are separated by a distance larger than the wavelength, experimentally we are able to address each area with a diffraction-limited beam (generated by a computer generated hologram (CGH), described below). The areas CL and CR, respectively, correspond to QD_{LL} and QD_{LR} , and thus CL and CR are also indicated in Fig. 2(a).

We fabricated QD samples using the procedure where a lithography and a lift-off technique were repeated twice. We used commercially available colloidal CdSe/ZnS core-shell QDs (manufactured by Quantum Design, Inc.). The core-diameters of QD_S and QD_L were 2.5 nm and 3.2 nm, and the first excited states (schematically shown in Fig. 2(a)) were $S_1 = 2.36$ eV (525 nm) and $LR_1 = LL_1 = 2.11$ eV (588 nm), respectively. With such a combination of QDs, the energy level S_1 is resonant with the second excited states of the larger dots, that is, LR_2 and LL_2 .²⁵ (1) First, by using e-beam lithography on a silica substrate coated with resist (ZEP-520 A, Zeon Corp.) with a thickness of around 100 nm, (2) the two areas in which QD_L s were to be deposited were formed. (3) Next, the QD_L solution was dripped onto the substrate and was allowed to dry naturally at room temperature. (4) By removing the resist, we obtained the QD_L structure on the substrate. (5) Next, resist was formed on top of the structure and (6) using e-beam lithography once again, the structures on which QD_S s were to be deposited were formed by aligning their positions with the former QD_L structures. (7) After developing the resist, we dripped the QD_S solution onto the substrate. (8) Finally, the resist was removed to obtain the final structure. Figure 2(c) shows a fluorescence microscope image obtained when the fabricated sample was excited with a mercury-vapor lamp. The irradiation ultraviolet light from a mercury-vapor lamp efficiently excites CdSe/ZnS core-shell QDs, allowing us to observe the entire device structure in the visible region. The QD_S and QD_L structures were, respectively, observed as green and yellow colors. Due mainly to alignment precision errors in the liftoff processes, the distances between the center of the QD_S area and the two QD_L areas (left-hand and right-hand sides) were 2.01 μm and 3.85 μm , which are, respectively, indicated by dotted and dashed lines.

The radiation of the output light is correlated with the radiation from the smaller dots (QD_S s) located around the

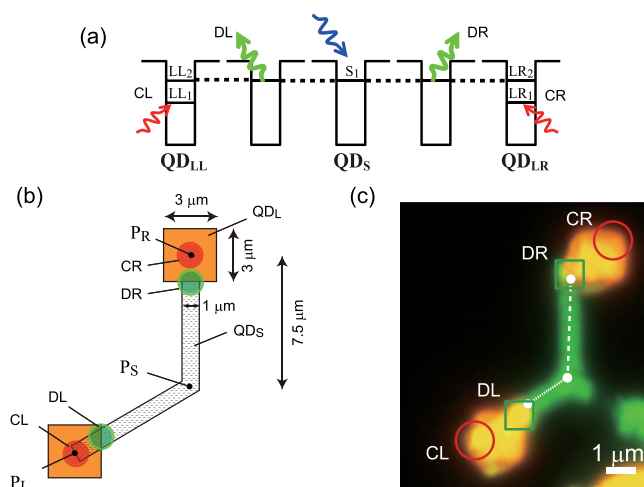


FIG. 2. Quantum dot devices for decision making. (a) Schematic architecture of the experimental device used in the decision making demonstration. (b) Design of the quantum dot-based device. (c) Light emission image from the fabricated quantum dot device.

edge of the lanes or the area intersecting with QD_{L} s, which are denoted by DL and DR as indicated by the circles in Fig. 2(b). The higher the occupation probability of the first excited state of QD_{L} , the more the energy transfer to the designated QD_{L} is prohibited, leading to increased radiation from QD_{S} s located in their proximity. Such a mechanism exhibits the same character as that theoretically demonstrated in Ref. 10 in the sense that more radiation from the output dot (QD_{M}) results from more state filling in its neighboring QD_{L} . The areas DL and DR, respectively, correspond to QD_{S} s located close to QD_{LL} and QD_{LR} in Fig. 2(a), and thus DL and DR are also indicated in Fig. 2(a).

C. Experimental systems

After the experimental device fabrication by using lift-off techniques and two kinds of colloidal quantum dots, the next important concern in implementing decision making functions is how to apply the two control light beams to irradiate the areas CL and CR. For this purpose, we introduced a phase-only spatial light modulator (SLM), based on liquid crystal on silicon (LCOS) technology (LCOS-SLM X10468-01, Hamamatsu Co., Ltd.). It has 792×600 pixels with a pixel pitch of $20 \mu\text{m}$, corresponding to a maximum spatial frequency of 25 lp/mm, designed for the wavelength region between 400 nm and 700 nm, and each pixel can modulate the phase in 256 grayscale levels. The diffraction efficiency of the LCOS-SLM is about 30% for a spatial frequency of 25 lp/mm.

Continuous-wave (CW) light at a wavelength of 589 nm produced by a diode-pumped solid-state laser (Shanghai Dream Laser Inc., MGL-W-589-1 W) was incident normally on the SLM, and the reflected light was collected by an objective lens with a numerical aperture (NA) of 0.40 and supplied to the sample. The experimental setup is schematically shown in Fig. 3(a). Computer-generated holograms (CGHs) with a size of 256×256 pixels, with 256 grayscale levels, were displayed on the SLM. The CGHs were designed so that their Fourier transform yielded two points corresponding to the first diffraction orders with intensities that can be independently adjusted. Let G_{L} and G_{R} denote the grayscale levels of the respective areas. For example, with the combination $(G_{\text{L}}, G_{\text{R}}) = (128, 128)$, the control light beams radiated onto the areas CL and CR have equal intensities, whereas the combination $(G_{\text{L}}, G_{\text{R}}) = (255, 1)$ means that the area CL is irradiated much more intensely than CR is. We prepared multiple CGHs beforehand and switched between them during the characterization of the device and the decision making demonstration shown below.

The optical excitation in the smaller QDs is generated by incident light focused on the position around P_{S} from a Ti:sapphire laser (Coherent Inc., Mira900) with a wavelength of 360 nm, a pulse width of 2 ps, and a repetition frequency of 80 MHz through the objective lens that the above control light also passes through. The radiation from the device was observed from the back surface through an objective lens with an NA of 0.55, followed by a bandpass filter with a pass wavelength of $540 \text{ nm} \pm 5 \text{ nm}$, and was captured by an electron multiplying CCD camera (Hamamatsu Co., Ltd., Imagem C9100-13 H) which acquired images with a 16-bit grayscale

and 512×512 pixels with a resolution of $0.37 \mu\text{m}/\text{pixel}$. Figure 3(b) shows the ratio of the control light intensity obtained by evaluating the average pixel values in the areas CR and CL shown in Fig. 2(c). We extracted two regions-of-interest (ROIs) consisting of 3×3 pixels from the image captured by the EMCCD camera, which corresponds to a $1.1 \mu\text{m} \times 1.1 \mu\text{m}$ area in the QD device. The G_{R} value of the CGH was adjusted while maintaining $G_{\text{L}} + G_{\text{R}} = 256$. As shown in Fig. 3(b), as the G_{R} value increased, the light intensity at CR, denoted by circular marks, increased; whereas that at CL, denoted by square marks, decreased.

We then evaluated the basic character of optical excitation transfer. The square and circular marks in Fig. 3(c), respectively, indicate the average pixel values corresponding to the areas DL and DR, obtained by extracting two 3×3 pixel ROIs, as a function of the ratio of the control light intensity incident on CR. The signal levels at DR (circular marks) increased, whereas those at DL (square marks) decreased as the imbalance of the intense control light intensity was shifted from left to right, which is consistent with the theoretical investigation discussed earlier. The absolute values in the areas DL and DR should ideally be symmetric when the same intensity of light is radiated onto CL and CR, but the experimental results shown in Fig. 3(c) did not exhibit such perfect symmetry. Also, the variance of the signal in DR was larger than that in DL; this is because, as shown in Fig. 2(c), the device structure was not perfectly symmetric due to the fabrication process, mainly because of the second liftoff step. In addition, optical misalignment of the overall experimental system may have caused a certain imbalance with respect to both light irradiation and observation. Nevertheless, it should be emphasized that the dependencies of the output signals from DL and DR on the imbalance of the control light controlled by the CGHs followed the “tug-of-war”-type behavior, meaning that the increase of the signal at one side and the decrease at the other side are correlated. This is one critical feature for the decision making mechanism.

Despite the device imperfections described above, one *presumable* reason behind the low-contrast for DL and the high-contrast for DR is as follows. Suppose that the distance between DL (or DR) and P_{S} is correlated with the likelihood of radiation from DL (or DR). When state-filling light is radiated at CL, radiation from DL is more likely to be induced regardless of the power of the state-filling light radiated at CL, and thus the resulting contrast is low. On the other hand, when state-filling light is radiated at CR, the radiation from DR depends more sensitively on CR, and thus the contrast is high. In other words, due to the large distance between DR and P_{S} , an optical excitation around DR is more strongly affected by the excitations in CR, resulting in high contrast. Note, however, that the above mechanism regarding the contrast is merely speculation, and it will be an interesting topic to examine in a future study.

III. DECISION MAKING DEMONSTRATIONS

From the nature of optical excitation transfer observed in Fig. 3(c), the probability of observing a photon from either

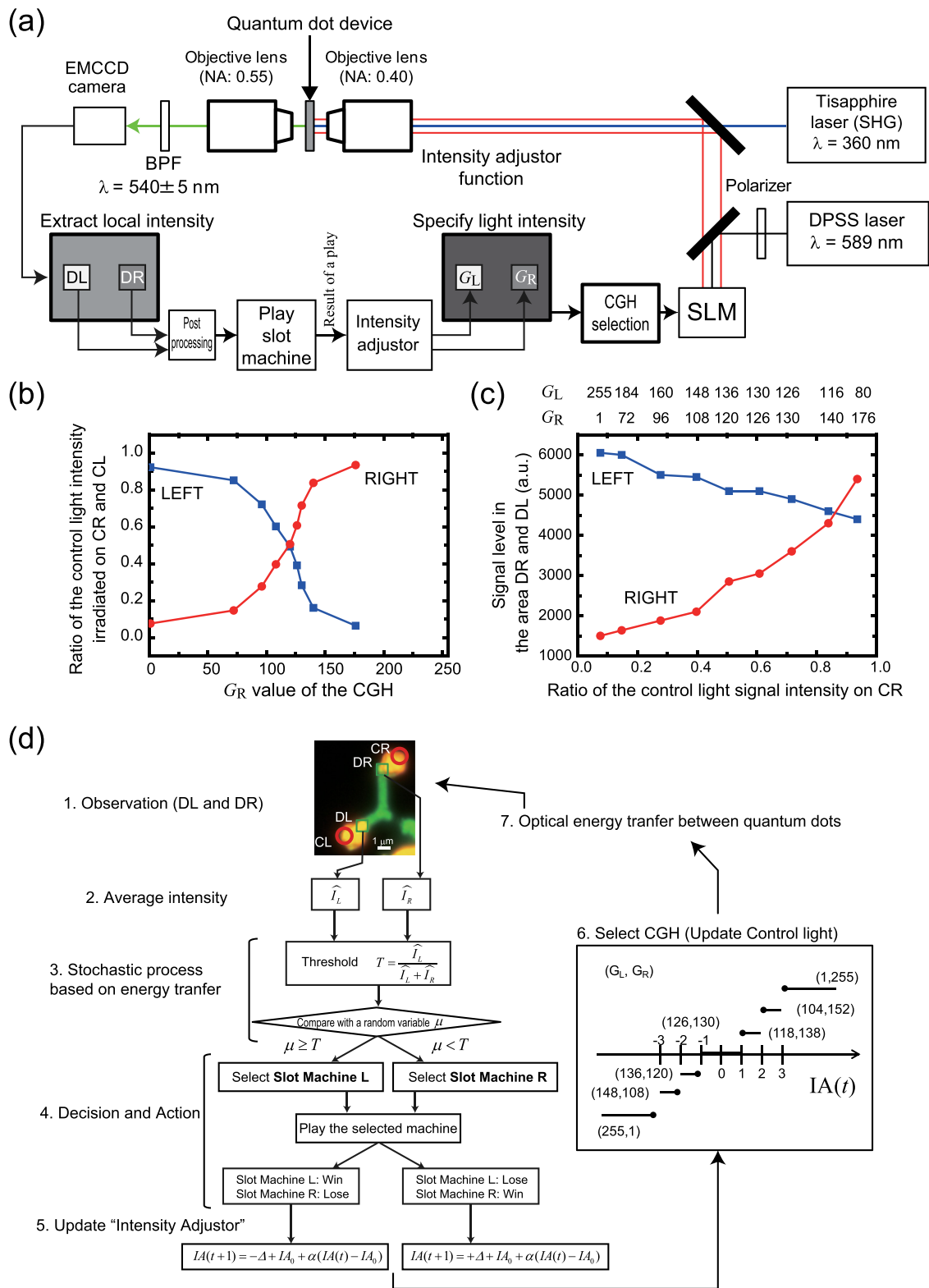


FIG. 3. Experimental systems for the quantum dot-based decision maker. (a) Schematic diagram of the experimental system. (b) Ratio of the control light intensity irradiated onto the areas CR and CL (in Figure 2(c)) as a function of CGH setup. (c) Signal levels from the areas DR and DL (in Figure 2(c)) as a function of the imbalance of control light intensities incident on CR and CL. (d) The overall mechanism of the experimental system used in solving the multi-armed bandit problem.

QD_{LL} or QD_{LR} is determined by the IA. Thus, an immediate single photon measurement determines the decision of which slot machine to choose, whereas the photon observation probability is engineered by state-filling effects. By utilizing

the experimentally observed characteristics of optical energy transfer and by representing its probabilistic nature, in the work described in this paper, we took the following approach rather than directly employing a single photon measurement.

Such an approach also takes account of the above-mentioned experimentally unavoidable imbalance in the fabricated device. Moreover, we consider that the demonstration will lead to more sophisticated experimental systems, including single photon measurement systems.

Let the intensities observed at DL and DR be denoted by I_L and I_R . These values are then calibrated by using the expressions $\hat{I}_L = A_L I_L - B_L$ and $\hat{I}_R = A_R I_R - B_R$, where A_L , A_R , B_L , and B_R are constants. Based on these values, a *threshold* value is defined by

$$T = \frac{\hat{I}_L}{\hat{I}_L + \hat{I}_R}. \tag{1}$$

The threshold T is compared with a random number between 0 and 1 generated at the host computer. If the random number is equal to or larger than T , the decision is made to choose the slot machine L, whereas if it is smaller than T the decision is made to choose the slot machine R.

The IA is implemented as follows. The grayscale values for the left- and right-hand sides at cycle t are given by

$$G_L(t) = CGH_L(\lceil IA(t) \rceil), \tag{2}$$

$$G_R(t) = CGH_R(\lceil IA(t) \rceil), \tag{3}$$

where $\lceil \cdot \rceil$ means the floor function, which truncates the decimal part. The functions $CGH_L(n)$ and $CGH_R(n)$ specify the grayscale values for CL and CR, respectively, when the truncated IA value is given by n . Let the initial IA value be IA_0 . If the slot machine L yields a reward in cycle t , the IA value is updated based on

$$IA(t + 1) = -\Delta + IA_0 + \alpha(IA(t) - IA_0), \tag{4}$$

where α is referred to as a forgetting parameter and Δ is a constant increment of IA,¹⁰ which is assumed to be unity in the experiments. In the case where the machine R gives a reward at the cycle t , the update rule is given by

$$IA(t + 1) = +\Delta + IA_0 + \alpha(IA(t) - IA_0). \tag{5}$$

In the following decision making demonstration, the truncated integer values of the IA value are assumed to take a natural number $-3, -2, -1, 0, 1, 2$, or 3 . When $IA(t) \geq 4$ or $IA(t) \leq -4$, the truncated IA value is, respectively, given by $\lceil IA(t) \rceil = +3$ or $\lceil IA(t) \rceil = -3$. The particular G_L and G_R values are specified by seven CGHs, providing the (G_L, G_R) pairs with pixel values $(255,1), (148,108), (136,120), (126,130), (118,138), (104,152)$, and $(1,255)$, which, respectively, correspond to truncated intensity adjustor values of $-3, -2, -1, 0, 1, 2$, and 3 . Figure 3(d) summarizes the mechanism of the experimental system used to solve the multi-armed bandit problem.

Let the reward probability of the machine L be $P_L = 0.8$ and the reward probability of the machine R be $P_R = 0.2$, where the total probability, $P_L + P_R$, is unity, which is the same condition imposed in the model results discussed in Ref. 10. Furthermore, the reward probability is dynamically changed from time to time; the occurrence of a “change” of the reward probability is not notified to the player. In the

experiment, the values of P_L and P_R are swapped every 150 plays. The solid curve in Fig. 4(a) shows the evolution of the “success rate,” taking a value between 0 and 1, for 600 consecutive plays. Such 600 plays of the slot machines were repeated 10 times. “Success” means choosing the slot machine with the higher reward probability. The success rate is evaluated by calculating the number of successes divided by the number of repeat cycles. The success rate increases as time evolves. As a result of swapping the reward probabilities, the success rate drops every 150 plays but quickly recovers. Such rapid and accurate adaptability to the external environment demonstrates the success of the method of solving the multi-armed bandit problem considered in this paper. Note that the “correct” machine is not, of course, notified to the player; the player may know the “winning rate,” which is the ratio of getting coins from the chosen slot machine, which fluctuates considerably. Nevertheless, the “correct selection rate” does indeed approach unity after a certain number of cycles.

The dotted curve in Fig. 4(a) shows the evolution of the success rate with the reward probabilities $P_L = 0.6$ and $P_R = 0.4$. Like the former case, the reward probabilities were switched every 150 plays. Since the difference between the reward probability is smaller than in the former case, accurate decision making is difficult, which is manifested by the fact that the dashed curve stays lower than the former solid curve. However, what is remarkable is that the success rate again increases as time evolves, and the adaptive behavior is also observed in such a difficult situation. Since the machine with the higher reward probability may not dispense a reward in some trials, the “winning rate,” which is the ratio of getting coins from the chosen slot machine, is different from the success rate. Figure 4(b) shows the evolution of the winning rate, where we can observe that it approaches 0.8 and 0.6, denoted by solid and dotted curves, respectively, which is the higher probability of the assumed slot machine’s reward probability, indicating that the winning rates approach achievable limits.

Behind such success in selecting a higher-reward machine is the way in which the intensity adjustor mechanism works. Figure 4(c) represents the evolution of the IA value, which evolves toward a smaller value (choosing the **slot machine L** is more likely) and a larger one (choosing the **slot machine R** is more likely), and this is consistent with the given reward probabilities. We should also note that, in the case of $P_L = 0.8$ and $P_R = 0.2$, the duration required to recover unity (that is, 100%) “correct selection rate” after a sudden environmental change is not constant; the durations are about 50, 30, and 20 cycles. These are correlated with the value of IA. At cycle 150, IA is about -500 ; whereas at cycle 300, IA is about 400. Such a difference in the value of IA, and its associated performance differences, also clearly suggests that our proposed dynamics of IA and the quantum-dot based devices play a key role. In other words, the probabilistic attributes of the IA and the fact that the probability is determined by optical excitation transfer are key. While Fig. 4 demonstrates the dynamics of the proposed decision making mechanism, Fig. 3(c) confirms one important internal process involving optical excitation

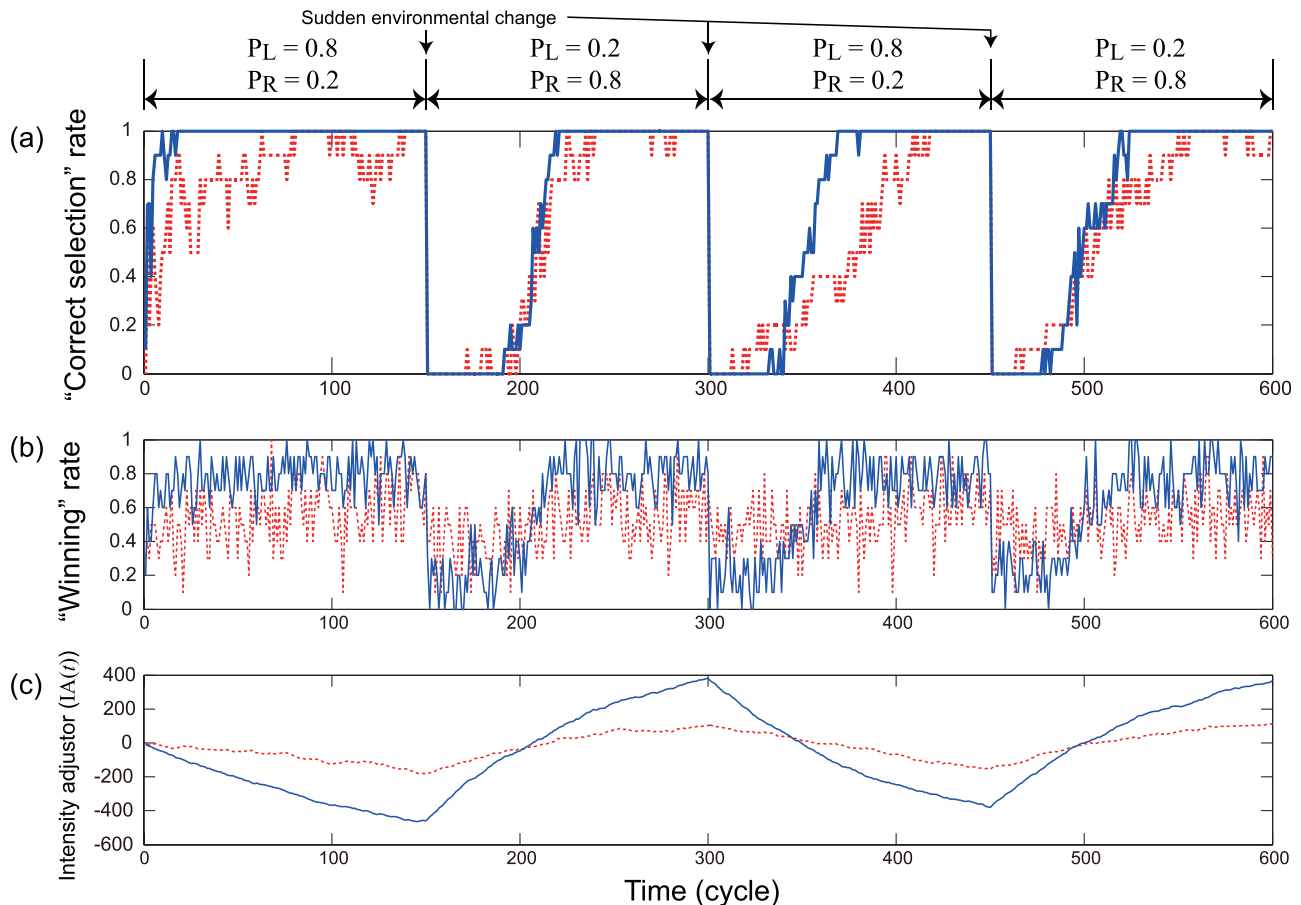


FIG. 4. Decision making demonstration. (a) Correct selection rate, (b) winning rate, and (c) the value of the IA.

transfer. In addition, the variance in the recovery time indicates that a more intelligent architecture for the IA may be possible. These results demonstrate the accurate and adaptive decision making ability of the decision maker based on quantum dots mediated by optical near-field interactions.

Finally, we make a remark regarding possible processing speeds and minimum power requirements of this device. The speed of the optical excitation transfer between quantum dots is on the order of 100 ps, and the radiation from QDs is on nanosecond order; in principle, therefore, the operating speed of the QD device itself can be as fast as 100 MHz to GHz order.²⁶ In the present experimental system, however, the primary bottlenecks are image acquisition (EMCCD camera), and data transfer to the host computer and post processing, which takes about 2 s/frame. Such a problem can be resolved by incorporating a fully parallel architecture, such as the one proposed by Ishikawa *et al.* in Ref. 27. The minimum power “dissipation” of optical energy transfer is about 10⁴-times smaller than that of the bit flip energy of electrical devices, for which theoretical²⁸ and experimental²⁶ values have been reported. The minimum power “requirement,” however, has not been clarified yet, and this will be an important research topic in the future.

IV. SUMMARY

In summary, we experimentally demonstrated the ability to solve multi-armed bandit problems on the basis of optical

excitation transfer via near-field interactions by using different-sized colloidal quantum dots. Small- and large-sized QDs were arranged in a geometry-controlled manner by repeating two lithography and lift-off processes. The patterns of optical excitation transfer, from smaller QDs to larger ones, were dynamically reconfigured by modulating the intensity of control light radiated onto the region occupied by the larger QDs to induce state filling, which was experimentally implemented by computer-generated holograms displayed on a spatial light modulator. The basic character of optical excitation transfer was evaluated, and accurate and adaptive decision making was successfully demonstrated. In the future, it would be rewarding to develop genuine sub-wavelength decision makers and to engineer related processes using single photon sources, for instance, from nanodiamonds,²⁹ to establish single-photon decision makers.

ACKNOWLEDGMENTS

This work was supported in part by Strategic Information and Communications R&D Promotion Programme (SCOPE) of the Ministry of Internal Affairs and Communications and the Core-to-Core Program, A. Advanced Research Networks from the Japan Society for the Promotion of Science.

¹M. Ohtsu, K. Kobayashi, T. Kawazoe, S. Sangu, and T. Yatsui, *IEEE J. Sel. Top. Quantum Electron.* **8**, 839–862 (2002).

²S. A. Crooker, J. A. Hollingsworth, S. Tretiak, and V. I. Klimov, *Phys. Rev. Lett.* **89**, 186802 (2002).

- ³T. Franzl, T. A. Klar, S. Schietinger, A. L. Rogach, and J. Feldmann, *Nano Lett.* **4**, 1599–1603 (2004).
- ⁴J. R. Zurita-Sánchez and L. Novotny, *J. Opt. Soc. Am. B* **19**, 1355–1362 (2002).
- ⁵C. Pistol, C. Dwyer, and A. R. Lebeck, *IEEE Micro* **28**, 7–18 (2008).
- ⁶T. Kawazoe, M. Ohtsu, S. Aso, Y. Sawado, Y. Hosoda, K. Yoshizawa, K. Akahane, N. Yamamoto, and M. Naruse, *Appl. Phys. B* **103**, 537–546 (2011).
- ⁷H. Dong, W. Gao, F. Yan, H. Ji, and H. Ju, *Anal. Chem.* **82**, 5511–5517 (2010).
- ⁸M. Naruse, M. Aono, S.-J. Kim, T. Kawazoe, W. Nomura, H. Hori, M. Hara, and M. Ohtsu, *Phys. Rev. B* **86**, 125407 (2012).
- ⁹M. Aono, M. Naruse, S.-J. Kim, M. Wakabayashi, H. Hori, M. Ohtsu, and M. Hara, *Langmuir* **29**, 7557–7564 (2013).
- ¹⁰S.-J. Kim, M. Naruse, M. Aono, M. Ohtsu, and M. Hara, *Sci. Rep.* **3**, 2370 (2013).
- ¹¹D. Brunner, M. C. Soriano, C. R. Mirasso, and I. Fischer, *Nat. Commun.* **4**, 1364 (2013).
- ¹²S. Utsunomiya, K. Takata, and Y. Yamamoto, *Opt. Express* **19**, 18091–18108 (2011).
- ¹³K. Wu, J. G. de Abajo, C. Soci, P. P. Shum, and N. I. Zheludev, *Light Sci. Appl.* **3**, e147 (2014).
- ¹⁴M. Naruse, N. Tate, M. Aono, and M. Ohtsu, *Rep. Prog. Phys.* **76**, 056401 (2013).
- ¹⁵S. Raymond, S. Fafard, P. J. Poole, A. Wojs, P. Hawrylak, S. Charbonneau, D. Leonard, R. Leon, P. M. Petroff, and J. L. Merz, *Phys. Rev. B* **54**, 11548 (1996).
- ¹⁶S. Grosse, J. H. H. Sandmann, G. von Plessen, J. Feldmann, H. Lipsanen, M. Sapanen, J. Tulkki, and J. Ahopelto, *Phys. Rev. B* **55**, 4473 (1997).
- ¹⁷R. Prasanth, J. E. M. Haverkort, A. Deepthy, E. W. Bogaart, J. J. G. M. van der Tol, E. A. Patent, G. Zhao, Q. Gong, P. J. van Veldhoven, R. Nötzel, and J. H. Wolter, *Appl. Phys. Lett.* **84**, 4059–4061 (2004).
- ¹⁸N. Daw, J. O'Doherty, P. Dayan, B. Seymour, and R. Dolan, *Nature* **441**, 876–879 (2006).
- ¹⁹L. Lai, H. Gamal, H. Jiang, and V. Poor, *IEEE Trans. Mob. Comput.* **10**, 239–253 (2011).
- ²⁰S.-J. Kim and M. Aono, *NOLTA* **5**, 198–209 (2014).
- ²¹D. Agarwal, B.-C. Chen, and P. Elango, in *Proceedings of IEEE International Conference on Data Mining* (2009), pp. 1–10.
- ²²L. Kocsis and C. Szepesvári, *Machine Learning: ECML* (Springer, 2006), Vol. 4212, pp. 282–293.
- ²³H. Takahashi, *Neurosci. Res.* **75**, 269–274 (2013).
- ²⁴S.-J. Kim, M. Aono, and M. Hara, *Biosystems* **101**, 29–36 (2010).
- ²⁵W. Nomura, T. Yatsui, T. Kawazoe, M. Naruse, and M. Ohtsu, *Appl. Phys. B* **100**, 181–187 (2010).
- ²⁶M. Naruse, P. Holmström, T. Kawazoe, K. Akahane, N. Yamamoto, L. Thylén, and M. Ohtsu, *Appl. Phys. Lett.* **100**, 241102 (2012).
- ²⁷T. Komuro, S. Kagami, I. Ishii, and M. Ishikawa, *J. Rob. Mechatron.* **12**, 515–520 (2000).
- ²⁸M. Naruse, H. Hori, K. Kobayashi, P. Holmström, L. Thylén, and M. Ohtsu, *Opt. Express* **18**, A544–A553 (2010).
- ²⁹A. Cuche, A. Drezet, Y. Sonnefraud, O. Faklaris, F. Treussart, J. F. Roch, and S. Huant, *Opt. Express* **17**, 19969 (2009).

Unidirectional light propagation through two-layer nanostructures based on optical near-field interactions

Makoto Naruse,^{1,*} Hirokazu Hori,² Satoshi Ishii,³ Aurélien Drezet,⁴ Serge Huant,⁴ Morihisa Hoga,⁵ Yasuyuki Ohyagi,⁵ Tsutomu Matsumoto,⁶ Naoya Tate,⁷ and Motoichi Ohtsu⁷

¹Photonic Network Research Institute, National Institute of Information and Communications Technology, 4-2-1 Nukui-kita, Koganei, Tokyo 184-8795, Japan

²University of Yamanashi, Takeda, Kofu, Yamanashi 400-8511, Japan

³Advanced ICT Research Institute, National Institute of Information and Communications Technology, 588-2, Iwaoka, Nishi-ku, Kobe, Hyogo 651-2492, Japan

⁴Institut Néel, CNRS and Université Joseph Fourier, 25 rue des Martyrs BP 166, 38042 Grenoble Cedex 9, France

⁵Dai Nippon Printing Co. Ltd., 250-1 Wakashiba, Kashiwa, Chiba 277-0871, Japan

⁶Yokohama National University, Hodogaya, Yokohama, Kanagawa 240-8501, Japan

⁷Department of Electrical Engineering and Information Systems, Graduate School of Engineering,

The University of Tokyo, 2-11-16 Yayoi, Bunkyo-ku, Tokyo 113-8656, Japan

*Corresponding author: naruse@nict.go.jp

Received May 7, 2014; revised July 26, 2014; accepted August 15, 2014;
posted August 15, 2014 (Doc. ID 211608); published September 22, 2014

We theoretically demonstrate direction-dependent polarization conversion efficiency, yielding unidirectional light transmission, through a two-layer nanostructure by using the angular spectrum representation of optical near fields. The theory provides results that are consistent with electromagnetic numerical simulations. This study reveals that optical near-field interactions among nanostructured matter can provide unique optical properties, such as the unidirectionality observed here, and offers fundamental guiding principles for understanding and engineering nanostructures for realizing novel functionalities. © 2014 Optical Society of America

OCIS codes: (260.5430) Polarization; (310.6628) Subwavelength structures, nanostructures; (160.3918) Metamaterials.

<http://dx.doi.org/10.1364/JOSAB.31.002404>

1. INTRODUCTION

Unidirectional light propagation has been studied intensively because of its crucial importance in practical optical systems, such as to achieve one-way signal transfer or to avoid back-reflections. Nonreciprocal light propagation [1,2] has been achieved in magneto-optical materials. The Faraday effect is the most well-known example [3], and this effect is used in a variety of device architectures, such as waveguides with different propagation constants in the forward and backward directions [4], different propagation losses [5], and polarization conversion [6]. By using isotropic materials, Lockyear *et al.* demonstrated a one-way diffraction grating that exhibits diffracted beams from one surface only [7], and unidirectional light transmission has also been shown [8,9]. Asymmetric transmission of linearly or circularly polarized light by optical metamaterials has also been demonstrated [10–12].

Regarding isotropic-material-based nanostructures that exhibit unidirectional/asymmetric light transmission [7–9,12], a common feature is that they contain subwavelength-scale three-dimensional architectures, typically consisting of two-layer structures. Interactions among nanostructured two-layer systems yield interesting optical properties. Nevertheless, the physical reasoning and formalism have been limited to the notion of far-field optics [12,13]. Coupling of surface plasmon polaritons has been postulated as the elemental physical

process [9]; however, a detailed formalism concerning near-field processes and unidirectional transmission has not been investigated yet.

In this paper, we present a rigorous theoretical foundation for characterizing unidirectional signal transfer in two-layer nanostructured matter based on the angular spectrum representation of optical near fields. The evanescent wave is the most remarkable manifestation of optical near fields that propagate parallel to the boundary surface and exhibit exponential decay in the direction normal to the surface [14–16]. In the near-field regime, the angular spectrum of the scattered fields involves evanescent waves with wave vectors (or momentum) along the surface much larger than that of optical waves in free space [17]. In addition, with respect to an arbitrary assumed planar boundary, the angular spectrum representation of optical near fields is a very useful basis. Therefore, the angular spectrum theory of optical near fields has been successful in revealing multipole radiation near a planar boundary [16], localized hierarchical optical interactions on the subwavelength scale [18], and asymmetric polarization conversion [19].

What we particularly address in this paper is to demonstrate theoretically and numerically that the polarization conversion efficiency from x -polarized input light to y -polarized output light in the forward direction differs from the

polarization conversion efficiency from a y -polarization input to an x -polarization output in the backward direction through a two-layer planar nanostructure. By considering the polarization conversion in the forward and backward directions based on the angular spectrum theory of optical near fields, the unidirectional transmission can be grasped clearly. Also, the ability of the angular-spectrum-based theory to explicitly deal with multiple multipoles, including dipoles, that are located at arbitrary positions is utilized fully in characterizing the relevance between the geometrical features of the nanostructures and the resultant direction-dependent polarization properties.

Before proceeding, it is instructive to consider the intuitive physical meaning of the angular spectrum with respect to the polarization conversion problem mentioned above. Consider the dispersion relation of photons,

$$\left(\frac{\omega}{c}\right)^2 - k_{\parallel}^2 - k_{\perp}^2 = 0, \quad (1)$$

where ω is the temporal angular frequency, and k_{\parallel} and k_{\perp} are, respectively, wavenumbers parallel and perpendicular to an assumed planar boundary [20]. When the wavenumber parallel to the boundary is larger than that of free space, that is, $k_{\parallel}^2 > k^2 = k_{\parallel}^2 + k_{\perp}^2$, then $k_{\perp}^2 < 0$ should hold, meaning that the wavenumber perpendicular to the boundary is an imaginary number that corresponds to evanescent waves. The angular spectrum representation is a momentum-space expansion of arbitrary scattered fields with respect to an assumed planar boundary in a series of plane waves that include complex wavenumbers. The exchange or transfer of momentum (or wavenumber) parallel to the boundary (k_{\parallel}), which is much larger than that in free space regarding near-field components, is explicitly dealt with by the angular spectrum formulation. It should also be noted that the large momentum originates from polarizations in the nanostructured matter induced by incident light in free space, and it is also correlated with scattered light or radiation from the nanostructure. In this paper, the problem of polarization conversion in two-layer nanostructured matter is analyzed as a “filtering” of evanescent components, or transfer of momentum, with respect to an assumed planar boundary. The asymmetric architecture of the nanostructure is explicitly incorporated into the angular spectrum-based formulation, and the direction-dependent polarization conversion and irreversibility of light transmission involving optical near-field processes is described clearly.

This paper is organized as follows: in Section 2, the theoretical elements and an outline of the method of dealing with unidirectionality are presented. Section 3 describes a concrete example of a two-layer nanostructured system in which the above-mentioned direction-dependent polarization conversion takes place. Section 4 presents a theoretical analysis of the polarization conversion shown in Section 3. Section 5 concludes the paper.

2. ANGULAR SPECTRUM REPRESENTATION OF OPTICAL NEAR FIELDS: THE BASIS OF DIRECTION-DEPENDENT POLARIZATION CONVERSION

In order to deal with light scattering based on subwavelength-scale interactions involving exchange of momentum, it is convenient to expand the vector multipole field into vector plane

waves with respect to an arbitrary assumed planar boundary by means of the angular spectrum representation [16]. The state of vector plane waves propagating in an arbitrary direction is characterized by the wavenumber K , the directional angles α and β of the wave vector, and the polarization state μ (for a transverse electric wave, $\mu = \text{TE}$, and for a transverse magnetic wave, $\mu = \text{TM}$) with respect to the wave vector. The total angular momentum is denoted by J and its z -projection (magnetic quantum number) is denoted by m . The vector plane wave is described in the form $\boldsymbol{\epsilon}(s^{(+)}, \mu) \exp(iKs^{(+)} \cdot \mathbf{r})$ ($\mu = \text{TE}, \text{TM}$), where

$$\begin{aligned} s^{(+)} &= (s_x, s_y, s_z) = (\sin \alpha \cos \beta, \sin \alpha \sin \beta, \cos \alpha), \\ \boldsymbol{\epsilon}(s^{(+)}, \text{TM}) &= (\cos \alpha \cos \beta, \cos \alpha \sin \beta, -\sin \alpha), \\ \boldsymbol{\epsilon}(s^{(+)}, \text{TE}) &= (-\sin \beta, \cos \beta, 0), \end{aligned} \quad (2)$$

which are illustrated schematically in Fig. 1(a). Then, the vector spherical waves are expanded into a vector plane wave:

$$\begin{aligned} A_{K,J,m}(\mathbf{r}) &= \frac{1}{2\pi} \sum_{\mu=\text{TE}}^{\text{TM}} \int_{C_+} \int_{-\pi}^{\pi} d\Omega_S(\mu, \alpha, \beta | \lambda, J, m) \boldsymbol{\epsilon}(s^{(+)}, \mu) \\ &\quad \times \exp(iKs^{(+)} \cdot \mathbf{r}), \end{aligned} \quad (3)$$

where $d\Omega_S = \sin \alpha d\alpha d\beta$ [15,16]. The expansion coefficient $(\mu, \alpha, \beta | \lambda, J, m)$ is given in Ref. [16]. This corresponds to the angular spectrum representation of a multipole. What is remarkable is that, whereas angle β is real ($-\pi \leq \beta < \pi$), α takes a complex value, leading to an explicit and intuitive expression for the optical near field. In the particular case of this paper, α follows a contour shown by C_+ in Fig. 1(b). Regarding the contour C_+ , the region $0 \leq \text{Re}(\alpha) < \pi/2$ corresponds to a homogeneous mode and the region $\text{Im}(\alpha) \leq 0$ corresponds to an evanescent mode. It is useful to introduce $s_{\parallel} = \sin \alpha$, which allows us to write a parameter s_z of the wave vector $s^{(+)}$ as

$$s_z = \begin{cases} \sqrt{1 - s_{\parallel}^2} & \text{for } 0 \leq s_{\parallel} < 1 \\ i\sqrt{s_{\parallel}^2 - 1} & \text{for } 1 \leq s_{\parallel} < +\infty, \end{cases} \quad (4)$$

meaning that pure imaginary values of s_z describe an evanescent wave propagating parallel to the boundary plane and showing exponential decay with increasing distance from the boundary. A remarkable benefit is that the value of s_{\parallel} specifies the property of a plane wave as a homogeneous wave ($0 \leq s_{\parallel} < 1$) or an evanescent wave ($1 \leq s_{\parallel} < +\infty$). In the case of an electric dipole \mathbf{d} as the source, the electric field is given by [17]

$$\begin{aligned} \mathbf{E}(\mathbf{r}) &= \left(\frac{iK^3}{8\pi^2 \epsilon_0}\right) \sum_{\mu=\text{TE}}^{\text{TM}} \int_0^{2\pi} d\beta \int_0^{\infty} ds_{\parallel} \frac{s_{\parallel}}{s_z} [\boldsymbol{\epsilon}(s^{(+)}, \mu) \\ &\quad \cdot \mathbf{d}] \boldsymbol{\epsilon}(s^{(+)}, \mu) \exp(iKs^{(+)} \cdot \mathbf{r}). \end{aligned} \quad (5)$$

We investigate the angular spectrum derived from Eq. (5) in the case of multiple dipoles arranged on a subwavelength scale in Section 4. In this section, we outline the essential idea of representing the direction-dependent polarization, which is followed by electromagnetic simulations in Section 3 and

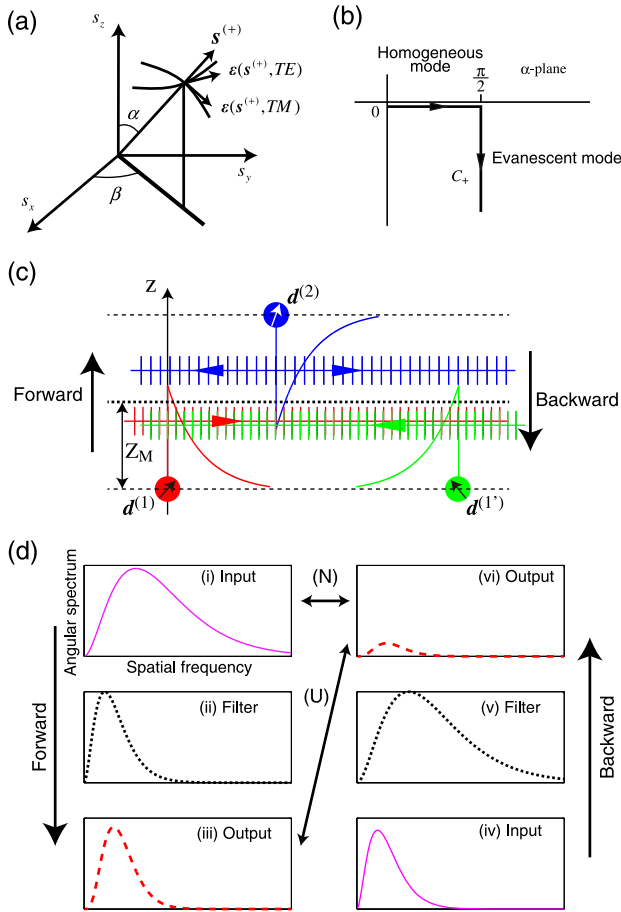


Fig. 1. (a) Geometrical relation of wave vector and polarization vectors. (b) Contour of the integration for rotation angle α . (c) Schematic illustration of direction-dependent polarization conversion via optical near-field interactions. (d) Schematic diagrams of forward- and backward-dependent polarization conversion based on the angular spectrum representation of optical near fields.

concrete theoretical applications in Section 4. Since we consider optical interactions in the subwavelength regime, where evanescent components are dominant and homogeneous ones are negligible, we characterize the angular spectra in the regime $1 \leq s_{\parallel} < +\infty$. We refer to s_{\parallel} as “spatial frequency” hereafter.

(1) Suppose x -polarized input light in the forward direction induces an electric dipole $d^{(1)}$. We can derive an angular spectrum representation of the radiation originating from the dipole $d^{(1)}$ at a plane at a distance Z_M from the source [Fig. 1(c)]. The forward-direction input light polarization may excite other dipoles at other positions, such as $d^{(1)}$ illustrated in Fig. 1(c), whose angular spectra are also considered simultaneously at the same boundary. In this manner, the angular spectrum triggered by the forward-direction x -polarized input light is obtained. Plot (i) in Fig. 1(d) shows a schematic illustration of such an angular spectrum as a function of spatial frequency s_{\parallel} . One remark to make here is that Fig. 1(c) is a “conceptual” schematic; the dipoles $d^{(1)}$ and $d^{(1)}$ are located on the same plane, and thus, the abscissa represented by the dashed line means the spatial position, whereas the decaying solid curves and the array of vertical lines shown in the middle conceptually indicate the exponentially decaying nature and

the high spatial frequency of the evanescent components of the electric fields, respectively.

(2) At the same time, we consider that “ideal” y -polarized output light is related with the radiation from an electric dipole $d^{(2)}$. The angular spectrum originating from the dipole $d^{(2)}$ can also be considered at a virtual boundary plane corresponding to the one introduced in Step (1). The “ideal” output light may also involve other dipole(s) [not shown in Fig. 1(c)] whose angular spectra are considered as well. We call the corresponding angular spectrum a “filter” angular spectrum [plot (ii), Fig. 1(d)].

(3) In characterizing the amount of y -polarized output light in the forward direction originating from the x -polarized input light, we consider that a limited portion of the angular spectrum triggered by the forward-direction input light is “filtered” by the angular spectrum specified in Step (2) [plot (iii), Fig. 1(d)]. Suppose the polarization conversion from x -polarization to y -polarization takes place perfectly. Then the entire angular spectrum given in Step (1) should correspond to the angular spectrum given in Step (2). As described in the introduction, the angular spectrum corresponds to momentum parallel to the assumed boundary, and thus, the perfect conversion efficiency means a perfect exchange of momentum for all wavenumbers, whereas less-than-perfect conversion indicates that the momentum exchange is suppressed at certain wavenumbers.

(4) Next, we consider the backward direction. The y -polarized input light of the backward direction excites an electric dipole $d^{(2)}$. Note that this dipole $d^{(2)}$ is equivalent to the dipole $d^{(2)}$ considered in Step (2). In this manner, the angular spectrum triggered by the backward-direction input light is obtained [plot (iv), Fig. 1(d)].

(5) In the backward direction, by following the exact same formalism regarding the forward direction shown in Step (2), the “filter” is specified by $d^{(1)}$ (and $d^{(1)}$), which yields x -polarized output light in the backward direction [plot (v), Fig. 1(d)].

(6) The output light polarization in the backward direction is characterized by the angular spectrum such that a portion of the input angular spectrum, obtained in Step (4), is chosen by the filter specified by the angular spectrum given in Step (5) [plot (vi), Fig. 1(d)].

The “unidirectionality” means that the angular spectra of the forward and backward output light could differ from each other, which is denoted by letter (U) in Fig. 1(d). Moreover, if the input angular spectrum of the forward direction differs from the output angular spectrum of the backward direction, then the system could be regarded as having irreversibility or nonreciprocity, denoted by letter (N) in Fig. 1(d), in the sense that the forward-direction input light polarization is not retrievable when it passes through the system in the forward direction and comes back in the backward direction via optical near-field interactions.

The notion of “nonreciprocity,” however, has been referred to as a phenomenon that breaks Lorentz reciprocity in the literature [21]; the reciprocity theorem holds provided the electrical permittivity and magnetic permeability are symmetric. We should note that our study, at this stage, has not yet addressed the relation between optical near-field processes and Lorentz reciprocity; this is an important and interesting future issue to be examined in light–matter interactions on the nanometer scale, where the applicability of the notion of

macroscale concepts, such as permittivity and permeability, should be investigated in greater depth. Carminati *et al.* studied the reciprocity of evanescent electromagnetic waves where the generalized reflection and transmission coefficients of vector wave fields containing evanescent components were investigated [22]. Whereas the scatter under study in Ref. [22] was considered as a united system, our study deals with two separate systems divided by a virtual boundary plane that are interacting via optical near fields, where we introduce the notion of exchange of momentum. Meanwhile, our study deals with limited cases of linearly polarized light with respect to the layout of nanostructures, whereas Carminati *et al.* dealt with arbitrarily polarizations. For these reasons, we use the term “unidirectionality,” not “nonreciprocity,” throughout the rest of the paper to remove any ambiguity. Nevertheless, we emphasize that this paper should provide a theoretical foundation for investigating polarization of light from the viewpoint of optical near-field processes.

3. ELECTROMAGNETIC SIMULATIONS

This section proposes a particular two-layer nanostructure consisting of gold (Au) embedded in SiO₂ substrates [Fig. 2(a)]. Considering realistic experimental two-layer devices consisting of gold nanostructures embedded in substrates, such as the one demonstrated by Tate *et al.* in Ref. [23], we choose a surrounding environment consisting of SiO₂.

The nanostructure in the first layer, which is the entrance for the forward-direction input light, consists of gratings parallel to y axis with a horizontal interval of G_X [Fig. 2(b)]. The second-layer nanostructure is composed of an array of pairs of L-shaped structures. The horizontal (x) and vertical (y) lengths of each L-shape are indicated by L . The two L-shaped structures in a pair face each other with a relative rotation of 180 degrees and are separated horizontally by a distance G_L . These L-shaped pairs are arrayed horizontally with an interval of G_X , which is the same as the inter-grating gap of the first layer, and vertically with an interval of G_Y . The heights and widths of all gold structures, as indicated by h and w , respectively, are the same. The interlayer gap distance between the first and second layers is denoted by G .

We calculate the optical properties in both the near field and far field based on the finite-difference time domain method [24], using the Poynting for Optics software, a product of Fujitsu, Japan. The permittivity of gold is expressed by the Drude model, in which the refractive index and extinction ratio are 0.16 and 3.8, respectively, at a wavelength of 688 nm [25]. The SiO₂ substrate is an isotropic dielectric material with a refractive index of 1.457. The light source is placed 500 nm away from the surface of the first layer with respect to the forward direction, whereas it is placed 500 nm away from the surface of the second layer with respect to the backward direction. We assume periodic boundary conditions at the

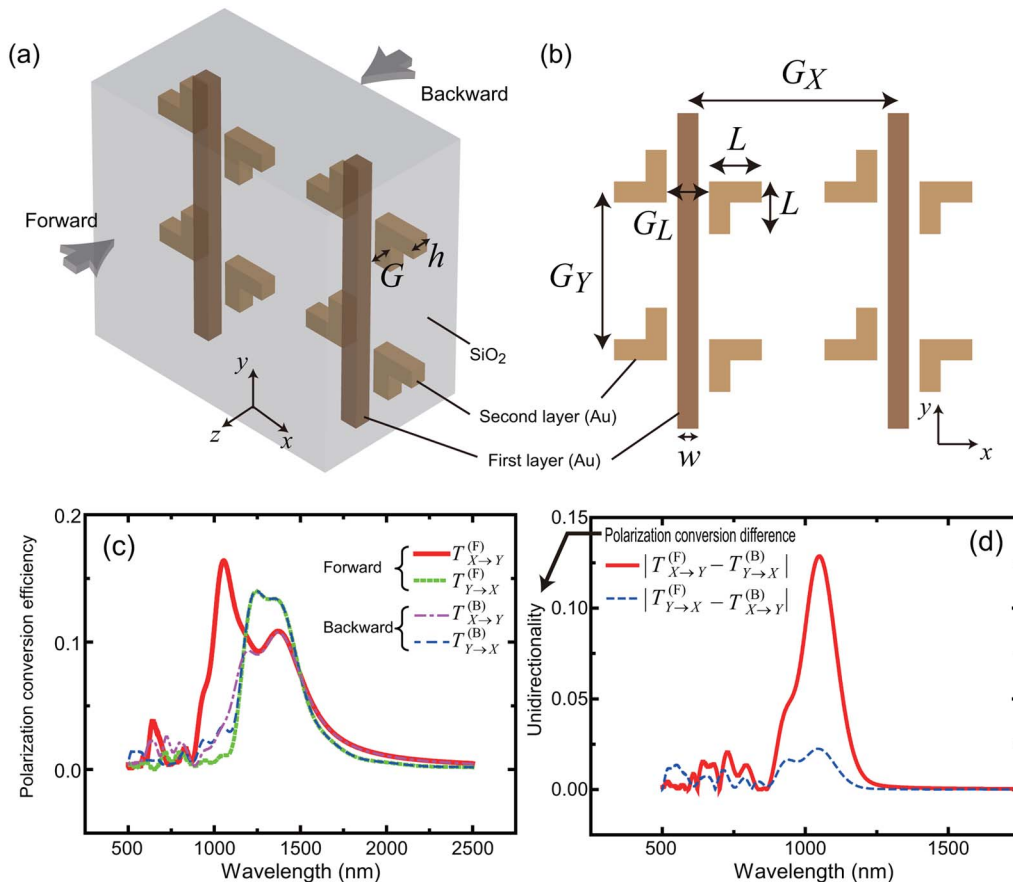


Fig. 2. (a) Example of two-layer nanostructures and some associated notations for the geometrical features. (b) Cross-sectional view of the two-layer nanostructures. (c) Polarization conversion efficiency regarding x -polarized input light to y -polarized output light ($T_{X \rightarrow Y}^{(F)}$) and that regarding y -polarized input light to x -polarized output light ($T_{Y \rightarrow X}^{(F)}$) for the forward direction, and those for the backward direction ($T_{X \rightarrow Y}^{(B)}$ and $T_{Y \rightarrow X}^{(B)}$). (d) Differences in polarization conversion efficiencies $|T_{X \rightarrow Y}^{(F)} - T_{Y \rightarrow X}^{(B)}|$ and $|T_{Y \rightarrow X}^{(F)} - T_{X \rightarrow Y}^{(B)}|$, which correspond to a measure used to quantify unidirectionality.

edges in the x - and y -directions, and perfectly absorbing boundaries in the z -direction.

In the representative structures, the parameters of the structures are assigned the following values: elemental-structure-related specifications: w (width), 80 nm; h (thickness), 80 nm; L , 200 nm; and G_L , 180 nm. Layout-related specifications: G_X , 800 nm; G_Y , 600 nm; and G (interlayer gap distance), 200 nm.

The far-field optical response is calculated at a plane 2.25 μm away from the surface of the structure opposite to the light source for both the forward and backward directions. We assume an input optical pulse with a differential Gaussian form, whose duration is 0.9 fs, that covers the wavelength regime studied in this paper. The transmission efficiency is obtained by dividing the Fourier transform of the electric field at the far-field output plane by the Fourier transform of the electric field at the light source. We assume that SiO_2 occupies the entire computational area in the calculation; this allows us to characterize the essential optical processes while considering the environmental effects of SiO_2 . Another possibility is to assume a vacuum environment, which actually yields similar characteristics, except that the wavelength regime where unidirectionality occurs (shown below) is shifted to a shorter wavelength range.

We are interested in the polarization conversion efficiency from x -polarized (or y -polarized) input light to y -polarized (or x -polarized) output light for both the forward and backward directions. The “forward” direction is assigned to the case where the input light enters the two-layer device from the first layer. The polarization conversion efficiency from x -polarized input light to y -polarized output light for the forward direction is given by

$$T_{X \rightarrow Y}^{(F)}(\omega) = \left| \frac{\hat{E}_{y,\text{output}}(\omega)}{\hat{E}_{x,\text{input}}(\omega)} \right|, \quad (6)$$

where $\hat{E}_{y,\text{output}}(\omega)$ denotes the Fourier transform of the y -component of the electric field evaluated at the output plane and $\hat{E}_{x,\text{input}}(\omega)$ shows the Fourier transform of the x -component of the input electric field. Similarly, the polarization conversion efficiency from y -polarization to x -polarization for the forward direction is $T_{Y \rightarrow X}^{(F)}$. Likewise, the polarization conversion efficiencies for the backward direction are $T_{X \rightarrow Y}^{(B)}$ and $T_{Y \rightarrow X}^{(B)}$.

The solid, dotted, dotted-dashed, and dashed curves in Fig. 2(c) represent, respectively, the calculated $T_{X \rightarrow Y}^{(F)}$, $T_{Y \rightarrow X}^{(F)}$, $T_{X \rightarrow Y}^{(B)}$, and $T_{Y \rightarrow X}^{(B)}$. Based on the optical reciprocity theorem, the values of $T_{X \rightarrow Y}^{(F)}$ and $T_{Y \rightarrow X}^{(B)}$ should be the same, and the values of $T_{Y \rightarrow X}^{(F)}$ and $T_{X \rightarrow Y}^{(B)}$ should be the same; we can observe such a characteristic in the wavelength region longer than about 1200 nm. However, especially in the wavelength region between 900 and 1200 nm, the differences in the polarization conversion efficiencies, given by $|T_{X \rightarrow Y}^{(F)} - T_{Y \rightarrow X}^{(B)}|$ and $|T_{Y \rightarrow X}^{(F)} - T_{X \rightarrow Y}^{(B)}|$, emerge as shown by the solid and dashed curves, respectively, in Fig. 2(d); namely, direction-dependent polarization conversion efficiencies result. If we associate $T_{X \rightarrow Y}^{(F)}$ with the forward transmission and $T_{Y \rightarrow X}^{(B)}$ with the backward transmission, then Fig. 2(d) demonstrates unidirectional light transmission. Regarding the metric $|T_{X \rightarrow Y}^{(F)} - T_{Y \rightarrow X}^{(B)}|$, if two polarizers are employed in the system in a crossed-Nicol manner to extract the x -polarized far-field light on the first layer-side and the y -polarized far-field light on the second layer-side, then the metric represents a performance measure of unidirectionality even for unpolarized light; this should help to give an intuitive understanding of the metric defined above as the unidirectionality in this study.

Before moving to a theoretical investigation based on the angular spectrum, here we note some relevant features. Figure 3(a) characterizes the direction-dependent polarization conversion efficiency ($|T_{X \rightarrow Y}^{(F)} - T_{Y \rightarrow X}^{(B)}|$) as a function of the interlayer gap distance (G). Specifically, the average value of $|T_{X \rightarrow Y}^{(F)} - T_{Y \rightarrow X}^{(B)}|$ in the spectral region from 900 to 1200 nm is quantified, which is called the “average unidirectionality”. It should be noted that both too small and too large gap distances deteriorate the average unidirectionality; that is, direction-dependent polarization conversion disappears. The maximum average unidirectionality is obtained around a gap distance of 200–300 nm. Such a feature is one of the important concerns in the theoretical treatment to be made.

While keeping the gap distance at 200 nm, Fig. 3(b) characterizes the unidirectionality, given by $|T_{X \rightarrow Y}^{(F)} - T_{Y \rightarrow X}^{(B)}|$, as a function of the “layout” regarding the pairs of L-shaped structures located in the second layer. The solid, dashed, and dotted curves correspond, respectively, to the specifications [G_X : 800, G_Y : 600], [G_X : 700, G_Y : 500], and [G_X : 600, G_Y : 400], while keeping other parameter specifications constant (the

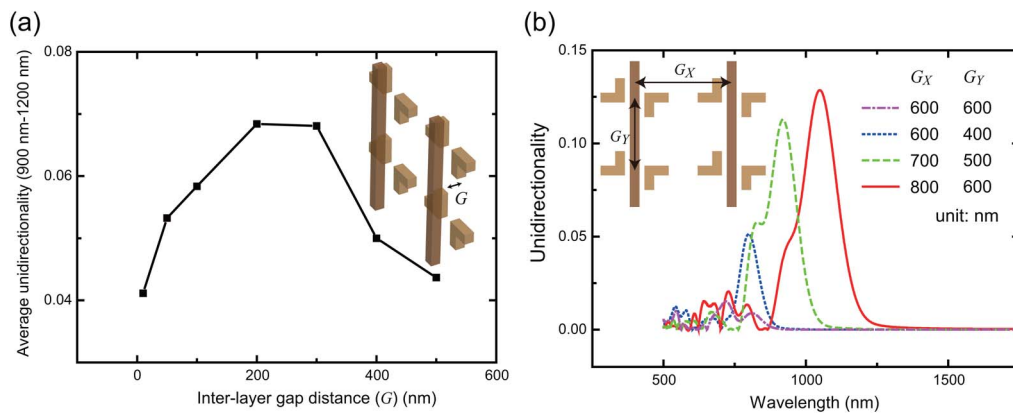


Fig. 3. (a) Average value of $|T_{X \rightarrow Y}^{(F)} - T_{Y \rightarrow X}^{(B)}|$, referred to as average unidirectionality, in the wavelength region 900–1200 nm as a function of interlayer gap distance, G . (b) Unidirectionality, $|T_{X \rightarrow Y}^{(F)} - T_{Y \rightarrow X}^{(B)}|$, with respect to asymmetric and symmetric arrangements of the L-shaped structures in the second layer.

measurement unit of these values is nanometers). As G_X and G_Y decrease, the wave band that exhibits unidirectionality is blue-shifted. Furthermore, the unidirectionality disappears when the layout has a symmetric configuration, as shown by the dashed-dotted curve in Fig. 3(b), where G_X and G_Y are both 600 nm.

Figure 4 shows the cross-sectional electric field intensity distributions for the cases when a considerable level of unidirectionality appears. The factors G_X and G_Y are 800 and 600 nm, respectively, for the “asymmetric layout,” whereas both G_X and G_Y are 600 nm for the “symmetric layout.” In order to obtain field distributions, we radiate continuous-wave (CW) input light at a wavelength of 1127 nm, and the refractive index and extinction ratio of the gold structures are 0.312 and 7.93, respectively [25]. The near-field intensities of the y -polarized field ($|E_y|^2$) and the x -polarized field ($|E_x|^2$) are evaluated by irradiating forward-direction x -polarized input light and backward-direction y -polarized input light, respectively. An evident difference between the forward and backward directions is observed for the asymmetric layout, whereas no evident interactions are observed in the case of the symmetric layout, especially regarding the “forward” direction.

4. THEORY OF UNIDIRECTIONAL LIGHT PROPAGATION VIA OPTICAL NEAR FIELDS BASED ON ANGULAR SPECTRUM REPRESENTATION

Based on the theoretical approach outlined in Section 2, we characterize the direction-dependent polarization conversion, or unidirectionality, by using the angular spectrum representation of optical near fields. The two-layer system is shown

schematically in Fig. 5(a), in which a “virtual intermediate layer” is assumed in the middle of the two layers.

With x -polarized forward-direction input light, the electron charges in each of the grating structures in the first-layer structure are concentrated at the left and right edges with different signs, thanks to the coupling between the input light and electrons in the metal. We model such a situation by an array of induced oscillating electrical dipoles appearing at the left and right edges of the gratings [Fig. 5(b)]. The dipoles are oriented parallel to x axis and a pair of dipoles located at both edges has a phase difference of π .

On the other hand, with y -polarized backward-direction input light, the electron charges are concentrated at the corners of the L-shaped elemental structures, whereby the signs of the induced electron charges at the corners of a single L-shape structure are opposite to each other. Similarly to the above-mentioned forward-direction input light modeling, we consider that an array of oscillating electrical dipoles is induced at the positions indicated by the arrows shown in Fig. 5(c). Referring to the physical dimensions in the electromagnetic simulations in Section 3, we specify the relative distances between the dipoles as shown in Fig. 5(c); note that the dimensions are given in units of wavelength. Also, in order to equate the power of the total input light for both the forward and backward directions, the numbers of induced electrical dipoles are assumed to be the same between the forward x -polarized input light and backward y -polarized input light, and the amplitudes of all induced dipoles are also assumed to be the same.

In order to quantify the angular spectra triggered by these arrays of dipoles, we introduce the following model: suppose the dipole $\mathbf{d}^{(k)}$ is oriented at an angle $\theta^{(k)}$ with respect to

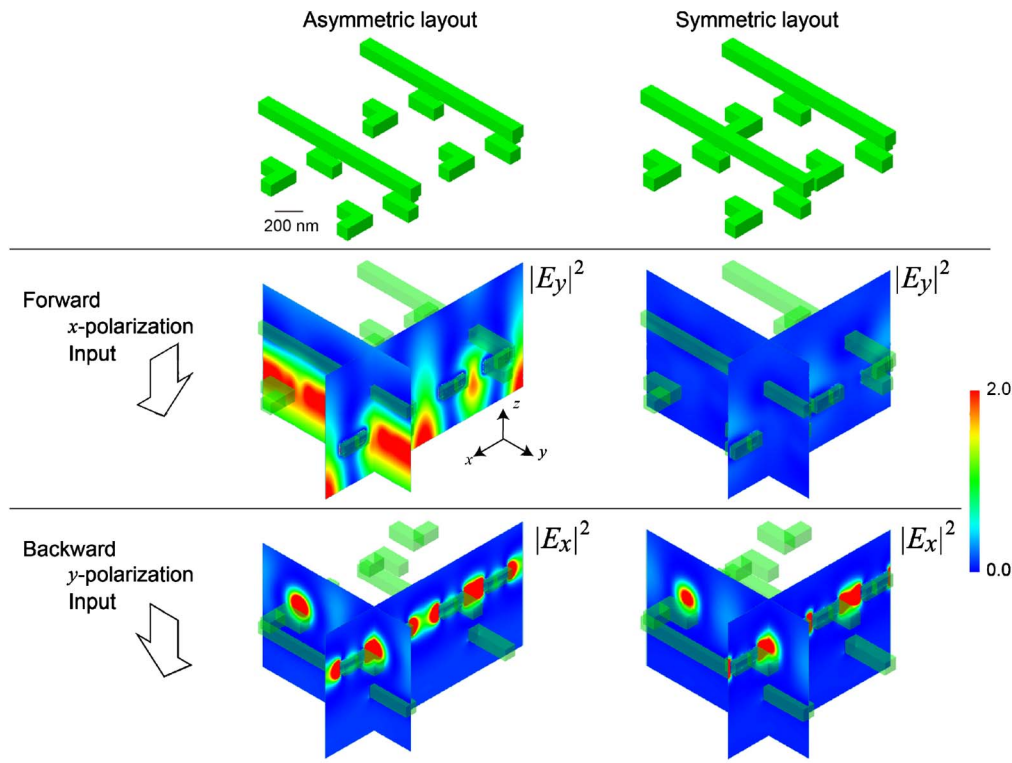


Fig. 4. Cross-sectional electric field intensity distributions when the asymmetric and symmetric structures are irradiated with CW input light at a wavelength of 1127 nm.

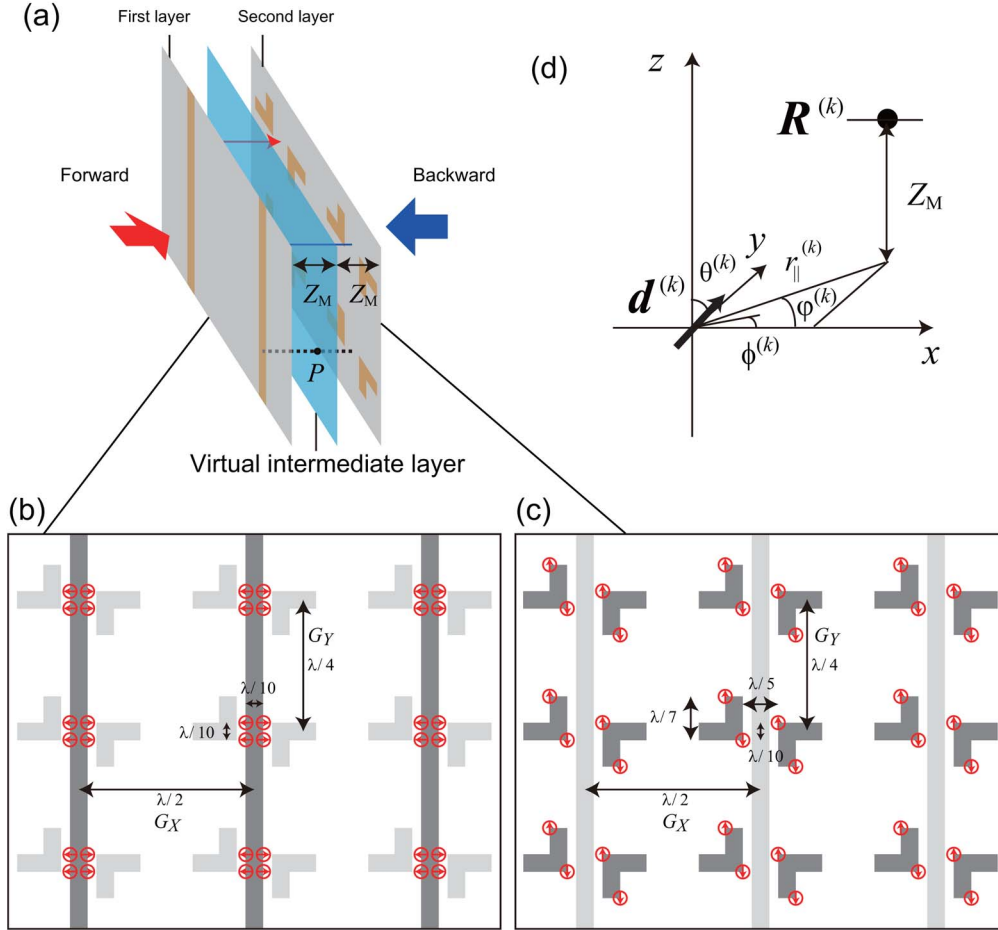


Fig. 5. Theoretical model based on angular spectrum representation. (a) Virtual intermediate layer, which is equidistant from the first and second layers by distance Z_M . (b) Array of dipoles induced at the first layer by x -polarized input light for the forward direction. (c) Array of dipoles induced at the second layer by y -polarized input light for the backward direction. (d) Geometrical illustration of the orientation of dipoles and the relative position where the angular spectrum representation is evaluated.

z axis and at an angle $\phi^{(k)}$ in the x - y plane, that is, $\mathbf{d}^{(k)} = d^{(k)}(\sin \theta^{(k)} \cos \phi^{(k)}, \sin \theta^{(k)} \sin \phi^{(k)}, \cos \theta^{(k)})$, as shown schematically in Fig. 5(d). Suppose also that we observe the radiation from $\mathbf{d}^{(k)}$ at a position displaced from the dipole by $\mathbf{R}^{(k)} = (r_{\parallel}^{(k)} \cos \phi^{(k)}, r_{\parallel}^{(k)} \sin \phi^{(k)}, Z_M)$. In such a case, based on Eq. (5), the angular spectrum representation of the z -component of the electric field at position \mathbf{R} in the assumed boundary plane for evanescent waves (namely, $1 \leq s_{\parallel} < +\infty$) is given by [18]

$$E_z(\mathbf{R}) = \left(\frac{iK^3}{4\pi\epsilon_0} \right) \sum_k \int_1^{\infty} ds_{\parallel} \frac{s_{\parallel}}{s_z} f_z^{(k)}(s_{\parallel}, \mathbf{d}^{(k)}, \mathbf{R}^{(k)}), \quad (7)$$

where

$$\begin{aligned} f_z^{(k)}(s_{\parallel}, \mathbf{d}^{(k)}, \mathbf{R}^{(k)}) &= ds_{\parallel} \sqrt{s_{\parallel}^2 - 1} \sin \theta^{(k)} \cos(\phi^{(k)} - \varphi^{(k)}) J_1(Kr_{\parallel}^{(k)} s_{\parallel}) \\ &\quad \times \exp(-KZ_M \sqrt{s_{\parallel}^2 - 1}) \\ &\quad + ds_{\parallel}^2 \cos \theta^{(k)} J_0(Kr_{\parallel}^{(k)} s_{\parallel}) \exp(-KZ_M \sqrt{s_{\parallel}^2 - 1}). \end{aligned} \quad (8)$$

Here, $J_n(x)$ represents a Bessel function of the first kind, where n is an integer, and the term $\sum_k f_z^{(k)}(s_{\parallel}, \mathbf{d}^{(k)}, \mathbf{R}^{(k)})$

corresponds to the angular spectrum of the electric field originating from an array of dipoles $\mathbf{d}^{(k)}$.

Here, we focus on the point P at the virtual intermediate layer whose horizontal and vertical positions lie directly above the center of the pair of L-shaped elements in the second-layer structure [Fig. 5(a)]. Furthermore, in order to take account of the layout dependencies of the second-layer structure, the angular spectrum concerns dipoles located on the left, right, upper, and lower neighboring areas with respect to the point P .

Assuming Z_M is $\lambda/10$, the angular spectrum at the virtual boundary plane originating from an array of dipoles induced in the first layer by the x -polarized forward input light, which is denoted by $f_{X \rightarrow M}^{(F)}$, is given by Eq. (8) and is shown by the solid curve in plot (i) ($Z_M = \lambda/10$) in Fig. 6. Similarly, an array of dipoles induced in the second layer by the y -polarized backward input light gives the angular spectrum denoted by $f_{Y \rightarrow M}^{(B)}$, as shown by the dashed curve in plot (i) ($Z_M = \lambda/10$) in Fig. 6.

As outlined in Section 2, a portion of the angular spectrum induced by the forward-direction x -polarized input light polarization can contribute to the y -polarized output light from the second layer. Ideally, the perfect y -polarized forward-direction output light is equivalent to a situation where y -polarized backward-direction input light induces an array of

dipoles in the second layer. Therefore, we consider that the “filter” that chooses portions that constitute the y -polarized output light from the angular spectrum $f_{X_{IN} \rightarrow M}^{(F)}$ is based on $f_{Y_{IN} \rightarrow M}^{(B)}$. Specifically, we normalize $f_{Y_{IN} \rightarrow M}^{(B)}$ by either the maximum or minimum value of $f_{Y_{IN} \rightarrow M}^{(B)}$ so that the resultant “filter,” which is now denoted by $\hat{f}_{Y_{IN} \rightarrow M}^{(B)}$, is in the range between $[+1, -1]$ [plot (ii) ($Z_M = \lambda/10$), Fig. 6]. As a result, the angular spectrum for the y -polarized output light in the forward direction is given by

$$f_{X_{IN} \rightarrow Y_{OUT}}^{(F)} = f_{X_{IN} \rightarrow M}^{(F)} \times \hat{f}_{Y_{IN} \rightarrow M}^{(B)}, \quad (9)$$

where the multiplication is applied for each spatial frequency (s_{\parallel}), and is shown by the solid curve in plot (iii) ($Z_M = \lambda/10$) in Fig. 6. Following the same approach, the angular spectrum for the x -polarized output light in the backward direction is given by

$$f_{Y_{IN} \rightarrow X_{OUT}}^{(B)} = f_{Y_{IN} \rightarrow M}^{(B)} \times \hat{f}_{X_{IN} \rightarrow M}^{(F)}, \quad (10)$$

where $\hat{f}_{X_{IN} \rightarrow M}^{(F)}$ and $f_{Y_{IN} \rightarrow X_{OUT}}^{(B)}$ are, respectively, obtained as the dashed curves in plot (ii) ($Z_M = \lambda/10$) and plot (iii) ($Z_M = \lambda/10$) in Fig. 6.

It should be noted that the resultant angular spectra $f_{X_{IN} \rightarrow Y_{OUT}}^{(F)}$ and $f_{Y_{IN} \rightarrow X_{OUT}}^{(B)}$ exhibit different curves, meaning that the polarization conversion efficiency is direction-dependent, which is consistent with the numerical demonstrations shown in Fig. 2(c).

Furthermore, when Z_M is assumed to have either a smaller value ($\lambda/20$) or a larger one ($\lambda/4$), the angular spectra are, respectively, derived as shown in the rows $Z_M = \lambda/20$ and $Z_M = \lambda/4$ in Fig. 6. The differences between the resultant angular spectra of the forward and backward directions are smaller than those in the former case $Z_M = \lambda/10$, which are quantified by calculating $f_{X_{IN} \rightarrow Y_{OUT}}^{(F)} / f_{Y_{IN} \rightarrow X_{OUT}}^{(B)}$ at each spatial frequency, and we refer to this as the figure of merit (FoM) of unidirectionality. This FoM can be defined with respect to spatial frequencies for which the denominator is nonzero; the FoM results in a constant value at valid spatial frequencies. This FoM of unidirectionality depends on the interlayer distance ($2 \times Z_M$), as demonstrated in Fig. 7(a), indicating that the unidirectionality is maximized at distances that are neither too small nor too large; this is consistent with the electromagnetic simulations shown in Fig. 3(a).

Such an attribute is physically reasonable by considering the explicit representation of optical near fields by the angular spectrum. The angular spectrum representation of optical near fields, given by Eq. (7), indicates that the penetration depth of evanescent waves is very small for larger spatial frequencies (s_{\parallel}), whereas it is large for smaller spatial frequencies; such an attribute is clearly indicated in plot (i) in Fig. 6, where the angular spectra can exist at larger spatial frequencies as Z_M decreases. Also, the resultant hierarchical attributes of optical near fields [18] suggest that near-field effects originating from spatial fine structures cannot be transferred to a distant plane; therefore, it is reasonable that the angular spectra of the forward and backward directions

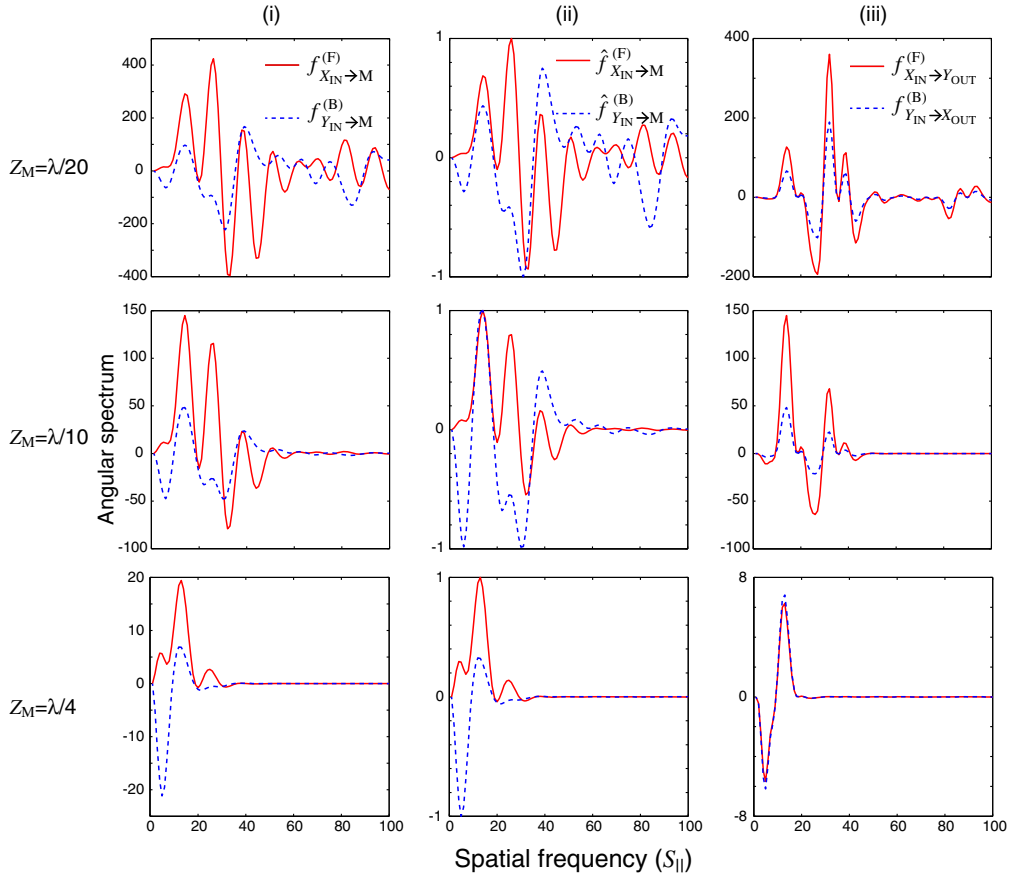


Fig. 6. Angular spectrum of (i) the input, (ii) the filter, and (iii) the output with respect to different values of Z_M ($\lambda/20, \lambda/10, \lambda/4$).

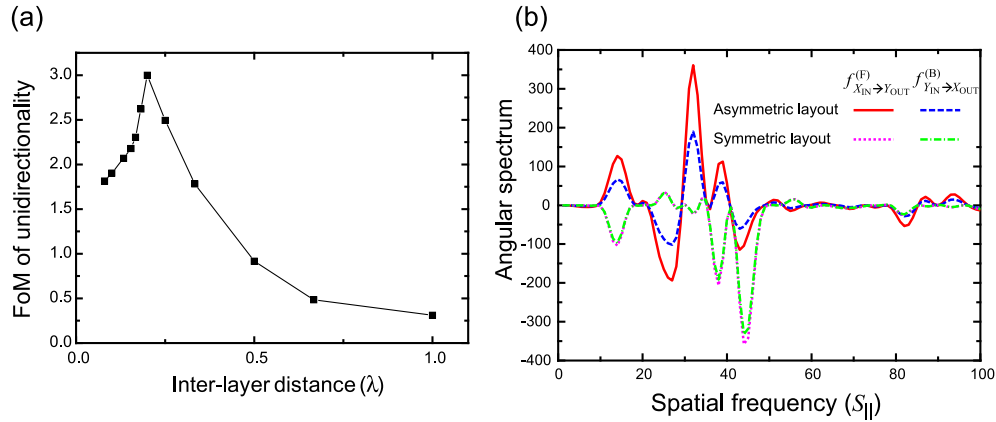


Fig. 7. FoM for the unidirectionality, given by $f_{X_{IN} \rightarrow Y_{OUT}}^{(F)} / f_{Y_{IN} \rightarrow X_{OUT}}^{(B)}$, as a function of interlayer distance. An interlayer distance that is neither too small nor too large provides better unidirectionality, which is consistent with the electromagnetic simulations demonstrated in Fig. 3(a). (b) Angular spectra of the symmetric and asymmetric layouts for the second-layer nanostructures. A symmetric layout causes the difference between the angular spectra ($f_{X_{IN} \rightarrow Y_{OUT}}^{(F)}$ and $f_{Y_{IN} \rightarrow X_{OUT}}^{(B)}$) to diminish, which is consistent with the simulation results shown in Fig. 3(b).

($f_{X_{IN} \rightarrow Y_{OUT}}^{(F)}$ and $f_{Y_{IN} \rightarrow X_{OUT}}^{(B)}$) follow similar traces with larger Z_M ($\lambda/4$). In other words, the near-field effects are negligible as Z_M increases. On the other hand, too small a value of Z_M indicates that coarse-scale spatial attributes, that is, the asymmetric layout of the dipole arrangements specified by G_X and G_Y , are difficult to be delivered through near-field interactions, resulting in the relatively similar angular spectra, as in the case of $Z_M = \lambda/20$.

In order to address the layout dependency, the dotted and dotted-dashed curves in Fig. 7(b) indicate, respectively, the angular spectrum of the forward ($f_{X_{IN} \rightarrow Y_{OUT}}^{(F)}$) and backward directions ($f_{Y_{IN} \rightarrow X_{OUT}}^{(B)}$) when the second-layer L-shapes are arranged in a symmetric manner while Z_M is given by $\lambda/20$. Specifically, both G_X and G_Y [specified in Figs. 5(b) and 5(c)] are $\lambda/2$ for the symmetric architecture. The two angular spectra follow nearly the same traces, meaning that the symmetric layout of the second-layer structure causes the unidirectionality to diminish, which is indeed consistent with the simulation results demonstrated in Fig. 3(b). The solid and dashed curves in Fig. 6(b) are, respectively, the forward and backward angular spectra when the L-shapes are arranged asymmetrically, which behave differently from each other. [These curves are the same as the ones shown in plot (iii) ($Z_M = \lambda/20$) in Fig. 6.]

Finally, we make a few remarks about the results of the present study. The first is a comment regarding the fact that the unidirectionality appears in a particular wavelength range (900–1200 nm) but not at other wavelengths. This is based on the resonance of the input light and the nanostructured matter placed at the entrance side of the input light; in the case of gold embedded in SiO_2 , the unidirectionality appears in the range presented. The second is a comment about the polarization conversion efficiencies ($T_{X \rightarrow Y}^{(F)}$, $T_{Y \rightarrow X}^{(F)}$, $T_{X \rightarrow Y}^{(B)}$, and $T_{Y \rightarrow X}^{(B)}$), which take small values, in general, lower than 10%. Clarifying the upper bound of the achievable polarization conversion efficiencies and unidirectionality will be an interesting topic of a future study. Also, similarly to the first remark, material dependence may be present, which could be exploited to increase the unidirectionality. The third is a comment regarding the applications of this study. As noted repeatedly in the paper, we consider that the significance of the angular-spectrum-based approach shown here is that

we can explicitly grasp the unidirectionality based on the notion of transfer of momentum via optical near fields. In this context, the principle proposed has advantages in terms of its general-purpose properties or utility. Also, based on the results and/or theoretical elements shown in this paper, we may be able to seek the origin of unidirectionality at a more fundamental level. Meanwhile, as is also mentioned in the literature [1,2,4–13], the potential industrial applications of unidirectional optical devices are vast, including optical isolators, one-way mirrors, etc.

5. SUMMARY

In summary, we demonstrate a theoretical foundation for direction-dependent polarization conversion efficiency, yielding unidirectional light transmission, in two-layer isotropic nanostructured matter based on the angular spectrum representation of optical near fields. The interlayer distance dependencies and the asymmetric and symmetric layout dependencies of nanostructured matter exhibit agreement between electromagnetic numerical simulations and the theoretical calculations. The explicit representation of optical near fields by the angular spectrum, which is a decomposition of evanescent waves with different decay lengths, provides a physically intuitive picture in considering polarization conversion involving subwavelength structures. This study provides insights into unique optical properties, such as unidirectionality, stemming from isotropic shape-engineered nanostructured matter, which will lead to fundamental guiding principles for understanding and engineering nanostructures for novel functionalities.

ACKNOWLEDGMENTS

This work was supported in part by the Strategic Information and Communications R&D Promotion Programme (SCOPE) of the Ministry of Internal Affairs and Communications, and by Grants-in-Aid for Scientific Research and the Core-to-Core Program, A. Advanced Research Networks from the Japan Society for the Promotion of Science.

REFERENCES

1. R. J. Potton, "Reciprocity in optics," *Rep. Prog. Phys.* **67**, 717–754 (2004).

2. A. Drezet and C. Genet, "Reciprocity and optical chirality," in *Singular and Chiral Nanoplasmonics*, N. Zheludev and S. V. Boriskina, eds. (Pan Stanford Publishing) (to be published).
3. B. E. A. Saleh and M. C. Teich, *Fundamentals of Photonics* (Wiley-Interscience, 2007), Chap. 6.
4. H. Dötsch, N. Bahlmann, O. Zhuromskyy, M. Hammer, L. Wilkens, R. Gerhardt, P. Hertel, and A. F. Popkov, "Applications of magneto-optical waveguides in integrated optics: review," *J. Opt. Soc. Am. B* **22**, 240–253 (2005).
5. W. Van Parys, B. Moeyersoon, D. Van Thourhout, R. Baets, M. Vanwolleghem, B. Dagens, J. Decobert, O. Le Gouezigou, D. Make, R. Vanheertum, and L. Lagae, "Transverse magnetic mode nonreciprocal propagation in an amplifying AlGaInAs/InP optical waveguide isolator," *Appl. Phys. Lett.* **88**, 071115 (2006).
6. T. Amemiya, K. Abe, T. Tanemura, T. Mizumoto, and Y. Nakano, "Nonreciprocal polarization conversion in asymmetric magneto-optic waveguide," *IEEE J. Quantum Electron.* **46**, 1662–1669 (2010).
7. M. J. Lockyear, A. P. Hibbins, K. R. White, and J. R. Sambles, "One-way diffraction grating," *Phys. Rev. E* **74**, 056611 (2006).
8. W.-M. Ye, X.-D. Yuan, and C. Zeng, "Unidirectional transmission realized by two nonparallel gratings made of isotropic media," *Opt. Lett.* **36**, 2842–2844 (2011).
9. J. Xu, C. Cheng, M. Kang, J. Chen, Z. Zheng, Y.-X. Fan, and H.-T. Wang, "Unidirectional optical transmission in dual-metal gratings in the absence of anisotropic and nonlinear materials," *Opt. Lett.* **36**, 1905–1907 (2011).
10. V. A. Fedotov, P. L. Mladyonov, S. L. Prosvirnin, A. V. Rogacheva, Y. Chen, and N. I. Zheludev, "Asymmetric propagation of electromagnetic waves through a planar chiral structure," *Phys. Rev. Lett.* **97**, 167401 (2006).
11. A. Drezet, C. Genet, J.-Y. Laluet, and T. W. Ebbesen, "Optical chirality without optical activity: How surface plasmons give a twist to light," *Opt. Express* **16**, 12559–12570 (2008).
12. C. Menzel, C. Helgert, C. Rockstuhl, E. B. Kley, A. Tünnermann, T. Pertsch, and F. Lederer, "Asymmetric transmission of linearly polarized light at optical metamaterials," *Phys. Rev. Lett.* **104**, 253902 (2010).
13. C. Cheng, J. Chen, D.-J. Shi, Q.-Y. Wu, F.-F. Ren, J. Xu, Y.-X. Fan, J. Ding, and H.-T. Wang, "Physical mechanism of extraordinary electromagnetic transmission in dual-metallic grating structures," *Phys. Rev. B* **78**, 075406 (2008).
14. E. Wolf and M. Nieto-Vesperinas, "Analyticity of the angular spectrum amplitude of scattered fields and some of its consequences," *J. Opt. Soc. Am. A* **2**, 886–890 (1985).
15. T. Inoue and H. Hori, "Representations and transforms of vector field as the basis of near-field optics," *Opt. Rev.* **3**, 458–462 (1996).
16. T. Inoue and H. Hori, "Theoretical treatment of electric and magnetic multipole radiation near a planar dielectric surface based on angular spectrum representation of vector field," *Opt. Rev.* **5**, 295–302 (1998).
17. T. Inoue and H. Hori, "Quantum theory of radiation in optical near field based on quantization of evanescent electromagnetic waves using detector mode," in *Progress in Nano-Electro-Optics IV*, M. Ohtsu, ed. (Springer, 2005), pp. 127–199.
18. M. Naruse, T. Inoue, and H. Hori, "Analysis and synthesis of hierarchy in optical near-field interactions at the nanoscale based on angular spectrum," *Jpn. J. Appl. Phys.* **46**, 6095–6103 (2007).
19. M. Naruse, N. Tate, Y. Ohyagi, M. Hoga, T. Matsumoto, H. Hori, A. Drezet, S. Huan, and M. Ohtsu, "Optical near-field-mediated polarization asymmetry induced by two-layer nanostructures," *Opt. Express* **21**, 21857–21870 (2013).
20. M. Ohtsu and H. Hori, *Near-Field Nano-Optics* (Kluwer Academic/Plenum, 1999).
21. D. Jalas, A. Petrov, M. Eich, W. Freude, S. Fan, Z. Yu, R. Baets, M. Popovic, A. Melloni, J. D. Joannopoulos, M. Vanwolleghem, C. R. Doerr, and H. Renner, "What is—and what is not—an optical isolator," *Nat. Photonics* **7**, 579–582 (2013).
22. R. Carminati, M. Nieto-Vesperinas, and J.-J. Greffet, "Reciprocity of evanescent electromagnetic waves," *J. Opt. Soc. Am.* **15**, 706–712 (1998).
23. N. Tate, H. Sugiyama, M. Naruse, W. Nomura, T. Yatsui, T. Kawazoe, and M. Ohtsu, "Quadrupole–dipole transform based on optical near-field interactions in engineered nanostructures," *Opt. Express* **17**, 11113–11121 (2009).
24. A. Taflov and S. C. Hagness, *Computational Electrodynamics: The Finite-Difference Time-Domain Method* (Artech House, 2005).
25. D. W. Lynch and W. R. Hunter, "Comments on the optical constants of metals and an introduction to the data for several metals," in *Handbook of Optical Constants of Solids*, E. D. Palik, ed. (Academic, 1985), pp. 275–367.

Novel sub-100 nm surface chemical modification by optical near-field induced photocatalytic reaction

Thu Hac Huong Le · Kazuma Mawatari ·
Yuriy Pihosh · Tadashi Kawazoe · Takashi Yatsui ·
Motoichi Ohtsu · Takehiko Kitamori

Received: 4 October 2013 / Accepted: 2 February 2014 / Published online: 14 February 2014
© Springer-Verlag Berlin Heidelberg 2014

Abstract The surface modification is indispensable to facilitate new functional applications of micro/nanofluidics devices. Among many modification techniques developed so far, the photo-induced chemical modification is the most versatile method in terms of robustness, process simplicity, and feasibility of chemical functionality. In particular, the method is useful for closed spaces, such as post-bonded devices. However, the limitation by optical diffraction limit is still a challenging issue in scaling down the pattern sizes to nanoscale. Here, we demonstrated a novel surface modification on sub-100 nm scale utilizing the novel optical near-field (ONF) generated on nanostructures of photocatalyst (TiO₂). The minimum pattern size of 40 nm, which was much smaller than diffraction limit, was achieved using a visible light source (488 nm) and a conventional irradiation setup. The controllability of pattern size by light intensity, the feasibility of functionality, and the non-contact working mode have impacts on surface patterning of post-bonded micro/nanofluidics devices. It is also worthy to note that our results verified for the first time the ONF on nanostructures of non-metal materials and its ability to manipulate the chemical reaction on nanoscale.

Keywords Surface modification on nanoscale · Modification of bonded chip · Optical near-field · Photocatalytic chemical modification

1 Introduction

Surface properties of microfluidic devices are of significance to facilitate many applications including analytical or biological devices, fluidic control, and chemical reaction (Delamarche et al. 2005; West et al. 2008). Moreover, the downscaling of fluidic devices to 10¹–10³ nm scale, which is referred as extended-nano fluidics, has resulted in a very high surface-to-volume ratio and significantly dominant surface effects. Surface properties induced unique properties of liquid in extended-nano fluidics such as ion enrichment (Pu et al. 2004), fast proton transfer (Tsukahara et al. 2007), and viscosity increase (Hibara et al. 2003). These unique properties are quite promising for next functional nanofluidic devices, and controlling the surface properties is indispensable to realize those devices. Chemical modification of surface is the key technology not only in microfluidics/nanofluidics, but also in many research fields including optical and electronic field, cell biology, and tissue engineering. Selective functional modification, together with the scaling down of modified features to nanoscale, has been of great importance to exploit new value, unique properties of materials, and practical applications of devices (Xia and Whitesides 1998; Wouters and Schubert 2004; Qi et al. 2004; Ganesan et al. 2010). For example, selective patterning of surface has made it possible to attach nanomaterials, biomolecules, or polymers for functional nanodevices (Mendes et al. 2007). In biosensing application, the selective functionalization is necessary to render chemical

Electronic supplementary material The online version of this article (doi:10.1007/s10404-014-1361-7) contains supplementary material, which is available to authorized users.

T. H. H. Le · K. Mawatari · Y. Pihosh · T. Kitamori (✉)
Department of Applied Chemistry, Graduate School of
Engineering, The University of Tokyo, Hongo 7-3-1,
Bunkyo-ku, Tokyo 113-8656, Japan
e-mail: kitamori@icl.t.u-tokyo.ac.jp

T. Kawazoe · T. Yatsui · M. Ohtsu
Department of Electrical Engineering and Information Systems,
Graduate School of Engineering, The University of Tokyo,
Tokyo, Japan

specificity toward analytes, as well as to improve the sensitivity (Jane et al. 2009). Generally, the spatial resolution and chemical functionality are two crucial requirements in modification. Specifically, for microfluidic/nanofluidic devices, the fabrication (bonding) process usually consists of thermal/plasma treatment, and strong acidic/alkali washing that may damage the modified patterns, especially for soft materials or biomaterials. Thus, the techniques that allow the chemical modification after the devices are sealed are highly desirable (Priest 2010).

Numerous techniques including photolithography, nanolithography, self-assembly of supramolecules have been developed to realize the chemical patterning with resolution from several micrometers to several nanometers. Nanolithography such as dip-pen nanolithography (Huo et al. 2008), nanoimprinting, and scanning probe lithography (Tseng et al. 2005) has demonstrated prominent spatial resolution, yet the scanning and probing principle limit their application to modification of open surfaces, and modification to post-bonded devices is difficult. Those techniques also require expensive equipment and do not have a high throughput. There have been many efforts to realize the chemical patterning that work on non-contact mode such as using thermal (Park et al. 2007), electrical, or electrochemistry (Bunimovich et al. 2004), but they still have limitation in spatial resolution and chemical feasibility.

In microscale, the photo-induced methods are widely used, owing to their outstanding feasibility of chemical functionality, controllability, and robustness. However, in principle, the diffraction limit of light is the bottle-neck in improving the spatial resolution. Some optical near-field (ONF) techniques have been introduced to overcome the optical diffraction limit. One of beneficial property of ONF is its ability to optically induced physical and chemical processes at the nanometer scale. These techniques are usually enabled by embedding metal nanostructure as local field hot spot, or using the scanning near-field microscopy (SNOM) (Menard 2007; König et al. 2012; Ueno et al. 2008; Luo and Ishihara 2004). For example, Ohtsu et al. succeeded in the photolithography with the groove width of 50 nm, using the non-adiabatic photochemical reaction induced by the ONF generated on a Cr mask (Yonemitsu et al. 2005), but this method still need the contact of mask and modified surface.

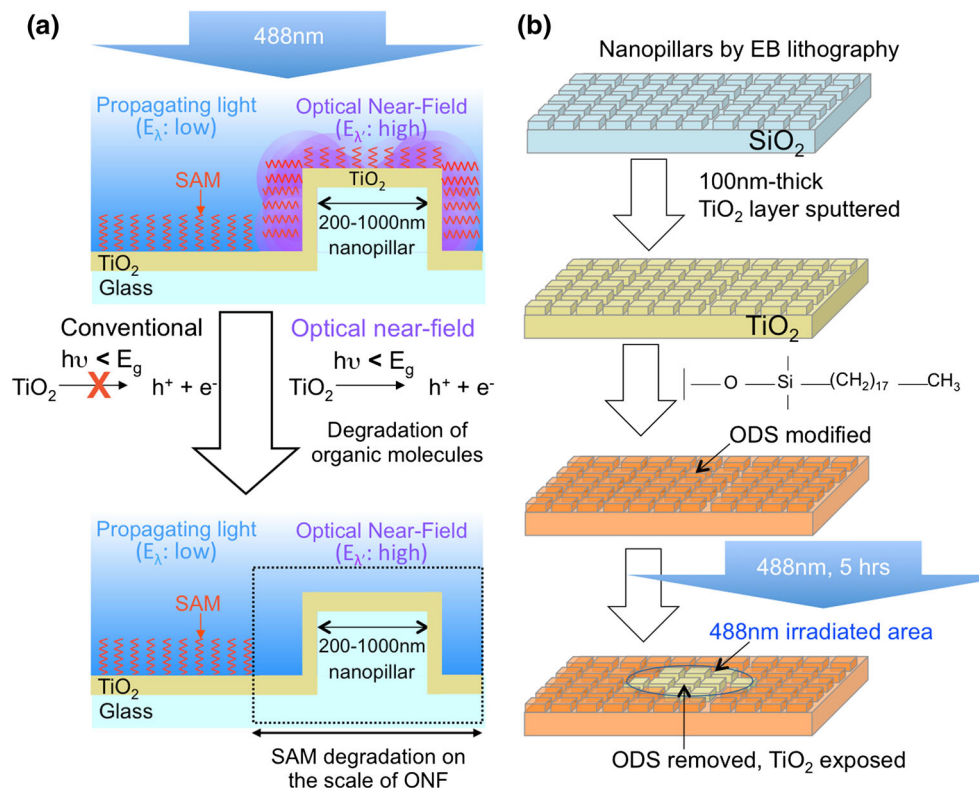
In this work, we have realized a novel chemical modification using the ONF generated on nanostructures of photocatalyst (TiO_2) that can work well for close spaces. Here, the ONF allowed the scaling down of pattern size to several tens of nanometers, and the photocatalytic property of TiO_2 offered many potential modification strategies such as destructive modification (decomposition) or constructive modification (self-assembly, polymerization, etc.).

2 Principle

The principle of this method is based on our previous reports about the ONF generation on nanostructure TiO_2 and the ONF-induced visible response photocatalytic water splitting (Le et al. 2011, 2012). The bandgap energy of TiO_2 is 3.2 eV (wavelength: ~ 380 nm); thus, conventionally, an UV-photon is required to excite an electron from valence band to conduction band of TiO_2 . However, even under visible (488 nm) irradiation, the ONF generated on nanostructures TiO_2 can excite the coherent phonons in the nanostructures, together with the ONF. These excited coherent phonons form a coupled state, which is called exciton-phonon-polariton. This coupled state contributes to the so-called phonon-assisted process, which excites an electron in the valence band of TiO_2 to the higher phonon level and successively to the conduction band by normal light absorption, even though the energy of incident photon is lower than its bandgap energy. This excitation process is allowed by the ONF, even though the transition is an electric-dipole forbidden process. It should be noted that although this is multi-step excitation via the phonon level (real states), it is totally different with the nonlinear multi-photon absorption using virtual states. In other words, ONF has an apparent energy higher than the incident photons. The novel property of ONF has also been experimentally verified and widely applied as non-adiabatic photolithography (Kawazoe et al. 2007), novel self-organized photochemical etching (Yatsui et al. 2008), optical frequency up-conversion (Kawazoe et al. 2009), and semiconductor photovoltaic (Yukutake et al. 2010), etc. These results have inspired us to apply this concept to the photocatalytic chemical reactions on nanostructure TiO_2 for modification, since the superior spatial resolution of ONF and the size/structure dependency could manipulate the chemical reaction at nanoscale.

The concept in Fig. 1a generally describes how the ONF is generated and the photocatalytic modification is controlled on nanoscale on TiO_2 nanostructures. As TiO_2 nanostructure is irradiated with visible propagating light (wavelength: 488 nm), ONF is generated at the edges of nanostructures. This ONF has apparent higher energy (apparent UV-photon), which allows the excitation of TiO_2 , following by the photocatalytic reaction of TiO_2 , even under visible light irradiation. The usage of visible light results in the selective excitation of TiO_2 at ONF-generated sites only, since at other sites, without ONF, 488 nm light cannot excite TiO_2 . Consequently, it is expected that the photocatalytic reaction occurs exactly at ONF-generated sites. For example, when the size of nanostructures was small enough (below 200 nm), it was possible to control the chemical reaction on the whole single nanostructures. While in larger nanostructures, the

Fig. 1 ONF-induced partial surface modification: **a** concept of ONF-induced photocatalytic degradation of ODS monolayer on TiO₂ and **b** protocol of the whole modification process: fabrication of TiO₂ nanostructures by EBL and sputtering, surface modification of ODS, and selective degradation of ODS



chemical reaction was likely to enhance at the edges, remaining the center of pillar untreated (Le et al. 2012). Interestingly, we have also verified the dependency of ONF generation on the light intensity that indicates the controllability of pattern size by irradiation power. In this study, we demonstrated the photocatalytic degradation of the octadecylsilyl (ODS) as the representative process to realize hydrophobic/hydrophilic patterning. The protocol for the whole process is shown in Fig. 1b. Here, the top-down fabrication method, which allowed the construction of uniform, scalable, and shape specific nanostructures, was chosen.

3 Experimental

3.1 Fabrication and characterization of TiO₂ film

The nanopillar or nanogap structures were fabricated onto a fused-silica substrate by electron-beam lithography (EBL), followed by a dry etching process. The substrate was then deposited with a 20-nm-thick tin-doped indium oxide (ITO) and 100-nm-thick TiO₂ layer by a sputtering method. The ITO layer was used as a conducting layer during electron-beam microscopy (SEM) measurements. The fabricated TiO₂ thin film was then undergoing a post-annealing at 450 °C in 4 h to convert it into anatase crystalline phase.

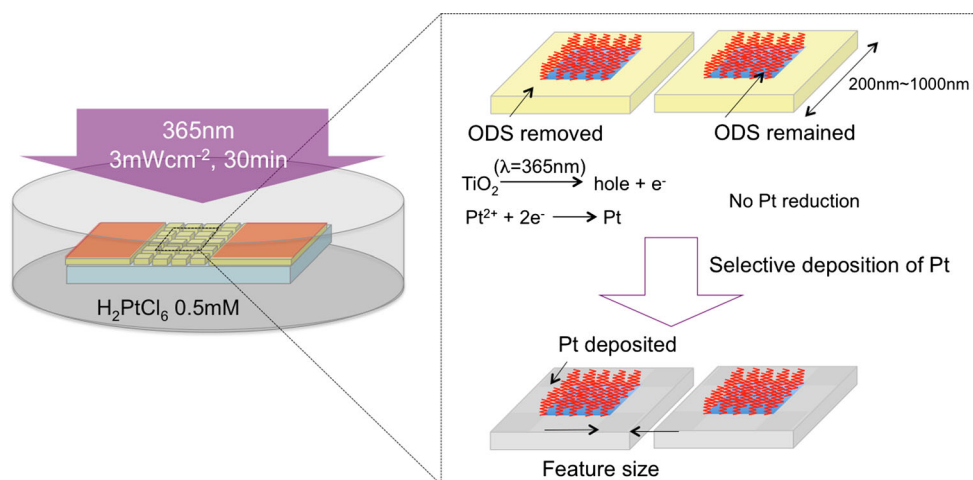
The surface was modified with ODS by wet protocol [see supporting information (2)].

3.2 Optical near-field induced degradation of ODS and evaluation

In the ODS degradation experiment, the film with nanostructures was irradiated with 488 nm light (Ar⁺ ion laser, Coherent Japan Inc., Japan) in 5 h by changing the intensity in the range of 5.0×10^2 – 1.0×10^4 W cm⁻². The usage of visible light led to the selective degradation of ODS at ONF-generated sites only, since 488 nm could not excite TiO₂ on the remaining areas. In order to evaluate the ODS degradation, the whole film was stained by fluorescent dye Rhodamine B (25 μM) and observed by fluorescence microscopy. Rhodamine B is likely to adsorb onto hydrophobic surfaces; therefore, rhodamine B is expected to adsorb onto the ODS-remaining area (hydrophobic area). The substrate was then cleaned and observed by a fluorescence microscope.

Since the ODS degradation was induced by ONF, it was expected that the ODS was not removed uniformly on single nanostructures, yet the ODS degradation should be significantly enhanced at their edges, compared with the center. The main reason is the enhancement of ONF at the edges of nanostructures that have been previously reported (Kawazoe et al. 2007). This effect is also similar to the

Fig. 2 High-resolution visualization method of ODS degradation by SEM after selective photodeposition of Pt onto the ODS-degraded area



enhanced local electric field at the edges of metal nanostructures in case of plasmonic field (Valev et al. 2012). However, the optical diffraction limit of fluorescence microscopy cannot allow us to observe this phenomenon with nanometer scale resolution. In order to observe the degradation of ODS with nanometer scale resolution, we used the selective photodeposition of Pt onto the ODS-degraded area and observed the Pt patterns by SEM as shown in Fig. 2. The details of Pt photodeposition protocol were described in supporting information (3). The Pt was expected to be photodeposited at the ODS-degraded area, while remaining ODS layer kept the area from reacting with Pt ions (Juodkazis et al. 2001). As a result, Pt was deposited onto the ODS-degraded area only. The deposited Pt was observed using SEM, and the existence of Pt was confirmed by the energy-dispersive X-ray (EDX) mapping [see supporting information (4)]. The achieved Pt patterns were useful for exactly evaluating the size of ODS-degraded area on single nanostructures.

4 Results and discussion

4.1 Evaluation of ODS degradation by fluorescence (FL) microscopy

Figure 3a shows the ODS degradation of a substrate with nanostructures (width 180 nm \times gap 20 nm \times height 50 nm). On the 488 nm irradiated area, the ODS degradation or the exposure of TiO_2 appeared as the dark spot, while ODS was remained and stained by a fluorescent dye (rhodamine B) at the non-irradiated area. As a negative control experiment, we also carried out the same experiment on a flat TiO_2 substrate without nanostructures. The degradation ratio was evaluated using the equation in Fig. 3a. The dependency of ODS degradation ratio on 488 nm irradiation intensity in Fig. 3b shows that there was a significant enhancement (enhancement factor

larger than 8) of ODS degradation ratio on nanopillars TiO_2 compared with that of the flat substrate, though ODS on flat TiO_2 film was also slightly degraded under 488 nm irradiation. This result strongly supports our principle that the ODS degradation was induced by ONF at nanostructures.

4.2 Evaluation of modified pattern size based on Pt patterns

In order to exactly evaluate the ODS degradation patterns, the Pt photodeposition process was carried out. The result is shown in Fig. 4. The SEM and SEM-EDX images in Fig. 4 verified that outside the 488 nm irradiated spot, there was no Pt deposited on the surface, while inside the 488 nm irradiated spot, Pt appeared as bright patterns at the edges of nanostructures. It indicated that the Pt was deposited onto the ODS degradation area.

Figure 5 shows various modified features manipulated by the irradiation intensity and design of nanostructures. As expected, it was clear that Pt was detected at the edges of nanostructures, whereas there was no Pt deposited at the center. Interestingly, we found out that the size of pillar did not affect the size of modified features, but the 488 nm irradiation intensity did determine the size of Pt patterns. The minimum size of 40 nm was achieved with nanostructures of width 180 nm \times gap 20 nm \times height 50 nm under irradiation intensity of 0.8 kW cm^{-2} (Fig. 5a), which was much smaller than the wavelength of using light. As increasing the irradiation intensity up to 14.1 kW cm^{-2} on nanostructures of width 900 nm \times gap 100 nm \times height 50 nm (Fig. 5b), the modified patterns with a half-pitch of 350 nm were achieved (Fig. 5b).

The dependency of pattern size on the 488 nm light intensity was also investigated as shown in Fig. 5c. Details about evaluation of pattern sizes were described in supporting information (5). The larger pattern sizes were achieved by increasing irradiation intensity. For example,

Fig. 3 Visualization of ODS degradation by fluorescence microscopy after staining the remaining ODS with rhodamine B: **a** microscope image and **b** dependence of degradation ratio on irradiation intensity of 488 nm light. The $I_{background}$ represents the intensity of substrate before rhodamine B staining

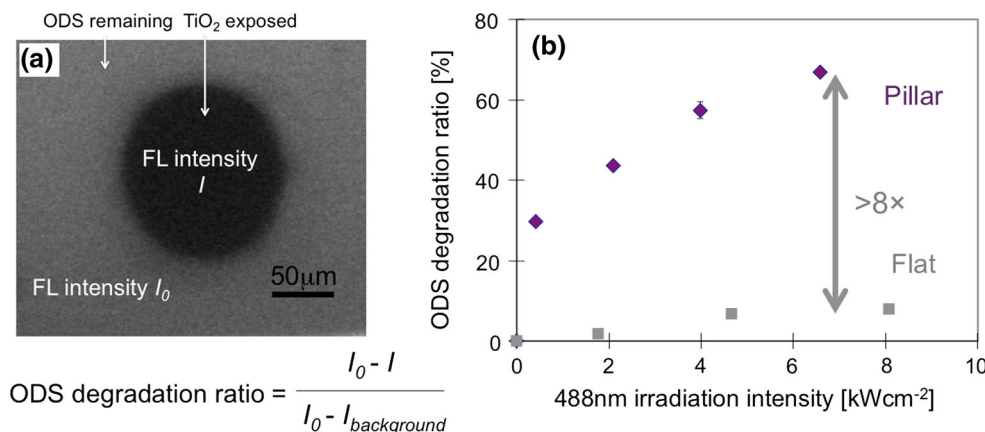
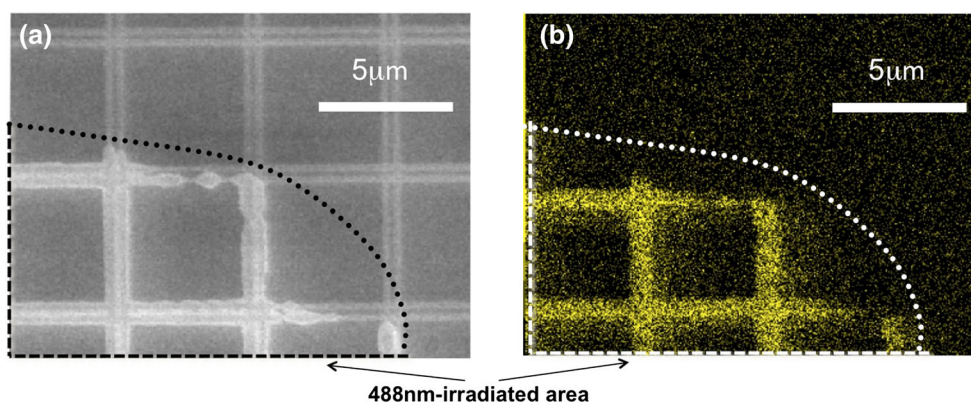


Fig. 4 Visualization of ODS degradation: **a** SEM image and **b** EDX mapping of Pt element



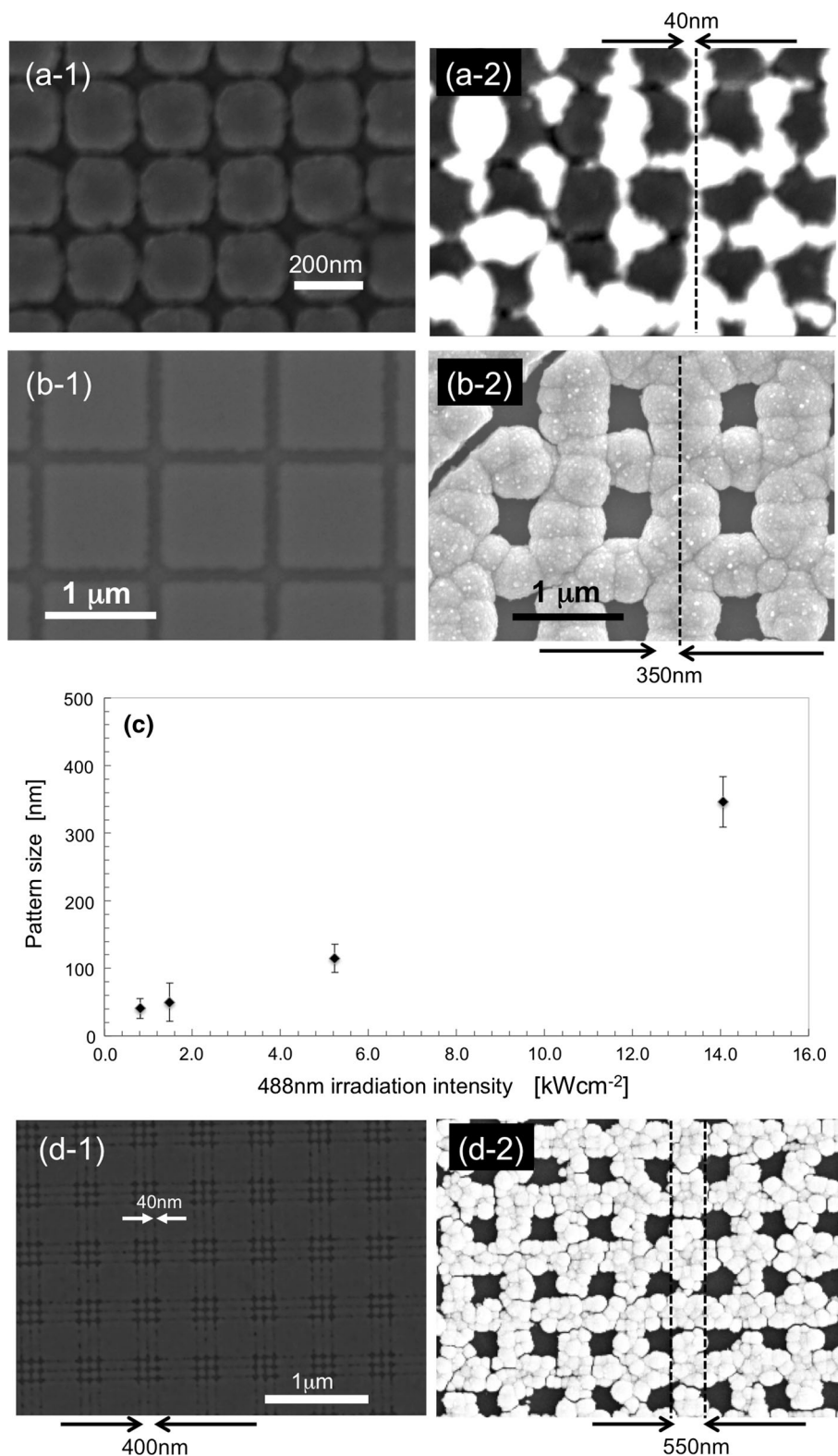
the increase of irradiation intensity in Fig. 5a by one order of magnitude in Fig. 5b resulted in the increase in pattern sizes from several tens of nanometers to several hundreds of nanometers. It is also suggested that the modified features could be easily manipulated by irradiation intensity and design of nanostructures. As mentioned above, the deposited Pt could be considered as the trace of ODS-degraded area. The ODS degradation at edges of nanostructures was consistent with previous reports about photolithography using visible optical near-fields generated on Cr mask (Kawazoe et al. 2007). The enhancement of ONF at the edges is similar to the enhancement of local electric fields at edges of metal nanostructures, according to numerical calculation model, as well as experimental results (Valev et al. 2012).

The non-uniform deposition of Pt on nanopillars strongly supported our conclusion that ODS was degraded by ONF effect. Since the ONF generation at edges of nanostructures was confirmed, we demonstrated modification using nanochannel structures. For example, in Fig. 5d, 40 nm-wide channel structures with 160 nm gap between channels were drawn by EBL. This design generated pattern size of 550 nm (Fig. 5d-2).

Although the experiments were carried out on an open substrate, the working principle that does not need masks or the contact to surfaces suggested that our method was applicable to post-bonded micro/nanofluidics devices. Moreover, the high photocatalytic activity of TiO₂ would offer a wide range of chemical modification. The ODS degradation in our experiments results in the partial tailoring wettability of surface (ODS is hydrophobic while TiO₂ is hydrophilic) at sub-100 nm scale. It should contribute an effective technique to realize two-phase flow (Hibara et al. 2002) or Laplace valve (Mawatari et al. 2013) for nanofluidics, which are difficult to realize by conventional photo-induced methods.

In our experiments, it took five hours for the total degradation of ODS layer at irradiation intensity of $\sim \text{kW cm}^{-2}$, but we believe that the increase in intensity by several orders of magnitude could significantly improve the chemical reaction rate toward the rapid manipulation of surface chemical reaction. Thus, it is expected to open a new perspective in optical manipulation of surface chemistry in restricted small spaces. In this case, the spatial resolution could be manipulated by the size of nanostructures.

Fig. 5 SEM images of ODS degradation with different nanostructures: **a** non-irradiated area (**a1**) and irradiated area (**a2**) with nanostructures of width $180\text{ nm} \times$ gap $20\text{ nm} \times$ height 50 nm (irradiation intensity of 0.8 kW cm^{-2}), **b** non-irradiated area (**b1**) and irradiated area (**b2**) with nanostructures of width $900\text{ nm} \times$ gap $100\text{ nm} \times$ height 50 nm (irradiation intensity of 14.1 kW cm^{-2}), **c** the dependency of pattern sizes on the irradiation intensity (see supporting information for the definition of the pattern size), and **d** an example using a nanochannel structure (40 nm -wide channel structures with 160 nm gap between channels) to demonstrate 550 nm pattern size



The plasmonic field enhancement on metal nanostructures has been intensively studied, yet there are still few studies on local field enhancement at nanostructures of materials other than metal. In the present work, the

observation of Pt as the trace of ONF generation could be considered as the first verification and visualization of ONF on semiconductor materials. Furthermore, the visualization showed that under linearly polarized light, there was no

significant difference between the vertical and longitudinal edges of square nanopillars. Unlike the strong dependence in polarization of light reported in case of plasmonic local field, the polarization dependence of ONF is negligibly small.

5 Conclusion

In summary, we have successfully realized a novel surface chemical modification that was enabled by the ONF generated on nanostructures of photocatalyst, though there was still a problem of non-uniform modified pattern at low irradiation intensity. The achievement of 40 nm patterns, the controllability of spatial resolution by irradiation intensity, and the feasibility of chemical functionality are main advantages of our method. Moreover, our method works well for closed spaces that may contribute to many practical applications for post-bonded micro/nanofluidic devices. Our method is conceptually novel in utilizing of ONF for photocatalysis, owing to its prominent spatial resolution and unique property in electronic excitation.

Acknowledgments This work was partially supported by JSPS Core-to-Core Program and the Grant-in-Aid for Specially Promoted Research. We also would like to thank to the Research Hub for Nano Characterization Center at the University of Tokyo for SEM measurement.

References

- Bunimovich Y, Ge G, Ries R, Beverly K, Hood L, Heath J (2004) Electrochemically programmed, spatially selective biofunctionalization of silicon wires. *Langmuir* 20:10630–10638
- Delamarche E, Juncker D, Schmid H (2005) Microfluidics for processing surfaces and miniaturizing biological assays. *Adv Mater* 17:2911–2933
- Ganesan R, Kratzka K, Lendlein A (2010) Multicomponent protein patterning of material surfaces. *J Mater Chem* 20:7322–7331
- Hibara A, Nonaka M, Hisamoto H, Uchiyama K, Kikutani Y, Tokeshi M, Kitamori T (2002) Stabilization of liquid interface and control of two-phase confluence and separation in glass microchips by utilizing octadecylsilane modification of microchannels. *Anal Chem* 74:1724–1728
- Hibara A, Takumi S, Kim H-B, Tokeshi M, Ooi T, Nakao M, Kitamori T (2003) Liquid properties investigation by time-resolved fluorescence measurements. *Anal Chem* 36:605–612
- Huo F, Zheng Z, Zheng G, Giam LR, Zhang H, Mirkin CA (2008) Polymer pen lithography. *Science* 321:1658–1660
- Jane A, Dronov R, Hodges A, Voelcker NH (2009) Porous silicon biosensors on the advance. *Trends Biotechnol* 27:230–240
- Juodkazis S, Yamaguchi A, Ishii H, Matsuo S, Takagi H, Misawa H (2001) Photo-electrochemical deposition of platinum on TiO₂ with resolution of twenty nanometers using a mask elaborated with electron-beam lithography. *Jpn J Appl Phys* 40:4246–4251
- Kawazoe T, Ohtsu M, Inao Y, Kuroda R (2007) Exposure dependence of the developed depth in nonadiabatic photolithography using visible optical near fields. *J Nanophoton* 1:011595
- Kawazoe T, Fujiwara H, Kobayashi K, Ohtsu M (2009) Visible light emission from dye molecular grains via infrared excitation based on the nonadiabatic transition induced by the optical near field. *J Sel Top Quantum Electron* 15:1380–1386
- König T, Sekhara YN, Santer S (2012) Surface plasmon nanolithography: impact of dynamically varying near-field boundary conditions at the air–polymer interface. *J Mater Chem* 22:5945–5950
- Le THH, Mawatari K, Pihosh Y, Kawazoe T, Yatsui T, Ohtsu M, Tosa M, Kitamori T (2011) Optical near-field induced visible response photoelectrochemical water splitting on nanorod TiO₂. *Appl Phys Lett* 99:213105–213108
- Le THH, Mawatari K, Hasumoto N, Pihosh Y, Kitamura K, Kawazoe T, Yatsui T, Naruse M, Ohtsu M, Kitamori T (2012) Optical near-field induced chemical partial hydrophobic/hydrophilic modification with sub-diffraction limit resolution. In: *Proceedings of the 16th μTAS conference*, pp 222–224
- Luo X, Ishihara T (2004) Subwavelength photolithography based on surface-plasmon polariton resonance. *Opt Express* 12:3055
- Mawatari K, Kubota S, Xu Y, Priest C, Sedev R, Ralston J, Kitamori T (2013) Femtoliter droplet handling in nanofluidic channels: a Laplace nanovalve. *Anal Chem* 84:10812–10816
- Menard E (2007) Micro- and nanopatterning techniques for organic electronic and optoelectronic systems. *Chem Rev* 107:1117–1160
- Mendes PM, Yeung CL, Preece JA (2007) Bio-nanopatterning of surfaces. *Nanoscale Res Lett* 2:373–384
- Park I, Li Z, Pisano AP, Williams RS (2007) Selective surface functionalization of silicon nanowires via nanoscale Joule heating. *Nano Lett* 7:3106–3111
- Priest C (2010) Surface patterning of bonded microfluidic channels. *Biomicrofluidic* 4(3):32206–32219
- Pu Q, Yun JS, Temkin H, Liu SR (2004) Ion-enrichment and ion-depletion effect of nanochannel structures. *Nano Lett* 4:1099–1103
- Qi M, Lidorikis E, Rakich PK, Johnson SG, Joannopoulos JD, Ippen EP, Smith HI (2004) A three-dimensional optical photonic crystal with designed point defects. *Nature* 429:538–542
- Tseng AA, Notargiacomo A, Chen TP (2005) Nanofabrication by scanning probe microscope lithography: a review. *J Vac Sci Technol B* 23:877–894
- Tsukahara T, Hibara A, Ikeda K, Kitamori T (2007) NMR study of water molecules confined in extended nanospaces. *Angew Chem Int Ed* 46:1180–1183
- Ueno K, Juodkazis S, Shibuya T, Yokota Y, Mizeikis V, Sasaki K, Misawa H (2008) Nanoparticle plasmon-assisted two-photon polymerization induced by incoherent excitation source. *J Am Chem Soc* 130:6928–6929
- Valev VK, De Clercq B, Biris CG, Zheng X, Vandendriessche S, Hojeij M, Denkova D, Jeyaram Y, Panoui NC, Ekinci Y, Silhanek AV, Volskiy V, Vandenbosch GAE, Ameloot M, Moshchalkov VV, Verbiest T (2012) Distributing the optical near-field for efficient field-enhancements in nanostructures. *Adv Opt Mater* 24:208–215
- West J, Becher M, Tombrink S, Manz A (2008) Micro total analysis systems: latest achievements. *Anal Chem* 80:4403–4419
- Wouters D, Schubert US (2004) Nanolithography and nanochemistry: probe-related patterning techniques and chemical modification for nanometer-sized devices. *Angew Chem Int Ed* 43:2480–2495
- Xia Y, Whitesides GM (1998) Soft lithography. *Angew Chem Int Ed* 37:550–575
- Yatsui T, Hirata K, Nomura W, Tabata Y, Ohtsu M (2008) Realization of an ultra-flat silica surface with angstrom-scale average roughness using nonadiabatic optical near-field etching. *Appl Phys B* 93:55–57

- Yonemitsu H, Kawazoe T, Kobayashi K, Ohtsu M (2005) Nonadiabatic photochemical reaction and application to photolithography. *J Lumin* 122:230–233
- Yukutake S, Kawazoe T, Yatsui T, Hirata K, Nomura W, Kitamura K, Ohtsu M (2010) Selective photocurrent generation in the transparent wavelength range of a semiconductor photovoltaic device using a phonon-assisted optical near-field process. *Appl Phys B* 99:415–422

High-field electroluminescence in semiconductor tunnel junctions with a Mn-doped GaAs layer

Pham Nam Hai,^{1,2} Takashi Yatsui,^{1,3} Motoichi Ohtsu,^{1,3} and Masaaki Tanaka^{1,3}

¹Department of Electrical Engineering and Information Systems, The University of Tokyo, 7-3-1 Hongo, Bunkyo-ku, Tokyo 113-8656, Japan

²Department of Physical Electronics, Tokyo Institute of Technology, 2-12-1 Ookayama, Meguro-ku, Tokyo 152-0033, Japan

³Nanophotonics Research Center, The University of Tokyo, 7-3-1 Hongo, Bunkyo-ku, Tokyo 113-8656, Japan

(Received 27 June 2014; accepted 3 September 2014; published online 16 September 2014)

We investigated high-field electroluminescence (EL) in semiconductor tunnel junctions with a Mn-doped GaAs layer (here, referred to as GaAs:Mn). Besides the band-gap emission of GaAs, the EL spectra show visible light emissions with two peaks at 1.94 eV and 2.19 eV, which are caused by *d-d* transitions of the Mn atoms excited by hot electrons. The threshold voltages for band-gap and visible light EL in the tunnel junctions with a GaAs:Mn electrode are 1.3 V higher than those of GaAs:Mn excited by hot holes in reverse biased p^+-n junctions, which is consistent with the hot carrier transport in the band profiles of these structures. Our EL results at room temperature show that the electron temperature in GaAs:Mn can be as high as ~ 700 K for a low input electrical power density of 0.4 W/cm^2 , while the lattice temperature of the GaAs:Mn layer can be kept at 340 K.

© 2014 AIP Publishing LLC. [<http://dx.doi.org/10.1063/1.4895700>]

I. INTRODUCTION

High-field electroluminescence (EL) due to the *d-d* transitions in transition metal (TM)-doped wide-gap II-VI semiconductors have been well studied for display applications.¹ The most well-studied material is Mn-doped ZnS (ZnS:Mn), which was commercialized as an electroluminescent phosphor used in flat panel displays from the late 80s to early 90s. Since the band gap of ZnS ($\sim 3.7 \text{ eV}$) is neither too large nor too small, electrical excitation of Mn^{2+} ions is realized by applying a high electric field (10^6 V/cm) directly to ZnS:Mn. Under this high electric field, electron carriers are accelerated to sufficiently high energy, such that they can excite the Mn^{2+} atoms by impact excitation. Such light emissions due to *d-d* transitions have several advantages over conventional band-gap emissions. The most important advantage is that *d-d* transitions can occur even in indirect band-gap semiconductors, where the band-gap emission is not effective. While EL due to the *d-d* transitions of TM atoms in II-VI semiconductors are well-known, realization of EL by the same mechanism in more widely used semiconductors, such as GaAs and Si, is very challenging due to the very low equilibrium solubility of TM atoms in GaAs and Si and the high conductivity of TM-doped GaAs and Si. Therefore, electrical excitation of TM atoms by a high electric field cannot be realized in the same manner as was done in TM-doped II-VI semiconductors. Recently, we have demonstrated visible light EL due to the *d-d* transitions in p^+-n light-emitting diodes (LEDs) with a Mn-doped GaAs (GaAs:Mn) layer, in the temperature range from 4 K up to room temperature.² EL due to the *d-d* transitions in GaAs:Mn is particularly interesting, since GaAs:Mn is a model material system for studying the ferromagnetism in TM-doped semiconductors,^{3,4} but very little is known about its luminescence characteristics, especially its high-field EL due to the *d-d* transitions. In GaAs:Mn, the low

equilibrium solubility of Mn in GaAs was overcome by using the low-temperature molecular-beam epitaxy (LTMBE) method,⁵ which allows us to dope Mn in GaAs up to a few percents. Since Mn atoms are acceptors in III-V semiconductors, GaAs:Mn is a p^+ semiconductor with a hole concentration as high as $10^{20} \sim 10^{21} \text{ cm}^{-3}$ and a resistivity as low as $10^{-2} \sim 10^{-3} \text{ } \Omega \text{ cm}$. Therefore, in order to realize LEDs using the *d-d* transitions in GaAs:Mn, unconventional device structures should be carefully designed such that hot carriers can be injected to GaAs:Mn layers for impact excitation of Mn *d* electrons. In this paper, we introduce a general strategy to design such structures using semiconductor band engineering techniques. Then, we describe suitable device structures, such as p^+-n junctions (which have already been demonstrated) and tunnel junctions. Finally, we report on high-field EL in semiconductor tunnel junctions with a Mn-doped GaAs layer.

II. DEVICE STRUCTURES FOR LIGHT-EMITTING DEVICES

In order to electrically excite the Mn *d* electrons in very conducting GaAs:Mn layers, we propose a basic device structure consisting of three different layers; (i) a carrier injection layer, (ii) a carrier acceleration layer with a high electric field, which lies next to (iii) a luminescent GaAs:Mn layer, as schematically shown in Fig. 1(a). In this basic structure, charge carriers (electrons or holes) are injected from the carrier injection layer to the carrier acceleration layer. Then, the charge carriers are accelerated by the high electric field in the acceleration layer, such that they can gain sufficiently high energy when they exit the acceleration layer. Finally, these hot carriers can excite Mn atoms by impact excitation when they encounter them in the luminescent GaAs:Mn layer. In this way, we can electrically excite the Mn atoms even in the very conducting GaAs:Mn layer. In

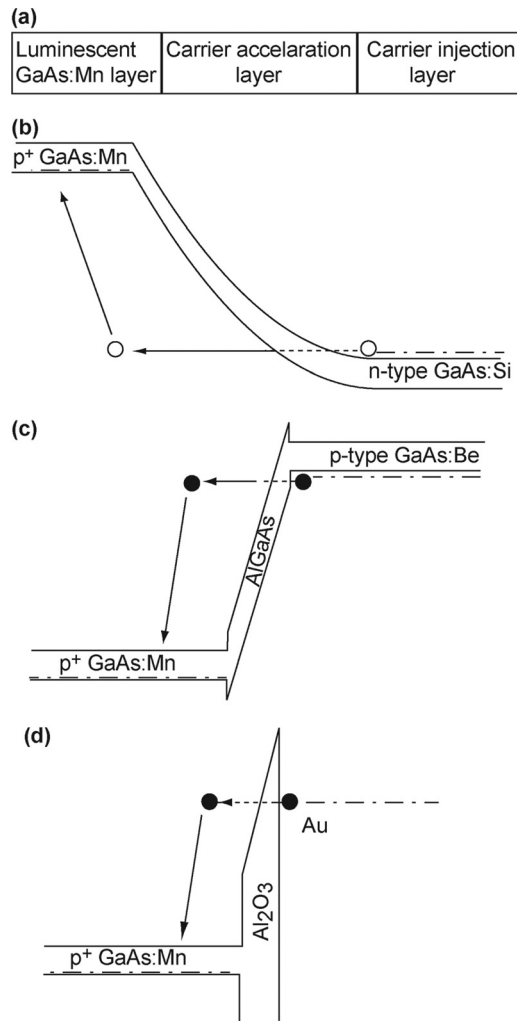


FIG. 1. (a) General structure for high-field EL devices using conductive Mn-doped GaAs, which consists of a carrier injection layer, a carrier acceleration layer, and a luminescent GaAs:Mn layer. Implementations of such a structure can be (b) reverse biased p^+ - n junctions, (c) semiconductor tunnel junctions, and (d) MIS junctions with a luminescent GaAs:Mn layer. (b)–(d) show the band profile of each device structure, where solid lines are the conduction band top and valence band bottom, and chained lines are the quasi Fermi levels. Solid circles and blank circles are electrons and holes, respectively.

the following, we describe our device structures in more details. Figures 1(b)–1(d) show the band profiles of our device structures.

(A) Semiconductor p^+ - n junctions containing a p^+ GaAs:Mn layer, such as a p^+ -type Mn-doped GaAs (GaAs:Mn)/ n -type Si-doped GaAs (GaAs:Si) junction, as shown in Fig. 1(b). When a high reverse bias voltage (i.e., -6 V) is applied to the p^+ - n junction, an intense electric field ($\sim 10^6$ V/cm) builds up in the depletion layer of the p^+ - n junction. Holes are injected from the GaAs:Si to the depletion layer by Zener tunneling. These holes are accelerated to sufficiently high energy by the high electric field in the depletion layer, such that these hot holes can excite the d electrons of the Mn atoms by impact excitation when they exit the depletion layer and are injected into the GaAs:Mn layer. This device structure can be driven only by a direct current (DC) source.

(B) Semiconductor tunnel junctions with at least one p^+ GaAs:Mn layer, such as a p^+ GaAs:Mn/AlGaAs tunnel

barrier/ p -type GaAs:Be structure, as shown in Fig. 1(c). Under a high bias voltage, electrons are injected from the valence band of the GaAs:Be layer to the conduction band of the tunnel barrier by Fowler–Nordheim type inter-band tunneling. These electrons are accelerated by the high electric field in the tunnel barrier, such that they can excite Mn atoms by impact excitation when they are injected into the GaAs:Mn layer. If both the electrodes are GaAs:Mn, this device structure can be driven by an alternating current (AC) source. A similar device structure with the same operating mechanism is a metal-insulator-semiconductor (MIS) structure, such as an Au/Al₂O₃/GaAs:Mn tunnel junction as shown in Fig. 1(d). In the MIS structure, the metal layer acts as a carrier injector. However, the MIS structure can only be driven by a DC source.

In our previous study, we demonstrated visible reddish yellow EL due to the d - d transitions of Mn in structure (A), which is GaAs:Mn/GaAs:Si p^+ - n junctions, and confirmed that these visible light EL emissions originate from the d - d transitions of Mn.² In this work, we investigate visible light EL due to the d - d transitions of Mn in structure (B) at room temperature, which gives us more insightful information on the characteristics of the luminescent GaAs:Mn layers under impact excitation. We will show that the electron temperature in GaAs:Mn can be as high as ~ 700 K, while the lattice temperature of the GaAs:Mn can be kept as low as 340 K. We then discuss the impact excitation efficiency by hot electrons in the GaAs:Mn layers.

III. SEMICONDUCTOR TUNNEL JUNCTION AND POTENTIAL PROFILE

Figure 2(a) shows the schematic device structure of our tunnel junctions, whose layered structure is 20 nm-thick p^+ GaAs:Mn (Mn 1%)/100 nm-thick undoped Al_{0.7}Ga_{0.3}As tunnel barrier/50 nm-thick p -type GaAs:Be (hole concentration $p = 3 \times 10^{18}$ cm⁻³), from the top to the bottom, grown on a p^+ GaAs:Zn substrate by MBE. The p -type GaAs:Be layer and the Al_{0.7}Ga_{0.3}As tunnel barrier were grown at 580 °C, while the top p^+ GaAs:Mn layer was grown at 330 °C. The tunnel junctions were processed into 2×2 mm² mesa diodes by using photolithography and wet etching. A 20 nm-thick Au thin film was evaporated on the surface of the GaAs:Mn layer and the p^+ GaAs substrate as electrodes. Figure 2(b) shows the calculated potential profile of this LED, when a bias voltage $V = 6$ V is applied to the junction. Electrons are injected from the valence band of the GaAs:Be layer to the conduction band of the Al_{0.7}Ga_{0.3}As tunnel barrier by Fowler–Nordheim type interband tunneling. These electrons are accelerated to high energy by the intense electric field (6×10^5 V/cm) in the Al_{0.7}Ga_{0.3}As tunnel barrier, and excite the d electrons of Mn in the p^+ GaAs:Mn layer by impact excitation. The excited d electrons emit visible light when they relax back to their ground states. At the same time, the hot electrons can also generate electron-hole pairs in the GaAs:Mn layer by impact ionization of the GaAs host, which then recombine by either non-radiative or radiative processes. The radiative recombination processes result in band-gap emissions from the GaAs:Mn layer. The band-gap

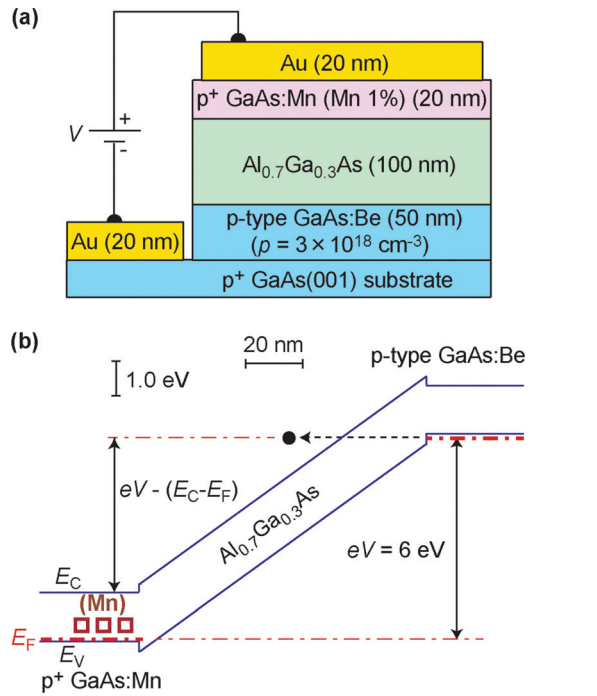


FIG. 2. (a) Schematic device structure of our semiconductor tunnel junctions. (b) Calculated band profile of a tunnel junction, when biased by a voltage of 6 V. Electrons are injected to the conduction band of the $\text{Al}_{0.7}\text{Ga}_{0.3}\text{As}$ tunnel barrier by Fowler–Nordheim tunneling from the valence band of the p-type GaAs:Be layer.

emissions give us useful information on the characteristics of the GaAs:Mn layer under impact excitation, as discussed later.

IV. ELECTRONIC STRUCTURE OF GaAs:Mn AND HIGH-FIELD EL SPECTRUM

Next, we discuss on the electronic structure of the d electrons of Mn atoms in GaAs as derived from the first principle calculations,^{6,7} which is shown in Fig. 3(a), and compare it with our results. In the case of Mn atoms doped in insulating oxides or wide-gap II–VI semiconductors, the electronic states of the d electrons are described by a configuration model based on the atomic orbitals of free Mn atoms, such as ${}^6A_1({}^6S)$, ${}^4T_1({}^4G)$, ${}^4A_2({}^4F)$ states, etc. In the configuration model, the p - d hybridization is treated as a perturbation that breaks the forbidden rules of d - d transitions. However, for Mn doped in GaAs, p - d hybridization is quite strong, thus the d electrons of Mn are not in pure d orbitals.^{6,7} In this case, a single-electron description of the d electrons taking into account the strong p - d hybridization is more suitable. Let us discuss on the p - d hybridized states of a single Mn atom at a Ga site, as shown in the left panel of Fig. 3(a). The optical ground states of a Mn atom in GaAs are the three-fold degenerate p - d hybridized up-spin anti-bonding t_1^a states (d_{xy} , d_{xz} , d_{yz}), which are close to the top of the valence band. The t_1^a states are partially filled with two electrons and one hole at each Mn site. The optical excited states are the two-fold degenerate down-spin non-bonding e_\downarrow (d_{z^2} , $d_{x^2-y^2}$) and the three-fold degenerate p - d hybridized down-spin anti-bonding t_1^b (d_{xy} , d_{xz} , d_{yz}) states. As discussed in our previous work,²

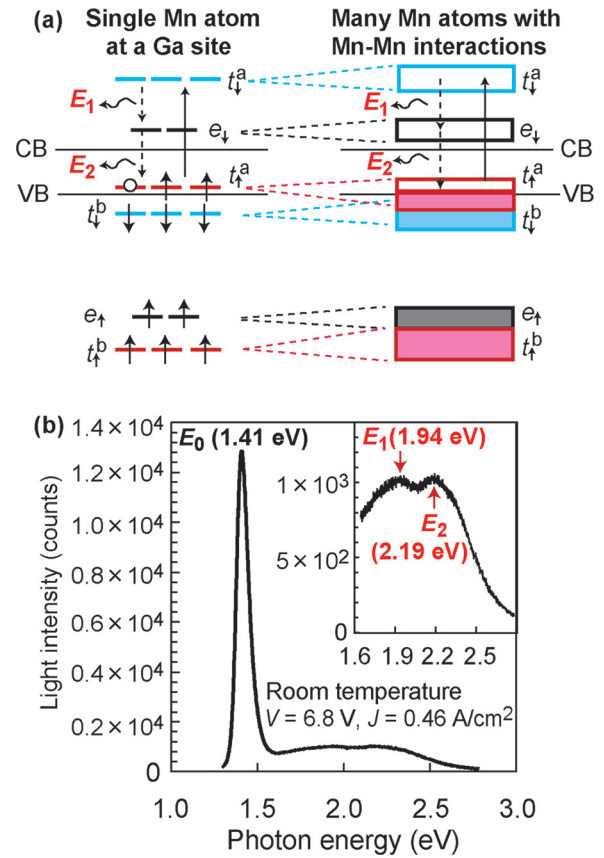


FIG. 3. (a) Electronic structures of a single Mn atom (left) and many Mn atoms with Mn-Mn interactions (right). Here, $t_{1(\downarrow)}^{a(b)}$ represent the three-fold degenerate p - d hybridized d_{xy} , d_{xz} , d_{yz} orbitals, while $e_{1(\downarrow)}$ represent the two-fold degenerate d_{z^2} , $d_{x^2-y^2}$ orbitals of Mn d electrons. The subscripts \uparrow and \downarrow represent spin-up and spin-down orbitals, respectively. The superscripts a and b represent the anti-bonding and bonding orbitals, respectively, formed by the d orbitals of Mn and p orbitals of Ga vacancy dangling bonds.^{6,7} Note that $e_{1(\downarrow)}$ remain non-bonding. CB and VB indicate the conduction band and valence band edge of GaAs. The t_1^a states are optical ground states. The e_\downarrow and t_1^a states are optical excited states. For many Mn atoms, Mn-Mn interactions result in broad bands. (b) EL spectrum of a device when biased at $V = 6.8$ V and a current density $J = 0.46$ A/cm² at room temperature. The inset shows the magnified view of the visible light spectrum. Besides a band-gap emission at $E_0 = 1.41$ eV, there are visible light emissions at $E_1 = 1.94$ eV and $E_2 = 2.19$ eV, corresponding to the $t_1^a \rightarrow e_\downarrow$ and $e_\downarrow \rightarrow t_1^a$ transitions as indicated in (a).

transitions from the t_1^a states to the e_\downarrow state in the single-electron model corresponds to that of ${}^4A_2({}^4F) \rightarrow {}^4T_1({}^4G)$ transition of Mn d electrons ($E_1 = 1.89$ eV in ZnS:Mn), while the transition from the e_\downarrow states to the t_1^a corresponds to that of ${}^4T_1({}^4G) \rightarrow {}^6A_1({}^6S)$ transition ($E_2 = 2.16$ eV in ZnS:Mn) in the configuration model.

Figure 3(b) shows a representative EL spectrum of a tunnel junction device with the structure of Fig. 2, biased at a voltage of $V = 6.7$ V and a current density $J = 0.46$ A/cm², measured at room temperature. We observe a strong band-gap emission at $E_0 = 1.41$ eV, which is due to the radiative recombination of electron-hole pairs that are generated by impact ionization in the GaAs host. Besides the band-gap emission, our LED shows visible light yellow-reddish emission at $E_1 = 1.94$ eV and $E_2 = 2.19$ eV. Note that these two peaks are much higher than $E_0 + \Delta_0 \sim 1.8$ eV for p⁺ GaAs.

Furthermore, these peaks cannot be explained by the band-to-band transitions in the $\text{Al}_{0.7}\text{Ga}_{0.3}\text{As}$ tunnel barrier, because $\text{Al}_{0.7}\text{Ga}_{0.3}\text{As}$ is an indirect band-gap semiconductor with an indirect band gap of 2.06 eV at the X point and a direct band-gap of 2.41 eV at the Γ point. However, the E_1 and E_2 peak are nearly the same as those of visible light emissions due to the d - d transitions (at 1.89 eV and 2.16 eV) observed in ZnS:Mn crystals⁸ and reverse biased $\text{GaAs:Mn/GaAs:Si p}^+-\text{n}$ junctions.² In our previous study, the d - d transition nature of these peaks from GaAs:Mn of the reverse biased p^+-n junctions has been confirmed by their insensitivity to temperature and bias current density, which is contrasting to the strong temperature and bias-current-density dependence of the band-to-band transitions, and by their good agreement with the ${}^4\text{A}_2({}^4\text{F}) \rightarrow {}^4\text{T}_1({}^4\text{G})$ (1.89 eV) and ${}^4\text{T}_1({}^4\text{G}) \rightarrow {}^6\text{A}_1({}^6\text{S})$ (2.16 eV) transitions in ZnS:Mn .^{2,8} However, we observe a small blue-shift of peak E_1 and E_2 in the present devices compared with those observed in reverse biased $\text{GaAs:Mn/GaAs:Si p}^+-\text{n}$ junctions.² The origin of the small blue-shift is not clear, but we suggest that the small blue-shift is probably due to the difference in the tetrahedral crystal field of As atoms, which is affected by the Mn-As distance. Since the Mn-As distance can be changed by many factors depending on the growth condition, such as excess As anti-sites in the GaAs:Mn layer due to the low growth temperature, the strength of the crystal-field can also be slightly changed by the growth condition, which may slightly affect the energy levels of Mn d electrons. Note that similar shift of the ${}^4\text{T}_1({}^4\text{G}) \rightarrow {}^6\text{A}_1({}^6\text{S})$ transition energy has also been observed in Mn-doped II-VI semiconductors. For example, the ${}^4\text{T}_1({}^4\text{G}) \rightarrow {}^6\text{A}_1({}^6\text{S})$ transition in ZnSe:Mn can shift from 2.150 eV to 2.195 eV, depending on the Mn concentration.⁹

Another distinct characteristic of the d - d transitions in GaAs:Mn is their broad linewidth compared with those of ZnS:Mn . This can be explained by the formation of broad Mn-induced d bands due to Mn-Mn interactions in III-V semiconductors. According to the first principle calculations,^{6,7} the t_{\uparrow}^a , t_{\downarrow}^a , and e_{\downarrow} states of neighboring Mn atoms can interact with each other to form broad electronic bands, as shown in the right panel of Fig. 3(a). Particularly, the t_{\uparrow}^a states can form an “impurity band” near the top of the valence band, which was recently observed by soft x-ray angle-resolved photoemission spectroscopy.¹⁰ Note that the formation of “impurity band” allows the metallic conduction of holes, and eventually spin ordering (ferromagnetism),¹¹ since such an “impurity band” can reduce the total energy of holes due to the double-exchange-like mechanism.¹² Similar broad bands are expected for the other states. Therefore, the linewidth of the d - d transitions in GaAs:Mn is much broader than that of the d - d transitions in ZnS:Mn .

V. CURRENT-DENSITY DEPENDENCE

Figure 4 shows the EL peak intensity-current density characteristics of the E_0 (squares) and E_1 peak (circles), and the voltage-current density characteristic (diamonds) of a LED device placed in air at room temperature. The E_0 peak appears above a threshold of $V_{\text{th-0}} = 4.9$ V, while E_1 appears above a threshold of $V_{\text{th-1}} = 5.4$ V. In the case of p^+-n

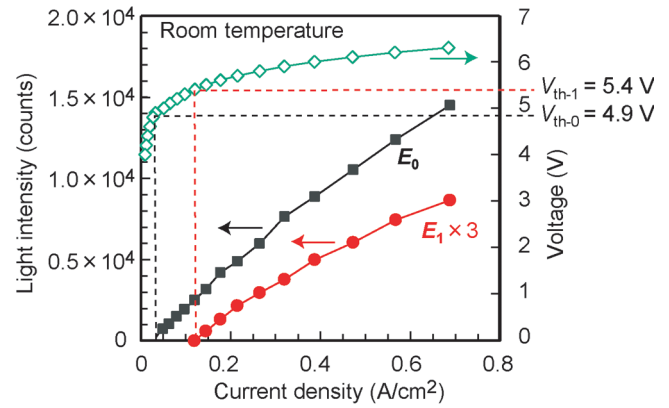


FIG. 4. Current-density dependence of the peak E_0 (squares) and E_1 (circles) intensity, and the voltage-current density characteristic (diamonds) of a device measured at room temperature.

junctions, where the GaAs:Mn layer is excited by hot holes, the threshold voltages are about -3.6 V and -4.1 V for the band-gap and visible light EL, corresponding to the impact ionization (excitation) threshold energy of 3.6 eV and 4.1 eV for GaAs and Mn atoms, respectively.² Note that the impact excitation energy of 4.1 eV for Mn atoms is equal to $E_1 + E_2$, which is needed for one-step excitation of Mn atoms from the t_{\uparrow}^a ground states to the t_{\downarrow}^a excited states, as shown in Fig. 3(a). The absolute values of the threshold voltages for the band-gap and visible light EL in the present devices are therefore 1.3 V higher than those of p^+-n junctions. This can be explained by the impact excitation process by *hot electrons*, in contrast to the impact excitation process by hot holes as in the case of p^+-n junctions. As depicted in Figs. 2(b) and 1(c), the maximum energy of electrons available for impact excitation is given by $eV - (E_C - E_F)$. Here, $E_C - E_F$ is the energy difference between the conduction band bottom E_C and the quasi Fermi level E_F of holes in the GaAs:Mn layer. This is because the injected *hot electrons* relax to the bottom of the *conduction band* of the GaAs:Mn layer, which is higher than the quasi Fermi level in the GaAs:Mn layer by an amount of $E_C - E_F$. In contrast, in the case of p^+-n junctions (see Fig. 1(b)), all of the electrical energy $e|V|$ of the injected *hot holes* can be spent for impact excitation, because hot holes relax to the quasi Fermi level of the p^+ GaAs:Mn layer.² This is an important difference between the impact excitation process by hot holes in structure (A) and by hot electrons in structure (B) and, as shown in Figs. 1(b) and 1(c), respectively. Let us numerically estimate the value of $E_C - E_F$ and compare it with the experimental result. In the “impurity band” picture of GaAs:Mn , the Fermi level in GaAs:Mn lies somewhere between the top of the valence band E_V and the impurity level of Mn in GaAs (110 meV above E_V),¹³ i.e., $0 \leq E_F - E_V \leq 0.11$ eV. At the same time, the band gap is reduced to $E_C - E_V = 1.37$ eV at the threshold voltages (4.9–5.4 V) due to lattice heating (see later). Therefore, $E_C - E_F = (E_C - E_V) - (E_F - E_V)$ should be somewhere between 1.26 eV and 1.37 eV, which is consistent with our experimental result of 1.3 eV. The observation of the higher threshold for E_0 in the present LED indicates that the observed band-gap emissions originate from electron-hole

pairs generated due to the impact ionization by *hot electrons* in the GaAs:Mn layer. Therefore, the E_0 peak can give us insightful information on the characteristics of the GaAs:Mn under impact excitation by hot electrons.

VI. ELECTRON AND LATTICE TEMPERATURE OF THE GaAs:Mn LAYER

We now investigate the electron and lattice temperature of the GaAs:Mn layer under the impact excitation by hot electrons. Figure 5(a) shows a representative spectrum near the E_0 peak of the same device in Fig. 4, when biased at $V = 6.3$ V and $J = 0.69$ A/cm² at room temperature. The electron temperature T_E is estimated by fitting the exponential function of the photon energy E , i.e., $I(E) \sim \exp[-E/k_B T_E]$, to the observed high-energy tail of the light intensity spectrum $I(E)$, as shown by the dashed line in Fig. 5(a). Figure 5(b) shows the estimated T_E by this fitting as a function of J . It is found that T_E abruptly increases up to about 653 K when 0.05 A/cm² $< J \leq 0.098$ A/cm² and 5.0 V $< V \leq 5.3$ V (area I). However, when 0.098 A/cm² $< J \leq 0.27$ A/cm² and 5.3 V $< V \leq 5.8$ V (area II), T_E increases more slowly and shows small oscillating behavior. One can see that the abrupt change in the $T_E - J$ characteristic at the border between area I and II coincides with the threshold voltage $V_{th-1} = 5.4$ V for impact excitation of the d electrons. This coincidence can be explained as follows. Since $V_{th-0} < V_{th-1}$, the energy required for impact ionization of GaAs (~ 3.6 eV) is smaller than that of impact excitation of Mn (~ 4.1 eV). At 4.9 V $\leq V \leq 5.3$ V (area I), all of the hot electrons can contribute to the impact ionization of the host GaAs but not of Mn, because 3.6 eV $\leq e|V| - 1.3$ eV ≤ 4.0 eV. As J and V increase, the population of excess electrons at the bottom of the conduction band of GaAs:Mn also increases rapidly. As a result, T_E abruptly increases with J and V . However, when $V > 5.4$ V (area II), a part of hot electrons can contribute to the impact excitation of Mn d electrons in addition to the impact excitation of the host GaAs. Therefore, the population of excess electrons at the bottom of the conduction band increases more slowly. This explains the abrupt change in the $T_E - J$ characteristic at $V_{th-1} = 5.4$ V. The origin of the small oscillation of T_E in area II (5.3 V $< V \leq 5.8$ V) is unclear, but it may be due to the oscillating distribution of hot electrons in the range 5.3 V $< V \leq 5.8$ V. Finally, we observe that T_E increases slowly and monotonously when $J > 0.27$ A/cm² and $V > 5.8$ V (area III). T_E can be as high as ~ 700 K even at a current density J as small as 0.69 A/cm². For comparison, we note that such a high T_E in GaAs grown by LTMBE can only be obtained by photon excitation with a laser whose wavelength is 720 nm (1.72 eV) and whose input optical power density is as large as 5 kW/cm², corresponding to a photon flux of 10^{22} cm⁻²s⁻¹ (Ref. 14). In contrast, the same T_E in our device can be obtained by an input electrical power density of 0.4 W/cm² and a hot electron flux of 10^{18} cm⁻²s⁻¹. This indicates that impact ionization (excitation) by hot electrons with high energy is much more effective than by photons with lower energy.

The lattice temperature T_L of GaAs:Mn is estimated by using the following relation: $E_0 = E_g(T_L) + k_B T_E/2$. Here,

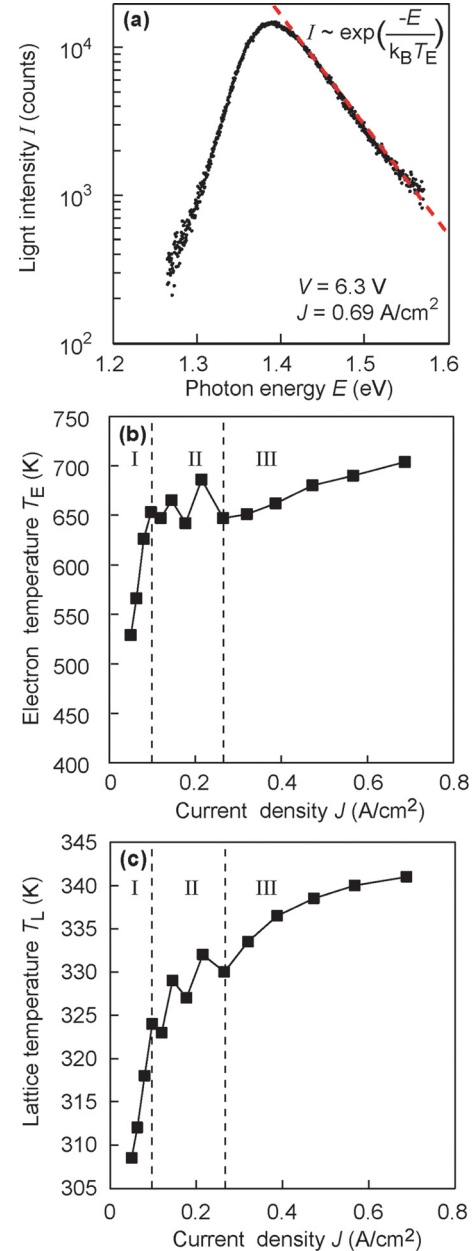


FIG. 5. (a) Room-temperature EL spectrum of the same device in Fig. 4 near the band-gap emission, measured at $V = 6.3$ V and $J = 0.69$ A/cm². The dashed line shows the fitting of the exponential function of the photon energy E to the high-energy tail of the spectrum (see text). (b) Electron temperature T_E in the GaAs:Mn layer as a function of current density J . (c) Lattice temperature T_L of the GaAs:Mn layer as a function of current density J . In (b) and (c), T_E and T_L show rapid increasing in area I, slow increasing and oscillation in area II, and slow increasing in area III with increasing J .

$E_g(T_L)$ is the band-gap energy at temperature T_L , given by $E_g(T_L) = E_g(0) - \alpha T_L^2 / (\beta + T_L)$, where $E_g(0) = 1.519$ eV is the band-gap energy of GaAs at 0 K, $\alpha = 5.41 \times 10^{-4}$ eV K⁻¹, and $\beta = 204$ K.¹⁵ Figure 5(c) shows the estimated T_L as a function of J . The $T_L - J$ characteristic is similar to the $T_E - J$, indicating that phonon-scattering of hot electrons is also associated with the same phenomena discussed in Fig. 5(b). However, the lattice temperature of the GaAs:Mn is as low as 340 K (67 °C) at the highest J .

VII. CONCLUSIONS

We have observed high-field EL in semiconductor tunnel junctions with a GaAs:Mn layer at room temperature. Besides the band-gap emission of GaAs, we observed visible light EL due to the $d-d$ transitions of Mn atoms at 1.94 eV and 2.19 eV, which are similar to those observed in reverse biased p^+-n junctions with a GaAs:Mn layer. The threshold voltages for the band-gap and visible light EL are 1.3 V higher than those of GaAs:Mn excited by hot holes in reverse biased p^+-n junctions, which is well explained by the impact ionization (excitation) process by hot electrons. We show that the electron temperature in GaAs:Mn can be as high as ~ 700 K for a low input electrical power density of 0.4 W/cm², while the lattice temperature of the GaAs:Mn layer can be kept at as low as 340 K. This shows that impact ionization (excitation) by hot electrons is more effective than by photons with lower energy. Our results open a way to utilize $d-d$ transitions as a light-emission mechanism in TM-doped semiconductors.

ACKNOWLEDGMENTS

This work was supported by Grant-in-Aids for Scientific Research including the Specially Promoted Research, and the Project for Developing Innovation Systems of MEXT.

P.N.H. acknowledges support from the Foundation of Ando Laboratory.

- ¹Y. A. Ono, *Electroluminescent Displays* (Word Scientific, Singapore, 1995).
- ²P. N. Hai, D. Maruo, and M. Tanaka, *Appl. Phys. Lett.* **104**, 122409 (2014).
- ³H. Ohno, A. Shen, F. Matsukura, A. Oiwa, A. Endo, S. Katsumoto, and Y. Iye, *Appl. Phys. Lett.* **69**, 363 (1996).
- ⁴T. Hayashi, M. Tanaka, T. Nishinaga, H. Shimada, H. Tsuchiya, and Y. Otuka, *J. Cryst. Growth* **175–176**, 1063 (1997).
- ⁵H. Munekata, H. Ohno, S. von Molnar, A. Segmüller, L. L. Chang, and L. Esaki, *Phys. Rev. Lett.* **63**, 1849 (1989).
- ⁶P. Mahadevan and A. Zunger, *Phys. Rev. B* **69**, 115211 (2004).
- ⁷A. Zunger, S. Lany, and H. Raebiger, *Physics* **3**, 53 (2010).
- ⁸T. Kushida, Y. Tanaka, and Y. Oka, *J. Phys. Soc. Jpn.* **37**, 1341 (1974).
- ⁹J. F. Suyver, S. F. Wuister, J. J. Kelly, and A. Meijerink, *Phys. Chem. Chem. Phys.* **2**, 5445 (2000).
- ¹⁰M. Kobayashi, I. Muneta, Y. Takeda, Y. Harada, A. Fujimori, J. Krempasky, T. Schmitt, S. Ohya, M. Tanaka, M. Oshima, and V. N. Strocov, *Phys. Rev. B* **89**, 205204 (2014).
- ¹¹M. Dobrowolska, K. Tivakornsasithorn, X. Liu, J. K. Furdyna, M. Berciu, K. M. Yu, and W. Walukiewicz, *Nature Mater.* **11**, 444 (2012).
- ¹²K. Sato, L. Bergqvist, J. Kudrnovský, P. H. Dederichs, O. Eriksson, I. Turek, B. Sanyal, G. Bouzerar, H. Katayama-Yoshida, V. A. Dinh, T. Fukushima, H. Kizaki, and R. Zeller, *Rev. Mod. Phys.* **82**, 1633 (2010).
- ¹³I. Muneta, H. Terada, S. Ohya, and M. Tanaka, *Appl. Phys. Lett.* **103**, 032411 (2013).
- ¹⁴X. Q. Zhou, H. M. van Driel, W. W. Ruhle, Z. Gogolak, and K. Ploog, *Appl. Phys. Lett.* **61**, 3020 (1992).
- ¹⁵C. D. Thurmond, *J. Electrochem. Soc.* **122**, 1133 (1975).



OPEN

Nano-artifact metrics based on random collapse of resist

SUBJECT AREAS:

INFORMATION
TECHNOLOGY

SYNTHESIS AND PROCESSING

ELECTRICAL AND ELECTRONIC
ENGINEERINGReceived
15 May 2014Accepted
23 July 2014Published
21 August 2014Correspondence and
requests for materials
should be addressed to
T.M. (tsutomu@ynu.ac.
jp)Tsutomu Matsumoto¹, Morihisa Hoga², Yasuyuki Ohyagi², Mikio Ishikawa², Makoto Naruse³,
Kenta Hanaki¹, Ryosuke Suzuki¹, Daiki Sekiguchi¹, Naoya Tate⁴ & Motoichi Ohtsu⁴

¹Graduate School of Environment and Information Sciences, Yokohama National University, Hodogaya, Yokohama, Kanagawa 240-8501, Japan, ²Dai Nippon Printing Co. Ltd., 250-1 Wakashiba, Kashiwa, Chiba 277-0871, Japan, ³Photonic Network Research Institute, National Institute of Information and Communications Technology, 4-2-1 Nukui-kita, Koganei, Tokyo 184-8795, Japan, ⁴Department of Electrical Engineering and Information Systems, Graduate School of Engineering, The University of Tokyo, 2-11-16 Yayoi, Bunkyo-ku, Tokyo 113-8656, Japan.

Artifact metrics is an information security technology that uses the intrinsic characteristics of a physical object for authentication and clone resistance. Here, we demonstrate nano-artifact metrics based on silicon nanostructures formed via an array of resist pillars that randomly collapse when exposed to electron-beam lithography. The proposed technique uses conventional and scalable lithography processes, and because of the random collapse of resist, the resultant structure has extremely fine-scale morphology with a minimum dimension below 10 nm, which is less than the resolution of current lithography capabilities. By evaluating false match, false non-match and clone-resistance rates, we clarify that the nanostructured patterns based on resist collapse satisfy the requirements for high-performance security applications.

Artifact metrics¹ uses physical features unique to individual objects in terms of their physical properties or combinations of these properties, including electromagnetic^{2,3}, mechanical and optical properties^{4,5}. For an artifact metric to function, it should satisfy several conditions, such as (1) the extracted characters should vary between individual objects (individuality), (2) a given response should be consistently obtained for each measurement (measurement stability), (3) they should be robust against degradation caused by common use (durability) and (4) fabricated clones having an equivalent physical characteristic should be extremely difficult (clone resistance). Examples of existing artifact metrics include ordinary paper⁵, paper containing magnetic microfibers⁶, plastics and semiconductor chips. A physical unclonable function⁷ is a type of artifact metrics that is essentially equivalent to what Matsumoto *et al.* examined under the name of ‘clone-resistant modules’ in 1997⁸.

The critical-security battlefield in which artifact metrics are used is analogous to a defender and attacker relationship in which the former tries to produce patterns that are difficult copies, and the latter seeks to counterfeit these patterns. In view of recent technological advancements in microfabrication and its strong demand in society and industry (e.g. optical document security⁹), new technology must go beyond that developed so far, which has been limited to micrometre-scale precision, and be founded on the ultimate principles of physics. Here, we propose and demonstrate a nano-artifact metrics that is robust against cloning attacks. The proposed metric uses nanometre-scale structures obtained from the random collapse of resists induced by exposure to conventional electron-beam (e-beam) lithography.

E-beam lithography is a mature and fundamental technology for prototyping fine structures. Minimum feature size is an important metric for lithography to produce the designated structures. To quantify the achievable minimum size, we use a two-dimensional array of pillars. The decrease in the minimum pitch of a pillar array over the last few years is summarized in Fig. 1a. The circles denoted (1), (2) and (3) in Fig. 1a are based on Refs. 10, 11 and 12, respectively and the dotted line, which represents an estimated pitch-resolution limit, is based on Refs. 13 and 14. Figure 1a also suggests that these feature sizes may be fabricated by attackers who use the available technology to make clones.

Meanwhile, we must also consider the extent to which we can precisely measure fine structures with the available technology such as a scanning electron microscopy (SEM). Critical-dimension scanning electron microscopy (CD-SEM), which is specialized in measuring length and offers precision in the sub-nanometre scale, may be assumed¹⁵. For an artifact metrics to be made using silicon nanostructures fabricated based on conventional e-beam lithography, the defender, who wants to prevent counterfeiting, must fabricate fine-structured patterns such that the attacker, who wants to copy the authentic device, will not be able to intentionally

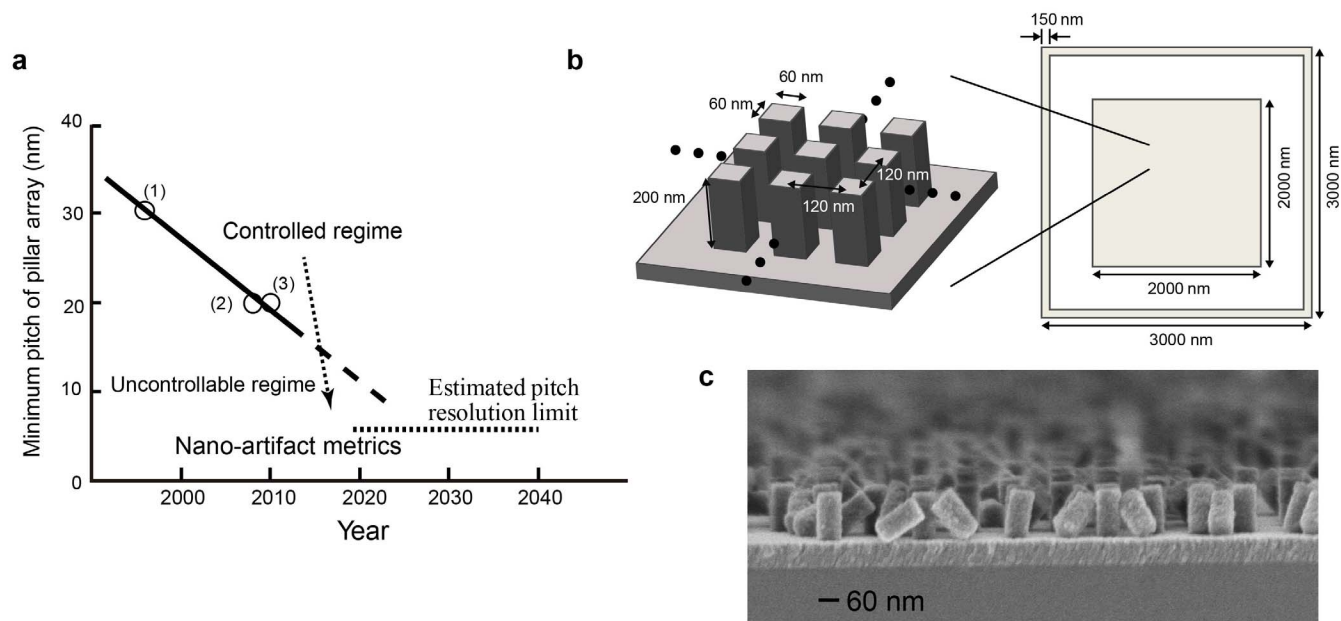


Figure 1 | Nano-artifact metrics based on random collapse of resist in electron-beam lithography. (a) Roadmap showing the minimum size of pillars formed by e-beam lithography. Using the phenomenon of randomly induced resist collapse, nano-artifact metrics contain length scales below the minimum dimension available in conventional lithography methods. (b) Schematic of array of pillars. (c) SEM image of collapsed resist.

reproduce the pattern based on the information obtained by CD-SEM. However, this condition imposes a paradoxical requirement that fine structures which are smaller than the resolution limit of the state-of-the-art e-beam lithography should be fabricated. Otherwise, the authentic devices may be easily cloned.

To overcome this paradox, we exploit the well-known phenomenon of the random collapse of resist¹⁶. Resist collapse may occur during the rinse process of lithography and depends on the pattern resolution, resist thickness and duration of e-beam exposure. The end result is the collapse of the intended pattern¹⁶. To produce a desired pattern, resist collapse must be suppressed in e-beam lithography, which can be achieved by deployment of ‘anticollapse rinses’. However, from the standpoint of nano-artifact metrics, resist collapse occasionally provides structures finer than the original technological limitation. Furthermore, resist collapse occurs randomly. Therefore, as shown in Fig. 1a, we can use resist collapse to benefit from the uncertainty in position that is less than the resolution of nanofabrication and achieve nano-artifact-metric functionalities.

To verify this notion, we fabricated an array of pillars from a layer of resist. The pillars had cross section area of 60 nm × 60 nm, were 200 nm high and were positioned on a grid of 120 nm × 120 nm squares that filled a 2 μm × 2 μm square, as shown in Fig. 1b. As a guide for facilitating alignment, a 3 μm × 3 μm square frame was drawn outside the pillar array area. We used a JEOL JBX-9300FS e-beam lithography system with the acceleration voltage set at 100 kV and with a dose of 37 μC/cm². After post-exposure bake and resist development, the structure is rinsed, which is when the random collapse of resist pillars occurs. Figure 1c shows an SEM image of an array of collapsed resist pillars. The wafer is then etched with HBr-based gas using inductively coupled plasma (ICP)-type reactive ion etching (RIE), and the resist is stripped by oxygen ashing. The resulting nanostructured-silicon patterns were imaged by a CD-SEM (Hitachi High-Technologies CG4000). We fabricated 2401 samples on a single 200-mm-diameter wafer and used 2383 of these samples to evaluate their use for security applications.

Figure 2a shows an image of a nanostructured-silicon pattern. The image contains 1024 × 1024 pixels, has eight-bit resolution (256 levels) and was obtained by averaging eight frames acquired by CD-SEM. A variety of different morphologies were obtained, as

shown in Fig. 2b. Figures 2b.i and 2b.iii show that the structural details in the patterns are as small as 9.23 nm.

Here, one minor remark is that the sizes and the layout of the original array of pillars have not been optimized so that the resultant security performances, described below, are maximized. Nevertheless, as shortly demonstrated, quite good properties have been obtained. This indicates that further advancements could be possible by engineering the original pillar (or not-like-a-pillar) structures to be collapsed, which could be an interesting future study. Meanwhile, we have experimentally confirmed that a proper dose of electron beam is necessary in order to induce versatile collapse of resist pillars; Figs. 2c and 2d show CD-SEM images when the dose was 30 and 40 μC/cm², respectively, indicating that too low or too high doses do not yield versatile resultant patterns.

To determine whether these patterns may be used as artifact metrics, we conducted the following analysis: A 512 pixel × 512 pixel, 8 bit (256 levels) greyscale image was extracted from the centre of an image of a pillar array and smoothed by an 11 × 11 median filter. In comparing any two patterns, $A(i, j)$ and $B(i, j)$, we first created a ‘mask’ pattern defined by

$$M(i, j) = \begin{cases} 1, & A(i, j) > T \text{ or } B(i, j) > T \\ 0 & \text{otherwise,} \end{cases} \quad (1)$$

where T is a given threshold value. Because the patterns are fabricated by conventional lithographic processes, they consist of areas of varying heights. Therefore, two peaks appear in the statistics of pixel values, with a valley between the two peaks. Specifically, the number of times higher and lower peak values occur was approximately 130 and 80, respectively, and the incidence of the valley (i.e. the threshold T) between the two peaks was 90. Here, a remark is that the pixel value in images is given by 8 bit (0–255), and the particular values of 130, 80 and 90 are related to the greyscale pixel values of the given images. As indicated by Fig. 1c and Fig. 2, the greyscale value is related to the height of the nanostructured pattern. We do not calibrate the pixel value to the actual height (i.e. $A(i, j)$ and $B(i, j)$ are dimensionless values), but it does not cause any problem in this particular study. Also, 1 pixel occupies approximately a 3.3 nm square area.

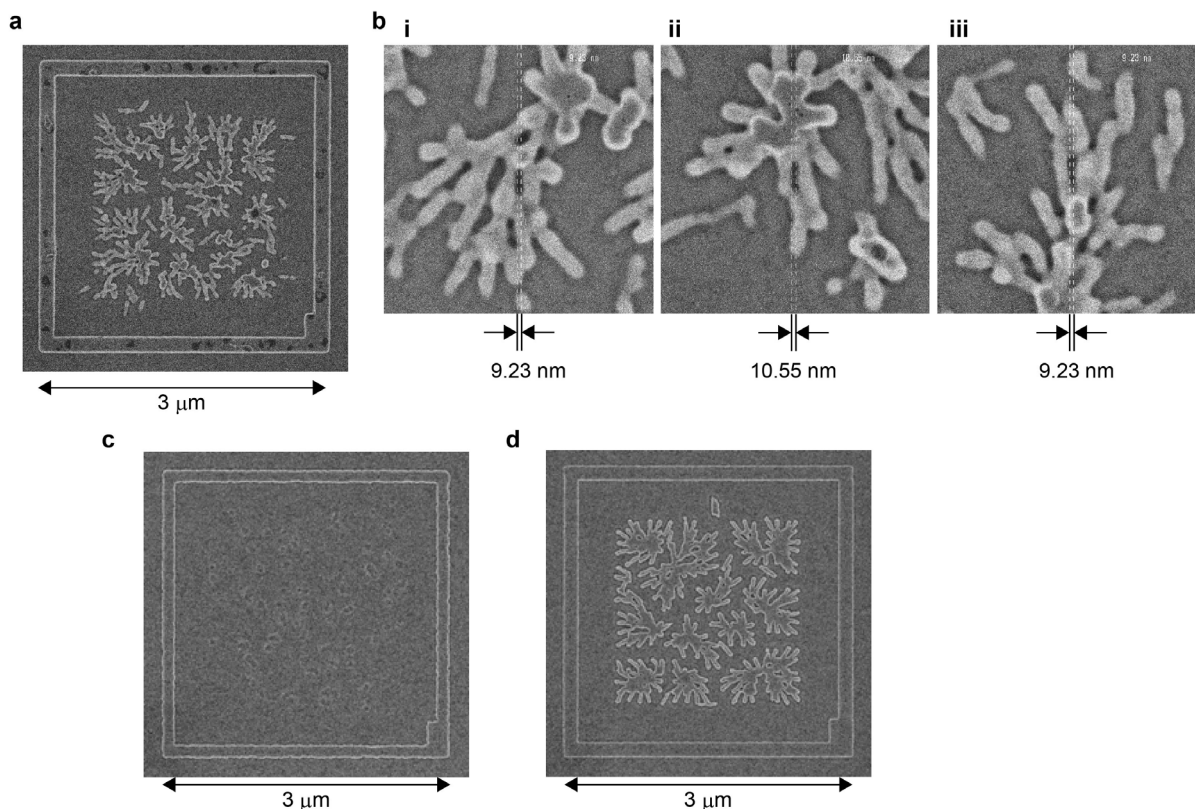


Figure 2 | Versatile morphology in silicon nanostructures obtained from collapsed resist. (a) Example of entire region of fabricated silicon nanostructure. (b) Magnified view of several areas from the panel (a). The minimum feature size is indicated in each image. Note that feature sizes are smaller than the minimum feature size of the original array of pillars. In other words, the uncertainty obtained in this versatile morphology is less than that available directly by current technology. (c,d) Silicon nanostructure when the dose quantity in the e-beam lithography was (c) 30 and (d) 40 $\mu\text{C}/\text{cm}^2$, respectively. Too low or too high doses do not yield versatile resultant patterns.

By applying the mask, we obtain two images, $\hat{A}(i, j) = M(i, j) \times A(i, j)$ and $\hat{B}(i, j) = M(i, j) \times B(i, j)$, which means that we ignore regions where both patterns $A(i, j)$ and $B(i, j)$ are low (i.e. the pattern is not high). The correlation, or similarity, between the two patterns is evaluated by the Pearson correlation coefficient

$$R = \frac{\sum_i \sum_j [\hat{A}(i, j) - \bar{\hat{A}}] [\hat{B}(i, j) - \bar{\hat{B}}]}{\sqrt{\sum_i \sum_j [\hat{A}(i, j) - \bar{\hat{A}}]^2 [\hat{B}(i, j) - \bar{\hat{B}}]^2}}, \quad (2)$$

where $\bar{\hat{A}}$ and $\bar{\hat{B}}$ indicate the average of $\hat{A}(i, j)$ and $\hat{B}(i, j)$, respectively. R is a dimensionless value. If R is negative, it is set to zero. Furthermore, each value of $A(i, j)$ and $B(i, j)$ is shifted between one and five pixels to the upper, lower, left and right side, and R is calculated for each shifted position. The maximum R from these positions (no shift, left, right, up and down shifts) is used as the similarity between $A(i, j)$ and $B(i, j)$.

We next calculate the false match rate (FMR) and false non-match rate (FNMR). FMR and FNMR are indicators of individuality and measurement stability, respectively. To calculate the FMR, all 2383 images were used. If the similarity given by Eq. (2) is greater than the given threshold, the two patterns are considered to be similar to each other, which is extremely likely to be a false decision. Since we had 2383 samples, we conducted 2383×2382 comparisons in calculating the FMR for threshold values between 0 and 1. To have an intuitive picture, suppose that only 1 case among the 2383×2382 comparisons resulted in a false decision. In this case, the 'error rate' would be $1/(2383 \times 2383) \approx 1.76 \times 10^{-7}$. From such calculation, the logarithmic scale for the FMR in the y-axis of Fig. 3 is naturally recognized.

From Fig. 3, the FMR drops below the error rate of 10^{-6} as the threshold is just above zero, indicating that the occurrence of false decisions among all comparisons are extremely small.

To calculate the FNMR, we used images created from 100 images of each of the 74 samples. If the similarity is less than the given threshold, the two images are considered different from each other. In other words, identical samples are considered different, which is a

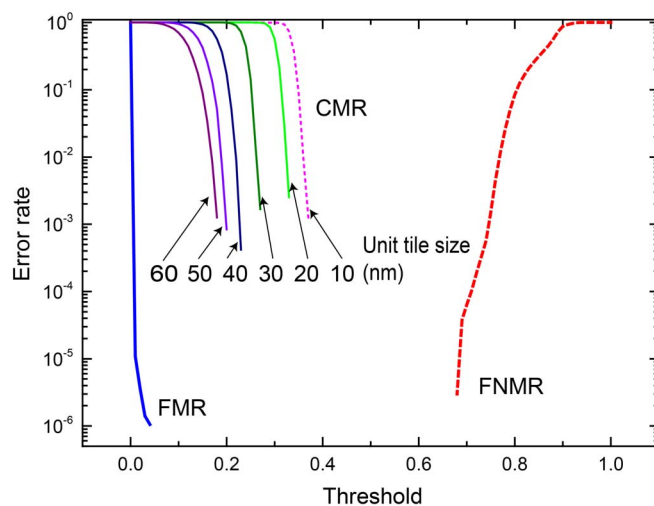


Figure 3 | Evaluation of security performance. Error rate as a function of the threshold. False match rate (FMR) and false non-match rate (FNMR) are labelled. The curves labelled 60, 50, 40, 30, 20 and 10 nm are the clone match rate (CMR) for the given minimum unit tile size.



Table 1 | Assumptions for cloning technology

Unit tile size of virtual clone image	Actual physical size
15 × 15 pixels	50-nm-square
12 × 12 pixels	40-nm-square
9 × 9 pixels	30-nm-square
6 × 6 pixels	20-nm-square
3 × 3 pixels	10-nm-square

false decision. The leftmost and rightmost curves in Fig. 3 show the FMR and FNMR, respectively. The FMR is substantially smaller than the FNMR, even with a smaller threshold value. In addition, the FMR and FNMR curves are well separated from each other, which means that it is possible to obtain sufficiently small FMR and FNMR by choosing adequate threshold values.

In addition, using the following method, we examined the clone match rate (CMR). Suppose that attackers capture the authentic device pattern and precisely fabricate a pattern in such a manner that an average over every $k \times k$ pixel area is essentially equivalent to the authentic device pattern. To quantify such a cloning process, we transformed each of the 2383 images into ‘virtually cloned images’. Let the pixel value for a $k \times k$ area be denoted by $p(i, j)$. If the average value in this area is greater than the threshold T , we consider this area to have the higher average value (130). Thus, this pixel value of the virtually cloned image is $p'(i, j) = 130$. If the average value in the $k \times k$ area is less than or equal to the threshold T , we consider this area to have the lower average value (80). Thus, this pixel value of the virtually cloned image is $p'(i, j) = 80$. The clone image thus obtained is then compared with the authentic image using Eq. (2). If the similarity exceeds the threshold value, the clone successfully mimics the original. The CMR is calculated by performing the above evaluation for all the 2383 samples.

This scheme constitutes a very strict evaluation of the cloning resistance. Table 1 summarizes the assumed cloning technologies. For example, if $k = 3$, a 3×3 pixel area (or ‘unit tile size’) corresponds to a $10 \text{ nm} \times 10 \text{ nm}$ square because, as mentioned earlier, 1 pixel occupies approximately a 3.3 nm square area, which may be regarded as state-of-the-art for the current nanofabrication technology. Nevertheless, the similarity cannot be greater than 0.4, as indicated by the calculated CMR shown by the purple dotted curve in Fig. 3. Considering that this value is considerably lower than the similarity between images of identical samples (i.e. the FNMR curve), such a clone does not pose a serious threat. In other words, the original authentic pattern is sufficiently random. Furthermore, were it possible to detect that a given pattern was formed from a combination of square units, it would presumably be determined that, based on such a feature, the pattern is a non-authentic device (or clone); this strategy is similar to liveness detection in biometrics¹⁷. Finally, note that the signal processing scheme described above is relatively simple yet requires highly skilled attackers. Based on these considerations and the results of the FMR, FNMR and CMR analysis, we conclude that the proposed nanostructured patterns based on the random collapse of resist could serve as superior nano-artifact metrics.

Finally, we put forward few remarks on the demonstrated principles and technologies.

First, the proposed principle is based on the ‘uncertainty’ inherent in conventional e-beam lithography technologies. Moreover, e-beam lithography is one of the widely spreading nanotechnologies including silicon fabrications. In this context, the proposed principle also has advantages in its general purpose properties or utilities.

Second is a comment regarding optical lithography. Optical lithography in silicon nanostructuring is based on the so-called reticle, which is subjected to reduced-projection exposure. A reticle is four times larger in scale than the intended nanostructured pattern and is

fabricated by e-beam lithography. It is impossible to fabricate patterns by optical lithography in the same resolution of the randomly collapsed silicon nanostructures demonstrated in this study. In other words, optical lithography may not be useful for attackers in copying the demonstrated devices.

The third remark concerns the term ‘nano-artifact metrics’. In Ref. [1], Matsumoto *et al.* proposed ‘artifact metrics’. The notion of artifact metrics is conceptually similar to ‘biometrics’, for which uniqueness in biological entities is utilized. Unlike biometrics, artifact metrics utilizes uniqueness in physical objects/things, physical processes or their combinations. We should emphasize that there are no implications such as ‘defective patterns’ in the word ‘artifact’. One may imagine that ‘nanoscale fingerprint’ might be more appropriate than ‘nano-artifact metrics’. However, the term ‘fingerprint’ implies information hiding, watermarking and their related technologies in the field of information security, which do not apply to our study. Furthermore, as discussed at the beginning of this paper, we showed four important requirements for artifact metrics to function (i.e. individuality, measurement stability, durability, clone resistance). Here, it should be noted that a total system as a whole is important, not just the elemental processes; this is another reason we describe the concept by ‘nano-artifact metrics’, which includes the notion of a total system while avoiding the use of ‘nanoscale fingerprint’.

In summary, with the goal of exploiting the fundamental laws of physics to produce nano-artifact metrics, we demonstrated nano-artifact metrics based on the random collapse of resist pillars in e-beam lithography. As qualitative significance for information security, this study opens new design principles and degrees-of-freedom by exploiting uncertainty at the nanometre scale. Moreover, by developing sophisticated image preprocessing means and similarity indices for matching, the security performance of these metrics is further enhanced. This is also a qualitatively novel aspect for information security in the sense that the combinations of physical process and logical signal processing means provide new values. Note that our use of SEM technology is not a particularly important aspect of this study. To construct practical systems, many additional issues must be considered, such as reducing measurement cost and verifying interoperability for the case when different measurement devices are used for sample registration and authentication. Nevertheless, this study demonstrates that sufficiently good security performance can be achieved by the random collapse of resist in e-beam lithography; the enemy of silicon processing in previous studies turns out to be a strong enabler for information security in this study.

1. Matsumoto, H. & Matsumoto, T. Clone match rate evaluation for an artifact-metric system. *IPSI J.* **44**, 1991–2001 (2003).
2. Lim, D., Lee, J. W., Gassend, B., Suh, G. E., van Dijk, M. & Devadas, S. Extracting secret keys from integrated circuits. *IEEE T. VLSI Syst.* **13**, 1200–1205 (2005).
3. DeJean, G. & Darko, K. RF-DNA: Radio-frequency certificates of authenticity. *Cryptographic Hardware and Embedded Systems-CHES 2007* (Vienna, 10–13 September 2007) Lecture Notes in Computer Science **4727**, 2007, pp. 346–363, DOI: 10.1007/978-3-540-74735-2_24.
4. Buchanan, J. D., Cowburn, R. P., Jausovec, A. V., Petit, D., Seem, P., Xiong, G. & Bryan, M. T. Fingerprinting documents and packaging. *Nature* **436**, 475 (2005).
5. Yamakoshi, M., Tanaka, J., Furuie, M., Hirabayashi, M. & Matsumoto, T. Individuality evaluation for paper based artifact-metrics using transmitted light image. *Proc. SPIE* **6819**, 68190H-1–68190H-10 (2008).
6. Ikeda, T., Hiroe, S., Yamada, T., Matsumoto, T. & Takemura, Y. Evaluation of equal error rate in document authentication system using magnetic fiber. *3rd Intl. Conf. Anti-counterfeiting, Security, and Identification in Communication 2009* (Hong Kong, 20–22 August 2009) pp. 382–385, 2009. DOI: 10.1109/ICASID.2009.5276959
7. Pappu, R., Recht, B., Taylor, J. & Gershenfeld, N. Physical one-way functions. *Science* **297**, 2026–2030 (2002).
8. Matsumoto, T. *et al.* Proposal of authentication method based on cloning resistance. *Proceedings of the IEICE Symposium on Cryptography and Information Security 1997* (Fukuoka, 29 January–1 February 1997), SCIS 97-19C, The Institute of Electronics, Information and Communication Engineers (in Japanese).



9. van Renesse, R. L. *Optical document security* (Artech House, Boston, 2004).
10. Broers, A. N., Hoole, A. C. F. & Ryan, J. M. Electron beam lithography—resolution limits. *Microelectron. Eng.* **32**, 131–142 (1996).
11. Hosaka, S. *et al.* Extremely small proximity effect in 30 keV electron beam drawing with thin Calixarene for 20×20 nm² pitch dot array. *Appl. Phys. Express* **1**, 027003 (2008).
12. Duan, H. *et al.* Sub-10-nm half-pitch electron-beam lithography by using poly(methyl methacrylate) as a negative resist. *J. Vac. Sci. Technol. B* **28**, C6C58 (2010).
13. Lee, K. W. *et al.* Secondary electron generation in electron-beam-irradiated solids: resolution limits to nanolithography. *J. Kor. Phys. Soc.* **55**, 1720–1723 (2009).
14. Manfrinato, V. R. *et al.* Resolution limits of electron-beam lithography toward the atomic scale. *Nano Lett.* **13**, 1555–1558 (2013).
15. Hibino, D. *et al.* High-accuracy OPC-modeling by using advanced CD-SEM based contours in the next-generation lithography. *SPIE Advanced Lithography* 76381X–76381X (2010).
16. Namatsu, H., Kurihara, K., Nagase, M., Iwadata, K. & Murase, K. Dimensional limitations of silicon nanolines resulting from pattern distortion due to surface tension of rinse water. *Appl. Phys. Lett.* **66**, 2655–2657 (1995).
17. Nixon, K. A. *et al.* Novel spectroscopy-based technology for biometric and liveness verification. *Proc. SPIE* **5404**, 287–295 (2004).

Acknowledgments

The authors thank Hitachi High-Technologies Cooperation in operating the CD-SEM. The authors thank Mr. Nakagawa from JOEL Co. Ltd. for his helpful discussions regarding the

resolution limits of e-beam lithography. This work was supported in part by the Strategic Information and Communications R&D Promotion Programme (SCOPE) of the Ministry of Internal Affairs and Communications and by the Core-to-Core Program of the Japan Society for the Promotion of Science.

Author contributions

T.M., M.N. and M.O. directed the project; T.M., M.N., M.H. and N.T. designed the system architecture and experiments; M.H., Y.O. and M.I. performed experimental device fabrication; M.H. performed SEM measurements; T.M., K.H., R.S. and D.S. conducted image processing and performance analysis; and T.M. and M.N. wrote the paper.

Additional information

Competing financial interests: The authors declare no competing financial interests.

How to cite this article: Matsumoto, T. *et al.* Nano-artifact metrics based on random collapse of resist. *Sci. Rep.* **4**, 6142; DOI:10.1038/srep06142 (2014).



This work is licensed under a Creative Commons Attribution-NonCommercial-NoDerivs 4.0 International License. The images or other third party material in this article are included in the article's Creative Commons license, unless indicated otherwise in the credit line; if the material is not included under the Creative Commons license, users will need to obtain permission from the license holder in order to reproduce the material. To view a copy of this license, visit <http://creativecommons.org/licenses/by-nc-nd/4.0/>



Observation and analysis of structural changes in fused silica by continuous irradiation with femtosecond laser light having an energy density below the laser-induced damage threshold

Wataru Nomura^{*1}, Tadashi Kawazoe¹, Takashi Yatsui¹, Makoto Naruse² and Motoichi Ohtsu¹

Full Research Paper

Open Access

Address:

¹School of Engineering, The University of Tokyo, and The Nanophotonics Research Center, The University of Tokyo, 2-11-16 Yayoi, Bunkyo-ku, Tokyo, 113-8656 Japan, and ²National Institute of Information and Communications Technology, 4-2-1 Nukui-kita, Koganei, Tokyo 184-8795, Japan

Email:

Wataru Nomura^{*} - nomura@nanophotonics.t.u-tokyo.ac.jp

* Corresponding author

Keywords:

compositional change in molecular; femtosecond laser; fused silica; laser-induced damage; laser-induced degradation

Beilstein J. Nanotechnol. **2014**, *5*, 1334–1340.

doi:10.3762/bjnano.5.146

Received: 28 April 2014

Accepted: 26 July 2014

Published: 21 August 2014

This article is part of the Thematic Series "Optical near-fields & nearfield optics".

Guest Editors: A. J. Meixner and P. Leiderer

© 2014 Nomura et al; licensee Beilstein-Institut.

License and terms: see end of document.

Abstract

The laser-induced damage threshold (LIDT) is widely used as an index for evaluating an optical component's resistance to laser light. However, a degradation in the performance of an optical component is also caused by continuous irradiation with laser light having an energy density below the LIDT. Therefore, here we focused on the degradation in performance of an optical component caused by continuous irradiation with femtosecond laser light having a low energy density, i.e., laser-induced degradation. We performed an in situ observation and analysis of an increase in scattering light intensity in fused silica substrates. In experiments conducted using a pulsed laser with a wavelength of 800 nm, a pulse width of 160 fs and pulse repetition rate of 1 kHz, we found that the scattered light intensity increased starting from a specific accumulated fluence, namely, that the laser-induced degradation had a threshold. We evaluated the threshold fluence F_t as 6.27 J/cm² and 9.21 J/cm² for the fused silica substrates with surface roughnesses of 0.20 nm and 0.13 nm in R_a value, respectively, showing that the threshold decreased as the surface roughness increased. In addition, we found that the reflected light spectrum changed as degradation proceeded. We analyzed the details of the degradation by measuring instantaneous reflectance changes with a pump-probe method; we observed an increase in the generation probability of photogenerated carriers in a degraded silica substrate and a damaged silica substrate and observed a Raman signal originating from a specific molecular structure of silica. From these findings, we concluded that compositional changes in the molecular structure occurred during degradation due to femtosecond laser irradiation having an energy density below the LIDT.

Introduction

Since the invention of the laser, it has been widely known that damages occur at the surface or interior of optical components when irradiated with laser light having a high energy density. A lot of research has been conducted in the area of laser-induced damage. For example: mechanism for picosecond [1,2] and femtosecond (fs) laser [3,4], effect of surface geometry [5,6], damage threshold [7,8], and so on. The laser-induced damage originates in photoionization of molecules caused by local electric fields generated at ultrafine structures in the substrates, such as indentations/protrusions in the surface or impurities in the interior. Recently, with advances made in the development of light sources, such as the trend towards lasers with higher power, shorter pulses, and shorter wavelengths, there has been a demand for the development of optical components having even higher damage resistance. Laser resistance is evaluated by an index called the laser-induced damage threshold (LIDT), which is measured by the 200-on-1 method according to ISO 11254-2 [9,10], for example. With this method, 200 locations on a sample surface are irradiated with single shots of pulsed laser light having different energy densities. The presence/absence of damage sites due to the irradiation is visually checked, and the minimum energy density at which damages are found is defined as the LIDT. However, the practical problem is that the performance of an optical component, such as transmittance, reflectance, etc., is degraded by continuous irradiation with laser light having an energy density below the LIDT. The cause of such degradation in performance, namely, laser-induced degradation of the optical component, is not fully understood. In addition, the resistance cannot be evaluated by tests based on ISO 11254-2, and therefore, a technique for the quantitative evaluation of such degradation would be useful. Furthermore, if the relation between laser-induced degradation and surface roughness is revealed, it may contribute to the development of a surface polishing technology for optical components with higher resistance against not only laser-induced damage but also degradation. Moreover, the clarification of the mechanism and knowledge about the details of the laser-induced degradation may provide an opportunity to develop novel laser processing techniques. Thus, our study about laser-induced degradation is a contribution to the progress in nanotechnology.

Therefore, we performed in situ a quantitative detection of laser-induced degradation in flat fused silica substrates, serving as the target material. The continuous irradiation with fs pulsed laser light has an energy density below the LIDT. We also analyzed the origin of the laser-induced degradation. Section 1 in Results and Discussion describes experiments in which we continuously irradiated substrates with fs pulsed laser light having a low energy density below the LIDT and detected the laser-induced degradation by measuring the scattered light. In

addition, by simultaneously measuring the reflected-light spectrum during this process, we observed spectral changes as the laser-induced degradation proceeded. Section 2 in Results and Discussion describes the measurement of instantaneous reflectance changes using a pump–probe method carried out to analyze the details of these spectral changes. From an increase in photo-generated carriers and the power spectrum of their relaxation lifetime, we found that compositional changes in the molecular structure occurred as laser-induced degradation proceeded.

Results and Discussion

1 Evaluation of laser-induced degradation of fused silica

1.1 Surface roughness dependence of threshold fluence in laser-induced degradation

First, to quantitatively observe laser-induced degradation due to continuous irradiation with a laser light having an energy density below the LIDT, we conducted an experiment in which we continuously irradiated a silica substrate with fs laser light and measured the relative increase in scattered light from the substrate surface. As measurement samples, we used high-purity fused silica flat substrates in which the OH impurity content was 0.8 ppm or less. We used two samples: sample A, which was prepared by planarizing a substrate using standard chemical-mechanical polishing (CMP) [11], and sample B, which was prepared by performing optical near-field etching on a substrate prepared under the same conditions as sample A. The samples A and B had a minimum average surfaces roughnesses R_a of 0.20 nm and 0.13 nm, respectively [12]. Since we employed a continuous-wave laser with the wavelength of 532 nm and power of 2 W for optical near-field etching, the sample B did not have any laser-induced damage or degradation caused by this preparation. Optical near-field etching is a surface planarization technique for selectively removing only minute protrusions in the surface of a substrate, and can flatten the planer substrate polished by CMP. Thus, it is effective in reducing the drop in LIDT caused by electric field enhancement induced by the surface structure [5,6]. It has been reported that a dielectric multilayer mirror fabricated by using a silica substrate planarized by this technique exhibited an LIDT that was increased from 8.2 J/cm² to 14 J/cm² compared with the mirror before planarization processing, according to a 200-on-1 laser resistance test based on ISO 11254-2 [13].

Figure 1a shows the experimental set-up. For the light source, we used a regeneratively amplified fs Ti:sapphire laser (Coherent, Inc., Legend Elite F-1K) with a wavelength of 800 nm, a power of 1.0 W, a repetition frequency of 1 kHz, and a pulse width of 160 fs. The laser light was incident on the

surface of the substrates at an incident angle of 45° and with an energy density of 6.0 mJ/cm^2 . This energy density is sufficiently lower than the LIDT of fused silica for the same wavelength and pulse width, namely, about 0.5 J/cm^2 [14,15]. Scattered light from the samples was collected by a Si photodiode (Hamamatsu Photonics K.K., S3883) placed perpendicularly to the substrate, and lock-in detection was performed at the repetition frequency of the laser using a lock-in amplifier (Stanford Research Systems, Inc., SR830).

We evaluated the two silica substrates using the relative increase in the scattered light intensity S , $\Delta S(F) = (S(F) - S(0))/S(0)$, versus the accumulated fluence F (J/cm^2) of the irradiated light. In the experiment, we continuously irradiated samples A and B with laser light having fluences up to $F = 3.5 \times 10^4 \text{ J/cm}^2$ and $8.8 \times 10^4 \text{ J/cm}^2$, respectively, and after the experiment, we confirmed that there were no sites showing laser-induced damage in the surfaces of the samples by using an optical microscope. The results of measuring $\Delta S(F)$ for samples A and B, ΔS_A and ΔS_B , are shown by the black and red solid lines in Figure 1b, respectively. We observed a tendency for the scattered light to increase with continuing irradiation, showing that this method succeeded in quantitatively measuring the laser-induced degradation. In addition, for both ΔS_A and ΔS_B , the scattered light intensity increased logarithmically from specific fluences, showing that there was a threshold fluence at which laser-induced degradation started. To determine this threshold fluence, F_t , the regions where ΔS_A and ΔS_B rose were fitted with an approximation $g(F) = P \log(F) - Q$. The approximation curves are shown by the green and blue dotted lines in Figure 1b, where $g_A(F)$ was defined over the range

$6.3 \times 10^3 \text{ J/cm}^2 < F < 1.2 \times 10^4 \text{ J/cm}^2$ for ΔS_A , and $g_B(F)$ was defined over the range $F > 9.2 \times 10^3 \text{ J/cm}^2$ for ΔS_B . The constants P and Q are as shown in Table 1. When F_t at which $g_A(F) = 0$ and $g_B(F) = 0$ is determined from these equations, for the samples A and B, we calculated $F_{tA} = 6.3 \times 10^3 \text{ J/cm}^2$ (1.1×10^6 shots) and $F_{tB} = 9.2 \times 10^3 \text{ J/cm}^2$ (1.5×10^6 shots), under the laser energy density of 6.0 mJ/cm^2 . This result shows that the degradation starting threshold for sample B is 1.4-times higher than that for sample A. As described above, sample B was a substrate prepared by selectively removing only the ultra-fine surface structure from the substrate of sample A, and the LIDT of a mirror using a substrate identical to this was improved by a factor of 1.7 [13]. Since the degradation starting threshold F_t and the LIDT improvement factor are in good agreement, this result indicates the laser-induced degradation occurs with a partly similar mechanism of laser-induced damage, namely multiphoton ionization caused by local electric fields generated at indentations or protrusions. Also, the constants P which define the rate of increase of $g_A(F)$ and $g_B(F)$ are $P_A = 0.062$ and $P_B = 0.016$, differing by a factor of 3.9, which shows that laser-induced degradation originating from the surface structure proceeds more rapidly.

Table 1: Constants P and Q for approximation curves $g_A(F)$ and $g_B(F)$.

	P	Q
$g_A(F)$	0.062	0.24
$g_B(F)$	0.016	0.062

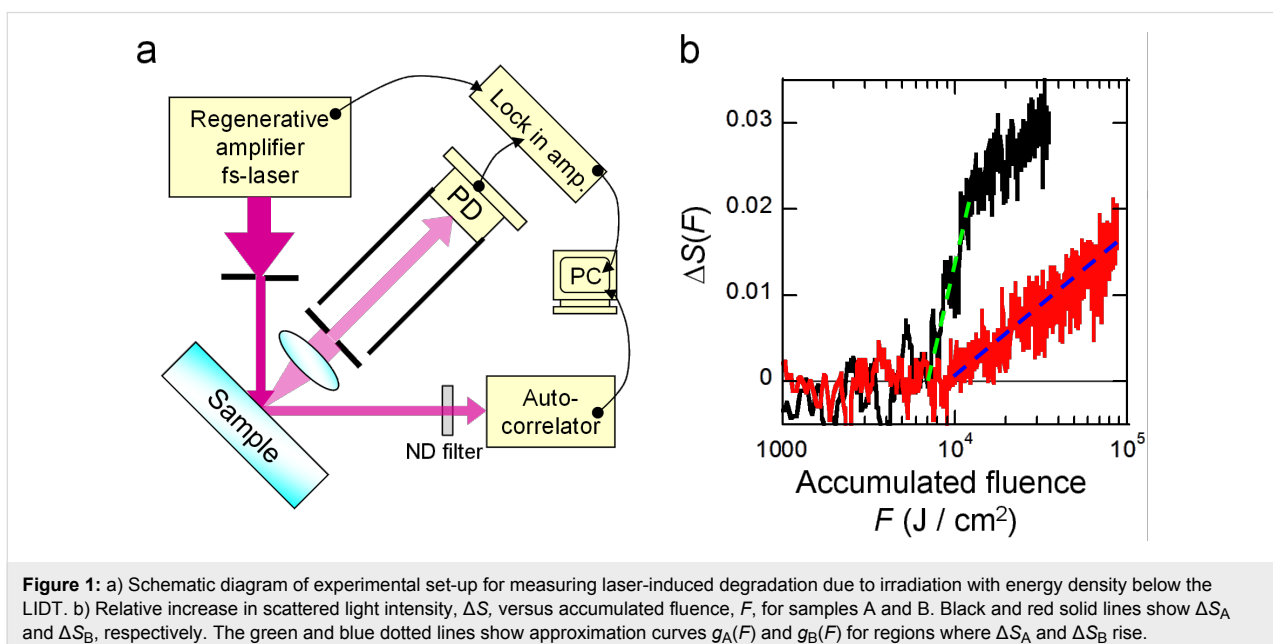


Figure 1: a) Schematic diagram of experimental set-up for measuring laser-induced degradation due to irradiation with energy density below the LIDT. b) Relative increase in scattered light intensity, ΔS , versus accumulated fluence, F , for samples A and B. Black and red solid lines show ΔS_A and ΔS_B , respectively. The green and blue dotted lines show approximation curves $g_A(F)$ and $g_B(F)$ for regions where ΔS_A and ΔS_B rise.

1.2 In situ evaluation of spectral change in reflected light

To analyze the laser-induced degradation, we evaluated the reflected light spectrum at the same time as the scattered light intensity measurement. As shown in Figure 1a, reflected light was introduced from the sample into an autocorrelator with a spectrometer function (APE GmbH, pulseCheck). We used a fused silica substrate identical to sample A and set the energy density of incident light on the substrate to 17 mJ/cm^2 , which is below the LIDT. Spectral data was obtained at four fluences, namely, $F_1 = 5.1 \times 10^3 \text{ J/cm}^2$, $F_2 = 1.9 \times 10^5 \text{ J/cm}^2$, $F_3 = 5.9 \times 10^5 \text{ J/cm}^2$, and $F_4 = 1.3 \times 10^6 \text{ J/cm}^2$.

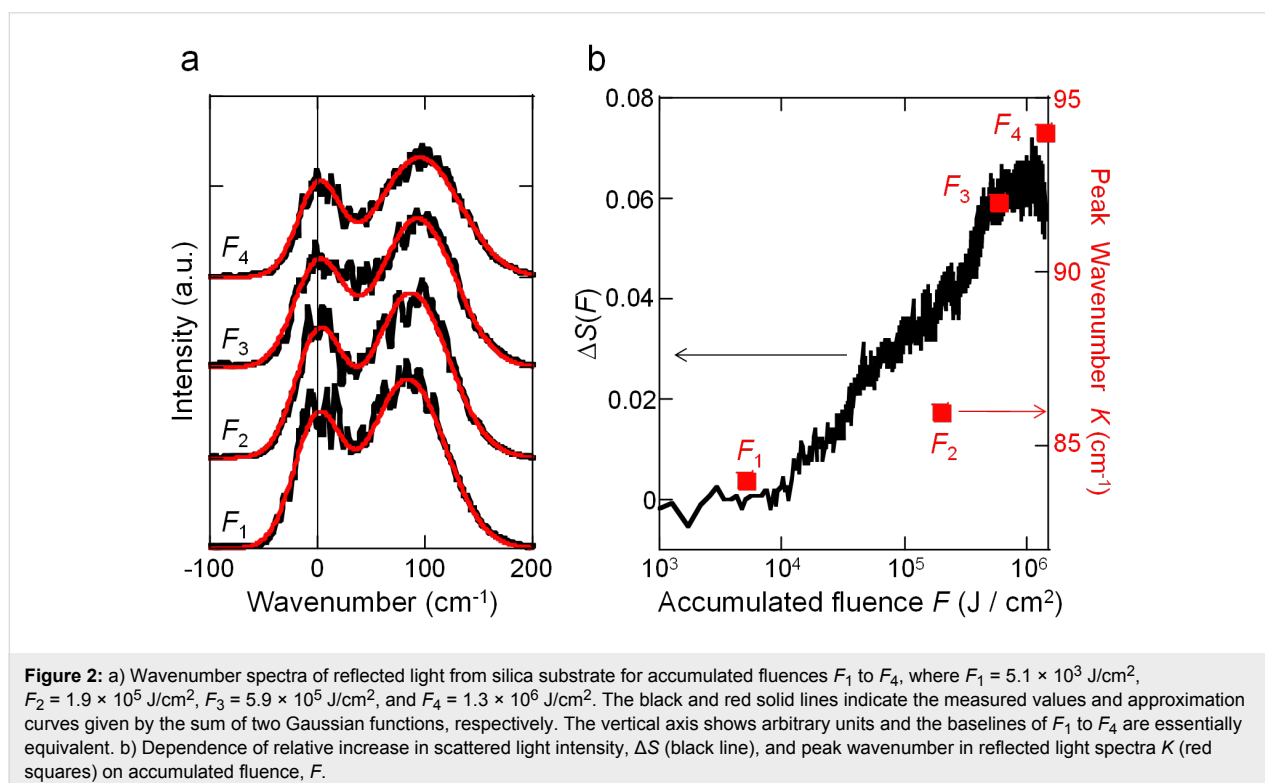
The solid black line in Figure 2a shows the wavenumber spectra of the reflected light, centered on the central wavelength of the laser (800 nm). Under all conditions, in addition to the central frequency of the laser, we observed the 2nd peak on the long-wavelength side. When these wavenumber spectra were fitted with the sum of two Gaussian functions, as shown by the solid red lines in Figure 2a, the center wavenumbers on the 2nd peaks K were determined to be $K_1 = 84 \text{ cm}^{-1}$, $K_2 = 86 \text{ cm}^{-1}$, $K_3 = 92 \text{ cm}^{-1}$, and $K_4 = 94 \text{ cm}^{-1}$ for the fluences F_1 to F_4 , respectively. The relative increase in the scattered light intensity, ΔS , and K versus the irradiated fluence, F , are plotted in the black solid line and the red squares in Figure 2b, respectively. The monotonically increasing trends with respect to F agreed well in both ΔS and K , showing that the 2nd peak of the spec-

trum shifted to lower energy side as the degradation proceeded. We estimated the origin of the 2nd peaks were Raman signals of degraded silica and this result represented the compositional changes in the molecular proceeds with the laser-induced degradation proceeded.

2 Analysis of degradation via pump–probe method

2.1 Time-resolved measurement of reflectance

To analyze in detail the spectral changes occurring with laser-induced degradation due to continuous irradiation with laser light having an energy density below the LIDT, as confirmed in the previous section, we conducted an experiment to evaluate the time-resolved changes in reflectance via a pump–probe method. The experimental setup is shown in Figure 3. The laser used was a mode-locked Ti:sapphire laser (Coherent, Inc., Mira Optima 900-D) with a wavelength of 750 nm, a pulse width of 90 fs, and a repetition frequency of 80 MHz. Using a beam-splitter, the laser light was split with an intensity ratio of reflected light to transmitted light of 1:19. As pump light, the transmitted light was made perpendicularly incident on the sample surface via an optical delay and a chopper with a frequency of 2 kHz. P-polarized probe light, with a polarization orthogonal to that of the pump light, was incident on the substrate at an angle of incidence of about 70° , and the reflected probe light was received by a Si photodiode (Hamamatsu Photonics K.K., S3883). The received signal was detected with



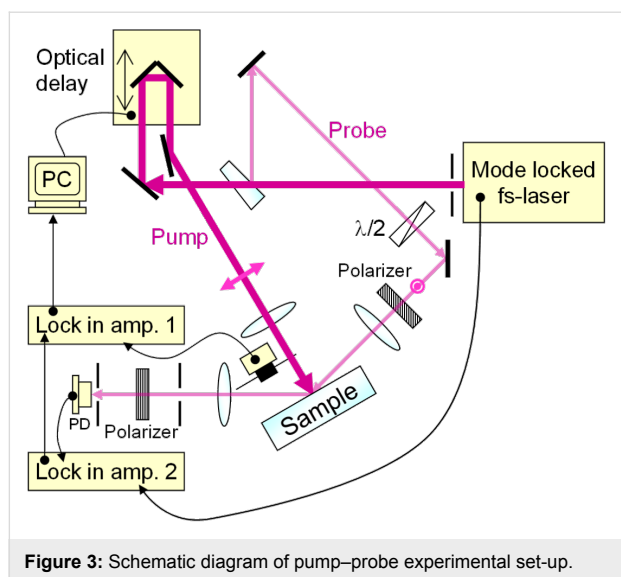


Figure 3: Schematic diagram of pump-probe experimental set-up.

double lock-in detection using two lock-in amplifiers (Stanford Research Systems, Inc., SR844 and SR830) based on the repetition frequency of the laser pulses and the frequency of the chopper. The laser light used as the pump light in this experiment had an energy density of $1.6 \mu\text{J}/\text{cm}^2$, and no increase in light scattering was observed even when the silica substrate was continuously irradiated with this laser light with an accumulated fluence exceeding $1.0 \times 10^7 \text{ J}/\text{cm}^2$, thus confirming that the progression of laser-induced degradation could be ignored in this pump-probe experiment. We performed measurements on three samples, which were all high-purity fused silica substrates polished by CMP, identical to sample A: Sample C, on which no laser was irradiated; Sample D, which showed laser-induced degradation by being irradiated with the regeneratively amplified fs laser with a wavelength of 800 nm, an energy density of

$17 \text{ mJ}/\text{cm}^2$, a repetition frequency of 1 kHz and a pulse width of 160 fs to an accumulated fluence of $3.5 \times 10^4 \text{ J}/\text{cm}^2$, namely 2.1×10^7 shots; and Sample E, in which laser-induced damage visually recognizable as damage sites was caused by 1000 shots of irradiation with an energy density of $100 \text{ mJ}/\text{cm}^2$ using the same fs laser.

In the evaluation, we used a relative change $\Delta R = (R - R_0)/R_0$, where R_0 is the reflected light intensity in the case where only the probe light was radiated, and R is the reflected light intensity obtained in the pump-probe experiment. The measurement results ΔR_C , ΔR_D , and ΔR_E for samples C, D, and E are plotted in Figure 4a as black squares, blue circles, and red triangles, respectively. The horizontal axis of the graph is the time delay, t , of the probe light relative to the pump light, where the peak of ΔR_C is taken as $t = 0$. ΔR_C is well-approximated by $\Delta R_{\text{fit}} = 5.5 \text{ sech}^2(t/(9 \times 10^{-14}))$, which is shown by the green solid line in Figure 4a, and nonlinear polarization reflecting the pulse width of the laser was observed. In contrast, ΔR_D , and ΔR_E showed temporal broadenings of about several 100 fs. Because these decay times are close to the photogenerated carrier lifetime of silica 150 fs [16,17], it is assumed the temporal changes in the reflectance were originated from the photogenerated carrier in samples D and E. In other words, in Samples D and E, we concluded that the generation probability of photogenerated carriers was higher than in Sample C because electric field enhancement occurred due to laser-induced degradation and laser-induced damage.

2.2 Spectrum analysis

To analyze this in more detail, we obtained the power spectrum by subtracting the nonlinear polarization component represented by ΔR_{fit} from ΔR_D , and ΔR_E . The results are shown by

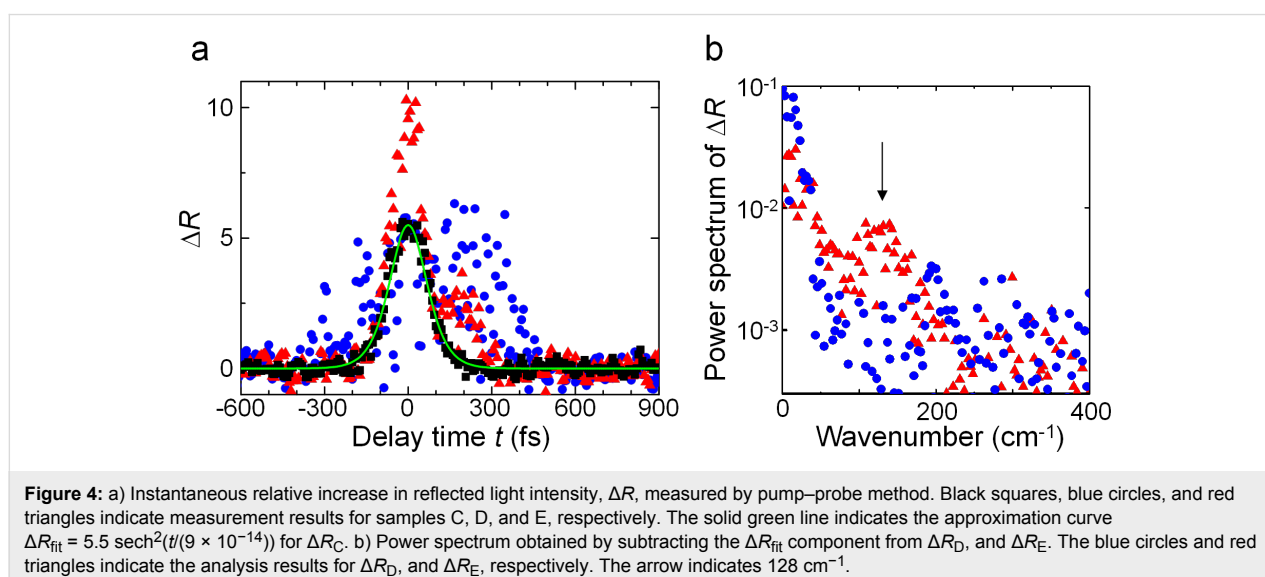


Figure 4: a) Instantaneous relative increase in reflected light intensity, ΔR , measured by pump-probe method. Black squares, blue circles, and red triangles indicate measurement results for samples C, D, and E, respectively. The solid green line indicates the approximation curve $\Delta R_{\text{fit}} = 5.5 \text{ sech}^2(t/(9 \times 10^{-14}))$ for ΔR_C . b) Power spectrum obtained by subtracting the ΔR_{fit} component from ΔR_D , and ΔR_E . The blue circles and red triangles indicate the analysis results for ΔR_D , and ΔR_E , respectively. The arrow indicates 128 cm^{-1} .

the blue circles and red triangles in Figure 4b, respectively. For sample D, a signal having a weak peak close to 195 cm^{-1} was obtained, whereas for sample E, a broad peak around 128 cm^{-1} was found, thus giving different signals. The peak at 128 cm^{-1} was consistent with the Raman signal of α -quartz, which is formed of six-membered rings of Si and O [18]. It has been reported that the Raman signal from silica with a specific molecular structure is increased by irradiation with fs laser light having an energy density above the LIDT [19], and sample E is also thought to be mainly formed of six-membered rings in a similar fashion. Although there is no molecular structure of silica that corresponds to the peak for sample D, the result indicates that compositional changes occur due to laser-induced degradation. As we found in section 1.1, the laser-induced degradation originates in multiphoton ionization. The laser-induced damage by fs laser occurs by multiphoton ionization and consequent avalanche ionization [3,4]. Since there are no breakdowns, it is estimated that avalanche ionization does not occur in the laser-induced degradation due to its low energy density. While the carriers generated by just multiphoton ionization are not enough to cause breakdown, they change amorphous silica to a more stable molecular structure. As also indicated in the results in section 1.2, the spectrum shifted, namely the compositional change carried on as laser-induced degradation proceeds. It provides nanoscale nonuniformity of the refractive index which increases scattering of light, decreases transmittance, and accelerates the progress of the laser-induced degradation.

Conclusion

In this paper, we focused on the degradation in performance of optical components due to continuous irradiation with laser light having an energy density below the LIDT, i.e., laser-induced degradation. We examined the degradation of fused silica substrates in response to fs laser irradiation and performed an in situ observation of the laser-induced degradation, as well as an analysis of the underlying mechanism. By monitoring the scattered light intensity versus the accumulated irradiation fluence, we succeeded in quantitatively detecting the laser-induced degradation. We confirmed that the total irradiation threshold at which laser-induced degradation starts changed depending on the size of the ultrafine structure in the surface. In addition, we also found that the spectrum of reflected light shifted as the laser-induced degradation proceeded. By analyzing the details of this behavior with a pump-probe method, we observed an increase in photogenerated carriers, and from the power spectrum, we obtained results indicating that the molecular structure of the silica undergoes compositional changes due to the laser-induced degradation.

From the findings we obtained in this study, it can be concluded that, to increase the resistance of a substrate to laser-induced de-

gradation, it is effective to improve the substrate's flatness, similarly to the case of the LIDT. In addition, because it is possible to estimate the molecular structure formed by the laser-induced degradation from the spectral information, there is a possibility of achieving more effective measures against laser-induced degradation. The measurement method employed here for the fs laser light and the flat fused silica substrates can also be applied to other types of laser and optical components and is expected to contribute to the development of optical components having high resistance to laser-induced degradation in the future.

Acknowledgements

The authors would like to thank Prof. Dr. M. Haraguchi of The University of Tokushima, Mr. Y. Tabata and Mr. K. Hirata of SIGMA KOKI Co., Ltd., for helpful discussions. This work was partially supported by the New Energy and Industrial Technology Development Organization (NEDO) under the program of Strategic Development on Rationalization Technology using Energy and under the program of Comprehensive Activity for Personnel Training and Industry-Academia Collaboration based on the NEDO project.

References

- Bliss, E. S. *Opto-electronics (London)* **1971**, 3, 99–108. doi:10.1007/BF01424087
- Wood, R. M. *Laser Damage in Optical Materials*; Hilger: Boston, 2002.
- Schaffer, C. B.; Brodeur, A.; Mazur, E. *Meas. Sci. Technol.* **2001**, 12, 1784–1794. doi:10.1088/0957-0233/12/11/305
- Mao, S. S.; Quéré, F.; Guizard, S.; Mao, X.; Russo, R. E.; Petite, G.; Martin, P. *Appl. Phys. A* **2004**, 79, 1695–1709. doi:10.1007/s00339-004-2684-0
- Génin, F. Y.; Salleo, A.; Pistor, T. V.; Chase, L. L. *J. Opt. Soc. Am. A* **2001**, 18, 2607–2616. doi:10.1364/JOSAA.18.002607
- Bloembergen, N. *Appl. Opt.* **1973**, 12, 661–664. doi:10.1364/AO.12.000661
- Stuart, B. C.; Feit, M. D.; Herman, S.; Rubenchik, A. M.; Shore, B. W.; Perry, M. D. *Phys. Rev. B* **1996**, 53, 1749–1761. doi:10.1103/PhysRevB.53.1749
- Jia, T. Q.; Li, R. X.; Liu, Z.; Xu, Z. Z. *Appl. Phys. A* **2002**, 74, 503–507. doi:10.1007/s003390100903
- Becker, J.; Bernhardt, A. *Proc. SPIE* **1994**, 2114, 703–713. doi:10.1117/12.180881
- ISO 11254–2, *Test methods for laser induced damage threshold of optical surfaces. Part 2: S on 1 test*, International Organization for Standardization. 2001.
- Cook, L. M. *J. Non-Cryst. Solids* **1990**, 120, 152–171. doi:10.1016/0022-3093(90)90200-6
- Yatsui, T.; Hirata, K.; Nomura, W.; Tabata, Y.; Ohtsu, M. *Appl. Phys. B* **2008**, 93, 55–57. doi:10.1007/s00340-008-3142-z
- Hirata, K. *Proc. SPIE* **2011**, 7921, 79210M. doi:10.1117/12.875808
- Miura, K.; Qiu, J.; Inouye, H.; Mitsuyu, T.; Hirao, K. *Appl. Phys. Lett.* **1997**, 71, 3329–3331. doi:10.1063/1.120327

15. Sudrie, L.; Couairon, A.; Franco, M.; Lamouroux, B.; Prade, B.; Tzortzakis, S.; Mysyrowicz, A. *Phys. Rev. Lett.* **2002**, *89*, 186601. doi:10.1103/PhysRevLett.89.186601
16. Audebert, P.; Daguzan, P.; Dos Santos, A.; Gauthier, J. C.; Geindre, J. P.; Guizard, S.; Hamoniaux, G.; Krastev, K.; Martin, P.; Petite, G.; Antonetti, A. *Phys. Rev. Lett.* **1994**, *73*, 1990–1993. doi:10.1103/PhysRevLett.73.1990
17. Saeta, P. N.; Greene, B. I. *Phys. Rev. Lett.* **1993**, *70*, 3588–3591. doi:10.1103/PhysRevLett.70.3588
18. Bates, J. B. *J. Chem. Phys.* **1972**, *56*, 1910–1917. doi:10.1063/1.1677474
19. Chan, J. W.; Huser, T.; Risbud, S.; Krol, D. M. *Opt. Lett.* **2001**, *26*, 1726–1728. doi:10.1364/OL.26.001726

License and Terms

This is an Open Access article under the terms of the Creative Commons Attribution License (<http://creativecommons.org/licenses/by/2.0>), which permits unrestricted use, distribution, and reproduction in any medium, provided the original work is properly cited.

The license is subject to the *Beilstein Journal of Nanotechnology* terms and conditions: (<http://www.beilstein-journals.org/bjnano>)

The definitive version of this article is the electronic one which can be found at:
[doi:10.3762/bjnano.5.146](https://doi.org/10.3762/bjnano.5.146)



OPEN

Randomness in highly reflective silver nanoparticles and their localized optical fields

SUBJECT AREAS:
NANOPHOTONICS AND
PLASMONICS
STATISTICSReceived
6 May 2014Accepted
15 July 2014Published
15 August 2014Correspondence and
requests for materials
should be addressed to
M.N. (naruse@nict.go.
ip)Makoto Naruse^{1,2}, Takeharu Tani³, Hideki Yasuda³, Naoya Tate^{2,4}, Motoichi Ohtsu^{2,4} & Masayuki Naya³

¹Photonic Network Research Institute, National Institute of Information and Communications Technology, 4-2-1 Nukui-kita, Koganei, Tokyo 184-8795, Japan, ²Nanophotonics Research Center, Graduate School of Engineering, The University of Tokyo, 2-11-16 Yayoi, Bunkyo-ku, Tokyo 113-8656, Japan, ³Frontier Core-Technology Laboratories, Research and Development Management Headquarters, Fujifilm Corporation, Nakanuma, Minamiashigara, Kanagawa 250-0193, Japan, ⁴Department of Electrical Engineering and Information Systems, Graduate School of Engineering, The University of Tokyo, 2-11-16 Yayoi, Bunkyo-ku, Tokyo 113-8656, Japan.

Reflection of near-infrared light is important for preventing heat transfer in energy saving applications. A large-area, mass-producible reflector that contains randomly distributed disk-shaped silver nanoparticles and that exhibits high reflection at near-infrared wavelengths was demonstrated. Although resonant coupling between incident light and the nanostructure of the reflector plays some role, what is more important is the geometrical randomness of the nanoparticles, which serves as the origin of a particle-dependent localization and hierarchical distribution of optical near-fields in the vicinity of the nanostructure. Here we show and clarified the unique optical near-field processes associated with the randomness seen in experimentally fabricated silver nanostructures by adapting a rigorous theory of optical near-fields based on an angular spectrum and detailed electromagnetic calculations.

Near-infrared light-reflecting films attached to windows etc. are important for preventing heat transfer from sunlight, thus saving energy for cooling rooms in summer¹⁻⁴. At the same time, it is important to maintain higher transmission efficiency in the visible range to ensure good visibility, as well as in radio frequency bands so as not to interfere with wireless communications. A large area and mass-producibility are also critical for market deployment. Fujifilm Co. Ltd. has proposed and realized a device named NASIP (Nano Silver Pavement), which satisfies all of the above requirements, consisting of randomly distributed disk-shaped silver nanoparticles for reflecting near-infrared light¹. An actual device is shown in Fig. 1a, and a scanning electron microscope image of the surface is shown in Fig. 1b². The elemental silver nanostructure has a diameter of about 120 to 150 nm and a thickness of 10 nm. From Fig. 1b, we can see that the nanoparticles contain randomness in terms of their individual shapes and layout. Figure 1c shows experimentally observed spectral properties of the fabricated device, which exhibits high reflectance for near-infrared light while maintaining a high transmittance in the visible and far-infrared regions.

The physical principle of the device has been attributed to plasmon resonances between the incoming light and the individual nanostructured matter¹. However, as introduced later with Fig. 2b, whereas strong light localization indeed occurs in certain nanoparticles at the resonant wavelengths, not-so-evident localization has also been observed in some nanoparticles. Also, strong localization is observed even at non-resonant wavelengths in some nanoparticles. Such features may be attributed to the above-mentioned randomness of nanostructures. Furthermore, unlike uniformly distributed, uniformly shaped nanoparticles, interesting optical near-field distributions are present in a device containing geometrical randomness.

In this paper, by investigating the inherent randomness of silver nanoparticles while adapting a rigorous theory of optical near-fields based on an angular spectrum, we clarified the unique optical near-field processes associated with randomness in nanostructures, which are not observed in uniformly arranged nanostructures. Unlike the well-known Anderson localization⁵ scheme, where multiple coherent scattering and the constructive interference of certain scattering paths are the origin of the localization phenomena⁶, with our approach we are able to highlight near-field interactions and “hierarchical” attributes in the vicinity of nanostructures. The word “hierarchical” here indicates that localized electromagnetic fields exist in a plane distant from the surface of the nanostructure; such a feature is manifested via the angular-spectrum-based theory, as shown below. Regarding

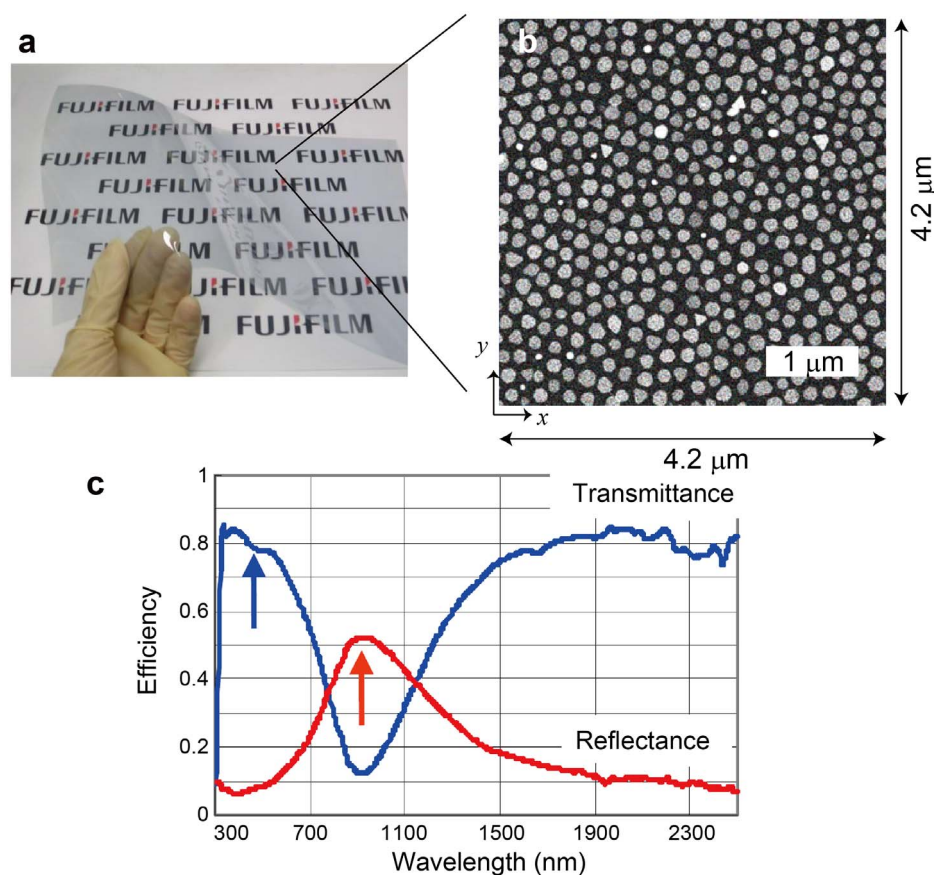


Figure 1 | Overview of the fabricated near-infrared light reflection film composed of silver nanoparticles (NASIP (Nano Silver Pavement)). (a) A picture of the fabricated and deployed near-infrared light reflection film. (b) Its thickness is 10 nm, and the average diameter of the silver nanoparticles is about 100 nm to 120 nm. (c) Experimentally measured transmittance and reflectance spectra of the device.

random media and light localization, Gréillon *et al.* did pioneering work by evaluating a metal–dielectric film having a random surface profile using near-field scanning microscopy^{7,8}. Birowosuto *et al.* observed fluctuations in the local density of states in random photonic media⁹, and Krachmalnicoff did so on disordered metal films¹⁰. With respect to statistical insights in related fields, Le Ru *et al.* investigated a power law distribution of electromagnetic enhancement and its relation to the detection of single molecules¹¹, and Sapienza *et al.* investigated the long-tail statistics of the Purcell factor in disordered media¹². With our work, we would like to contribute to the understanding of the fundamental aspects of randomness in an array of nanoparticles and their localized optical fields by adapting a rigorous theory of optical near-fields based on an angular spectrum and detailed electromagnetic calculations.

It is well-known that the resonance between far-field light and metal nanostructures depends on the type of metal, geometries such as size or shape, environmental materials, and so forth¹³. Silver has been chosen for such devices since it exhibits a remarkable resonance with near-infrared light¹. Regarding planar metal nanostructures, it is known that the resonant wavelength can be engineered in the range from visible to infrared by modifying the aspect ratio¹⁴. A 10 nm-thick layer containing about 100 nm-diameter silver nanoparticles, shown in Fig. 1b, which corresponds to an aspect ratio of 10, realizes a resonant wavelength in the near-infrared region. We assume a surrounding dielectric material whose refractive index is 1.5.

In order to characterize the electromagnetic properties associated with experimentally fabricated devices in detail, the geometries of the fabricated silver nanoparticles are converted to a numerical model consisting of a vast number of voxels. Specifically, the SEM image shown in Fig. 1b, which occupies an area of $4.2 \mu\text{m} \times 4.2 \mu\text{m}$, is

digitized into binary values with a spatial resolution of 2.5 nm both horizontally and vertically. The pixels occupied by silver take values of one, whereas those specified by the substrate material take values of zero. The thickness of the silver nanoparticles may exhibit certain position-dependent variations, as indicated by the grayscale differences observed in Fig. 1b; but we consider that they do not significantly affect the overall optical properties, and thus assume that the thickness is constant.

As a result, the silver nanoparticles, of which total number N is 468, are numerically modeled by $4200 \times 4200 \times 5$ voxels in an xyz Cartesian coordinate system, giving a total of 88.2 M voxels. This model is then simulated with a finite-difference time-domain-based electromagnetic simulator with assuming continuous-wave (CW) x -polarized light incident normally on the surface of the silver nanostructures (Fig. 2a). The details are shown in Methods section. Figure 2b summarizes electromagnetic intensity distributions calculated at a position 5 nm away from the surface of the silver nanoparticles on which the input light is incident. The wavelength is from 300 nm to 2000 nm in 100 nm intervals. Around the wavelength of 1000 nm, highly localized electric fields are observed in the vicinity of silver nanoparticles, but it should also be noted that not all nanoparticles have accompanying high-intensity fields. Also, even at some off-resonant wavelengths, most of the nanoparticles carry low-intensity electric fields, but a few of them carry high-intensity electric fields.

In order to characterize the localization of optical near-fields stemming from the geometrical randomness of the silver nanoparticles, we take the following strategy. First, we derive the induced charge distributions in silver nanostructures. Specifically, we calculate the divergence of the calculated electric fields at planes within the silver

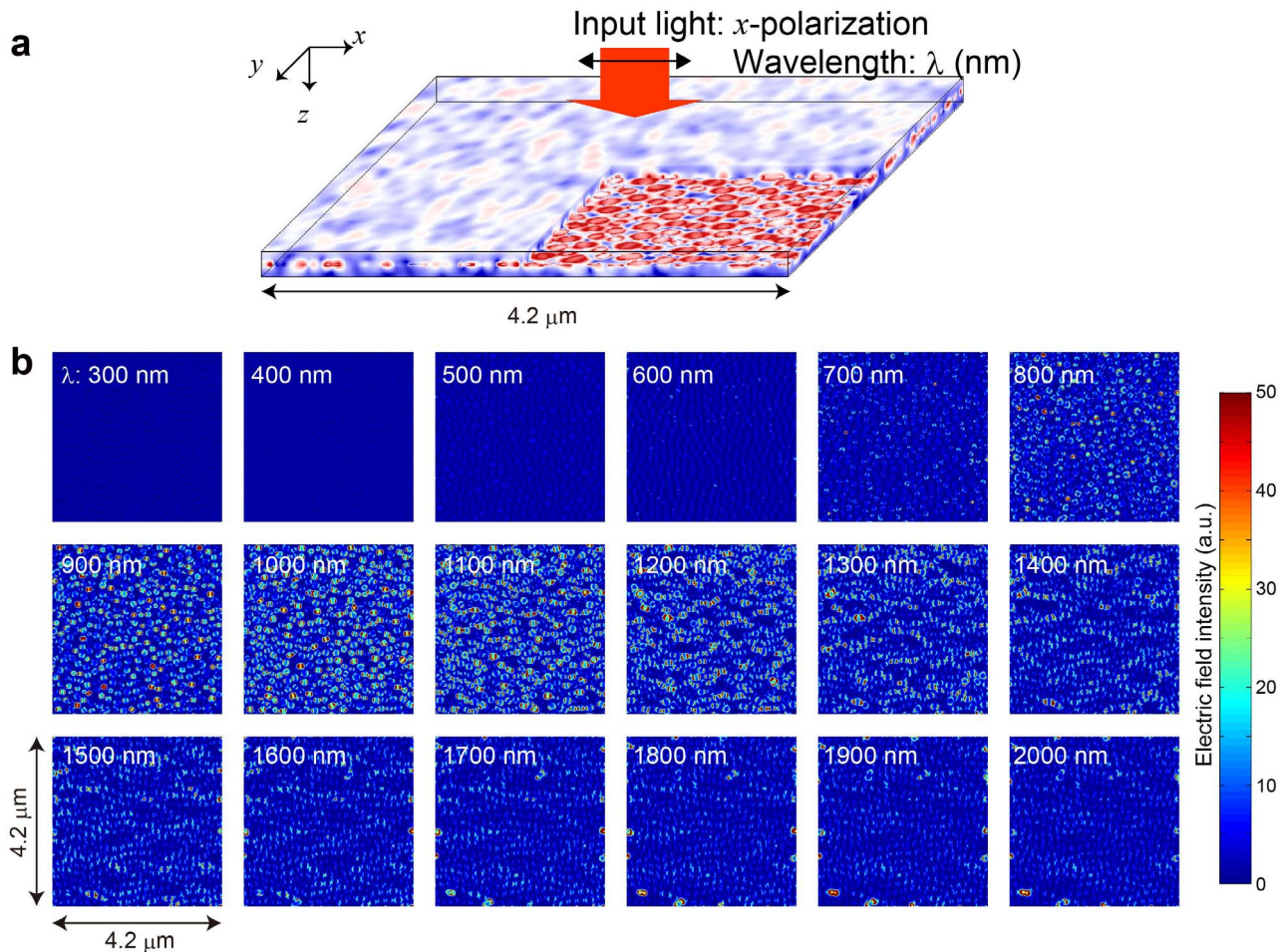


Figure 2 | Electromagnetic computational evaluations based on experimentally fabricated silver nanoparticles. (a) A schematic illustration of numerical evaluation of silver nanoparticles experimentally fabricated as shown in Fig. 1(b). (b) Calculated electric field intensity distributions at a position 5 nm away from the silver nanostructure when the wavelength of the normally incident light was 300 nm to 2000 nm in 100 nm intervals.

nanostructure, and sum up along the Z-direction to represent the charge density distributions. Figure 3a shows such a charge distribution, denoted by $\rho(x, y)$ brought about by 1000 nm-wavelength light.

Now, we characterize the induced charge distribution at each nanoparticle as an oscillating electric dipole. Figure 3b schematically illustrates a nanoparticle identified by index i ($i = 1, \dots, N$). The position of the center of gravity of the nanoparticle i is given by

$$G^{(i)} = \left(\frac{\sum_{P^{(i)}} xp(x,y)}{\sum_{P^{(i)}} p(x,y)}, \frac{\sum_{P^{(i)}} yp(x,y)}{\sum_{P^{(i)}} p(x,y)} \right), \quad p(x,y) = \begin{cases} 1 & (x,y) \in P^{(i)} \\ 0 & \text{otherwise} \end{cases} \quad (1)$$

where $P^{(i)}$ indicates the area that the nanoparticle i occupies. We consider that the imbalance of the induced charge regarding the vertical and horizontal half spaces divided by $G^{(i)}$ is represented by an induced dipole given by

$$\mathbf{d}^{(i)} = \left(\sum_{x \geq G^{(i)}(x)} \rho(x,y) - \sum_{x < G^{(i)}(x)} \rho(x,y), \sum_{y \geq G^{(i)}(y)} \rho(x,y) - \sum_{y < G^{(i)}(y)} \rho(x,y) \right) \quad (2)$$

$$= d^{(i)} \exp(i\phi^{(i)})$$

where $d^{(i)}$ and $\phi^{(i)}$ ($-\pi < \phi^{(i)} \leq \pi$) respectively represent the magnitude and phase of $\mathbf{d}^{(i)}$. Here the charge density distributions, $\rho(x, y)$, are temporally oscillating variables; we represent $d^{(i)}$ by its maximum value during a single period of lightwave oscillation, and $\phi^{(i)}$ is determined accordingly. Figure 3c schematically indicates the calculated

dipoles, where both the magnitude and the phase seems to contain certain randomness.

To quantify such randomness, the incidence patterns of the magnitude and the phase of the induced dipoles are analyzed as shown respectively in Fig. 4a and Fig. 4b with respect to all wavelengths. (The incidence patterns at the wavelengths of 300 nm, 500 nm, ..., and 1900 nm are not shown.) The magnitude of the dipoles exhibits some variation around the wavelength of 1200 nm, and the phase shows significant variation at 1000 nm. The square and circular marks in Fig. 4c and Fig. 4d respectively represent the average and the standard deviation of the magnitude and the phase of the dipoles. From Fig. 4d, the average phase is changed by π for 1000 nm light, which might be a manifestation of the resonance between the incident light and the silver nanostructured matter. If the nanoparticles have the same shape and are arranged uniformly, no such diversity in induced dipoles is observed; therefore, it is concluded that the geometrical randomness of the silver nanostructure must contribute to these electromagnetic characteristics.

Moreover, such variations in phase or magnitude, or both, lead to a variety of electronic localizations of the electronic fields, not just in the close vicinity of the silver nanostructures shown in Fig. 2b. We also evaluate the electric field intensity distributions at planes distant from the surface by 20, 50, 100, 200, 500, and 1000 nm, respectively, for all wavelengths. For these analyses, we conducted other numerical simulations by converting the above 2.5 nm-grid silver nanostructure model to a 10 nm-grid model. In addition, 1100 nm-thick and 1090 nm-thick volumes were assumed in the electromagnetic

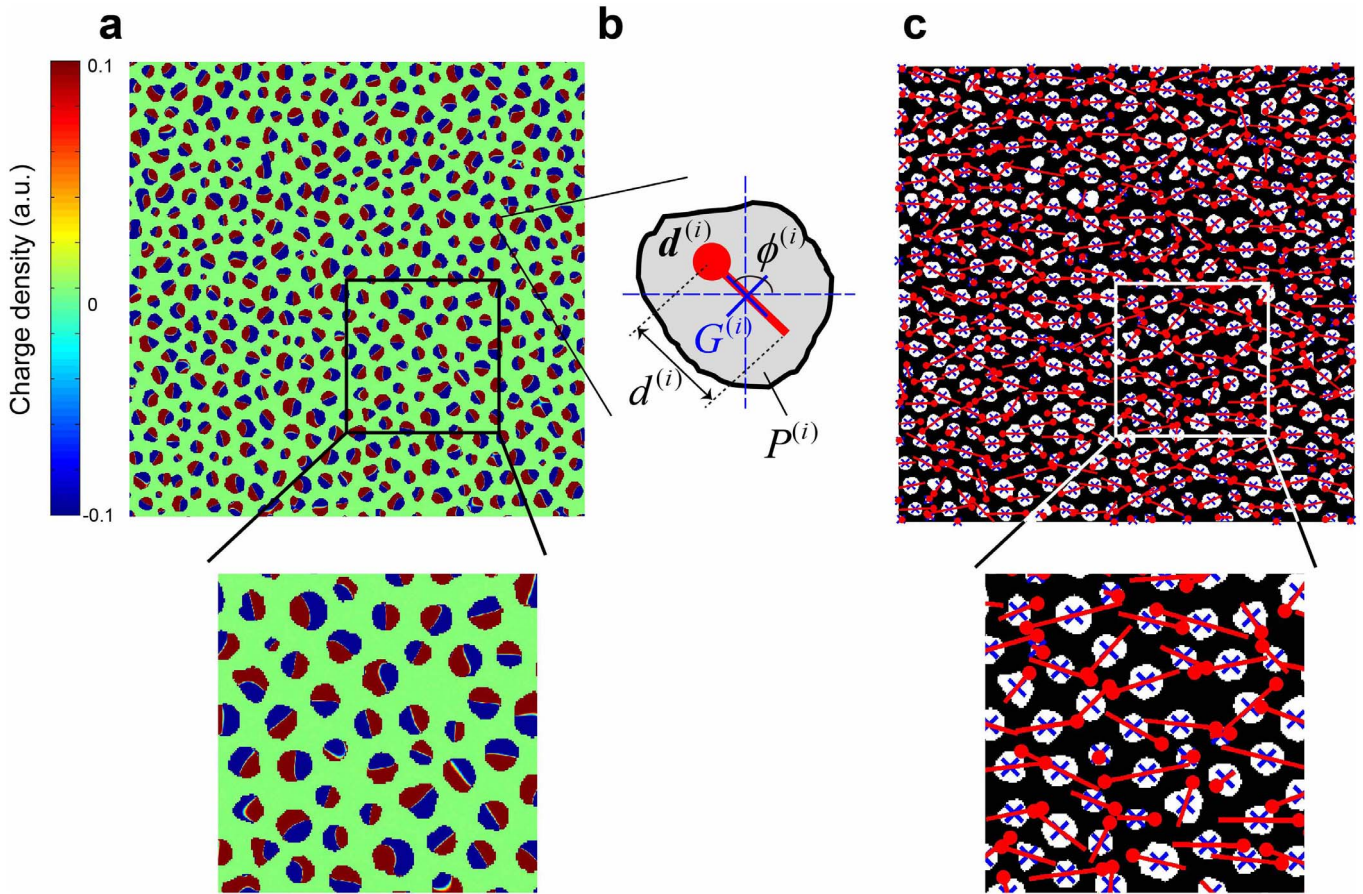


Figure 3 | Dipole-based modeling for randomly distributed silver nanoparticles. (a) Induced charge distributions in the silver nanostructures, showing magnified view below. (b) A schematic diagram of a silver nanoparticle, identified by the index i . The position of the center of gravity is given by $G^{(i)}$, and a dipole $\mathbf{d}^{(i)} = d^{(i)} \exp(i\phi^{(i)})$ based on the imbalance of induced electron charges with respect to $G^{(i)}$. (c) A schematic diagram of the induced dipoles, showing magnified view below.

calculation above and beneath the silver nanostructures. The CW light source was located 1070 nm away from the surface of the silver nanostructure.

Figure 5 summarizes incidence patterns of the electric field intensity at different heights for all wavelengths. (The patterns with respect to the wavelengths of 300 nm, 500 nm, ..., and 1900 nm are not shown.) It is evident that the electric field intensity exhibits a variety of values even 100 nm away, for the wavelengths between 1000 nm and 2000 nm. As the distance from the surface increases to larger than 200 nm, the variation in the electric field intensity decreases. However, it should be noted that at the resonant frequency, at the wavelength of 1000 nm, even a distant plane (1000 nm away from the silver nanoparticles) contains some variation in the electric field intensity. Such a nature has never been found in the electric fields accompanying uniform-shaped, uniformly distributed nanostructures. In the following, we provide the theoretical background behind such attributes.

The angular spectrum representation of an electromagnetic field involves decomposing an optical field as a superposition of plane waves including evanescent components^{15,16}, which allows us to explicitly represent and quantify optical near-fields. The details of the angular spectrum representation used in this paper are shown in the Supplementary Information and in Fig. 6a. The electric field $\mathbf{E}(\mathbf{r})$ originated by a point dipole $\mathbf{d}^{(i)}$ with frequency K is given in the form¹⁰

$$\mathbf{E}(\mathbf{r}) = \left(\frac{iK^3}{8\pi^2\epsilon_0} \right) \sum_{\mu=TE}^{TM} \int_{-\infty}^{\infty} \int_{-\infty}^{\infty} ds_x ds_y \frac{1}{s_z} [\mathbf{e}(\mathbf{s}^{(+)}, \mu) \cdot \mathbf{d}^{(i)}] \mathbf{e}(\mathbf{s}^{(+)}, \mu) \exp(iK\mathbf{s}^{(+)} \cdot \mathbf{r}). \quad (3)$$

Suppose that the dipole is oriented in the xz plane and is given by $\mathbf{d}^{(i)} = d^{(i)}(\sin\theta^{(i)}, 0, \cos\theta^{(i)})$, and that the point \mathbf{r} is also on the xz plane and is given by the displacement from the dipole, or $\mathbf{R}^{(i)} = (X^{(i)}, 0, Z^{(i)})$ (Fig. 6b). In such a case, the angular spectrum representation of the z component of the electric field in the evanescent regime (namely, $1 \leq s_{||} < +\infty$) based on eq. (3) is given by^{17,18}

$$E_z(\mathbf{R}^{(i)}) = \left(\frac{iK^3}{4\pi\epsilon_0} \right) \int_1^{\infty} ds_{||} \frac{s_{||}}{s_z} f_z^{(i)}(s_{||}, \mathbf{d}^{(i)}), \quad (4)$$

where

$$f_z^{(i)}(s_{||}, \mathbf{d}^{(i)}) = ds_{||} \sqrt{s_{||}^2 - 1} \sin\theta^{(i)} J_1(KX^{(i)}s_{||}) \exp(-KZ^{(i)}\sqrt{s_{||}^2 - 1}) + ds_{||}^2 \cos\theta^{(i)} J_0(KX^{(i)}s_{||}) \exp(-KZ^{(i)}\sqrt{s_{||}^2 - 1}). \quad (5)$$

Here, $J_n(x)$ represents a Bessel function of the first kind, where n is an integer. One minor remark here is that the dipole model derived in eq. (2) spans in the xy plane, whereas the dipole used in the above angular spectrum theory is oriented in the xz plane. Although it is possible to assume a dipole oriented in the xy plane in the angular spectrum theory^{16,17}, we consider that the resulting mathematical representations and the formula for the angular spectrum would be unnecessarily much more complex, whereas assuming dipoles in the xz plane preserves the essential attributes of the discussion of randomness in this paper while keeping the mathematical formula simpler.

In order to examine the character of optical near-fields that originate from the structural randomness, we consider two virtual

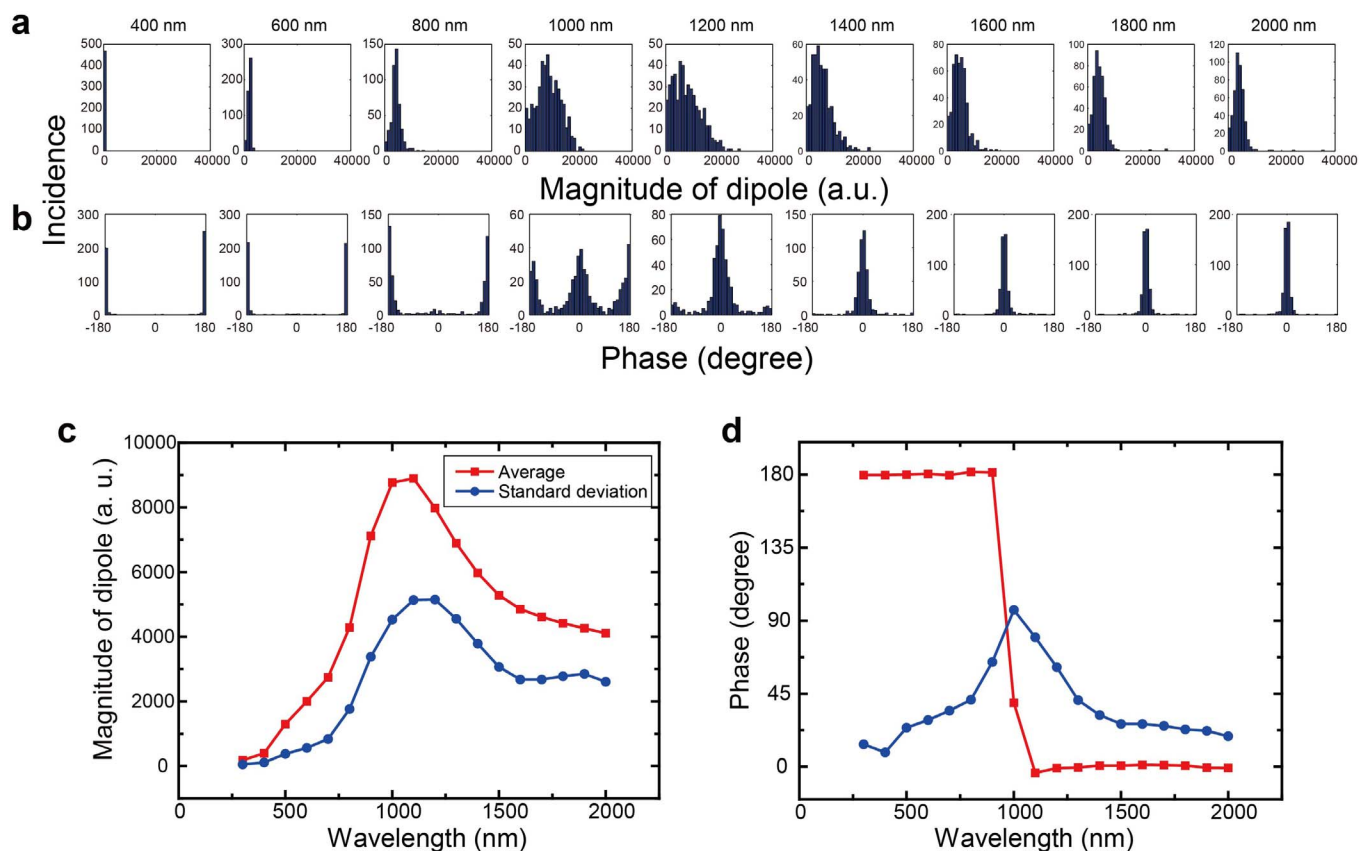


Figure 4 | Statistical properties inherent in the induced dipoles. (a,b) Incidence patterns of (a) the magnitude and (b) the phase of the induced electric dipoles as a function of the wavelength of irradiated light. (c,d) The average and the standard deviation of (a) the magnitude and (b) the phase are evaluated at each wavelength.

dipoles $\mathbf{d}^{(1)}$ and $\mathbf{d}^{(2)}$ located on the x -axis and separated from each other by a small distance G , as shown in Fig. 6c. Now, supposing that the magnitude and the orientation of these dipoles are chosen in a random manner, we investigate the resultant near-fields. Specifically, we evaluate the angular spectra at a position equidistant from both $\mathbf{d}^{(1)}$ and $\mathbf{d}^{(2)}$ and a distance Z away from the x -axis. Let the magnitude of a dipole be given by a random number that follows a normal distribution whose average and standard deviation are given by 2 and $1/2$, respectively. The phase is also specified by a random number following a normal distribution whose average and standard deviation are both given by $\pi/2$. We characterized 10,000 kinds of such angular spectra based on pairs of dipoles, each of which was randomly chosen. Figure 7a shows ten example angular spectra obtained when G was $\lambda/4$ and Z was $\lambda/16$, whose differences are evident.

On the other hand, when the randomness associated with the dipoles is smaller, for example, in the case of the amplitude, the random number follows a normal distribution with an average of 2 and a standard deviation of $1/20$, and in the case of the phase, the random number follows a normal distribution with average $\pi/2$ and standard deviation $\pi/20$. Ten example angular spectra, out of 10,000, are shown in Fig. 7b, where the differences among the angular spectra are considerably smaller.

The integral of the angular spectrum along the spatial frequency is correlated with the electric field intensity¹⁶. Figures 7c,i and 7d,i respectively represent the incidence patterns of the integral of 10,000 kinds of angular spectra, showing the variation in electric field intensity, with respect to the former highly random dipole pairs and the latter less-random ones. It should be noted that considerable variation appears in the case of the higher randomness, whereas the electric field intensity is almost uniquely low with the less-random dipoles. As the distance from the dipole, namely Z , increases,

the variation of the angular spectra, and their resultant electric field intensity, decreases. However, as is shown in Figs. 7c,ii and 7c,iii, which are for the cases $Z=\lambda/8$ and $Z=\lambda/2$, respectively, the electric field intensity histogram still contains some variation; that is to say, highly localized optical near-fields could exist in some cases. On the other hand, such an intensity variation is *never* observed in the case of less-randomly formed dipole pairs, as shown in Figs. 7d,ii and 7d,iii. These theoretically obtained characteristics agree well with the former results shown in Fig. 5 derived by electromagnetic calculations based on experimentally observed randomly organized silver nanostructures.

One minor remark that we should make regarding the analysis is that the distance between the two dipoles is kept constant, and this distance could be set in a random manner. We consider that the geometrical randomness causes the imbalance of the magnitude and the phase of dipoles, and thus, investigating the attributes of optical near-fields by taking account of the randomness associated with dipoles is the most important matter at this stage. The geometrical randomness of the nanostructures and the randomness in the induced dipoles may have certain complex correlations, and such issues should be investigated in future work.

Finally, the diamond and triangular marks in Fig. 8 show the reflection efficiencies based on electromagnetic calculations in the cases of the random structure based on the experimentally observed silver nanoparticles and an “ordered” structure, respectively. Here, the “ordered” structure consisted of an array of constant-diameter (128 nm), 10 nm-thick silver nanoparticles, and the total area and the total number of nanostructures were equivalent to the case of the random structure. Although the reflectance of the ordered structure exhibits a higher value than that of the random structure at the resonant frequency (1000 nm), the average reflectance between the

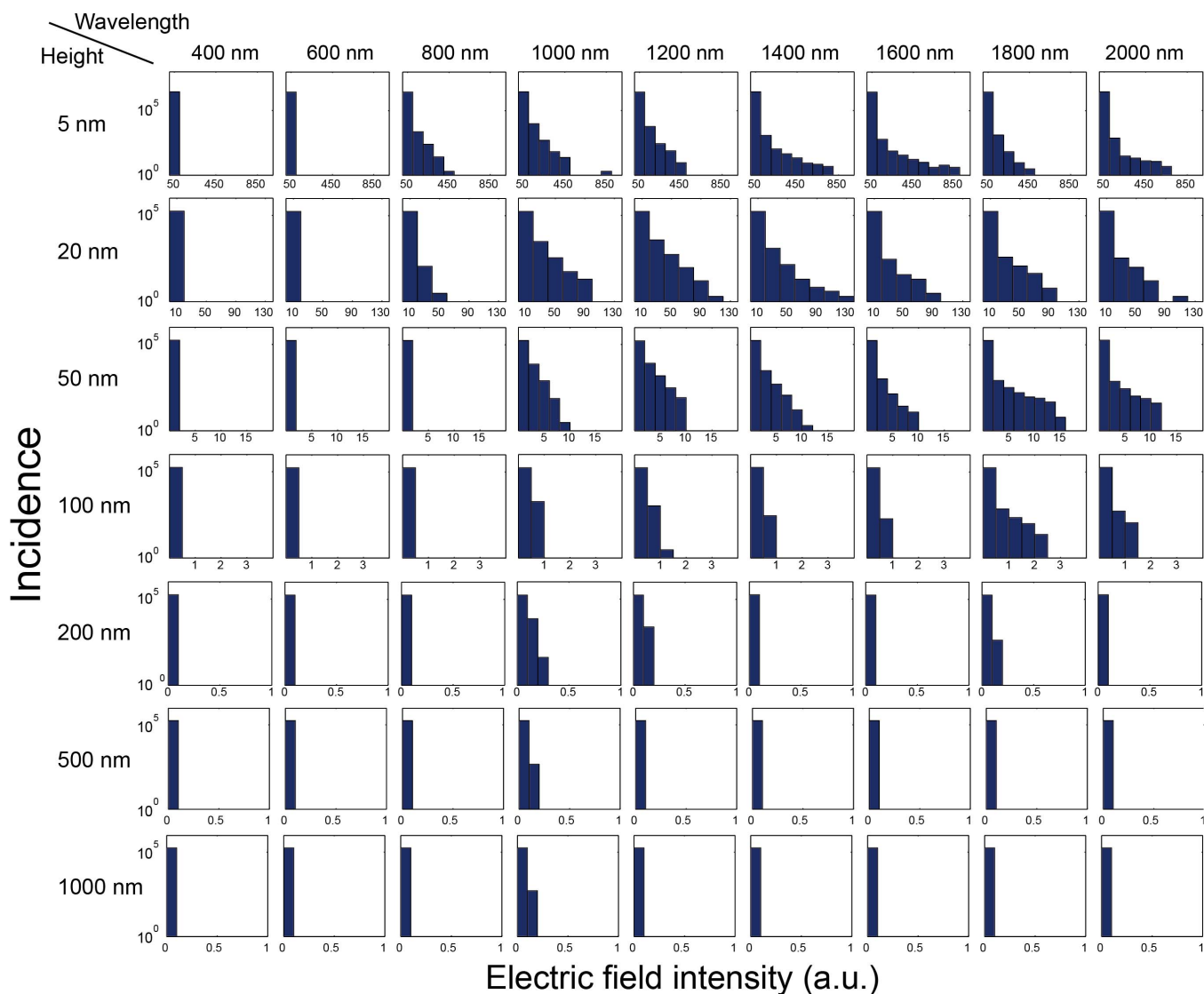


Figure 5 | Statistical properties of optical near-field distributions associated with the random silver nanoparticles. The incidence patterns of electric field intensity at planes away from the surface of the silver nanostructure by distances 5, 20, 50, 100, 200, 500, and 1000 nm for each wavelength.

wavelengths of 1000 nm and 2000 nm results in a higher value in the case of the random structure (0.171) than in the case of the ordered one (0.138). The square and circular marks in Fig. 8 represent the transmittances for the random and ordered structures, respectively, whose averages in the spectral range between 1000 nm and 2000 nm are given by 0.710 and 0.805, meaning that the random structure provides lower transmittance. Thus, we have shown that a silver nanostructured material having randomness yields different performance figures of the near-infrared reflection film compared with

those of a reflection film containing an equivalent amount of uniformly distributed silver nanoparticles.

In summary, we examined the optical near-fields associated with randomly organized silver nanoparticles by using electromagnetic calculations based on experimentally fabricated devices, and we clarified the fact that they stemmed from the structural randomness of the silver nanoparticles by adapting a theory of optical near-fields based on an angular spectrum. One of the most interesting challenges in near-field optics and nanophotonics in future will be to gain a

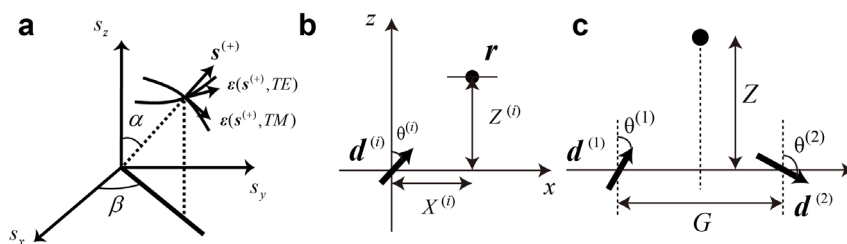


Figure 6 | Theoretical modeling of optical near-fields based on angular spectrum representation. (a) A schematic diagram of a wave vector and polarization vectors for the angular spectrum representation of optical near-fields. For evanescent components, α takes an imaginary number. (b) Orientation of a dipole $d^{(i)}$ and the point of evaluation r . (c) A two-dipole system located in close proximity. The magnitude and the orientation of each dipole is specified by randomly generated numbers.

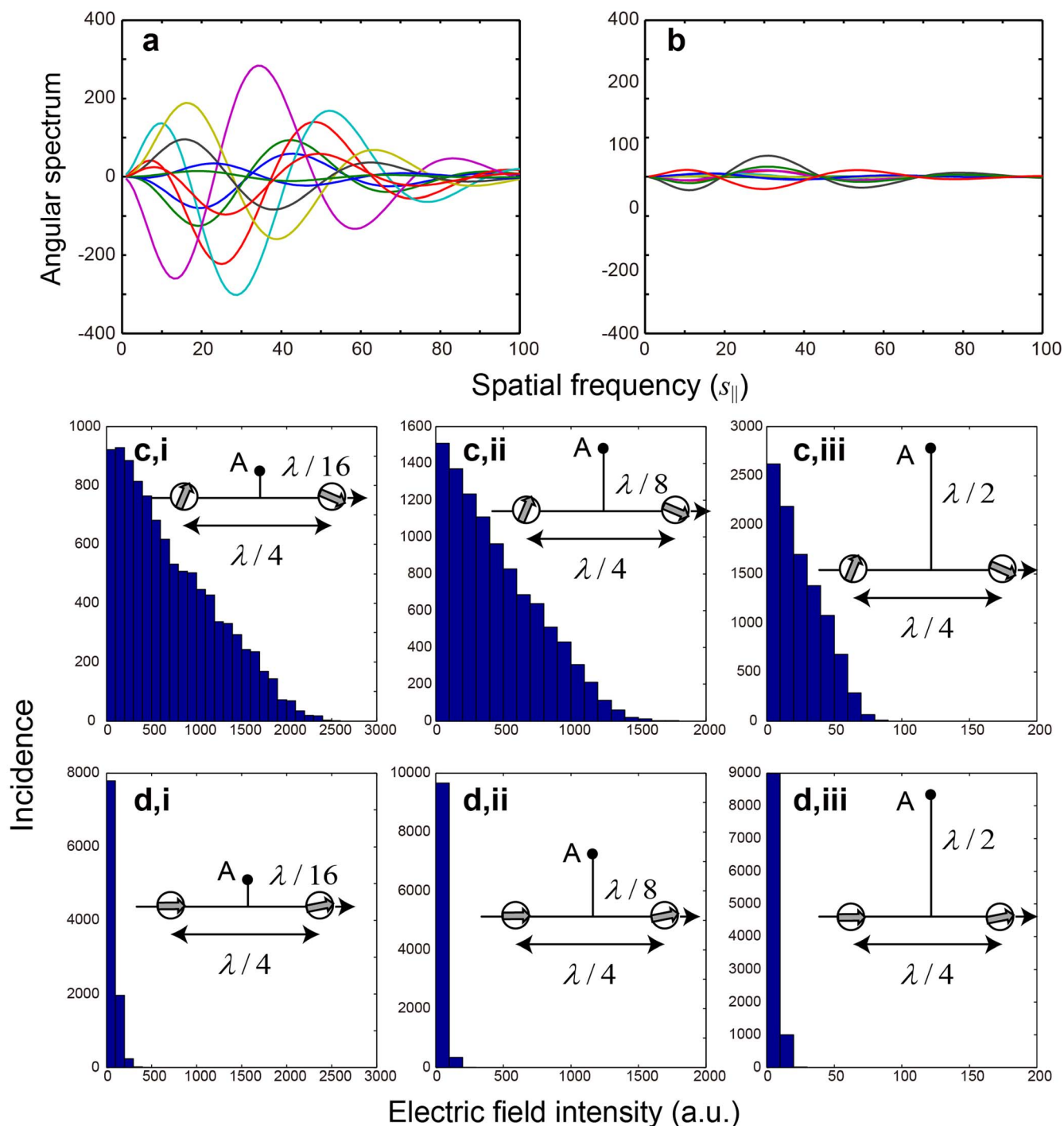


Figure 7 | Characterization of randomness in optical near-fields by the angular spectrum-based theoretical analysis. (a,b) A differently-specified dipole pair gives a different angular spectrum. (a) Moderate randomness yields significantly different spectra, whereas (b) less randomness gives nearly identical spectra. (c) The incidence patterns of the near-field electric field intensity, given by the integral of the angular spectrum, based on dipole pairs that follow random statistics show some variation even as the distance from the silver nanostructures increases. (d) On the other hand, with less-random dipole pairs, such a tendency is not observed. These are clear manifestations of the hierarchical attributes of optical near-fields.

deeper understanding of randomness; further detailed modeling, analysis, and even to exploit it and optimize it for practical applications would be expected. We consider that this study paves the way to gaining fundamental insights regarding optical near-field processes associated with randomness in the subwavelength regime.

Methods

Electromagnetic numerical simulations. Above and beneath the 10 nm-thick silver nanoparticles model area, we assume 100 nm-thick and 90 nm-thick spaces,

as schematically shown in Fig. 2a. Continuous-wave (CW) x -polarized light, irradiating the surface of the sample from a distance of 92.5 nm, is normally incident on the surface of the silver nanostructures. Absorbing boundary conditions are assumed for the z -direction, and periodic boundary conditions are assumed in both the x - and y -directions. Some of the silver nanoparticles near the boundaries touch the periodic boundaries, meaning that they may be interconnected between upper and lower ends and/or between left and right ends in the computational model. Such conditions may trigger artifacts in the simulations, but we consider that our computational area is large enough, and the total number of nanoparticles in the region is large enough ($N = 468$ particles), and thus the issue of the periodic boundary is marginal. In addition, it is likely

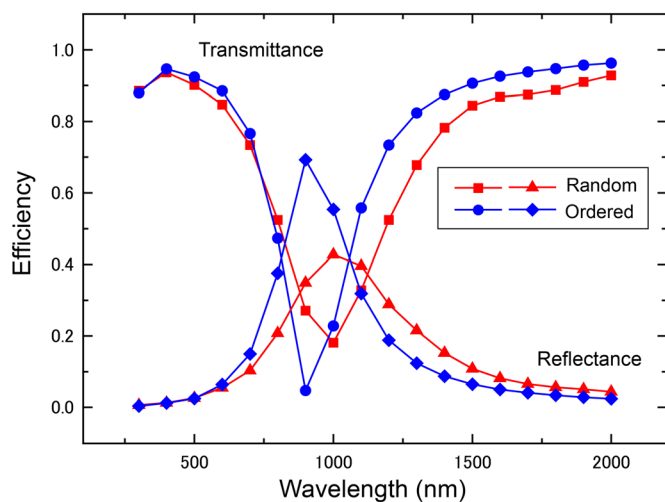


Figure 8 | Comparison of calculated spectra for the random structure and an ordered one. Comparison of calculated transmittance and reflectance spectra for the random structure based on the experimentally fabricated silver nanostructure and an “ordered” one, which is virtually constructed in such a way that the sizes of the nanoparticles are the same and the layouts are uniform, whereas the total area and the total number of particles is equivalent to the case of the former random structures. The average reflectance and the average transmittance of the random structure in the wavelength regime between 1000 nm and 2000 nm are respectively higher and lower compared with those of the ordered one.

that the size of nanoparticles located at the boundaries is smaller, and the periodic boundary conditions are even reasonable in our particular analysis.

1. Kiyoto, N., Hakuta, S., Tani, T., Naya, M. & Kamada, K. Development of a Near-infrared Reflective Film Using Disk-shaped Silver Nanoparticles. *Fujifilm Res. & Dev.* **58-2013**, 55–58 (2013).
2. Tani, T., Hakuta, S., Kiyoto, N. & Naya, M. Transparent near-infrared reflector metasurface with randomly dispersed silver nanodisks. *Opt. Express* **22**, 9262–9270 (2014).
3. Granqvist, C. G. Smart Optics. *Advances in Science and Technology (Volume 55)*, Vincenzini P. & Righini G. (eds.) 205–212 (Trans. Tech. Publishing, Switzerland, 2008).
4. Wang, H., Wu, H., Ding, Y. & Zhou, X. Modeling and Analysis on the Cooling Energy Efficiency of Sun-Shading of External Windows in Hot Summer and Warm Winter Zone. *Int'l Conf. Mater. Renew. Energ. & Environ. (ICMREE)*. 1086–1090 (2011).
5. Anderson, P. W. Absence of diffusion in certain random lattices. *Phys. Rev.* **109**, 1492–1505 (1958).
6. Mascheck, M. *et al.* Observing the localization of light in space and time by ultrafast second-harmonic microscopy. *Nat. Photonics* **6**, 293–298 (2012).
7. Grésillon, S. *et al.* Experimental observation of localized optical excitations in random metal-dielectric films. *Phys. Rev. Lett.* **82**, 4520–4523 (1999).

8. Ducourtieux, S. *et al.* Near-field optical studies of semicontinuous metal films. *Phys. Rev. B* **64**, 165403 (2001).
9. Birowosuto, M. D., Skipetrov, S. E., Vos, W. L. & Mosk, A. P. Observation of spatial fluctuations of the local density of states in random photonic media. *Phys. Rev. Lett.* **105**, 013904 (2010).
10. Krachmalnicoff, V., Castanié, E., De Wilde, Y. & Carminati, R. Fluctuations of the local density of states probe localized surface plasmons on disordered metal films. *Phys. Rev. Lett.* **105**, 183901 (2010).
11. Le Ru, E. C., Etchegoin, P. G. & Meyer, M. Enhancement factor distribution around a single surface-enhanced Raman scattering hot spot and its relation to single molecule detection. *J. Chem. Phys.* **125**, 204701 (2006).
12. Sapienza, R. *et al.* Long-tail statistics of the Purcell factor in disordered media driven by near-field interactions. *Phys. Rev. Lett.* **106**, 163902 (2011).
13. Homola, J., Yee, S. S. & Gauglitz, G. Surface plasmon resonance sensors: review. *Sens. Actu. B.* **54**, 3–15 (1999).
14. Jin, R. *et al.* Controlling anisotropic nanoparticle growth through plasmon excitation. *Nature* **425**, 487–490 (2003).
15. Wolf, E. & Nieto-Vesperinas, M. Analyticity of the angular spectrum amplitude of scattered fields and some of its consequences. *J. Opt. Soc. Am. A* **2**, 886–889 (1985).
16. Inoue, T. & Hori, H. Quantum theory of radiation in optical near field based on quantization of evanescent electromagnetic waves using detector mode. Ohtsu, M. (ed.) 127–199 *Progress in Nano-Electro-Optics IV* (Springer, Berlin, 2005).
17. Naruse, M., Inoue, T. & Hori, H. Analysis and synthesis of hierarchy in optical near-field interactions at the nanoscale based on angular spectrum. *Jpn. J. Appl. Phys.* **46**, 6095–6103 (2007).
18. Naruse, M. *et al.* Optical near-field-mediated polarization asymmetry induced by two-layer nanostructures. *Opt. Express* **21**, 21857–21870 (2013).

Acknowledgments

This work was supported in part by Grants-in-Aid for Scientific Research (2330031) and the Core-to-Core Program A. Advanced Research Networks from the Japan Society for the Promotion of Science.

Author contributions

M.Naruse, M.O. and M.Naya directed the project; T.T., H.Y. and M.Naya designed experimental devices, and their experimental characterizations; T.T. and H.Y. performed numerical simulations; M.Naruse and N.T. conducted theoretical modeling and analysis; M.N. conducted analysis of numerical simulation results; M.N., T.T. and H.Y. wrote the paper.

Additional information

Supplementary information accompanies this paper at <http://www.nature.com/scientificreports>

Competing financial interests: The authors declare no competing financial interests.

How to cite this article: Naruse, M. *et al.* Randomness in highly reflective silver nanoparticles and their localized optical fields. *Sci. Rep.* **4**, 6077; DOI:10.1038/srep06077 (2014).



This work is licensed under a Creative Commons Attribution-NonCommercial-NoDerivs 4.0 International License. The images or other third party material in this article are included in the article's Creative Commons license, unless indicated otherwise in the credit line; if the material is not included under the Creative Commons license, users will need to obtain permission from the license holder in order to reproduce the material. To view a copy of this license, visit <http://creativecommons.org/licenses/by-nc-nd/4.0/>



OPEN

Chaotic oscillation and random-number generation based on nanoscale optical-energy transfer

SUBJECT AREAS:
NANOPHOTONICS AND
PLASMONICS
COMPUTER SCIENCEMakoto Naruse¹, Song-Ju Kim², Masashi Aono^{3,4}, Hirokazu Hori⁵ & Motoichi Ohtsu⁶Received
7 May 2014Accepted
25 July 2014Published
12 August 2014Correspondence and
requests for materials
should be addressed to
M.N. (naruse@nict.go.
ip)

¹Photonic Network Research Institute, National Institute of Information and Communications Technology, 4-2-1 Nukui-kita, Koganei, Tokyo 184-8795, Japan, ²WPI Center for Materials Nanoarchitectonics, National Institute for Materials Science, 1-1 Namiki, Tsukuba, Ibaraki 305-0044, Japan, ³Earth-Life Science Institute, Tokyo Institute of Technology, 2-12-1 Ookayama, Meguro-ku, Tokyo 152-8550, Japan, ⁴PRESTO, Japan Science and Technology Agency, 4-1-8 Honcho, Kawaguchi-shi, Saitama 332-0012, Japan, ⁵Interdisciplinary Graduate School of Medicine and Engineering, University of Yamanashi, 4-3-11 Takeda, Kofu, Yamanashi 400-8511, Japan, ⁶Department of Electrical Engineering and Information Systems, Graduate School of Engineering, The University of Tokyo, 2-11-16 Yayoi, Bunkyo-ku, Tokyo 113-8656, Japan.

By using nanoscale energy-transfer dynamics and density matrix formalism, we demonstrate theoretically and numerically that chaotic oscillation and random-number generation occur in a nanoscale system. The physical system consists of a pair of quantum dots (QDs), with one QD smaller than the other, between which energy transfers via optical near-field interactions. When the system is pumped by continuous-wave radiation and incorporates a timing delay between two energy transfers within the system, it emits optical pulses. We refer to such QD pairs as nano-optical pulsers (NOPs). Irradiating an NOP with external periodic optical pulses causes the oscillating frequency of the NOP to synchronize with the external stimulus. We find that chaotic oscillation occurs in the NOP population when they are connected by an external time delay. Moreover, by evaluating the time-domain signals by statistical-test suites, we confirm that the signals are sufficiently random to qualify the system as a random-number generator (RNG). This study reveals that even relatively simple nanodevices that interact locally with each other through optical energy transfer at scales far below the wavelength of irradiating light can exhibit complex oscillatory dynamics. These findings are significant for applications such as ultrasmall RNGs.

Modern neuroscience currently considers that the complex interactions between spiking pulses in human brains are at the origin of intelligence¹. It is clear that humans cannot live without the rhythmic patterns of signals or material flows such as the circadian rhythm². Moreover, even relatively simple biological organisms such as single-celled amoeboid organisms (e.g., *P. polycephalum*) exhibit complex spatiotemporal dynamics including chaotic oscillatory dynamics^{3,4}. This intriguing real-world observation raises the following question: What is the ultimate physical architecture in nature that exhibits complex pulsation dynamics?

To address this question, we use theory and numerical analysis to examine intriguing oscillatory dynamics that are based on optical-near-field-mediated energy transfer at a scale far below the wavelength of irradiating light. The insights obtained herein can help us understand the complex oscillatory phenomena observed in micro- and nanoscale engineering devices and natural biological organisms. Moreover, they can help the development of practical applications such as random-number generators⁵, which are critical in cryptography⁶ and computer simulations⁷, as well as in designing “nano intelligence”^{8–10}.

Energy transfer based on optical near-field interactions between nanoscale materials has been thoroughly studied by fundamental theory^{11,12} as well as experiments^{13–16}. Generating periodic optical pulses is one of the most important functions of digital systems¹⁷. To study the generation of optical pulses based on optical near-field processes in the subwavelength regime, Shojiguchi *et al.* theoretically investigated the generation of super-radiance in N two-level systems connected by optical near-field interactions¹⁸. By substantially simplifying Shojiguchi’s architecture, Naruse *et al.* theoretically demonstrated optical pulsation in a system composed of two subsystems, each of which involved energy transfer from a smaller to a larger quantum dot (QD). The energy transfer occurs via optical near-field interactions and is driven by a continuous wave (cw) irradiation¹⁹, which



results in the emission by the QD system of an optical pulse train. Thus, we refer to the QDs in this context as “nano-optical pulsers” (NOPs).

In many versatile systems in nature and in engineering devices and systems, synchronization and chaos are important phenomena connected to periodic signals^{20–22}. For example, injection locking of lasers is of fundamental importance, and stability, instability, and chaos in such systems have been thoroughly studied from basic and practical perspectives^{21,23}. In addition, rather than suppressing such chaotic behavior in lasers, the phenomenon can be exploited by applications that secure data communications^{24,25}. In associated research, optical random-number generators (RNGs) were intensively investigated^{6,26}, and chaos generated in quantum-dot microlasers with external feedback was also reported²⁷.

However, these studies of synchronized, chaotic, and random oscillatory dynamics require far-field optics, which means that the devices and systems are constrained by the diffraction limit of light. This physical restriction means that *macroscale* devices are inherently required. In contrast, the present study focuses on *nanoscale* oscillatory dynamics, which are free from the diffraction limit imposed by optical far fields. By revealing the basic functions made possible by synchronization and chaos in near-field optics, we provide guiding design principles for future devices, systems and methods to evaluate their performance. Note that the pulsation, synchronization, and chaos, as discussed in this paper, are related to *optical pulses* for which the carrying frequencies are fixed, whereas the conventional literature on synchronization and chaos in lasers²¹ discusses the oscillation frequency of the radiation itself.

We now give a brief outline of the paper. Reference 19 discusses the combination of two energy transfers by near-field interactions, one of which is delayed with respect to the other. When pumped by cw irradiation, the system emits an optical pulse train. This phenomenon was explained using a density matrix formalism involving six energy levels. In our study, we first further simplify such a pulse-generating mechanism by replacing one of the energy-transfer paths by a delay function. This approach allows us to confirm the emission of a pulsed output. Second, we demonstrate that such an NOP can be synchronized with a periodic external signal. We show that the synchronization bandwidth depends on the intensity of the external stimulus and that the “sensitivity” (defined later) to the external stimulus increases for weaker cw excitation of the NOP. Third, we characterize bifurcations and chaos by combining NOPs with an external timing delay between energy transfers. Finally, by using security-test suites to evaluate the chaotic signals, we checked the randomness inherent in those signals to determine if such devices can be used as an RNG.

Uchida *et al.* experimentally demonstrated an RNG based on semiconductor lasers and achieved 1.7 Gb/s random-number generation⁶. The rate obtained was excellent and devices were developed on the basis of solid and sophisticated principles in the literature on optical communications. However, because these results are based on far-field optics, they suffer from a fundamental difficulty that they cannot be miniaturized beyond the diffraction limit of light²⁸. NOPs, however, are based on energy transfer and thus are not diffraction limited. In addition, cw light sources, such as light-emitting diodes and lasers, have now been developed on the basis of principles of near-field optics^{29,30}, which suggests that optical pulsation and RNGs can be implemented on the basis of nanophotonic principles and technologies.

Results

Nano-optical pulser based on energy transfer. Previous work presented a theory of a pulse-generating mechanism in a system of

four QDs. This mechanism combines two energy-transfer pathways in which one pathway experiences a timing delay¹⁹. Here, we first introduce a simpler theory based on a pair of QDs, with one QD smaller than the other.

In the long-wavelength approximation, the electric-field operator is constant in the Hamiltonian, which describes the interaction between an electron and an electric field, because the electric field of the propagating light is considered to be uniform on the nanometer scale. For cubic QDs, optical selection rules prohibit transitions to states described by even quantum numbers. However, this restriction is relaxed when optical near fields are concerned because of the localized nature of optical near fields in the vicinity of nanoscale matter. Energy in QDs can be optically transferred to neighboring QDs via optical near-field interactions¹¹. For instance, assume that two cubic quantum dots—QD_S and QD_L, where S and L refer to small and large, and whose side lengths are a and $\sqrt{2}a$, respectively—are located close to each other, as shown in Fig. 1a. Also, suppose that the energy eigenvalues for the quantized exciton energy level specified by quantum numbers (n_x, n_y, n_z) in QD_S are given by

$$E_{(n_x, n_y, n_z)} = E_B + \frac{\hbar^2 \pi^2}{2Ma^2} (n_x^2 + n_y^2 + n_z^2), \quad (1)$$

where E_B is the energy of the bulk exciton and M is the effective mass of the exciton. A resonance exists between the energy level of QD_S with quantum numbers (1,1,1) (denoted as S_1 in Fig. 1a) and that of QD_L with quantum numbers (2,1,1) (denoted as L_2 in Fig. 1a). Because of the steep localized electric field in the vicinity of QD_S and QD_L, an optical near-field interaction occurs between the two QDs. This interaction is denoted by U in Fig. 1a, and the steep electric field is schematically indicated by the orange triangle. Therefore, energy in S_1 can be optically transferred to L_2 and vice versa. Normally, such a transition would be dipole forbidden because L_2 has an even quantum number. This means that diffraction-limited far-field light irradiation from external systems can couple only to S_1 ³¹. In QD_L, optical-energy dissipation, described by Γ is faster than the near-field interaction, so the optical energy deposited into the (2,1,1) level can relax to the (1,1,1) level of QD_L (denoted by L_1).

Similar optical-excitation transfer via near-field interactions has been reported for various material systems, including CuCl QDs¹¹, InAs QDs³², CdSe QDs³³, and hybrid systems^{13,14}. Also, the theoretical foundations describing such phenomena, including the optimal near-field interaction that maximizes optical excitation transfer, have been developed by Sangu *et al.* in Ref. [11]. Because the primary focus of the present study is to investigate the possibility of synchronization, chaos, and random-number generation based on optical excitation transfer, we do not assume a particular implementation, as explained in the discussion section. In this study, based on experimental observations of energy transfer in ZnO nanorods³⁴, we assume a sublevel relaxation $\Gamma^{-1} = 10$ ps and radiative decay times for QD_S and QD_L of $\gamma_S^{-1} = 443$ ps and $\gamma_L^{-1} = 190$ ps, respectively, which are typical values for these parameters. The optical near-field interaction is given by $U^{-1} = 120$ ps. As shown in Fig. 1b, these parameter values lead to an evolution of populations involving the energy level L_1 , assuming an initial excitation at S_1 . These results clearly indicate that optical excitation transfer occurs from S_1 to L_1 .

When the lower level of QD_L (L_1) is occupied, the optical excitation in QD_S cannot transfer to that level in QD_L because of the state-filling effect¹¹. Optical pulsation based on optical energy transfer forms because of the architecture, where the state filling in L_1 is triggered by the radiation from S_1 with a delay with respect to the energy transfer from L_1 , as shown schematically in Fig. 1c. If QD_S is

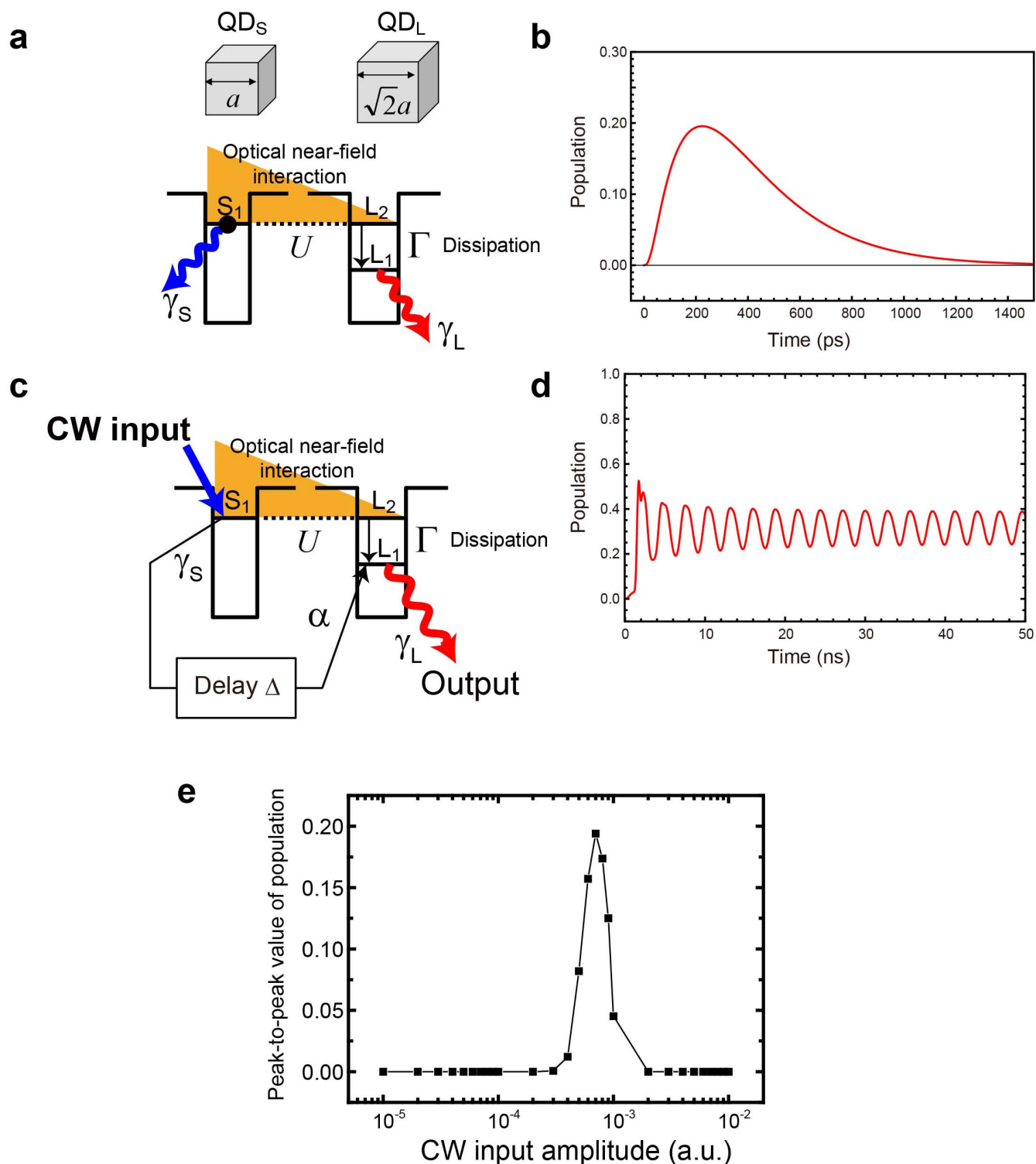


Figure 1 | Nanoscale optical pulser architecture. (a) Optical excitation transfer via near-field interactions between closely located smaller and larger quantum dots (QDs). (b) Example of optical excitation transfer from a smaller to a larger QD. (c) By incorporating a time delay, optical pulsation becomes possible. (d) Example of optical pulses induced by cw optical excitation. (e) Peak-to-peak value of pulsed population as a function of cw excitation amplitude.

irradiated with cw radiation, such triggers should occur periodically and continuously at constant intervals. In other words, a pulsed signal should result.

We describe the above dynamics by using a density matrix formalism. The radiative relaxation rates from S₁ and L₁ are denoted as γ_S and γ_L , respectively. The quantum master equation is³⁵



$$\begin{aligned} \frac{d\rho^{\text{NOP}}(t)}{dt} = & -\frac{i}{\hbar} [H_{\text{int}} + H_{\text{ext}}^{\text{CW}}(t) + H_{\Delta}(t), \rho^{\text{NOP}}(t)] \\ & + \sum_{i=S,L} \frac{\gamma_i}{2} \left[2R_i \rho^{\text{NOP}}(t) R_i^{\dagger} - R_i^{\dagger} R_i \rho^{\text{NOP}}(t) - \rho^{\text{NOP}}(t) R_i^{\dagger} R_i \right] \\ & + \frac{\Gamma}{2} [2S \rho^{\text{NOP}}(t) S^{\dagger} - S^{\dagger} S \rho^{\text{NOP}}(t) - \rho^{\text{NOP}}(t) S^{\dagger} S], \end{aligned} \quad (2)$$

where H_{int} represents the interaction Hamiltonian. Matrices R_i ($i = S, L$) are annihilation operators, which annihilate excitations in S_1 and L_1 , respectively, via radiative relaxations. Matrices R_i^{\dagger} ($i = S, L$) are creation operators given by transposes of matrices R_i . The matrix S is an annihilation operator that annihilates the excitation in L_2 via sublevel relaxations. The external Hamiltonian $H_{\text{ext}}^{\text{CW}}(t)$ represents the external cw optical excitation that populates the energy level S_1 of QD_S . This Hamiltonian is given by

$$H_{\text{ext}}^{\text{CW}}(t) = \text{CW}(R_{S_1}^{\dagger} + R_{S_1}), \quad (3)$$

where CW specifies the amplitude of the external cw radiation. The other external Hamiltonian $H_{\Delta}(t)$ represents radiation from the lower-energy level of QD_S , which affects the lower-energy level of QD_L or L_2 with a delay Δ . The Hamiltonian is given by

$$H_{\Delta}(t) = \alpha \rho_{S_1}^{\text{NOP}}(t - \Delta) (R_{L_1}^{\dagger} + R_{L_1}), \quad (4)$$

where $\rho_{S_1}^{\text{NOP}}(t)$ indicates the population of energy level S_1 and α indicates the coupling efficiency. In the original theory of the pulse-generating mechanism¹⁹, the delay line was represented by a different QD combination, giving another density matrix, and the overall dynamics was analyzed by solving the system of equations. In our simplified system, the delay is incorporated into Eq. (4).

In addition to the typical parameter values based on ZnO nanorods³⁴ introduced earlier, the coupling efficiency α is assumed to be 0.1, and the cw input amplitude is $\text{CW} = 0.0007$. Figure 1d shows the dynamics of the population of the lower level of QD_L (L_1) when the interdot optical near-field interaction $U^{-1} = 120$ ps and $\Delta = 1000$ ps. The population dynamics become pulsed, so we use this model for the following discussion. The period of the oscillating population is approximately 2849 ps, which gives a pulse frequency of approximately 351 MHz.

As reported in Ref. 19, no pulse train occurs for a cw excitation that is either too intense or too weak. Figure 1e shows the peak-to-peak population as a function of the cw input amplitude. Pulses occur for a cw input amplitude between approximately 0.0003 and 0.002.

Synchronization in nano-optics. We now consider irradiating the NOP with periodic external radiation, as shown schematically in Fig. 2a, and investigate whether synchronization is induced in the system. Consider the system subjected to an external periodic stimulus given by a sinusoidal perturbation:

$$H_T^{\text{Periodic}}(t) = A \sin(2\pi t/T) (R_{S_1}^{\dagger} + R_{S_1}), \quad (5)$$

where A and T are the amplitude and period of the periodic signal, respectively. By adding the Hamiltonian represented by Eq. (5) to Eq. (2), synchronization is characterized by solving

$$\begin{aligned} \frac{d\rho^{\text{Sync}}(t)}{dt} = & -\frac{i}{\hbar} [H_{\text{int}} + H_{\text{ext}}^{\text{CW}}(t) + H_{\Delta}(t) + H_T^{\text{Periodic}}(t), \rho^{\text{Sync}}(t)] \\ & + \sum_{i=S,L} \frac{\gamma_i}{2} \left[2R_i \rho^{\text{Sync}}(t) R_i^{\dagger} \right. \\ & \left. - R_i^{\dagger} R_i \rho^{\text{Sync}}(t) - \rho^{\text{Sync}}(t) R_i^{\dagger} R_i \right] \\ & + \frac{\Gamma}{2} [2S \rho^{\text{Sync}}(t) S^{\dagger} - S^{\dagger} S \rho^{\text{Sync}}(t) - \rho^{\text{Sync}}(t) S^{\dagger} S]. \end{aligned} \quad (6)$$

Let the parameters associated with the NOP be the same as those for the previous discussion. Let the period of the external signal be given by $T = 3500$ ps (or approximately 286 MHz) and $A = 0.0001$. The dashed and solid curves in Fig. 2b show the evolution of the population associated with the energy level L_1 with and without an external input. The oscillation period is synchronized with the input signal.

While maintaining the parameters associated with the NOP, Fig. 2c characterizes synchronization, or more specifically, the frequency of the external periodic signal that maximizes the spectral peak of the output signal. The dashed curve shows that the oscillating frequency is equal to the frequency of the external signal when the latter is between 244 and 500 MHz. For frequencies outside this locking range, the oscillating frequency is approximately 366 MHz, which is nearly equal to the oscillating frequency of the original NOP exposed to a cw input amplitude of 0.0008. This is consistent with the fact that the system is irradiated with cw radiation (0.0007) in addition to a periodic signal with amplitude 0.0001.

The locking range depends on the amplitude of the external irradiation. The solid, dot-dashed, and dotted curves in Fig. 2c indicate the locking range of synchronization for external irradiation amplitudes A of 0.0015, 0.0012, and 0.0008. The larger the amplitude of the external signal, the larger the bandwidth of synchronization. This property is similar to the mode-locking phenomenon observed in conventional lasers²¹ and other systems such as phase-locked loops³⁶. Furthermore, we find that an external stimulus with excessively large amplitude does not lead to synchronization; rather, the system is overwhelmed by optical energy and enters a static state.

Figure 2d considers the case in which the amplitude of the external periodic signal is maintained ($A = 0.0001$). Based on the results shown in Fig. 2d, we investigate the *sensitivity* of the NOP to the external system by changing the amplitude of the original cw pumping light. Recall that the locking range is between 244 and 500 MHz for $\text{CW} = 0.0007$ and an external periodic signal amplitude of 0.0001, respectively. The circles in Fig. 2d show the maximum spectrum obtained when the NOP is exposed to an external input divided by the maximum spectrum of the original pulser without the external input. We refer to this ratio as *sensitivity*, which is larger in the locking range. Moreover, it increases with decreasing cw-excitation power ($\text{CW} = 0.0006$), as indicated by the squares in Fig. 2d. In contrast, as shown by the triangles in Fig. 2d, greater cw excitation power ($\text{CW} = 0.0008$) leads to a decrease in sensitivity. Such properties are also similar to those of conventional mode-locked lasers and are referred to as the *dependence on relative excitation*³⁷.

These results clearly imply that the physics of near-field optical systems can lead to synchronized phenomena.

Chaos in nano-optics. Lasers are known to undergo chaotic oscillation when connected with a delayed feedback^{21,23}. Here, we address the question of whether chaos is possible in the subwavelength regime. In other words, we investigate the possibility of chaos evolving from nanoscale optical-energy transfer.

When an external delay line is added to the original NOP system, as shown schematically in Fig. 3a, the overall dynamics are described by solving

$$\begin{aligned} \frac{d\rho^{\text{Chaos}}(t)}{dt} = & -\frac{i}{\hbar} [H_{\text{int}} + H_{\text{ext}}^{\text{CW}}(t) + H_{\Delta}(t) + H_{\Delta_c}(t), \rho^{\text{Chaos}}(t)] \\ & + \sum_{i=S,L} \frac{\gamma_i}{2} \left[2R_i \rho^{\text{Chaos}}(t) R_i^{\dagger} \right. \\ & \left. - R_i^{\dagger} R_i \rho^{\text{Chaos}}(t) - \rho^{\text{Chaos}}(t) R_i^{\dagger} R_i \right] \\ & + \frac{\Gamma}{2} [2S \rho^{\text{Chaos}}(t) S^{\dagger} - S^{\dagger} S \rho^{\text{Chaos}}(t) - \rho^{\text{Chaos}}(t) S^{\dagger} S], \end{aligned} \quad (7)$$

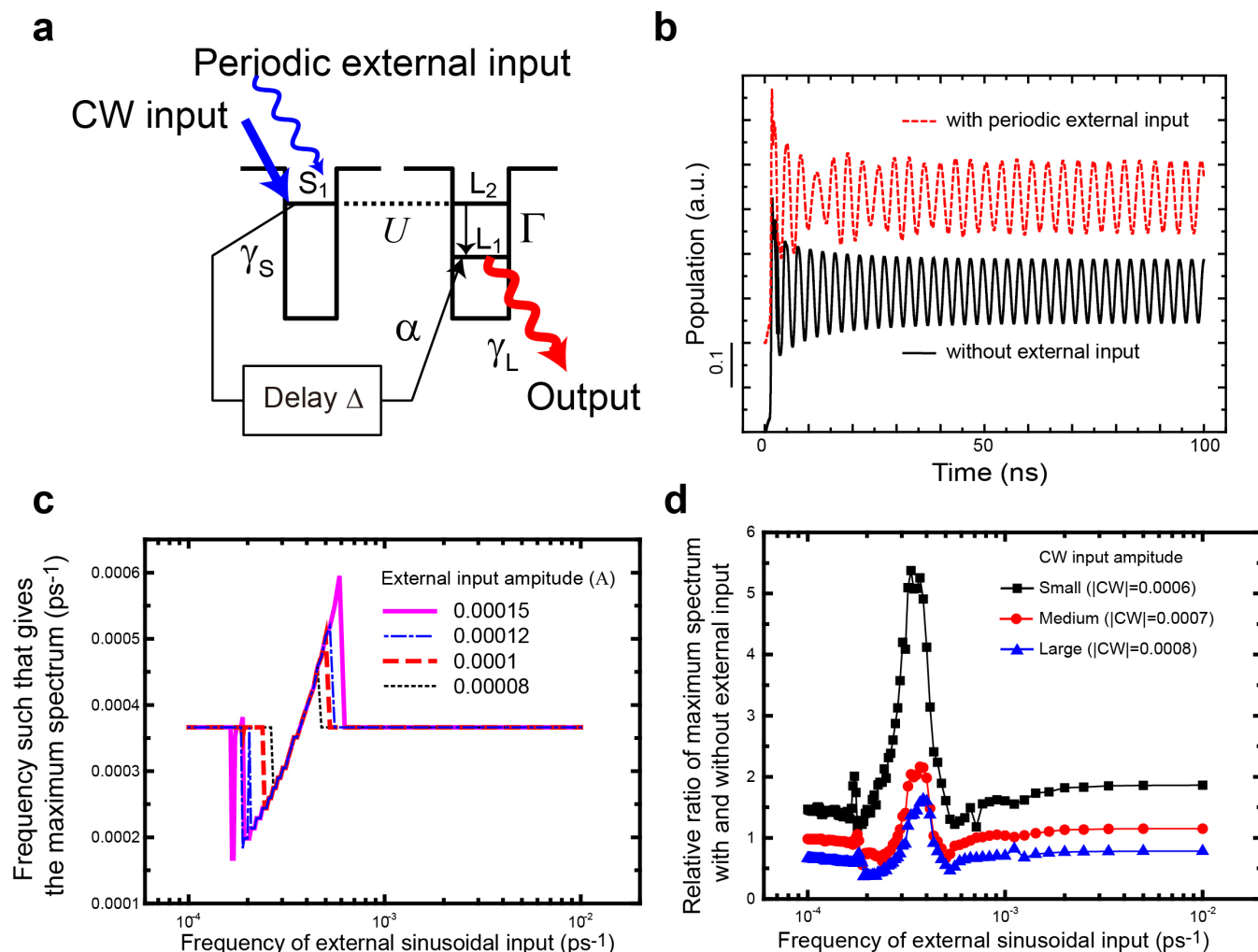


Figure 2 | Synchronization in NOP. (a) Schematic of system where NOP is subjected to external periodic signal. (b) Evolution of population with and without external input. (c) Synchronization of NOP to external input radiation. The bandwidth of the frequency locking increases with the amplitude of the external input. (d) Analysis of sensitivity of synchronization. Synchronization of weakly excited NOP is more sensitive to external input.

where the lower energy level L_2 of QD_L is fed back to the same energy level after time delay Δ . This effect is taken into account by adding the following external Hamiltonian to the original master equation:

$$H_{\Delta_C}(t) = -\alpha_C \rho_{L_1}^{\text{Chaos}}(t - \Delta_C) (R_{L_1}^\dagger + R_{L_1}), \quad (8)$$

where α_C and Δ_C are the coupling constant and timing delay, respectively. The quantity $\rho_{L_1}^{\text{Chaos}}(t)$ is the population of L_1 .

Parameter values for the systems are based on experimental observations from ZnO nanorods²⁸: $\gamma_S^{-1} = 443$ ps, $\gamma_L^{-1} = 190$ ps, $\Gamma^{-1} = 10$ ps, $\Delta = 3000$ ps, $\alpha = 0.1$, and $U^{-1} = 100$ ps. Figure 3b considers the situation in which delay lines with $\Delta_C = 1000$ ps are incorporated. Figure 3b shows populations when the coupling constant α_C is 0.001, 0.01, 0.02, and 0.05 (see Fig. 3b-i, 3b-ii, 3b-iii, and 3b-iv, respectively). Case (i) exhibits a periodic signal, whereas case (iv) converges to a constant population. Cases (ii) and (iii) exhibit more complicated dynamics.

To quantitatively characterize the dynamics, we evaluate the local maxima and minima of populations as a function of the coupling constant α_C . When the population dynamics is periodic or constant, there is no diversity in the local maxima and minima, whereas the maxima and minima take on a variety of values when the signal is chaotic²¹, which leads to bifurcations and chaos in signal trains.

The circles and crosses in Fig. 3c show the local maxima and minima, respectively, in the population between 500 000 and 1 000

001 ps. For α_C between 0.001 and approximately 0.0025, the variation in local maxima and minima is limited, whereas for $\alpha_C = 0.0025$, the variation is greater. From $\alpha_C > \sim 0.0025$ to nearly 0.009, the variation is again limited, whereas from approximately 0.009 to 0.0228, the variation increases again. Beyond $\alpha_C = 0.0228$, the local maxima and minima have similar values, so no oscillations occur. These results indicate that a system based on optical energy transfer exhibits bifurcation and chaotic behavior, which is evidence of chaos.

Another criterion satisfied by chaos is expressed by the maximal Lyapunov exponent (MLE)^{22,23}. Suppose that a trajectory exhibits chaotic behavior, which means that the final difference between two trajectories with a subtle initial difference δZ_0 grows exponentially. In other words, $|\delta Z(t)| \approx \exp(\lambda t) |\delta Z_0|$. The MLE is defined by

$$\lambda = \lim_{t \rightarrow \infty} \lim_{\delta Z_0 \rightarrow 0} \frac{1}{t} \ln \frac{|\delta Z(t)|}{|\delta Z_0|}, \quad (9)$$

where $\lambda \leq 0$ indicates no chaos^{20,22}. We used the FET1 code developed by Wolf *et al.*³⁸ to estimate the MLE from a time series. Figure 4a shows the calculated MLE as a function of the control parameter α_C . The results show that, for instance, λ is positive for $0.0148 < \alpha_C < 0.0225$. This particular range coincides with the range over which chaos occurs in the local maxima and minima (Fig. 3b). Also, for the 78 points in this particular regime, there are 26 points that satisfy the random-number conditions discussed below. This

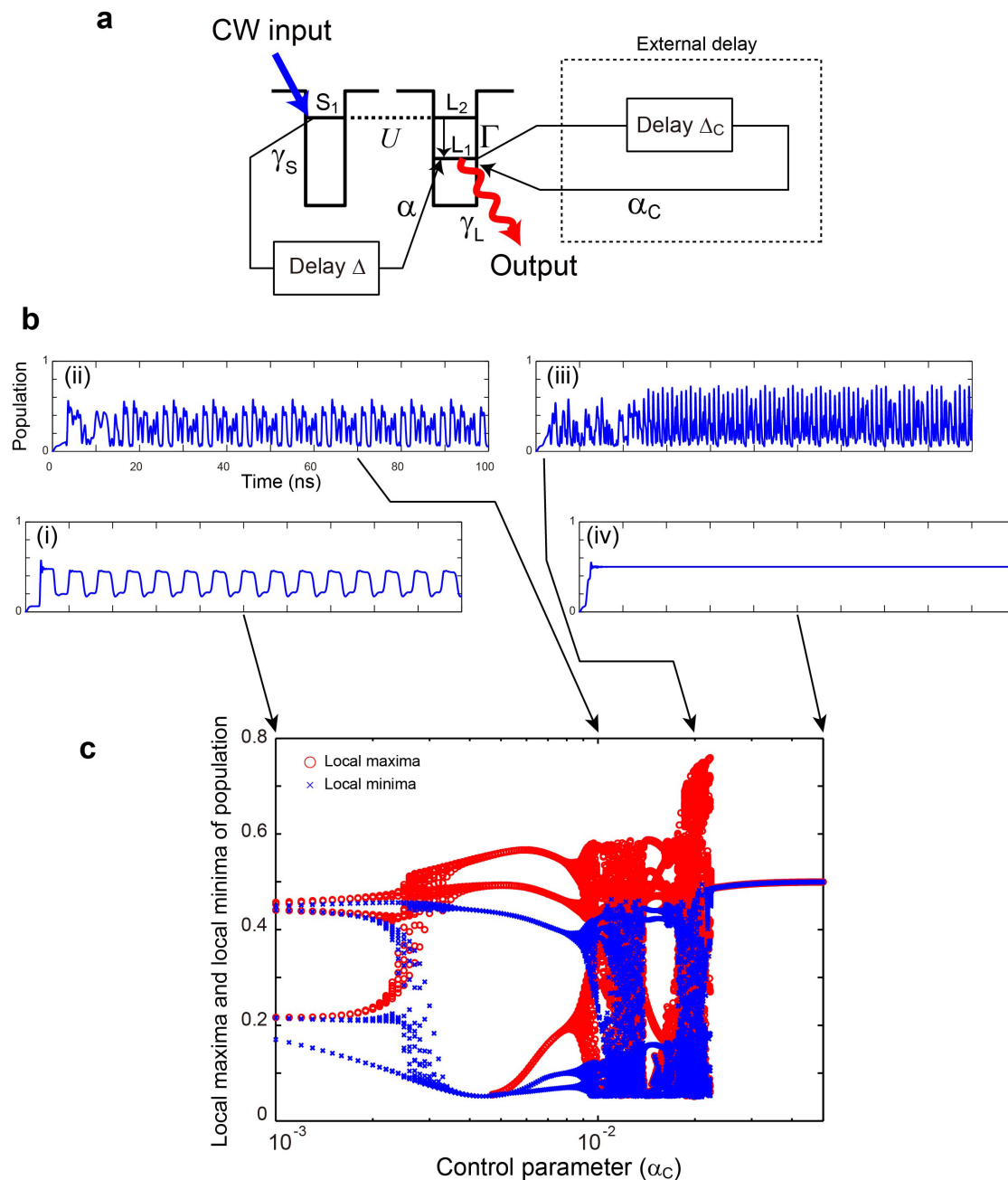


Figure 3 | Chaos in nano optical pulser. (a) Schematic of system where NOP is connected with external delay. (b) Evolution of population with four different parameters: (i) Periodic signal occurs. (ii) and (iii) Rather complex trains occur. (iv) Population is saturated at a certain level. (c) Local maxima and minima of populations as a function of control parameter α_C .

result clearly indicates that the physics of near-field optics allows for chaotic phenomena.

Random-number generation by nano-optics. Finally, to determine if NOPs can be used as RNGs, we use statistical-test suites to evaluate the randomness inherent in the chaotic dynamics of populations. Many well-known statistical-test suites, such as NIST 800-22^{39,40}, FIPS 140-2^{41,42}, and Diehard⁴³, are proposed in the literature. We use the FIPS 140-2 statistical-test suite (hereafter the “FIPS test”) because it is the most simple and user-friendly test suite. It offers the following four basic tests: (i) *the monobit test*, (ii) *poker test*, (iii) *run test*, and (iv) *long-run test*. Because of its simplicity, it has been used to supplement RNGs in many hardware implementations^{44,45}.

Kim *et al.* recalculated the requirement of the FIPS test for a 2500-bit sequence to give an identical significance level $\alpha = 10^{-2}$, which is a

commonly used value in cryptography. This significance level is defined as the probability of a false rejection of the null hypothesis in a statistical test. In other words, it is the probability that a perfect RNG generates a “failure” sequence. A summary of the “improved FIPS test”, which we use in the analysis, is available in the supplementary information, and further details may be found in Refs. [46] and [47].

We obtained temporal signals from $t = 0$ to $t = 1\,000\,000$ for each member of the population with a resolution of 1 ps. The population at each time increment is converted to a 16-bit-precision fixed-point number and the lowest significant bit is used for a binary value. In other words, 1 000 001 binary bits are obtained from a single run. Ignoring the initial time range from $t = 0$ to 100 000, the total length is reduced to 900 000 bits. The signals are then divided into increments of 2500 (i.e., 2500 ps duration); the number of 2500-bit bin-

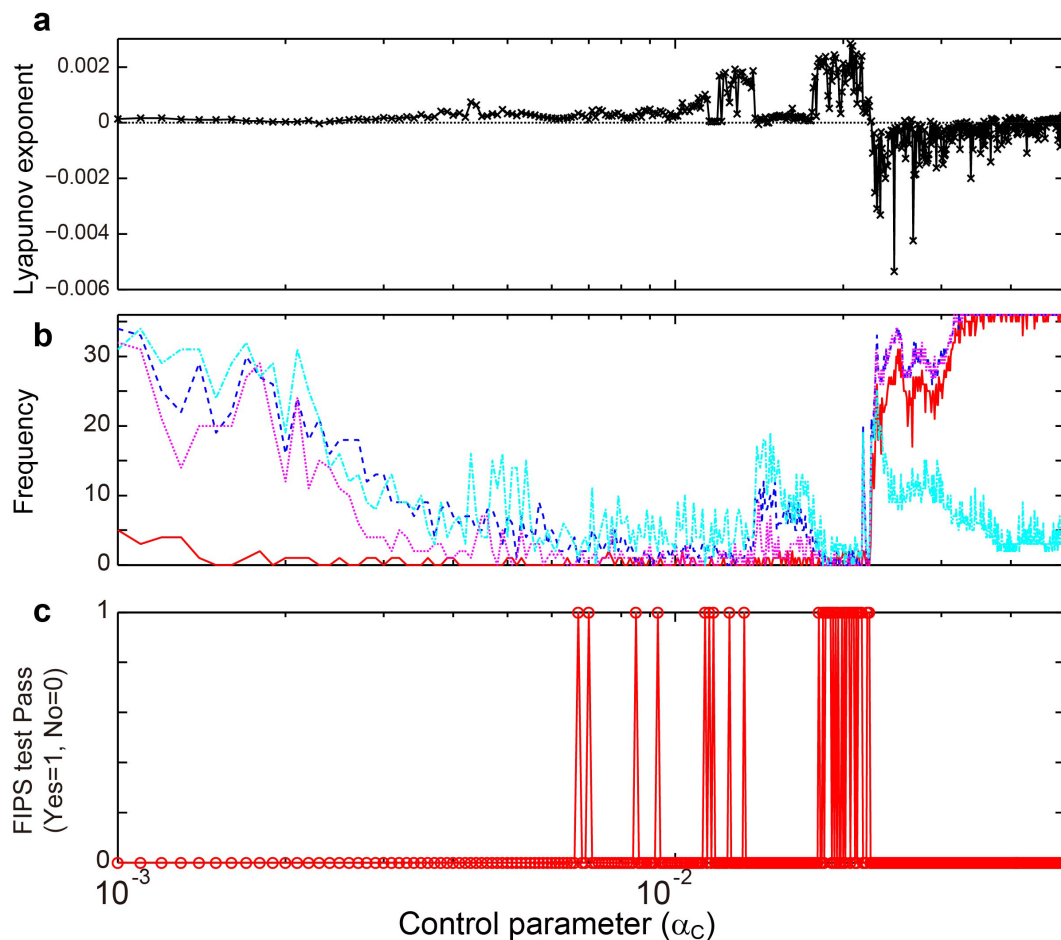


Figure 4 | Chaos and random-number generation in nanosized system. (a) Lyapunov exponents as a function of control parameter α_C . We used the following FET1 parameters, dimension = 7, delay = 10, evolve = 1, $\text{Scale}_{\min} = 10^{-5}$, and $\text{Scale}_{\max} = 0.7$. The Lyapunov exponent $\lambda \leq 0$ indicates no chaos. The dotted line shows $\lambda = 0$ (b) Analysis of properties of random numbers based on the improved FIPS test. (c) Schematic of cases that pass the improved FIPS test. For all 35 cases that pass the improved FIPS test, the corresponding Lyapunov exponent is positive [see panel (a)].

ary-signal sets is 36. By subjecting all 36 sets to the improved FIPS test described above, we can determine whether they qualify as random numbers. If all bit sets pass the test or if the number of failures is at most two for each test, then the answer is yes. Two failures are deemed acceptable in this particular case because the acceptable interval is determined to be in the 99.73% range of normal distribution. For details, see section 4.2.1 of Ref. [39].

The solid, dashed, dotted, and dot-dashed curves in Fig. 4b show the frequency of the FIPS-test failure for the monobit, poker, run, and long-run tests, respectively, as a function of the control parameter α_C . The FIPS test is passed in a total of 35 cases, which used the following control parameters: 0.0058, 0.0061, 0.0076, 0.0084, 0.0104, 0.0106, 0.0108, 0.0116, 0.0124, 0.0172, 0.0175, 0.0177–0.0180, 0.0181, 0.0183, 0.0185, 0.0187, 0.0190, 0.0192, 0.0194–0.0196, 0.0198–0.0200, 0.0202, 0.0204–0.0207, and 0.0212–0.0214. The evaluation was based on an α_C interval of 10^{-3} , as shown in Fig. 4c. Moreover, for all control parameters for which the improved FIPS test was passed, the corresponding MLEs are positive (see Fig. 4a).

The chaotic signal behaves differently depending on other parameters. Focusing on the external delay, which plays a crucial role in generating chaos, Fig. 5 characterizes the pass–no-pass results of the FIPS test for time delay Δ_C ranging from 0 to 3000 ps. The number of cases that pass the FIPS test is given on the right side of Fig. 5 (where $\Delta_C = 200$ ps yields the maximum number of cases that pass the FIPS test). From this analysis, we conclude that chaotic phenomena based on near-field local optical interactions can form the basis of ultra-small RNGs.

Discussion

As mentioned in the introduction, complex oscillatory dynamics are observed in various systems in the real world. Our study indicates that local nanoscale interactions may lead to synchronization, chaos, and even random-number generation. The optical near-field interactions examined in this study contain the “necessary conditions” required for generating complex oscillatory dynamics; that is, nanoscale optical near-field interactions generate physical properties that are functionally equivalent to those observed in other physical systems exhibiting complex dynamics. Moreover, using the optical near field yields the additional benefit of overcoming the diffraction limit of light.

However, several important unresolved issues remain that complicate the science of near-field optics. The function of delay, in particular, needs more study, both theoretically and experimentally. Optical excitation transfer depends on the architecture of nanostructures as well as on the population of energy levels therein. For example, in Ref. 48, Naruse *et al.* discusses topology-dependent, autonomous optical excitation transfer, and how an excitation “waits” in a multi-quantum-dot system. In addition, the coupling between semiconductor quantum dots and nanocavities has been intensively studied^{49–51}. These investigations are analogous to the present work in that they consider how to realize further functionalities by using near-field optics, but we need to be careful because the notion of “cavity” implies diffraction-limited macroscale entities. We will thus conduct further investigations into the theoretical foundation of delay in near-field optics. Experimentally, on the other

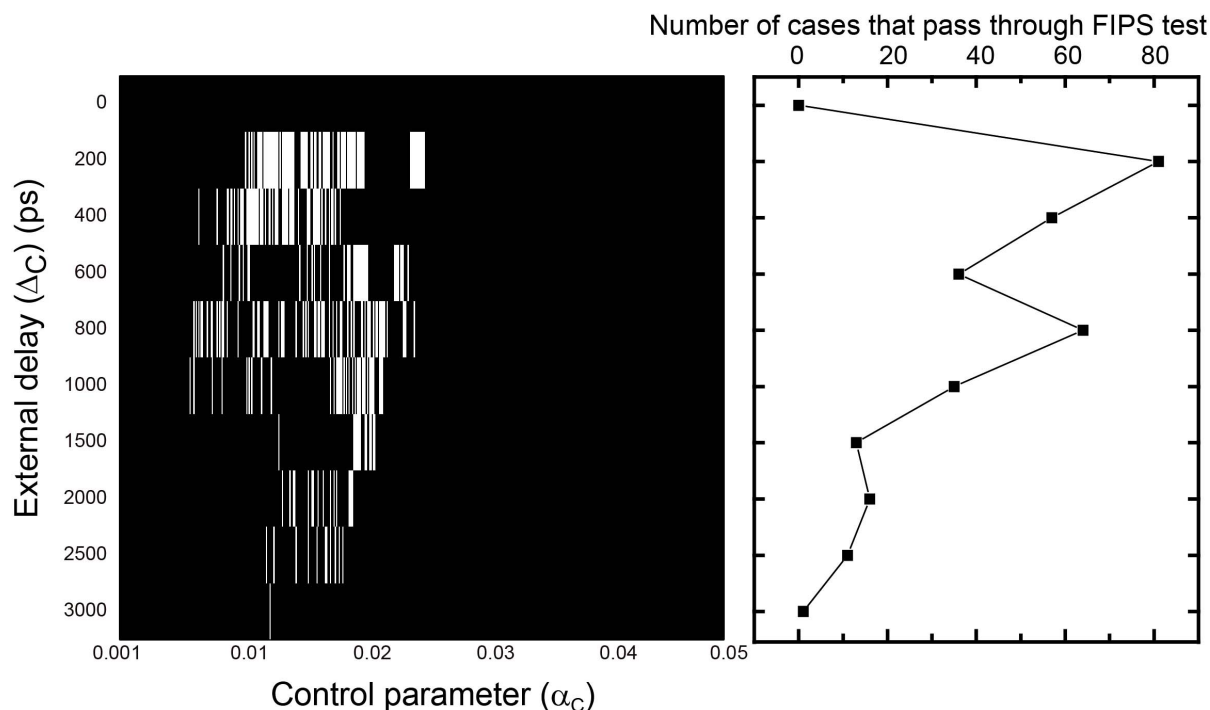


Figure 5 | Distributions of cases that pass the improved FIPS test. The randomness observed in output populations depends on the external delay Δ_C and control parameter α_C . The squares at the right give the number of case that pass the improved FIPS test as a function of external delay.

hand, Nomura *et al.* demonstrated a chain of colloidal CdSe QDs⁵². Also, QD arrangements of graded size have been demonstrated by Kawazoe *et al.*⁵³ and Franzl *et al.*⁵⁴, which could provide the basic resources to implement delay functions¹⁹. To fabricate devices in the future, fluctuations in size, layout, etc., in the quantum nanostructure may be of concern, and tolerance and robustness would need to be clarified. A step in this direction has already been taken by Naruse *et al.*, who built a stochastic model to systematically characterize optical excitation transfer in multilayer InAs QDs formed by molecular beam epitaxy⁵⁵.

Other unique optical near-field processes can be considered. For example, the hierarchical properties of the optical near field means that near-field interactions behave differently depending on the length scale involved⁵⁶. This property is notably different from that encountered in conventional optics and photonics. Another interesting topic is the impact of the hierarchical properties of optical near fields on synchronization and chaos. As techniques to fabricate nanophotonic devices continue to be developed, experimental verification and fabrication of practical devices are important routes for future work^{13–16,29,30,34,55}.

1. Brown, E. N., Kass, R. E. & Mitra, P. P. Multiple neural spike train data analysis: state-of-the-art and future challenges. *Nat. Neurosci.* **7**, 456–61 (2004).
2. Takahashi, J. S. & Zatz, M. Regulation of circadian rhythmicity. *Science* **217**, 1104–1111 (1982).
3. Aono, M., Hirata, Y., Hara, M. & Aihara, K. Amoeba-based chaotic neurocomputing: combinatorial optimization by coupled biological oscillators. *New Generation Comput.* **27**, 129–157 (2009).
4. Hirata, Y., Aono, M., Hara, M. & Aihara, K. Spontaneous mode switching in coupled oscillators competing for constant amounts of resources. *Chaos* **20**, 013117 (2010).
5. Knuth, D. *The Art of Computer Programming*. (Addison-Wesley, Massachusetts, 1997).
6. Uchida, A. *et al.* Fast physical random bit generation with chaotic semiconductor lasers. *Nat. Photonics* **2**, 728–732 (2008).
7. Meteopolis, N. & Ulam, S. The Monte Carlo method. *J. Am. Stat. Assoc.* **44**, 335–341 (1949).
8. Naruse, M. *et al.* Spatiotemporal dynamics in optical energy transfer on the nanoscale and its application to constraint satisfaction problems. *Phys. Rev. B* **86**, 125407 (2012).

9. Aono, M. *et al.* Amoeba-inspired nanoarchitectonic computing: solving intractable computational problems using nanoscale photoexcitation transfer dynamics. *Langmuir* **29**, 7557–7564 (2013).
10. Kim, S.-J., Naruse, M., Aono, M., Ohtsu, M. & Hara, M. Decision maker based on nanoscale photo-excitation transfer. *Sci. Rep.* **3**, 2370 (2013).
11. Sangu, S., Kobayashi, K., Shojiguchi, A., Kawazoe, T. & Ohtsu, M. Excitation energy transfer and population dynamics in a quantum dot system induced by optical near-field interaction. *J. Appl. Phys.* **93**, 2937 (2003).
12. Zurita-Sánchez, J. R. & Novotny, L. Multipolar interband absorption in a semiconductor quantum dot. I. Electric quadrupole enhancement. *J. Opt. Soc. Am. B* **19**, 1355–1362 (2002).
13. Cox, J. D., Singh, M. R., Gumbs, G., Anton, M. A. & Carreno, F. Dipole-dipole interaction between a quantum dot and a graphene nanodisk. *Phys. Rev. B* **86**, 125452 (2012).
14. Racknor, C., Singh, M. R., Zhang, Y., Birch, D. J. S. & Chen, Y. Methods, energy transfer between a biological labeling dye and gold nanorods. *Appl. Fluoresc.* **2**, 015002 (2014).
15. Naruse, M., Tate, N., Aono, M. & Ohtsu, M. Information physics fundamentals of nanophotonics. *Rep. Prog. Phys.* **76**, 056401 (2013).
16. Pistol, C., Dwyer, C. & Lebeck, A. R. Nanoscale optical computing using resonance energy transfer logic. *IEEE Micro* **28**, 7–18 (2008).
17. Haykin, S. *Communication Systems*. (John Wiley & Sons, New York, 2001).
18. Shojiguchi, A., Kobayashi, K., Sangu, S., Kitahara, K. & Ohtsu, M. Superradiance and dipole ordering of an N two-level system interacting with optical near fields. *J. Phys. Soc. Jpn.* **72**, 2984–3001 (2003).
19. Naruse, M., Hori, H., Kobayashi, K., Kawazoe, T. & Ohtsu, M. Optical pulsation mechanism based on optical near-field interactions. *Appl. Phys. B* **102**, 717–723 (2011).
20. Cencini, M., Cecconi, F. & Vulpiani, A. *Chaos from simple models to complex systems*. (World Scientific, Singapore, 2009).
21. Ohtsubo, J. *Semiconductor Lasers, Stability, Instability and Chaos*. (Springer, Heidelberg, 2013).
22. Uchida, A. *Optical Communication with Chaotic Lasers*. (Wiley-VCH, Weinheim, 2012).
23. Haken, H. *Light, Volume 2 Laser Light Dynamics*. (North-Holland Physics Publishing, Amsterdam, 1985).
24. VanWiggeren, G. D. & Roy, R. Communication with chaotic lasers. *Science* **279**, 1198–1200 (2011).
25. Argyris, A. *et al.* Chaos-based communications at high bit rates using commercial fibre-optic links. *Nature* **438**, 343–346 (2005).
26. Kanter, I., Aviad, Y., Reidler, I., Cohen, E. & Rosenbluh, M. An optical ultrafast random bit generator. *Nat. Photonics* **4**, 58–61 (2010).
27. Albert, F. *et al.* Observing chaos for quantum-dot microlasers with external feedback. *Nat. Commun.* **2**, 366 (2011).
28. Ohtsu, M. & Hori, H. *Near-Field Nano-Optics*. (Kluwer Academic/Plenum Publisher, New York, 1999).



29. Kawazoe, T., Mueed, M. A. & Ohtsu, M. Highly efficient and broadband Si homojunction structured near-infrared light emitting diodes based on the phonon-assisted optical near-field process. *Appl. Phys. B* **104**, 747–754 (2011).
30. Kawazoe, T., Ohtsu, M., Akahane, K. & Yamamoto, N. Si homojunction structured near-infrared laser based on a phonon-assisted process. *Appl. Phys. B* **107**, 659–663 (2012).
31. Naruse, M., Kawazoe, T., Sangu, S., Kobayashi, K. & Ohtsu, M. Optical interconnects based on optical far- and near-field interactions for high-density data broadcasting. *Opt. Express* **14**, 306–313 (2006).
32. Akahane, K. *et al.* Energy transfer in multi-stacked InAs quantum dots. *Jpn. J. Appl. Phys.* **50**, 04DH05 (2011).
33. Somers, R. C., Snee, P. T., Bawendi, M. G. & Nocera, D. G. Energy transfer of CdSe/ZnS nanocrystals encapsulated with rhodamine-dye functionalized poly(acrylic acid). *J. Photochem. Photobiol. A* **248**, 24 (2012).
34. Yatsui, T., Jeong, H. & Ohtsu, M. Controlling the energy transfer between near-field optically coupled ZnO quantum dots. *Appl. Phys. B* **93**, 199–202 (2008).
35. Carmichael, H. J. *Statistical Methods in Quantum Optics 1*. (Springer-Verlag, Berlin, 1999).
36. Li, P., Silveira, L. M. & Feldmann, P. (eds.) *Simulation and Verification of Electronic and Biological Systems*. (Springer, Heidelberg, 2011).
37. Lang, R. Injection locking properties of a semiconductor laser. *IEEE J. Quantum Electron.* **18**, 976–983 (1982).
38. Wolf, A., Swift, J. B., Swinney, H. L. & Vastano, J. A. Determining Lyapunov exponents from a time series. *Physica D* **16**, 285–317 (1985).
39. Ruhin, A. *et al.* *A Statistical Test Suite for Random and Pseudorandom Number Generators for Cryptographic Applications*. Computer Security National Institute of Standards and Technology. <http://csrc.nist.gov/groups/ST/toolkit/rng/documents/SP800-22rev1a.pdf>, (2010) (Date of access:2/7/2014).
40. Kim, S.-J., Umeno, K. & Hasegawa, A. Corrections of the NIST statistical test suite for randomness. *Cryptography* ePrint Archive 2004/018 (2004).
41. FIPS PUB 140-2. Security Requirements for Cryptographic Modules. U.S. Department of Commerce, Technology Administration, National Institute of Standards and Technology. <http://csrc.nist.gov/publications/fips/fips140-2/fips1402.pdf>, (2001) (Date of access:2/7/2014).
42. Kim, S.-J., Umeno, K. & Hasegawa, A. FIPS 140-2 statistical test suite has inappropriate significance levels. *ISM Report on Research and Education* **17**, 326–327 (2003).
43. The Marsaglia Random Number CDROM including the Diehard Battery of Tests of Randomness. <http://stat.fsu.edu/pub/diehard/>, (1995) (Date of access:2/7/2014).
44. Hasegawa, A., Kim, S.-J. & Umeno, K. IP core of statistical test suite of FIPS PUB 140-2. *Proc. of IP Based SoC Design* 2003, 111–114 (2003).
45. Lee, J. S., Choi, P., Kim, S.-J., Choi, B. D. & Kim, D. K. Built-in hardware random number test module for physical unclonable functions. *NOLTA* **5**, 101–112 (2014).
46. Ikezoe, Y., Kim, S.-J., Yamashita, I. & Hara, M. Random number generation for two-dimensional crystal of protein molecules. *Langmuir* **25**, 4293–4297 (2009).
47. Ikezoe, Y., Kim, S.-J., Kim, D., Lee, S. B. & Hara, M. Nanoscale shuffling in a template-assisted self-assembly of binary colloidal particles. *J. Nanosci. Nanotechnol.* **12**, 2934–2938 (2012).
48. Naruse, M. *et al.* Autonomy in excitation transfer via optical near-field interactions and its implications for information networking. *Nano Commun. Net.* **2**, 189–195 (2011).
49. Reitzenstein, S. *et al.* Coherent photonic coupling of semiconductor quantum dots. *Opt. Lett.* **31**, 1738–1740 (2006).
50. Laucht, A. *et al.* Mutual coupling of two semiconductor quantum dots via an optical nanocavity. *Phys. Rev. B* **82**, 075305 (2010).
51. Albert, F. *et al.* Microcavity controlled coupling of excitonic qubits. *Nat. Commun.* **4**, 1747 (2013).
52. Nomura, W., Yatsui, T., Kawazoe, T., Naruse, M. & Ohtsu, M. Structural dependency of optical excitation transfer via optical near-field interactions between semiconductor quantum dots. *Appl. Phys. B* **100**, 181 (2010).
53. Kawazoe, T., Kobayashi, K. & Ohtsu, M. Optical nanofountain: A biomimetic device that concentrates optical energy in a nanometric region. *Appl. Phys. Lett.* **86**, 103102 (2005).
54. Franzl, T., Klar, T. A., Schietinger, S., Rogach, A. L. & Feldmann, J. Exciton recycling in graded gap nanocrystal structures. *Nano Lett.* **4**, 1599 (2004).
55. Naruse, M. *et al.* Analysis of optical near-field energy transfer by stochastic model unifying architectural dependencies. *J. Appl. Phys.* **115**, 154306 (2014).
56. Naruse, M., Inoue, T. & Hori, H. Analysis and synthesis of hierarchy in optical near-field interactions at the nanoscale based on angular spectrum. *Jpn. J. Appl. Phys.* **46**, 6095–6103 (2007).

Acknowledgments

This work was supported in part by the Core-to-Core Program, A. Advanced Research Networks from the Japan Society for the Promotion of Science.

Author contributions

M.N. and S.-J.K. directed the project; M.N. and S.-J.K. designed systems; M.N. and S.-J.K. analyzed the data; M.A., H.H. and M.O. discussed physical modeling; M.N. and S.-J.K. wrote the paper.

Additional information

Supplementary information accompanies this paper at <http://www.nature.com/scientificreports>

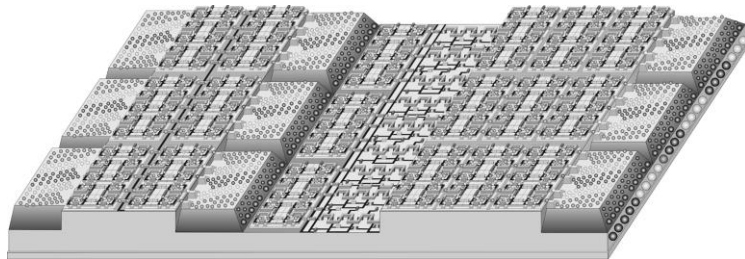
Competing financial interests: The authors declare no competing financial interests.

How to cite this article: Naruse, M., Kim, S.-J., Aono, M., Hori, H. & Ohtsu, M. Chaotic oscillation and random-number generation based on nanoscale optical-energy transfer. *Sci. Rep.* **4**, 6039; DOI:10.1038/srep06039 (2014).



This work is licensed under a Creative Commons Attribution-NonCommercial-NoDerivs 4.0 International License. The images or other third party material in this article are included in the article's Creative Commons license, unless indicated otherwise in the credit line; if the material is not included under the Creative Commons license, users will need to obtain permission from the license holder in order to reproduce the material. To view a copy of this license, visit <http://creativecommons.org/licenses/by-nc-nd/4.0/>

**[II] PRESENTATIONS
IN
INTERNATIONAL CONFERENCES**



The p-n homojunction GaP LED fabricated by dressed photon phonon assisted annealing

Jun Hyoung Kim¹, Tadashi Kawazoe^{1,2}, and Motoichi Ohtsu^{1,2}

¹Department of Electrical Engineering and Information Systems, Graduate School of Engineering, The University of Tokyo

²Nanophotonic Research Center, Graduate School of Engineering, The University of Tokyo

E-mail address: kimjh@nanophotonics.t.u-tokyo.ac.jp

Abstract: As a new solution to the so-called green-gap problem, we fabricated a GaP LED using dressed-photon–phonon assisted annealing. As a result, we increased the light emission intensity in an energy band above 2.33 eV. In this paper, we will introduce the results and discuss this light emission phenomenon.

The bandgap energy, E_g , of GaP is 2.26 eV, which corresponds to a wavelength of 546 nm. Thus, GaP could be regarded as a candidate material for solving the so-called green-gap problem [1]. However, the light emission efficiency of GaP is known to be extremely low, since GaP is an indirect-transition-type semiconductor. To overcome the limitations originating from the transition type, we adopted a dressed-photon–phonon (DPP) assisted annealing method, which uses simultaneous forward-bias current and laser irradiation to perform annealing. As a result, we increased the light emission intensity in an energy band higher than E_g [2].

We used an S-doped n-type GaP wafer, and Zn ions were implanted into this wafer to form a p–n junction. Next, a forward bias current of 9.9 A/cm² was applied to the device, while irradiating it with 532 nm wavelength (2.33eV) laser light with an intensity of 35.4 W/cm². The laser irradiation and current generated localized heating, causing random diffusion of the dopant. During this random change, if a local region takes a certain impurity distribution suitable for generating DPPs, electrons could couple with coherent multimode phonons in that region, and the limitation due to the wavenumber conservation law would be relaxed, thus enabling stimulated emission via DPP levels, even in an indirect-transition-type semiconductor. This means the applied energy would turn into photons, not heat. As a result, the diffusion rate around this region would be reduced. After this process proceeds for a sufficient amount of time, an LED that emits light with a wavelength of 532 nm can be fabricated, since the probabilities of stimulated emission and spontaneous emission are proportional to each other.

Fig. 1 shows the rate of increase of the EL spectral intensity. The red curve shows that light emission with an energy higher than E_g was significantly increased after DPP-assisted annealing. To verify that surface damage due to implantation did not affect this result, we carried out the same process on a thermally annealed sample. The blue curve shows the result, which is similar to the red curve. By performing experiments without irradiation light (Fig. 1, green curve), we also demonstrated the effectiveness of the DPP-assisted annealing.

Considering the principle of the DPP-assisted annealing method, the EL spectrum is expected to show some dependence on the process conditions. Using the same device and experimental set-up, we checked the correlation between the EL spectrum and the DPP-assisted annealing conditions. Fig. 2 shows the result. The x-axis and y-axis denote the current and the laser intensity during annealing, respectively. Numbers expressed as a percentage denote the rate of increase of the EL spectral intensity at 532 nm (2.33 eV). The result shows that the rate of increase becomes higher as the conditions become closer to those of the blue dashed line in Fig. 2. This can be interpreted as follows: In region A in Fig. 2, the number of surplus photons increases as the conditions deviate from those of the blue dashed line. Those surplus photons generate local heat through nonradiative relaxation. In region B, the number of surplus electrons increases, and those electrons also generate heat locally through scattering. In both cases, the suppression of heat generation through stimulated emission would be weakened. Thus, this surplus energy inhibits the formation of the optimum impurity distribution. As a result, we

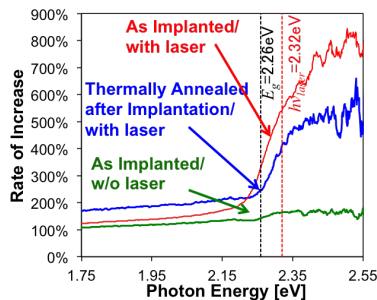


Fig. 1 Rate of increase of spectral intensity.

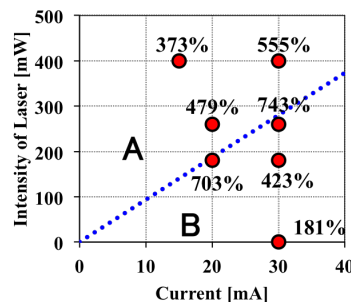


Fig. 2 Dependence of GaP LED output on processing conditions.

can conclude that there is an optimal ratio (blue dashed line) between the number of electrons and photons during the DPP-assisted annealing process.

This work was partially supported by a Grant-in-Aid for Scientific Research (B) (No. 24360023) of MEXT and the Core-to-Core Program of JSPS.

[1] S. Nakamura, MRS bulletin **34**, 101-107 (2009).

[2] J. H. Kim, T. Kawazoe, M. Ohtsu, Advances in Optical Technologies (2014). In press

Contr 1-5 / ST 2

Visible Si-LED with lateral p-n homojunction

Maiku Yamaguchi, Tadashi Kawazoe, Takashi Yatsui, Motoichi Ohtsu

Dept. Eng. Univ. Tokyo

E-mail address: yamaguchi@nanophotonics.t.u-tokyo.ac.jp

Abstract: We developed a silicon light emitting diode (Si-LED) that emits in the visible range using a dressed-photon-phonon (DPP) assisted annealing method. To solve the problem of the light extraction efficiency, which is essential for visible Si-LEDs, we fabricated the LED structure with a lateral p-n homojunction. By applying DPP-assisted annealing, involving injecting a forward current into the p-n homojunction while irradiating it with visible laser light, we realized a Si-LED with EL emission in the blue range via a phonon-assisted process.

Fabricating light emitters with silicon (Si) is a challenge because of its low light emission efficiency derived from its indirect-type band gap. Many researchers have been worked on improving the emission of Si, for example, by using quantum confinement effects in nanostructures, such as porous-Si [1] or quantum dots [2]. However, the efficiency of electroluminescence (EL) from those emitters is still low due to the difficulty of injecting current into such nanostructures. To solve this problem, the authors have been developing light emitting diodes (LED) using bulk Si which have achieved an EL efficiency of 15 % by using an annealing method assisted by a dressed-photon-phonon (DPP), which is a coupled state of an electron-hole pair and a phonon [3]. In this method, we illuminate a Si p-n homojunction with laser light while injecting a forward current. After annealing, DPPs are generated in the p-n homojunction. DPPs cause an optical process, called a phonon-assisted process, in which the wavenumber supplied from phonons via DPPs enables the electron-hole pair to recombine radiatively. The photon energy of the light emitted by the LED after DPP-assisted annealing is determined not by the band gap energy (E_g) of Si but by the photon energy of the laser light irradiated during annealing. By utilizing this property, we have fabricated a visible Si-LED by irradiating it with visible light [4].

However, an intrinsic problem with visible Si-LEDs is the low light extraction efficiency due to absorption loss. Since semiconductors absorb light with a higher photon energy than E_g , visible photons emitted by the p-n homojunction in a Si-LED are absorbed before they can be extracted from the device. To overcome this issue, we fabricated a device with a lateral p-n homojunction, as illustrated in the inset of Fig. 1. In this structure, the absorption loss is drastically reduced because the p-n homojunction is formed in the surface of the Si-LED. We deposited Cr/Pt layers serving as electrodes on an SOI substrate. After B-doped Si nanocrystals were spin-coated on the substrate, it was irradiated with pulsed laser light with a wavelength of 527 nm and a power density of 4 J/cm²/pulse in order to melt the nanocrystals and form a B-doped p-layer. Then, we conducted DPP-assisted annealing by applying a forward bias voltage of 15 V and irradiating the device with 405 nm CW laser light (photon energy $h\nu = 3.06$ eV) with an intensity of 2.0 W/cm².

Fig. 1 shows the EL spectra of the Si-LED obtained before annealing, and 30 and 90 minutes after starting annealing. Even before DPP-assisted annealing, blue light emission occurred at around 3 eV, corresponding to the direct transition in Si. This light emission could be measured owing to the high light extraction efficiency of the lateral p-n junction structure. Furthermore, we succeeded in enhancing the EL emission in the blue band (~3 eV) by increasing the annealing time. The selective EL enhancement around $h\nu = 3.06$ eV shows that the emission was via a phonon-assisted process caused by DPPs.

The authors thank Teijin Co. Ltd. for providing the NanoGram® Si ink. This research was supported by a Grant-in-Aid for the JSPS Core-to-Core Program, A. Advanced Research Networks.

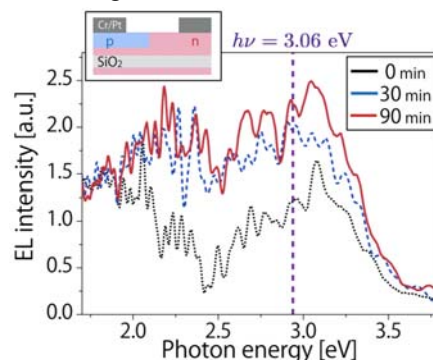


Fig. 1. EL emission spectra of Si-LED obtained before (black dotted line) and 30 minutes (blue dashed line) and 90 min. (red solid line) after starting DPP assisted annealing

[1] L.T. Canham, Appl. Phys. Lett., **57**, 1046-1048 (1990).

[2] D. Kovalev, H. Heckler, M. Ben-Chorin, G. Polisski, M. Schwartzkopff, and F. Koch, Phys. Rev. Lett., **81**, 2803-2806 (1998).

[3] T. Kawazoe, M.A. Mueed, and M. Ohtsu, Appl. Phys. B, **104**, 747-754 (2011).

[4] M.A. Tran, T. Kawazoe, and M. Ohtsu, Appl. Phys. A, **115**, 105-111 (2014).

Contr 1-6 / ST 3

Evaluation of optical gain using dressed photons in a Si laser waveguide

Hajime Tanaka¹, Tadashi Kawazoe^{1,2}, Motoichi Ohtsu^{1,2}, Kouichi Akahane³, Naokatsu Yamamoto³
¹Dept. Eng., The Univ. of Tokyo, ²International Center for Nano Electron and Photon Technology, The Univ. of Tokyo, ³NICT
 tanaka@nanophotonics.t.u-tokyo.ac.jp

Abstract: We used an SOI substrate to fabricate light waveguides and evaluated the optical gain. Optical gain is proportional to injected current density and is expected to be larger when the incident light power is low. By adopting an SOI substrate, the transparent current density was reduced, which contributed to a lower leakage current.

We successfully developed a Si LED with a homojunction for the first time in the world, as well as a Si laser operating in the 1.3 μm wavelength band and capable of continuous oscillation at room temperature [1]. Since these Si light emitting devices emit light whose photon energy is lower than the bandgap energy of Si, there is little absorption loss, which allows the threshold current density of a Si laser to be drastically reduced. We have designed laser waveguides with a high optical confinement factor, allowing us to realize a Si laser with a very low threshold current density, for example, as low as 40 A/cm^2 [2].

To realize highly efficient laser oscillation, we adopted a method in which we fabricate laser waveguides with a small width after acquiring high-efficiency light emission from waveguides with a large width using an SOI substrate. As a first step, we fabricated light waveguides (Fig. 1) using an SOI substrate, and confirmed the existence of optical gain by generating dressed-photons efficiently at a p-n junction interface. To measure the gain coefficient, the edge of the light waveguide was illuminated with laser light (wavelength 1.3 μm , optical power 40 mW), and the emitted light intensity I from the other edge was measured as a function of the current density (triangle wave current, current density 0–40 A/cm^2 (current 0–600 mA), voltage 0–3 V, frequency 1 Hz). We fitted the measurement result normalized by the light intensity when no current was injected with the expression $I = \exp(Gd)$ (where $G = gJ$, d is the length of the waveguide, which was 2000 μm , g is the differential gain coefficient, and J is the injection current density) and calculated the optical gain value G . Fig. 2 shows the dependency of G on J . We confirmed that the optical gain was proportional to the injection current density. We also applied linear fitting to this result and estimated the transparent current density (the value of J when $G = 0$), J_{tr} , to be 0.47 A/cm^2 . This value was one-fifth of the value (2.5 A/cm^2) we measured by another method [3]. This was because of the reduced leakage current due to the use of a light waveguide in the SOI substrate. G was measured to be smaller than the original value because gain saturation occurred due to the high power of the laser light (40 mW) used in this gain measurement. By taking into account this effect, the gain G at a lower light power, which is important when laser oscillation begins, is expected to be higher than the value we measured this time.

[Acknowledgement] This research was supported in part by Grant-in-Aid for JSPS Fellows Number 25 905 and the JSPS Core-to-Core Program, A. Advanced Research Networks.

This research was performed in part by the Advanced ICT Research Institute of NICT.

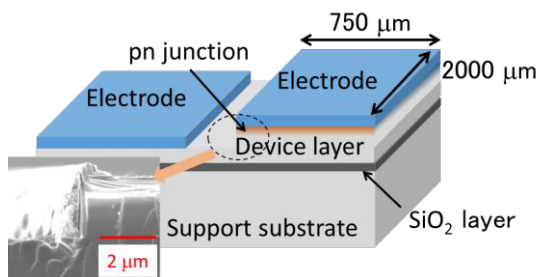


Fig. 1 Light waveguide using SOI substrate and SEM cross-sectional images of light waveguide.

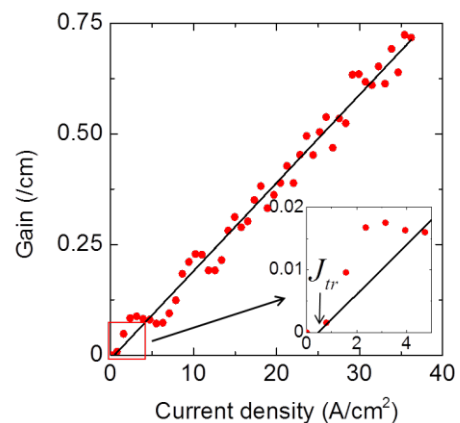


Fig. 2 Measurement results of dependency of gain G on forward current density J . Black: Estimation of transparent current density by linear regression.

[1] T. Kawazoe, M. Ohtsu, K. Akahane, N. Yamamoto, Appl. Phys. B, **107**, 659 (2012).

[2] H. Tanaka, T. Kawazoe, M. Ohtsu, K. Akahane, The 75th JSAP Autumn Meeting 18p-C1-4, Hokkaido university, Hokkaido, September 2014.

[3] H. Tanaka, T. Kawazoe, M. Ohtsu, The 74th JSAP Autumn Meeting 18p-C14-14, Doshisha university, Kyoto, September 2013.

Decision Making Based on Optical Excitation Transfer via Near-Field Interactions

M. Naruse¹, W. Nomura², M. Aono^{3,4}, M. Ohtsu², A. Drezet⁵, S. Huant⁵, and S.-J. Kim⁶

¹ National Institute of Information and Communications Technology, Tokyo, Japan

² The University of Tokyo, Tokyo, Japan

³ Tokyo Institute of Technology, Tokyo, Japan. ⁵ PRESTO, Japan Science and Technology Agency, Saitama, Japan

⁵ Institut Néel, CNRS and Université Joseph Fourier, Grenoble, France

⁶ National Institute for Materials Science, Tsukuba, Japan

E-mail address: naruse@nict.go.jp

Abstract: We experimentally demonstrate decision making based on optical excitation transfer via near-field interactions in quantum dots of different sizes formed on a geometry-controlled substrate, paving a way toward intellectual capabilities by near-field optics.

Optical near-field interactions between nanostructured matter, such as quantum dots, provide unidirectional optical excitation transfer when energy dissipation is induced. This results in versatile spatiotemporal dynamics of the optical excitation, which can be controlled by engineering the dissipation processes and exploited to realize intelligent capabilities such as solution searching and decision making [1-4].

Consider the particular case of a decision making problem in which a player should make a quick and accurate decision in choosing, from many available ones, a slot machine that has the highest probability of paying out a reward so that the player can get as much reward as possible. To accomplish this, the player should test and evaluate which machine is the best; however, too much testing or exploration to search for the best machine may result in a significant loss. Moreover, the best machine may change with time. (In the experiment, the number of slot machines was two.) In other words, there is a trade-off between exploration and exploitation, referred to as the *exploration-exploitation dilemma* [5]. Such a problem, called the *multi-armed bandit problem*, is the foundation of many important applications in information and communication technologies [3]. Kim *et al.* proposed an algorithm called tug-of-war model (TOW) [6], of which physical implementation is later theoretically proposed in [3]. It was demonstrated that the resultant decision making performance exhibits even better than that of the conventionally known best algorithm called Softmax [5] as shown in [3]. Here we *experimentally* demonstrate the ability of decision making on the basis of optical excitation transfer [4].

We fabricated QD samples using 2.5- and 3.2-nm-diameter CdSe/ZnS core-shell QDs formed on a geometry controlled substrates (Fig. 1(a)). The control lights irradiated on the sample were configured by a spatial light modulator (SLM) based on the optical excitation transfer observed in the QD sample. Figure 1(b) shows an experimental demonstration. Here the reward probability of the two slot machines are given by 0.8 and 0.2; thus choosing the higher-reward-probability machine is the correct decision. Furthermore, the reward probability is dynamically changed from time to time; the occurrence of a “change” of the reward probability is not notified to the player. In the experiment, the reward probabilities are swapped every 150 plays. The solid curve in Fig. 1(b) shows the evolution of the “success rate”, taking a value between 0 and 1, for 300 consecutive plays. The success rate is evaluated by calculating the number of successes divided by the number of repeat cycles. The success rate increases as time evolves. As a result of swapping the reward probabilities, the success rate drops every 150 plays but quickly recovers. Such rapid and accurate adaptability to the external environment demonstrates the success in solving the multi-armed bandit problem based on optical excitation transfer via optical near-field interactions between quantum dots.

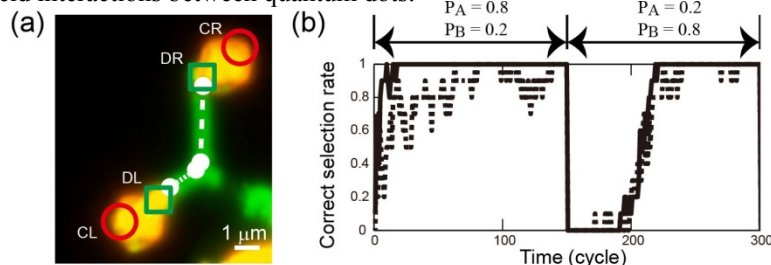


Fig. 1. Experimental demonstration of decision making: (a) experimental device. (b) decision making in uncertain environments.

Acknowledgements: This work was supported in part by Core-to-Core Program, A. Advanced Research Networks from JSPS. [1] M. Naruse, N. Tate, M. Aono, and M. Ohtsu, Rep. Prog. Phys. **76**, 056401 (2013). [2] M. Aono, M. Naruse, S.-J. Kim, M. Wakabayashi, H. Hori, M. Ohtsu, and M. Hara, Langmuir **29**, 7557-7564 (2013). [3] S.-J. Kim, M. Naruse, M. Aono, M. Ohtsu, and M. Hara, Sci. Rep. **3**, 2370 (2013). [4] M. Naruse, W. Nomura, M. Aono, M. Ohtsu, Y. Sonnefraud, A. Drezet, S. Huant, and S.-J. Kim, J. Appl. Phys. **116**, 154303 (2014) [5] N. Daw, J. O’Doherty, P. Dayan, B. Seymour, and R. Dolan, Nature **441**, 876-879 (2006). [6] S.-J. Kim, M. Aono, and M. Hara, Biosystems **101**, 29-36 (2010).

Motoichi OHTSU

Dept. EEIS, Graduate School of Eng., Univ. Tokyo
 (also with the International Center for Nano-Electron and Photon Technol., Univ. Tokyo)
 E-mail address: ohtsu@ee.t.u-tokyo.ac.jp

Abstract: This presentation reviews how to see the optical near field (ONF) and relevant problems to be solved in future. Several phenomena observed in nature that have similar features to those of the ONF are also presented.

It is essential to detect and/or see the optical near field (ONF) in order to promote the nano-optics and nanophotonics. With regard to seeing the ONF and identifying its origin, the following facts have been recognized:

- (1) The ONF is a virtual photon, and therefore, it cannot be described by Maxwell's equations because the uncertainties of the wavenumber and the energy of the ONF are too large due to its small spatial extent and short duration.
- (2) For describing the ONF, a novel quantum field theory has been developed, even though a virtual cavity for the field quantization cannot be defined in a nanometric space [1]. This theory has derived quantum operators representing the creation and annihilation of the ONF.
- (3) The ONF is a dressed photon because it is created by the interaction between a photon and electrons in a nanometric material.
- (4) The ONF couples with phonons to create a dressed-photon-phonon in a nanometric material.
- (5) Nobody can see the ONF without detecting the energy transfer from the nano-system to the surrounding macro-system through energy dissipation. The essential problem is that these energy transfer and dissipation processes cannot be described by conventional quantum mechanics. This is because the nano-system in which the ONF is created is connected with a macroscopic reservoir system. To solve this problem, the projection operator method has been developed based on the renormalization theory [1].

For more advanced methods that will allow us to see the ONF and to describe its origin, further studies on the energy transfer from the nano- to macro-systems are required. In particular, for describing the specific features due to the inherent hierarchy of the ONF, the physics of this complex system have to be developed based on micro-macro duality in quantum physics [2] and category theory[3]. Furthermore, for describing the energy dissipation, a novel theoretical model has to be developed based on the non-equilibrium statistical mechanics of the open system.

Many phenomena in nature have similar features to those of the ONF, and these have been observed in a variety of systems, including nano-systems, macro-systems, inorganic materials, and organic materials. Examples include: the meson, light-dependent magnetosensitivity in drosophila [4], a light-harvesting photosynthetic system [5], natural computing observed in single-celled amoeboid organisms [6], weathering of rocks, photon breeding in the radiation energy dissipation from relativistic jets in blazars [7], and a close binary star [8]. By clarifying the similarities and differences between these phenomena and those of the ONF, we expect that it will be possible to establish a method of seeing the ONF more precisely. As a result, this method will demonstrate that near field optics is a universal science and can be used to realize a generic technology of the 21st century. It should be pointed out that the search for this method corresponds to “exploring the future of light in the nanoscale”, which is the title of this special session.

References

- [1] M. Ohtsu, *Dressed Photons –Concepts of Light-Matter Fusion Technology–* (Springer, 2014).
- [2] I. Ojima, “Micro-macro duality in quantum physics,” Proc. Intern. Conf. of Stochastic Analysis, ed. by T. Hida (World Scientific, 2005) arXiv:math-ph/0502038.
- [3] S. MacLane, *Categories for the Working Mathematician* (Springer, 1971).
- [4] R.J. Gegear, A. Casselman, S. Waddell, and S.M. Reppert, “Cryptochrome mediates light-dependent magnetosensitivity in *Drosophila*,” *Nature*, **454**, 1014-1018 (2008).
- [5] G. McDermott, S.M. Prince, A.A. Freer, A. M. Hawthornthwaite-Lawless, M.Z. Papiz, R.J. Cogdell, and N.W. Isaacs, “Crystal structure of an integral membrane photosynthetic bacteria,” *Nature (London)*, **374**, 517-521 (1995).
- [6] M. Aono, S.-J. Kim, M. Naruse, M. Wakabayashi, H. Hori, M. Ohtsu, and M. Hara, “Amoeba-Inspired Nanoarchitectonic Computing: Solving Intractable Computational Problems Using Nanoscale Photoexcitation Transfer Dynamics,” *Langmuir*, **29**, 7557-7564 (2013).
- [7] B.E. Stern and J. Poutanen, “Radiation from relativistic jets in blazars and the efficient dissipation of their bulk energy via photon breeding,” *Mon. Not. R. Astronom. Soc.*, **383**, 1695-1712 (2008).
- [8] R.W. Hilditch, *An Introduction to Close Binary Stars* (Cambridge University Press, 2001).

Non-scanning optical near-field microscopy for nanophotonic security

Naoya Tate¹, Makoto Naruse², Tsutomu Matsumoto³,
Morihsa Hoga⁴, Yasuyuki Ohyagi⁴, Shumpei Nishio⁴, and Motoichi Ohtsu⁵

¹Kyushu University, ²National Institute of Information and Communications Technology, ³Yokohama National University,
⁴Dai Nippon Printing Co., Ltd., ⁵The University of Tokyo
tate@ed.kyushu-u.ac.jp

Abstract: We propose a novel method for observing nanometrically fluctuating signals due to optical near-field interactions between a probe and a target in near-field optical microscopy. By utilizing the hierarchy of these interactions, the method can observe spatial distribution-dependent outputs without requiring any scanning process. As an experimental demonstration, output signals due to interactions between a SiO₂ probe and Al nanorods were observed by using near-field optical microscopy at a single observation point. Using an original algorithm that we developed, we quantitatively evaluated these signals and their potential use in applications such as authentication.

In near-field optical microscopy (NOM), optical near-field interactions are induced between the probe and target, and output signals reflecting molecular attraction and optical responses due to the interactions are sequentially obtained. Generally, an NOM system includes a scanning mechanism, so that it can obtain a two-dimensional distribution of optical near-fields. By using systematic control via a feedback loop, the probe should be kept at a constant distance from the target. An important point is that the probe position inevitably fluctuates during the observation, and based on the concept of hierarchy [1], various scales of interactions are induced during this fluctuation. That is to say, NOM can observe *compressed* information that contains information about the spatial distribution of the target structure, without the need for any scanning process. Such information can be quantitatively evaluated by applying an original algorithm that we developed, including feature extraction and similarity calculation.

As an experimental demonstration to verify the basics of our proposed method, as the probe and target, we used an Au-coated SiO₂ probe and Al nanorods on a sample substrate [2], respectively. Fig. 1(a) shows the signal intensities of molecular attractions and optical responses at a single observation point. In order to quantitatively evaluate these results, the results were coded to produce the filled-in binary pattern shown in Fig. 1(b), and features of this pattern, namely, the coordinates of the corners, were extracted by applying the accelerated segment test (FAST) method [3]. A similar process was applied to other patterns obtained at different observation points, and their features were compared by calculating their mutual similarity values. Fig. 1(c) shows the results of the comparison, in which the bars and solid line represent the results of our method and the compared pixel values obtained from an SEM image of the target, respectively. As shown, both results revealed similar cyclic patterns. Because the solid line corresponds to a conventional scanning process, the similarity indicates that the output signals from a single observation point reflect the two-dimensional distribution of the target structure, as intended in our proposed method.

Generally, observation methods using NOM require a long processing time due to their scanning process. On the other hand, in the case of a security system, such as an authentication application, an accurate two-dimensional image of the target is not necessarily required. Our proposed method is suitable for such applications, and we expect that it can be used to develop novel applications of NOM.

This work was partially supported by a JSPS Core-to-Core Program (A. Advanced Research Networks).

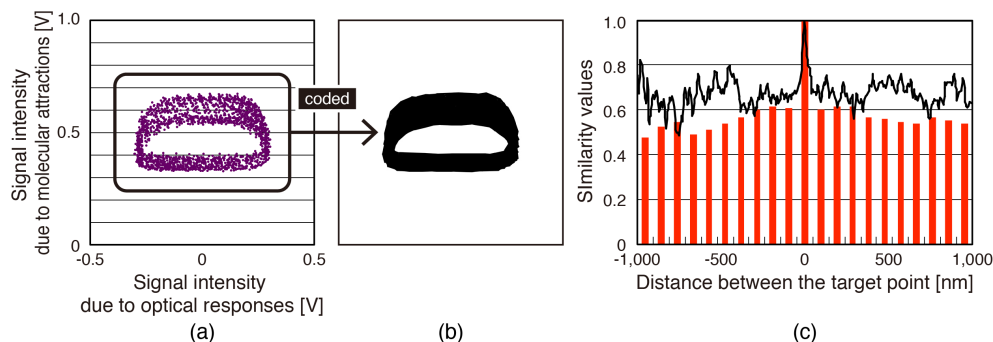


Fig. 1. (a) Mapped signals due to molecular attractions and optical responses during optical near-field interactions, and (b) their coded pattern. (c) Calculated similarity values between a reference pattern at $d=0$ and other positions.

[1] M. Naruse et al., *Optics Express*, **13**, No. 23, pp. 9265-9271 (2005).

[2] Y. Pihosh, et al., *ECS Trans.* Vol. 16, No. 5, pp. 49-58 (2009).

[3] E. Rosten et al., *European Conference on Computer Vision*, pp. 430-443 (2006).

High-speed flattening of a composite crystallized glass material by dressed-photon–phonon etching

Wataru Nomura¹, Takashi Yatsui¹, Tadashi Kawazoe¹, Naoya Tate², and Motoichi Ohtsu¹

1) School of Engineering, The University of Tokyo, and The Nanophotonics Research Center, The University of Tokyo, Bunkyo-ku, Tokyo 113-8656, Japan

2) Faculty of Information Science and electrical Engineering, Kyushu University, 744 Motoooka Nishi-ku Fukuoka 819-0395, Japan
E-mail address: yatsui@ee.t.u-tokyo.ac.jp

Abstract: We performed dressed-photon–phonon etching of a composite crystallized glass substrate using a laser beam with a high power density. The sample was successfully flattened in a processing time of under 5 seconds. The Ra value was reduced from 93 nm to 5.5 nm. We found some minor components on the surface after DPP etching due to differences in etching rates.

1. Background

Dressed-photon–phonon (DPP) etching is a novel non-contact processing technique that can realize ultra-flat surfaces. Its mechanism is as follows: DPPs [1] generated at nanometric protrusions on the surface dissociate reactive gas molecules to radicals, which then selectively etch the protrusions, making the surface flatter [2]. It has been reported that flat surfaces with an average roughness (Ra) value of approximately 0.1 nm were obtained by DPP etching of quartz glass substrates, plastic films, semiconductor crystal substrates, and so on [2]. In this talk, we report our results of using DPP etching to flatten a composite crystallized glass substrate used for a hard disc, which initially has a rough surface.

2. Experiment

The target material was an SiO₂-based composite crystallized glass substrate used for manufacturing a 2.5” hard disc, which was prepared by lapping using diamond abrasive grains. Fig. 1 shows a schematic diagram of the DPP etching set-up. The sample was irradiated with CW laser light with a wavelength of 532 nm, a power of 13 W, and a spot diameter of 0.2 mm, under a 200 Pa Cl₂ atmosphere. The surfaces before and after DPP etching were measured with an atomic force microscope (AFM), and the surface roughness values, Ra, were evaluated in a 5 μm × 5 μm region.

3. Results

Figures 2(a) and (b) show AFM images of the surfaces before and after DPP etching, respectively. The large bumps with a height of about 500 nm in Fig. 2 (a) were removed, and several small protrusions with a height of about 50 nm remained, as shown in Fig. 2(b). The Ra values calculated from Figs. 2(a) and (b) were greatly reduced, from 93 nm to 5.5 nm. The Ra value of 5.5 nm is approximately equal to that of a planar mirror substrate prepared by chemical mechanical polishing. The protrusions were assumed to be some small components of the ceramic glass material which appeared on the surface due to differences in etching rates. From these results, we successfully shortened the process time of DPP etching by using light with a high power density.

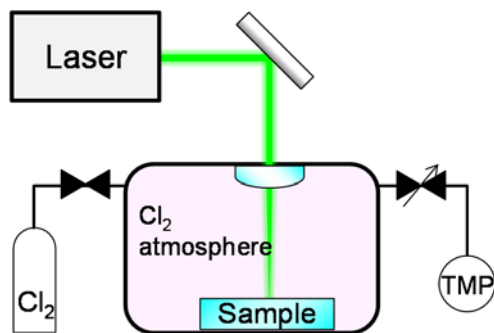


Fig. 1 Schematic image of experimental setup.

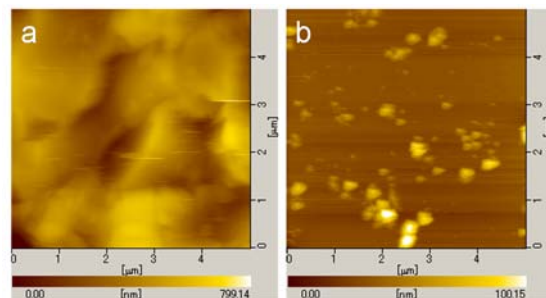


Fig. 2 AFM images of glass samples (a) before and (b) after DPP etching.

Acknowledgement

The sample substrate was provided by Showa Denko K.K.

References

- [1] M. Ohtsu, T. Kawazoe, T. Yatsui, and M. Naruse, IEEE J. of Selected Topics in Quantum Electronics, **14**, 1404 (2008).
- [2] T. Yatsui, W. Nomura, F. Stehlin, O. Soppera, M. Naruse, and M. Ohtsu, Beilstein J. Nanotech., **4**, 875–885 (2013).

P 2-1 Blue-ultraviolet Si photodetector with optical gain due to dressed photons

Masaki Ikegawa, Tadashi Kawazoe, Motoichi Ohtsu

Univ. of Tokyo

E-mail address: ikegawa@nanophotonics.t.u-tokyo.ac.jp

Abstract: Conventional Si photodetectors do not have high gain for blue-ultraviolet light. On the other hand, the photodetector that we fabricated using dressed photons has high gain in this spectral range. In addition, we made a lateral p-n junction not inside but on the surface of the photodetector with a new method.

Optical read/write devices with high density are needed in many applications. Also, the size of light sources has been getting shorter, and the number of device layers has been increasing. In addition, the speed of reading/writing to such high-density devices must become higher. Such optical devices need highly sensitive photodetectors.

Silicon (Si) can be used as a suitable photodetector (PD) for visible light. However, its photon efficiency in the short-wavelength region (blue-ultraviolet light) is low because of loss due to optical absorption. One well-known way to increase the efficiency is avalanche amplification, but this has the problem of dead time [1]. In order to solve this problem, we propose a Si-PD with optical gain due to dressed photons.

A dressed photon (DP) is a quasi-particle representing a coupled state of a photon and an electron-hole pair. Moreover, a dressed-photon-phonon (DPP) consists of a DP coupled with multi-mode coherent phonons. The Si-PD we propose has a boron (B) dopant distribution that easily produces DPPs on the p-n junction surface.

We created a unique distribution by performing DPP-assisted annealing of the device. Because the annealing process involved stimulated emission, the Si-PD after DPP-assisted annealing exhibited a light-amplification effect, resulting in high optical efficiency.

Our research group already realized a Si-PD that has a quantum efficiency of 336% in a 1.1 μm -long device [2].

In this study, we applied this amplifying function to blue-ultraviolet light. To prevent the Si from absorbing blue-ultraviolet light, we created a device that has a horizontal p-n junction on the surface (Fig. 1).

When doping the device with B, we adopted a new method of coating the device with Si-nanoparticles containing B and irradiating it with pulsed laser light. Furthermore, to increase the p-n junction area, we designed a comb-shaped p-n junction structure (Fig. 2).

Fig. 3 shows the current-voltage characteristics of the device we fabricated. When the device was irradiated with 405 nm laser light, we measured a current of 100 μA . In the presentation, we will

discuss the variation of the I-V characteristics before and after DPP-assisted annealing, as well as the device fabrication method.

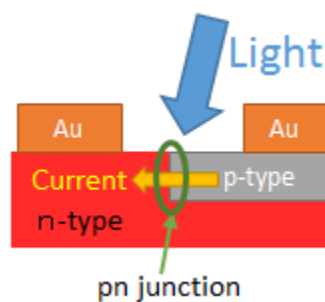


Fig. 1 Cross-sectional structure

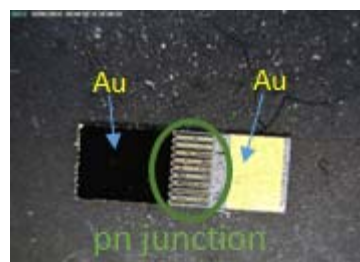


Fig. 2 The top view of a fabricated device

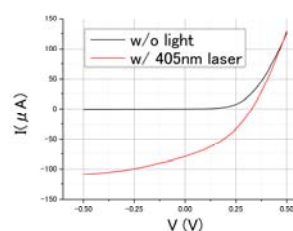


Fig. 3 Current-voltage characteristics

We thank Teijin Co., Ltd. for providing us with the NanoGram® Si ink used in this study.

[1]H. Dautet, P. Deschamps, B. Dion, A. D. MacGregor, D. Macsween, R. J. McIntyre, C. Trotter, P. P. Webb, *Applied Optics*, 32, 21, 3894-3900(1993)

[2]H. Tanaka, T. Kawazoe, M. Ohtsu, *Appl. Phys. B*, **108**, 51-56(2012)

P 2-2 Polarization control of Si-LED by photon breeding effect

Katsuhiko Nishioka, Tadashi Kawazoe, Takashi Yatsui, and Motoichi Ohtsu

Univ. of Tokyo

E-mail address: nishioka@nanophotonics.t.u-tokyo.ac.jp

Abstract: We performed dressed-photon–phonon assisted annealing on a bulk Si crystal. During this process, the Si was irradiated with light linearly polarized in a particular direction using a polarizing plate. As a result, the emission intensity of light polarized in the same direction as the linearly polarized laser light used during the annealing increased. A degree of polarization of 0.05 was obtained.

LEDs use mainly direct-transition-type semiconductors. Since indirect-transition-type semiconductors have a low radiative recombination probability, the light emission efficiency has been low; however, in our group, we have successfully achieved light emission from Si and SiC using a method known as dressed-photon–phonon assisted annealing [1][2], and have also realized laser oscillation [3]. In dressed-photon–phonon assisted annealing, a p–n junction is irradiated with laser light while causing a forward-bias current to flow. The photons emitted from the fabricated LED inherit the characteristics of the photons in the laser light irradiated during annealing. This effect is known as photon breeding [4]. This effect also applies to the polarization characteristics and has been used to realize a SiC LED exhibiting polarization [4].

Although an LED having polarization dependence at a particular angle by utilizing structural anisotropy has been reported [5], in general, LEDs emit unpolarized light in the normal direction. The aims of this research are to use Si having an isotropic crystal structure to fabricate an LED exhibiting polarized light emission, by focusing on the photon breeding effect related to polarization and using dressed-photon–phonon assisted annealing, and also to obtain knowledge about polarized light emitting structures.

We fabricated the device shown in Fig. 1 using a Si bulk crystal. The device was irradiated with laser light having a wavelength 1342 nm (0.924 eV) and a power of 1.2 W while causing a current to flow at a current density of 1.67 A/cm². During this process, the device was irradiated with linearly polarized light in a particular direction using a polarizing plate. During spectral measurement, the spectra of components parallel to and perpendicular to the polarization direction used in annealing were measured.

Fig. 2 shows the spectrum for each polarization component after annealing (the component parallel to (//) and perpendicular to (⊥) the polarization direction of the laser light using during annealing), as well as the degree of polarization calculated from these spectra. Spectra in which the peak was assigned to the Si band edge emission were obtained, and the degree of polarization at the wavelength of the light used during annealing was 0.05. Also, in the vicinity of the annealing wavelength, the degree of polarization showed a point-symmetric structure centered on the annealing wavelength, which shows a similar tendency to the annealing results reported for SiC [4]. In addition, the degree of polarization showed a tendency to increase with increasing annealing time. One possible reason for this degree of polarization behavior is orientation dependency of the dopant distribution involved in the generation of dressed-photon–phonons, and therefore, we intend to also present the results of analysis using the 3D atom probe method.

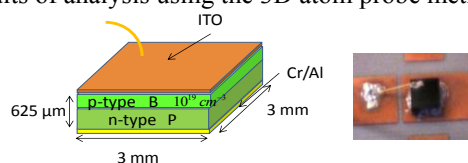


Fig. 1 Structure and photograph of the device.

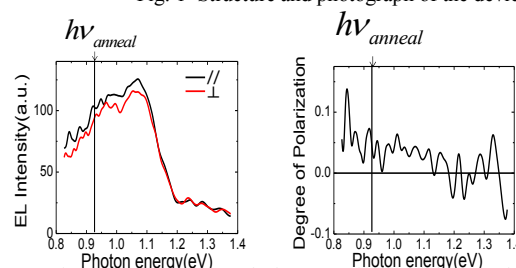


Fig. 2 Spectra observed after annealing and degree of polarization.

- [1] T. Kawazoe, M. A. Mueed, M. Ohtsu, Appl. Phys. B, 104, 747 (2011).
- [2] T. Kawazoe, M. Ohtsu, Appl. Phys. A, 115, 127 (2014).
- [3] T. Kawazoe et al. Appl. Phys. B, 107, 659 (2012).
- [4] T. Kawazoe, K. Nishioka, M. Ohtsu, The 75th JSAP Autumn Meeting, 18p-C1-2 (2014).
- [5] Martin F. Schubert et al. Appl. Phys. Lett. 91, 051117 (2007).

PLENARY

DRESSED PHOTON TECHNOLOGY FOR SILICON PHOTON BREEDING DEVICES

Motoichi Ohtsu^{1,2}*1 Dept. EEIS, Graduate School of Engineering, University of Tokyo, Tokyo, Japan**2 International Center for Nano Electron and Photon Technology, University of Tokyo, Tokyo, Japan**Contact: ohtsu@ee.t.u-tokyo.ac.jp*

Keywords: photon breeding, dressed photon, coherent phonon, silicon, silicon carbide, LED, laser

Although a photon breeding device (PBD) looks like a light emitting diode (LED) at first glance, its principle of operation, characteristics, and fabrication method are very different [1]. There has been a long-held belief in materials science and technology that indirect-transition-type semiconductors, such as silicon (Si), are not suitable for use in LEDs and lasers; however, they *can* be used as the device material in PBDs.

For fabricating such a device, a forward bias current is injected into a p-n homojunction in a Si bulk crystal to bring about annealing by Joule heat while irradiating the device with light. The PBD fabricated by this method exhibits unique characteristics: When current is injected for device operation, the device emits a photon whose energy is identical to that of the light irradiated during annealing; it is not determined by the bandgap energy of Si. Furthermore, the spin (polarization) and the momentum (wave-vector) of the emitted photon are also identical to those of the light irradiated during annealing. These characteristics are the origin of the name “photon breeding device”.

Photon breeding is caused by dressed photons (DPs), which are created at the boron (B) atoms (the p-type dopants) in the p-n homojunction by the light irradiated during annealing. The DP is a quasi-particle created as a result of the interaction between a photon and an electron in a nanometric space [2]. Furthermore, the DP excites multimode coherent phonons, and they couple to create a novel quasi-particle called a dressed-photon–phonon (DPP). Since the light irradiated during annealing triggers stimulated emission of light with the help of the DPP, the crystal temperature decreases, and the diffusion of the B atoms is decelerated, reaching a stationary spatial distribution of B atoms. Since this distribution is the optimum one for creating multimode coherent phonons most efficiently when a forward bias current is injected for device operation, the electrons in the conduction band can exchange momentum with the created phonons. As a result of this exchange, the PBD efficiently emits light. Furthermore, since the spatial distribution of B atoms has been controlled and optimized by the light irradiated during annealing, the energy, spin, and momentum of the emitted photon are governed by the created coherent phonons. Therefore, the photon is bred from the light irradiated during annealing and this bred photon is emitted.

The first topic of this presentation is the principle of creating DPs and DPPs. Second, the fabrication and characteristics of the PBD are reviewed. Novel devices to be discussed include visible LED-type PBDs using Si and infrared LED-type PBDs using SiC. Furthermore, visible LED-type PBDs using SiC, which is also a typical indirect-transition-type semiconductor, are also demonstrated. Infrared laser-type PBDs using Si are also reviewed.

Finally, several phenomena occurring in nature and which have similar features to those of DPs are reviewed. They have been observed in a variety of systems, including nano-systems, macro-systems, inorganic materials, and organic materials. Examples include: the meson, light-dependent magnetosensitivity in *Drosophila* [3], a light-harvesting photosynthetic system [4], natural computing observed in single-celled amoeboid organisms [5], weathering of rocks, photon breeding in the radiation energy dissipation from relativistic jets in blazars [6], and a close binary star [7]. By clarifying the similarities and differences between these phenomena and those of DPs, it will be possible to demonstrate that DPs are a key element in modern optical science and can be used to realize a generic technology of the 21st century.

1. M. Ohtsu, “Silicon Light Emitting Diodes and Lasers Using Dressed Photons,” in *Progress in Nanophotonics 3*, (ed. by M. Ohtsu) (Springer, 2014), pp.1-56.

2. M. Ohtsu, *Dressed Photons –Concepts of Light-Matter Fusion Technology–* (Springer, 2014).

3. R.J. Gegear, A. Casselman, S. Waddell, and S.M. Reppert, “Cryptochrome mediates light-dependent magnetosensitivity in *Drosophila*,” *Nature*, **454**, 1014-1018 (2008).

4. G. McDormott, S.M. Prince, A.A. Freer, A. M. Hawthornthwaite-Lawless, M.Z. Papiz, R.J. Cogdell, and N.W. Isaacs, “Crystal structure of an integral membrane photosynthetic bacteria,” *Nature (London)*, **374**, 517-521 (1995).

5. M. Aono, S.-J. Kim, M. Naruse, M. Wakabayashi, H. Hori, M. Ohtsu, and M. Hara, “Amoeba-Inspired Nanoarchitectonic Computing: Solving Intractable Computational Problems Using Nanoscale Photoexcitation Transfer Dynamics,” *Langmuir*, **29**, 7557-7564 (2013).

6. B.E. Stern and J. Poutanen, “Radiation from relativistic jets in blazars and the efficient dissipation of their bulk energy via photon breeding,” *Mon. Not. R. Astronom. Soc.*, **383**, 1695-1712 (2008).

7. R.W. Hilditch, *An Introduction to Close Binary Stars* (Cambridge University Press, 2001).

Giant-magneto-optic light modulator using p–n homojunction-structured ZnO crystal

Naoya Tate¹, Tadashi Kawazoe², and Motoichi Ohtsu²

¹Kyushu University, 744 Motoooka, Nishi-ku, Fukuoka 819-0395, Japan

²The University of Tokyo, 2-11-16 Yayoi, Bunkyo-ku, Tokyo 113-8656, Japan
tate@ed.kyushu-u.ac.jp

Abstract: We experimentally demonstrated large optical phase modulation using a p–n homojunction-structured zinc oxide single crystal. This device was fabricated using a method that we have developed, what we call dressed-photon-assisted annealing. Our device exhibited quantitatively superior performance in several applications, such as optical path switching and speckle reduction.

1. Introduction

Light modulators are one of the most fundamental optical devices in various applications of optical information processing. To keep up with recent developments in today's information society, there is a strong demand for light modulators with improved modulating speed, power consumption, and package size. The operating principle of conventional light modulators is typically based on modulation of the refractive index. Therefore, suitable materials for light modulators had been limited to specific materials such as nonlinear optical crystals and liquid crystals.

With crystals of oxide semiconductors, on the other hand, there are technical difficulties in implementing electro- or magneto-induced optical functionalities with general doping methods, because acceptors from the dopants are generally compensated with donors from the numerous oxygen vacancies and interstitial metals. However, according to recent research by the authors' group [1-7], novel electro-optical functions using various indirect- and direct-transition semiconductors have been successfully realized by employing a method that we have developed, what we call dressed-photon (DP) assisted annealing. The method automatically generates a distribution of p-type dopants that forms a appropriate p–n homojunction in the n-type material, and, as a result, a sufficiently large current can be applied to the device for inducing the magneto-optical effect in response to input light. The effect is fundamentally due to interactions between localized optical energy fields, namely, DPs, and electronic spins of the material, and does not require any external devices, such as magnetic field sources or mechanical controls. Here, we describe the basics of DP-assisted annealing and our giant-magneto-optic light modulator using a ZnO single crystal [8]. Moreover, we show the results of experimental demonstrations of some applications of our device and discuss the device characteristics.

2. Basics of DP-assisted annealing

A DP is a quasi-particle representing the coupled state of a photon and an electron in a nanometric space [9]. A DP excites a multi-mode coherent phonon in a nanometric material, and the DP state is coupled with excited coherent phonon states in the material. Because this coupled state can be regarded as an intermediate state during the electron transition process in the material, multistep transitions and corresponding electro-optical functions can be induced.

In order to effectively generate DPs, the device is subjected to DP-assisted annealing to optimize the distribution of dopants [1-7]; namely, it is annealed with Joule heating by applying a current while irradiating the device with light having a lower photon energy than the band gap energy of the material. While applying a forward bias current to generate Joule heating, the dopants are randomly diffused in the material and converge to a homogeneous distribution. However, at the same time, DPs are generated by radiated light. The generated DPs can excite multimode coherent phonons in the material [10], resulting in a state where the DPs and phonons are coupled; in other words, a multi-step electron transition occurs via energy levels corresponding to the coupled state. As a result, part of the electrical energy given by the forward bias current is efficiently converted to the photon energy of stimulated emission, and diffusion of the dopants subsequently stops. The distribution of dopants works as an appropriate structure for effective generation of DPs. On the other hand, in a distribution in which DPs are hardly generated, dopants continue to diffuse in the material until they form specific distributions that are suitable for generating DPs. Finally, high-efficiency DP generation is exhibited in all regions of the material. That is to say, an electro-optical device that exhibits high efficiency due to the higher applied current is successfully realized.

3. Specifications of giant-magneto-optic light modulator

Here, we used an n-type bulk ZnO crystal implanted with N^+ and N^{2+} ions serving as p-type dopants. A schematic diagram of our device is shown in Fig. 1. In this case, the device was irradiated with laser light having a photon energy $h\nu = 3.05$ eV during the DP-assisted annealing. After the annealing, Ag electrodes were formed on the same surface of the device for applying a bias current in the in-plane direction in the device, instead of the p–n direction. In this configuration, magnetic fields due to the applied current effectively affect the specific distribution of dopants in the

device, and, as a result, interactions between light and the material via the generated DPs in regions around the dopants are expected to occur. In order to qualitatively confirm the electro-optical characteristics of the device, the degree of polarization rotation in response to linearly-polarized input light was observed. Figures 2 (a) and (b) show the setup and the result, respectively. As shown, a polarization rotation of π radians was obtained per 15 mA of induced current, and a maximum rotation of more than 20π radians was found over a light propagation distance of only 1 mm in the device. These results are several orders of magnitude larger than the optical rotation levels achieved using conventional magneto-optical materials [11-13].

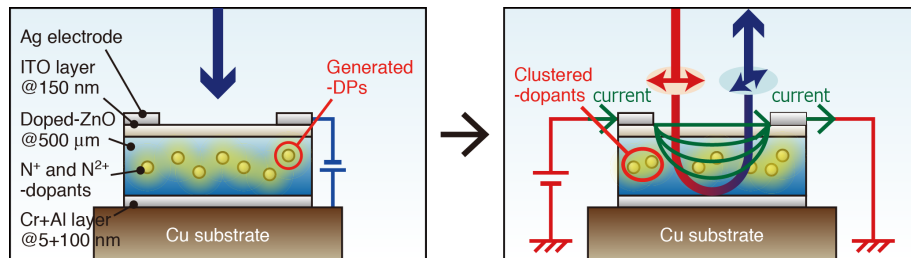


Fig. 1. Schematic diagram of DP-assisted annealing method (left) and setup for achieving optical phase modulation (right).

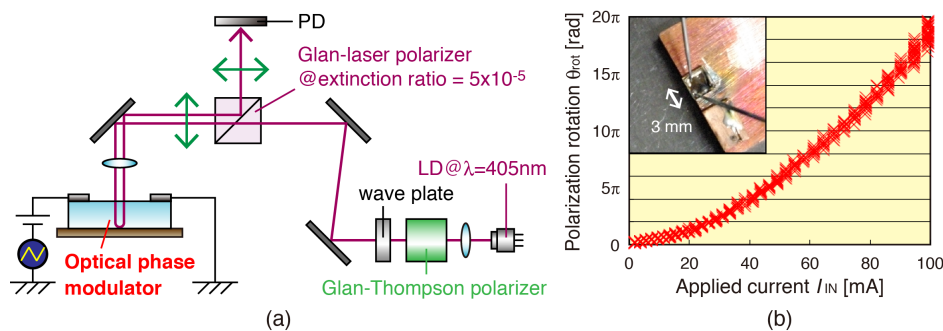


Fig. 2. (a) Experimental setup for measuring optical polarization rotation. Only modulated elements of the light are successfully observed by the PD. (b) Experimentally obtained relation between applied current and polarization rotation of our device.

4. Summary

We developed a giant-magneto-optic light modulator by using a doped ZnO single crystal in which we fabricated an appropriate p-n homojunction structure via a DP-assisted annealing method. We have already demonstrated that our device showed adequate performance in several applications, such as optical path switching and speckle reduction [10]. Such a large level of phase modulation will surely lead to the development of novel research fields, especially related to the field of optical processing.

References

- [1] T. Kawazoe, M. A. Mueed, and M. Ohtsu, "Highly efficient and broadband Si homojunction structured near-infrared light emitting diodes based on the phonon-assisted optical near-field process," *Appl. Phys. B-Lasers and Optics*, **104**, No. 4, 747–754 (2011).
- [2] K. Kitamura, T. Kawazoe, and M. Ohtsu, "Homojunction-structured ZnO light-emitting diodes fabricated by dressed-photon assisted annealing," *Appl. Phys. B-Lasers and Optics*, **107**, No. 2, 293–299 (2012).
- [3] T. Kawazoe, M. Ohtsu, K. Akahane, and N. Yamamoto, "Si homojunction structured near-infrared laser based on a phonon-assisted process," *Appl. Phys. B-Lasers and Optics*, **107**, No.3, 659–663 (2012).
- [4] H. Tanaka, T. Kawazoe, and M. Ohtsu, "Increasing Si photodetector photosensitivity in near-infrared region and manifestation of optical amplification by dressed photons," *Appl. Phys. B-Lasers and Optics*, **108**, No. 1, 51–56 (2012).
- [5] N. Wada, T. Kawazoe, and M. Ohtsu, "An optical and electrical relaxation oscillator using a Si homojunction structured light emitting diode," *Appl. Phys. B-Lasers and Optics*, **108**, No.1, 25–29 (2012).
- [6] M. A. Tran, T. Kawazoe, and M. Ohtsu, "Fabrication of a bulk silicon p-n homojunction-structured light-emitting diode showing visible electroluminescence at room temperature," *Appl. Phys. A*, **115**, Issue 1, 105–111 (2014).
- [7] T. Kawazoe and M. Ohtsu, "Bulk crystal SiC blue LED with p-n homojunction structure fabricated by dressed-photon-phonon-assisted annealing," *Appl. Phys. A*, **115**, Issue 1, 127–133 (2014).
- [8] N. Tate, T. Kawazoe, and M. Ohtsu, "Speckle reduction by current-induced magneto-optical effect using p-type ZnO device," *The 21st International Display Workshops (Niigata, 2014)*, PRJ3-1.
- [9] M. Ohtsu, *Dressed Photons - Concepts of Light-Matter Fusion Technology* (Springer, 2013).
- [10] Y. Tanaka and K. Kobayashi, "Spatial localization of an optical near field in one-dimensional nanomaterial system," *Physica E*, **40**, Issue 2, 297–300 (2007).
- [11] F. J. Kahn, and P. S. Pershan, and J. P. Remeika, "Ultraviolet Magneto-Optical Properties of Single-Crystal Orthoferrites, Garnets, and Other Ferric Oxide Compounds," *Phys. Rev.* **186**, 891-918 (1969).
- [12] J. K. Furdyna, "Diluted magnetic semiconductors," *J. Appl. Phys.* **64**, R29-R64 (1988).
- [13] K. H. J. Buschow, P. G. van Engen, and R. Jongebreur, "Magneto-optical properties of metallic ferromagnetic materials," *J. Magn. Magn. Mater.* **38**, Issue 1, 1-22 (1983).

Speckle reduction by current-induced magneto-optical effect using p-type ZnO device

Naoya Tate, Tadashi Kawazoe, Motoichi Ohtsu

The University of Tokyo, 2-11-16 Yayoi, Bunkyo-ku, Tokyo 113-8656, Japan

Keywords: speckle reduction, zinc oxide, nanophotonics, dressed-photon, dressed-photon-phonon annealing

ABSTRACT

We experimentally demonstrated giant optical phase modulation using a p-type ZnO device fabricated using a technique that we developed. We achieved a sufficient reduction in the speckle noise of laser light by utilizing this effect to decrease the contrast of time-averaged speckle patterns.

1. INTRODUCTION

When a screen is irradiated with a laser beam, unwanted interference patterns are generated on the displayed images due to the high coherence of laser light; these interference patterns are called *speckle noise* [1]. Because speckle noise is a critical issue in displaying high-resolution images by laser scanning, reducing speckle noise is one of the most important issues in realizing practical laser displays [2]. Recently, several approaches for reducing speckle noise have been investigated, including a method of decreasing the coherence of laser light so that beams do not interfere with each other [3-5], and generating fluctuating speckle patterns to display lower-contrast time-averaged patterns [6-8].

As one example of the latter approach, we have experimentally demonstrated a new technique for reducing speckle noise with a novel optical phase modulation technique using a p-type zinc oxide (ZnO) device [9] that exhibits giant magneto-optical effect. This device was realized by using a method that we developed, what we call dressed-photon (DP) assisted annealing [10]. The method automatically encourages a distribution of p-type dopants that forms a good p-n junction in the material, and, as a result, sufficiently large currents can be applied to the device for inducing the magneto-optical effect in response to input light. Because the effect is fundamentally due to interactions between localized optical energy fields, namely, DPs, and electronic spins of the material, and does not require any external devices, such as magnetic field sources or mechanical controls, high-speed, energy-conservative, and compact implementations are expected. Here, we describe the basics of the p-type ZnO device and its experimental specifications. Then, we show the results of some simple experimental demonstrations for speckle control using the p-type ZnO device and we discuss the implications of these results.

2. p-TYPE ZnO DEVICE

According to previous reports by the authors' group [9-12], a good p-n homojunction layer for implementing electro-optical-based functions in various types of indirect-transition semiconductors can be sufficiently realized by DP assisted annealing. In this study, we used an n-type bulk ZnO crystal implanted with N^+ and N^{2+} ions serving as p-type dopants. A DP is a quasi-particle representing the coupled state of a photon and an electron in a nanometric space [13]. A DP excites a multi-mode coherent phonon in a nanometric material, and the DP state is coupled with excited coherent phonon states in the material. Because this coupled state can be regarded as an intermediate state during the electron transition process in the material, multistep transitions and corresponding electro-optical functions can be induced.

In order to effectively generate DPs, in our previous work [9-12], the devices were subjected to DP-assisted annealing to optimize the distribution of dopants; namely, they were annealed with Joule heating by applying a current while irradiating the device with light having a lower photon energy than the band gap energy of the material. While applying a forward bias current to generate Joule heating, the dopants were randomly diffused in the material and converged to a homogeneous distribution. However, at the same time, DPs were generated by radiating light in the spatial vicinity of the exciton polaritons due to the formation of localized electrons and holes at regions where a specific distribution of dopants was present. The generated DPs can excite multimode coherent phonons in the material [14], resulting in a state where the DPs and phonons are coupled; in other words, a multi-step electron transition occurs via energy levels corresponding to the coupled state. As a result, part of the electrical energy given by the forward bias current is efficiently converted to the photon energy of stimulated emission, and diffusion of the dopants subsequently stops. The distribution of dopants works as an appropriate structure for effective generation of DPs. On the other hand, in a distribution in which DPs are hardly generated, dopants continue to diffuse in the material until they form specific distributions that are suitable for generating DPs. Finally,

high-efficiency DP generation is exhibited in all regions of the material. That is to say, a high-efficiency electro-optical device is successfully realized.

A schematic diagram of our p-type ZnO device is shown in Fig. 1(a). In this case, the device was irradiated with laser light having a photon energy $h\nu = 3.05$ eV during the DP assisted annealing. After the annealing, Ag electrodes were formed on the same surface of the device for in-plane induction of a bias current in the device, instead of the p-n direction. In this configuration, magnetic fields due to the applied current effectively affect the specific distribution of dopants in the device, and, as a result, interactions between light and the material via the generated DPs in regions around the dopants are expected to occur. In order to qualitatively confirm the electro-optical characteristics of the device, polarization rotation in response to linearly-polarized input light was experimentally demonstrated. Figure 1(b) shows the result. As shown, a polarization rotation of π radians was obtained per 15 mA of induced current, and a maximum rotation of more than 20π radians was found over a light propagation distance of only 1 mm in the device. These results are several orders of magnitude larger than conventional optical rotation using magneto-optical materials [15-17].

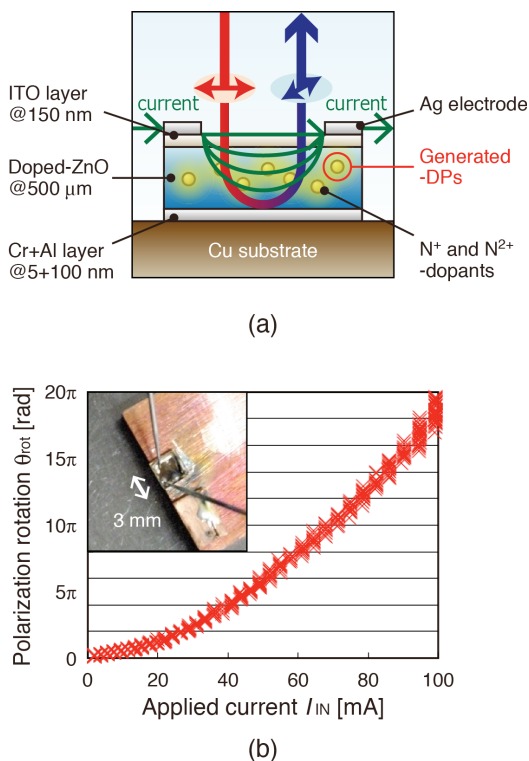


Fig. 1 (a) Schematic diagram of the p-type ZnO device. (b) Relation between applied current and polarization rotation obtained with the device.

3. EXPERIMENTAL DEMONSTRATION

Speckle control using our p-type ZnO device was demonstrated by using the experimental setup shown in Fig. 2(a). A linearly-polarized CW laser beam at a wavelength of 405 nm was vertically input to the device. To simplify the discussion, electrical modulation was applied to the device in the form of a triangular wave at a frequency of 1 Hz. The output light was radiated onto a commercially available frosted-diffuser plate (DFB1 #1000; Sigma Koki Co., Ltd.). The speckle pattern generated by the diffuser was observed and recorded using a CCD camera (DFK-21AU618; Imaging Source). The exposure time was set to 1/250 s. Some observed patterns are shown in Fig. 2(b). As shown, non-correlated patterns were successfully obtained by applying modulation to the device.

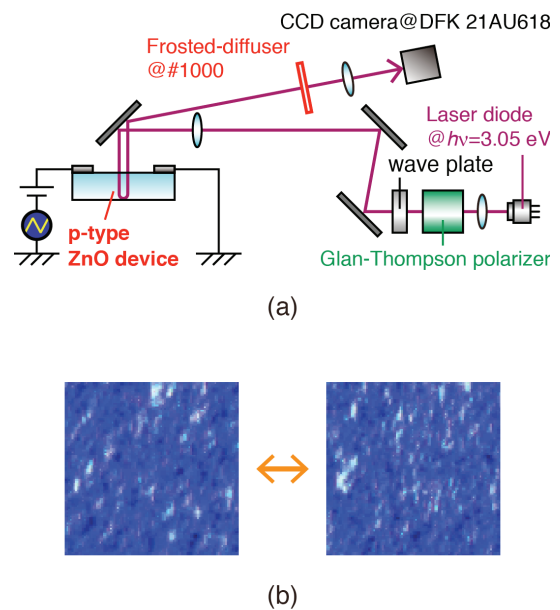


Fig. 2 (a) Schematic diagram of experimental setup for demonstration of speckle control and (b) observed speckle patterns.

For a quantitative discussion of the observed speckle patterns, image analyses were performed. Here, difference images between each pattern and a reference pattern were obtained, and their average pixel values were calculated. This value indicates the variation of the speckle patterns during modulation in response to input light. A higher variation is preferred for obtaining lower-contrast time-averaged patterns as a speckle reduction technique. Figure 3(a) shows the results. As shown, the application of a larger current induces larger variations of the speckle patterns. Moreover, these variations were made to converge by applying high currents of more than 50 mA, because a polarization rotation of 2π radians showed a speckle pattern similar to the default pattern. Then, the

time-averaged speckle patterns were examined by using image addition of the observed patterns. Each pattern was added sequentially, and their contrast C was calculated in each case. The results of C are plotted in Fig. 3(b). As shown, a reduction in C was obtained by applying a sufficiently high current to the device. The time required for convergence of C , which was about 0.25 s, corresponds to 1/4 cycle at the modulation frequency.

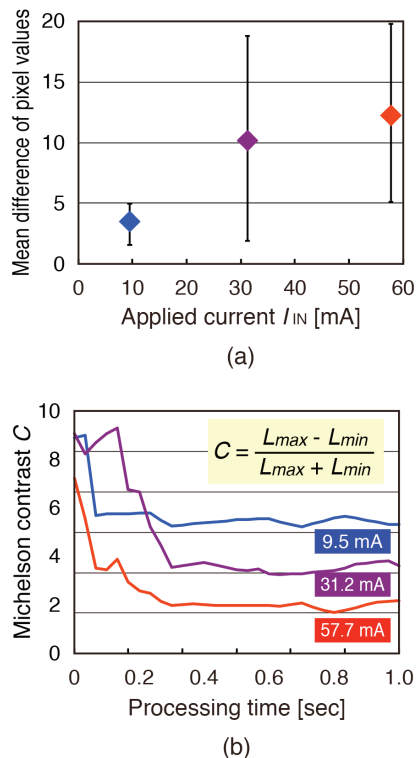


Fig. 3 (a) Variation of speckle patterns depends on applied current. (b) Contrast reduction of time-averaged speckle patterns during processing.

4. SUMMARY

We have proposed and experimentally demonstrated a method of controlling the speckle patterns of laser light by using a novel optical phase modulator, namely, a p-type ZnO device. In this study, we applied a lower modulation frequency to the device and used a lower output rate of the images observed by the camera to simplify the experimental demonstration and the discussion. In future researches, we plan to quantitatively verify the response characteristics of the device in the case where a higher modulation frequency is used for practical application to laser displays in the near future.

REFERENCES

[1] J. W. Goodman, *Speckle Phenomena in Optics* (Roberts and Co., Greenwood Village, CO, 2007).
 [2] M. Kuwata, H. Sugiura, T. Sasagawa, A. Michimori, E. Toide, T. Yanagisawa, S. Yamamoto, Y. Hirano, M.

Usui, S. Teramatsu, and J. Someya, "A 65-in. slim (255-mm depth) laser TV with wide-angle projection optical system," *J. Soc. Inf. Disp.* **17**, Issue 11, pp. 875-882 (2009).

[3] N. George and A. Jain, "Speckle Reduction Using Multiple Tones of Illumination," *Appl. Opt.* **12**, Issue 6, pp. 1202-1212 (1973).
 [4] F. Riechert, G. Craggs, Y. Meuret, B. V. Giel, H. Thienpont, U. Lemmer, and G. Verschaffelt, "Low-speckle laser projection with a broad-area vertical-cavity surface-emitting laser in the nonmodal emission regime," *Appl. Opt.* **48**, Issue 4, pp. 792-798 (2009).
 [5] H. Murata, K. Furusho, K. Yamamoto, and Y. Okamura, "New Speckle Control Technique Using High-Speed Electro-Optic Modulators with Resonant Electrode and Polarization-Reversed Structures," *Opt. Rev.* **19**, No. 6, pp. 436-439 (2012).
 [6] K. Kasazumi, Yasuo Kitaoka, Kiminori Mizuuchi and Kazuhisa Yamamoto, "A Practical Laser Projector with New Illumination Optics for Reduction of Speckle Noise," *Jpn. J. Appl. Phys.* **43**, No. 8B, pp. 5904-5906 (2004).
 [7] C.-Y. Chen, W.-C. Su, C.-H. Lin, M.-D. Ke, Q.-L. Deng, and K.-Y. Chiu, "Reduction of Speckles and Distortion in Projection System by Using a Rotating Diffuser," *Opt. Rev.* **19**, No. 6, pp. 440-443 (2012).
 [8] D. Li, D. P. Kelly, and J. T. Sheridan, "Speckle suppression by doubly scattering systems," *Appl. Opt.* **52**, Issue 35, pp. 8617-8626 (2013).
 [9] K. Kitamura, T. Kawazoe, and M. Ohtsu, "Homojunction-structured ZnO light-emitting diodes fabricated by dressed-photon assisted annealing," *Appl. Phys. B*, **107**, Issue 2, pp. 293-299, (2012).
 [10] T. Kawazoe, M. Ohtsu, K. Akahane, and N. Yamamoto, "Si homojunction structured near-infrared laser based on a phonon-assisted process," *Appl. Phys. B*, **107**, Issue 3, pp. 659-663, (2012).
 [11] T. Kawazoe, M. A. Mueed, and M. Ohtsu, "Highly efficient and broadband Si homojunction structured near-infrared light emitting diodes based on the phonon-assisted optical near-field process," *Appl. Phys. B*, **104**, Issue 4, pp. 747-754 (2011).
 [12] T. Kawazoe and M. Ohtsu, "Bulk crystal SiC blue LED with p-n homojunction structure fabricated by dressed-photon-phonon-assisted annealing," *Appl. Phys. A*, **115**, Issue 1, pp. 127-133 (2014).
 [13] M. Ohtsu, *Dressed Photons - Concepts of Light-Matter Fusion Technology* (Springer, 2013).
 [14] Y. Tanaka and K. Kobayashi, "Spatial localization of an optical near field in one-dimensional nanomaterial system," *Physica E*, **40**, Issue 2, pp. 297-300 (2007).
 [15] F. J. Kahn, and P. S. Pershan, and J. P. Remeika,

"Ultraviolet Magneto-Optical Properties of Single-Crystal Orthoferrites, Garnets, and Other Ferric Oxide Compounds," Phys. Rev. **186**, pp. 891-918 (1969).
[16] J. K. Furdyna, "Diluted magnetic semiconductors," J.

Appl. Phys. **64**, pp. R29-R64 (1988).
[17] K. H. J. Buschow, P. G. van Engen, and R. Jongebreur, "Magneto-optical properties of metallic ferromagnetic materials," J. Magn. Magn. Mater. **38**, Issue 1, pp. 1-22 (1983).

SiC light emitting diode and its polarization control using dressed photons

Tadashi Kawazoe^{1,2}, Katsuhiro Nishioka¹, and Motoichi Ohtsu^{1,2}

¹Department of Electrical Engineering and Information Systems, Graduate School of Engineering, The University of Tokyo, 2-11-16 Yayoi, Bunkyo-ku, Tokyo 113-8656, Japan

²Nanophotonic Research Center, Graduate School of Engineering, The University of Tokyo, 2-11-16 Yayoi, Bunkyo-ku, Tokyo 113-8656, Japan

Keywords: Nanophotonics, Polarization, LED, SiC, Dressed photon

ABSTRACT

An optically polarized SiC light emitting diode was demonstrated. To fabricate this device, it was annealed by Joule heating brought about by a forward bias current under laser irradiation (dressed-photon–phonon (DPP) annealing). The emission peak wavelength and polarization both corresponded to those of the laser light irradiated during annealing.

1. INTRODUCTION

Electroluminescence (EL) devices with high optical polarization ratios have the potential to improve laser diode (LD) performance and to reduce power consumption in backlight systems for displays. So far, several studies on optically polarized LEDs using the anisotropic optical properties of nonpolar InGaN quantum wells on GaN and SiC substrates have been reported [1–3]. In these GaN-based LEDs, the optically polarized spontaneous emission and absorption are explained by the crystal field oriented along the c axis and its effect on the valence band [4]. The degree of polarization of the emitted light is close to 0.8. However, they are not suitable for display backlight systems because a large degree of polarization and controllability of the emission wavelength are incompatible in these devices.

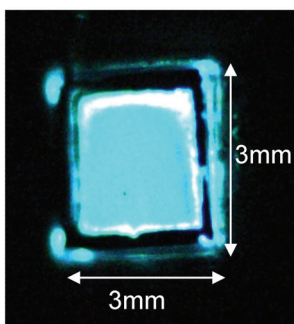


Fig. 1. Photograph of a SiC LED emitting blue-white light fabricated by DPP annealing.

Recently, we proposed indirect-transition-type semiconductor LEDs with p – n homojunctions

including SiC [5–8]. They are fabricated by a dressed-photon–phonon (DPP) annealing method. This process results in an optimized spatial distribution of an Al dopant which generates DPPs via an injected current (electrons and holes), allowing the annealed SiC bulk crystal with the p – n homojunction structure to work as an efficient LED, even though SiC is an indirect-transition-type semiconductor. In this device, the created DPPs are efficiently converted to photons. Figure 1 shows a photograph of a SiC LED emitting blue-white light, fabricated by DPP annealing. A 10% internal quantum efficiency of the EL emission was achieved [5]. The emission light inherits properties from the light source used in the DPP annealing via the stimulated emission. Thus, the emission wavelength is controllable by changing the wavelength of the light source used in the DPP annealing. In the same manner, we speculated that the polarization of the generated photons is also inherited from the light source used in the DPP annealing. In the work described in this report, we demonstrated a SiC LED whose polarization was controlled by the polarized light source used in the DPP annealing.

2. PRINCIPLE

A dressed-photon–phonon (DPP) is a quasi-particle representing the coupled state between a DP and a multimode coherent phonon in a nano-scale region [9]. The SiC LED emission originates from the generation of DPPs in the p – n junction by current injection. The generated DPPs relax to photons or photons and phonons. These photons are observed as the electroluminescence from the SiC LED. Here, the wavenumber conservation law, which is the barrier for recombination of an electron–hole pair, is satisfied by the large wavenumber of the phonon component of the DPP. The DPP annealing mechanism is described briefly here. During the DPP annealing, Joule heating due to a forward bias current causes the Al dopant in the SiC to diffuse,

modifying its spatial distribution. During this process, the device is irradiated with laser light for generating DPPs at the surface of the dopant sites. These DPPs excite multimode coherent phonons, forming DPPs. Since the density of states of these DPPs is much higher than the density of states of conduction electrons, a population inversion is formed. Therefore, stimulated emission is generated via a two-step transition driven by the incident light. Thus, part of the Joule heat is spent for the stimulated emission of photons, controlling the progress of the annealing. Because the stimulated emission probability and spontaneous emission probability are proportional to each other, in regions where the DPP-mediated stimulated emission process easily occurs, DPP-mediated spontaneous emission also easily occurs. This induces the DPP-assisted process, which modifies the Al diffusion due to annealing, leading to the self-organized formation of a unique minute inhomogeneous distribution of the dopant. It is expected that the distribution of the dopants will be optimal for efficient spontaneous emission.

3. EXPERIMENTAL

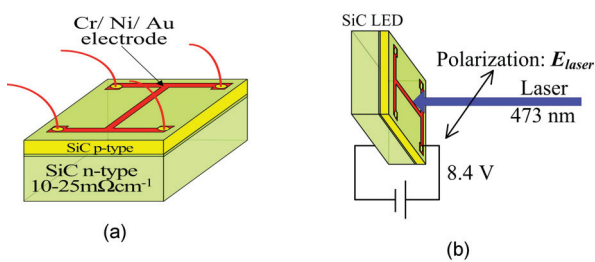


Fig. 2. (a) Schematic illustration of the fabricated device. (b) The setup used for DPP annealing.

First, we prepared a SiC p-n homojunction formed by ion implantation in n n-type bulk wafer. Next, electrodes were fabricated on the p-n homojunction SiC wafer by sputtering. Then, individual devices with the electrodes were singulated from the SiC wafer. The devices were annealed by Joule heating brought about by a forward bias current under laser irradiation, a process which is referred to as DPP annealing. For this annealing, we used a linearly polarized 473 nm ($h\nu=2.62$ eV) laser with a power of 20 mW. Figure 2(a) shows a schematic illustration of the fabricated device. The set-up used for the DPP annealing is explained in Fig. 2(b). The polarization of the laser used for the annealing was selected by a Glan-laser calcite polarizer.

Figure 3(a) shows the EL emission spectra

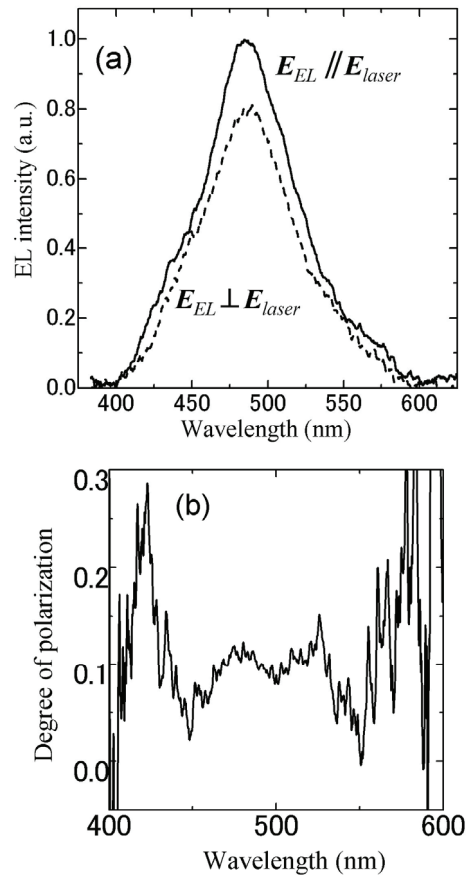


Fig. 3. (a) EL emission spectra from the SiC LED, showing polarization components parallel (solid curve) and orthogonal (broken curve) to the polarization of the laser light irradiated during DPP annealing. (b) The degree-of-polarization spectrum of the EL emission.

from the SiC LED, showing the polarization components parallel (solid curve) and orthogonal (broken curve) to the polarization of the laser light irradiated during DPP annealing. In both components, spectral peaks appeared at 480 nm. The spectral peak was controllable by changing the wavelength of the laser light irradiated during DPP annealing. A detailed discussion of the wavelength control has been reported elsewhere [5-8]. It should be noted that the parallel polarization component was stronger than that of the orthogonal polarization component. Figure 3(b) shows the degree-of-polarization spectrum of the EL emission. The degree of polarization was 12 % at 480 nm.

Figure 4 shows the dependency of the degree of polarization on the DPP annealing time. Before the annealing, the degree of polarization was negligibly small, and it increased as DPP annealing

progressed. At an annealing time of 5.5 hours, the degree of polarization reached 12 %. The polarization direction could be freely selected by changing the polarization of the light irradiated during the DPP annealing.

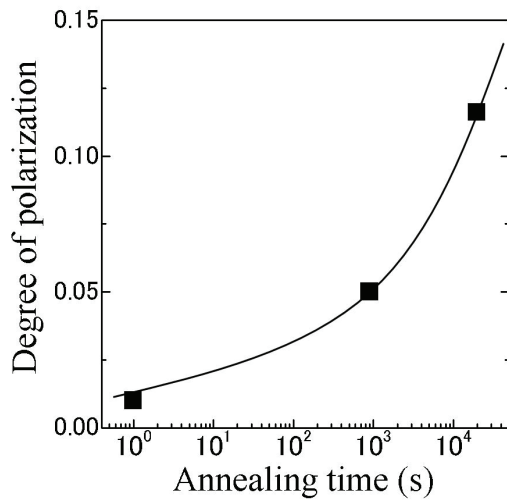


Fig. 4. The dependency of the degree of polarization on the DPP annealing time.

4. SUMMARY

We demonstrated a SiC light emitting diode and its polarization control by using DPP annealing. To fabricate this device, it was annealed by Joule heating brought about by a forward bias current under laser irradiation (dressed-photon–phonon

(DPP) annealing). In this process, polarized light was used. The annealed device emitted light with a polarization parallel to that of the annealing light. The device fabricated with a DPP annealing time of 5.5 hours showed a degree of polarization of 12%.

REFERENCES

- [1] M. F. Schubert, S. Chhajed, J. K. Kim, E. F. Schubert, and J. Cho, *Appl. Phys. Lett.* **91**, 051117 (2007).
- [2] N. F. Gardner, J. C. Kim, J. J. Wierer, Y. C. Shen, and M. R. Krames, *Appl. Phys. Lett.* **86**, 111101 (2005).
- [3] L. Schade, U. T. Schwarz, T. Wernicke, J. Rass, S. Ploch, M. Weyers, and M. Kneissl, *Appl. Phys. Lett.* **99**, 051103 (2011).
- [4] K. Domen, K. Horino, A. Kuramata, and T. Tanahashi, *Appl. Phys. Lett.* **71**, 1996 (1997).
- [5] T. Kawazoe & M. Ohtsu, *Appl. Phys. A* **115**, 127 (2014).
- [6] T. Kawazoe, M. A. Mueed, and M. Ohtsu. *Appl. Phys. B* **104**, 747 (2012).
- [7] T. Kawazoe, M. Ohtsu, K. Akahane, and N. Yamamoto, *Appl. Phys. B*, **107**, 659 (2012).
- [8] N. Wada, T. Kawazoe, and M. Ohtsu, *Appl. Phys. B*, **108**, 25 (2012).
- [9] M. Ohtsu, *Nanophotonic*. **1**, 83 (2012).

Dressed photon technology

Motoichi OHTSU

¹Department of Electrical Engineering and Information Systems, Graduate School of Eng.,
The University of Tokyo,

² International Center for Nano Electron and Photon Technology, Graduate School of Eng.,
The University of Tokyo,

2-11-16 Yayoi, Bunkyo-ku, Tokyo 113-8656, Japan

Email: ohtsu@ee.t.u-tokyo.ac.jp

Light–matter interactions in nanometric space can exhibit unique variations in the values of the physical quantities of nanomaterials, such as energy and momentum. Novel theories have succeeded in describing these interactions, which was outside the scope of conventional classical and quantum optics that were designed for light propagating through macroscopic space¹). Assuming an infinite number of electromagnetic modes (with infinite frequencies, polarization states, and energies) and an infinite number of energy states for the electrons and holes, the total Hamiltonian was derived to define the creation and annihilation operators of a quasi-particle in order to represent the light–matter interaction in a nanometric space. Since these operators are given by the sum of the operators of photons and electron–hole pairs, this quasi-particle was named a dressed photon (DP), which is a virtual photon that dresses the material energy, i.e., the energy of the electron–hole pair.

Several applications have been developed by using the intrinsic features of the DP-mediated interaction, the resultant DP energy transfer, and its dissipation. They are optical functional devices, nano-fabrication, energy conversion, and information processing systems. As an example of electrical-to-optical energy conversion, novel near infrared and visible light emitting diodes (LEDs) have been realized by using Si crystals even though Si is an indirect transition-type semiconductor. For fabricating the LEDs, the spatial distribution of doped boron atoms was autonomously modified by the DP-phonon–assisted annealing method, resulting in efficient momentum transfer between electrons and phonons in Si. It should be noted that the irradiation light during the DP-phonon–assisted annealing serves as a “breeder” that generates light with the same photon energy of the irradiation light; that is, a novel phenomenon that we call photon breeding takes place in this LED²). After the autonomous modification, the Huang-Rhys factor, a parameter representing the magnitude of the coupling between electron–hole pairs and phonons, was determined to be 4.08 ± 0.02 , which is 10^2 – 10^3 times higher than that of a conventional Si crystal device. Furthermore, it was confirmed that the DPs coupled with the coherent phonons of the longitudinal optical mode, creating DP-phonons. Besides Si, an indirect transition-type GaP semiconductor has been used for fabricating an LED emitting

yellow-green light. An indirect transition-type SiC semiconductor has also been used for fabricating LED emitting blue-violet light, ultraviolet light, and white light. In addition to LEDs, an optical and electrical relaxation oscillator and a near infrared laser have been realized by using crystalline Si.

As a future outlook, it should be pointed out that there still remain problems to be solved for gaining a deeper understanding of DPs and exploring more applications. These include: Improving the accuracy of the physical picture of the quasi-particle representing the coupled state of a photon, an electron, and a phonon in a nanometric space. Elucidating the details of energy transfer and dissipation between nanomaterials, mediated by DPs. Elucidating the details of phonon-assisted light–matter interactions in nanometric space. Elucidating the physical origins of autonomy and hierarchy.

References

- 1) M. Ohtsu, *Dressed Photons* (Springer, Berlin, 2013) 324pages.
- 2) M. Ohtsu and T. Kawazoe, “Silicon light emitting diodes and lasers using dressed photons”, in *Prog. Nanophotonics 3*, ed. M. Ohtsu, (Springer, Berlin, 2014) pp.1-66.



Motoichi Ohtsu received the Dr. E. degrees in electronics engineering from the Tokyo Institute of Technology, Tokyo in 1978. He was appointed a Research Associate, an Associate professor, a Professor at the Tokyo Institute of Technology. From 1986 to 1987, while on leave from the Tokyo Institute of Technology, he joined the Crawford Hill Laboratory, AT&T Bell Laboratories, Holmdel, NJ. In 2004, he moved to the University of Tokyo as a professor. He has been the leader of several Japanese national projects for academia-industry collaborations. He has written over 509 papers and received 83 patents. He is the author, co-author, and editor of 62 books, including 27 in English. In 2000, he was appointed as the President of the IEEE LEOS Japan Chapter. From 2000, he is an executive director of the Japan Society of Applied Physics. He is a Fellow of the Optical Society of America, and a Fellow of the Japan Society of Applied Physics. He is also a Tandem Member of the Science Council of Japan. He has been awarded 14 prizes from academic institutions, including the Issac Koga Gold Medal of URSI in 1984, the Japan IBM Science Award in 1988, two awards from the Japan Society of Applied Physics in 1982 and 1990, the Inoue Science Foundation Award in 1999, the Japan Royal Medal with a Purple Ribbon from the Japanese Government in 2004, H. Inoue Award from JST in 2005, the Distinguished Achievement Award from the IEICE of Japan in 2007, Julius Springer Prize for Applied Physics in 2009, and Fuji-Sankei Business Eye Award in 2012.

Visible Si-LED with lateral pn junction for efficient light extraction

M. Yamaguchi, T. Kawazoe, and M. Ohtsu

Univ. Tokyo

2-11-16 Yayoi, Bunkyo-ku, Tokyo 113-8656, Japan

Email: yamaguchi@nanophotonics.t.u-tokyo.ac.jp

Silicon (Si) is widely used semiconductor in electronics because of its high crystal quality, abundance, and low toxicity. However, it has never been used for active optical devices such as LED or LASER since light emission efficiency of Si is very low due to indirect band-gap. In order to solve this problem, we have invented the novel annealing process called phonon-assisted annealing which enhances the probability of the light emission, by activating the coupling between electron-hole pairs and phonons. Until now, we have succeeded in realizing Si-LED emitting infrared[1,2] and visible[3] light.

As for the light emission with the photon energy higher than the band-gap energy, there is a problem of low light extraction efficiency due to the absorption loss. The light extraction efficiency of visible Si-LED we fabricated before[3] was very low (0.01% in blue band). To overcome this problem, we have developed a novel LED structure with lateral pn-junction, drawn in inset of Fig.1. This structure enables photons to extract efficiently because active layer is formed on the surface of the LED.

We deposited chromium/platinum layers as electrodes on n-type device layer of SOI substrate. After that, diffusion agent of p-type dopant boron was applied by spin-coating, and diffused by annealing at 600 °C. The rectifying characteristic observed in I-V curve shown in Fig.1 indicated the formation of pn-junction. We conducted phonon-assisted annealing by applying forward-bias voltage to the device while illuminating it with 2.3 eV photon energy light. As a result of annealing, we succeeded in fabricating Si-LED with emission peak at 1.9 eV (Fig.2). The external quantum efficiency is estimated to be about 10 times higher than previous research [3]. We can further improve the efficiency by optimizing the annealing the profile using this structure.

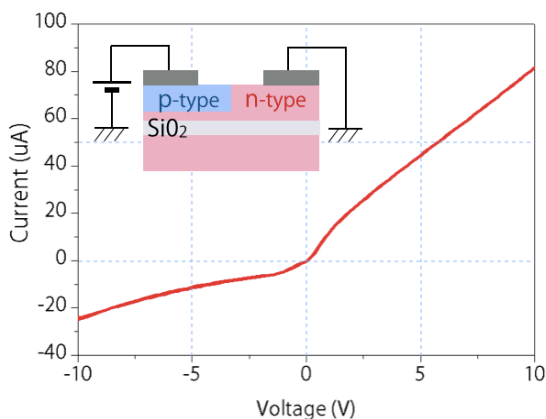


Fig.1 I-V characteristic and schematic diagram of novel LED structure

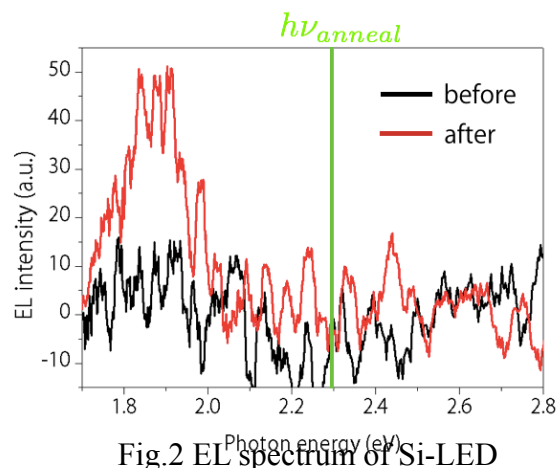


Fig.2 EL spectrum of Si-LED

- [1] T. Kawazoe et al., Appl. Phys. B, **104**, 747 (2011) [2] M. Yamaguchi et al., Appl. Phys. A, **115**, 119 (2014) [3] M.A. Tran et al., Appl. Phys. A, **115**, 105 (2014)

Ultralow-threshold current density Si lasers using dressed photons

H. Tanaka¹, T. Kawazoe¹, M. Ohtsu¹, K. Akahane²

Univ. Tokyo¹, NICT²

2-11-16 Yayoi, Bunkyo-ku, Tokyo 113-8656, Japan¹,

4-2-1, Nukui-Kitamachi, Koganei, Tokyo, Japan²

Email: tanaka@nanophotonics.t.u-tokyo.ac.jp

We fabricated a Silicon (Si) laser by applying dressed-photon-phonon assisted annealing process to a light waveguide we fabricated on silicon on insulator (SOI). We evaluated near-infrared Si photodetector having optical gain [1] for differential gain coefficient to design a light waveguide. This Si photodetector was also fabricated by the same annealing process. We designed the light waveguide, whose schematic structure is inset of Fig. 1, with 15 μm thickness of a device layer to realize large optical confinement factor. Fig.1 is laser spectrum and we confirmed that this Si laser oscillated at 1.4 μm . The intensity of amplified spontaneous emission (ASE) was so low that we could not confirm. It is because that threshold current density was so low that the Si laser oscillated right after amplifying spontaneous emission light. We estimated threshold current density by current-voltage characteristic (Fig.2). The threshold current density was 40 A/cm^2 because we confirmed minuscule current depression at 40 A/cm^2 by the Si laser oscillation. This threshold current density was one twenty-eighth of that of Si lasers we realized before [2].

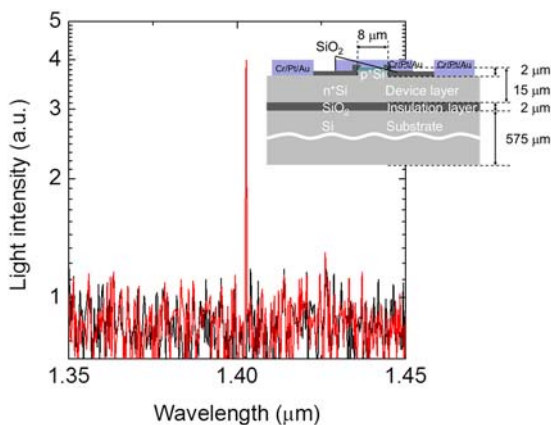


Fig. 1 Schematic device structure and laser spectrum Red: Above threshold current density ($J/J_{th} = 1.05$) Black: Below threshold current density ($J/J_{th} = 0.95$)

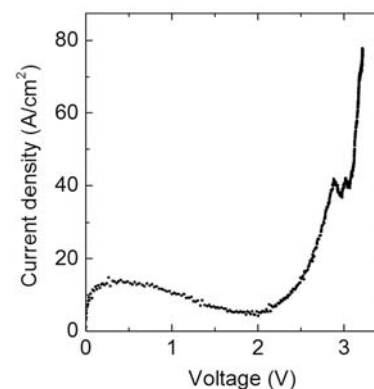


Fig. 2 Current-voltage characteristic of the laser 30 minutes after starting dressed-photon-phonon annealing.

Acknowledgement

This research was supported in part by Grant-in-Aid for JSPS Fellows Number 25 905 and JSPS Core-to-Core Program, A. Advanced Research Networks. This research was implemented in part by advanced ICT research institute of NICT. We thank N. Yamamoto for enlightening discussions.

[1] H. Tanaka, T. Kawazoe, and M. Ohtsu, Applied Physics B 108, 1, 51 (2012)

[2] T. Kawazoe, M. Ohtsu, and K. Akahane, Applied Physics B 107, 3, 659 (2012).

GaP homojunction LEDs fabricated by dressed-photon-phonon assisted annealing

Jun Hyoung Kim, Tadashi Kawazoe, and Motoichi Ohtsu

Department of Electrical Engineering and Information Systems, Graduate School of Engineering, The University of Tokyo, 2-11-16 Yayoi, Bunkyo-ku, Tokyo, 113-8656, Japan

Email: kimjh@nanophotonics.t.u-tokyo.ac.jp

We successfully fabricated a light-emitting device by forming a p–n junction via ion implantation in a bulk GaP crystal, which is an indirect-transition type semiconductor, and by using DPP (Dressed-photon-phonon) assisted annealing. As shown in the figure 1, the EL spectrum of the device fabricated by this method was governed by the light used during processing, not by the band structure of the semiconductor. In practice, the light emission from energy levels higher than 2.32 eV was increased by more than 550% (E_g of GaP is 2.26 eV) by using 532 nm (2.32 eV) light irradiation during the DPP-assisted annealing. In contrast, the rate of increase in the energy region below 2.2 eV was limited to 150–250%. As shown in figure 2, by performing experiments with and without irradiation light, we also observed a phenomenon whereby the light emission intensity from higher energy levels was increased as a result of the DPP-assisted annealing, thus demonstrating the effectiveness of the DPP-assisted process. In addition, it was also confirmed experimentally that this light was emitted from a single crystal, and was not due to amorphization (Fig. 2 blue straight line).

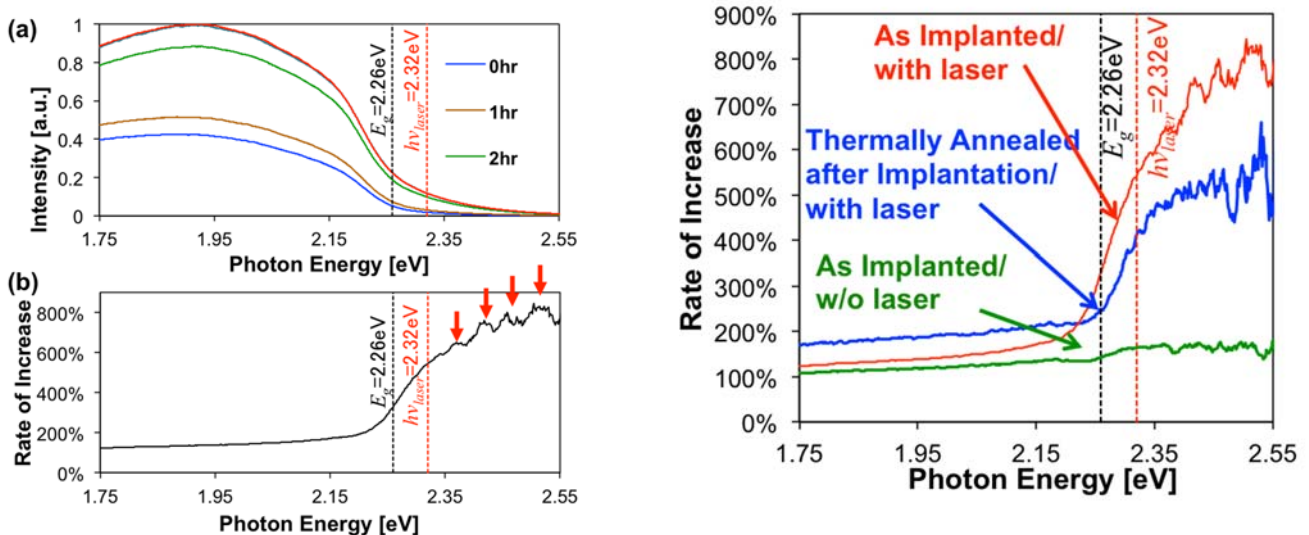


Fig. 1 Result of DPP assisted annealing. (a) Temporal evolution of spectrum. (b) Rate of increase

Fig. 2 Measured results of rate of increase.

[Invited Talk]

Processing based on fluctuations in a nanometric space and corresponding optical applications in a macroscopic space

Naoya Tate,[†] Makoto Naruse,[‡] Tadashi Kawazoe,[†] and Motoichi Ohtsu[†]

[†]The University of Tokyo

2-11-16 Yayoi, Bunkyo-ku, Tokyo, 113-8656, Japan, Japan

[‡]National Institute of Information and Communications Technology

4-2-1 Nukuikita, Koganei, Tokyo, 184-8795, Japan

Email: tate@nanophotonics.t.u-tokyo.ac.jp, naruse@nict.go.jp, kawazoe@ee.t.u-tokyo.ac.jp, ohtsu@ee.t.u-tokyo.ac.jp

Abstract—Effective utilization of fluctuations in a nanometric physical system is one of the fundamental issues that will be faced in the practical implementation of future processing systems. While fluctuations themselves often show random behavior, it is expected that optimized nanometric structures will be realized by development of a suitable control method on the nanometric scale. On the other hand, recent research on nanophotonics utilizing the characteristic behavior of dressed photons has resulted in several novel applications that work at macroscopic scales. The fundamental principle on which such techniques are based is controlled fluctuations involving interactions between light and materials in a nanometric space, and their corresponding macroscale optical functions. This paper describes concepts, experimental demonstrations, and applications of some recent activity on fluctuation-based nanophotonics, including nanophotonic droplets, dressed photon-assisted giant optical rotation, and compressive near-field optical microscopy.

1. Introduction

Recent research in the field of *beyond von Neumann computing* [1] suggests that effective utilization of fluctuations in a physical system will form an essential part of future processing systems. It is expected that degrees-of-freedom based on fluctuations will be utilized to implement innovative large-scale processing systems. Especially on the nanometric scale, fluctuations in a physical system are one of the most fundamental issues faced in the practical implementation of a processing system. To implement a *fluctuation-based nanometric processing system*, it is essential to develop novel concepts and logic that will replace the conventional ones.

On the other hand, the field of *nanophotonics*, which exploits the local interactions between nanometric particles via optical near fields induced by incident light, has seen rapid progress in recent years, and various studies have been performed [2]. Several of the characteristics of optical near fields can be explained by the behavior of a *dressed photon* (DP), which is a quasi-particle representing the coupled state of a photon and an electron in a nano-

metric space [3]. A DP excites a multi-mode coherent phonon in a nanometric material, and the DP state is coupled with states of the excited coherent phonon [4, 5, 6, 7]. Because this coupled state can be regarded as an intermediate state during the excitation and relaxation process of the material, multistep excitation and relaxation, and corresponding optical functions, are allowed. Some experimental demonstrations utilizing this phenomenon, called a DP-assisted transition, have been reported, for example, high-yield emission of up-converted optical energy by using organic dye grains [5, 8] and high-intensity emission from indirect transition type semiconductors [6, 7, 9].

The important point in these demonstrations, is that the behavior fundamentally depends on fluctuations of components in a nanometric space, and the optical functions were revealed at a macroscopic scale. This means that precisely controlled fluctuations in a nanometric space can be effectively utilized as characteristic optical functions and processing in a macroscopic space. In this paper, we focus on DPs and related technologies, and we describe concepts and experimental demonstrations on *nanophotonic droplets*, *DP-assisted giant optical rotation*, and *compressive near-field optical microscopy*, which all exhibit macroscopic optical functions based on precisely controlled fluctuations in nanometric spaces.

2. Nanophotonic droplets

We have previously demonstrated a novel technique for autonomous fabrication of a *nanophotonic droplet* (ND) [10, 11, 12], which is a micro-scale spherical polymer structure that contains coupled heterogeneous nanometric components, such as quantum dots (QDs) and organic dye molecules. The sort-selectivity and alignment accuracy of the nanometric components in each ND, as well as the related homogeneity of their optical functions, are due to a characteristic coupling process based on a DP-assisted photo-curing method involving dressed-photon-phonon interactions [13]. The method only requires irradiating a mixture of components with light to induce optical near-field interactions between each component, and subsequent processes based on these interactions. The principle of our

method is schematically shown in Fig. 1.

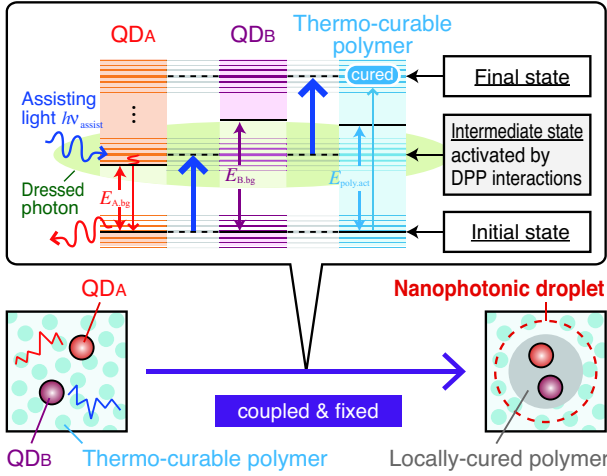


Figure 1: Schematic diagram of process of forming a thermo-curable polymer-based ND via the phonon-assisted photo-curing process.

The ND fabrication process can be induced when energies $E_{A:bg}$, $E_{B:bg}$, $E_{poly:act}$, and $h\nu_{assist}$ satisfy the condition:

$$E_{A:bg} < h\nu_{assist} < E_{poly:act} < E_{B:bg}. \quad (1)$$

. Here, if the density is sufficiently high that the QDs can frequently encounter each other, multistep photo-curing occurs due to generation of DPPs and corresponding optical near-field interactions between two neighboring QDs, QD_A and QD_B . As a result, the thermo-curable polymer is locally cured, and the spatial alignment of the QDs that encountered each other is physically fixed by the cured polymer. Because the fabrication of NDs fundamentally depends on components encountering each other due to thermal fluctuations in the mixture, thermal dependency of the process was theoretically and experimentally verified in a previous report by the authors [12].

Figure 2 shows a fluorescence image of the NDs formed using commercially available CdSe-QDs (Sigma-Aldrich, *Lumidots*), CdS-QDs (NN-Labs, *Nanocrystals*), and thermo-curable polymer (Dow Corning Toray, *Sylgard 184*) irradiated with assisting light from a 200 mW laser diode with a wavelength of 457 nm for 30 minutes. As shown, a number of NDs with similar sizes and emission intensities were successfully obtained.

These similarities of massively fabricated NDs are due to the accuracy and homogeneity of their alignment and the combinations of QDs in each ND. Due to the particular structural characteristics of their constituent elements, we have reported an experimental demonstration of effective wavelength conversion based on the novel optical functions of NDs [14]. Because the formation process is induced only when fluctuating heterogeneous QDs encounter each other at the optimum distance to induce appropriate optical near field interactions between the two, their relative spatial positions and corresponding optical functions are au-

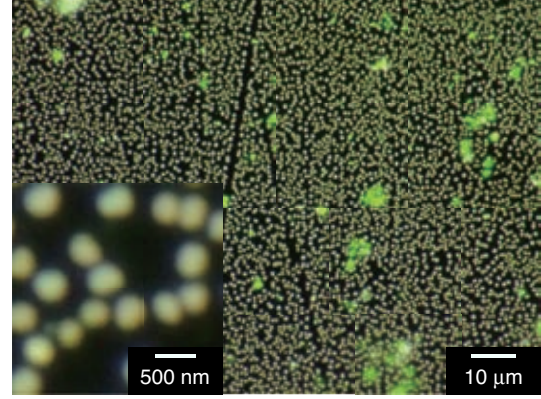


Figure 2: Microscope fluorescence image of densely formed NDs under UV light irradiation and (inset) a magnified view.

tonomously determined. This means that thermal fluctuations of components in the mixture realized optimal nanometric structures, and corresponding optical functions were revealed at a macroscopic scale in the form of light emission from the NDs.

3. DP-assisted giant optical rotation

Oxide semiconductors are known to be direct-transition materials with a wide bandgap. Due to their natural abundance, innocuity, and transparency to visible light, they are expected to be widely applied to various optical devices [15]. However, although such oxide semiconductors are highly promising, it is difficult to realize electro- or magneto-induced optical functionalities by general doping methods, because acceptors from the dopants are generally compensated with donors from the numerous oxygen vacancies and interstitial metals in the crystal. On the other hand, according to recent research by the authors' group, a p-type ZnO device, which is one of the most common oxide semiconductors, has been successfully realized by employing annealing using dressed photons [16], a technique known as *DP-assisted annealing*. By using the p-type ZnO device, realization of a p-n homojunction-structured LED that emits at room temperature has been successfully demonstrated. More recently, we applied a voltage to p-type ZnO devices in the in-plane direction instead of the direction perpendicular to the p-n homojunction plane, and experimentally demonstrated novel optical phenomena quite similar to but much larger than the well-known magneto-optical effect. The essential point of that work is that the distribution of dopants is autonomously optimized by utilizing DP-assisted annealing. DP-assisted annealing controls the fluctuations of dopants in the crystal, causing them to converge to an optimized distribution for inducing DPPs and, as a result, corresponding optical functions are exhibited.

In this study, we used an n-type bulk ZnO crystal implanted with N ions (N dopant) serving as a p-type dopant.

A p-n homojunction was formed in the crystal by implanting N ions; however, because this structure was simple, the electrons and holes both exhibited wide spatial distributions, and their recombination probability and the emission intensity were low. Therefore, the devices were subjected to DP-assisted annealing to optimize the dopant distributions; namely, they were annealed with Joule heat by applying a current. During this process, the substrate surface was irradiated with light having a photon energy $h\nu = 3.05$ eV, which is smaller than the bandgap energy of ZnO, $E_g = 3.40$ eV, so as to control the spatial distribution of the N concentration at the p-n junction in a self-organized manner. As a result, DPs were efficiently generated in the N regions, and electrons and holes recombined via these DPs, producing spontaneous emission based on the existence of a good p-n homojunction.

In order to demonstrate giant optical rotation using the p-type ZnO device, the experimental setup shown in Fig. 3 was prepared for observing modulated light among the incident orthogonally polarized light. As shown, a bias current was induced in the device in the in-plane direction instead of the p-n homojunction direction. In such a situation, the magnetic field due to the induced current affected the p-n homojunction. Incident light to the device was temporarily converted to DPs via the dopant, and these DPs interacted with the magnetic field. As the result, corresponding optical modulation was applied to the incident light.

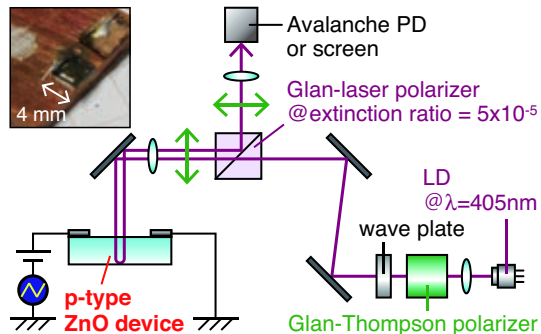


Figure 3: Schematic diagram of experimental setup for measuring optical rotation with orthogonally polarized light. (Inset) Appearance of the prototype p-type ZnO device.

Figure 4 shows the relation between the applied voltage to the device and the polarization rotation. Although the original ZnO crystal does not reveal such large optical rotation of the incident light, extremely large optical rotation was observed in our p-type ZnO device.

The characteristic behavior observed in this research was a result of the optimized distribution of dopants and the corresponding interactions between induced DPs and incident light. What is important is that fluctuations of the dopants due to the Joule heat were effectively controlled by DP-assisted annealing to make the distribution converge to one appropriate for generating DPs and the corresponding op-

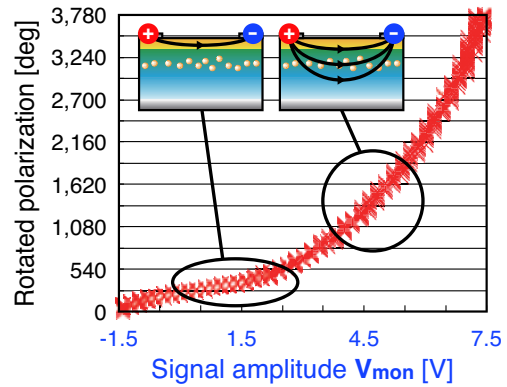


Figure 4: Relation between applied voltage to the device and polarization rotation.

tical functions.

4. Compressive near-field optical microscopy

A *Reader* and a *Device* are fundamental elements of a general authentication system. Recently, the authors developed a novel authentication system based on nanophotonics, what we call a *nanometric artifact-metric system*. Whereas in a conventional system, the Reader reads data from the Device and then their validities are authenticated, in the case of our proposed system, the data to be authenticated is a result of optical near-field interactions between the Reader and the Device in a nanometric space. Because the result of the interactions is strictly dependent on the uniqueness of the physical properties of both the Reader and the Device, security of the system is fundamentally guaranteed. For a simple demonstration of this approach, we previously used a conventional scanning near-field optical microscope (SNOM) as a Reader and a sample containing nanorods, grown by the glancing angle deposition (GLAD) method, as a Device. However, the SNOM required a scanning process, making it quite inconvenient to use the SNOM in a practicable system.

Against such a background, we proposed the concept of a *compressive near-field optical microscope* (CNOM) to demonstrate a practicable nanometric artifact-metric system instead of using an SNOM. A schematic diagram illustrating the concept of the CNOM is shown in Fig. 5.

As shown, the readout results from the probe of the Reader constantly fluctuated based on the feedback setup of NOM, which prevents a collision between the probe and the Device by sensing the shear force between them. This means that the probe constantly reads the result of different scales of interaction during the fluctuation. Because the result of an interaction depends on the element size of the Device at an appropriate scale, which is determined by the readout distance between the probe and the Device, the readout results are expected to contain not only data about a single point but also data about a two-dimensional area in the surroundings. Therefore, we can read out two-

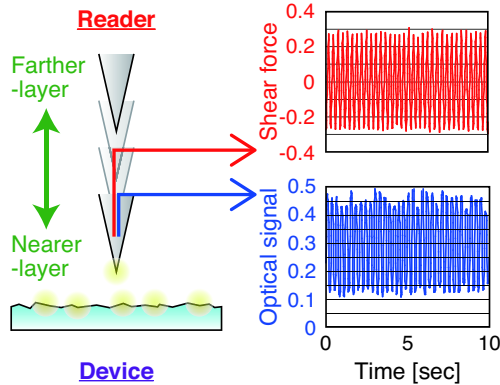


Figure 5: Schematic diagram illustrating concept of a compressive near-field optical microscope (CNOM).

dimensional data without any scanning process by utilizing the fluctuations of the probe. In the case where a basic NOM system is used, readout data from the probe consists of signals due to shear force and the optical response. Here we defined these two types of data as parameter that identifies each Device, and verified their individualities by using different Devices.

For an experimental demonstration, we used the NOM system in an illumination-collection mode with an Au-coated glass fiber probe having a radius of curvature of 50 nm. To control the observation distance, the probe sensitivity to the shear force between the probe tip and the sample was electrically adjusted in multiple steps. A laser diode (LD) with an operating wavelength of 650 nm was used as the light source. Figure 6 shows readout results obtained using two different Devices, Device 1 and Device 2, which consisted of smaller (35 nm diameter) and larger (75 nm diameter) Al nanorods, respectively.

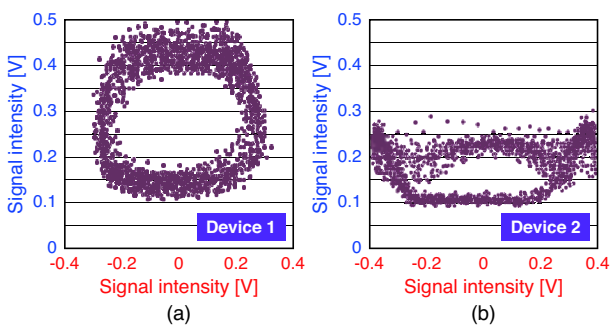


Figure 6: Readout results obtained by using different Devices, which consisted of (a) smaller nanorods and (b) larger nanorods.

As shown, distinct differences were observed between the two. Moreover, because the basic shape of each result surely corresponds to the two-dimensional distribution of nanorods, the characteristic value of each Device is expected to be analogize based on further statistical results, which are obtained without any scanning processes.

5. Summary

We have described some the concepts and experimental demonstrations of some recent activity in research on nanophotonic droplets, dressed photon-assisted giant optical rotation, and compressive near-field optical microscopy. A common point in these systems is that their nanometric mechanisms were optimized by controlled fluctuations of the components based on the behavior of dressed photons, and the results of the optimization were revealed as characteristic optical functions at the macroscopic scale. Focusing on such controlled fluctuations and related technologies is expected to lead to further developments in the research and implementation of future processing systems.

Acknowledgments

A part of this work was supported by the “Development of next-generation high-performance technology for photovoltaic power generation system” program of the New Energy and Industrial Technology Development Organization (NEDO), Japan.

References

- [1] E. Verhulst, *Networks on Chip* (Springer, 2004).
- [2] M. Ohtsu, K. Kobayashi, T. Kawazoe, T. Yatsui, and M. Naruse (eds.), *Principles of Nanophotonics* (Taylor and Francis, 2008).
- [3] M. Ohtsu, *Dressed Photons* (Springer-Verlag, 2013).
- [4] S. Yukutake et al., *Appl. Phys. B* **99**(3), 415-422 (2010).
- [5] H. Fujiwara et al., *Appl. Phys. B* **98**(2-3), 283-289 (2010).
- [6] T. Kawazoe et al., *Appl. Phys. B* **104**(4), 747-754 (2011).
- [7] K. Kitamura et al., *Appl. Phys. B* **107**(2), 293-299 (2012).
- [8] T. Kawazoe et al., *J. Sel. Top. Quantum Electron.* **15**(5), 1380-1386 (2009).
- [9] N. Wada et al., *Appl. Phys. B* **108**(1), 25-29 (2012).
- [10] N. Tate, et al., *Appl. Phys. B*, **110**(1), 39-45 (2013).
- [11] N. Tate, et al., *Appl. Phys. B*, **110**(3), 293-297 (2013).
- [12] N. Tate, et al., *Appl. Phys. B*, **112**(4), 587-592 (2013).
- [13] M. Ohtsu, et al., *IEEE J. Sel. Top. Quant. Ele.*, **14**(6), 1404-1417 (2008).
- [14] N. Tate, et al., *Opt. Exp.*, **22**(9), 10262-10269 (2014).
- [15] Y.-S. Choi et al., *IEEE Trans. Electron Devices* **57**(1), 26-41 (2010).
- [16] T. Kawazoe et al., *J. Chem. Phys.*, **122**, 024715 (2005).

[Invited Talk]

Near-field Nanophotonics for Intelligent Information Functions

Makoto Naruse¹, Masashi Aono², Song-Ju Kim³, Naoya Tate⁴, and Motoichi Ohtsu⁴

¹ Photonic Network Research Institute, National Institute of Information and Communications Technology, 4-2-1 Nukui-kita, Koganei, Tokyo 184-8795, Japan

² Earth-Life Science Institute, Tokyo Institute of Technology, 2-12-1 Ookayama, Meguro-ku, Tokyo 152-8550, Japan

³ WPI Center for Materials Nanoarchitectonics, National Institute for Materials Science, 1-1 Namiki, Tsukuba, Ibaraki 305-0044, Japan

⁴ Department of Electrical Engineering and Information Systems, Graduate School of Engineering, The University of Tokyo, 2-11-16 Yayoi, Bunkyo-ku, Tokyo 113-8656, Japan

Abstract— This paper reviews recent theoretical and experimental investigations toward realizing intelligent information functionalities by utilizing unique physical processes occurring at a scale below the wavelength of light, which is called nanophotonics.

There is a great demand for novel computing devices and architectures that can overcome the limitations of conventional technologies based solely on electron transfer, including the need to reduce energy consumption and solve computationally demanding problems [1-3]. Security is becoming ubiquitously important to safeguard against threats [4,5]. A promising solution is near-field nanophotonics [6], which has been extensively studied with the aim of unveiling and exploiting light-matter interactions that occur at a scale below the wavelength of light, and recent progress made in experimental technologies—both in nanomaterial fabrication and in characterization—is driving further advancements in the field.

We demonstrate that the dynamics of optical energy transfer mediated by near-fields interactions can be exploited to solve solution searching [7] and decision making problems [8]. By introducing simple state-filling mechanisms for controlling the energy transfer among multiple quantum dots, we successfully solved a constraint satisfaction problem [7] and the multi-armed bandit problem [8]. The emergent intellectual abilities of these near-field nanophotonic systems are attributed to the probabilistic and nonlocal nature inherent in the optical-near-field-mediated energy transfer dynamics.

Also, we theoretically and experimentally demonstrate information security applications, such as information hiding and authentication, by using hierarchical properties of optical near-fields [9]. Shape-engineered nanostructures can play a key role for security functionalities thanks to their abilities of, for instance, asymmetric polarization conversion [10].

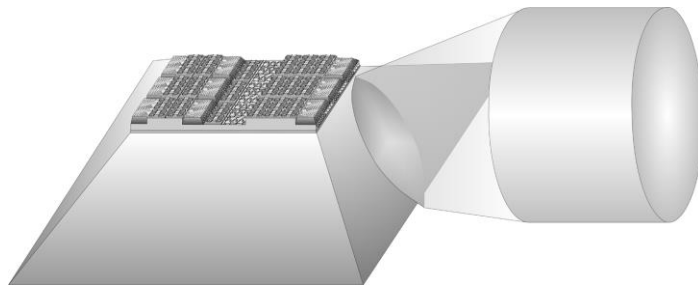
Acknowledgments

This work is supported in part by the Core-to-Core Program by the Japan Society for the Promotion of Science.

References

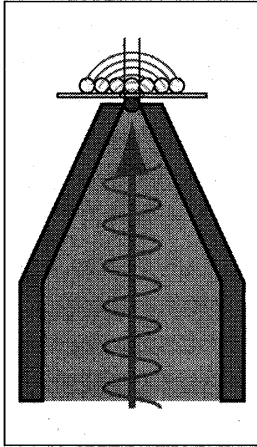
- [1] M. Naruse, N. Tate, M. Aono, and M. Ohtsu, Information physics fundamentals of nanophotonics, Reports on Progress in Physics, vol. 76, pp. 056401, 2013.
- [2] D. Brunner, M. C. Soriano, C. R. Mirasso, and I. Fischer, “Parallel photonic information processing at gigabyte per second data rates using transient states,” Nature Commun., vol. 4, 1364, 2013.
- [3] S. Utsunomiya, K. Takata, and Y. Yamamoto, Mapping of Ising models onto injection-locked laser systems. Optics express, vol. 19, pp. 18091-18108, 2011.
- [4] H. Matsumoto and T. Matsumoto, Clone match rate evaluation for an artifact-metric system, IPSJ J., vol. 44, pp. 1991-2001, 2003.
- [5] R. Pappu, B. Recht, J. Taylor, and N. Gershenfeld, Physical One-Way Functions, Science, vol. 297, pp. 2026-2030, 2002.
- [6] M. Ohtsu, K. Kobayashi, T. Kawazoe, S. Sangu, T. Yatsui, Nanophotonics: design, fabrication, and operation of nanometric devices using optical near fields, IEEE J. Sel. Top. Quantum Electron., vol. 8, pp. 839-862, 2002.
- [7] M. Naruse, M. Aono, S.-J. Kim, T. Kawazoe, W. Nomura, H. Hori, M. Hara, and M. Ohtsu, Spatiotemporal dynamics in optical energy transfer on the nanoscale and its application to constraint satisfaction problems, Phys. Rev. B, 86, pp. 125407, 2012.
- [8] S.-J. Kim, M. Naruse, M. Aono, M. Ohtsu, and M. Hara, Decision Maker based on Nanoscale Photo-excitation Transfer, Scientific Reports, vol. 3, 2370, 2013.
- [9] M. Naruse, N. Tate, and M. Ohtsu, Optical security based on near-field processes at the nanoscale, J.Optics, vol. 14, pp. 094002, 2012.
- [10] M. Naruse, N. Tate, Y. Ohyagi, M. Hoga, T. Matsumoto, H. Hori, A. Drezet, S. Huant, and M. Ohtsu, Optical near-field-mediated polarization asymmetry induced by two-layer nanostructures, Optics Express, vol. 21, pp. 21857-21870, 2013.

[III] REVIEW PAPERS



近接場光学の過去, 現在, 未来

東京大学
大津元一



1. はじめに

近接場光とは光が照射されたナノ寸法物質（ナノ物質）の表面近傍に発生する小さな光であるが、それはいまや国語辞典でも解説されるほど広く知られている¹⁾。近接場光を扱う科学技術は「近接場光学」であり、これは筆者が命名したものであるが²⁾、この末尾の二文字は「光学」ではなく「近接場光」の「学」を意味しており、近接場光を学び使うことを意図している。従来の光学で扱う光は遠くへと伝わる伝搬光であり、光子と物質との相互作用の観点からは実光子(real photon)である。一方、近接場光は非伝搬であり、仮想光子(virtual photon)である³⁻⁵⁾。この根本的な違いに注意すると近接場光をどのように理解し、どのように応用すればよいかがわかる。本稿では近接場光の科学技術の歴史とともに、応用例を紹介する。なお、近接場光の応用技術は今や包括的技術として育っており、その活用分野は多岐にわたるが、ここでは頁数の制限上、発光素子への応用を中心に紹介する。

2. 歴史

一般に科学技術の出発点を何時と捉えるかは、その科学技術の定義に依存する⁶⁾。近接場光の科学技術の場合、その「古典的」な時代では近接場光を高分解能の光学顕微鏡に応用する提案の論文発表が出発点と捉えられていた⁷⁾。その後マイクロ波を用いてこれが検証された⁸⁾。さらに微小開口からの電磁波の回折と放射の現象が理論的に解析され^{9,10)}、多体効果を取り入れた自己無撞着の理論も展開された¹¹⁾。一方、実験面では近接場光学顕微鏡が世界の数カ所ではほぼ同時期に開発され¹²⁾、物質の形状や構造の計測と分析の新たな手段を提供した。以上の研究は全て波動光学の枠組みで議論されている。

顕微鏡は測定対象である物質の形状や構造を非破壊測定するために使われるが、この非破壊測定は近接場光の性質と整合しないことが認識され、近接場光を顕微鏡に使う「古典的」な時代は終焉し、「現代的」な新しい近接場光の科学技術が誕生した。すなわちそれは近接場光が関わる光と物質の相互作用を明らかにする研究、およびその幅広い応用である。

「近接場光」の名前はエバネッセント光と同様、物質表面に発生することに起因し「古典的」な時代に採用された。しかし近接場光が関わる光と物質の相互作用では光波長以下の寸法を持つ物質および光波長以下の距離での相互作用を絶えず扱う。従って近接場光の研究はナノ寸法空間での光と物質の相互作用の研究に他ならず、扱うナノ寸法物質（ナノ物質）の種類に依存し、大きく分けて二つの方向へと進んだ。その第一は半導体や有機分子のナノ物質、さらには気体分子を対象とする研究である。この研究ではナノ物質の中の電子正孔対または気体分子中の電子の離散化したエネルギー準位とエネルギー散逸とを考慮して光と物質の相互作用が調べられ、量子力学的な現象を発現する「現代的」な近接場光の応用技術としての新機能の光デバイスなどが実現した³⁻⁵⁾。第二は金属のナノ物質や薄膜を対象とするが、これらは半導体のナノ物質にくらべ製造加工が容易なことから、多くの研究がなされている。その結果、金属中の自由電子のプラズマ振動の様子を表すプラズモンと光の結合を利用し

たプラズモニクスと呼ばれる技術が開発された¹³⁾。この場合には電子の集団運動が関与しているため、光のエネルギーはいち早く電子のプラズマ振動に変換され、また電子の位相緩和時間は非常に短いため、たとえ金属に入射する光が特殊な量子力学的な性質を持っていたとしても、光の当初の性質は失われる。従ってプラズモニクスでは波動の物理現象を表す屈折率、波数、導波モード、分散関係などの用語を用いて現象が解析されており、上記の顕微鏡の研究と同様の「古典的」な波動光学の範疇に含まれる。

3. ドレスト光子としての描像

本節では近接場光の「現代的」な側面を中心として、物理的描像を記述しよう。ナノ寸法空間での光と物質の相互作用の結果、光と物質のエネルギーや運動量などの物理量が独特の形態で増減する。従ってこの相互作用について調べるにはその増減の様子を知ることが必須である。そのためには次の点に注意する必要がある。

- (1) ナノ寸法空間での光と物質の相互作用を調べるには、場の量子論によりエネルギーの増減すなわち光子と電子正孔対の数の増減を多体系の物理として記述し、これらの粒子の生成消滅演算子を定義する必要がある。しかし光波長以下の寸法の空間を取り扱うので、量子化の基礎となる光のモードが定義できないことから、光の波長（波数）と光子の運動量が確定せず、従って光エネルギーのハミルトニアンが書き下せないという問題がある。従来の光の量子論¹⁴⁾では架空の共振器の特定のモードの光を考え、それを量子化の対象としているが、ここではこの問題によりそれが不可能である。
- (2) 近接場光は光照射により物質表面に誘起された分極の間の相互作用を媒介する仮想光子（物質表面に発生する非伝搬の光）なので、それを観測・検出するためには第二のナノ物質を近づけて近接場光を多重散乱させ、伝搬光（実光子）に変換する必要がある。その後この伝搬光を遠方にて測定する。これにより近接場光の発生と検出の過程が終了する。この場合、近接場光発生用の第一のナノ物質を近接場光源、第二のナノ物質を近接場光検出器と考えることができるが、従来の光学現象と異なり、ナノ寸法空間ではこの光源と光検出器はもはや独立ではなく、近接場光を通じて結合している。すなわち近接場光は光源と光検出器の間に多重散乱されていることから、近接場光源と近接場光検出器とを区別できない。このため、従来の光学で用いられてきた屈折率（入射光に対する物質の応答の位相遅れを表す）は基本的な物理量にはなりえない。
- (3) 上記(2)に記したように、ナノ寸法空間において二つ（またはそれ以上）ナノ物質が近接場光を介して結合している系（ナノ系）は周囲の巨視的な系とも相互作用している。この巨視系はナノ物質が置かれている基板、または埋もれている母結晶といった巨視的物質、および近接場光発生用の入射光、散乱されて伝搬していく光といった巨視的電磁場からなる。すなわちナノ系は熱浴としての巨視系に囲まれそれと相互作用し、ナノ系の一部のエネルギーは巨視系へと散逸する。

以上の各項目に注意し、波動光学の枠組みを脱した新しい理論が構築され、次の知見が得られている。

- (a) 上記(1)で指摘された問題を解決するには、環境系を含む無数のモードの光子、無数のエネルギー準位をもつ電子正孔対の相互作用を考える必要がある。そのハミルトニアンを書き下し、相互作用の様子を表す準粒子を抽出して、近接場光による相互作用を代表する準粒子の生成消滅演算子を定義する理論体系が構築された¹⁵⁾。この演算子が光子の生成消滅演算子と電子正孔対の生成消滅演算子の和から構成されていることから、この準粒子は電子正孔対の衣をまとった光子、すなわちドレスト光子（dressed photon ; DP）と名づけられた³⁻⁵⁾。DPは無数のモードの光子を含むので、そのスペクトルは周波数変調され無数の側波帯を有する。すなわち第一のナノ物質に単一モードの光が入射した場合でも、発生するDPは無数の周波数成分からなる。なお、さらにDPは物質中の多モードのコヒーレント状態のフォノンとも結合し、ドレスト光子フォノン（dressed-photon—phonon ; DPP）と呼ばれる準粒子を形成することが見出され、その生成消滅演算子も導出された¹⁶⁾。

- (b) 上記 (2) の指摘を反映し、二つのナノ物質間の相互作用は DP または DPP の交換によって表されるようになった。それらは上記の生成消滅演算子によって表される。なお、上記の周波数変調の結果、第一のナノ物質に生ずる側波帯のエネルギーを第二のナノ物質が吸収すれば、このナノ物質は伝搬光を吸収した場合とは異なる光学応答を示すことも理論と実験の両面から示された¹⁷⁾。
- (c) 上記 (3) の指摘を反映し、かつ (a) と (b) の理論に基づけば、巨視系のもつ多数の物理定数と自由度のうち、ナノ系と巨視系との相互作用を記述する為に直接必要ではないものは繰り込みの手法を用いて理論式中の適切な定数に置き換えることができる¹⁸⁾。この手法により、ナノ系の二つのナノ物質間の相互作用の大きさとその空間分布が求められた¹⁹⁾。この分布は中間子と同様の湯川関数により表され、DP の場の空間的減衰長はナノ物質の寸法に相当する。すなわちナノ物質表面に発生する近接場光の厚みはその物質の寸法程度である。これは「古典的」な時代から実験を通じて経験的に知られている近接場光の性質であるが、ナノ寸法空間での光と物質の相互作用を調べる「現代的」な研究により定式化することができた。さらに物質の寸法程度の空間分布をもつ近接場光のエネルギーが二つのナノ物質間を移動する際、その効率二つの物質の寸法が等しいときに最大となるという性質、すなわち「寸法依存共鳴」の現象も定式化された²⁰⁾。これらの性質に起因し、上記 (2) にも示した伝搬光の場合とは異なる次のような光学応答が見出された：ナノ物質の場合、この減衰長は光波長よりずっと短いので、DP による光と物質との相互作用では、従来の伝搬光が関与する相互作用において使われていた長波長近似とそれに付随する保存則等が有効ではなくなる。すなわち従来の電気双極子禁制遷移が「現代的」な近接場光学では許容される。

以上の「現代的」な研究の結果、仮想光子である近接場光は今やナノ寸法空間で結合している光子と電子正孔対からなる準粒子である DP という描像で記述されている。「近接場光」という用語はナノ物質表面に発生する光の空間的分布を表すのに適しており、「古典的」な時代にはその空間分布の一部の性質はこれまで波動光学の概念によって説明されていたが、「現代的」な研究の結果、その発生の起源である光と物質の相互作用のようすが DP の描像により表されるようになった。

4. 応用技術

近接場光はかつて高分解能の顕微鏡などの光学計測へ応用されていたが、DP のエネルギーが二つのナノ物質間で移動することから、測定対象のナノ物質の状態が近接場光で摂動を受ける。従って計測の非破壊性が保証されず計測結果の物理的解釈が困難である。近接場光の優れた性質を活用する本来の方向は DP のエネルギー移動を利用して微小な光デバイスを作ったり、また微細加工、エネルギー変換を行うことであり、最近では下記の技術が発展している。

(1) 微小な光デバイス：

半導体のナノ物質の間での DP を介したエネルギー移動を利用することによりナノ寸法の光デバイス、すなわちドレスト光子デバイスが作られている³⁻⁵⁾。このデバイスでは特定の寸法比をもつ大小二つのナノ物質の間でのエネルギー移動、それにより第二のナノ物質中に励起された電子正孔対の緩和によるエネルギー散逸を利用して光信号を伝送し取り出す。これまでに多様なデバイスが開発されており、さらにこれらを用いたナノ寸法の光コンピューティングのシステムや情報セキュリティのシステムが開発されている^{21,22)}。

(2) 微細加工：

フォトマスク開口端部に発生させた DPP によるリソグラフィ²³⁾、さらにはフォトマスク等の特別な部品を使わず被加工物質表面の小さな突起に発生する DPP を用いた自己組織的な表面平坦化技術²⁴⁾などが開発されている。

(3) 光エネルギー変換：

DP は入射光の周波数のみでなく、多くの側波帯を含んでいるのでエネルギー上方または下方変換の現象が生じる。例えば色素微粒子の間での DPP のエネルギー移動の際のエネルギー上方変

換を利用し、近赤外線が可視光に変換されている²⁵⁾。一方、下方変換を利用し紫外光を可視光に変換する技術も進展している^{26,27)}。

(4) 第三の光源：

従来の光源には発光ダイオード (LED)、レーザーなどがあるが、これらに対し、本技術による発光デバイスはその原理、作製方法、特性が全て異なることから「第三の光源」と位置づけられている。なお、この光源が発する光の色、伝搬方向、偏光は、作製時に DPP を発生させるために照射した光のそれらと同等である。すなわち作製の際に照射した光の特性が発光へと遺伝している。この遺伝現象は光子ブリーディング (photon breeding, PB) と名づけられ、この現象を発揮するデバイスは光子ブリーディングデバイス (PBD) と呼ばれている²⁸⁾。従来技術で LED やレーザーを作る際、発光させたい光の波長に応じ種々の直接遷移型半導体を選んで使っているが、PBD では光の色によらずシリコン (Si) の結晶を使えばよい。Si は電子技術では古くから使われてきた材料であるが間接遷移型半導体なので、長い光技術の歴史において「光らない」と考えられてきた。しかし Si 結晶中の DPP の発生を制御して伝導帯の電子とフォノンとの間で運動量を授受させることにより近赤外光、可視光を高効率で発生する LED 型 PBD、近赤外線を発生するレーザー型 PBD が実現した。さらには Si と同様の間接遷移型半導体の SiC や GaP を用いた LED 型 PBD も開発された。以下ではこれらの革新技术を概説する。

DPP はナノ物質中の結晶格子に不純物原子が含まれている場合、そこに局在しやすい³⁵⁾。これによりフォノンが関与する新規の励起・脱励起が可能となるので、対象となるナノ物質についてはその中の電子の状態のみでなく、それとフォノンの励起状態との直積で表される状態を考える必要が生ずる。間接遷移型半導体の場合、伝導帯、価電子帯のエネルギー帯の底、頂点における電子と正孔の波数ベクトル (運動量) の向きと大きさは互いに異なるので帯間遷移のためには運動量の異なる電子と正孔とが再結合しなければならない。その際、運動量の保存則を満たすためには光子の他にフォノンも同時に放出する必要があるが、電子とフォノンの相互作用は小さく、その確率は低い。しかし上記の DPP はフォノンを含むので、伝導帯中の電子とフォノンと相互作用は大きく、間接遷移型半導体でも再結合による自然放出の確率は直接遷移型半導体における確率と同程度まで高くなる。その結果 DPP が自然放出されるが、その一部は伝搬光に変換されるので発光素子を実現する。

Si のバルク結晶を用いて発光素子を実現するためには DPP を二回使う (図1)。その一つは発光素子を作製する際、自然放出に適した p 型ドーパントのボロン (B) 原子の空間分布を制御するためである。すなわちアニール加工の際、照射により発生する DPP による原子の空間分布を制御し、伝導帯中の電子とフォノンとの間での運動量の授受が可能となる空間分布形状を自律的に形成させる。もう一つは自然放出光を発生させ発光素子として動作させるためである。前者の詳細については文献²⁸⁾を参照して頂くことにし、本節では後者について記す。

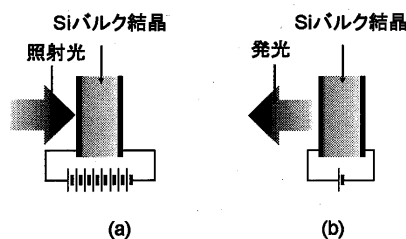


図1 PBDの作製と動作

(a)ジュール熱アニールによる作製。アニール時に光も照射する。(b)動作方法。動作時には(a)に示す光を照射する必要はない。

まず近赤外線を発生するLED型PBDの主な特性を紹介しよう。図2中の写真は各々電流非注入時、電流注入時のPBDの外観を赤外 CCD カメラにより撮影した画像である²⁹⁾。発光パワーは1.1Wに達しており、これはInGaAs(直接遷移型半導体)を用いて実用化されている波長1.3 μm のLEDの値(2.8mW,株式会社浜松ホトニクス製L12771)の300倍以上の大きな値である。高パワー発光している。曲線Aは30分間のアニールにより作製されたPBDの発光スペクトルである。なお既存の方法で作製された市販のSiフォトダイオード(株式会社浜松ホトニクス製S3590)もわずかに発光するので、参考のためにその微弱な発光スペクトルを曲線Bに示す。曲線Bの発光スペクトルはバンドギャップエネルギー($E_g=1.12\text{eV}$)より高エネルギー側に分布しているが、これはSi中のフォノン散乱による間接遷移の結果生ずる発光である。曲線Aは曲線Bと大きく異なっており、発光スペクトルは E_g 以下の低エネルギー側に広がっている。 E_g の位置に明瞭な発光ピークは存在せず、作製の際に照射した光の光子エネルギー(0.95eV, 波長1.30 μm)に相当する領域にピーク(下向き矢印)が現れており、これは照射光によってB濃度の空間分布が制御された結果、光子エネルギーに関するPBの効果が発現したことを意味する。なお、二つの上向き矢印の位置(0.83eV, 0.89eV)および下向き矢印の位置の間隔は各々0.06eVであり、これはSiの光学フォノンのエネルギーと一致している。すなわち0.95eVのエネルギーを持つDPPが一個の光学フォノンを放出し通常の光子に変わる過程、および二個の光学フォノンを放出して光子に変わる過程に各々対応している。これらの過程はここで議論している発光がフォノンのエネルギー準位を中間状態として使われることを証明している。

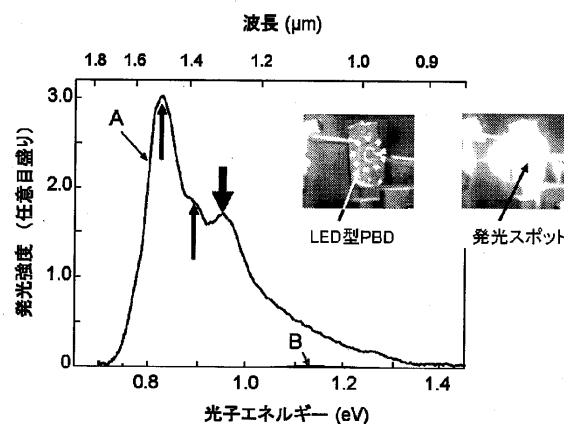


図2 近赤外線のLED型PBDの発光スペクトル²⁹⁾
 曲線AはPBDの発光スペクトル。曲線Bは市販のSiフォトダイオードの発光スペクトル。
 挿入写真はPBDの外観と発光スポット像。

上記の近赤外線のPBDの外部量子効率の値は15%に達しており、上記と同様の実用化LEDの値(2%~5%, 株式会社浜松ホトニクス製L7866, L10822)よりずっと大きい。技術開発の積み重ねによりこの効率の値は着実に増加しているが、その様子は個体群成長、技術の進歩、商品の販売数の変化などを表すのに使われているロジスティクス曲線に沿っていることから、本技術が従来の多くの技術開発と同様の進展をしていることがわかる²⁸⁾。さらに最近の話題として、アニール加工の際に偏光を照射することにより、作製されたPBDからの発光も同様に偏光していることが確認されている³⁰⁾。これは上記の光の特性の遺伝(PB)のうち、光子スピンのに関するものである。

関連研究の結果、電子正孔対とフォノンとの結合の大きさを表すHuang-Rhys因子が4.08と推定されているが³¹⁾、これは通常のSiバルク結晶の値にくらべ $10^2\sim 10^3$ 倍大きく、PBDの発光がDPPに起因することを示している。また、コヒーレント状態の縦モード光学フォノンがDPと結合しDPPを形成していることも確認されている³²⁾。

以上の他、Siのバルク結晶を用いて赤・緑・青色の可視光を発生するLED型PBD³³⁾が作製されている。さらにSiと同様の間接遷移型半導体のGaPを用い黄・緑色の可視光を発生するLED型PBD³⁴⁾、

SiCを用い青～紫色³⁵⁾、紫外³⁶⁾、さらには白色³⁷⁾を発生するLED型PBDが作製され、Siの場合と同様にその偏光も制御されている³⁸⁾。加えて関連する発光素子としてSiを用いたLED型PBDによる光・電気弛張発振器³⁹⁾、さらには偏光変調素子⁴⁰⁾などが作製されている。

次に近赤外線を発生するレーザー型PBD⁴¹⁾を紹介しよう。これは長さ500 μm のリッジ導波路を有するファブリペロー共振器型の構造となっており、LED型PBDと同様の方法で作製される。その発振しきい値電流密度は1.1kA/cm²である。図3(a)、(b)は各々しきい値以上、しきい値以下の発振スペクトルであり、前者の鋭い発振スペクトルから発振波長が1.27 μm （作製の際に照射した光の波長と同等：光子エネルギーに関するPB効果）であることがわかる。また、最近ではSOI基板の使用によりしきい値電流密度は著しく減少し40A/cm²に達している^{42,43)}。光閉じ込め効果をさらに高める事により、しきい値電流密度の値はさらに減少すると期待されている⁴⁴⁾。しきい値電流密度の減少の様子を図4に示す。

このレーザー型PBDの特徴を、従来の直接遷移型半導体によるレーザーと比較すると次のとおりである。(a) 光閉じ込め部位が基板層内なので、光ビーム形状は円形に近い。また偏光はTEモードではなく、アニール用の光の偏光に依存する。これもLED型PBEと同様の光子スピンに関するPBの効果である。(b) 横モードは導波路の幅の値ではなく、アニール用の光の横モードに依存する。(c) 縦モードは単一である。これは正味利得が大きいため、たとえ共振器が長く、縦モード間隔が狭くとも他の縦モードの利得アニール用光の光子エネルギー付近の縦モードの発振のために消費されるからである。以上の特徴は従来のレーザーのそれらとは大きく異なることがわかるであろう。

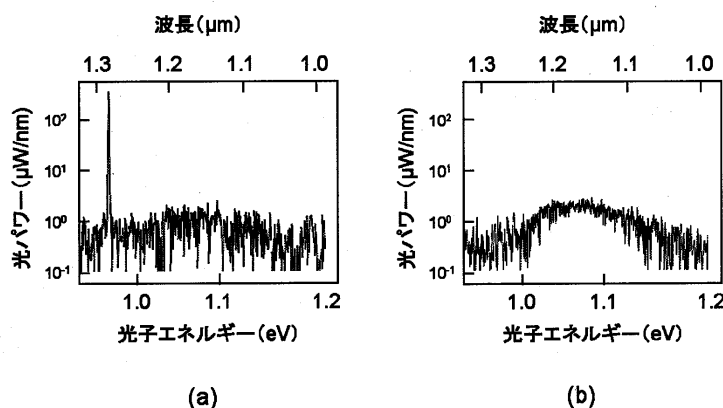


図3 近赤外線のレーザー型PBDの発光スペクトル
(a)発振しきい値以上。(b)発振しきい値以下。

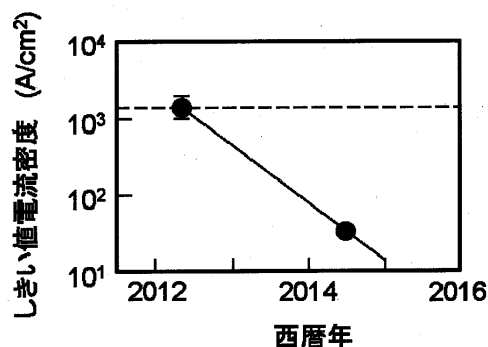


図4 発振しきい値の減少の様子
破線は従来の直接遷移型半導体（化合物半導体）からなるレーザーのしきい値電流密度の例⁴⁵⁾。

LED型、レーザー型ともPBDではPBの効果により作製の際に照射した光の特性が発光へと遺伝するので、前述のように発光させたい光の色によらずSiの結晶を使うことができる。これにより従来の材料科学に基づいて新しい物質を探索する必要はなくなった。実現したPBDの発光波長は近赤外線～可視域全体をカバーする。

これらの光源を用い次の応用が考えられている：

《LED型PBD》

Siを用いて赤外領域における高パワー、高効率PBDが開発されているので、熱源、医療機器、赤外センサー用光源など。また可視域ではSiCを用いた高効率、広波長域PBDが開発されているので情報表示用光源など。

《レーザー型PBD》

Siを用いて赤外領域における高パワー、低しきい値デバイスが開発されているので、加工用光源、通信用光源など。

なお、PBDの製作と同様の方法を用いてDPPに起因する上方変換を利用した光電変換素子が開発されている。その例として、有機分子薄膜フォトダイオード⁴⁶⁾、Siフォトダイオード⁴⁷⁾などがある。これらにより E_g 以下の光子エネルギーをもつ光が入射した場合にも光電変換が実現している。特にSiフォトダイオードは光増幅機能を有することが確認されている。

5. 展望

これまでに明らかになっている事実は次のとおりである³⁻⁵⁾。

- (1) 近接場光は仮想光子である。
- (2) 近接場光の発生はMaxwell方程式では記述できない。なぜならMaxwell方程式は位置、時間に関して電場と磁場の間の因果関係を記述する微分方程式であるため、それらの導出には積分操作が必要であるが、この操作により仮想光子成分は消失するからである。言い換えると、近接場光の場合は位置と時間の範囲が小さいので場の運動量、さらにはエネルギーが不確定となるからである。
- (3) 近接場光はナノ物質中の電子と光とが相互作用する事により生ずるので、物質エネルギーの衣をまとっている。すなわちDPである。
- (4) 近接場光はフォノンとも結合し、フォノンのエネルギーの衣をまとう。すなわちDPPが発生する。
- (5) 近接場光の存在を確認するには（すなわち、近接場光を観測するには）、近接場光が発生するナノ系から、それを取り囲むマクロ系へのエネルギー移動と散逸を使う必要がある。すなわち、ナノ系はマクロ系と接続し外部に向けて開放されているので、近接場光の観測は量子力学が取り扱う閉じた系の中の現象の範囲を超えている。

次に、近接場光をさらに深く理解し応用範囲を広げるために今後必要となることを列挙する。

- (a) ナノ系とマクロ系とのエネルギー移動および階層性の理解のために複雑系の物理学を利用する。そのためには量子場におけるマイクロ・マクロ双対性に関する考え方⁴⁸⁾、理論⁴⁹⁾の導入が必要である。
 - (b) エネルギーの散逸の理解のために非平衡・開放系の統計力学の導入が必要である。
 - (c) 自己組織性を記述するための数理科学モデルの構築とシミュレーション手法の導入が必要である
- 最後に、近接場光に類似する現象は自然界に多数見られることを指摘しよう。それらはナノ系、マクロ系、無機物、有機物など多岐にわたる（図5）。たとえば、中間子、光活性の磁気センサータンパク質⁵⁰⁾、光合成バクテリアの光捕獲システム⁵¹⁾、粘菌コンピューティング⁵²⁾、岩石の風化、宇宙空間の相対論的ジェット中に見られる放射エネルギー上方変換⁵³⁾、近接連星⁵⁴⁾などである。これらの現象との共通点、差異を明らかにすることにより近接場光学が自然界をつかさどる普遍的学問であることが確認されるであろう。

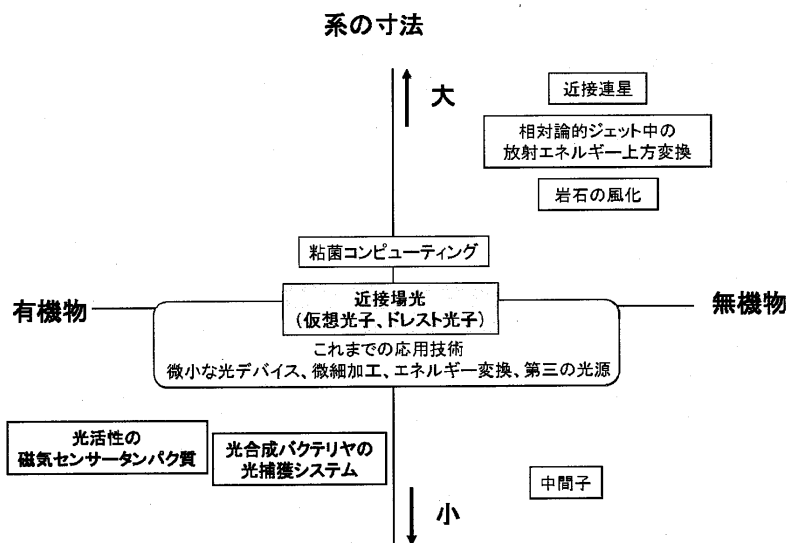


図5 近接場光に類似の現象

6. おわりに

本稿ではまず高分解能の顕微鏡に使うための近接場光に関する波動光学の研究の歴史を述べ、そのような「古典的」な時代がすでに終焉したことを指摘した。次に近接場光の性質を正確に記述するには波動光学の枠組みを超えた理論的描像が必要であり、さらに顕微鏡以外への応用を開発することが本質的であることを指摘した。この指摘に基づき、「現代的」な研究から DP という描像が生まれ、波動光学から脱却して進展していることを示した。その応用技術の例として光デバイス、微細加工、エネルギー変換、第三の光源である PBD を紹介した。「近接場光」の「学」は短期間のうちに多くの実用的な技術へと繋がった典型的な現代科学である。これは近接場光を発生する局所環境を制御できること、言い換えると近接場光を効率よく発生するようにナノ領域の物質環境を制御できることが決め手であった。今や現在の光の科学と技術の多くを近接場光により置換えることのできる包括的な科学と技術の時代が到来したといえよう。

参考文献

- 1) 松村明編:「近接」の項, 大辞林 第三版, (三省堂, 東京, 2006) .
- 2) 大津元一: “第 2 回近接場光学国際会議報告”, 応用物理, **63** (1994) p.77.
- 3) 大津元一: ドレスト光子, (朝倉書店, 東京, 2013) .
- 4) M. Ohtsu: *Dressed Photons*, Springer, 2014.
- 5) 大津元一: ドレスト光子はやわかり, (丸善プラネット, 東京, 2014) .
- 6) M. Ohtsu; “From Classical to Modern Near-Field Optics and the Future,” *Opt. Rev.*, **21** (2014) pp.905-910.
- 7) E.H.Synge: “A Suggested Method for Extending Microscopic Resolution into the Ultra-Microscopic Region,” *Phil. Mag.*, **6** (1928) pp.356-362.
- 8) E. A. Ash and G. Nicholls: “Super-Resolution Aperture Scanning Microscope,” *Nature*, **237** (1972) pp.510-516.
- 9) H. Bethe: “Theory of diffraction by small holes,” *Phys. Rev.*, **66** (1944) pp.163-182.
- 10) C.J. Bouwkamp: “On the Diffraction of Electro-Magnetic Waves by Small Circular Discs and Holes,” *Philips Res. Rep.*, **5** (1950) pp.401-422.
- 11) C. Girard and D. Courjon: “Model for scanning tunneling optical microscopy: A microscopic

- self-consistent approach,” *Phys. Rev., B* **42** (1990) pp.9340-9439.
- 12) D.W. Pohl and D.Courjon (ed.): *Near Field Optics* (Kluwer, Dordrecht, 1993) p.1-324.
 - 13) V.A. Podolskiy, A.K. Sarychev, and V.M. Shalaev: “Plasmon modes and negative refraction in metal nanowire composites,” *Opt. Express*, **11** (2003) pp.735-745.
 - 14) J.J. Sakurai: *Advanced Quantum Mechanics* (Addison-Wesley, Reading, 1967) p.20-74.
 - 15) 小林潔: “ナノ領域における光近接場現象とその応用”, *表面科学*, **30** (2009) pp.638-641.
 - 16) Y. Tanaka and K. Kobayashi: “Spatial localization of an optical near field in one-dimensional nanomaterial system,” *Physica, E* **40** (2007) pp.297-300.
 - 17) T. Kawazoe, K. Kobayashi, S. Takubo, and M. Ohtsu: “Nonadiabatic photodissociation process using an optical near field,” *J. Chem. Phys.*, **122** (2005) 024715.
 - 18) H. Hyuga and H. Ohtsubo: “Breakdown of the Siegert theorem and the many-body charge density operators,” *Nucl. Phys.*, **A294** (1978) pp.348-356.
 - 19) K. Kobayashi and M. Ohtsu: “Quantum theoretical approach to a near field optical system,” *J. Microscopy*, **194** (1999) pp.249-254.
 - 20) S. Sangu, K. Kobayashi, and M. Ohtsu: “Optical near fields as photon-matter interacting systems,” *J. Microscopy*, **202** (2001) pp.279-285.
 - 21) M. Naruse, M. Aono, S.-J. Kim, T. Kawazoe, W. Nomura, H. Hori, M. Hara, and M. Ohtsu: “Spatiotemporal dynamics in optical energy transfer on the nanoscale and its application to constraint satisfaction problems,” *Phys. Rev. B*, **86** (2012) 125407.
 - 22) N. Tate, M. Naruse, T. Yatsui, T. Kawazoe, M. Hoga, Y. Ohyagi, T. Fukuyama, M. Kitamura, and M. Ohtsu: “Nanophotonic code embedded in embossed hologram for hierarchical information retrieval,” *Opt. Express*, **18** (2010) pp.7497-7505.
 - 23) T. Kawazoe, T. Takahashi, and M. Ohtsu: “Evaluation of the dynamic range and spatial resolution of nonadiabatic optical near-field lithography through fabrication of Fresnel zone plates,” *Appl. Phys.B*, **98** (2010) pp.5-11.
 - 24) T. Yatsui, W. Nomura, M. Naruse, and M. Ohtsu: “Realization of an atomically flat surface of diamond using dressed photon-phonon etching,” *J. Phys.D*, **45** (2012) 475302.
 - 25) T. Kawazoe, H. Fujiwara, K. Kobayashi, M. Ohtsu: “Visible light emission from dye molecular grains via infrared excitation based on the nonadiabatic transition induced by the optical near field,” *IEEE J. Select. Top. on Quantum Electron.*, **15** (2009) pp.1380-1386.
 - 26) N. Tate, Y. Liu, T. Kawazoe, M. Naruse, T. Yatsui, and M. Ohtsu: “Fixed-distance coupling and encapsulation heterogeneous quantum dots using phonon-assisted photo-curing,” *Appl. Phys.B*, **110** (2013) pp.39-45.
 - 27) 川添忠, 雨海千秋, 大津元一: “ドレスト光子利用波長変換フィルムによる結晶シリコン太陽電池の高効率化”, 第 62 回応用物理学会春季学術講演会予稿集 (応用物理学会, 2015) 11p-A12-7.
 - 28) M. Ohtsu: “Silicon Light Emitting Diodes and Lasers Using Dressed Photons,” *Prog. Nanophotonics* **3** (ed. M. Ohtsu), (Springer, 2014) pp.1-56.
 - 29) T. Kawazoe, M.A. Mueed and M. Ohtsu: “Highly efficient and broadband Si homojunction structured near-infrared light emitting diodes based on the phonon-assisted optical near-field process,” *Appl. Phys.B*, **104** (2011) pp.747-754.
 - 30) 西岡克紘, 川添忠, 大津元一: “フォトンブリーディング効果による Si-LED の偏光制御”, 第 62 回応用物理学会春季学術講演会予稿集 (応用物理学会, 2015) 11p-A12-9.
 - 31) M. Yamaguchi, T. Kawazoe and M. Ohtsu: “Evaluating the coupling strength of electron-hole pairs and phonons in a 0.9 μm -wavelength silicon light emitting diode using dressed-photon-phonons,” *Appl. Phys.A*, **115** (2014) pp.119-125.

- 32) N. Wada, M.-A. Tran, T. Kawazoe and M. Ohtsu: "Measurement of multimode coherent phonons in nanometric spaces in a homojunction-structured silicon light emitting diode," *Appl. Phys.A*, **115** (2014) pp.113-118.
- 33) M. -A. Tran, T. Kawazoe and M. Ohtsu: "Fabrication of a bulk silicon p-n homojunction-structured light-emitting diode showing visible electroluminescence at room temperature," *Appl. Phys.A*, **115** (2014) pp.105-111.
- 34) J.-H. Kim, T. Kawazoe, and M. Ohtsu: "GaP Homojunction LEDs Fabricated by Dressed-Photon—Phonon-Assisted Annealing," *Adv. Opt. Technol.*, **2015** (2015) Article ID 236014.
- 35) T. Kawazoe and M. Ohtsu: "Bulk crystal SiC blue LED with p-n homojunction structure fabricated by dressed-photon-phonon-assisted annealing," *Appl. Phys.A*, **115**(2014) pp.127-133.
- 36) Q. H. Vo, 川添忠, 大津元一: "二光源によるドレスト光子フォノン援用アニール法を用いたSiC-LEDの作製", 第61回応用物理学会春季学術講演会予稿集 (応用物理学会, 2014) 18a-F12-10.
- 37) 川添忠, 大津元一: "ドレスト光子援用アニール法により作製されたホモ接合SiCの白色LED", 第73回応用物理学会学術講演会予稿集 (応用物理学会, 2012) 13p-F8-10.
- 38) T. Kawazoe, K. Nishioka, and M. Ohtsu: "SiC light emitting diode and its polarization control using dressed photons," Abstract of the 21st Int. Display Workshop (Soc. Inf. Display, 2014) PRJ1-1.
- 39) N. Wada, T. Kawazoe and M. Ohtsu: "An optical and electrical relaxation oscillator using a Si homojunction structured light emitting diode," *Appl. Phys.B*, **108** (2012) pp.25-29.
- 40) N. Tate, T. Kawazoe, and M. Ohtsu: "Giant-magneto optic light modulator using p-n homojunction-structured ZnO crystal" The 4th Japan-Korea Workshop on Digital Holography and Information Photonics, (16-18 Dec. 2014, Okinawa) paper number TuP1.
- 41) T. Kawazoe, M. Ohtsu, K. Akahane and N. Yamamoto: "Si homojunction structured near-infrared laser based on a phonon-assisted process," *Appl. Phys.B*, **107** (2012) pp.659-663.
- 42) 田中肇, 川添忠, 大津元一, 赤羽浩一: "ドレスト光子を利用したSiレーザーの超低しきい値化", 田尾75回応用物理学会秋期学術講演会予稿集 (応用物理学会, 2014) 18p-C1-4.
- 43) H. Tanaka, T. Kawazoe, M. Ohtsu, and K. Akahane: "Degreasing the threshold current density by Si lasers fabricated by using dressed-photons," *Fluo. Mat.*, **1**(2015) pp.1-7.
- 44) 田中肇, 川添忠, 大津元一, 赤羽浩一, 山本直克: "ドレスト光子を利用したSiレーザー導波路の光増幅利得の評価", 第62回応用物理学会春季学術講演会予稿集 (応用物理学会, 2015) 11p-A12-12.
- 45) Zh. I. Alferov, "The history and future of semiconductor heterostructures," *Semiconductors*, **31** (1998) pp.1-115.
- 46) S. Yukutake ,T. Kawazoe, T. Yatsui, W. Nomura, K. Kitamura, and M. Ohtsu, "Selective photocurrent generation in the transparent wavelength range of a semiconductor photovoltaic device using a phonon-assisted optical near-field process," *Appl. Phys. B*, **99** (2010) pp.415-412.
- 47) H. Tanaka, T. Kawazoe, and M. Ohtsu, "Increasing Si photodetector photosensitivity in near-infrared region and manifestation of optical amplification by dressed photons," *Appl. Phys. B*, **108** (2012) pp.51-56.
- 48) S. MacLane: *Categories for the Working Mathematician* (Springer, 1971).
- 49) 小嶋泉: *量子場とマイクロ・マクロ双対性*, (丸善, 東京, 2013) pp.1-222.

- 50) R.J. Gegear, A. Casselman, S. Waddell, and S.M. Reppert: "Cryptochrome mediates light-dependent magnetosensitivity in *Drosophila*," *Nature*, **454**, (2008) pp.1014-1018.
- 51) G. McDermott, S.M. Prince, A.A. Freer, A. M. Hawthornthwaite-Lawless, M.Z. Papiz, R.J. Cogdell, and N.W. Isaacs: "Crystal structure of an integral membrane photosynthetic bacteria," *Nature (London)*, **374** (1995) pp.517-521.
- 52) M. Aono, S.-J. Kim, M. Naruse, M. Wakabayashi, H. Hori, M. Ohtsu, and M. Hara: "Amoeba-Inspired Nanoarchitectonic Computing: Solving Intractable Computational Problems Using Nanoscale Photoexcitation Transfer Dynamics," *Langmuir*, **29** (2013) pp.7557-7564.
- 53) B.E. Stern and J. Poutanen: "Radiation from relativistic jets in blazars and the efficient dissipation of their bulk energy via photon breeding," *Mon. Not. R. Astronom. Soc.*, **383** (2008) pp.1695-1712.
- 54) R.W. Hilditch: *An Introduction to Close Binary Stars* (Cambridge University Press, 2001).



大津元一 OHTSU, Motoichi

東京大学 大学院工学系研究科 電気系工学専攻

〒113-8656 東京都文京区弥生 2-11-16 工学部 9 号館

近接場光の科学と技術

大津元一

■「古典」から「現代」へ

近接場光とは光が照射されたナノ寸法物質（ナノ物質）の表面近傍に発生する小さな光であるが、それはいまや国語辞典でも解説されるほど広く知られている¹⁾。近接場光の「古典」的な科学と技術は電磁気学と波動光学の範疇にあり、回折限界を超える高倍率の顕微鏡をつくるという80年以上前の提案²⁾を世界の数か所で二十数年前に同時期に実現することから始まった³⁾。しかし近接場光は測定対象である微小物質の形や構造をわずかに変えてしまい、その測定結果を古典的に解釈できないことから「古典」的な科学と技術は終焉を迎えた。とはいえこの顕微鏡は2014年ノーベル化学賞の受賞理由にもかかわっており、科学技術の大きな進歩をもたらす威力があったといえよう。

近接場光が微小物質の形や構造を変えることに注目し十数年前には「現代」的な近接場光の科学が誕生した。それはナノ寸法空間において近接場光がかかわる光と物質の相互作用の研究であり、とり扱うナノ物質の種類に依存し2つの方向に進んだ。その第1は半導体などのナノ物質や分子をとり扱い、電子の離散化したエネルギー準位間の遷移とエネルギー

散逸とを考慮して光と物質の相互作用を調べる方向である。これにより量子力学的な現象の発現、およびナノ空間での散逸過程を用いた観測が関与する科学が大きく発展した⁴⁾。第2は金属の微粒子や薄膜をとり扱い自由電子のプラズマ振動と光の波の共鳴的相互作用による電場増強を利用する方向である。これらの材料は半導体ナノ構造に比べ容易につくれることから多く研究され、その応用技術はプラズモニクスとよばれている⁵⁾。ただしこの相互作用は電子の集団運動を基礎としており、波動的性質を示す光は電子のプラズマ振動に結合することから、たとえ金属に入射する光が特殊な量子力学的性質をもっているとしてもその性質はいち早く失われてしまう。

■ 近接場光の現代科学

将来の発展につなげるため上記の第1の方向の歩みを紹介しよう。光と物質の相互作用を記述するには光子および電子の生成・消滅を表す量子力学的な場の演算子が必要であるが、ここでは光の波長よりずっと小さいナノ空間をとり扱うので従来の光の量子論のように共振器を仮定できず、共振器モードにもとづく場の演算子を考えることはできない。この困難を克服するためにナノ空間の環境系を記

述しうる無数のモードの光子と無数のエネルギー準位をもつ電子を考え、その間の相互作用をもとに近接場光の量子論を組み立て、場の生成・消滅演算子が導出された。これは光子および電子の生成・消滅演算子からなることから、それらが表す準粒子は電子正孔対の衣をまとった光子、すなわちドレスト光子(dressed photon, DP)と名づけられた。さらにDPはナノからマクロへと接続される環境系に相当する物質中のコヒーレント状態のフォノンとも結合しドレスト光子フォノン(dressed-photon-phonon, DPP)とよばれる準粒子を生成することも明らかになった。

近接場光は従来の光の量子論が扱う伝搬光(実光子)とは異なり光照射下のナノ物質に発生する分極の間の相互作用を媒介する仮想光子であることから、それを観測・検出するためには第2のナノ物質を近づけて多重散乱により実光子に変換する必要がある。このとき、ナノ物質の間でDPまたはDPPが交換されるので両ナノ物質はたがいに結合した状態になっている。この状態を利用し、つぎに示す多くの革新技术が生まれた。

■ 近接場光の革新技术,そして包括的な科学と技術へ

本稿冒頭の顕微鏡では近接場光を発生させるためにファイバークローブなどの特殊な道具が使われていた。しかし近接場光はナノ物質の表面、巨視的物質表面の微小な突起の先端、巨視的物質中の不純物原子など、光を照射すればいろいろなところに自然発生する。このことに着目し、ファイバークローブのような特殊器具を使わずにDPを発生させることにより、新しい光デバイス、微細加工、エネルギー変換、情報セキュリティーなど多くの革新技术が生まれた⁶⁾。これらのうち最近のめざましい成果として新しい発光ダイオード(LED)、レーザーの発明がある。従来技術ではこれらのデバイス

をつくるさい、発光させたい光の波長に応じ種々の直接遷移型半導体を選んで使っている。たとえば2014年ノーベル物理学賞では青色LEDをつくるためには窒化ガリウム(GaN)を使った。しかし近接場光の技術では光の色によらずシリコン(Si)の結晶を使えばよい。Siは電子技術では古くから使われてきた材料であるが間接遷移型半導体なので、長い光技術の歴史において「光らない」と考えられてきた。しかしSi結晶中のDPPの発生を制御して伝導帯の電子とフォノンとの間で運動量を授受させることにより、近赤外光、可視光を高効率で発生するLED、近赤外線を発生するレーザーが相次いで実現したのである⁷⁾。さらにはSiと同様の間接遷移型半導体のSiCやGaPを用いたLEDも開発された。

これらのLED、レーザーが発する光の色、伝播方向、偏光は、作製時にDPPを発生させるために照射した光のそれらと同等であることが注目を浴びている。すなわち発生する光は製作に使われた光の複写になっており、この性質は光子ブリーディング(photon breeding, PB)と名づけられている。とくに光の色が複写されるので上記のように発光させたい光の色によらずシリコン(Si)の結晶を使うことができるのである。これにより従来の材料科学にもとづいてわざわざ新しい物質を探索する必要はなくなった。

近接場光の現代科学は短期間のうちに多くの実用的な技術へとつながった典型的な例である。これは近接場光を発生する局所環境を制御できること、いい換えると特殊な近接場光が自然に発生するようなナノ領域の物質環境が制御できることが決め手となっている。近接場光の現代科学が生まれて二十数年たったいま、現在の光の科学と技術の多くを近接場光により置き換えることのできる包括的な科学と技術の時代がいよいよ到来した。

参考文献

- 1) 松村明編：「近接」の項、『大辞林』第3版、三省堂(2006)。
- 2) E. H. Syge: *Phil. Mag.* **6**, 356(1928)。
- 3) D. W. Pohl and D. Courjon (ed.): *Near Field Optics*, Kluwer, Dordrecht(1993)pp. 1-324.
- 4) 大津元一：『ドレスト光子』朝倉書店(2013)。
- 5) V. A. Podolskiy, A. K. Sarychev and V. M. Shalaev: *Opt. Express* **11**(2003)735.
- 6) 大津元一：『ドレスト光子はやわかり』丸善プラネット(2014)。
- 7) M. Ohtsu and T. Kawazoe: "Silicon light emitting diodes and lasers using dressed photons", M. Ohtsu (ed.), *Progress in Nanophotonics* **3**, Springer, Berlin(2014) pp. 1-67.

From Classical to Modern Near-Field Optics and the Future

Motoichi OHTSU^{1,2}

¹*Department of Electrical Engineering and Information Systems, Graduate School of Engineering, The University of Tokyo, Bunkyo, Tokyo 113-8656, Japan*

²*Nanophotonic Research Center, Graduate School of Engineering, The University of Tokyo, Bunkyo, Tokyo 113-8656, Japan*

(Received April 25, 2014; Accepted June 9, 2014)

This paper reviews the framework of classical near-field optics and recent progress in modern near-field optics. Some applications are also reviewed, including novel optical functional devices, nano-fabrication technologies, energy conversion technologies, and information processing systems. Novel theoretical models based on mathematical science are also presented, as well as an outlook for the future, hinting at the possibilities of near-field optics.

© 2014 The Japan Society of Applied Physics

Keywords: optical near field, photon, electron, phonon, device, fabrication, energy conversion

1. Introduction

Science and technology, in general, have clearly demarcated classical and modern ages. In the case of near-field optics, it has been recognized that the classical age started with the proposal to use optical near fields for high-resolution optical microscopy.¹⁾ The viability of this proposal was subsequently supported through experiments using microwaves.²⁾ Theoretical studies were undertaken to analyze the diffraction and radiation of electromagnetic waves through a small aperture.^{3,4)} Afterward, a self-consistent theory was developed to solve many-body problems for analyzing the optical microscope image of a specimen.⁵⁾ Several institutes around the world embarked, almost simultaneously, on experimental studies on near-field optical microscopy,⁶⁾ which provided a new methodology for measuring and analyzing the conformation and structure of sub-wavelength sized specimens. It should be noted that the studies in this classical age were carried out in the framework of wave optics.

In the case where the optical near field is applied to microscopy, however, an important problem is that non-demolition measurement is not guaranteed because the optical properties of the specimen are inevitably perturbed by optical near field energy transferred from the tip of the probe to the specimen. This non-demolition has been pointed out in the many-body problems described above, which means that microscopy may not be the most appropriate application of the optical near field. In other words, there is a strong desire to advance from the classical age of near-field optics. In response to this, the modern age of near-field optics started, and appropriate applications have been found.

Since sub-wavelength sized nanometric materials (nanomaterials) are placed in close proximity to each other and are involved in the interaction mediated by the optical near field, the study of the optical near field is nothing more than the study of a light–matter interaction in nanometric space. This investigation progressed in two directions in the modern age, depending on the species of nanomaterials used.

One uses molecules or semiconductor nanomaterials. The light–matter interactions involving these specimens were analyzed by considering the discrete energy levels of the electrons in the molecules or those of the electron–hole pairs in the semiconductor. A successful and appropriate example application of this in the modern age is novel quantum optical functional devices developed based on this approach.⁷⁾

The other uses metallic nanoparticles or metallic films. Since it is fairly easy to fabricate and use these specimens, a variety of studies have been carried out. The mainstream approach was to study phenomena that originate from the coupling between the lightwave and plasmons, by which the plasma oscillation of the free electrons in a metal was manifested.⁸⁾ Since the collective motion of electrons is involved in this coupling, optical energy is converted promptly to plasma oscillation energy. Furthermore, since the phase-relaxation time of the electrons is very short, the unique properties of light, such as its quantum optical properties, can be promptly lost in the metal. Therefore, to analyze these plasmonic phenomena, it was sufficient to use quantities from conventional wave optics, such as refractive index, wave-number, guiding mode, and the dispersion relation. In other words, these analyses were still based on the wave-optics principles of the classical age, as with the case of optical microscopy described above.

This paper reviews recent progress in modern near-field optics. This includes theoretical studies that present an intuitive physical picture of the optical near field for analyzing light–matter interactions in nanometric space, applications to novel optical functional devices, nano-fabrication, energy conversion, and information processing systems. A future outlook of near-field optics will be also given, hinting at the possibilities in this field.

2. The Dressed Photon as a Physical Picture of an Optical Near Field

Light–matter interactions in nanometric space can exhibit unique variations in the values of the physical quantities of nanomaterials, such as energy and momentum. There are

unsolved problems and untouched subjects in analyzing these variations, including:

(1) Quantum field theory is required to describe the numbers of photons and electron–hole pairs in a many-particle system, which can vary as a result of light–matter interactions in a nanometric space. For this description, creation and annihilation operators have to be defined by quantizing the light and elementary particles. However, in the conventional quantum theory of light, the concept of a photon has been established by quantizing the electromagnetic field of light that propagates through macroscopic free space whose size is larger than the wavelength of light.⁹⁾ A photon corresponds to an electromagnetic mode in a virtual cavity defined in free space for quantizing light. However, a serious problem in near-field optics is that a virtual cavity cannot be defined in a sub-wavelength sized nanometric space, which makes it difficult to derive the Hamiltonian of the optical energy. In addition, the wavelength (wavenumber) of light and the photon momentum have large uncertainties due to the sub-wavelength size of the space under study.

(2) The optical near field is generated and localized on the surface of a nanomaterial under light irradiation. In other words, the optical near field corresponds to virtual photons mediating the interaction between the polarizations induced on the nanomaterial surface. Therefore, for detecting the optical near field, another nanomaterial has to be placed in close proximity to convert the optical near field to propagating light (i.e., from a virtual photon to a real photon) via multiple scattering of the optical near field. This conversion enables detection of the optical near field through detection of the scattered light in the far field region. Through these processes, generation and detection of the optical near field are achieved. Here, the first and the second nanomaterials may be regarded as the source and detector of the optical near field, respectively. However, in contrast to conventional optical phenomena, the source and detector are not independent of each other but are coupled via the optical near field. In other words, the source and detector cannot be distinguished from each other. As a result, the refractive index of the nanomaterial, for example, which has been commonly used in conventional wave-optics in order to represent the phase delay in the optical response of a material to an incident lightwave, cannot be used for analysis.

(3) In practice, nanomaterials are fixed on a macroscopic substrate or buried in a macroscopic host crystal. Furthermore, they are surrounded by macroscopic electromagnetic fields belonging to the applied propagating light and scattered light. In short, since the nanomaterials in an actual nanometric subsystem are always surrounded by a macroscopic subsystem composed of macroscopic materials and electromagnetic fields, the contribution from the macroscopic subsystem must be taken into account to analyze the interaction between the nanomaterials for estimating the magnitude of the resultant energy transfer and dissipation in the nanometric subsystem.

Novel theories have been developed to solve problems (1)–(3) above, and these theories have succeeded in painting

a physical picture of the optical near field, which was outside the scope of conventional classical and quantum optics that were designed for light propagating through macroscopic space. Solutions to problems (1)–(3) are:

(a) In order to solve problem (1), an infinite number of electromagnetic modes with infinite frequencies, polarization states, and energies was assumed. An infinite number of energy states was also assumed for the electrons and holes. Based on these assumptions, the total Hamiltonian was derived to define the creation and annihilation operators of a quasi-particle in order to represent the light–matter interaction in a nanometric space.¹⁰⁾ Since these operators are given by the sum of the operators of photons and electron–hole pairs, this quasi-particle was named a dressed photon (DP), which is a photon that dresses the material energy, i.e., the energy of the electron–hole pair.¹¹⁾ It was found that the DP was modulated temporally and spatially because of the infinite electromagnetic modes and infinite energy states. The temporal modulation feature was represented by an infinite number of modulation sidebands. That is, even though the nanomaterial was irradiated with propagating light of a single mode, the generated DP had an infinite number of modulation sidebands. It was also found that the DP could couple with multi-mode coherent phonons in the nanomaterial to create another quasi-particle, named the dressed-photon–phonon (DPP).¹²⁾

(b) In order solve problem (2), the theoretical approach reviewed in (a) was used to analyze the interaction between the two nanomaterials by using the concepts of the annihilation of a DP from the first nanomaterial and its creation on the second nanomaterial. Furthermore, it was also found from experimental and theoretical studies that the second particle exhibits a unique optical response if it absorbs the energy of the modulation sideband described in (a), which is different from the conventional optical response induced by absorbing propagating light.¹³⁾

(c) In order to solve problem (3), the near-field optical interaction between the nanomaterials in the nanometric subsystem was analyzed by renormalizing the effects originating from the macroscopic subsystem in a consistent and systematic way. This renormalization was carried out by using the projection operator method.¹⁴⁾ As a result, the spatial distribution of the near-field optical interaction energy was derived and expressed by using a Yukawa function, which also succeeded in representing the interaction between the two nanomaterials mediated by the DP (DP-mediated interaction).¹⁵⁾ This function quantitatively showed that the interaction range was equivalent to the size of the nanomaterial and did not depend on the wavelength of the incident propagating light. Originating from this size-dependent interaction range, novel optical response characteristics were found: Since the DP is localized in nanometric space, the long-wavelength approximation, which is valid for conventional light–matter interactions in macroscopic space, is not valid for the DP-mediated interaction. As a result, an electric dipole-forbidden transition turned out to be allowed. Furthermore, size-dependent resonance was also found.¹⁶⁾ That is to say, the efficiency of

the energy transfer between nanomaterials depends on the size of the nanomaterials that are interacting. It should be noted that this resonance is unrelated to diffraction that governs the conventional wave-optical phenomena.

In the classical age, the name optical near field has been used for representing the spatial features of the light generated on the surface of a nanomaterial, which has been described by using the technical terms of wave-optics. In the modern age, the term optical near field was replaced by DP, which is the quasi-particle representing the coupled state of photons and electron–hole pairs in a nanometric space. This replacement has been successful in painting a more physically intuitive picture of the optical near field and in describing the light–matter interactions in a nanometric space more precisely.

3. Applications of the Optical Near Field

This section reviews several applications that have been developed by using the intrinsic features of the DP-mediated interaction and the resultant DP energy transfer described in Sect. 2. Novel theoretical models based on mathematical science, different from the theory described in (a)–(c) of Sect. 2, are also described, as well as a future outlook of near-field optics.

3.1 Optical functional devices

Novel optical functional devices, named DP devices, have been developed by using semiconductor nanomaterials. They enabled the transmission and readout of optical signals by the energy transfer and subsequent dissipation of the DP energy. The operation of these DP devices was analyzed by using a quantum mechanical master equation based on a density matrix formulation for describing the DP-mediated interaction between nanomaterials.¹⁷⁾

Examples of DP devices developed so far are: a logic gate device for controlling optical signals,⁷⁾ an energy transmitter for transmitting optical signals between DP devices,¹⁸⁾ and an input interface device for converting incident propagating light to a DP.¹⁹⁾ Furthermore, a unique delayed-feedback-type optical pulse generator has been proposed for use as a DP signal pulse generator.²⁰⁾ Practical NOT gate and AND gate devices that operate at room temperature have also been fabricated by using InAs nanomaterials.²¹⁾

One advantage of these devices is their extremely small volume, far beyond the diffraction limit of propagating light. Other advantages are their superior performance levels and unique functionality, such as high figures of merit,²²⁾ low energy consumption,²³⁾ tamper-resistance,²⁴⁾ skew-resistance,²⁵⁾ and autonomous energy transfer,²⁶⁾ all of which originate from the unique operating principles of DP devices, utilizing electric-dipole-forbidden transitions and size-dependent resonance of DP-mediated interactions, as described in (c) of Sect. 2.

3.2 Nano-fabrication

This subsection reviews two examples of nano-fabrication technologies based on the intrinsic nature of the DP. The first example is lithography using DPs generated at the aperture

of a photo-mask. In classical near field optical technology, linearly-aligned aperture patterns on a photo-mask have been transcribed to a photo-resist film;²⁷⁾ however, sufficiently high resolution has not been obtained because the photo-resist is exposed also by the diffracted propagating light transmitted through the aperture pattern. In order to avoid this exposure, a novel method has been developed by irradiating a UV-sensitive photo-resist with visible propagating light. It should be noted that the UV-sensitive photo-resist can be excited by DPs even though they are generated from visible propagating light. This is possible because the DPP has high-frequency sidebands of modulation, generated as a result of temporal modulation (refer to Sect. 2). In other words, this is possible due to the energy up-conversion via energy levels of coherent phonons in DPPs. As a result, the photo-mask pattern can be accurately transcribed to the photo-resist while the photo-resist remains un-exposed by the visible propagating light transmitted through the apertures.²⁸⁾ With this method, a diffraction-free resolution as high as that determined by the aperture size has been realized by a compact lithography machine for practical use.²⁹⁾ This method has enabled duplication of an integrated circuit pattern, multiple exposure, and patterning using an optically inactive photo-resist.²⁸⁾ As applications of this method, a two-dimensional array of DP devices,³⁰⁾ a diffraction grating for soft-X rays,³¹⁾ and a Fresnel zone plate for soft-X rays³²⁾ have been fabricated.

The second example is smoothing a material surface by photo-etching. In this process, bumps on a rough material surface are autonomously removed by chemically radical atoms. These atoms are created by photo-dissociating gaseous molecules using energy up-conversion, as was the case with the lithography described above, due to DPP energy transfer from the apex of the bump to the molecules under visible light irradiation.³³⁾ Using this method, the surfaces of glass substrates have been smoothed for use as high-power laser mirrors,³⁴⁾ for magnetic storage memory disks,³⁵⁾ and for EUV masks.³⁶⁾ Side walls of densely aligned corrugations of a diffraction grating have been also smoothed.³⁷⁾ This method has been applied to other materials, such as plastic PMMA,³⁸⁾ crystalline GaN,³⁹⁾ and crystalline diamond.⁴⁰⁾ This method realizes high-throughput smoothing because no special devices, like a fiber probe or a photo-mask, are required for generating the DPs and DPPs. Furthermore, because no mechanical components are required, this method can be more advantageous than conventional chemical–mechanical polishing,⁴¹⁾ which uses a sliding pad on the material surface to be polished. Based on a principle equivalent to the smoothing reviewed above, scratches on a transparent poly-Al₂O₃ crystal surface have been filled-in by using chemical vapor deposition in order to smooth the substrate surface for ceramic laser media applications.⁴²⁾

3.3 Energy conversion

Conversions between optical and electrical energies have been realized based on energy up- or down-conversions by using DPs and DPPs. These include:

(1) Optical-to-optical energy conversion: Near infrared light has been converted to visible light by using energy up-conversion in the process of DPP energy transfer between organic dye particles. Red, green, and blue light has been emitted from DCM, coumarine 540A, and stilbene 420 particles, respectively, by irradiating them with 0.8–1.3 μm wavelength infrared light.^{43,44} These conversion methods have been applied to infrared optical pulse shape measurements.⁴⁵

On the other hand, energy down-conversion by DPPs has been applied to convert short-wavelength light to long-wavelength light. For example, a high-efficiency down-conversion method has been developed by using nanometric droplets autonomously grown in an optically curable resin.^{46–48}

(2) Optical-to-electrical energy conversion: Novel devices have been developed for efficiently converting optical energy to electrical energy, using the energy up-conversion via DPPs. One example is a photovoltaic device using an organic film of P3HT. The electrode surface conformation of this device was autonomously modified by using novel DPP-assisted deposition of silver particles for efficient DPP generation.⁴⁹ Another example is a Si photodiode in which the spatial distribution of doped boron atoms was autonomously modified by a novel DPP-assisted annealing method.⁵⁰ In these two examples, effective energy conversion has been confirmed even when the photon energy of the incident light is lower than the bandgap energy of the semiconductor materials used. Furthermore, in the case of the Si photodiode, an optical amplification capability was confirmed, which was due to stimulated emission triggered by the DP.

(3) Electrical-to-optical energy conversion: Novel near infrared and visible light emitting diodes (LEDs) have been realized by using Si crystals even though Si is an indirect transition-type semiconductor.^{51,52} The autonomous modification method reviewed in (2) above was also used, resulting in efficient momentum transfer between electrons and phonons in Si. After the autonomous modification, the Huang–Rhys factor,⁵³ a parameter representing the magnitude of the coupling between electron–hole pairs and phonons, was determined to be 4.08 ± 0.02 ,⁵⁴ which is 10^2 – 10^3 times higher than that of a conventional Si crystal device. Furthermore, it was confirmed that the DPs coupled with the coherent phonons of the longitudinal optical mode, creating DPPs.⁵⁵ Besides Si, an indirect transition-type GaP semiconductor has been used for fabricating an LED emitting yellow-green light.⁵⁶ An indirect transition-type SiC semiconductor has also been used for fabricating LED emitting blue-violet light,⁵⁷ ultraviolet light,⁵⁸ and white light.⁵⁹ In addition to LEDs, an optical and electrical relaxation oscillator⁶⁰ and a near infrared laser have been realized by using crystalline Si.⁶¹

3.4 Information processing systems

Novel information processing systems using the DP devices reviewed in Sect. 3.1 have been proposed.^{62,63} A first example is a nanometric optical computing system

utilizing the DP energy transfer.⁶⁴ Although several optical methods have been proposed by following the concepts of Von Neumann computing systems, the collapse of the scaling-law for computing time and energy consumption has remained a critical problem. In order to solve these problems, a non-Von Neumann computing system has been proposed by using DP devices, and its ability to solve decision making problems,^{65,66} constraint satisfaction problems,⁶⁷ and intractable computational problems⁶⁸ has been demonstrated.

A second example is an information processing system using the dissipations and fluctuations of the DP energy.⁶⁹ The last example is an information security system that uses the size-dependent resonance of the DP energy transfer described in Sect. 2.⁷⁰ This system has realized a hierarchical hologram,⁷¹ a lock-and-key,⁷² and nonsymmetric polarization transformation.⁷³

3.5 Novel theoretical models and future outlook

Novel theoretical models based on mathematical science, different from the theory described in (a)–(c) of Sect. 2, have been proposed for analyzing the spatio-temporal properties of DP energy transfer. By using these theoretical models, a novel information processing method has been developed by taking the hierarchy of the DP energy transfer into account.⁷⁴ These models have also been applied to analyze the dynamic process of material surface smoothing by photo-etching, reviewed in Sect. 3.2.⁷⁵ Furthermore, they have been applied to analyze nano-fabrication processes, such as morphological- and arrayed-structure formations on a material surface.^{76,77} It should be noted that the DP-mediated processes described in Sects. 3.2 and 3.3 were governed by the autonomy of DP creation and annihilation. Therefore, for designing these processes, it is difficult to employ the deterministic methods that have been used to design and fabricate conventional materials and devices. In other words, since the autonomous creation and annihilation of DPs take place in multiple nanometric areas on the surface or inside the material, deterministic theoretical models of these processes inevitably involve an extremely long computing time. In order to shorten the computing time, the validity of the theoretical models above has been confirmed by the work described above.

In contrast to these models, a non-uniform light–matter interaction theory that directly solves the Schrödinger equation and Maxwell equation simultaneously has been recently proposed.⁷⁸ This theory is expected to provide a powerful tool for rigorously analyzing light–matter interactions in nanometric space.

As a future outlook, it should be pointed out that there still remain problems to be solved for gaining a deeper understanding of DPs and exploring more applications. These include: (1) Improving the accuracy of the physical picture of the quasi-particle representing the coupled state of a photon, an electron, and a phonon in a nanometric space. (2) Elucidating the details of energy transfer and dissipation between nanomaterials, mediated by DPs or DPPs. (3) Elucidating the details of phonon-assisted light–matter

interactions in nanometric space. (4) Elucidating the physical origins of autonomy and hierarchy. (5) Developing technical methods based on statistical mechanics, mathematical science, and numerical simulation to analyze and solve problems (1)–(4) above.

A novel optical technology, called light–matter fusion technology in this article, is expected to be established in the future via further studies of DPs, e.g., by investigating the possibility of coupling DPs not only with phonons but also with other types of primary excitations.

4. Summary

This paper has reviewed the framework of classical near-field optics and recent progress in modern near-field optics. After reviewing the wave-optical approach for application to high-resolution microscopy, it was pointed out that a novel theory was required for painting a more precise physical picture of the optical near field. To meet this requirement, the novel physical concept of the dressed photon was described. Applications made possible by this modern picture were reviewed, including optical functional devices, nano-fabrication technologies, energy conversion technologies, and information processing systems. Furthermore, theoretical models based on mathematical science were introduced, and finally, a future outlook of near-field optics was presented.

References

- 1) E. H. Syngé: *Philos. Mag.* **6** (1928) 356.
- 2) E. A. Ash and G. Nicholls: *Nature* **237** (1972) 510.
- 3) H. A. Bethe: *Phys. Rev.* **66** (1944) 163.
- 4) C. J. Bouwkamp: *Philips Res. Rep.* **5** (1950) 401.
- 5) C. Girard and D. Courjon: *Phys. Rev. B* **42** (1990) 9340.
- 6) *Near Field Optics*, ed. D. W. Pohl and D. Courjon (Kluwer, Dordrecht, 1993) pp. 1–324.
- 7) T. Kawazoe, K. Kobayashi, S. Sangu, and M. Ohtsu: *Appl. Phys. Lett.* **82** (2003) 2957.
- 8) V. A. Podolskiy, A. K. Sarychev, and V. M. Shalaev: *Opt. Express* **11** (2003) 735.
- 9) J. J. Sakurai: *Advanced Quantum Mechanics* (Addison-Wesley, Reading, MA, 1967) pp. 20–74.
- 10) K. Kobayashi: *Hyomen Kagaku* **30** (2009) 638 [in Japanese].
- 11) M. Ohtsu: *Dressed Photons* (Springer, Berlin, 2013) pp. 11–36.
- 12) Y. Tanaka and K. Kobayashi: *Physica E* **40** (2007) 297.
- 13) T. Kawazoe, K. Kobayashi, S. Takubo, and M. Ohtsu: *J. Chem. Phys.* **122** (2005) 024715.
- 14) H. Hyuga and H. Ohtsubo: *Nucl. Phys. A* **294** (1978) 348.
- 15) K. Kobayashi and M. Ohtsu: *J. Microsc.* **194** (1999) 249.
- 16) S. Sangu, K. Kobayashi, and M. Ohtsu: *J. Microsc.* **202** (2001) 279.
- 17) S. Sangu, K. Kobayashi, A. Shojiguchi, and M. Ohtsu: *Phys. Rev. B* **69** (2004) 115334.
- 18) W. Nomura, T. Yatsui, T. Kawazoe, and M. Ohtsu: *J. Nanophotonics* **1** (2007) 011591.
- 19) T. Kawazoe, K. Kobayashi, and M. Ohtsu: *Appl. Phys. Lett.* **86** (2005) 103102.
- 20) M. Naruse, H. Hori, K. Kobayashi, T. Kawazoe, and M. Ohtsu: *Appl. Phys. B* **102** (2011) 717.
- 21) T. Kawazoe, M. Ohtsu, S. Aso, Y. Sawado, Y. Hosoda, K. Yoshizawa, K. Akahane, N. Yamamoto, and M. Naruse: *Appl. Phys. B* **103** (2011) 537.
- 22) M. Ohtsu, K. Kobayashi, T. Kawazoe, T. Yatsui, and M. Naruse: *Principles of Nanophotonics* (CRC Press, Boca Raton, FL, 2008) p. 122.
- 23) M. Naruse, P. Holmström, T. Kawazoe, K. Akahane, N. Yamamoto, L. Thylén, and M. Ohtsu: *Appl. Phys. Lett.* **100** (2012) 241102.
- 24) M. Naruse, H. Hori, K. Kobayashi, and M. Ohtsu: *Opt. Lett.* **32** (2007) 1761.
- 25) M. Naruse, F. Peper, K. Akahane, N. Yamamoto, T. Kawazoe, N. Tate, and M. Ohtsu: *ACM J. Emerging Technol. Comput. Syst.* **8** (2012) 1.
- 26) M. Naruse, K. Leibnitz, F. Peper, N. Tate, W. Nomura, T. Kawazoe, M. Murata, and M. Ohtsu: *Nano Commun. Networks* **2** (2011) 189.
- 27) M. M. Alkai, R. J. Blaikie, S. J. McNab, R. Cheung, and D. R. S. Cumming: *Appl. Phys. Lett.* **75** (1999) 3560.
- 28) H. Yonemitsu, T. Kawazoe, K. Kobayashi, and M. Ohtsu: *J. Photolumin.* **122–123** (2007) 230.
- 29) Y. Inao, S. Nakasato, R. Kuroda, and M. Ohtsu: *Microelectron. Eng.* **84** (2007) 705.
- 30) T. Kawazoe, K. Kobayashi, K. Akahane, M. Naruse, N. Yamamoto, and M. Ohtsu: *Appl. Phys. B* **84** (2006) 243.
- 31) T. Kawazoe, T. Takahashi, and M. Ohtsu: *Appl. Phys. B* **98** (2010) 5.
- 32) M. Koike, S. Miyauchi, K. Sano, and T. Imazono: in *Nanophotonics and Nanofabrication*, ed. M. Ohtsu (Wiley-VCH, Weinheim, 2009) p. 179.
- 33) T. Yatsui, K. Hirata, W. Nomura, Y. Tabata, and M. Ohtsu: *Appl. Phys. B* **93** (2008) 55.
- 34) T. Yatsui, K. Hirata, Y. Tabata, W. Nomura, T. Kawazoe, M. Naruse, and M. Ohtsu: *Nanotechnology* **21** (2010) 355303.
- 35) W. Nomura, T. Yatsui, T. Kawazoe, and M. Ohtsu: Ext. Abstr. (59th Spring Meet., 2012); Japan Society of Applied Physics and Related Societies, 17p-B11-14 [in Japanese].
- 36) R. Teki, A. John Kadaksham, M. House, J. Harris-Jones, A. Ma, S. V. Babu, A. Hariprasad, P. Dumas, R. Jenkins, J. Provine, A. Richmann, J. Stowers, S. Meyers, U. Dietze, T. Kusumoto, T. Yatsui, M. Ohtsu, and F. Goodwin: *Proc. SPIE* **8322** (2012) 83220B.
- 37) T. Yatsui, K. Hirata, Y. Tabata, Y. Miyake, Y. Akita, M. Yoshimoto, W. Nomura, T. Kawazoe, M. Naruse, and M. Ohtsu: *Appl. Phys. B* **103** (2011) 527.
- 38) T. Morimoto, K. Hirata, Y. Tabata, W. Nomura, T. Kawazoe, T. Yatsui, and M. Ohtsu: Ext. Abstr. (59th Spring Meet., 2012); Japan Society of Applied Physics and Related Societies, 17p-B11-13 [in Japanese].
- 39) T. Yatsui, W. Nomura, F. Stehlin, O. Soppera, M. Naruse, and M. Ohtsu: *Beilstein J. Nanotechnol.* **4** (2013) 875.
- 40) T. Yatsui, W. Nomura, M. Naruse, and M. Ohtsu: *J. Phys. D* **45** (2012) 475302.
- 41) Y. Hirabayashi: *Proc. SPIE* **8166** (2011) 81663T.
- 42) W. Nomura, T. Yatsui, Y. Yanase, K. Suzuki, M. Fujita, A. Kamata, M. Naruse, and M. Ohtsu: *Appl. Phys. B* **99** (2010) 75.
- 43) T. Kawazoe, H. Fujiwara, K. Kobayashi, and M. Ohtsu: *IEEE J. Sel. Top. Quantum Electron.* **15** (2009) 1380.
- 44) H. Fujiwara, T. Kawazoe, and M. Ohtsu: *Appl. Phys. B* **98** (2010) 283.
- 45) H. Fujiwara, T. Kawazoe, and M. Ohtsu: *Appl. Phys. B* **100** (2010) 85.
- 46) N. Tate, Y. Liu, T. Kawazoe, M. Naruse, T. Yatsui, and M.

- Ohtsu: *Appl. Phys. B* **110** (2013) 293.
- 47) N. Tate, Y. Liu, T. Kawazoe, M. Naruse, T. Yatsui, and M. Ohtsu: *Appl. Phys. B* **110** (2013) 39.
- 48) N. Tate, M. Naruse, Y. Liu, T. Kawazoe, T. Yatsui, and M. Ohtsu: *Appl. Phys. B* **112** (2013) 587.
- 49) S. Yukutake, T. Kawazoe, T. Yatsui, W. Nomura, K. Kitamura, and M. Ohtsu: *Appl. Phys. B* **99** (2010) 415.
- 50) H. Tanaka, T. Kawazoe, and M. Ohtsu: *Appl. Phys. B* **108** (2012) 51.
- 51) T. Kawazoe, M. A. Mueed, and M. Ohtsu: *Appl. Phys. B* **104** (2011) 747.
- 52) M. A. Tran, T. Kawazoe, and M. Ohtsu: *Appl. Phys. A* **115** (2014) 105.
- 53) K. Huang and A. Rhy: *Proc. R. Soc. London, Ser. A* **204** (1950) 406.
- 54) M. Yamaguchi, T. Kawazoe, and M. Ohtsu: *Appl. Phys. A* **115** (2014) 119.
- 55) N. Wada, M. A. Tran, T. Kawazoe, and M. Ohtsu: *Appl. Phys. A* **115** (2014) 113.
- 56) T. Hayashi, T. Kawazoe, and M. Ohtsu: Ext. Abstr. (73rd Autumn Meet., 2012); Japan Society of Applied Physics and Related Societies, 13p-F8-11 [in Japanese].
- 57) T. Kawazoe and M. Ohtsu: *Appl. Phys. A* **115** (2014) 127.
- 58) Q. H. Vo, T. Kawazoe, and M. Ohtsu: Ext. Abstr. (61st Spring Meet., 2014); Japan Society of Applied Physics and Related Societies, 18A-F12-10 [in Japanese].
- 59) T. Kawazoe and M. Ohtsu: Ext. Abstr. (59th Spring Meet., 2012); Japan Society of Applied Physics and Related Societies, 17p-B11-1 [in Japanese].
- 60) N. Wada, T. Kawazoe, and M. Ohtsu: *Appl. Phys. B* **108** (2012) 25.
- 61) T. Kawazoe, M. Ohtsu, K. Akahane, and N. Yamamoto: *Appl. Phys. B* **107** (2012) 659.
- 62) M. Naruse, N. Tate, M. Aono, and M. Ohtsu: in *Nanophotonic Information Physics*, ed. M. Naruse (Springer, Berlin, 2013) p. 1.
- 63) M. Naruse, N. Tate, M. Aono, and M. Ohtsu: *Rep. Prog. Phys.* **76** (2013) 056401.
- 64) C. Pistol, C. Dwyer, and A. R. Lebeck: *IEEE Micro* **28** [6] (2008) 7.
- 65) M. Naruse, M. Aono, and S.-J. Kim: *IEICE Trans. Commun.* **E96-B** (2013) 2724.
- 66) S.-J. Kim, M. Naruse, M. Aono, M. Ohtsu, and M. Hara: *Sci. Rep.* **3** (2013) 2370.
- 67) M. Naruse, M. Aono, S.-J. Kim, T. Kawazoe, W. Nomura, H. Hori, M. Hara, and M. Ohtsu: *Phys. Rev. B* **86** (2012) 125407.
- 68) M. Aono, M. Naruse, S.-J. Kim, M. Wakabayashi, H. Hori, M. Ohtsu, and M. Hara: *Langmuir* **29** (2013) 7557.
- 69) M. Takahashi, N. S. Humam, N. Tsumori, T. Saiki, P. Regreny, and M. Gendry: *Appl. Phys. Lett.* **102** (2013) 093120.
- 70) M. Naruse, N. Tate, and M. Ohtsu: *J. Opt.* **14** (2012) 094002.
- 71) N. Tate, M. Naruse, T. Yatsui, T. Kawazoe, M. Hoga, Y. Ohyagi, T. Fukuyama, M. Kitamura, and M. Ohtsu: *Opt. Express* **18** (2010) 7497.
- 72) N. Tate, H. Sugiyama, M. Naruse, W. Nomura, T. Yatsui, T. Kawazoe, and M. Ohtsu: *Opt. Express* **17** (2009) 11113.
- 73) M. Naruse, N. Tate, Y. Ohyagi, M. Hoga, T. Matsumoto, H. Hori, A. Drezet, S. Huant, and M. Ohtsu: *Opt. Express* **21** (2013) 21857.
- 74) M. Naruse, H. Hori, K. Kobayashi, M. Ishikawa, K. Leibnitz, M. Murata, N. Tate, and M. Ohtsu: *J. Opt. Soc. Am. B* **26** (2009) 1772.
- 75) M. Naruse, T. Yatsui, W. Nomura, T. Kawazoe, M. Aida, and M. Ohtsu: *Appl. Phys. Lett.* **102** (2013) 071603.
- 76) M. Naruse, T. Kawazoe, T. Yatsui, N. Tate, and M. Ohtsu: *Appl. Phys. B* **105** (2011) 185.
- 77) M. Naruse, Y. Liu, W. Nomura, T. Yatsui, M. Aida, L. B. Kish, and M. Ohtsu: *Appl. Phys. Lett.* **100** (2012) 193106.
- 78) T. Iwasa and K. Nobusada: *Phys. Rev. A* **80** (2009) 043409.

ドレスト光子によるバルク結晶シリコン発光素子

大津 元一・川 添 忠

Bulk Crystal Silicon Light Emitting Devices Using Dressed Photons

Motoichi OHTSU and Tadashi KAWAZOE

Physical pictures of dressed photons and dressed-photon-phonons are described. Based on the principle of dressed photon generation, fabrication and operation of light emitting devices using a bulk crystal silicon are reviewed. For fabrication, unique annealing is used by the dressed-photon-phonons. Light emission characteristics of near infrared light emitting diode are presented. Characteristics of visible light emitting diodes, near infrared laser, and related devices are also reviewed.

Key words: dressed photon, phonon, silicon, light emitting diode, laser

シリコン (Si) は古くから電子回路用素子に使われているが、間接遷移型半導体であるため発光効率が低く、発光素子用の材料としては不適當と考えられてきた。しかし最近ではこれを発光素子に使う試みが多くなされている。たとえば可視光領域では多孔質 Si¹⁾、Si と SiO₂ の超格子構造²⁾、SiO₂ 中の Si ナノ凝集粒子³⁾ が用いられ、赤外線領域では Er が添加された Si⁴⁾、Si と Ge の混晶量子構造⁵⁾ が用いられている。これらに対し、従来の電子素子に用いられているバルク結晶 Si の p-n 接合によって高効率の電界発光素子を実現すれば、応用範囲がひろがる。本稿では、ドレスト光子 (dressed photon: DP) の原理に基づきバルク結晶 Si を加工してこのような発光素子を実現する方法について紹介する。

1. ドレスト光子フォノンによる発光

ドレスト光子 (DP) はナノ寸法領域において光子と電子とが結合した状態を表す準粒子である^{6,7)}。なおナノ寸法領域では光の量子化のための共振器を設定することができず、波数と運動量は保存量とはならない。したがって単一周波数、単一モードの光がナノ寸法物質 (ナノ物質) に入射した場合でも、ナノ物質中および表面で生じる光・電子相互作用を記述するためには、無数のモードの光と無数のエネルギー準位の電子を考える必要がある。この相互作

用の結果生じる DP は入射光とは異なり無数の周波数を有し、そのスペクトルは無数の変調側波帯からなる。これらの側波帯が近隣のナノ物質中の電子を励起・脱励起すると新規な光吸収・放出が可能となる。また、DP の発生する系 (ナノ系) は巨視的寸法の光と物質 (巨視系) に囲まれているので、DP を介したナノ物質間の相互作用エネルギーは巨視系により遮蔽され、ナノ物質の寸法程度の有効長をもつ空間特性を示す。すなわち DP の場合は入射光の波長よりずっと小さい寸法で空間的に変調されナノ物質表面に局在するので、従来の光・物質相互作用で用いられてきた長波長近似が破綻し、その結果電気双極子禁制遷移も許容される。DP はさらにコヒーレント状態のフォノンとも結合し、ドレスト光子フォノン (DPP) とよばれる準粒子が発生する。この準粒子はナノ物質中の結晶格子に不純物原子が含まれている場合、そこに局在しやすい⁸⁾。これによりフォノンが関与する新規の励起・脱励起が可能となるので、対象となるナノ物質についてはその中の電子の状態のみでなく、それとフォノンの励起状態との直積で表される状態を考える必要が生じる。

間接遷移型半導体の場合、価電子帯、伝導帯のエネルギー帯の頂点、底における波数ベクトル (運動量) の向きと大きさは互いに異なるので、帯間遷移のためには運動量の異なる電子と正孔とが再結合しなければならない。その

際、運動量の保存則を満たすためには光子のほかに運動量をもつフォノンも同時に放出する必要があるが、電子・正孔対とフォノンの相互作用は小さく、その確率は低い。しかし上記の DPP はフォノンを含むので、伝導帯中の電子とフォノンの相互作用は大きく、間接遷移型半導体でも再結合による自然放出の確率は直接遷移型半導体における確率と同程度まで大きくなる。その結果 DPP が自然放出されるが、その一部は伝搬光に変換されるので発光素子が実現する。

2. 発光素子の自律的な加工

Si のバルク結晶を用いて発光素子を実現するためには DPP を 2 回使う。その 1 つは自然放出光を発生させ発光素子として動作させるためである。もう 1 つは発光素子を作製する際、自然放出に適した不純物濃度の空間分布を自律的に制御するためである。本章では後者について記し、前者の発光特性は次章で紹介する。

n 型 Si 結晶基板を用いて発光ダイオード (LED) を作製する場合を例にとろう。この基板の表面部分に不純物 (ボロン: B) を添加すると、添加部分は p 型になり、p-n ホモ接合が形成される。これに正負の電極用の金属膜を付けるが、そのうち正電極には透明な ITO 膜を用いる。その後順方向電流を注入し、ジュール熱を発生させて結晶基板を加熱しアニールを行う。これにより B は拡散し、その濃度の空間分布が変化する。その際 ITO 膜をとおして外部から光を結晶基板に照射し、B 濃度の空間分布を制御する。この制御に関して光照射の効果は、下記のように入射光の光子エネルギー $h\nu_{\text{anneal}}$ と、Si のバンドギャップエネルギー E_g ($= 1.12 \text{ eV}$: 吸収端波長 $\lambda_c = 1.11 \mu\text{m}$) との大小関係に依存する。

(1) $h\nu_{\text{anneal}} < E_g$ の場合: 照射光は Si に吸収されないため、B が低濃度・均一のため DPP が発生しにくい場所では光照射の効果は表れない。しかし高濃度・不均一の場合では前章で述べたように不純物原子としての B 周囲に DPP が発生し局在しやすいことから、光照射の効果が表れる。すなわち伝導帯中の電子は DPP に含まれるフォノンと運動量を授受し、価電子帯に脱励起する。その結果、入射光に駆動され誘導放出が生じ、伝搬光が発生する。この伝搬光は結晶基板外部に伝搬するので、電流注入により加えられた電気エネルギーの一部は光エネルギーとして外部に散逸する。すなわち、光照射により加熱量は減少し、アニールによる B の拡散は抑制される。ここで $h\nu_{\text{anneal}} < E_g$ であることから上記の脱励起は次の 2 段階からなる。第 1 段階では初期状態 (伝導帯の電子状態とフォノンの熱平衡

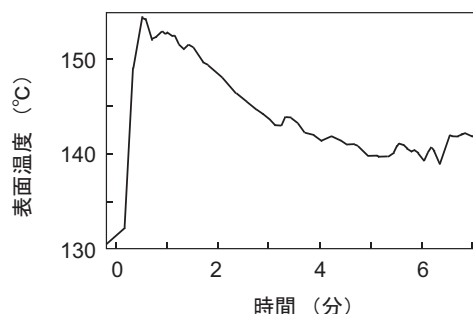


図 1 結晶基板の表面温度の時間変化。

状態との直積で表される状態) から入射光に駆動され、中間状態 (価電子帯の電子状態とフォノンの励起状態との直積で表される状態) に遷移する。これは電気双極子許容遷移なので、その際の誘導放出の結果 DPP とともに伝搬光が発生する。第 2 段階ではこの中間状態から終状態 (価電子帯の電子の基底状態および中間状態より低エネルギーのフォノンの励起状態との直積で表される状態) に遷移する。これは電気双極子禁制遷移なので DPP のみを発生する。その後フォノンは熱平衡状態へ緩和する。上記の第 1 段階で発生した伝搬光のエネルギーが結晶基板外部に散逸する。

(2) $h\nu_{\text{anneal}} > E_g$ の場合: DPP が発生しにくい場所では光吸収が生じ、電子は伝導帯へと励起される。この励起に寄与しない余剰のエネルギー ($h\nu_{\text{anneal}} - E_g$) は熱エネルギーに変わり結晶基板を加熱する。一方、DPP が発生しやすい場所では (1) と同様に誘導放出が生じ、伝搬光が発生する。すなわち光照射により加熱量は減少し、アニールによる B の拡散は抑制される。なお、この場合、 $h\nu_{\text{anneal}} > E_g$ であることから脱励起は 1 段階である。

(1), (2) の場合とも、B 濃度の空間分布に依存した DPP の発生しやすい程度に応じて B の拡散が自律的に制御され、B 濃度の独特の空間分布が形成される。(1), (2) の場合について、光照射により結晶基板温度が減少、増加する様子が測定されている^{9,10)}。(1) の例として、図 1 は光子エネルギー $h\nu_{\text{anneal}}$ の値が 0.95 eV (波長 $1.30 \mu\text{m}$) のレーザー光 (光パワー密度 10 W/cm^2) を照射した場合のアニール開始後の結晶表面温度の時間変化を示す¹¹⁾。表面温度は電流注入による発熱によって急上昇した後、光照射によって下降し一定値に達している。なお、結晶内部の温度は約 300°C 程度と推定されている。アニール前後での結晶内部での B 濃度の空間分布の差異はアトムプローブ法により計測されている¹²⁾。

上記 (1), (2) の過程が進むにつれ、発生した誘導放出光が結晶内部を伝搬するので、上記の過程は光照射領域に

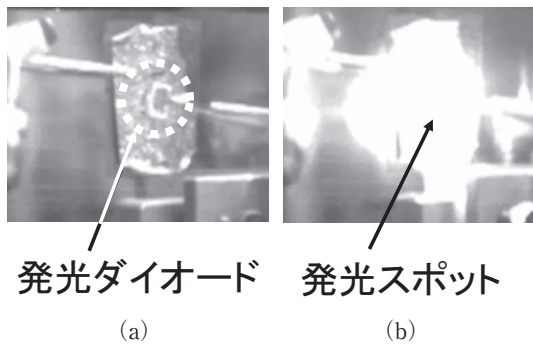


図2 作製されたLEDの外観。(a), (b)はおのおの電流非注入時, 注入時.

とどまらず結晶全体に自律的に広がる. こうして形成された領域境界でのB濃度の空間分布は, LEDとしての動作の際にDPPを効率よく誘起するのに適している. 誘導放出と自然放出の確率は互いに比例するので, DPPの発生しやすい領域では自然放出も起こりやすく, 十分効率の高いLEDが実現する. さらに, このB濃度の空間分布はアニール時の光照射によって形成されることから, 作製されたLEDはこの照射光の光子エネルギー $h\nu_{\text{anneal}}$ に相当する光を発生する. すなわち, 発光波長はアニールのために使用する照射光の光子エネルギーによって制御される.

3. 発光素子の特性

前章(1)の方法により作製された近赤外線LEDのおもな特性を紹介しよう. 図2(a), (b)はおのおの電流非注入時, 電流注入時のLEDの外観を赤外CCDカメラにより撮影した写真である¹¹⁾. 図2(b)の場合の投入電力は11W, 発光パワーは1.1Wに達し, 高輝度発光している. 図3は作製されたデバイスの発光スペクトルである(注入電流密度 1.5 A/cm^2). なお既存の方法で作製された市販のSiフォトダイオード(浜松ホトニクス製S3590)もわずかに発光するので, 参考のためにその発光スペクトルを曲線Aに示す(注入電流密度 0.2 A/cm^2). 曲線Aでは発光スペクトルが E_g より高エネルギー側に分布している¹³⁾. これはSi中のフォノン散乱による間接遷移の結果生じる微弱な発光である. 一方, 曲線B~Dは前章(1)に従いおのおの1分間, 7分間, 30分間のアニールにより作製されたLEDの発光スペクトルである. これらの形は曲線Aとは大きく異なっており, 発光スペクトルは E_g 以下の低エネルギー側に広がっている. 0.8 eV 以下での発光強度の減少は光検出器の感度限界に起因しており, 実際の発光スペクトルはさらに低エネルギー領域にも広がっている. これらのうち曲線Dでは, E_g の位置に明瞭な発光ピークは存在せず, 加工の際に照射した光の光子エネルギー $h\nu_{\text{anneal}}$ (=

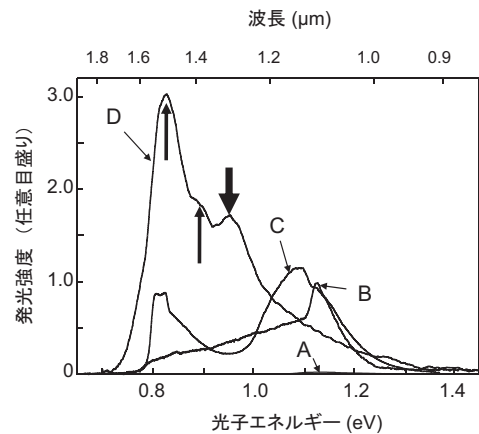


図3 発光スペクトル. 曲線Aは市販のSiフォトダイオード. 曲線B, C, Dはアニール時間がおのおの1分, 7分, 30分の場合. 下向き矢印はアニールの際に照射した光の光子エネルギー $h\nu_{\text{anneal}}$ の値を示す. 2つの上向き矢印はフォノンの寄与を示す.

0.95 eV , 波長 $1.30 \mu\text{m}$)に相当する領域にピーク(下向き矢印)が現れており, これは照射光によってB濃度の空間分布が制御されたことを意味する. なお, 2つの上向き矢印の位置 (0.83 eV , 0.89 eV) および下向き矢印の位置の間隔はおのおの 0.06 eV であり, これはSiの光学フォノンのエネルギーと一致している. すなわち 0.95 eV のエネルギーをもつDPPが1個の光学フォノンを放出し通常的光子になる過程, および2個の光学フォノンを放出して光子になる過程におのおの対応している. これらの過程は, ここで議論している発光が前章(1)のようにフォノンのエネルギー準位を中間状態として使われることを証明している.

フォノンに起因する発光スペクトルの特性とシミュレーションとの比較から, 電子正孔対とフォノンとの結合の大きさを表すHuang-Rhys因子¹⁴⁾は 4.08 ± 0.02 と推定されている¹⁵⁾. これは通常のSiバルク結晶の値に比べ $10^2 \sim 10^3$ 倍大きく, 本LEDの発光がDPPに起因することを示している. また, コヒーレント状態の縦モード光学フォノンがDPと結合しDPPを形成していることが, ポンププローブ分光により確認されている¹⁶⁾.

30分間のアニールで作製されたLEDからの発光のうち光子エネルギー $h\nu = 0.73 \text{ eV}$ (波長 $1.70 \mu\text{m}$) 以上での発光成分に関し, 外部電力変換効率 1.3% , 微分外部電力変換効率 5.0% であった(注入電力 11 W のとき). また電流密度 I_d と発光パワー密度 P_d の関係は二次式 $P_d = 0.04I_d^2$ で表された. これは前章(1)のように自然放出が2段階の過程によることに起因する¹¹⁾.

図4にはこれまでに作製された近赤外線LEDの外部量子効率の向上の様子を示す. 産学連携による技術開発の結

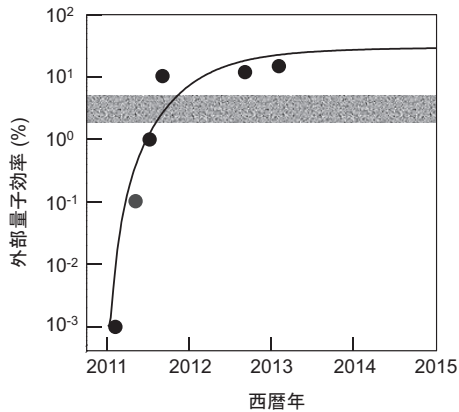


図4 近赤外線のLEDの外部量子効率の値の増加の様子。実線の曲線はロジスティック曲線を表す。網掛け部分は実用化されているInGaAs製の波長1.3 μm のLEDの値を示す。

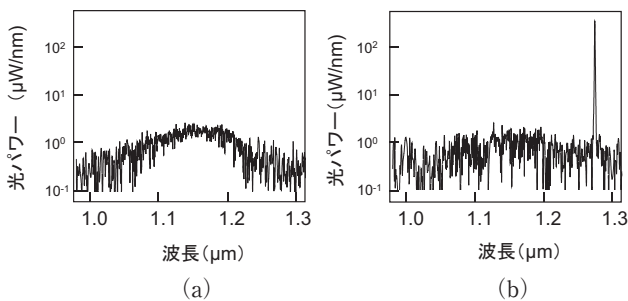


図5 レーザーの発振スペクトル。(a) 発振閾値以下、(b) 発振閾値以上。

果、2013年2月の段階で15%に達しており、この値はInGaAs(直接遷移型半導体)を用いて実用化されている波長1.3 μm のLEDの値(2%~5%, たとえば浜松ホトニクス製L7866, L10822)より大きい。図中の実線は個体群成長、技術の進歩、商品の販売数の変化などを表すのに使われているロジスティクス曲線であり、これは黒丸に示す数値にあてはめたものである。両者は互いによく合っており、技術が本従来の技術開発と同様の進展をしていることがわかる。

以上のほか、Siのバルク結晶を用いて赤・緑・青色の可視光を発生するLED¹⁰⁾が作製されている。さらに、Siと同様の間接遷移型半導体のGaPを用いて黄・緑色の可視光を発生するLED¹⁷⁾, SiCを用いて青~紫色¹⁸⁾, 紫外¹⁹⁾, さらには白色²⁰⁾を発生するLEDが作製されている。加えて関連する発光素子としてSiを用いたLEDによる光・電気弛張発振器²¹⁾, 光増幅機能を有する近赤外線のSiフォトダイオードなどが作製されている²²⁾。

最後に、前章と同様の方法で作製された近赤外線レーザー²³⁾を紹介しよう。これは長さ500 μm のリッジ導波路を有するファブリー・ペロー共振器型構造を有し、その発

振閾値電流密度は1.1 kA/cm^2 である。図5(a), (b)はおのの閾値以下、閾値以上の発振スペクトルであり、後者の鋭い発振スペクトルから発振波長が1.27 μm であることがわかる。

ドレスト光子の原理にもとづき、間接遷移型半導体であるSiのバルク結晶によりLED, レーザーなどの発光素子を実現した。この技術は関連する他の材料にも展開され、それらの発光波長は近赤外線~可視域全体をカバーしつつある。今後の技術開発とともに、新しい応用の発展が期待される。

本研究の一部は文部科学省科学研究費助成金(B)(課題番号24360023)「ドレスト光子フォノンによる間接遷移型半導体の電流注入発光とその波長制御」によった。

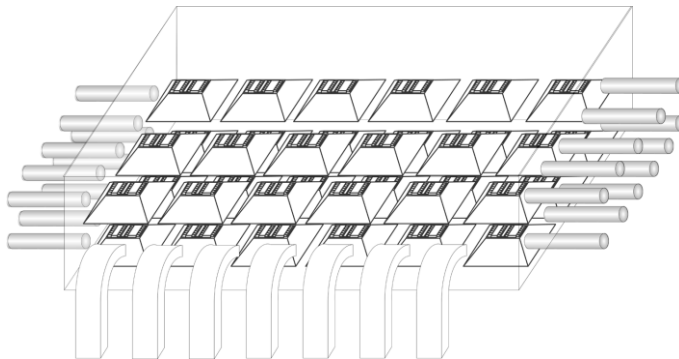
文 献

- 1) K. D. Hirschman, L. Tysbekov, S. P. Duttagupta and P. M. Fauchet: "Silicon-based visible light-emitting devices integrated into microelectronic circuits," *Nature*, **384** (1996) 338-341.
- 2) Z. H. Lu, D. J. Lockwood and J.-M. Baribeau: "Quantum confinement and light emission in SiO_2/Si superlattices," *Nature*, **378** (1995) 258-260.
- 3) T. Komoda, J. Kelly, E. Cristiano, A. Nejim, P. L. F. Hemment, K. P. Homewood, R. Gwilliam, J. E. Mynard and B. J. Sealy: "Visible photoluminescence at room temperature from microcrystalline silicon precipitates in SiO_2 formed by ion implantation," *Nucl. Instrum. Methods Phys. Res., Sect. B*, **96** (1995) 387-391.
- 4) S. Yerci, R. Li and L. Dal Negro: "Electroluminescence from Er-doped Si-rich silicon nitride light emitting diodes," *Appl. Phys. Lett.*, **97** (2010) 081109.
- 5) S. K. Ray, S. Das, R. K. Singha, S. Manna and A. Dhar: "Structural and optical properties of germanium nanostructures on Si (100) and embedded in high-k oxides," *Nanoscale Res. Lett.*, **6** (2011) 224-233.
- 6) 大津元一: ドレスト光子(朝倉書店, 2013) pp. 10-32.
- 7) M. Ohtsu: *Dressed Photons* (Springer, Berlin, 2013) pp. 11-36.
- 8) Y. Tanaka and K. Kobayashi: "Optical near field dressed by localized and coherent phonons," *J. Microscopy*, **229** (2008) 228-232.
- 9) K. Kitamura, T. Kawazoe and M. Ohtsu: "Homojunction-structured ZnO light-emitting diodes fabricated by dressed-photon assisted annealing," *Appl. Phys. B*, **107** (2012) 293-299.
- 10) M.-A. Tran, T. Kawazoe and M. Ohtsu: "Fabrication of a bulk silicon p-n homojunction-structured light-emitting diode showing visible electroluminescence at room temperature," *Appl. Phys. A*, **115** (2013) 105-111.
- 11) T. Kawazoe, M. A. Mueed and M. Ohtsu: "Highly efficient and broadband Si homojunction structured near-infrared light emitting diodes based on the phonon-assisted optical near-field process," *Appl. Phys. B*, **104** (2011) 747-754.
- 12) 和田直樹, 水島彩子, 川添 忠, 大津元一: "ELスペクトルの評価によるホモ接合Si-LED内のフォノンと電子正孔対との結合制御と評価", 第61回応用物理学学会春季学術講演会予稿集(2014) 18a-F12-7.
- 13) R. A. Milano, P. D. Dapkus and G. E. Stillman: "An analysis of the performance of heterojunction phototransistors for fiber

- optic communications,” IEEE Tran. Electron Devices, **29** (1982) 266-274.
- 14) K. Huang and A. Rhys: “Theory of light absorption and non-radiative transitions in *F*-centres,” Proc. R. Soc. London, Ser. A, **204** (1950) 406-423.
 - 15) M. Yamaguchi, T. Kawazoe and M. Ohtsu: “Evaluating the coupling strength of electron-hole pairs and phonons in a 0.9 μm -wavelength silicon light emitting diode using dressed-photon-phonons,” Appl. Phys. A, **115** (2013) 119-125.
 - 16) N. Wada, M.-A. Tran, T. Kawazoe and M. Ohtsu: “Measurement of multimode coherent phonons in nanometric spaces in a homojunction-structured silicon light emitting diode,” Appl. Phys. A, **115** (2013) 113-118.
 - 17) 林 拓朗, 川添 忠, 大津元一: “ホモ接合 GaP の高エネルギー準位からの EL 発光”, 第 73 回応用物理学会秋季学術講演会予稿集 (2012) 13p-F8-11.
 - 18) T. Kawazoe and M. Ohtsu: “Bulk crystal SiC blue LED with p-n homojunction structure fabricated by dressed-photon-phonon-assisted annealing,” Appl. Phys. A, **115** (2013) 127-133.
 - 19) Q. H. Vo, 川添 忠, 大津元一: “二光源によるドレスト光子フォノン援用アニール法を用いた SiC-LED の作製”, 第 61 回応用物理学会春季学術講演会予稿集 (2014) 18a-F12-10.
 - 20) 川添 忠, 大津元一: “ドレスト光子を利用したホモ接合 Si-LED の作製および動作原理と検証実験”, 第 59 回応用物理学会関連連合講演会予稿集 (2012) 17p-B11-1.
 - 21) N. Wada, T. Kawazoe and M. Ohtsu: “An optical and electrical relaxation oscillator using a Si homojunction structured light emitting diode,” Appl. Phys. B, **108** (2012) 25-29.
 - 22) H. Tanaka, T. Kawazoe and M. Ohtsu: “Increasing Si photo-detector photosensitivity in near-infrared region and manifestation of optical amplification by dressed photons,” Appl. Phys. B, **108** (2012) 51-56.
 - 23) T. Kawazoe, M. Ohtsu, K. Akahane and N. Yamamoto: “Si homo-junction structured near-infrared laser based on a phonon-assisted process,” Appl. Phys. B, **107** (2012) 659-663.

(2014 年 2 月 15 日受理)

[IV] PUBLISHED BOOKS



|イラストレイテッド|
光の科学

|大津元一 [監修]

|田所利康・石川 謙 [著]|

朝倉書店

目次

第1章 波としての光の性質	1
身の周りの光 2	波の重ね合わせ 14
光は電磁波 6	偏った光 / 自然の光 18
進む光の表し方 10	
第2章 ガラスの中で光は何をしているのか	23
光と電子はダンスを踊る 24	空の青、雲の白、夕焼けの赤 36
加速電子は光を放出する 28	周波数で変わる光の伝搬速度 40
重ね合わせが決める波の進み方 32	
第3章 光の振る舞いを調べる	45
多数決で進む光 46	強め合う光 / 弱め合う光 62
向きを変える光 50	回り込む光 66
遅くなる光 54	閉じ込めると広がる光 70
完全に反射する光 58	
第4章 なぜヒマワリは黄色く見えるのか	75
眼が感じる色彩 76	虹の不思議 92
色を重ねる 80	周期構造が色を作る 96
吸収が決める物の色 84	「色彩」は自然に学べ 100
光源で変わる色の見え方 88	偏った光が色彩を生む 104
キーワード解説	109
あとがき	114
索引	116

コラム

スペクトルを測定する 22
透けて見える LCD 22
半月の偏光写真 44
球状シリカ微粒子の多様な色彩 44
曲がる光の実験 74
セロハンテープのステンドグラスを作ろう 108
光の一方通行路 108